Journal of Turbomachinery

Published Quarterly by ASME

VOLUME 129 • NUMBER 3 • JULY 2007

TECHNICAL PAPERS

(Contents continued on inside back cover)

Editor, **DAVID C. WISLER (2008)**
Assistant to the Editor: **ELIZABETH WISLER**
Associate Editors
Gas Turbine (Review Chair)
K. MILLSAPS, JR. (2007)
Aeromechanics
M. MONTGOMERY (2008)
A. SINHA (2008)
Boundary Layers and Turbulence
G. WALKER (2008)
Computational Fluid Dynamics
J. ADAMCZYK (2008)
M. CASEY (2008)
Experimental Methods
W.-F. NG (2008)
Heat Transfer
R. BUNKER (2009)
J.-C. HAN (2008)
K. A. THOLE (2007)
Radial Turbomachinery
R. VAN DEN BRAEMBUSSCHE (2008)
Turbomachinery Aero
S. GALLIMORE (2008)
D. PRASAD (2008)
A. R. WADIA (2009)

PUBLICATIONS COMMITTEE
Chair, **BAHRAM RAVANI**

OFFICERS OF THE ASME
President, **SAM Y. ZAMRIK**
Executive Director, **VIRGIL R. CARTER**
Treasurer, **T. PESTORIUS**

PUBLISHING STAFF
Managing Director, Publishing
PHILIP DI VIETRO
Manager, Journals
COLIN MCATEER
Production Coordinator
JUDITH SIERANT
Production Assistant
MARISOL ANDINO

Transactions of the ASME, Journal of Turbomachinery (ISSN 0889-504X) is published quarterly (Jan., Apr., July, Oct.) by The American Society of Mechanical Engineers, Three Park Avenue, New York, NY 10016. Periodicals postage paid at New York, NY and additional mailing offices. POSTMASTER: Send address changes to Transactions of the ASME, Journal of Turbomachinery, c/o THE AMERICAN SOCIETY OF MECHANICAL ENGINEERS, 22 Law Drive, Box 2300, Fairfield, NJ 07007-2300. **CHANGES OF ADDRESS** must be received at Society headquarters seven weeks before they are to be effective. Please send old label and new address.

STATEMENT from By-Laws. The Society shall not be responsible for statements or opinions advanced in papers or ... printed in its publications (B7.1, Par. 3).

COPYRIGHT © 2007 by the American Society of Mechanical Engineers. For authorization to photocopy material for internal or personal use under those circumstances not falling within the fair use provisions of the Copyright Act, contact the Copyright Clearance Center (CCC), 222 Rosewood Drive, Danvers, MA 01923, tel: 978-750-8400, www.copyright.com. Request for special permission or bulk copying should be addressed to Reprints/Permission Department.

Canadian Goods & Services Tax Registration #126148048

This journal is printed on acid-free paper, which exceeds the ANSI Z39.48-1992 specification for permanence of paper and library materials. ♾™
♲ 85% recycled content, including 10% post-consumer fibers.

Downloaded 31 May 2010 to 128.113.26.88. Redistribution subject to ASME license or copyright; see http://www.asme.org/terms/Terms_Use.cfm

(**Contents continued**)

Journal of Turbomachinery **Volume 129, Number 3** **JULY 2007**

The ASME Journal of Turbomachinery is abstracted and indexed in the following:

Aluminum Industry Abstracts, Aquatic Science and Fisheries Abstracts, Ceramics Abstracts, Chemical Abstracts, Civil Engineering Abstracts, Compendex (The electronic equivalent of Engineering Index), Corrosion Abstracts, Current Contents, Ei EncompassLit, Electronics & Communications Abstracts, Energy Information Abstracts, Engineered Materials Abstracts, Engineering Index, Environmental Science and Pollution Management, Excerpta Medica, Fluidex, Fuel and Energy Abstracts, INSPEC, Index to Scientific Reviews, Materials Science Citation Index, Mechanical & Transportation Engineering Abstracts, Mechanical Engineering Abstracts, METADEX (The electronic equivalent of Metals Abstracts and Alloys Index), Metals Abstracts, Oceanic Abstracts, Pollution Abstracts, Referativnyi Zhurnal, Shock & Vibration Digest, Steels Alert

Development of a One-Dimensional Modular Dynamic Model for the Simulation of Surge in Compression Systems

M. Morini

M. Pinelli

M. Venturini
e-mail: mauro.venturini@unife.it

Engineering Department in Ferrara (ENDIF),
University of Ferrara,
Via Saragat 1,
44100 Ferrara, Italy

The paper deals with the development of a nonlinear one-dimensional modular dynamic model for the simulation of transient behavior of compression systems. The model is based on balance equations of mass, momentum, and energy, which are derived through a general approach and are written by using the finite difference method. The model also takes rotating mass dynamics into account through a lumped parameter approach. Moreover, it reproduces the behavior of the system in the presence of the surge phenomenon through steady-state performance maps, which represent the compressor operation in the inverse flow region by means of a third degree polynomial curve. The model is implemented through the Matlab Simulink tool, where the system of ordinary differential equations is solved by using a fourth- and fifth-order Runge–Kutta method. A sensitivity analysis is carried out to evaluate the influence on compressor outlet pressure oscillations of the model parameters, of the supplied torque, of ambient conditions and of the shape of the compressor characteristic curves. The results show that the model proves effective in capturing the physical essence of surge phenomenon without being computationally too heavy. [DOI: 10.1115/1.2447757]

Introduction

Models for the simulation of turbomachinery transient behavior are employed both for the design of new machines and for the analysis of those which are already in operation. These models are also used as signal generators for the study and the enhancement of control systems (rapid prototyping), these latter applications being focused in particular on the simulation of compressor instabilities such as rotating stall and surge. In fact, an experimental campaign can be expensive, mainly for large-size machines and, in any case, these phenomena are difficult to capture experimentally. Thus, the availability of well-tuned numerical models can allow a better understanding of the physics of the phenomena and of their influence on machine behavior. Moreover, they can help in simulating the behavior of gas turbines fed by low calorific value fuels, since gas turbines are usually designed for natural gas. In fact, in this case, the use of a low heating content gas leads to larger mass flow rates and so to an increased compressor ratio, which finally implies a rise in surge risk.

Two of the most successful models for simulating compressor instabilities are the Greitzer model [1] and the Moore and Greitzer (MG) model [2], which have been widely adopted by many authors in the literature both to study compressor instabilities and to set up devices to avoid compressor operation beyond the surge line.

Concerning compressor instabilities, in Ref. [3] the MG model has been applied to study surge effects on a turbocharger compressor and in Ref. [4] a control-theoretic form of MG model and a Liapounov stability analysis of rotating stall and surge were presented. The MG model was also adopted to perform bifurcational analyses (see for instance Refs. [5–7]). A nonlinear control law for active stall/surge controllers was derived in Ref. [8]. In Ref. [9] higher order Galerkin expansion of the MG model was investigated.

A great number of papers have also been published to address the problem of developing compressor control devices, for which the MG model was widely used. In Ref. [10] the use of pulsed air injection to control rotating stall in low speed axial flow compressors was presented and jet injection with a high order Galerkin method was studied in Ref. [11]. In Ref. [12], a close coupled valve for surge and rotating stall control was presented. In Refs. [13] and [14], a control device based on the aeroelastic coupling of the basic compression system with a hydraulic oscillator was illustrated. In Ref. [15], the MG model was applied to a system in which wet compression was used for active control of compression system instabilities.

Other successful models, which allow the simulation of compressor instabilities and mainly used for aeronautic applications, are the dynamic turbine engine compressor code model (DYNTECC) [16] and the aerodynamic turbine engine code, (ATEC) model which extended the DYNTECC model to consider the whole gas turbine [17,18]. In particular, the DYNTECC model was applied to study axial–centrifugal compressors off-design behavior [19,20].

Many other models can be found in literature. For instance, interesting models, which simulate the transient behavior of turbocharger compressors in diesel engines, and also the compressor surging and its emergency shutdown, are developed in Refs. [21–23]. In Ref. [24], a model was applied to a closed loop Brayton Cycle. Effects of surge on a hybrid system (Solid Oxide Fuel Cell and Gas Turbine) were also studied in Refs. [25,26].

Another important field where dynamic models have been used is the simulation of compression stations. For these applications, the effect of the surge onset can result in deterioration, damage and forced stops, which in turn can result in significant economic losses. A recent qualitative evaluation based on proprietary field data allowed the estimation of costs due to a forced stop of about 10 euro/h for each installed kW.

In Ref. [27], a model was developed and applied to three test

---

Contributed by the International Gas Turbine Institute of ASME for publication in the Journal of Turbomachinery. Manuscript received June 6, 2006; final manuscript received June 26, 2006. Review conducted by David Wisler. Paper presented at the ASME Turbo Expo 2006: Land, Sea and Air (GT2006), Barcelona, Spain, May 8–11, 2006. Paper No. GT2006-90134.

cases: a compressor surge protection control, a compressor startup for a single unit compressor station and a compressor station set point change for a compressor station composed of two compressors in series. In Ref. [28] the compressor deceleration during shutdown and the effects of recycle coolers on compressor surge were studied for a single unit compression station. Transient phenomena associated with gas recycling during compressor emergency shutdown have been studied both experimentally and numerically in Ref. [29]. A similar study was carried out in Refs. [30,31] on a compressor station composed of five multistage centrifugal compressors in parallel. In Ref. [32] a study was focused on the evaluation of the best arrangement in a two unit compressor station.

In this paper, a model for the simulation of the dynamic behavior of compression systems is developed. Mass, momentum, and energy balance equations and the spool momentum balance are written through a general approach. The model is implemented through the Matlab Simulink tool by using a finite difference method and the ordinary differential equation system is solved through the Runge–Kutta method. Compressor behavior is simulated through steady-state maps both for normal and unstable operating regions. The model response to surge (in terms of the oscillations of pressure at the outlet section of the compressor) is studied through a sensitivity analysis, by varying geometrical parameters and driving torque.

The main feature of the model is that it can be adopted for different geometrical configurations since the approach used for deriving model equations is general.

Moreover, the model is built as a tool which allows the study of the influence of external disturbances (e.g., boundary conditions) and takes into account the compressor outlet temperature through compressor efficiency characteristic curves. In fact, the presence of compressor outlet temperature is not always taken into account in literature. Models developed for applications in the aeronautic field, as for example DYNTECC [16–20], actually consider such a variable, since instabilities could occur on military aircraft due to the temperature increase as a result of the use of armaments. On the other hand, models derived from the Greitzer model [[1,2,33]], which are mainly oriented to industrial applications, do not consider this variable.

In addition to this, the model can be used to carry out diagnostic analyses, since it may allow the identification of malfunctions which can be detected during transient regimes by adapting compressor performance maps.

Finally, since the model is developed so that it requires a low computational effort, it may also be used for on-line applications. Thus, the model developed may be a useful tool for analyzing the behavior of compression systems under unsteady conditions, with particular reference to the simulation of operating points close or even beyond the surge line.

Overview of Compressor Instabilities

Compressor Instabilities. Many studies on compressor instabilities have been carried out since Emmons proposed an explanation of rotating stall phenomenon in 1955 [34]. Some of these studies are focused on modeling instabilities [1,2,4,5,11,33,35], while others are focused on experimental investigation of them [3,23,36–43].

Compressor unstable behavior is one of the major limiting factors of the entire gas turbine operating range, performance, and reliability. As reported in Ref. [44], Dean proposed a criterion which allows the definition of the onset of instabilities as the zero-slope point in the characteristic curve (surge point). The line connecting all the points at various rotating speeds is known as the surge line. As a general rule of thumb the instabilities, either in the form of both rotating stall and surge, occur at operating points with a low mass flow rate and high pressure ratio, where the compressor usually reaches high efficiency values.

Rotating stall is a bidimensional phenomenon [44] characterized by a distribution of the mass flow which is not axisymmetric, so that there are regions (known as cells) with lower mass flow rate which rotate at a speed equal to 40–70% of the compressor rotating speed [45]. Two different kinds of stall can be identified: progressive and abrupt. Progressive stall causes a small performance loss and its presence is indicated by a characteristic noise measurable through high frequency instruments. Abrupt stall is characterized by high performance losses, which are usually modeled as if the operating point abruptly passes from the surge point to a new performance characteristic curve called "stalled characteristic curve."

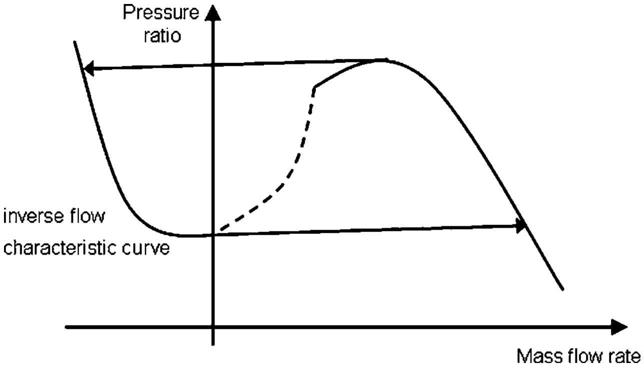

Fig. 1 Deep surge modeling through static performance maps with inverse flow

Surge is a one-dimensional phenomenon [44] that causes a variation in time of the mass flow rate. Different kinds of surge can be identified with respect to the amplitude and the frequency of the oscillations of the mass flow rate and of the pressure ratio [45]:

- Mild surge is characterized by the absence of mass flow inversion and small amplitude pulsation of the pressure ratio.
- Classic surge is characterized by the absence of mass flow inversion and pulsation of the pressure ratio with higher amplitude and lower frequency than the oscillation which characterizes the mild surge.
- Modified surge is a mix of rotating stall and classic surge (i.e., the flow is not axisymmetric).
- Deep surge, characterized by the inversion of the mass flow, is more severe than classic surge but the flow is axisymmetric, so that the operating point passes suddenly from the surge point to a branch of the compressor characteristic curve called "inverse flow characteristic curve" as represented in Fig. 1.

Surge and stall were originally treated separately, but they are now recognized as being coupled oscillation modes of the compression system: in fact, surge can be represented by a zeroth order or planar oscillation mode, while rotating stall is the limit cycle resulting from higher-order rotating-wave disturbances [4].

Both phenomena can lead to severe damage to the compression system because they cause an increase in the temperature of blades and an off-design distribution of stresses (e.g., due to shock waves associated to deep surge or to the not axisymmetric distribution of the flow in the rotating stall). For these reasons, different strategies to avoid compressor operation beyond the surge line have been developed [10,12,14,15,42,45–47].

In order to set up these strategies, many models for the simulation of stable and unstable behavior of compression systems have been developed in the literature.

Models for the Simulation of Surge and Stall in Compression Systems. Models for the simulation of surge and stall presented in the literature can be grouped depending on the dimension of the model.

One-dimensional models can correctly simulate surge, but not rotating stall, because stall is a bidimensional phenomenon. They are employed for compressors in which stability is recoverable after rotating stall has occurred, as is the case of centrifugal compressors [4].

The most famous model is Greitzer model [1]. This model is a nonlinear dynamic model of an axial compressor which was extended by Hansen et al. [48] to centrifugal compressors. The model is based on nondimensional mass and momentum balance equations and it represents surge through an oscillating pressure rise and stall through a loss in pressure rise.

Another important one-dimensional model is DYNTECC [16] developed by the Arnold Engineering Development Center (AEDC). DYNTECC is an one-dimensional stage-by-stage dynamic model for the simulation of axial compressors. This model is based on energy, momentum, and mass balance written by using the finite differences method for a series of elementary control volumes.

Bidimensional models were developed because many studies have emphasized that rotating stall is a precursor of surge [3,10,44]. In fact, an evolution of the Greitzer model was presented by Moore and Greitzer [2], where stall is described by a parameter obtained by applying a Galerkin procedure over the partial differential equation system composed by nondimensional balance equations for mass, momentum, and annulus-averaged momentum. Gravdahl and Egeland [33] completed the Moore and Greitzer model by adding the spool dynamics.

Three-dimensional models are based on computational fluid dynamics. Until recent years, the weak dependence of surge and stall on viscosity, the high computational power required, and the difficulties in obtaining data for code validation had limited the use of such tools to study surge and stall [49].

Model Development

General Balance Equation. The development of the mathematical model to determine the laws of conservation (mass, momentum, and energy) is carried out starting from a general approach.

The main features which characterize the model developed in the current paper are:

- this model is based on formulas for each material point, differently from other models in the literature which are based on integral formulas [50]. The procedure for deriving the balance equation for the generic quantity ψ (scalar or vector) is reported in Appendix A.1.
- use of finite difference method instead of a lumped parameter method. This allows the one-dimensional discretization of the problem. For instance, one or more elements may be adopted to represent each single component.
- modularity, so that every system configuration can be represented by means of basic components (valve, duct, compressor).
- use of dimensional quantities, which allows an easy-to-read analysis of the results, both in terms of physical interpretation and of practical quantification.

For any material point, Eq. (1) represents the balance equation for a general scalar intensive property and Eq. (2) is the balance equation for a general vectorial intensive property

$$\frac{\partial \psi}{\partial t} + \nabla \cdot (\psi \boldsymbol{\nu}) = -\nabla \cdot \boldsymbol{\varphi} + \rho r \tag{1}$$

$$\frac{\partial \boldsymbol{\psi}}{\partial t} + \nabla \cdot (\boldsymbol{\nu}^T \boldsymbol{\psi}) = \nabla \cdot \boldsymbol{\Phi} + \rho \mathbf{r} \tag{2}$$

Continuity Equation for Fluids. In this case, the scalar property is the density distribution $\rho = \rho(\mathbf{x}, t)$.

By assuming the validity of the conservation of mass principle the source term is null. Moreover, any configuration S_t is composed of the same points (independent of time t), so the flux term is null too.

For a one-dimensional system, density is a function of the curvilinear coordinate x and time and Eq. (1), is reduced to

$$\frac{\partial \rho}{\partial t} + \frac{\partial \rho v}{\partial x} = 0 \tag{3}$$

Moreover, by considering the gas as perfect, the equation of state is $p/\rho = RT$ and for a reversible adiabatic transformation $p/\rho^k = \text{const}$. So, Eq. (3) can be written as

$$\frac{\partial p}{\partial t} = -kRT\frac{\partial \rho v}{\partial x} \tag{4}$$

Let us consider a duct whose length is L and whose area is $A(x)$ and which is normal to the curvilinear abscissa x. Fluid properties can be assumed constant on each section and only variable on the curvilinear abscissa.

By denoting with the subscripts "i" and "f" the initial and final sections of the L length duct respectively, Eq. (4) can be written for these two sections as

$$\frac{\partial p_{i,f}}{\partial t} = -kRT_{i,f}\left(\frac{\partial \rho v}{\partial x}\right)_{i,f} \tag{5}$$

The Taylor series with Peano remainder of the function $\rho\nu$ can be expressed as

$$(\rho v)_f = (\rho v)_i + \left(\frac{\partial \rho v}{\partial x}\right)_i \cdot L + o(|L|) \tag{6a}$$

$$(\rho v)_i = (\rho v)_f + \left(\frac{\partial \rho v}{\partial x}\right)_f \cdot (-L) + o(|L|) \tag{6b}$$

By neglecting the remainders, Eq. (5) can be combined with Eqs. (6a) and (6b), and then it is possible to obtain

$$\frac{\partial p_{i,f}}{\partial t} = \frac{kRT_{i,f}}{A_i A_f} \cdot \frac{A_f w_i - A_i w_f}{L} \tag{7}$$

Momentum Balance for Fluids. In this case the vectorial property is the momentum $\rho(\mathbf{x}, t)\mathbf{v}(\mathbf{x}, t)$.

By noting that for a nonviscous fluid the stress tensor, which corresponds to $\boldsymbol{\Phi}$, is equal to $-p\mathbf{I}$ [51] and the source term $\boldsymbol{r}$ is equal to the vectorial sum of forces per unit mass working on the fluid, Eq. (2) can be reformulated as

$$\frac{\partial \rho v}{\partial t} + \nabla \cdot (\rho \mathbf{v}^T \mathbf{v}) = -\nabla \cdot p\mathbf{I} + \rho \sum \boldsymbol{f} \tag{8}$$

By considering a one-dimensional system, as made in the previous paragraph, Eq. (8) can be put in the form

$$\frac{\partial \rho v}{\partial t} + \frac{\partial \rho v^2}{\partial x} = -\frac{\partial p}{\partial x} + \rho \sum f \tag{9}$$

The friction force f_f and the gravitational force f_g per unit mass can be expressed as [50]

$$f_f = -\frac{\lambda}{D_h}\frac{\nu^2}{2} \tag{10}$$

$$f_g = g\frac{\partial x_g}{\partial x} \tag{11}$$

If the fluid is a gas, the gravitational term can be neglected. So, Eq. (9) can be written as

$$\frac{\partial \rho v}{\partial t} = -\frac{\partial p}{\partial x} - \frac{\partial \rho v^2}{\partial x} - \rho \frac{\lambda}{D_h} \frac{v^2}{2} \tag{12}$$

Let us assume that the kinetic energy of the fluid and its variation can both be neglected, and so Eq. (12) can be simplified to

$$\frac{\partial \rho v}{\partial t} = -\frac{\partial p}{\partial x} - \rho \frac{\lambda}{D_h} \frac{v^2}{2} \tag{13}$$

Equation (13) can be written for the initial and final section as

$$\frac{\partial (\rho v)_{i,f}}{\partial t} = \left(-\frac{\partial p}{\partial x}\right)_{i,f} - \rho_{i,f} \frac{\lambda_{i,f}}{D_{hi,f}} \frac{v_{i,f}^2}{2} \tag{14}$$

By proceeding as in the previous paragraph, the pressure for the initial and final section can be expressed through the Taylor series with Peano remainder retained up to the first order. By neglecting the remainders, and by using the perfect gas equation of state, the equation of momentum balance can be written as

$$\frac{\partial w_{i,f}}{\partial t} = -\frac{A_{i,f}}{L}(p_f - p_i) - \frac{\lambda_{i,f}}{D_{hi,f}} \frac{RT_{i,f}}{A_{i,f} p_{i,f}} \frac{w_{i,f}^2}{2} \tag{15}$$

Momentum Balance for Rotating Masses (Spool Dynamics). Let us consider a solid cylinder (length L and radius R) rotating around its axis with angular velocity ω.

By assuming pressure and shear stresses on the boundary surface to be negligible and by using cylindrical coordinates (r, θ, z), it is possible to write

$$v_\theta = \omega r \quad \forall\, P \in \Omega \tag{16a}$$

$$v_r = 0 \quad \forall\, P \in \Omega \tag{16b}$$

$$v_z = 0 \quad \forall\, P \in \Omega \tag{16c}$$

$$\mathbf{\Phi} = \mathbf{0} \quad \forall\, P \in \partial\Omega \tag{16d}$$

By adopting cylindrical coordinates, Eq. (2) for the momentum can be written for any point of the cylinder through the following scalar equation

$$\frac{\partial \rho \omega r}{\partial t} + \frac{1}{r} \frac{\partial \rho \omega^2 r^2}{\partial \theta} = \rho f_\theta \tag{17}$$

where f_θ is the resultant in θ direction of the forces per unit mass. By assuming a homogenous density for the cylinder and by noting that angular velocity and radius are independent of the tangential coordinate, Eq. (17) can be put in the form

$$\rho r \frac{\partial \omega}{\partial t} = \rho f_\theta \tag{18}$$

By defining the torque per unit mass as $c=2f_\theta r$ Eq. (18) becomes

$$\rho r^2 \frac{\partial \omega}{\partial t} = \rho \frac{c}{2} \tag{19}$$

By integrating Eq. (19) over the cylinder volume and by applying the integral mean value theorem to the second member, it is possible to obtain

$$J \frac{\partial \omega}{\partial t} = C \tag{20}$$

where C is the resultant of the torques applied to the cylinder and $J=MR^2$.

Energy Balance for Fluids. In this case the scalar property is the total energy e, defined as sum of internal energy u, kinetic energy e_k and potential energy e_p [52]

$$e = u + e_k + e_p \tag{21}$$

By denoting with r_e and $\boldsymbol{q}$ the source and flux terms, respectively, Eq. (1) can be written as

$$\frac{\partial \rho e}{\partial t} + \nabla \cdot (\rho e v) = -\nabla \cdot \boldsymbol{q} + \rho r_e + \xi \tag{22}$$

where ξ is a dissipation function which represents the energy dissipated due to internal friction. Since ξ is proportional to the velocity gradient, for a Newtonian fluid it can be written as

$$\xi = \{\lambda(\nabla \cdot v)\mathbf{I} + \mu[\nabla v + (\nabla v)^T]\}:(\nabla v)^T \tag{23}$$

Let us consider a perfect gas flowing through a duct as in previous paragraphs. By defining $e_p=p/\rho$, and since $h_t=u+p/\rho+e_k$, Eq. (22) can be written as

$$\frac{\partial \rho h_t}{\partial t} + \frac{\partial (\rho h_t v)}{dx} = -\nabla \cdot \boldsymbol{q} + \rho r_e + \mu \left(\frac{\partial v}{\partial x}\right)^2 \tag{24}$$

By assuming that the fluid is a nonviscous fluid (i.e., $\mu=0$) and the generation term is null, and by writing the total enthalpy as $h_t=c_p T_t$, Eq. (24) becomes

$$\frac{\partial (\rho c_p T_t)}{\partial t} + \frac{\partial (\rho c_p T_t v)}{\partial x} = -\nabla \cdot \boldsymbol{q} \tag{25}$$

By using the coordinate system (r, θ, x), where x is a curvilinear coordinate, and by assuming the thermal flux only in radial direction, Eq. (25) can be expressed in the form

$$\frac{\partial (\rho c_p T_t)}{\partial t} + \frac{\partial (\rho c_p T_t v)}{\partial x} = -\frac{1}{r} \frac{\partial (r q_r)}{\partial r} \tag{26}$$

By integrating over the surface $A(x)$

$$\frac{\partial (A \rho c_p T_t)}{\partial t} = -A \frac{\partial (\rho c_p T_t v)}{\partial x} - Q_r \tag{27}$$

By substituting the spatial derivative with its expression derived from Taylor series and by introducing the mass flow rate, Eq. (27) can be written for the initial and the final section

$$\frac{\partial (A \rho c_p T_t)_{i,f}}{\partial t} = -\frac{1}{A_{f,i}} \frac{A_i (w c_p T_t)_f - A_f (w c_p T_t)_i}{L} - (Q_r)_{i,f} \tag{28}$$

Energy Balance for a Pipe. Let us consider a pipe with internal radius $R(x)$ and thickness $s(x)$. Any point of this pipe has null velocity and, so, both the kinetic energy e_k in Eq. (21) and the dissipation function ξ in Eq. (22) are null. By assuming energy flux only in radial direction and by neglecting the potential energy, we deduce from Eq. (22)

$$\rho c_v \frac{\partial T}{\partial t} = -\frac{1}{r} \frac{\partial (r q)}{\partial r} \tag{29}$$

By integrating Eq. (29) on the section area of the pipe

$$\int_0^{2\pi} \int_R^{R+s} \rho c_v \frac{\partial T}{\partial t} r dr d\theta = -\int_0^{2\pi} \int_R^{R+s} \frac{1}{r} \frac{\partial (r q)}{\partial r} r dr d\theta \tag{30}$$

and then by assuming temperature, density, and specific heat constant on the section, for any value of curvilinear abscissa x the equation of energy balance for the duct can be written as

$$C \frac{\partial T}{\partial t} = 2\pi R Q_R + 2\pi (R+s) Q_{R+s} \tag{31}$$

where C is the thermal capacity per unit length and Q_R and Q_{R+s} are the thermal flux per unit length on internal and external surfaces, respectively.

Model Implementation

The system under consideration, schematically represented in Fig. 2, is made up of three components (as already done in Ref. [50]): intake duct (ID), compressor (C) and exhaust duct (ED).

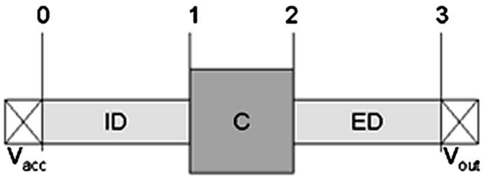

Fig. 2 Schematic representation of the system

Each duct has constant section. The system is isolated from the environment by two valves simulated through Eq. (A10) reported in Appendix A.2

Model equations are written for four control sections: inlet (0) section of the intake duct, inlet (1), and outlet (2) sections of the compressor and outlet (3) section of the exhaust duct.

Equations (32) and (33) represent the continuity equation written for sections 1 and 2, while Eqs. (34)–(36) express the momentum balance for sections 0, 1, and 3.

Energy balance equation, as reported in Eq. (28), is not adopted in the model. In fact, a preliminary investigation was carried out and the following assumptions have been made accordingly:

- In the intake duct, the thermal exchange can be assumed negligible and the difference between w_0 and w_1 is very small due to the fact that intake duct volume is small. Thus, the derivative with respect to time is assumed null.
- In the compressor, thermal exchange under steady conditions is implicitly taken into account by means of compressor characteristic curves [19], while thermal exchange under unsteady conditions is considered negligible, since the compressor is characterized by a small volume. The first term on the right-hand side of Eq. (28) can be also neglected because of compressor small volume.
- In the exhaust duct, the energy balance is not negligible. However, since it only affects the quantities in section 3, while it slightly affects the quantity considered to reveal the surge phenomenon (i.e. compressor outlet pressure), it is also neglected.

In any case, the choice of excluding the equation of energy balance from the model finds a further reason in the fact that in this way the model does not result computationally too heavy.

Equation (37) represents the spool dynamics. The torque supplied C_s is an input of the system, while the evaluation of the torque C_a absorbed by the compressor and of the friction torque C_f is reported in Appendix A.3

$$\frac{\partial p_1}{\partial t} = \frac{kRT_1}{A_1} \cdot \frac{w_1 - w_2}{L_C} \tag{32}$$

$$\frac{\partial p_2}{\partial t} = \frac{kRT_2}{A_2} \cdot \frac{w_2 - w_3}{L_{\mathrm{ED}}} \tag{33}$$

$$\frac{\partial w_0}{\partial t} = -\frac{A_0}{L_{\mathrm{ID}}}(p_1 - p_0) - \frac{\lambda_0}{D_{h0}}\frac{RT_0}{A_0 p_0}\frac{w_0^2}{2} \tag{34}$$

$$\frac{\partial w_1}{\partial t} = -\frac{A_1}{L_{\mathrm{ID}}}(p_1 - p_0) - \frac{\lambda_1}{D_{h1}}\frac{RT_1}{A_1 p_1}\frac{w_1^2}{2} \tag{35}$$

$$\frac{\partial w_3}{\partial t} = -\frac{A_3}{L_{\mathrm{ED}}}(p_3 - p_2) - \frac{\lambda_3}{D_{h3}}\frac{RT_3}{A_3 p_3}\frac{w_3^2}{2} \tag{36}$$

$$J\frac{\partial \omega}{\partial t} = C_s - C_a - C_f \tag{37}$$

In all the equations, temperature is a fundamental variable of the model. The presence of such a variable, whose importance has already been underlined above, allows the evaluation of the influence of inlet and outlet compressor temperature on compressor behavior. The outlet compressor temperature is estimated through the polytropic efficiency derived by using experimental maps. Moreover, the specific heats and, so, their ratio k depend on actual temperatures.

Compressor Characteristic Curves. Compressor characteristic curves are implemented in the model in the form suggested by Koff and Greitzer [35] for the inverse-flow characteristic and in a second degree polynomial form fitted over experimental data for the direct-flow characteristic. This solution of experimental data fitted by a parametric curve for the direct-flow region and polynomial curves for the inverse-flow region was already adopted in Ref. [53].

Direct-Flow Characteristic Curves. By using the test facility described in Ref. [54], different operating points at various corrected rotational speeds were recorded. Each set was interpolated by using a second degree polynomial curve, where the three coefficients depend on corrected rotational speed n_r.

Inverse-Flow Characteristic Curves. For the description of compressor behavior during surge, Koff and Greitzer [35] proposed a third degree polynomial curve where the coordinates were nondimensional pressure rise and nondimensional flow coefficient. In Ref. [21] the same equation is expressed by using pressure ratio and mass flow rate.

In the model presented in this paper a modified equation of the one proposed by Ref. [21] is adopted. In fact, instead of mass flow rate the equation is written by using corrected mass flow rate [22] and, thus, surge is modeled in the form of deep surge by using the following equation

$$\beta = \beta_0 + \left(\frac{\beta_{\max} - \beta_0}{2}\right)\left[1 + \frac{3}{2}\left(\frac{2 \cdot w_r}{w_{r_{\beta_{\max}}}} - 1\right) - \frac{1}{2}\left(\frac{2 \cdot w_r}{w_{r_{\beta_{\max}}}} - 1\right)^3\right] \tag{38}$$

where $\beta_{\max}$ is the maximum of the characteristic curve in the direct-flow region and is assumed to be the ordinate of the surge point. The parameter β_0 represents the intersection with pressure ratio axes and in the paper is expressed as

$$\beta_0 = f_s \cdot (\beta_{\max} - 1) + 1 \tag{39}$$

where f_s is a shape factor, which, in the paper, is assumed to be constant.

The parameter β_0 can be evaluated through both analytical and experimentally derived relations. For example, an analytical relation can be derived for centrifugal compressors, as shown in Refs. [21,22,28]. In the case of axial compressors, a detailed knowledge of compressor geometry is required, so that it could not be adopted for the considered axial–centrifugal compressor. On the other hand, the experimental evaluation of parameter β_0 requires the presence of a plenum large enough to make the surge occur, which at the moment is not present in the test rig [54]. In any case, the determination of such parameter is deeply influenced by the problems related to unsteady flow measurements, as discussed in Refs. [3,36,39]. Thus, the parameter β_0 was estimated through the shape factor f_s, on which an influence analysis will be carried out below.

The trend of the characteristic curve corresponding to the maximum measured corrected rotational speed, i.e., 1756 rpm/$\mathrm{K}^{0.5}$, is shown in Fig. 3 both in the direct-flow and inverse-flow region. The compressor actual working point is assumed to be quasi-steady and it always lies on the steady-state characteristic curve. A time lag in compressor response is not necessary for the simulation of deep surge as shown in Ref. [55].

The compressor efficiency map was also recorded by using the test facility described in Ref. [54]. These sets of points are processed in order to relate polytropic efficiency to corrected mass

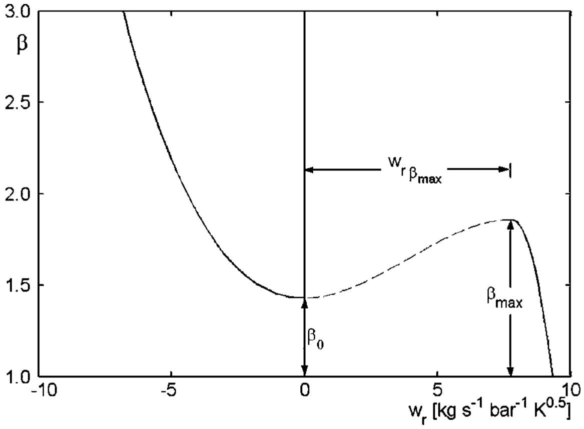

Fig. 3 Example of characteristic curves used for compressor behavior simulation in direct-flow and inverse-flow region—n_r=1756 rpm/K$^{0.5}$

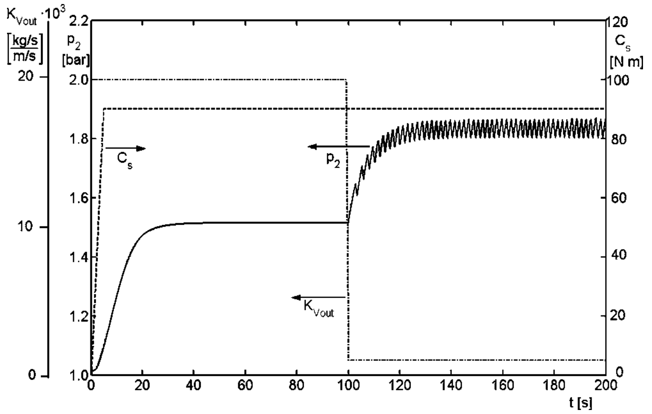

Fig. 4 Supplied torque (dotted line), outlet valve coefficient (dashed line), and compressor outlet pressure (solid line) during the base case simulation

flow rate for the operating points in the direct-flow region and then they are interpolated by means of a second degree polynomial equation.

Solver. To solve the system of ordinary differential equations, a fifth-order Runge–Kutta method with a fourth-order error control (the Dormand–Prince pair) is used. This method is implemented as a variable-step solver, which is named ODE45 and is supplied with Matlab. For the simulations, five ODE45 parameters have been set: maximum, minimum, and initial step size, and relative and absolute tolerance. The maximum step size, and the relative tolerance have been set equal to 0.1 s and 0.1%, respectively, while the rest has been set to "auto." The condition that the minimum step size is set to "auto" means that it is of the order of machine precision. Simulations are carried out by using a desktop PC with a 32 bit 1.4 GHz AMD processor and 1 GByte RAM memory.

According to Ref. [50], a solver based on the Runge–Kutta method of second- and third-order formulas (ODE23tb) was used at first but simulations failed when the inversion of the mass flow rate occurred: the convergence could not be reached even with the minimum step size allowed by the computer. Since the magnitude of the error is comparable to the minimum step raised to the maximum order of the method, a higher-order method was chosen, i.e., ODE45.

Results and Discussion

In order to analyze the dynamic response of a compression system, whose working fluid is assumed to be air, a parametric study is performed by evaluating the influence of geometrical parameters (length and diameter of intake duct and exhaust duct, outlet valve coefficient, and shaft inertia), of the supplied torque, of ambient conditions and of the shape factor f_s.

In Fig. 4, the forcing controlled variables (torque C_s and valve coefficient K_{Vout}) and their effect on compressor outlet pressure p_2 are reported for the base case configuration: the supplied torque and the valve coefficient are represented by a dotted line and a dashed line, respectively, while the solid line represents p_2. In fact, only this quantity will be analyzed below since it is usually considered the most significant quantity to reveal the surge phenomenon.

The imposed disturbance is simulated as a partial closure of the valve downstream the system through a decrease of the outlet valve coefficient K_{Vout}, as reported in Fig. 4. For the base case simulation, the steady-state condition is completely reached in about 30 s. However, the valve is closed at time t=99 s, so that the achievement of the steady-state condition for all performed simulations is guaranteed, even when the parameters considered for the sensitivity analyses are changed. The stroke time of the valve is 1 s, making a total of 100 s. Then, the simulation continues until t=200 s.

The supplied torque is zero at the start of the simulation and reaches its stationary value through a linear ramp in 5 s; then it is kept constant, as shown in Fig. 4.

The outputs of these 200 s of simulation (which require a computational time of about 15 min) are then analyzed by using a fast-Fourier transform (FFT) to determine the amplitude and the frequency of the spike of the surge phenomenon. In the paper, the frequency of the spike with the maximum amplitude is assumed to be the surge frequency.

Since the solver is variable step, to perform the FFT it is necessary to resample the simulated signal: the chosen resample frequency is 1 kHz. This value is chosen to avoid both the aliasing and hiding of the surge phenomenon. In Fig. 5, the FFT of p_2 is shown. As can be seen, the spike is located at 0.55 Hz, which is of the order of magnitude of surge phenomenon typical frequencies.

The base case parameters are summarized in Table 1. Regarding the values of geometrical parameters, it is very important to note that, for the analyses of transient phenomena, the cutoff frequency of the system, which is determined by the fluid residence time inside the largest volume, must be higher than the frequency characterizing the phenomenon [56]. Hence, in this case, the considered volumes of the elements (and so their lengths and diameters) are limited by the frequency of the studied phenomenon (in the case of surge, up to 10 Hz).

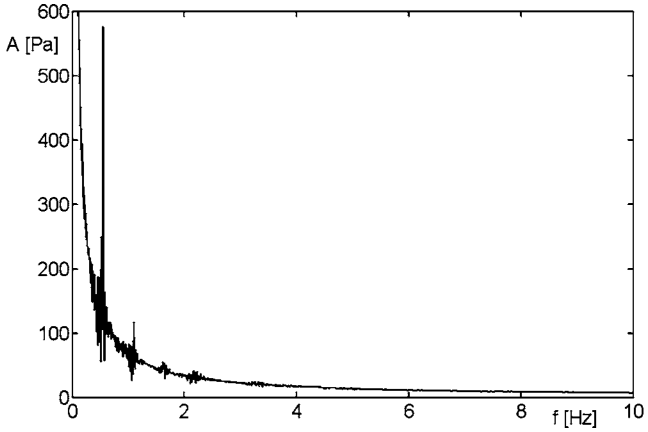

Fig. 5 Result of the fast Fourier transform of outlet compressor pressure

Table 1 Base case parameters

Property	Value
Hydraulic diameters $(D_{h0},D_{h1},D_{h2},D_{h3})$	0.1 m
Intake duct length L_{ID}	3.0 m
Compressor duct length L_C	0.4 m
Exhaust duct length L_{ED}	15 m
Friction factors $(\lambda_0,\lambda_1,\lambda_2,\lambda_3)$	0.2
Access valve coefficient $K_{\mathrm{Vacc}}\cdot 10^3$	10 (kg/s)/(m/s)
Initial outlet valve coefficient $K_{\mathrm{Vout}}\cdot 10^3$	20 (kg/s)/(m/s)
Final outlet valve coefficient $K_{\mathrm{Vout}}\cdot 10^3$	1.0 (kg/s)/(m/s)
Ambient pressure p_{amb}	101.3 kPa
Ambient temperature T_{amb}	15°C
Initial supplied torque C_s	0 N m
Final supplied torque C_s	90 N m
Polar inertia $J\cdot 10^3$	10.0 kg m^2
Shape factor f_s	0.5

Grid Sensitivity Analysis. According to the assumption of neglecting the remainders, as for instance in Eqs. (6*a*) and (6*b*) for the expression of pressure, simulation errors increase as the length of the computational element increases. So, a grid sensitivity analysis is carried out to evaluate the influence of the number of computational elements which are used to model each component. The analysis is carried out for the exhaust duct only, since this is the longest pipe and so the simulation error will be higher. The duct is divided into a number of elements (in the range of 1–60) with the same length and the results are reported in Fig. 6. It can be observed that by increasing the number of elements the frequency of the oscillations of the compressor outlet pressure increases towards an asymptotic value of about 0.81 Hz (47% higher than the value calculated by using one element only, i.e., 0.55 Hz).

The results of this analysis is that a component can actually be modeled through one element only, as often found in the literature for lumped parameter models [1–3,21,22,27–33]. In fact, even if the maximum percentage relative variation is high (47%), the frequency absolute value variation is not significant when the investigation is aimed at detecting surge occurrence.

Moreover, it should be noted that the computational time required for the simulation of 200 s increases from about 15 min to 1 day by increasing the number of elements from 1 to 60. Hence, since the use of one element does not affect the validity of the results, but only their accuracy, one element will be used in the following for modeling each component and, so, the results presented in this paper should be regarded comparatively.

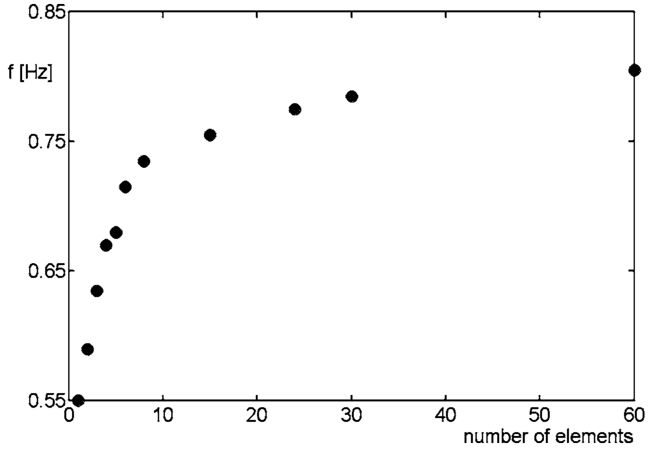

Fig. 6 Frequency of the oscillation of compressor outlet pressure vs. number of elements of the exhaust duct

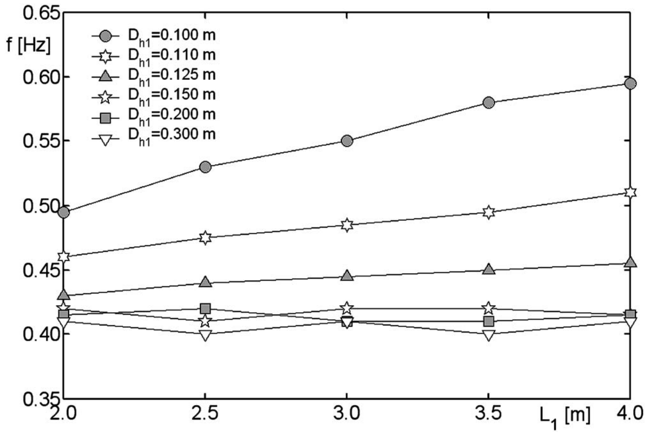

Fig. 7 Effects of the variation of the intake duct length on the frequency of the oscillations of the compressor outlet pressure

Intake Duct Geometry. The effect of the variation of the intake duct length on the p_2 oscillation frequency is shown in Fig. 7 for different values of the intake duct diameter. It can be seen that the frequency increases by increasing the length, although this effect is less marked when the intake duct diameter is increased. This behavior can be explained by considering that the higher the duct length is, the higher the friction forces are. Thus, in the case of reverse flow, this effect increases the pressure at the compressor inlet, so that the operating point moves toward the direct-flow region more rapidly as the duct length increases.

The figure also shows that by increasing the diameter of the intake duct the frequency decreases, and this effect is more marked by increasing the length (for a threefold increase of the diameter, the frequency varies by about 25% with respect to the base case at $L_1=3.0$ m). A saturation effect is noticeable at high values of intake diameter, which can be explained by the fact that, for high values of the diameter, friction forces decrease and so their variation is negligible with respect to the increase of the duct length.

Exhaust Duct Geometry. The analysis carried out by varying the length of the exhaust duct (figure omitted) shows that the p_2 oscillation frequency decreases by increasing the duct length, but the trend is not linear. In fact, for a decrease of the length of the exhaust duct of 33% (L_3 varies from 15 to 10 m), the frequency increases by about 10% with respect to the base case, while an increase in the exhaust duct length of 33% (L_3 varies from 15 to 20 m) causes a hardly appreciable decrease with respect to the base case. This can be explained by noting that, as observed in the previous paragraph, the increase of the duct length leads to higher friction forces and, so, the emptying and the draining of the plenum is slowed down.

Moreover, in this case, no effect is revealed by varying the exhaust duct diameter D_{h3} from 0.1 m (base case) to 0.3 m (exactly as was done for the intake duct diameter D_{h1}). The reason may be that in this case the D_h/L ratio is much smaller than in the case of the analyses performed for the intake duct.

Outlet Valve Coefficient. Figure 8 shows that, by increasing the outlet valve coefficient K_{Vout} (which corresponds to a higher valve opening), the frequency of the oscillation of the compressor outlet pressure decreases. The reason lies in the fact that the greater the valve coefficient is, the higher the mass flow rate through the valve is and so the plenum takes a longer time to be filled.

Shaft Inertia. Figure 8 also shows that by increasing shaft inertia the frequency of the oscillation of outlet compressor pressure decreases. This means that the system obviously responds

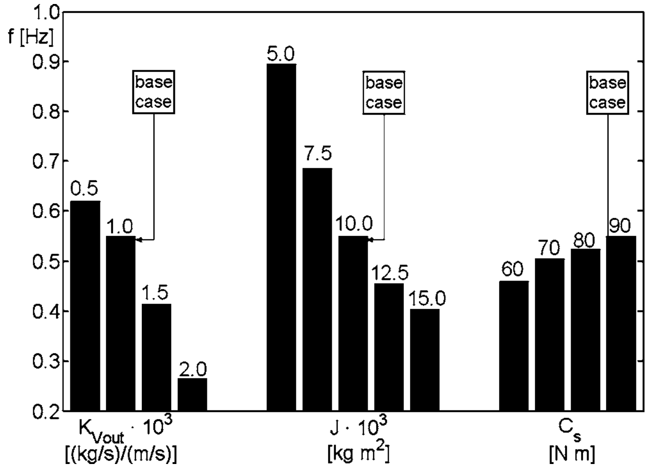

Fig. 8 Effects of the variation of final outlet valve coefficient K_{Vout}, of the supplied torque C_s, and of shaft inertia J on the frequency of compressor outlet pressure oscillations

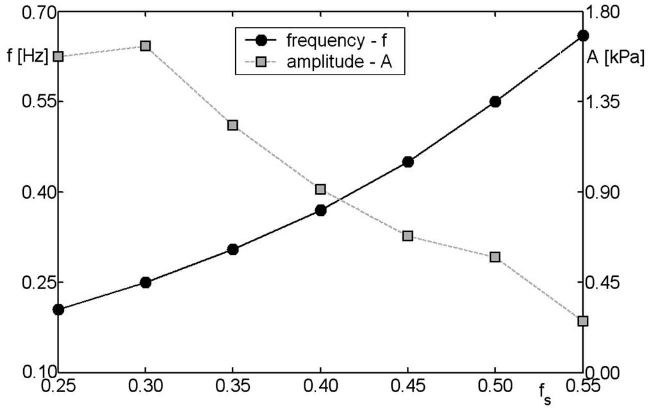

Fig. 10 Effects of the variation of f_s factor on the frequency f and on the amplitude A of the oscillations of outlet compressor pressure

faster if the inertia is lower. It can be observed that the correlation between f and the shaft inertia is not linear. In fact, for a decrease of 50%, the frequency increases by about 64% with respect to the base case, while an increase of 50% causes a decrease of about 25% with respect to the base case.

Supplied Torque. Finally, Fig. 8 shows that by increasing the supplied torque C_s the p_2 oscillation frequency increases. In fact, at high rotational speeds consequent to a higher supplied torque, higher mass flow rates are involved and, thus, the effect of filling and emptying the plenum is faster. This will be confirmed further by considering the influence of the shape of the curves, as shown in Fig. 11.

Ambient Conditions. The effect of the variation of ambient conditions (temperature and pressure) is shown in Fig. 9. An increase of the density of the fluid, due to a decrease of ambient temperature or an increase of ambient pressure, causes an increase of the p_2 oscillation frequency. In fact, the higher the density, the faster the emptying and the draining of the plenum.

Shape of Compressor Maps. Since experimental measurements on the test rig presented in Ref. [54] did not allow β_0 value to be determined, a sensitivity analysis is carried out to evaluate the influence of the shape of the characteristic curves (through the shape factor f_s) on the surge phenomenon. Figure 10 shows the results of the sensitivity analysis both in terms of frequency f and of amplitude A of compressor outlet pressure oscillations.

It can be noticed that an increase of f_s causes an increase of the p_2 oscillation frequency. This can be explained in the same way as for the supplied torque: high values of f_s mean very stretched curves and, so, high mass flow rates in the region of inverse flow, so that a faster draining of the plenum is allowed.

Figure 10 also shows the effect on the amplitude A of a variation of f_s, whose increase causes a decrease of the amplitude. This is due to the fact that the amplitude A in the presence of deep surge phenomenon is closely connected to the difference between $\beta_{\max}$ and β_0.

In order to clear up the effect of a variation of the shape factor, the compressor characteristic curves for two different values of the corrected rotational speed (500 and 2000 $\mathrm{rpm/K^{0.5}}$) are reported in Fig. 11 for two different values of the parameter f_s (0.25 and 0.50). It can be seen that the characteristic curves in the inverse flow region become less steep by increasing the f_s value, according to the choice of representing the compressor characteristic curves through Eqs. (38) and (39), as also done in Ref. [35].

Figure 11 also allows a better interpretation of the results pre-

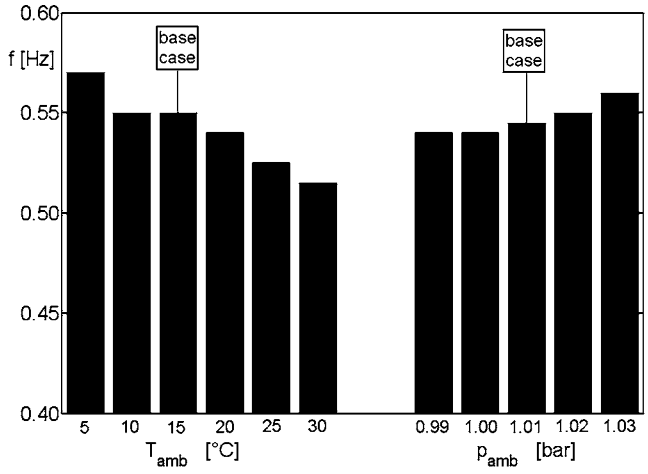

Fig. 9 Effects of the variation of ambient temperature and pressure on the frequency of compressor outlet pressure oscillations

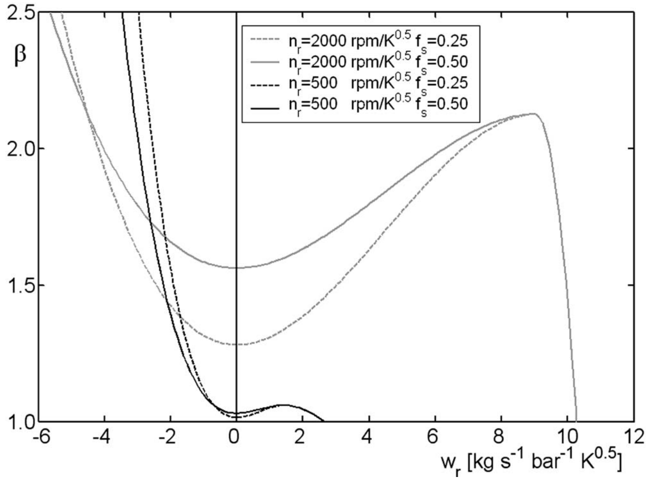

Fig. 11 Influence of the shape factor f_s on compressor characteristic curves for two values of the corrected rotational speed

sented in Fig. 8 for the supplied torque C_s.

In fact, if the corrected rotational speed is decreased for a given value of f_s, the slope of the curve in the inverse flow region (negative) deepens to even more negative values. This behavior explains the reason why an increase of the supplied torque, which also implies an increase in the corrected rotational speed, leads to an increase of the surge frequency. In fact, for higher corrected rotational speed values, the absolute value of the mass flow rate is higher both in the direct-flow region and in the inverse-flow region.

Conclusions

In the paper, a nonlinear one-dimensional modular dynamic model, implemented through a physics-based approach, was developed for the simulation of the transient behavior of compression systems.

The model also allows the simulation of compressor behavior in the presence of the surge phenomenon by means of steady-state performance maps, which represent the compressor operation in the inverse flow region.

A grid sensitivity analysis was preliminarily carried out to evaluate the influence of the number of computational elements which are used to reproduce each component. It was observed that by increasing the number of elements the frequency of the oscillations of the compressor outlet pressure increases toward an asymptotic value. In any case, for the analyses developed in the paper, each component was modeled through one element only since: (i) the frequency absolute value that is obtained by means of one element is not remarkably different from the one obtainable through tens of elements when the investigation is aimed at detecting surge occurrence; (ii) the computational time is reduced; and (iii) the validity of the results is maintained if the results are considered for comparative analyses only.

A sensitivity analysis was then carried out to evaluate the influence of the model parameters, of the supplied torque, and of ambient conditions. Some general conclusions can be highlighted.

The analysis of the influence of model parameters showed that the frequency of the oscillations of the compressor outlet pressure decreases when: (i) the intake duct length decreases or the exhaust duct length increases; (ii) the outlet valve coefficient increases (i.e., valve opening is higher); (iii) shaft inertia increases; (iv) the supplied torque decreases; or (v) the density of the fluid decreases (corresponding to an increase of ambient temperature or a decrease of ambient pressure). Moreover, a nonlinear response of the system with respect to model parameter variation was observed (e.g., by varying the intake duct diameter or the length of the exhaust duct). Thus, it may be difficult to define a scaling procedure for determining compression system behavior with respect to surge occurrence.

Finally, a compressor characteristic curve shape factor has been newly defined to relate the intersection with pressure ratio axes to a more easily measurable parameter, such as the maximum of the characteristic curves. From the sensitivity analysis, it has been observed that the frequency of compressor outlet pressure oscillations is remarkably influenced by the value of the shape factor, whose increase causes an increase of the frequency. In fact, high values of the shape factor mean less steep curves and, thus, high mass flow rates in the region of inverse flow, so that a faster draining of the plenum is allowed. An increase of the shape factor also causes a decrease of the amplitude, since the amplitude of the oscillations in the presence of deep surge phenomenon is closely connected to the difference between the maximum pressure ratio and the pressure ratio at null mass flow rate. Hence, this analysis suggested that it is advisable to estimate the intersection of compressor characteristic curve with pressure ratio axes (either experimentally or numerically) with an accuracy as high as possible.

As a final conclusion, the model proved effective in capturing the physical essence of surge without being computationally too heavy. Another important feature of the modular model developed in the paper is that it can be adopted for different system configurations since both the approach used for deriving model equations and their implementation are general. Finally, the model allows the study of the influence of external disturbances (e.g., boundary conditions) and it takes the compressor outlet temperature into account through compressor efficiency characteristic curves.

Future developments of the paper will be study of the dynamic behavior of a complete compression station. Moreover, the rapid prototyping of plant control system, based on a surge avoidance strategy, will be carried out by using the model as a compression station simulator.

Acknowledgment

The work was carried out with the support of the M.i.U.R. (Italian Ministry of University and Research). The authors gratefully acknowledge Professor Roberto Bettocchi and Professor Pier Ruggero Spina for the suggestions provided during the work.

Nomenclature

A = area, amplitude
B = body configuration
$\mathcal{B}$ = body
c = specific torque, specific heat
C = torque, thermal capacity
D_h = hydraulic mean diameter
e = specific energy
f = frequency, force per unit mass
f_s = shape factor
g = acceleration of gravity
h = specific enthalpy
$\mathbf{I}$ = identity matrix
J = polar inertia
k = c_p/c_v ratio of specific heats
K_V = valve coefficient
L = length
n_r = $(60/2\pi)(\omega/\sqrt{T})$ corrected rotational speed
M = $\pi R^2 L_\rho$ cylinder mass
p = pressure
P = material point
q = thermal flux per unit area
Q = thermal flux per unit length
r = source term per unit mass, radial coordinate
R = radius, gas constant
s = thickness
S = volume of the subsystem $(S \subset B)$
t = time
T = absolute temperature
u = specific internal energy
v = Eulerian velocity
w = $\rho v A$ mass flow rate
w_r = $w\sqrt{T}/p$ corrected mass flow rate
x = curvilinear coordinate
x_g = coordinate along gravity acceleration direction
z = axial coordinate
β = pressure ratio
η = efficiency
θ = tangential coordinate
λ = friction factor, second viscosity coefficient
μ = dynamic viscosity
ξ = dissipation function
ρ = density
$\boldsymbol{\varphi}, \boldsymbol{\Phi}$ = flux
ψ = generic intensive property
ω = angular speed
Ω = solid cylinder

Subscripts

0, 1, 2, 3 = model sections
a = absorbed
acc = access
amb = ambient
C = compressor
e = energy
ED = exhaust duct
f = final, friction
g = gravitational
i = initial
ID = intake duct
k = kinetic
out = outlet
p = potential
r = radial
rf = reverse flow
s = supplied
t = time, total
z = axial
θ = tangential

Appendix

A.1 General Balance Equation

Let us consider a generic scalar intensive property

$$\psi = \psi(\boldsymbol{x}, t) \tag{A1}$$

defined for $\mathbf{x} \in B_{\mathrm{t}}$, where B_{t} is the configuration of a generic body $\mathcal{B}$ at time t.

By using a Eulerian approach, the rate of variation of the property expressed through the substantial derivative over a finite volume $S_{\mathrm{t}} \subset B_{\mathrm{t}}$ can be written as

$$\frac{D}{D_t} \int_{S_t} \psi(\boldsymbol{x}, t) d\Omega \tag{A2}$$

where $d\Omega$ is the infinitesimal element of volume.

By assuming [57] that this variation is equal to the sum of two general contributions:

1. A flux term, written as

$$-\int_{\partial S_t} \boldsymbol{\varphi} \cdot \boldsymbol{n}\, d\sigma \tag{A3}$$

   where $\boldsymbol{\varphi}$ is the flux vector, $d\sigma$ is the infinitesimal element of area, and $\boldsymbol{n}$ is the external normal versor to boundary surface ∂S_t (the minus sign in Eq. (A3) is due to the versus of normal versor);
2. A source term

$$\int_{S_t} \rho r d\Omega \tag{A4}$$

   where r is the property generated per unit mass and per unit time and ρ is the density. Hence, Eq. (A2) can be written as

$$\frac{D}{Dt} \int_{S_t} \psi(\boldsymbol{x}, t) d\Omega = -\int_{\partial S_t} \boldsymbol{\varphi} \cdot \boldsymbol{n} d\sigma + \int_{S_t} \rho r\, d\Omega \tag{A5}$$

By applying the transport theorem to the first member of Eq. (A5) and the divergence theorem to the first term of the second member, Eq. (A5) can be expressed as

$$\int_{S_t} \left(\frac{D\psi}{Dt} + \psi \nabla \cdot \boldsymbol{v} \right) d\Omega = \int_{S_t} (-\nabla \cdot \boldsymbol{\varphi} + \rho r) d\Omega \tag{A6}$$

Since Eq. (A6) is valid for any $S_t \subset B_t$ and by assuming the continuity of the integral arguments, the balance equation can be written for any $\boldsymbol{x} \in B_t$ as

$$\frac{D\psi}{Dt} + \psi \nabla \cdot \boldsymbol{v} = -\nabla \cdot \boldsymbol{\varphi} + \rho r \tag{A7}$$

where $\boldsymbol{v}$ is the Eulerian velocity.

By using the definition of the substantial derivative, Eq. (A7) can be reformulated as

$$\frac{\partial \psi}{\partial t} + \nabla \cdot (\psi \boldsymbol{v}) = -\nabla \cdot \boldsymbol{\varphi} + \rho r \tag{A8}$$

For a vectorial intensive property $\boldsymbol{\psi} = \boldsymbol{\psi}(\boldsymbol{x}, t)$, by assuming that the flux through the boundary and the source term can be written as $\boldsymbol{\Phi n}$ and $\rho \boldsymbol{r}$ respectively, the balance equation for any $\boldsymbol{x} \in B_t$ is

$$\frac{\partial \boldsymbol{\psi}}{\partial t} + \nabla \cdot (\boldsymbol{v}^T \boldsymbol{\psi}) = \nabla \cdot \boldsymbol{\Phi} + \rho \boldsymbol{r} \tag{A9}$$

A.2 The Valve

The mass flow rate through a valve can be expressed as a function of the pressure differential [47]

$$w = \mathrm{sign}(p_i - p_f) \cdot K_V \sqrt{\frac{|p_i - p_f|}{\rho}} \tag{A10}$$

Thus, the pressure for the access and outlet valves can be written as

$$p_0 = p_{\mathrm{amb}} - \frac{\rho \cdot w_0 |w_0|}{K_{\mathrm{Vacc}}^2} \tag{A11a}$$

$$p_3 = p_{\mathrm{amb}} + \frac{\rho \cdot w_3 |w_3|}{K_{\mathrm{Vout}}^2} \tag{A11b}$$

In Eqs. (A11*a*) and (A11*b*), the density ρ is calculated as the mean value of the densities upstream and downstream of the valve.

A.3 The Torque Absorbed by the Compressor

The torque absorbed by the compressor is calculated in the case of direct flow by using the following expression

$$C_a = \frac{w_2 c_p T_1}{\omega} \left[\left(\frac{p_2}{p_1} \right)^{\frac{k-1}{k\eta}} - 1 \right] \tag{A12}$$

where η is the polytropic efficiency calculated by using the experimental maps.

According to Ref. [44], a centrifugal compressor where reverse flow is present can be approximated to a turbine. In this paper, this hypothesis is assumed valid even for an axial–centrifugal compressor. Hence, in the case of reverse flow, the absorbed torque C_a can be calculated as

$$C_a = \frac{w_2 c_p T_2}{\omega} \left[\left(\frac{p_1}{p_2} \right)^{\frac{\eta_{\mathrm{rf}}(k-1)}{k}} - 1 \right] \tag{A13}$$

where η_{rf} is the value of efficiency assumed equal to 0.1.

A.4 The Friction Torque

The friction torque C_f is estimated through a second degree polynomial function of compressor rotational speed, fitted over experimental data.

References

[1] Greitzer, E. M., 1976, “Surge and Rotating Stall in Axial Flow Compressor: Part 1, Theoretical Compression System Model” ASME J. Eng. Power, **98**, pp. 190–198.
[2] Moore, F. K., and Greitzer, E. M., 1986, “A Theory of Post-Stall Transients in

Axial Compression Systems: Part I-Development of Equations," ASME J. Eng. Gas Turbines Power, **108**, pp. 68–76.

[3] Fink, D. A., Cumpsty, N. A., and Greitzer, E. M., 1992, "Surge Dynamics in a Free-Spool Centrifugal Compressor System," ASME J. Turbomach., **114**, pp. 321–332.

[4] Mansoux, C. A., Gysling, D. L., Setiawan, J. D., and Paduano, J. D., 1994, "Distributed Nonlinear Modeling and Stability Analysis of Axial Compressor Stall And Surge," *Proceedings of American Control Conference*, Baltimore, MD, June 29–July 1, pp. 2305–2316.

[5] McCaughan, F. E., 1989, "Application of Bifurcation Theory to Axial Flow Compressor Instability," ASME J. Turbomach., **111**, pp. 426–433.

[6] McCaughan, F. E., 1990, "Bifurcational Analysis of Axial Flow Compressor Stability," SIAM J. Appl. Math., **50**(5), pp. 1232–1253.

[7] Hös, C., Champneys, A., and Kullmann, L., 2003, "Bifurcational Analysis of Surge and Rotating Stall in the Moore-Greitzer Compression System," IMA J. Appl. Math., **68**(2), pp. 205–228.

[8] Vaidya, U., Ananthkrishnan, N., and Walimbe, V., 2000, "Nonlinear Control of Surge and Stall in Axial Flow Compressor," *Proceedings of the 5th National Conference on Airbreathing Engines and Aerospace Propulsion (NCABE 2000)*, Hyderabad, India, December 21–23, pp. 102–110.

[9] Humbert, J. S., and Krener, A. J., 1998, "Dynamics and Control of Entrained Greitzer Compressor Models," Int. J. Control, **71**(5), pp. 807–821.

[10] D'Andrea, R., Behnken, R. L., and Murray, R. M., 1997, "Rotating Stall Control of an Axial Flow Compressor using Pulsed Air Injection," ASME J. Turbomach., **119**(4), pp. 742–752.

[11] Protz, M., and Paduano, J. D., 1997, "Rotating Stall and Surge: Alternate Modeling and Control Concepts," *Proceedings of the 1997 International Conference on Control Application*, Hartford, CN, October 5–7, pp. 866–873.

[12] Gravdahl, J. T., 1998, "Modeling and Control of Surge and Rotating Stall in Compressors," Ph.D. thesis, Norwegian University of Science and Technology, Trondheim, Norway.

[13] Arnulfi, G. L., Giannattasio, P., Giusto, C., Massardo, A. F., Micheli, D., and Pinamonti, P., 1998, "Multistage Centrifugal Compressor Surge Analysis: Part II–Numerical Simulation and Dynamic Control Parameters Evaluation," ASME J. Turbomach., **121**, pp. 312–320.

[14] Arnulfi, G. L., Giannattasio, P., Micheli, D., and Pinamonti, P., 2001, "An Innovative Device for Passive Control of Surge in Industrial Compression Systems," ASME J. Turbomach., **123**, pp. 473–482.

[15] Li, M., and Zheng, Q., 2004, "Wet Compression System Stability Analysis. Part I–Wet Compression Moore Greitzer Transient Model," ASME Paper No. GT 2004-54018.

[16] Hale, A. A., and Davis, M. W., 1992, "DYNamic Turbine Engine Compressor Code DYNTECC–Theory and Capabilities," AIAA-92-3190, *Proceedings of 28th AIAA/SAE/ASME/ASEE Joint Propulsion Conference and Exhibit*, Nashville, TN, July 6–8.

[17] Owen, A. K., Daugherty, A., Garrard, D., Reynolds, H. C., and Wright, R. D., 1999, "A Parametric Starting Study of an Axial-Centrifugal Gas Turbine Engine Using a One-Dimensional Dynamic Engine Model and Comparisons to Experimental Results: Part I–Model Development and Facility Description," ASME J. Eng. Gas Turbines Power, **121**, pp. 377–383.

[18] Owen, A. K., Daugherty, A., Garrard, D., Reynolds, H. C., and Wright, R. D., 1999, "A Parametric Starting Study of an Axial-Centrifugal Gas Turbine Engine Using a One-Dimensional Dynamic Engine Model and Comparisons to Experimental Results: Part II–Simulation Calibration and Trade-Off Study," ASME J. Eng. Gas Turbines Power, **121**, pp. 384–393.

[19] Owen, A. K., and Davis, M. W., Jr., 1994, "Modeling The Dynamic Behavior of an Axial-Centrifugal Compression System," AIAA-94-2802, *Proceedings of 30th AIAA/ASME/SAE/ASEE Joint Propulsion Conference*, Indianapolis, IN, June 27–29.

[20] Cousins, W. T., 1996, "The Dynamics of Stall and Surge Behavior in Axial-centrifugal Compressors," Ph.D. thesis, Virginia Polytechnic Institute and State University, Blacksburg, VA.

[21] Theotokatos, G., and Kyrtatos, N. P., 2003, "Investigation of a Large High-Speed Diesel Engine Transient Behavior Including Compressor Surging and Emergency Shutdown," ASME J. Eng. Gas Turbines Power, **125**, pp. 580–589.

[22] Theotokatos, G., and Kyrtatos, N. P., 2001, "Diesel Engine Transient Operation with Turbocharger Compressor Surging," SAE Paper No. 2001-01-1241.

[23] Schmitz, M. B., and Fitzky, G., 2004, "Surge Cycle of Turbochargers: Simulation and Comparison to Experiments," ASME Paper No. GT 2004-53036.

[24] Botha, B. W., du Toit, B., and Rousseau, P. G., 2003, "Development of a Mathematical Compressor Model to Predict Surge in a Closed Loop Brayton Cycle," ASME Paper No. GT 2003-38795.

[25] Hahn, A., 2000, "Modeling and control of Solid Oxide Fuel Cell–Gas Turbine Power Plant Systems," Ph.D. thesis, University of Pittsburgh, Pittsburgh, PA.

[26] Hildebrandt, A., Genrup, M., and Assadi, M., 2004, "Steady-State and Transient Compressor Surge Behaviour Within a SOFC-GT-Hybrid System," ASME Paper No. GT 2004-53892.

[27] Botros, K. K., Campbell, P. J., and Mah, D. B., 1991, "Dynamic Simulation of Compressor Station Operation Including Centrifugal Compressor and Gas Turbine," ASME J. Eng. Gas Turbines Power, **113**, pp. 300–311.

[28] Botros, K. K., 1994, "Transient Phenomena in Compressor Stations During Surge," ASME J. Eng. Gas Turbines Power, **116**, pp. 133–142.

[29] Botros, K. K., Jungowski, W. M., and Richards, D. J., 1996, "Compressor Station Recycle System Dynamics During Emergency Shutdown," ASME J. Eng. Gas Turbines Power, **118**, pp. 641–653.

[30] Bakken, L. E., Bjørge, T., Bradley, T. M., and Smith, N., 2002, "Validation of Compressor Transient Behaviour," ASME Paper No. GT-2002-30279.

[31] Tveit, G. B., Bjørge, T., and Bakken, L. E., 2005, "Impact of Compressor Protection System on Rundown Characteristics," ASME Paper No. GT 2005-68436.

[32] Ohanian, S., and Kurz, R., 2001, "Series or Parallel Arrangement in a Two-Unit Compression Station," ASME Paper No. 2001-GT-0230.

[33] Gravdahl, J. T., and Egeland, O., 1997, "A Moore-Greitzer Axial Compressor Model with Spool Dynamics," *Proceedings of the 36th IEEE Conference on Decision and Control* San Diego, CA, December 10–12, pp. 4714–4719.

[34] Emmons, H. W., Pearson, C. E., and Grant, H. P., 1955, "Compressor Surge and Stall Propagation," Trans. ASME, **77**, pp. 455–469.

[35] Koff, S. G., and Greitzer, E. M., 1984, "Stalled Flow Performance for Axial Compressors–I: Axisymmetric Characteristics," ASME Paper No. 84-GT-93.

[36] Greitzer, E. M., 1976, "Surge and Rotating Stall in Axial Flow Compressor: Part 2, Experimental Results and Comparison with Theory," ASME J. Eng. Power, **98**, pp. 199–211.

[37] Toyama, K., Runstadler, P. W., Jr., and Dean, R. C., Jr., 1976, "An Experimental Study of Surge in Centrifugal Compressors," ASME J. Fluids Eng., **99**, pp. 115–131.

[38] Lawless, P. B., Frey, K. K., and Fleeter, S., 1997, "Rotating Stall Spatial Domain Characterization in Axial and Centrifugal Compressors," *Turbomachinery Fluid Dynamics and Heat Transfer*, Marcel Dekker, New York, pp. 367–382.

[39] Arnulfi, G. L., Giannattasio, P., Giusto, C., Massardo, A. F., Micheli, D., and Pinamonti, P., 1998, "Multistage Centrifugal Compressor Surge Analysis: Part I–Experimental Investigation," ASME J. Turbomach., **121**, pp. 305–311.

[40] Hoss, B., Leinhos, D., and Fottner, L., 1998, "Stall Inception in the Compressor System of a Turbofan Engine," ASME Paper No. 98-GT-475.

[41] Nurzia, F., Palomba, C., and Puddu, P., 2000, "Experimental Investigation of Stall in a Two Stage Compressor," ASME Paper No. 2000-GT-0571.

[42] Skoch, G. J., 2003, "Experimental Investigation of Centrifugal Compressor Stabilization Techniques," J. Turbomach. **125**, pp. 704–713.

[43] Horodko, L., 2005, "Investigation of Centrifugal Compressor Surge with Wavelet Methods," *Proceedings of 6th Conference on TURBOMACHINERY Fluid Dynamics and Thermodynamics*, Lille, France, March 7–11.

[44] Gravdahl, J. T., and Egeland, O., 1999, *Compressor Surge and Rotating Stall Modeling and Control*, Springer, London.

[45] Tavakoli, S., Griffin, I., and Fleming, P., 2004, "An Overview of Compressor Instabilities: Basic Concepts and Control," *Proceedings of the 16th IFAC International Symposium on Automatic Control in Aerospace*, St. Petersburg, Russia, June 14–18.

[46] Vachtsevanos, G., Kang, H., Cheng, J., and Kim, I., 1992, "Detection and Identification of Axial Flow Compressor Instabilities," J. Guid. Control Dyn., **15**, pp. 1216–1223.

[47] Kurz, R., and White, R. C., 2004, "Surge avoidance in gas compression systems," ASME J. Turbomach., **126**, pp. 501–506.

[48] Hansen, K. E., Jorgensen, P., and Larsen, P. S., 1981, "Experimental and Theoretical Study of Surge in a Small Centrifugal Compressor," ASME J. Fluids Eng., **103**, pp. 391–394.

[49] Niazi, S., 2000, "Numerical Simulation of Rotating Stall and Surge Alleviation in Axial Compressors," Ph.D. thesis, Georgia Institute of Technology, Atlanta, GA.

[50] Venturini, M., 2005, "Development and Experimental Validation of a Compressor Dynamic Model," ASME J. Turbomach., **127**(3), pp. 599–608.

[51] Batchelor, G. K., 1973, *An Introduction to Fluid Dynamics*, Cambridge University Press, Cambridge, UK.

[52] Backus, G., 1997, *Continuum Mechanics*, Samizdat Press, USA.

[53] Gong, Y., 1999, "A Computational Model for Rotating Stall and Inlet Distortion in Multistage Compressors," Ph.D. thesis, Massachusetts Institute of Technology, Cambridge, MA.

[54] Bettocchi, R., Pinelli, M., and Spina, P. R., 2005, "A MultiStage Compressor Test Facility: Uncertainty Analysis and Preliminary Test Results," ASME J. Eng. Gas Turbines Power, **127**(1), pp. 170–177.

[55] Fink, D. A., 1988, "Surge Dynamics and Unsteady Flow Phenomena," Ph.D. thesis, Massachusetts Institute of Technology, Cambridge, MA.

[56] Van Essen, H. A., and de Lange, H. C., 2001, "Nonlinear Model Predictive Control Experiments on a Laboratory Gas Turbine Installation," ASME J. Eng. Gas Turbines Power, **123**, pp. 347–352.

[57] Šilhavý, M., 1997, *The Mechanics and Thermodynamics of Continuous Media*, Springer, Berlin, Germany.

Nobuyuki Tahara
Ishikawajima-Harima Heavy Industries,
Toyosu, Tokyo, 135-8710 Japan

Masahiro Kurosaki
Ishikawa National College of Technology,
Kahoku-gun, Ishikawa, 929-0392 Japan

Yutaka Ohta

Eisuke Outa

Waseda University,
Shinjuku, Tokyo, 169-8555 Japan

Takurou Nakajima

Tomofumi Nakakita

Ishikawajima-Harima Heavy Industries,
Toyosu, Tokyo, 135-8710 Japan

Early Stall Warning Technique for Axial-Flow Compressors

This paper proposes a unique stall risk index based on pressure signals by high-response transducers on the casing wall at the rotor leading-edge location. The aim of the research is to explore the possibility of reducing current excessive stall margin requirement for compressor design based on the worst-case scenario. The index is generated by computing correlation degradation of pressure time histories of current and one revolution before over each blade pitch. Tests conducted on a single-stage low-speed compressor exhibits that the correlation diminishes significantly with proximity to stall, and the proposed technique might have the capability of generating a stall warning signal sufficiently in advance of spike inception. Extensive experiments on a research compressor show that the degree of the index degradation depends on various factors, such as flow coefficient, tip clearance, and rotor blade incidence. In order to obtain a reliable stall warning signal in practical use, these effects must be carefully examined.

[DOI: 10.1115/1.2447948]

Introduction

Stall and surge are among the most burdensome problems that constrain the design of turbomachines. Because they are catastrophic, occurring near the peak of pressure-rise performance, compressor operation is limited to the negative slope range of the pressure-rise characteristic. One way to expand the stable operating range of compressors is to utilize control technologies. It is common in the aircraft engine industry to design engine matching so that the steady-state operating point of the compressor has $\sim$20% surge margin at all operations from idle to max power. Since a reliable stall warning system is not available, the surge margin requirement is a sum of possible causes, such as inlet distortion effect, performance deterioration, engine control tolerance, and engine transient effect based on the worst-case scenario. If a reliable stall warning signal can be generated sufficiently in advance of stall occurrence, it may be possible to reduce such a large surge margin requirement with conventional control means, such as acceleration fuel schedule reduction, compressor variable stator vane angle modulation, and compressor bleed valve actuation. Suppose that the margin can be reduced from 20% to 10%, roughly speaking, this is equivalent to a 10% increase of individual blade loading and would result in a two-stage reduction of a ten-stage compressor. A significant reduction of engine weight, cost, and direct operating cost of an air fleet would be expected.

Active compressor stall control was initially proposed by Epstein et al. [1] in 1986. They showed that the onset of stall and surge could be suppressed by actively controlling the stall inception process. Since then much research has been carried out. The challenge has been especially directed to detailed study of stall inception to reliably identify it as early as possible so that enough time could be secured to take actions to suppress incipient stall. In axial flow compressors, there are two typical stall inceptions currently known in general: a long-wavelength pattern referred to as "modal oscillation" and a short-wavelength pattern typically of the order of one or two blade passages referred to as "spike" [2]. The former is related to two-dimensional instability of the whole compression system and rotates at a relatively low speed of $<50\%$ of the rotor speed. It builds up gradually and can be observed from several tens to more than 100 rotor revolutions prior to stall. In contrast, the latter propagates more quickly at speeds between 60% and 80% of the rotor speed. It appears suddenly and grows directly into stall cells within several rotor revolutions. Its rapid growth makes it difficult for current actuation technologies to avoid stall even if the first appearance of spike inception is successfully detected. Thus, a good indicator of proximity to stall must be found earlier than the time of spike inception identification.

Since the flow in the tip region of a compressor rotor has significant effect on the compressor efficiency and stability, a great deal of research has been conducted in order to understand flow mechanism in that region. Because of the complicated flow structure and the increasing blade-loading requirement, investigations with advanced measurement techniques, such as DPIV (digital particle image velocimetry) and CFD (computational fluid dynamics) are ongoing.

Hoying et al. [3] showed by numerical experiments that the short length-scale inception process was linked to the behavior of the blade-passage flow-field structure, specifically the tip clearance vortex. At the higher flow coefficients, the vortex trajectory lies further back in the blade passage. As the flow coefficient is reduced, the clearance vortex trajectory becomes closer to perpendicular to the axial direction. They claim that a criterion for stall inception for the short length-scale phenomena requires that the tip vortex trajectory be perpendicular to the axial direction.

In the high blade-loading operating point case, DPIV measurements by Wernet et al. [4] revealed a large tip clearance vortex that extended further upstream than the design point case and a large flow blockage in the center of the blade passage that was not observed in the design operating measurements.

Tryfonidis et al. [5] studied prestall behavior of several high-speed compressors. Prestall refers to the period of time immediately prior to stall inception during which compressor operation is

---

Contributed by the International Gas Turbine Institute (IGTI) of ASME for publication in the JOURNAL OF TURBOMACHINERY. Manuscript received July 2, 2006; final manuscript received July 29, 2006. Review conducted by David Wisler. Paper presented at the ASME Turbo Expo 2004: Land, Sea and Air (GT2004), Vienna, Austria, June 14–17, 2004. Paper No. GT2004-53292.

steady but may exhibit small amplitude dynamics. They proposed a new technique based on spectral analysis of the spatial Fourier harmonics of measured case wall pressures.

Day et al. [6] reported test results for four high-speed compressors. One of their conclusions was that the variety of the stalling patterns and the ineffectiveness of stall warning procedures suggest that the ultimate goal of a flight worthy active control system remains distant. They also suggest that an alternative approach to active control is to disregard the physical details of the flow generating the incoming signals and to simply concentrate on deriving a stall risk index from the sum of all the inputs.

Hoenen and Arnold [7] proposed a monitoring algorithm for the prediction of unstable compressor operation that involves analyzing the signal patterns of dynamic pressure transducers mounted above the first rotor. As the compressor load approached the stability limit, the amplitude of the blade-passing frequency became reduced but new frequency peaks occurred and grew until the stability limit was reached. The stability parameter was calculated as follows. The blade-passing frequency and its harmonics were blanked out from the spectra. By means of numerical differentiation, taking absolute values and finally integration the stability parameter was calculated from the remaining signal.

Motivated by previous papers, the authors carried out a series of experiments on a research compressor and based on these results, here we propose a unique stall warning index. The proposed technique utilizes casing wall pressure at the rotor blade leading edge measured by high-response pressure transducers. It compares the pressure time histories of one blade pitch with that of the identical blade pitch one revolution before and computes their correlation to eliminate the effect of rotor blade geometry difference. The correlation diminishes significantly with proximity to stall, and based on the correlation degradation degree, a stall warning signal can be generated in practical application. The main feature of the proposed technique is the possibility of providing stall warning sufficiently in advance of spike inception.

The paper is organized as follows. First, measurements of case pressure in a rotor blade passage are described and then a signal processing technique to generate a stall warning index is proposed. Indication development generated from axially located pressure transducers is then described. Next, index development in the circumferential direction with uniform inlet flow is described in the casing and the rotor fixed frame, respectively. Tip clearances are measured and their relation with the circumferential distribution of the indices is described. Finally, the circumferential index development with a distorted inlet flow condition and axial and circumferential velocity measurements are presented and discussed. This sensitive stall warning technique will provide some novel information on stall initiation process.

Pressure-Field Measurements in Rotor Blade Passage

Detection of spike inception may be too late for stall avoidance even with advanced high-response control systems. The authors' research activity started with a study of a steady-state pressure-field structure in the rotor blade passage at various airflow rates to find clues that might exist prior to spike inception. Experiments were carried out at a facility illustrated in Fig. 1. The compressor is a low-speed single-stage axial-flow machine without inlet guide vanes. The main features of the research compressor are listed in Table 1, and the total-to-static pressure rise characteristics are shown in Fig. 2.

Figure 3 is a typical stalling pattern of the compressor captured by a circumferential array of six pressure transducers 1/5 aero chord ahead of the rotor leading edge. Circumferential locations of pressure transducers A through F are illustrated in Fig. 4. Clearly the compressor has a spike-type stall inception. Rotating with ~60% of the rotor speed, the spike grows into stall cells during several rotor rotations.

For a detailed pressure-field survey, a series of fast-response pressure transducers were placed along the rotor blade passage on the casing wall as shown in Fig. 5. The location of sensor *f* is right on the rotor leading edge, *a* through *e* are upstream of the leading edge and *g* through *n* are in the blade passage.

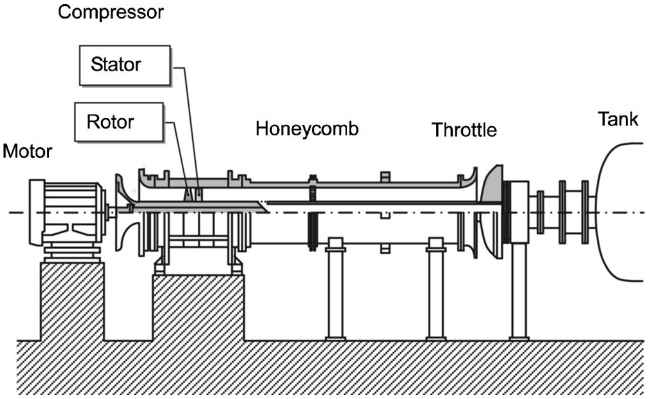

Fig. 1 Test facility

Figure 6 shows the steady-state pressure contours around the rotor blade measured by those pressure transducers at the design condition, near stall, and during stall transient, respectively. At the design condition, a pressure trough lies leeward in the blade passage from the low-pressure core on the suction surface. As the airflow rate decreased, the low-pressure core shifted slightly toward the leading edge. The pressure trough swung upstream toward the circumferential direction as a consequence. Near stall, the pressure trough becomes more perpendicular to the axial direction and impacted against the leading edge of the subsequent blade. During the transition into the fully developed stall, the pressure trough becomes obscure.

It is well known that a leakage vortex forms the low-pressure trough near the leading edge of the suction surface [8]. It is thought that the pressure troughs observed in the experiments are

Table 1 Compressor features

Article	Specification
Diameter of rotor	130.0 mm
Diameter of rotor hub	80.0 mm
Number of rotor blades	12
Chord of rotor blade	30.0 mm
Number of stator blades	15
Chord of stator blades	24.5 mm
Airfoil configuration	NACA65
Rotational speed	12,000 rpm
Airflow rate	0.37 kg/s
Pressure rise	1.48 kPa (151 mm Aq)

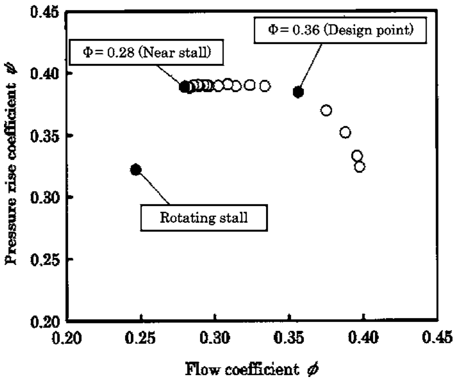

Fig. 2 Pressure-rise characteristic of the compressor

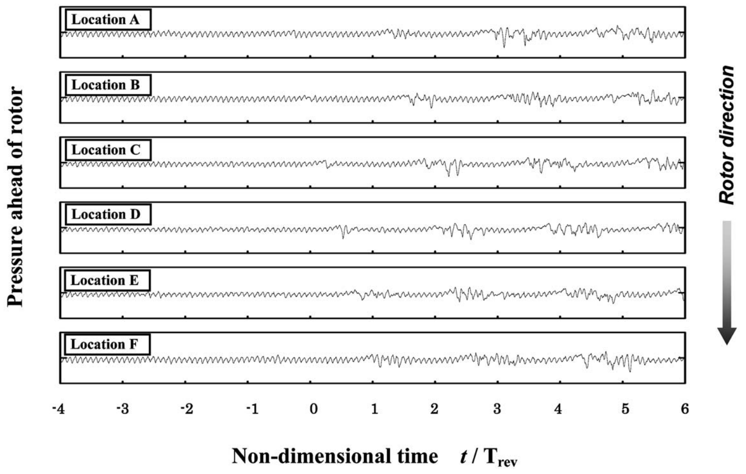

Fig. 3 Stalling pattern of the compressor

caused by tip leakage flow. The observed behavior of the tip leakage flow trajectory corresponds well to that described by Hoying et al. [3].

Signal-Processing Technique

If the trajectory of the low-pressure troughs can be detected in the blade passage, it could be utilized as a stall warning index. Since the tip leakage flow interferes with the main flow, it is expected that pressure signal in blade passage will fluctuate and that the fluctuation will shift upstream with an airflow rate decrease.

To have a quantitative evaluation of the fluctuation, time histories of current and one rotor revolution before of the same blade pitch are compared and the following correlation coefficient is computed as a candidate for the stall warning indices (refer to Fig. 7):

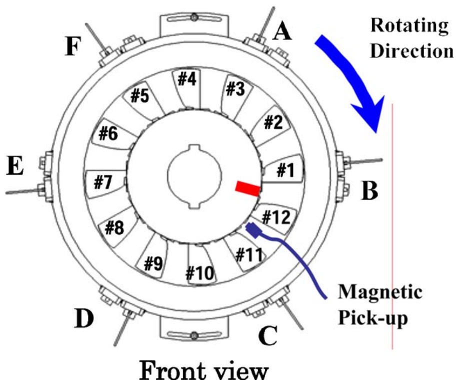

Fig. 4 Circumferential sensor locations and blade identification

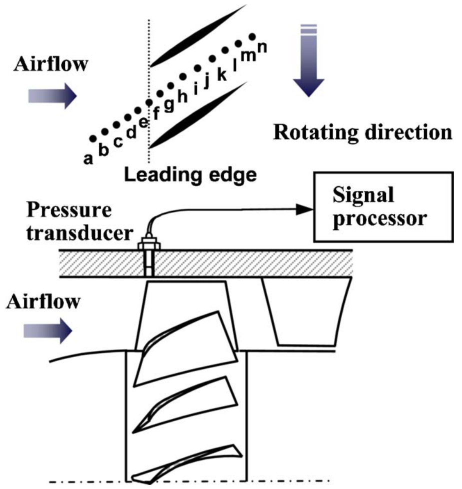

Fig. 5 Pressure field measurement

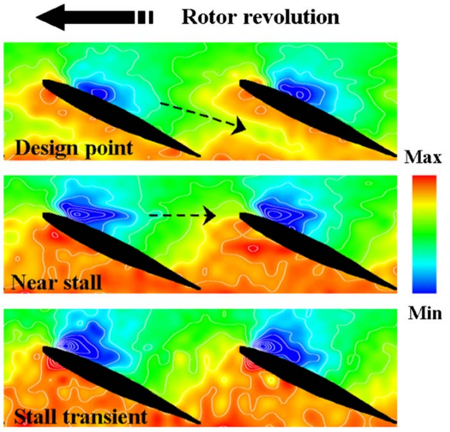

Fig. 6 Pressure contours (experimental results)

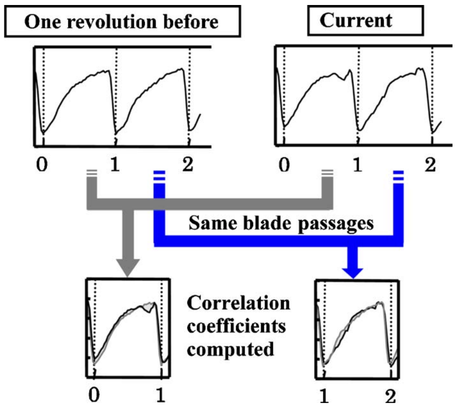

Fig. 7 Signal-processing technique

$$R = \frac{\int (P(t) - P_{av,n})(P(t-\tau) - P_{av,n-1})dt}{\sqrt{\int (P(t) - P_{av,n})^2 dt}\sqrt{\int (P(t-\tau) - P_{av,n-1})^2 dt}} \quad (1)$$

where τ is the time period of one rotor revolution, P_{av} is the average pressure over one blade pitch and the integration is taken for one blade pitch. For simplicity, the denominator is replaced with the average of two integrations to avoid computing a time-consuming root. When the flow does not have any fluctuation, the pressure signal is completely identical to that of one rotor revolution before. In this situation, the computed value becomes unity continuously. However, when fluctuation is present in the flow, the computed value is degraded and reduced toward zero with flow fluctuation increase.

Previous authors have used autocorrelation for studying the physics of stall initiation. It is well known that the casing wall pressure at the rotor blade leading edge is significantly affected by blade passing. Inoue et al. [9] eliminated the blade-passing waves by subtracting the phase-locked value and averaging values from the instantaneous signals. By taking autocorrelation of the time trace of a disturbance excluding the blade passing waves, they showed that the phase-locked pattern is periodic with blade spacing under the normal flow condition, but the periodicity collapses near stall inception. Their proposed detection parameter requires data acquisition over 200 or more rotor revolutions. This process results in the deterioration of sensitivity in the case of a rapid change in flow conditions.

The technique presented in this paper needs neither spectral analysis nor an autocorrelation calculation. Signal processing with this special artifice provides several attractive features as follows. First, computation is simple and suitable for real-time application. Second, the system is robust against manufacturing errors since the fluctuation caused by geometrical differences among rotor blades can be completely eliminated by comparing the pressure signals over the same blade pitches. Third, although signal noise may have adverse effects on the effectiveness of the method, it is still on the fail-safe side from the stall-preventing-system point of view. Moreover, since computation is carried out over one blade pitch, the condition of each blade pitch can be identified. This intriguing result, probably the first trial in archival as far as the authors know, is presented later. In the following sections, the performance of the index is shown in several experiments.

Indication Development in Axial Direction

The signal-processing technique mentioned in the previous section was applied to several dynamic experiments in which airflow was throttled at a constant rate from the design point to stall in ~4 s. Figure 8 shows a typical stalling pattern of the research compressor measured by pressure transducers at several axial locations, as illustrated in Fig. 5. Spike can be seen upstream of the leading edge in sensors *b*, *c*, and *d*. The abscissa is time normalized by revolution time of the rotor. The first appearance of a spike is set to zero in the time scale for stall transients hereafter as shown in Fig. 8.

Figure 9 shows results processed by the proposed technique. At higher airflow rates, the stall warning indices are constantly over 0.99 at the rotor leading edge sensor *f*, and slightly lower but nearly constant at the downstream sensor *j*. As the airflow rate is decreased, the first index degradation appears at sensor *j* and is followed by upstream sensor *i*.

About 100 rotor revolutions after the first appearance of index degradation at sensor *f*, the fully developed stall occurred, which was clearly recognized by the simultaneous significant index fluctuation at all sensors. The index at upstream sensor *d* did not show significant change until fully developed stall had occurred. As stated, closing speed of the throttle valve, the time scale, and its origin are same as in Fig. 8. The proposed technique provides stall warning sufficiently in advance of spike inception.

Since the flow in the tip region is very complex, it is not certain what flow mechanism causes the index degradation. The index degradation clearly advances upstream as the airflow rates decrease and the stall occurs shortly after it reaches the leading edge. Considering the diminished indices are uniquely observed only in the blade passage and obscure ahead of the rotor prior to stall initiation, it seems that they are not due to ordinary unsteadiness in the through flow. A detailed observation of raw pressure signals near the leading edge shows that fluctuations first appear in the

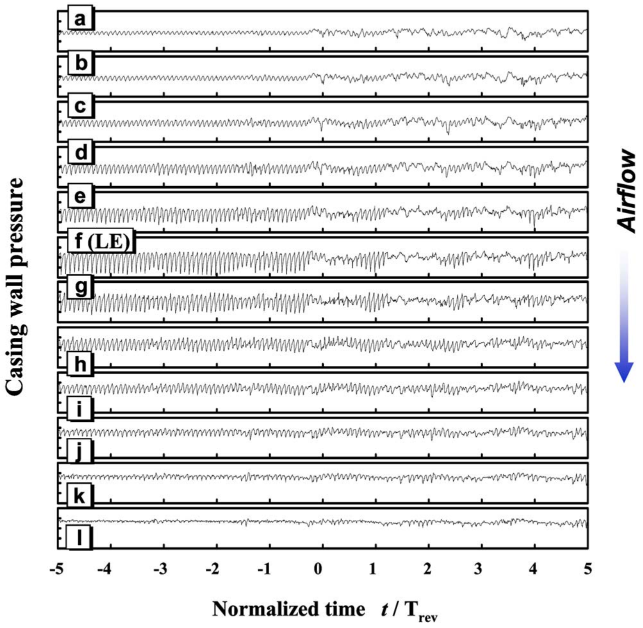

Fig. 8 Time history of pressure signal at axial locations

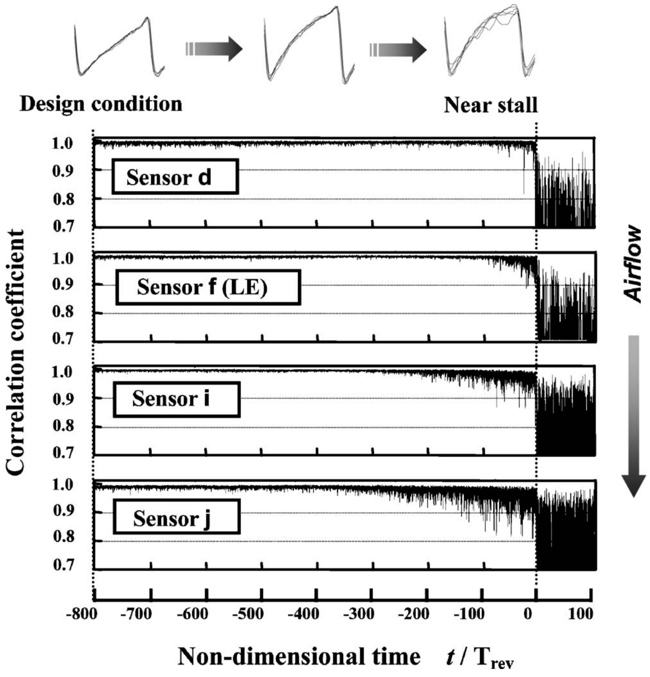

Fig. 9 Indication development in axial direction

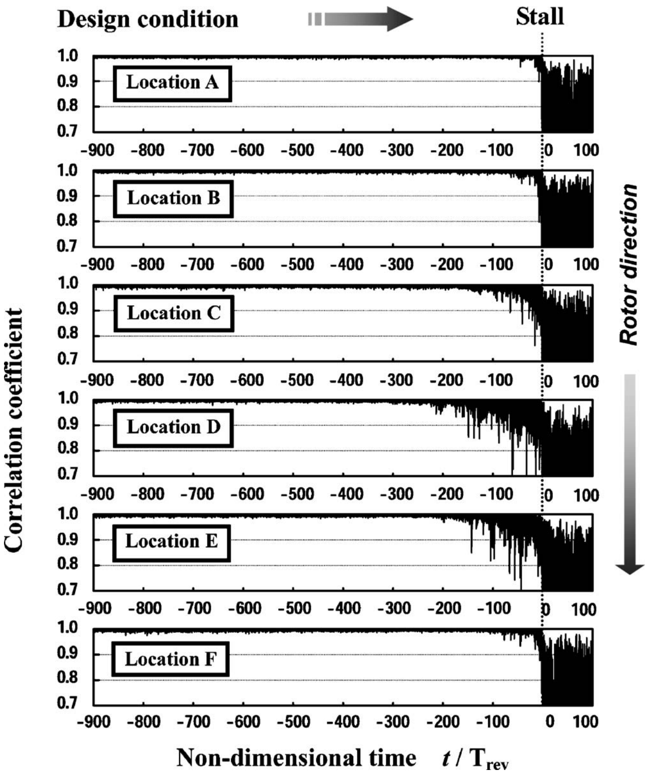

Fig. 10 Indication development in circumferential direction in uniform inlet flow

pressure side of the rotor blade rather than in the suction side as the airflow decreases. This indicates that the tip leakage flow is one probable cause of the index degradation.

Axial sensor location is an important factor for the stall warning system. As seen in Fig. 8, the pressure signals are less distinct near the midchord and the downstream regions. In Fig. 9, the index upstream of the leading edge is insensitive. On the other hand, the index near the leading edge shows no degradation until the operating point approaches the stall point. Hence, locations near the rotor leading edge are judged the most suitable axial sensor locations. Hereafter in authors' experiments, pressure transducers are placed on the casing wall at the rotor leading edge.

Indication Development in Circumference Direction in Uniform Inlet Flow

Another experiment was conducted to investigate circumferential index growth. Six pressure transducers were placed around the casing at the rotor leading-edge location shown in Fig. 4. The experiments consisted of two cases, one under normal conditions with uniform inlet flow and the other under distorted inlet conditions caused by a sector plate prefixed at the inlet bell mouth. The case with a uniform inlet flow is presented in this section, and the other is discussed in the next section.

Figure 10 shows the results of the uniform inlet flow condition. Closing speed of the throttle valve, the time scale, and the origin are same as in Fig. 8. The indices were constantly over 0.99 at all circumferential locations at higher airflow rates. Index degradation first appeared at location D as the airflow rate decreased. Signals at E and C, both adjacent to D, then showed the index degradation. As the airflow rate was further decreased, index degradation spread in both circumferential directions. Just after the index degradation was discernable at location A, deep stall initiates with significant fluctuation of indices at all circumferential locations simultaneously. Apparently, rotating disturbances, such as a modal wave or spike, will cause the index degradation at all circumferential locations. It is considered that diminished index spreading from its stationary region in both circumferential directions is not due to flow unsteadiness in the entire annulus but is due to a local disturbance existing on the duct.

Index Degradation Growth on Rotor Blades

The proposed signal-processing technique has an amazing feature that can individually identify the index of rotor blades. As explained previously, the indices are computed by using pressure signals of the current and one rotor revolution before of identical blade pitches. By appropriately sorting the indices of a particular circumferential location, the indices of each blade can be obtained. This unique characteristic of the technique is easy but useful since the state of individual rotor blades can be monitored by a single pressure transducer on the casing.

Location D, which exhibited the first and most significant index degradation in Fig. 10, was selected for analysis. Based on the electrical pulsations triggered once per rotor revolution, 12 rotor blades were identified from 1 through 12 in the order illustrated in Fig. 4. The indices at location D in Fig. 10 are sorted with blades 1–12, as shown in Fig. 11. The plots in Fig. 11 look sparse as compared to Fig. 10 because the number of plots for each blade in Fig. 11 is one-twelfth of that of location D in Fig. 10.

Time differences of index degradation appearance among the rotor blades were less distinct than that among duct circumferential locations. Careful examination of Fig. 11 reveals that the first index degradation appeared on blade 11.

Tip-Clearance Measurement

Since blade tip clearance is one of the most important factors that affect the flow mechanism in the tip region, comprehensive measurement of the tip-clearance gap was carried out on the research compressor. The average clearance against all rotor blades at case circumferential locations A, B, C, D, E, and F, and the clearance of each blade averaged around the casing were measured. They are shown in Fig. 12, respectively.

The maximum and minimum gap among the casing wall were location D and location A, respectively. These locations were 180 deg apart. The gaps among the casing circumferential locations vary smoothly and gradually. On the other hand, the gaps among the rotor blades had smaller differences and varied rather randomly. Based on these measurements, it is believed that the smooth gap distribution of the casing wall can be attributed to the assembling mismatch of the casing and the rotor and that the random gap distribution of the blades is due to manufacturing error. Dimension errors of blades are probably smaller than assembling mismatch, in general.

It is reasonable to conclude that development of degraded indices on the casing wall is consistent with the distribution of tip-clearance gap. It is natural to suppose that the locations with larger blade tip gap have more tip-clearance flow, which may cause greater disturbance in blade passages near stall. This data supports the assumption that the degraded indices may reflect disturbance caused by tip leakage flow interacting with the main flow.

Index Degradation Growth in Steady-State Experiment

In the previous dynamic experiments in which the throttling valve was closed automatically, it was unknown whether the index degradation grew by itself regardless of the throttling valve. Thus, it is suspected that the degree of index degradation may be dependent on airflow rate. A series of steady-state experiments at various flow rates was carried out to study index degradation versus flow rate. In Fig. 13, each figure shows how index degradation varies with airflow rate and rotor blade number at each duct location. The indices were averaged over 200 rotor revolutions. Averaged tip-clearance gaps at the circumferential locations are shown for reference in the center of the figure.

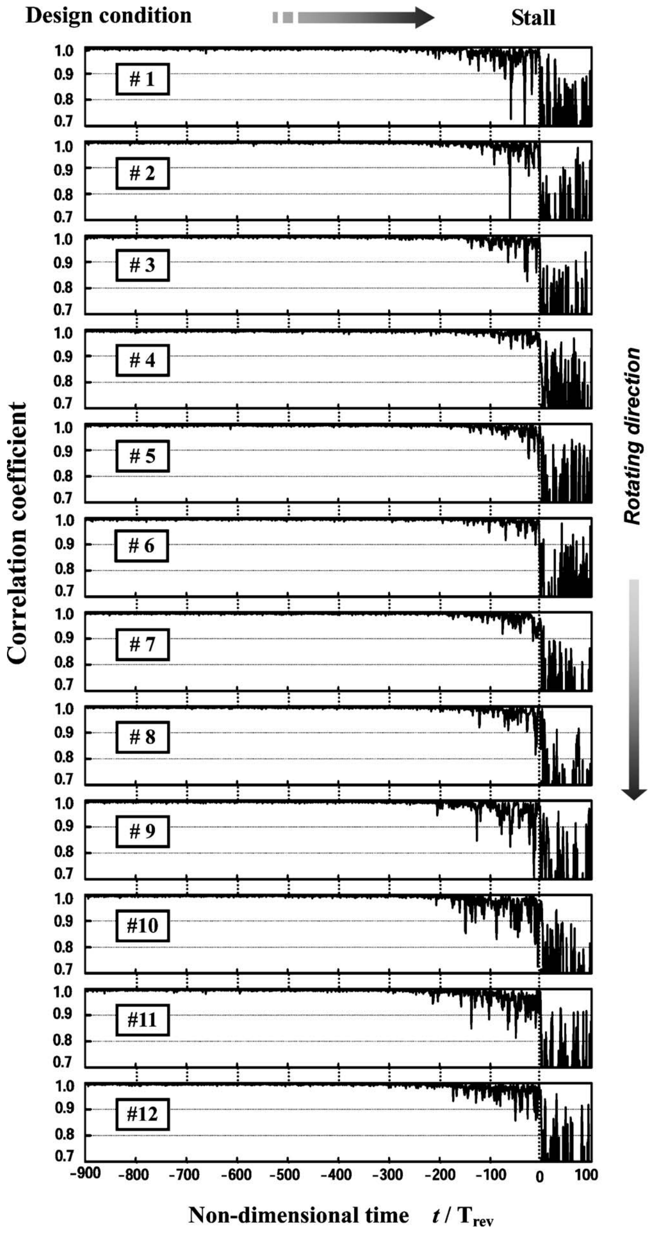

Fig. 11 Indication development on rotor blades

These steady-state experiments exhibited clearer and similar results to those of the previous transient experiments. Discernable index degradation first appeared at a flow coefficient of 0.30 at circumferential location D and rotor 11. That combination of the location and the blade has the largest tip clearance. As airflow rates decreased further, the indication grew to both adjacent locations C and E on the casing. It was confirmed that the index degradation does not grow by itself on the casing wall or rotor blades and is dependent on airflow rates. Near stall conditions at a flow coefficient of 0.28, location A, which had the minimum tip clearance, exhibited a slight depression in index value on rotor blades 9–12. However, at locations C, D, and E, which had larger clearances, there was considerable degradation on all rotor blades. Distributions of degraded indices on rotor blades were similar at those locations.

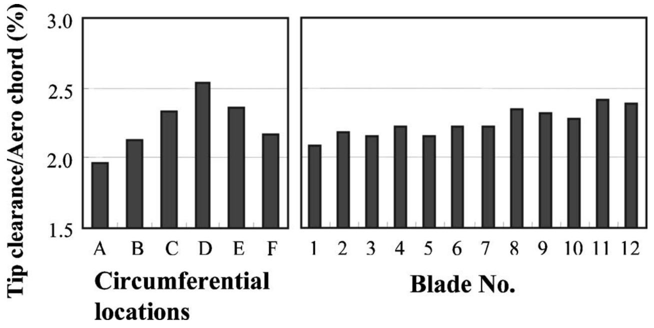

Fig. 12 Averaged tip-clearance gap

A possible explanation of index degradation with decreased airflow rates is as follows: (i) the index degradation appeared first at the circumferential location with the largest clearance when the rotor blade with the largest clearance passed that location, (ii) the indication disappeared when the blade left that location, and (iii) the region of degraded indices spread circumferentially on the casing in accordance with distribution of the tip clearance gap.

Indication Development in Distorted Inlet Flow

It is well known that inlet distortion reduces compressor stall margin. An experiment was conducted to study the capabilities of the proposed technique under distorted inlet conditions. A 90 deg sector plate was prefixed at the inlet bell mouth to provide severe distortion. The plate was placed at circumferential location A, which had the smallest tip clearance so that the effect of the inlet distortion could be separated from that of the tip clearance.

The results of the experiment with the distorted inlet flow are shown in Fig. 14. The flow coefficient of stall occurrence increased from 0.28 in normal inlet conditions to 0.295. The indices at location B show significant degradation even at the design flow coefficient. It is natural to interpret this as a result of distortion caused by the sector plate. The index degradation then started to appear in the rotating direction as the flow coefficient decreased. This is quite different from that of the uniform inlet flow in which the index degradation developed in both circumferential directions from the largest tip-clearance location. It seems that the effect of the tip-clearance gap was not apparent.

Severe disturbances caused by the 90 deg sector plate resulted in local significant index degradation at limited duct regions, which did not seem critical to stall. The regions of index degradation developed with reduced airflow rates and, when most locations showed degradation, stall initiated.

Flow-Field Measurement in Inlet Distortion

It is interesting to note that index degradation developed circumferentially in different ways. In uniform inlet flow, index degradation developed in both directions. In distorted inlet flow, index degradation developed in the rotor-rotating direction. In order to study the distorted flow condition, three-hole-yaw-meter measurements were made at 0.28 aero chords ahead of the rotor blade's leading edge. Although the flow field near the tip region was of interest, the probe was placed at 90% blade span from the hub due to large measurement errors in the tip region. Since the distortion effect was considered much larger than the tip-clearance effect in this experiment, the sector plate at the inlet bell mouth was relocated by 10 deg intervals with the probe prefixed on the casing.

Figure 15 shows the axial airflow velocity, circumferential airflow velocity, and incidence distribution at the rotor blade front for 270 deg of the casing annulus where stable measurements were obtained. A fairly smooth distribution of axial velocities at high flow coefficients becomes distorted with a flow coefficient decrease. Axial airflow velocity exhibits a marked depression at the circumferential location of the annulus just outside of the plate blockage at every flow coefficient. Circumferential airflow velocities are negative at several circumferential locations of the rotor just outside of the plate blockage and increase monotonically in the rotor-rotating direction to the maximum point of the rotor just

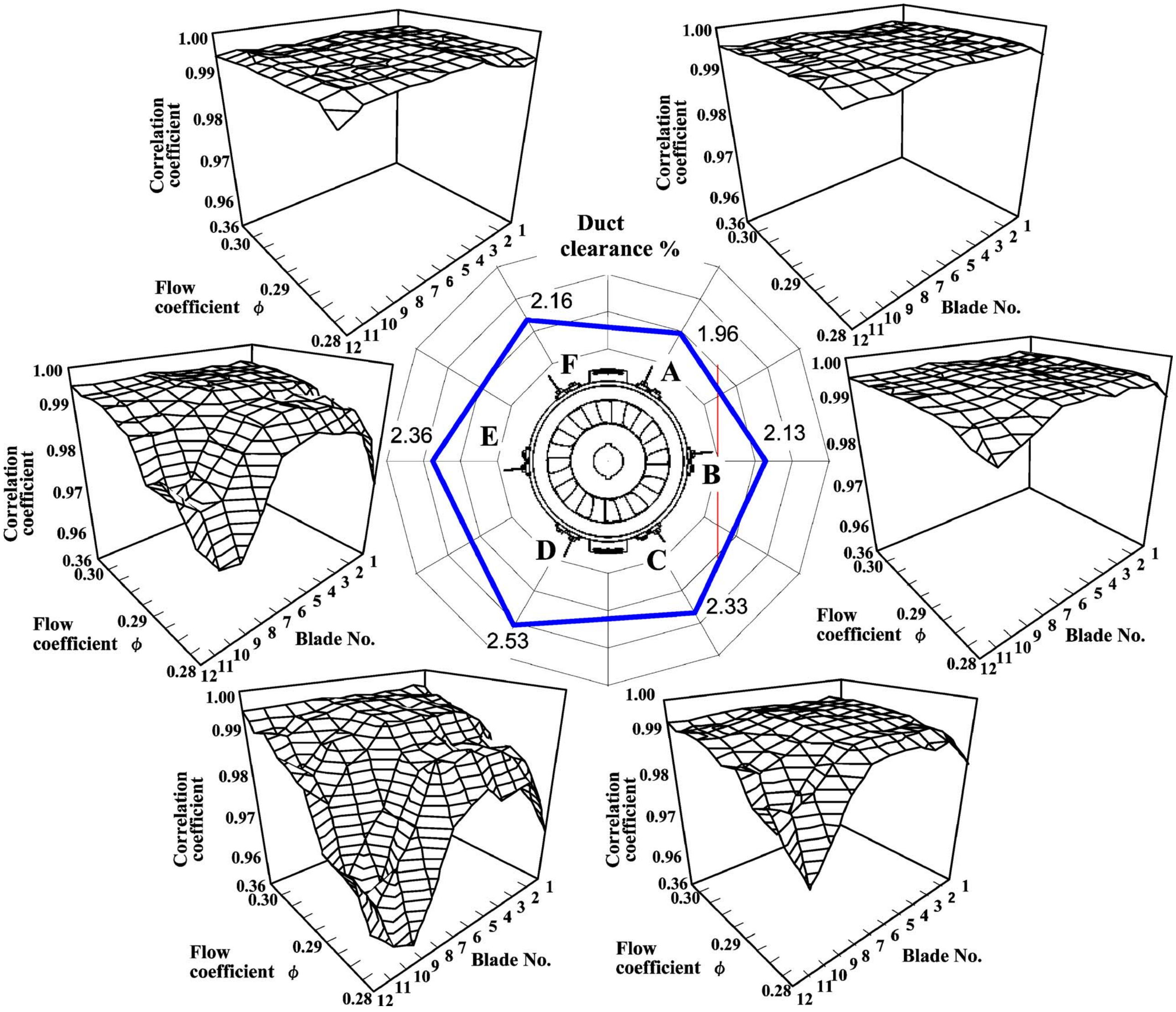

Fig. 13 Steady-state experiments with airflow rates

before the plate blockage at every flow coefficient. Because air flows in order to become uniform by compensating for the lack of airflow behind the plate blockage, it is reasonable to have such distribution of circumferential airflow velocity at the rotor front. Hence, the blade incidences exhibit the maximum at the location just outside of the rotor plate blockage and decrease in the rotor-rotating direction at every flow coefficient. The flow incidences of the blades at all circumferential locations become higher as the axial velocity decreases.

In order to compare the results of a flow-field survey with the index degradation, the proposed signal process was performed at relative circumferential locations *i* through *ix* at each airflow rate. The upper figures in Fig. 16 show flow incidence distribution at circumferential locations at design, medium, and near-stall flow conditions, respectively. The lower figures in Fig. 16 show computed indices at the same locations over 200 rotor revolutions. Each plot is averaged over one rotor revolution.

The locations with higher rotor incidence exhibit much larger index degradation. It is observed that, when the rotor incidence becomes >4 deg, the index degrades everywhere except locations *viii* and *ix* at near-stall conditions. The fact that the region of rotor incidence >4 deg expanded in the rotor-rotating direction as the airflow rates decreased explains why index degradation developed in the rotor-rotating direction in the case of distorted inlet conditions.

Discussion

The ultimate objective of this study was to establish a stall warning system for active stall control that may reduce the current excessive surge margin requirement for compressor design with current control means. In order to achieve this objective, it is essential to develop reliable techniques to recognize proximity to stall.

Motivated by the results of previous researchers, which showed that tip-leakage flow becomes perpendicular to the axial direction at near stall conditions, a unique stall-warning technique was proposed and tested on a single-stage low-speed compressor. The technique is intended to detect the tip-leakage trajectory by capturing pressure fluctuation caused by interactions between the tip-leakage vortex and the main flow. Time histories of current and one revolution before casing wall pressures over each blade pitch at the rotor blade leading edge were compared and their correlation was computed. When the interaction between the leakage flow and the main flow is present near the leading edge, correlation degradation is expected.

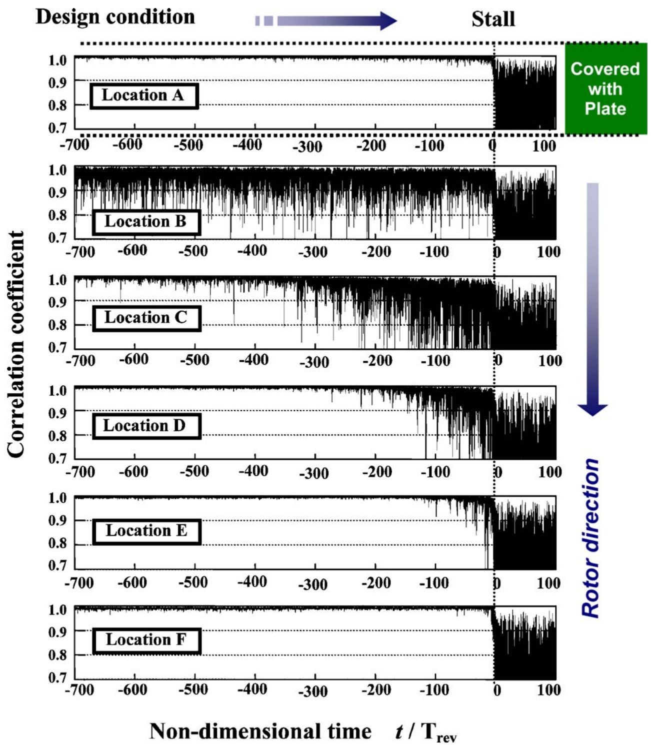

Fig. 14 Indication development during inlet distortion

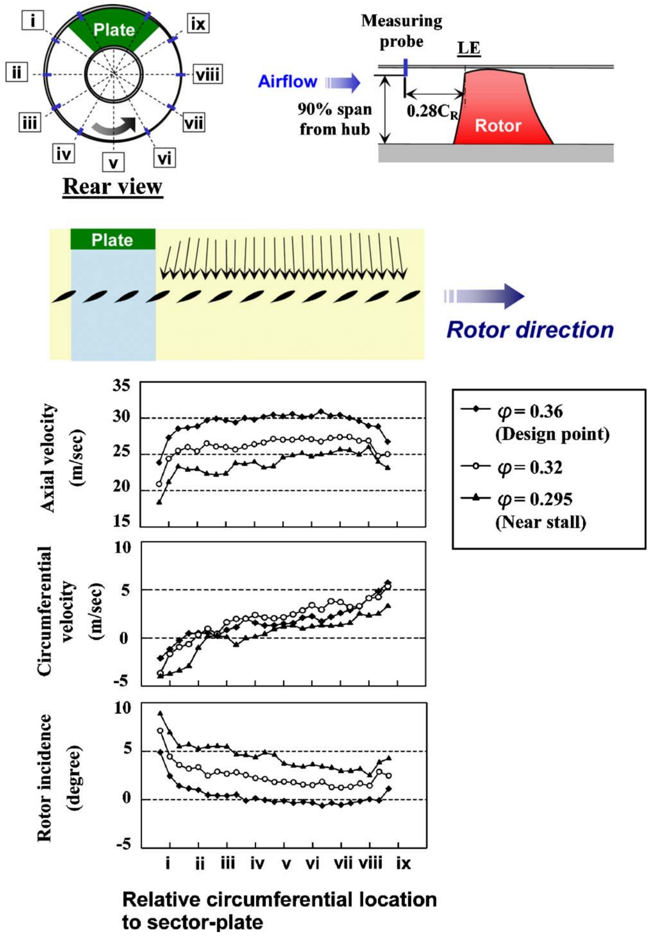

Fig. 15 Flow-field measurement during inlet distortion

Axially located pressure transducers revealed that the correlation degradation first appeared at the midchord location and advanced toward the leading edge with a decrease in flow coefficient as expected. The degree of the degradation monotonically increased with flow coefficient decrease. The most promising feature of this technique is that it has the potential to generate a stall-warning signal sufficiently in advance of spike inception so that stall avoidance actuation may have enough time to respond.

In the experiments with uniform inlet flow, circumferentially located sensors at the leading edge showed that correlation degradation started at the location with the largest tip clearance. As the flow coefficient was reduced, the correlation degradation developed circumferentially in both directions according to the magnitude of the tip clearance. Whether or not the disturbance was rotating in the region of degraded indices during their development along the casing was not confirmed.

In the experiments of the circumferentially distorted inlet condition, the correlation degradation existed at the location of the rotor just going out of the plate blockage even at design condition. As the flow coefficient was further reduced, the region of correlation degradation expanded in the rotor-rotating direction as opposed to circumferentially outward as in the uniform inlet flow condition. It was found that the degradation was related to rotor incidence.

In both normal and distorted inlet conditions, stall does not occur even with the significant degradation existing in partial circumferential location. The correlation degradation is the necessary condition of rotating stall, not the sufficient condition. This index reflects the stall risk at the location. It has the potential of providing a stall-warning signal; however, since the degree of the index degradation depends on tip clearance or rotor incidence, a simple threshold criteria at an arbitrary circumferential location does not work. Several sensors must be placed around the casing annulus.

The correlation degradation grew monotonically and rather continuously with reduction of the flow coefficient. Just before stall, correlation degradation was noted at all circumferential locations. Correlation degradation at the rotor leading edge reflects the local stall risk. Stall suppressing measures should be performed before the necessary conditions of rotating stall occurrence appear at all circumferential locations.

Multiple sensors and a sophisticated algorithm that simultaneously take account of sensor measurements are required to generate a reliable stall-warning signal. There are various factors that may cause correlation degradation, such as tip clearance, rotor incidence, sensor noise, etc. The effects of these factors must be carefully examined. The next step in further exploration of the capability of the proposed technique would require experiments on a high-speed multistage compressor.

Conclusion

1. A unique stall-warning technique based on index degradation computed from pressure signals from high-response transducers mounted on casing at the rotor leading-edge location was proposed. Test results conducted on a research compressor show that the proposed technique might have the capability of generating a stall-warning signal sufficiently in advance of spike inception. It is expected that this may help to reduce current excessive stall margin requirements for compressor design based on the worst-case scenario.
2. It was observed that index degradation shifted upstream with airflow rate decrease in an experiment with axially located pressure transducers. The flow mechanism that causes index degradation is not clear since the flow in the tip region is very complex. Pressure disturbances due to the interactions between the tip-leakage flow and the main flow is a leading candidate for index degradation.

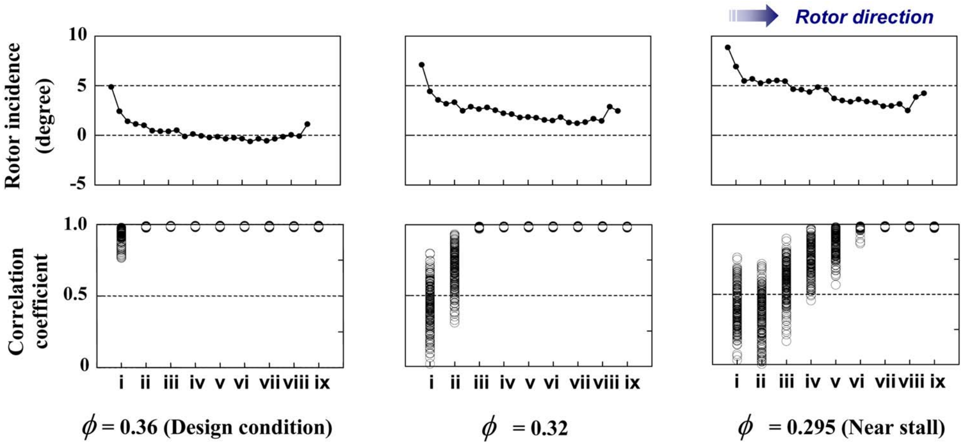

Fig. 16 Rotor incidence and indication development during inlet distortion

3. In the uniform inlet flow condition, the degree of index degradation depends on tip clearance. Index degradation first appears at the casing circumferential location with the largest radius when the rotor blade with the smallest span reaches the location and disappears when the rotor blade passes that location. With airflow decrease, the region of index degradation grows in both circumferential directions.
4. In the condition in which inlet flow is distorted by a sector plate at the bell mouth partially blocking airflow, the index degradation exists from the design airflow condition at the circumferential location of the rotor blade just outside of the plate blockage. Local index degradation at limited duct regions, even if significantly large, does not seem critical to stall. In contrast to the uniform flow case, the region of the index degradation expands only in the rotor rotating direction with airflow decrease.
5. Time-averaged measurements of rotor incidence show that incidence is maximum at the circumferential location of the rotor just outside of the plate blockage and lessen in the rotor rotating direction. This indicates that index degradation also depends on rotor incidence.
6. These observations suggest that the proposed signal process is sufficient for providing a proper stall risk index. The degree of the index degradation depends on various factors, such as flow coefficient, tip clearance, and rotor blade incidence. In order to obtain a reliable stall warning signal in practical use, these effects must be carefully examined.

Nomenclature

av = average over 1 blade pitch
C_R = chord of rotor blade
LE = leading edge
n = current sampling point
$n-1$ = a point 1 rotor revolution before current sampling point
P = pressure
R = correlation coefficient

$$R=\frac{\int (P(t)-P_{av,n})(P(t-\tau)-P_{av,n-1})dt}{\sqrt{\int (P(t)-P_{av,n})^2dt}\sqrt{\int (P(t-\tau)-P_{av,n-1})^2dt}}$$

t = time
T_{rev} = revolution time of compressor rotor
U = blade tip speed
ρ = air density
ϕ = airflow coefficient
ψ = pressure-rise coefficient (inlet total to exit static divided by $1/2\rho U^2$)
τ = one rotor revolution period for time lag

References

[1] Epstein, A. H., Efowcs Williams, J. E., and Greitzer, E. M., 1986, "Active Suppression of Aerodynamic Instabilities in Turbomachines," AIAA Paper No. AIAA86-1994.
[2] Camp, T. R., and Day, I. J., 1998, "A Study of Spike and Modal Stall Phenomena in a Low-Speed Axial Compressor," Transaction of the ASME, 120, pp. 393–401.
[3] Hoying, D. A., Tan, C. S., and Greitzer, E. M., 1998, "Role of Blade Passage Flow Structures in Axial Compressor Rotating Stall Inception," ASME Paper No. 98-GT-588.
[4] Wernet, M. P., Zante, D. V., Strazisar, T. J., John, W. T., and Prahst, P. S., 2002, "3-D Digital PIV Measurements of the Tip Clearance Flow in an Axial Compressor," ASME Paper No. GT-2002-30643.
[5] Tryfonidis, M., Etchevers, D., Paduano, J. D., Epstein, A. H., and Hendricks, G. J., 1995, "Prestall Behavior of Several High-Speed Compressors," ASME, 117, pp. 62–80.
[6] Day, I. J., Breuer, T., Escuret, J., Cherrett, M., and Wilson, A., 1999, "Stall Inception and the Prospects for Active Control in Four High-Speed Compressors," ASME, 121, pp. 18–27.
[7] Hoenen, H., and Arnold, T., 2003, "Development of a Surge Prediction System for Multi Stage Axial Compressors," IGTC2003Tokyo TS-040.
[8] Adamczyk, J. J., Celestina, M. L., and Greitzer, E. M., 1993, "The Role of Tip Clearance in High-Speed Fan Stall," ASME, 115, pp. 28–39.
[9] Inoue, M., Kuroumaru, M., and Ando, Y., 1993, "Pressure Fluctuation on Casing Wall of Isolated Axial Compressor Rotors at Low Flow Rate," ASME, 115, pp. 19–27.

Effect of Blade Passage Surface Heat Extraction on Axial Compressor Performance

P. N. Shah[1]
e-mail: parthiv@alum.mit.edu

C. S. Tan
e-mail: choon@mit.edu

Gas Turbine Laboratory,
Massachusetts Institute of Technology,
Cambridge, MA 02139

Axial compressor performance with heat extraction via blade passage surfaces (compressor cooling) is compared to its adiabatic counterpart, using computational experiments and mean line modeling. For a multistage compressor with an adiabatic design point, results at fixed corrected rotor speed indicate that, if available, compressor cooling would (i) raise the overall pressure ratio (at a given corrected flow), (ii) raise the maximum mass flow capability, (iii) raise the efficiency, defined as the ratio of isentropic work for a given pressure ratio to actual shaft work, and (iv) provide rear stage choking relief at low corrected speed. In addition, it is found that, if available, cooling in the front stages is better than in the rear stages. This is primarily a thermodynamic effect that results from the fact that, for a given gas, the compression work required to achieve a given pressure ratio decreases as the gas becomes colder. Heat transfer considerations indicate that the engineering challenges lie in achieving high enough heat transfer rates to provide a significant impact to the compressor's performance.

[DOI: 10.1115/1.2372776]

Introduction

In this paper we investigate the effect of blade passage surface heat removal on the performance of an axial compressor. We motivate our study by providing the example of a turbomachinery-based propulsion system for a flight vehicle having a low-to-high flight Mach number (0 to 4+) mission profile, where thermal management is a primary design concern. The beneficial effect of heat removal in the front end of the turbomachine (*precooling*, via heat exchange or mass injection) on specific thrust has been discussed by several authors [1–5]. We explore a novel concept, in which heat removal occurs in the compressor itself via the blade passage surfaces (*compressor cooling*), in order to extract a thermodynamic and aerodyanamic benefit. In this study we focus on the effect that this heat removal would have on axial compressor performance.

Blade passage simulations using computational fluid dynamics (CFD) indicate that the standard bulk figures of merit for blade passage flows, namely, nondimensional total pressure reduction and trailing edge deviation are improved with the removal of heat across blade passage surfaces. We quantify the beneficial effects of cooling in terms of incidence, inlet Mach number, and a new nondimensional heat transfer parameter, q^*, defined as the rate of heat removal normalized by relative inlet stagnation enthalpy flux. We then create a representative set of generic performance "rules" for blade passage flows with surface cooling, and apply these rules to the mean line analyses of a one-stage and an eight-stage compressor, both with adiabatic design points. Our results indicate that the presence of surface cooling results in the following:

1. An increase in the overall pressure ratio (at a given corrected flow).
2. An increase in the maximum mass flow capability
3. An increase in the efficiency, η, defined as the ratio of isentropic work for a given pressure ratio to actual shaft work (a brief discussion of an alternate, "nonadiabatic" efficiency, η_{na}, is provided in Appendix B)
4. Rear stage choking relief at a low corrected speed

Results from a three dimensional (3D) calculation of the transonic NASA Rotor 35 geometry with blade and casing surface cooling are in agreement with these conclusions.

In addition, we find that, if available, a given amount of nondimensional compressor cooling, q^*, defined as the rate of heat removal normalized by compressor inlet stagnation enthalpy flux, will yield superior performance in the front of the compressor versus in the rear. This is primarily a thermodynamic effect that comes from the fact that by cooling the air in the front, all stages downstream subsequently do work on colder air, which can be compressed to a higher pressure ratio for a given amount of work input.

Heat transfer considerations, the details of which are provided in Appendix A, underscore the importance of blade solidity (nominally, the ratio of the blade wetted area to the flow passage annulus area) and the ratio of wall temperature to free stream stagnation temperature, to achievable values of q^* in the blade passage. Clearly, higher q^* values may be achievable in the rear of a multistage compressor, where blade solidities tend to be higher and the temperature ratio between the gas path and coolant may be highest. The fact that higher values of q^* may be available in the rear means that this effect competes with the earlier finding that, thermodynamically, a given amount of cooling in the front is better than in the rear. This indicates that for a given compressor, an optimal stagewise cooling distribution should exist based upon cycle and compressor geometry, leaving an open design problem for future work.

Motivation: Low-to-High Flight Mach Number Mission

Low-to-high (4+) Mach number flight poses unique challenges to the aircraft system designer. As supersonic flight Mach numbers increase, the large stagnation temperature rise at the engine inlet imposes the need to keep aircraft system components to within acceptable temperature limits. This design requirement is loosely called thermal management, and applies to both the airframe and power plant.

---

[1] Author to whom all correspondence should be addressed.

Contributed by the International Gas Turbine Institute (IGTI) of ASME for publication in the Journal of Turbomachinery. Manuscript received October 1, 2004; final manuscript received February 1, 2005. IGTI Review Chair: K. C. Hall. Paper presented at the ASME Turbo Expo 2005: Land, Sea and Air, Reno, NV, June 6–9, 2005, Paper No. GT2005-68815.

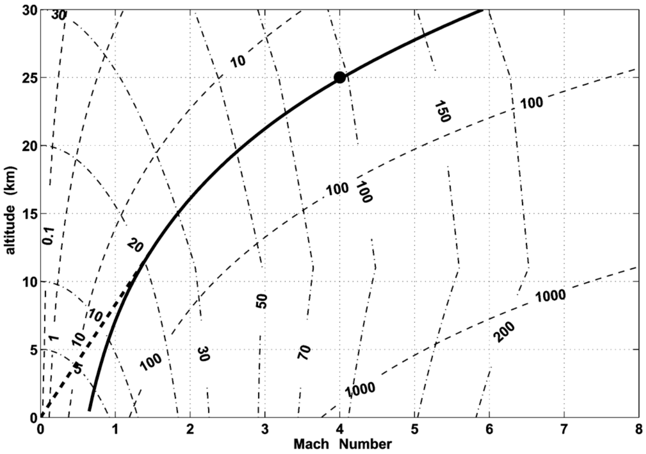

Fig. 1 Selected flight path. The heavy, broken line represents low Mach number trajectory. The heavy, solid line is $\rho u^2/2 = 28.4$ kPa, representing a high Mach number trajectory. Faint broken lines are isocontours of $\rho u^2/2$ in kPa. Faint dash-dotted lines are isocontours of specific energy, in km.

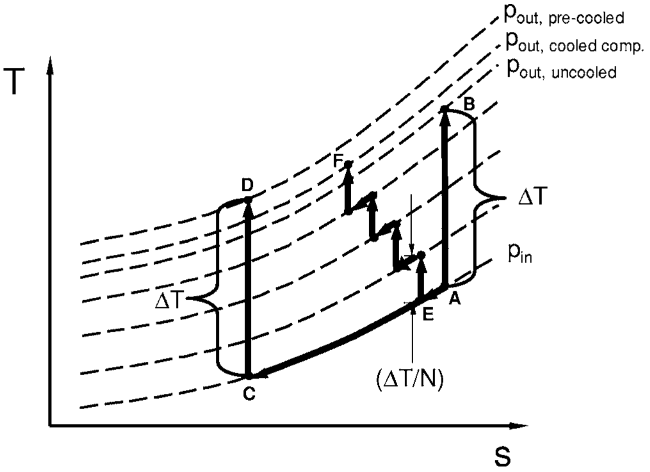

Fig. 2 Temperature, T versus entropy, s, for isentropic compression (A–B), isentropic compression with isobaric precooling (A–C–D), and interspersed isobaric cooling and isentropic compression in N steps (A–E–· · ·–F).

Thermal management is a complex vehicle-system level problem that requires a detailed, mission-specific analysis. In this paper, we do not tackle the problem of thermal management; rather, we use a simple mission profile to illustrate the need for thermal management in a low-to-high flight Mach number aircraft. We define a mission profile as the trajectory definition in the altitude-Mach number plane. Several types of representative mission profiles could be considered for a wide flight Mach number vehicle: (1) a minimum fuel to climb mission may be appropriate for a two-stage-to-orbit (TSTO) vehicle, since minimizing fuel would permit the second stage to maximize payload; (2) a minimum time to climb mission may be appropriate for an advanced fighter aircraft; (3) a constant dynamic pressure mission may be appropriate for vehicle structural reasons. For simplicity, we select a mission profile based upon a nearly constant dynamic pressure ($\rho u^2/2$) trajectory of 28.4 kPa (0.28 atm) at supersonic flight Mach numbers, as shown in Fig. 1. At "lower" Mach numbers, the trajectory is defined by the broken line, while at "high" Mach numbers the trajectory follows the solid line of constant $\rho u^2/2$. The dynamic pressure selected for the high Mach number portion of the trajectory corresponds to $M=4$ at an altitude of 25 km, and falls within design ranges typically given in the literature [6].

As the aircraft climbs, its Mach number increases, leading to increasing free stream total temperature (T_t) along the flight path. Free stream total temperatures at Mach 3, 4, and 5, are approximately 600, 900, and 1350 K, respectively. The rapid increase in T_t with Mach number is the primary reason that a single-spool turbojet (SSTJ) cycle fails to produce thrust at high Mach numbers. Current material temperature limits in both the compressor, and especially the turbine limit the production of thrust by reducing the heat addition capability of the fuel in the combustor. Cooling the air entering the compressor is one way to regain this heat addition capability, and leads to a cycle concept called the *precooled* turbojet (PCTJ). Typically, precooling of the inlet air would be achieved using a heat sink (such as a cryogenic fuel), or via mass injection (e.g., water or liquid oxygen). Variants of PCTJ cycles, both with and without afterburning, have been studied by several authors [1–5]. The general conclusion in the literature is that cooling of the order of several tens of degrees to a few hundred degrees Kelvin can theoretically result in enough specific thrust enhancement to push conventional turbomachinery out to flight Mach numbers of 4 to 6. The authors do cite numerous practical hurdles that must still be overcome in order to introduce this concept into an engine, such as weight penalties associated with precooler hardware.

Anticipated Effect of Compressor Cooling

Despite the practical challenges associated with the PCTJ, this propulsion concept provides us with a starting point for studying the potential cycle benefits of compressor cooling. To the authors' knowledge, there exist few or no examples in the literature of cooling within the compressor via blade passage surface heat extraction. It is first necessary, then, to compare the concept of the PCTJ to compressor cooling. The temperature-entropy diagram in Fig. 2 compares standard ideal compression (A–B) to constant pressure pre-cooling (A–C) followed by isentropic compression (C–D). The comparison is made on an equal work basis, meaning ΔT is the same for the isentropic compression process in both cases (a perfect gas is assumed). Process (A–E· · ·–· · ·–F) superimposes a third conceptualization, the case of N constant-pressure cooling steps interspersed with N equal work steps. It is implied by the temperature rise of $\Delta T/N$ that the total compression work for all three processes (A–B), (A–C–D), (A–E–· · ·–F) is equal. It is argued by the authors that process (A–E–· · ·–F) could represent: (1) an N stage compressor with constant-pressure cooling in an inlet guide vane and the first N-1 stators, or (2) perhaps, in the limit as N approaches infinity, a single stage device with a continuous cooling scheme. Both descriptions will be generally referred to as *cooled compressors*.

Under the perfect gas assumption, two lines of constant-pressure diverge on a T-s diagram with increasing temperature or entropy. The implication of this fact on the three processes shown is that the pressure rise capability of the *precooled compressor* is greatest, followed by the *cooled compressor* (schematically similar to intercooling), and finally the standard (adiabatic) compressor, because compression work done at a lower temperature results in a greater pressure rise. This idealized model fails, however, to account for the fact that a *real* precooler may create a significant loss of stagnation pressure, and that cooling within blade passage surfaces may have an additional *aerodynamic* benefit. Assuming that a cooled compressor introduces no new gas-path geometry, and hence no new loss generating solid boundaries, the cooled compressor underperformance may be mitigated or even reversed when compared to a real precooler. (In addition to the loss penalties associated with a real precooler, significant system weight penalties from heat exchanger hardware are also seen as a technological challenge, requiring lightweight heat exchanger materials to be surmounted [2]. In this paper we do not address the modeling of system weight. It would be necessary in any vehicle-system level study.)

The natural point of departure from this conceptual example is to examine the implication of blade surface heat extraction on compressor performance, in order to determine whether it may be a viable candidate for a low to high flight Mach number mission. In the remainder of the paper we use CFD experiments and mean-line analysis to model a *cooled compressor*.

Blade Passage Aerodynamics: 2D Cascade CFD

Two-dimensional CFD experiments using FLUENT have been performed on two different cascade geometries in order to produce bulk aerodynamic performance figures of merit. The two selected geometries are "representative" of airfoils used in multistage compressors. The first airfoil geometry is based upon a NACA 65 airfoil series blade definition, with an inlet and exit metal angle of $\chi_{\text{in}}=38°$ and $\chi_{\text{out}}=0°$, respectively, and a cascade solidity of 0.75. The second geometry has $\chi_{\text{in}}=51°$, $\chi_{\text{out}}=14°$, and solidity of 1.0, similar to the midspan metal angles of the NASA/GE E^3 compressor.

For both cascades, matrices of cases have been assembled by varying the flow inlet angle and the ratio of upstream total pressure to downstream static pressure. For cascade 1, cases have been generated using (1) adiabatic and (2) constant heat flux boundary conditions (BCs). For cascade 2, cases have been generated using (1) adiabatic airfoil walls and (2) a wall temperature BC for cooling equal to one-half the free stream value. We define a nondimensional cooling rate as the heat removed from the flow normalized by the inlet stagnation enthalpy flux:

$$q^* = \frac{\dot{Q}}{\dot{m}h_{t,\text{in,bl}}} = \frac{\Delta h_t}{h_{t,\text{in,bl}}} = \frac{\Delta T_t}{T_{t,\text{in,bl}}} < 0 \quad \text{(for cooling)} \tag{1}$$

Integrated bulk flow properties have been area or mass averaged one chord length upstream of the airfoil leading edge (inlet) and one chord length downstream of the trailing edge (outlet). For example, velocities have been mass-averaged, while pressures have been area-averaged. (It was found that the differences between area averaging and mass averaging were not appreciable in terms of the essential conclusions of this paper.) All of the results have been interpolated to a given set of inlet Mach numbers in order to produce bulk performance data. The primary figures of merit used to characterize bulk blade passage performance are nondimensional total pressure reduction (*loss buckets*), ω, and deviation (difference between air and blade metal exit angle), δ, defined as:

$$\omega = \frac{p_{t,\text{in}} - p_{t,\text{out}}}{p_{t,\text{in}} - p_i} \tag{2}$$

$$\delta = \beta_{\text{out}} - \chi_{\text{out}} \tag{3}$$

(Strictly speaking, the term *loss bucket* should be used with adiabatic blade-to-blade flows only, as in these flows entropy generation, i.e., lost work, is tied to loss a of total pressure alone. We use the term loss bucket per its conventional definition of total pressure reduction divided by inlet dynamic head.) Our computations reveal that cooling impacts blade passage flows in the following ways:

1. For a given value of q^* at a given inlet Mach number, cooling benefits performance by producing a relatively uniform reduction in ω across the loss bucket.
2. For a given value of q^* the reduction in ω increases as inlet Mach number increases.
3. The effect of reversible cooling on a one-dimensional channel flow given by

$$\frac{dp_t}{p_t} = -\frac{\gamma M^2}{2}\frac{dT_t}{T_t} \approx -\frac{\gamma M_{\text{in}}^2}{2} q^* \quad (|q^*| \ll 1) \tag{4}$$

provides a reasonable first approximation to the effect of cooling on total pressure change at *low* inlet Mach numbers, whereas at *high* subsonic inlet Mach numbers (e.g., $M_{\text{in}} \sim 0.8$), cooling appears to have a more beneficial impact above and beyond the bulk cooling of the working fluid. This is deduced by comparing the channel flow sensitivity coefficient [7] given in Eq. (4) to computed differences between cooled (na) and adiabatic (a) fractional total pressure change, $[(\Delta p_{t,\text{na}} - \Delta p_{t,a})/p_t]$, divided by cooled fractional temperature change, $\Delta T_{t,\text{na}}/T_t$.

Table 1 Average effect of $q^*=-0.001$ on flow turning for cascade 1, across a range of incidences

M_{in}	$\Delta\beta_{\text{na}}=-\Delta\delta_{\text{na}}$
0.4	0.1 deg
0.8	0.25 deg

4. Cooling increases the flow turning (or lowers δ). Table 1 summarizes the average level of change of flow turning for cascade 1, for $q^*=-0.001$.
5. Cooling reduces the exit Mach number. The effect of a Mach number reduction downstream (in most compressors) will be to reduce the inlet Mach number into the next blade row, thereby potentially reducing losses associated with locally supersonic regions on the blade.

$$\frac{dM^2}{M^2} = \frac{(1+\gamma M^2)\left(1+\frac{\gamma-1}{2}M^2\right)}{1-M^2}\frac{dT_t}{T_t} - \frac{2\left(1+\frac{\gamma-1}{2}M^2\right)}{1-M^2}\frac{dA}{A} \tag{5}$$

From the sensitivity coefficients for one-dimensional channel flow [7,8] in Eq. (5), we see subsonic cooling has the effect of *directly* reducing the Mach number (just as heating does the opposite, driving flow towards sonic conditions) by reducing the total temperature, and *indirectly* reducing the Mach number by an increase in effective exit flow area caused by a reduction in deviation.

6. Cooling decreases the exit stagnation temperature. This has a favorable effect on the downstream blade rows, as less work is required to compress colder air to a given pressure ratio.

Figure 3 shows the adiabatic and cooling wall BC ($T_{\text{wall}}/T_{t,\text{in}}=0.5$) *loss bucket* for cascade 2, at a low (0.4) and high (0.8) Mach number. Corresponding values of q^* for the nonadiabatic

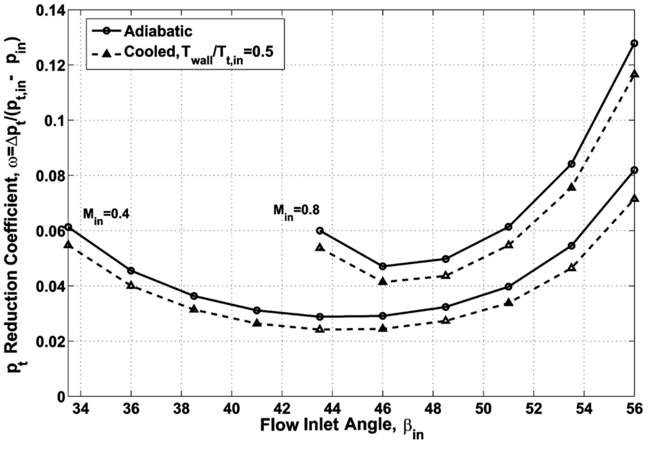

Fig. 3 Total pressure reduction coefficient, ω, versus the flow inlet angle at low (0.4) and high (0.8) inlet Mach number, for cascade 2. Solid lines are adiabatic wall BC; dashed lines are $T_{\text{wall}}/T_{t,\text{in}}=0.5$.

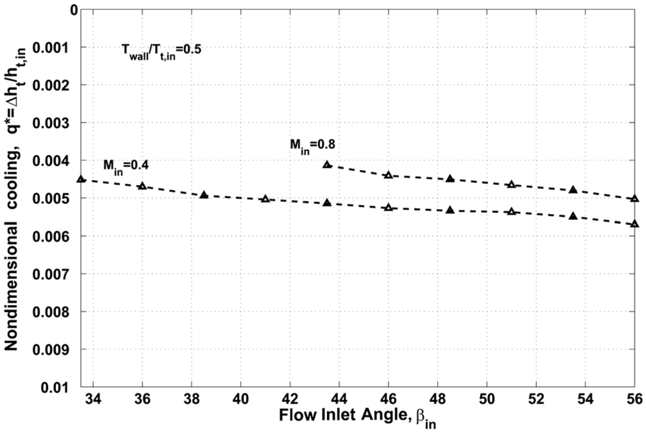

Fig. 4 Nondimensional cooling, q^* versus the flow inlet angle at low (0.4) and high (0.8) inlet Mach number, for cascade 2, cooled case, $T_{\mathrm{wall}}/T_{t,\mathrm{in}}=0.5$

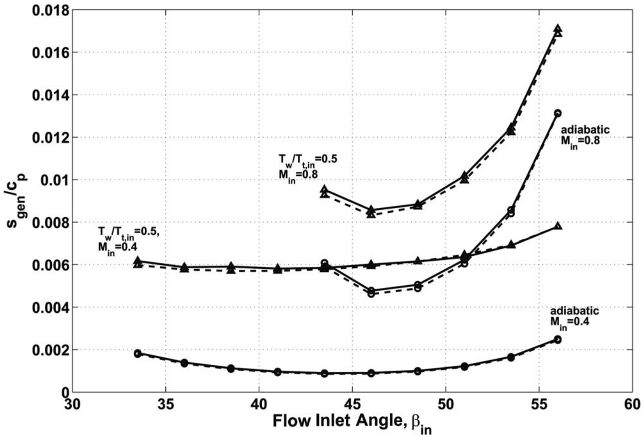

Fig. 5 Cascade 2, computed entropy generation versus incidence at low (0.4) and high (0.8) inlet Mach number using net entropy flux method (solid lines given by Eq. (6)) and direct volume integration (dashed lines given by Eq. (7)). Adiabatic and cooled ($T_{\mathrm{wall}}/T_{t,\mathrm{in}}=0.5$) cases shown.

case are shown in Fig. 4. From these plots we see that at the given wall temperature BC, there is a fairly uniform reduction in ω across the cascade operating range. As q^* shows a relatively slight variation for a given Mach number, we can conclude that this is consistent with oberservation 1. It is also apparent that the reduction in ω at a given wall temperature ratio increases with inlet Mach number. Further, as absolute values of q^* are shown to be lower at the higher Mach number, the benefit from cooling at a *fixed* q^* is further pronounced with increasing Mach number.

Observation 3 indicates that the reduction in ω from cooling occurs due to both compressibility effects (reversible cooling) and from the rebalancing of entropy generation (loss) inside the flow field with entropy removal across blade surfaces. The constant wall temperature BCs on the airfoil surfaces of cascade 2 allow us to easily compute the entropy flux across the blades themselves. From this, it is possible to compute the entropy generation, by considering the second law of thermodynamics over the computational domain, namely,

$$\frac{s_{\mathrm{gen}}}{c_p}=\frac{s_{\mathrm{out}}-s_{\mathrm{in}}}{c_p}-q^*\frac{T_{t,\mathrm{in}}}{T_{\mathrm{wall}}}=\frac{s_{\mathrm{out}}-s_{\mathrm{in}}}{c_p}-\frac{h_{t,\mathrm{out}}-h_{t,\mathrm{in}}}{c_pT_{\mathrm{wall}}} \tag{6}$$

The entropy generation is comprised of two components, viscous dissipation, and thermal dissipation [8], which can also be computed by numerical integration over the entire computational domain,

$$\frac{s_{\mathrm{gen}}}{c_p}=\frac{1}{\dot{m}c_p}\int\int_{\mathcal{V}}\int\left[\underbrace{\frac{1}{T}\tau_{ik}\left(\frac{\partial u_i}{\partial x_k}\right)}_{\text{viscous}}+\underbrace{\frac{k}{T^2}\left(\frac{\partial T}{\partial x_i}\frac{\partial T}{\partial x_i}\right)}_{\text{thermal}}\right]d\mathcal{V} \tag{7}$$

where

$$\tau_{ik}=\lambda\frac{\partial u_l}{\partial x_l}\delta_{ik}+\mu\left(\frac{\partial u_i}{\partial x_k}+\frac{\partial u_k}{\partial x_i}\right) \tag{8}$$

and the factor λ is assumed to be equal to $-\frac{2}{3}\mu$ [9]. It is important to note that in order to use Eqs. (7) and (8) to calculate the specific entropy generation for turbulent flows, it is appropriate to use the "effective" viscosity, μ (and "effective" thermal conductivity, k), which is the sum of the laminar and turbulent, or eddy, viscosities (and thermal conductivities).

Figure 5 shows that it is possible to reconstruct the entropy generation using both the technique of entropy flux bookeeping given in Eq. (6) and the direct integration of the viscous and thermal dissipaton terms given in Eq. (7). Figure 5 also shows that entropy generation is greater for the cooled cases versus the adiabatic cases. The net decrease in ω from cooling shown in Fig. 3 must therefore occur because the transfer of entropy across the blade surface counters additional entropy generation by thermal dissipation, such that the exit total pressure is higher in the cold wall case than for the adiabatic cascade. Specifically, let us use the entropy consitutive relation for a perfect gas (Eq. (9)) to manipulate the definition of ω (Eq. (10)). We see that the numerator of the right hand side of Eq. (10) shows that ω is affected both by the temperature reduction from cooling (the $1+q^*$ term), and the competition between entropy transfer and entropy generation in the exponential ($q^*<0$ for cooling).

$$\frac{s_{\mathrm{out}}-s_{\mathrm{in}}}{c_p}=\ln\frac{T_{t,\mathrm{out}}}{T_{t,\mathrm{in}}}-\frac{\gamma-1}{\gamma}\ln\frac{p_{t,\mathrm{out}}}{p_{t,\mathrm{in}}}=\frac{s_{\mathrm{gen}}}{c_p}+q^*\frac{T_{t,\mathrm{in}}}{T_{\mathrm{wall}}} \tag{9}$$

$$\omega=\frac{p_{t,\mathrm{in}}-p_{t,\mathrm{out}}}{p_{t,\mathrm{in}}-p_i}=\frac{1-\left[(1+q^*)\exp\left(-q^*\dfrac{T_{t,\mathrm{in}}}{T_{\mathrm{wall}}}-\dfrac{s_{\mathrm{gen}}}{c_p}\right)\right]^{\gamma/(\gamma-1)}}{1-\left[1+\dfrac{\gamma-1}{2}M_{\mathrm{in}}^2\right]^{\gamma/(1-\gamma)}} \tag{10}$$

Figure 6 shows bar charts of the viscous and thermal dissipation at a low (0.4) and high (0.8) inlet Mach number, for both the adiabatic and wall temperature boundary condition cases. From these charts, several interesting observations can be made. First, we notice that in the adiabatic cases virtually all of the entropy generation comes from viscous dissipation. Second, in the cases with $T_{\mathrm{wall}}/T_{t,\mathrm{in}}=0.5$, the relative magnitudes of viscous and thermal dissipation are highly Mach number dependent. At low Mach numbers, thermal dissipation is the larger contributor to total entropy generation, whereas at high Mach number viscous dissipation is the larger contributor. Our results show that viscous dissipation has a strong Mach number dependency, but is virtually independent of the cooling BC, whereas thermal dissipation has weak Mach number dependency but is, of course, highly dependent upon the wall temperature BC. Since the viscous dissipation term is dependent upon local strain rates in the flow field, this may suggest that the velocity boundary layer is fairly independent of the temperature boundary layer. This implies that a simple model for the effect of blade surface heat extraction on blade passage aerodynamic performance could be constructed by building two separate models for the viscous and thermal dissipation, where the viscous dissipation could come strictly from adiabatic computations.

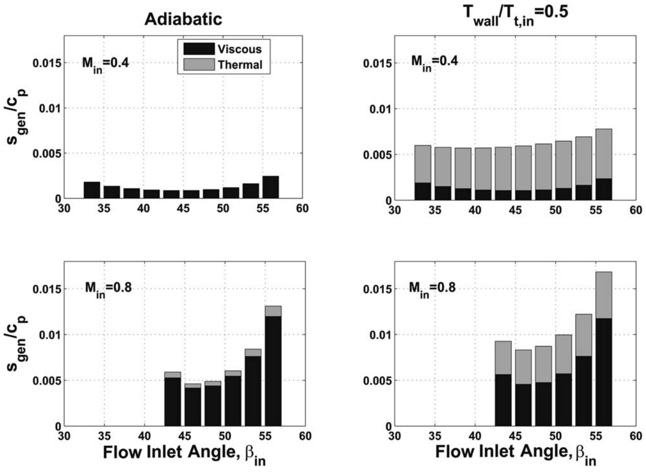

Fig. 6 Cascade 2, viscous (black), and thermal (gray) dissipation versus incidence at low (0.4) and high (0.8) inlet Mach number. Plots on the left are adiabatic wall BC; plots on the right are $T_{\text{wall}}/T_{t,\text{in}}=0.5$.

In summary, we have looked at blade passage flows in terms of traditional bulk figures of merit such as ω and δ, as well as considering the flow from a second law of thermodynamics perspective, for two different blade passage geometries. We find that the effect of cooling is to decrease the value of ω and δ, both of which favorably affect compressor performance. In addition, we expect that the decrease in the exit stagnation temperature and exit Mach number should both favorably affect subsequent downstream blade rows, due to the increased pressure rise capability on a relatively colder fluid and the decrease in ω with decreasing Mach number. Finally, we find that the loss generation mechanisms in the flow field, namely viscous and thermal dissipation, are relatively uncoupled, which indicates that a simple model for aerodynamic performance of nonadiabatic blade passage flows could be constructed using these components as the basis.

Generic Rules for Blade Passage Loss and Deviation

Generic rules for ω and δ have been created by postprocessing the CFD results shown in the previous section. The motivation for using generic rules comes from the fact that no detailed geometry information exists during the preliminary design of a compressor. These rules serve as a set of trends that can be used in a preliminary design.

By introducing cooling to the cascades, we have added an additional variable to the cascade performance, namely, the nondimensional cooling, q^*. For our mean line model, we assume that cooling takes place at a uniform rate over the airfoil surface. In fact, the details of the cooling distribution could also be a design variable. However, to make use of the data in a general sense, we simplify our definition to isolate the effect of each variable. The set of variables that describe the cascade performance parameters of interest are then,

$$\text{Cascade Performance} = f(\text{geometry}, i, M_{\text{in}}, \text{Re}_c, q^*) \qquad (11)$$

where geometry (including airfoil shape and cascade solidity, σ) is fixed for the experiment, i is the inlet flow incidence, M_{in} is the inlet Mach number, Re_c is the inlet Reynolds Number, using airfoil chord as an appropriate length scale, and q^* is the nondimensional cooling rate, defined as the ratio of the change in stagnation enthalpy due to cooling to the inlet stagnation enthalpy (see Eq. (1)). Because cooling involves heat removal, we have adopted a sign convention that q^* is always *negative* for cooled cascades.

For the situation where dependence on Re_c is weak, and the solidity only appears in the expression for "base" deviation (i.e., Carter's rule [10]), Eq. (11) simplifies to:

$$\omega, \Delta\delta = f(i, M_{\text{in}}, q^*) \qquad (12)$$

where ω is the total pressure reduction coefficient and $\Delta\delta$ is the change in deviation relative to the "base" deviation. For cascade 1, values of Re_c range from 100 000 to 200 000 and do not change appreciably between comparable adiabatic and cooled cases.

For a low level of cooling ($q^* \ll 1$), the channel flow sensitivity coefficient relating a differential change in stagnation temperature of a perfect gas to the resultant differential change in stagnation pressure is linear for a given Mach number, per Eq. (4). Thus, we assume that, to first order, it will be reasonable to scale the observed changes in ω linearly with the cooling rate.

Generic *loss buckets* have been developed by taking each loss bucket from the CFD data and referencing its minimum ω value as "zero" incidence. Polynomial fits have been used to define the bucket in the incidence range of −15° to 15° (for further details, see Shah [11]).

Nominal, or base deviation for adiabatic cascades at design (minimum ω) is predicted by using Carter's rule, $\delta_{\text{base}} = m\theta\sigma^{-n}$, where m is an empirical constant that depends on geometry, θ is the camber angle, and n is usually taken as 0.5 for decelerating cascades. This deviation is then modified for incidence, Mach number, and cooling rate. The first deviation modification, $\Delta\delta_a$, is the increase in deviation due to off-design incidence and Mach number for an adiabatic cascade. The second modification is a reduction of deviation due to cooling ($\Delta\delta_{\text{na}}$). The effect of inlet Mach number on $\Delta\delta_{\text{na}}$ has been included, while the effect of incidence has been neglected by averaging the values of $\Delta\delta_{\text{na}}$ at each Mach number. The generic deviation model is based upon the cascade 1 observations shown earlier in Table 1.

The changes in deviation due to cooling do not have as simple an analog as changes in p_t, and hence changes in ω. In this study we have assumed that the observed changes in deviation due to cooling will scale linearly for cooling rates up to $q^* = -0.01$. Our model is a significant simplification of the physical effect, but it is nonetheless valuable to include deviation effects to give the reader a sense of the potential impact of cooling on axial compressor performance. If levels of cooling such as this are available ($q^* \sim -0.01$), our model allows for two to three degrees of deviation to be recoverd from the blade rows at high subsonic Mach numbers. Two to three degrees of deviation reduction per blade row would make cooling a legitimate control variable to improve off-design matching. In the mean line analysis of the next section, we do select cooling rates up to ten times higher ($q^* = -0.01$), giving extrapolated turning values due to cooling of 2°–3° in the high Mach number stages of the compressor. We present a performance map in the next section that gives the reader an idea of the impact of the additional turning from deviation for the cooled, single stage compressor selected in this study.

On- and Off-Design Mean Line Analysis

Results from 2D CFD experiments have been used to assess the effect of cooling on a single stage and an eight stage compressor. As the number of stages increases, off-design matching becomes more challenging. The presence of cooling affects matching significantly, both in terms of the propagation of off-design perturbations to velocity triangles and in terms of the total pressure reduction. Results show that constant corrected speed lines (constant $N_c = N/\sqrt{T_{t,\text{in}}/T_{\text{ref}}}$) on a compressor map are raised relative to their adiabatic counterparts. Qualitatively, cooling affects low N_c lines differently than high N_c lines. This is primarily due to the Mach numbers seen by the airfoils at low and high values of N_c. At high values of N_c (and hence high rotor Mach numbers), there is a very narrow range of incidences in which the airfoils may operate successfully. There is also an increase of loss with increasing Mach number. Cooling (1) increases the pressure rise, (2) increases the turning, (3) decreases the downstream stagnation temperature, and also (4) slightly decreases the downstream Mach

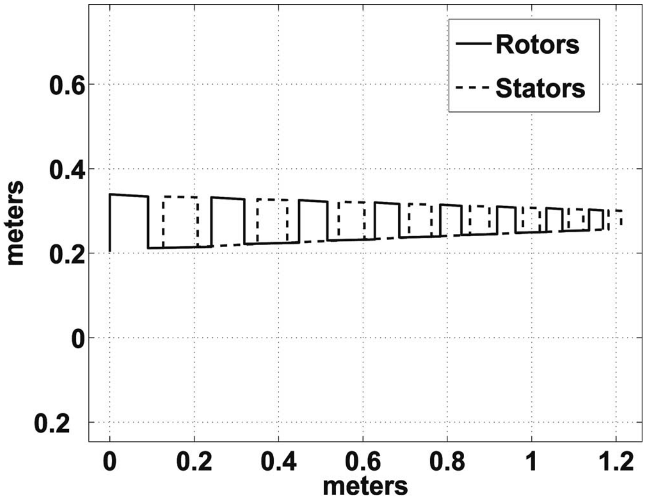

Fig. 7 Eight stage compressor layout. The first stage is also analyzed as a single stage fan.

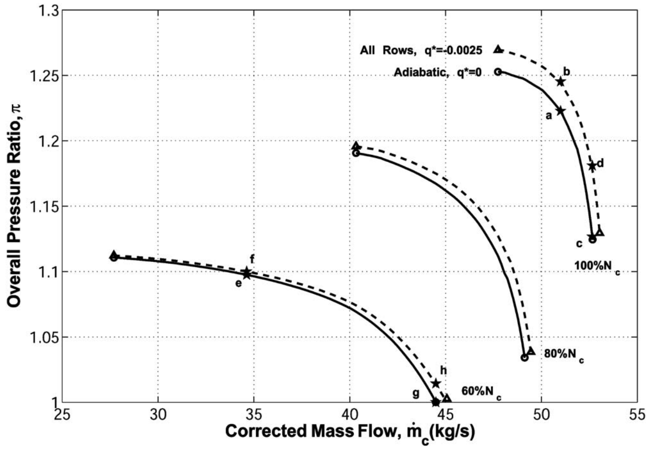

Fig. 8 Single stage compressor map, with and without cooling. The solid line is adiabatic; the dashed line is $q^*=-0.0025$ per blade row.

number. Effects (2), (3), and (4) all potentially affect the flow conditions into the next blade row in a favorable manner.

The eight stage compressor is designed by specifying compressor inlet conditions based upon a flight vehicle at 25 km altitude and a flight Mach number of 4, assuming that a lossless inlet exists upstream of the compressor. The overall pressure ratio at design is taken as 5, with each stage taken to produce the same pressure ratio, for simplicity. Air is assumed to behave as a perfect gas with $\gamma=1.4$. (In general, a variable specific heat thermodynamic model may be more accurate for a high flight Mach number vehicle in which air enters the compressor at a very high temperature. For consistency between our mean line analysis and our CFD computations, we have chosen $\gamma=1.4$. We expect no qualitative difference between a variable or fixed specific heat model). The compressor is sized for a "typical" high flight Mach number vehicle by specifying an inlet corrected flow $\dot{m}_c=\dot{m}\sqrt{T_t/T_{\text{ref}}}/(p_t/p_{\text{ref}})$ of 51 kg/s where T_{ref} and p_{ref} are standard day conditions. The hub and tip radii are chosen so as to keep the mean line radius constant from blade row to blade row. Each stage is designed to return the flow to the axial direction at the design point, so that we may also study the first stage as a single stage fan. The meridional layout of the eight stage compressor is shown in Fig. 7.

In order to compare various compressor cooling schemes, we nondimensionalize the local heat extraction by the compressor face inlet stagnation enthalpy:

$$q^*_{\text{comp}}=\frac{\dot{Q}}{\dot{m}h_{t,\text{in,comp}}}=\frac{\Delta h_t}{h_{t,\text{in,comp}}} \tag{13}$$

The subscript comp has been dropped in the subsequent discussion of compressor cooling, but it should be noted that the nondimensionalization follows Eq. (13). The results from the single stage and the eight stage compressors are presented in the next two subsections.

Single Stage Fan. The single stage fan map comparing an adiabatic and a cooled fan stage is shown in Fig. 8. For a nondimensional cooling value of $q^*=-0.0025$ per blade row, results indicate that the constant corrected speed line on a given compressor map (pressure ratio versus corrected mass flow) moves up in pressure ratio and in mass flow. (It should be noted that some of the chosen values of q^* in both the single stage and multistage examples lead to values of q^*, which require extrapolation of the two-dimensional cascade data presented earlier.) Thus, a cooled compressor produces a greater pressure rise at a given corrected mass flow and corrected speed. This also implies that as $\dot{m}_c$ increases along a given constant N_c line and the line approaches vertical (i.e., choked), a cooled compressor can pass greater corrected mass flow versus an adiabatic compressor. The increase in corrected mass flow occurs both at high and low corrected speed, but a constant value of q^* affects the corrected speed lines differently. At high N_c, the blade passages see higher inlet Mach numbers (and thus have a narrower range of operable incidences), resulting in a greater sensitivity to the beneficial effects of cooling. For example, at 100% N_c the "stall" side of the speed line shows a greater improvement in pressure ratio for the same corrected mass flow, than at 60% N_c. An examination of the one dimensional flow properties at the points shown explains why this is so. The 100% N_c line is in the *high subsonic* regime, where cooling has a more pronounced impact on ω and δ than the *low subsonic* regime that is encountered along the 60% N_c line. A comparison of the stator inlet and exit Mach numbers of points *c* (adiabatic) and *d* (cooled) shows that in the adiabatic case the stator behaves as a throttle, and is no longer diffusing the flow, whereas in the cooled case there is much less total pressure reduction and the stator is still diffusing the flow. The difference in stator incidence at these points varies by only 2.4°, but since the inlet Mach number is in the high subsonic regime, ω in the cooled stator is 50% lower than the adiabatic stator. Comparing these two points to their low N_c counterparts, points *g* and *h*, shows that the smaller change in total pressure reduction due to cooling is a result of less incidence change and lower inlet Mach numbers. Points *e* and *f* show even less change, as their Mach numbers are closer to the low subsonic regime.

Studies on the single stage fan reveal that the improvement in pressure rise capability seen on the compressor map is attributable to both the increase in stagnation pressure from cooling (lower ω) *and* the increased flow turning (lower δ). Figure 9 shows the change in cooled speed lines when the effects on total pressure reduction and flow turning are both isolated, and when they are both included. For the geometry we have selected, both these effects appear comparable when isolated and applied alone. This map also indicates that if the effects of deviation were not included, the predicted benefits would be lower, but the essential conclusions of our study would remain unchanged.

Eight Stage Compressor. Four different cases were analyzed on a hypothetical eight stage compressor using the mean line design framework. The cooling levels (per blade row) are $q^*=-0.01$ in the first two stages (rotor and stator cooling), $q^*=-0.0025$ in all eight stages, and $q^*=-0.01$ in the last two stages, as shown in Fig. 10. The three cooling rates are nondimensionally

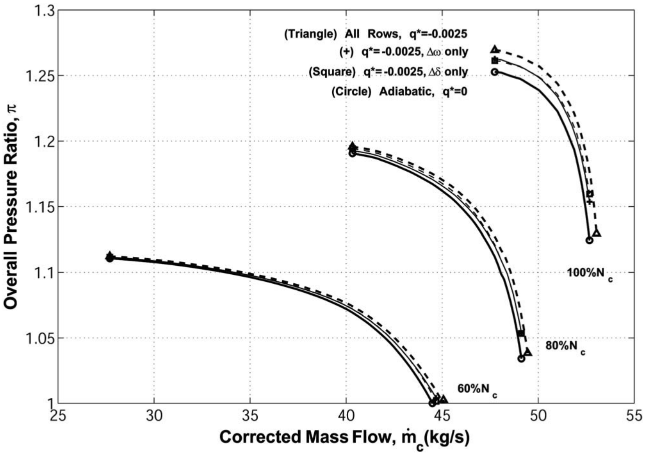

Fig. 9 A single stage compressor map, with and without different effects from a cooled cascade performance. The solid line with circles is adiabatic; the dashed line with squares shows the cooling effects of a change in deviation only; a solid line with plusses shows cooling effects of change in ω only; a dashed line with triangles shows both effects. For cooled cases, $q^*=-0.0025$ per blade row.

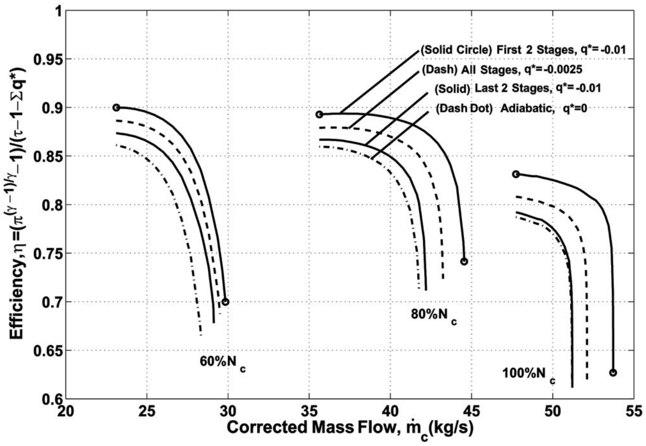

Fig. 11 Eight stage efficiency map, with and without cooling. A dash-dotted line is adiabatic; a solid line is $q^*=-0.01$ in the last two stages; a dashed line is $q^*=-0.0025$ in all stages; a solid line with circles is $q^*=-0.01$ in first two stages. q^* values are per blade row.

equivalent, so that for a given corrected mass flow, the same total cooling rate in units of power (e.g., Watts) applies.

$$\eta=\frac{\pi^{(\gamma-1)/\gamma}-1}{\tau-1-\Sigma q^*} \tag{14}$$

We define the efficiency, Eq. (14), using the "adiabatic" efficiency (η) definition of isentropic work required to achieve a given pressure ratio divided by the actual shaft work, which constitutes modifying the conventional adiabatic efficiency by accounting for the effect of cooling on the change in total temperature (i.e., the temperature ratio alone is no longer an indicator of shaft work). The use of this efficiency definition allows us to compare the actual work inputs of an adiabatic and a cooled compressor at a given pressure ratio, because we assume the same adiabatic refrence process in both cases. (An alternate, "nonadiabatic" efficiency (η_{na}) definition given in Appendix B compares the actual shaft work required to achieve the given pressure ratio to a lossless, nonadiabatic reference process. The definition of η_{na} accounts for the additional theoretically extractable work between the hot gas and cold wall, via a heat engine).

The efficiency map and compressor maps for an adiabatic case and three cooled cases are shown in Figs. 11 and 12, respectively. It is worthwhile to first consider the operating environments of the six adiabatic points, *i* through *n*, shown on the compressor map in Fig. 12. Points *i*, *j*, and *k* are on the high speed $(100\% N_c)$ line, and represent the *design point*, a *high speed stall side* point and a *high speed choke side* point, respectively. Points *l*, *m*, and *n* are on the low speed $(60\% N_c)$ line, and represent a point having the same throttle characteristic as point *i* (i.e., a *low speed throttle point*), a *low speed stall side point*, and a *low speed choke side point*, respectively. The incidence angles and inlet Mach numbers into the eight rotors and stators set the levels of ω and $\Delta\delta$. The adiabatic design point, *i*, has zero incidence into each rotor and stator. The Mach number into the rotors is in the high subsonic regime in the early stages, i.e., above 0.8. (Note, this represents an area of extrapolation in the generic loss bucket data, as $M_{\mathrm{in}}=0.8$ is the maximum Mach number included in the generic data. We expect consistency in the trends because this is a region where there is typically a strong divergence of flow properties, e.g., drag,

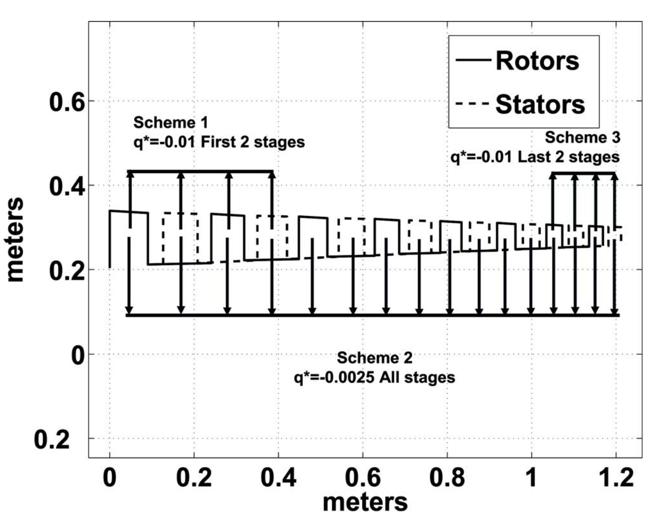

Fig. 10 Cooling schemes studied in eight stage compressor layout. q^* values are per blade row.

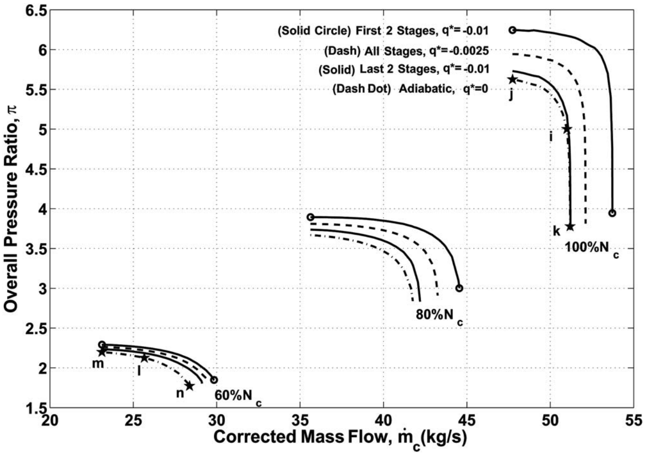

Fig. 12 Eight stage compressor map, with and without cooling. The dash-dotted line is adiabatic; the solid line is $q^*=-0.01$ in the last two stages; the dashed line is $q^*=-0.0025$ in all stages; the solid line with circles is $q^*=-0.01$ in first two stages. q^* values are per blade row.

or pressure coefficient.) As one moves along the speed line toward the stall side, i.e, in the direction of decreasing corrected mass flow, all of the rotor and stator incidences *increase* (point *j*) monotonically. In the opposite direction, toward point *k*, all the blade row incidences *decrease* monotonically. At low power, the *low speed throttle point*, point *l*, shows that the front stages are all operating at positive incidence, while the rear stages all operate toward negative incidence. The change in incidence from stage to stage progresses monotonically from the stall side to the choke side. Again, moving along the low speed line in the direction of lower mass flow increases the incidence on all blade rows, while moving in the opposite direction has the opposite effect.

An examination of the inlet Mach numbers from stage to stage reveal an important compressor characteristic. On the 100% N_c line Mach numbers primarily *decrease* from front to back, while on the 60% N_c line they *increase*. This is due to the fact that the annulus areas at low N_c are underdesigned to pass the required mass flow, versus at high N_c. Stated another way, at low speed the front stages provide relatively less charging pressure (or density rise) to pass the required mass flow leading to greater axial (and blade relative) Mach numbers. The degree to which the annular area is "underdesigned" on the low N_c line *increases* as the rear stages are reached. From the compressor map we see, therefore, that cooling in the last two stages alone has greater effect on the choke side of the *low* N_c line than on the choke side of the *high* N_c line.

The compressor map also clearly shows that at all corrected speeds for the cooling schemes presented, the highest pressure ratio is achieved by (1) cooling the first two stages, followed by (2) cooling all stages, (3) cooling the last two stages, and finally (4) the adiabatic case. This is consistent with the $T-s$ diagram shown in Fig. 2, which says that ideally, a *lossless precooler* is superior to *cooled compression*, because the fluid upon which shaft work is being done is at the lowest temperature possible, producing the highest total pressure rise. In other words, in addition to the *aerodynamic* benefit associated with cooling in the blade passages, there is a *thermodynamic* benefit associated with delivering colder, lower Mach number air to the downstream blade rows, making it most desirable to introduce a given amount of cooling, q^*, as far forward in the compressor as possible.

Finally, it is well known that at low N_c the rear of the compressor sets the mass flow capability. Moving along a low N_c speed line in the direction of increasing $\dot{m}_c$, the front stages provide lower and lower pressure (or density) rise, leading to higher and higher axial velocities in order to pass the required mass flow in the rear stages. The rearmost stator thus encounters flow at larger negative incidences, leading to higher losses, and reduced turning capability. Eventually, turning is reduced to such low amounts that throttle-like behavior occurs in the rearmost stator, increasing the compressor exit Mach number until it reaches the thermal choking limit of 1. *Since putting all the cooling in the first two stages produces the largest increase in corrected mass flow at all speeds, we may conclude that the presence of cooling in upstream blade rows relieves the adiabatic choking limit in the downstream rows. This effect arises both due to the increased pressure (or density) rise capabilty in the cooled upstream blade rows (aerodynamic effect), and the temperature reduction (relative to adiabatic) into the downstream blade rows (thermodynamic effect).*

Three Dimensional Transonic Rotor

Three dimensional CFD experiments have been performed on the transonic NASA Rotor 35 geometry using FLUENT. Selection of this single stage fan has the advantage of readily available test data in the literature [12]. An adiabatic and wall temperature BC speed line has been generated. Figure 13 shows the rotor geometry and the wall temperature BCs employed in the nonadiabatic computation. The *x* axis represents the positive axial direction. The inlet total temperature in both cases is 300 K. Static temperature BCs of 100 K have been placed on the blade surface and on the rotor casing in the nonadiabatic speed line computation. Since a real compressor is three dimensional, the ratio of the wetted surface area to the annular cross sectional area is higher than in a two dimensional cascade. Thus, we take advantage of a portion of this casing surface and allow heat transfers and entropy transfers to take place across it.

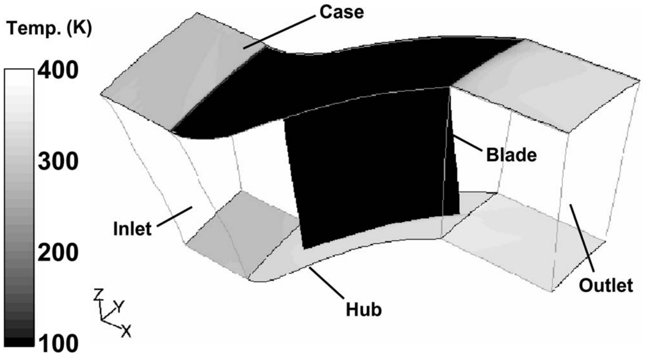

Fig. 13 Rotor 35 geometry and boundary conditions (single passage periodic) for nonadiabatic case. Filled static temperature contours on wall boundaries (hub, casing, and blade surfaces) show a BC of 100 K on the blade and middle portion of the outer casing surface. (The positive *x* axis is in the downstream axial direction).

Figure 14 shows the compressor map for the CFD cases studied, and compares it to test data at 90% and 100% corrected speed. The CFD cases have been run to a corrected speed of 93.7%. (The intent of these computations was to to determine whether the conclusions from the meanline analysis were relevant to higher performance geometries of practical interest. The computations were run at a speed *near* the absolute design speed and were corrected to the absolute and reference conditions given in the test report *a posteriori*, resulting in a corrected speed different from available data.) The pressure ratio computed in the CFD cases is based upon a mass average of the total pressure in the absolute frame of reference at the exit plane of the computational domain. We can see that the adiabatic CFD speed line is positioned reasonably well relative to the rig data. The nonadiabatic speed line is qualitatively similar to the nonadiabatic speed lines generated in the meanline analysis, in terms of increased pressure ratio and mass flow capability. For example, at a corrected flow of 19.27 kg/s, the nonadiabatic rotor computation shows a pressure ratio of 1.81, versus a pressure ratio of 1.76 at a similar corrected flow in the adiabatic case. The maximum mass flow capability

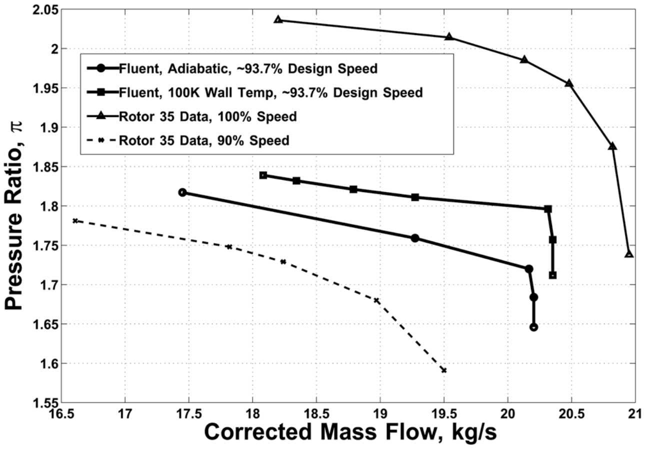

Fig. 14 Rotor 35 map

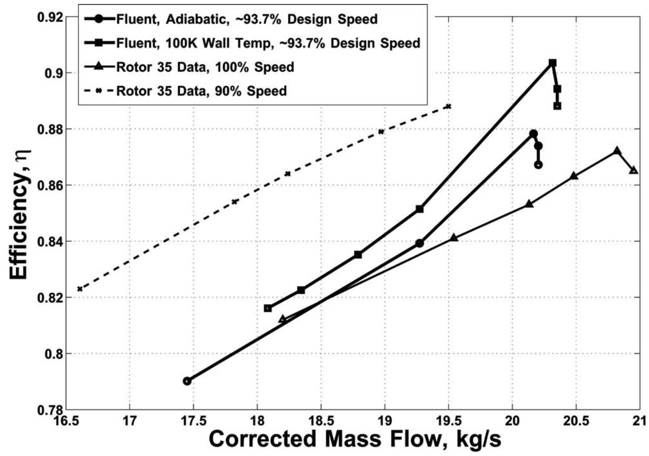

Fig. 15 Rotor 35 efficiency map

increases from 20.20 to 20.35 kg/s, or 0.7%. The value of q^* for the nonadiabatic speed line is of the order of −0.008 across the range of mass flows shown. Reference [13] provides a simple model for the purely *thermodynamic* effect of constant pressure heat exchange followed by compression at fixed adiabatic efficiency. The nonadiabatic pressure ratio, π_{na}, is related to the adiabatic pressure ratio, π_a by,

$$\pi_{\text{na}} = \left[\frac{1}{1+q^*}(\pi_a^{(\gamma-1)/\gamma} - 1) + 1\right]^{\gamma/(\gamma-1)} \qquad (15)$$

and the nonadiabatic mass flow, $\dot{m}_{\text{na}}$ is related to the adiabatic mass flow, $\dot{m}_a$, by,

$$\dot{m}_{\text{na}} = \dot{m}_a \frac{1}{1+q^*} \qquad (16)$$

If we consider the value of $q^* = -0.008$ and the adiabatic pressure ratio of 1.76, we see that Eq. (16) predicts the increased mass flow quite accurately (0.8%), whereas the increased pressure ratio is well underpredicted by Eq. (15). Thus, we can indirectly infer that it is primarily the *aerodynamic* performance improvement from blade passage surface heat extraction that provides the pressure rise shown in this computation, while the mass flow improvement is a purely *thermodynamic* effect. One can use these simple models to arrive at a similar conclusion for the compressors modeled earlier in the mean line analysis.

Figure 15 shows the efficiency map for the 93.7% speed line, as compared to the 90% and 100% rig test measurements. The efficiency definition for the transonic rotor CFD cases is consistent with that used in the mean line analyses, namely, the ratio of the isentropic work required to achieve the given pressure ratio to the actual (shaft) work done by the rotor. The actual shaft work is computed by integrating over the rotating surfaces to compute the axial torque ($\mathcal{T}_x$) and multiplying by the rotational shaft speed (Ω), as shown in Eq. (17).

$$\eta = \frac{\pi^{(\gamma-1)/\gamma} - 1}{\dfrac{\mathcal{T}_x \Omega}{\dot{m} h_{t,\text{in,comp}}}} \qquad (17)$$

From the efficiency map we see a peak efficiency increase of approximately 2% for the case with cooling BC, and 1%–2% at lower values of corrected flow. These efficiency improvements are consistent with those seen in the mean line cases.

Summary and Conclusions

We have used computational experiments and mean line modeling to investigate the effect of blade passage surface heat extraction on the performance of an axial compressor with an adiabatic design point. Two dimensional CFD experiments have given us the basis for a bulk performance model that has been applied to the mean line analyses of a single stage and an eight stage compressor. From this model, we deduce that surface cooling results in the following:

1. An increase in the overall pressure ratio (at a given corrected flow),
2. An increase in the maximum mass flow capability,
3. An increase in the efficiency, defined as the ratio of isentropic work for a given pressure ratio to actual shaft work,
4. Rear stage choking relief at low corrected speed.

Results from three dimensional computations on a state-of-the art transonic rotor are in accord with these conclusions.

In addition, our results suggest that, if available, a given amount of cooling is better in the front of the compressor than in the rear. This is primarily a thermodynamic effect resulting from the downstream stages compressing the colder air to a higher pressure ratio for a given amount of work.

Looking ahead, engineering issues that must be addressed include determination of achievable heat transfer levels inside a compressor. In Appendix A we provide a back-of-the-envelope heat transfer analysis based upon Reynolds Analogy over a flat plate, which underscores the importance of the blade solidity and the ratio of wall temperature to free stream stagnation temperature, to achievable cooling levels in the blade passage. The fact that the *rear* of the compressor may produce higher heat transfer rates competes with the finding that it is thermodynamically most desirable to have cooling in the *front* of the compressor. This indicates that for a given machine, an optimal stagewise cooling distribution should exist based upon cycle and compressor geometry, leaving an open design problem for future work.

Acknowledgment

Support for this work was provided by NASA Glenn under Grant No. NAG3-2767. We gratefully acknowledge the support of Dr. Kenneth Suder, technical monitor, and Dr. Arun Sehra, former director of programs and projects. We would like to thank Dr. Rod Chima of NASA Glenn for providing us with the Stage 35 gridded geometry. We thank Professor E. Greiter, Professor Z. Spakovszky, Dr. Y. Gong of MIT for their helpful discussions. We would also like to thank Prof. N. Cumpsty of Imperial College, London, Prof. F. Marble of CalTech, and Dr. J. Adamczyk and Dr. L. Larosiliere of NASA Glenn for their discussions and suggestions. Finally, we express our appreciation to the paper's reviewers for their insights and constructive criticisms, which have improved the technical clarity of the paper.

Nomenclature

c = specific heat (per unit mass)
C = used with subscript f as skin friction coefficient
h = specific enthalpy (per unit mass)
i = incidence
k = thermal conductivity
m = mass
m = Carter's rule constant
M = Mach number
n = Carter's rule exponent (0.5 for decelerating cascades)
N = rotational speed
p = pressure
q = heat transfer per unit mass
Q = heat transfer quantity
R = ideal gas constant (per unit mass)

Re = Reynolds number
s = specific entropy (per unit mass)
T = temperature
$\mathcal{T}$ = rotor torque
u = velocity
$\mathcal{V}$ = volume
x = spatial coordinate

Greek

β = blade air angle (measured from axial)
γ = ratio of specific heats
δ = deviation
δ = Kronecker delta
Δ = difference
η = efficiency
θ = net airfoil camber in degrees (used in Carter's rule)
μ = dynamic viscosity
π = total pressure ratio
ρ = density
σ = blade solidity, or chord-to-spacing ratio
τ = viscous stress tensor
χ = blade metal angle (measured from axial)
ω = nondimensional total pressure reduction
Ω = rotor rotational speed (radians/second)

Subscripts

a = adiabatic
av = average
base = adiabatic deviation at minimum loss
bl = blade (frame of reference)
c = Corrected to reference conditions (used with mass flow and rotational speed)
c = based upon chord length (used with Re)
comp = compressor face
f = used with C as skin friction coefficient
gen = generation (used w/entropy)
i = dummy index for orthonormal coordinate directions
in = inlet
k = dummy index for orthonormal coordinate directions
l = dummy index for orthonormal coordinate directions
lam = laminar
na = nonadiabatic
out = outlet
p = constant pressure (used with specific heats)
ref = reference conditions (e.g., standard day)
rev = reversible process
t = total or stagnation
turb = turbulent
v = constant volume (used with specific heats)
wall = at the wall
x = axial direction
∞ = free stream

Superscript

* = nondimensionalization relative to blade passage or compressor inlet

Oversymbols

$\dot{}$ = time rate of change
$\bar{}$ = average

Acronyms

BC = boundary condition(s)
CFD = computational fluid dynamics
PCTJ = precooled turbojet
SSTJ = single spool turbojet

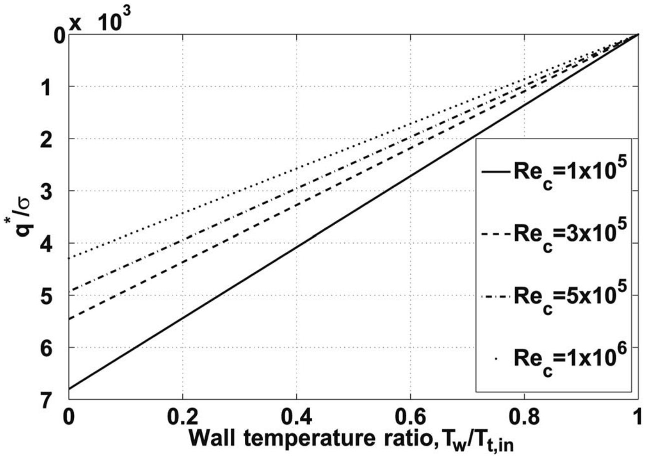

Fig. 16 Blade surface nondimensional heat transfer per unit solidity versus the wall temperature at various turbulent Reynolds numbers, generated using Reynolds analogy over a flat plate

Appendix A: Heat Transfer Considerations

CFD and mean line modeling on single stage and multistage compressor geometries having adiabatic design points show potential performance improvements through the presence of blade passage heat extraction (surface cooling). The obvious follow-up question is what types of cooling rates can be achieved. Although we are not able, at present, to offer details of what a practical cooling scheme might look like, we offer a first step toward identifying the answer. We have performed a back-of-the-envelope heat transfer analysis, using Reynolds analogy over a flat plate, assuming cooling on the blade surface alone (both pressure side and suction side). (It should be noted that this analysis has an element of conservatism in that cooling levels would increase if heat transfer was available along casing walls.) Using this approach, the available nondimensional cooling per unit solidity as a function of wall temperature ratio is approximated by:

$$\frac{q^*}{\sigma} \approx \bar{C}_f\left(\frac{T_{\text{wall}}}{T_{t,\text{in,bl}}} - 1\right) \tag{A1}$$

$\bar{C}_f$ is a representative mean skin friction coefficient that we estimate using expressions for laminar and turbulent flat plate skin friction coefficient [14] at a mid-chord Reynolds number:

$$\bar{C}_{f,\text{lam}} = \frac{0.664}{\overline{\text{Re}_x^{1/2}}} \approx \frac{0.664}{\text{Re}_{c/2}^{1/2}} = \frac{0.933}{\text{Re}_c^{1/2}} \tag{A2}$$

$$\bar{C}_{f,\text{turb}} = \frac{0.0592}{\overline{\text{Re}_x^{1/5}}} \approx \frac{0.0592}{\text{Re}_{c/2}^{1/5}} = \frac{0.068}{\text{Re}_c^{1/5}} \tag{A3}$$

Figure 16 shows an estimation of heat transfer capability using this model, for several turbulent Reynolds numbers between 100 000 and 1 000 000. Solidity, σ, is nominally the ratio of blade "wetted" area to the annular cross-sectional area. This analysis shows that for a representative Reynolds number and a fixed wall temperature ratio, q^* can be increased only by increasing σ. If we consider a Reynolds number of 300 000 and assume that the solidity is 1, then in order to achieve $q^* = -0.0025$ we need a wall temperature ratio of 0.54. Higher values of solidity can either increase the magnitude of the achievable q^*, or raise the required wall temperature ratio.

In a typical multistage compressor, solidities usually increase in the rear stages. In addition, the compression work leads to higher free stream temperatures ($T_{t,\text{inbl}}$), which can increase heat transfer capability with a fixed temperature heat exchanger fluid. The observation that heat transfer capability may be greatest in the rear of the compressor competes with the earlier finding that a given amount of cooling has the most impact in the front of the compressor. This opens the door to an optimization problem for future work.

Appendix B: Alternate, "Nonadiabatic" Efficiency Definition

The compressor efficiency definition (η) employed in the presentation of results throughout this paper is given by Eq. (14), and is interpreted as *the ratio of adiabatic, reversible work input required to achieve a given exit total pressure to the work input associated with the actual nonadiabatic, irreversible process*. The utility of this "adiabatic" efficiency definition is that it allows the work input into a real, adiabatic compressor to be compared to the corresponding work input into a real, nonadiabatic compressor, when compressing to the same exit total pressure. Stated another way, the actual work inputs of the two types of compressors may be compared to the same reference (ideal) process.

It would also be entirely reasonable to consider the efficiency of the nonadiabatic compressor on its merits alone. To do this requires that the reference, or ideal process against which the comparison is made, be a *nonadiabatic, reversible* process. We can clearly interpret such an efficiency definition as *the ratio of nonadiabatic, reversible work input required to achieve a given exit total pressure to the work input associated with the actual nonadiabatic, irreversible process*. Our purpose in this appendix is to derive such a definition.

We begin by considering a control volume (CV) around the entire compressor in steady operation. Mass may only cross the CV boundary at the inlet and outlet of the device, and the first law of thermodynamics is given by the steady flow energy equation as:

$$h_{t,\mathrm{out}} - h_{t,\mathrm{in}} = q + w_{\mathrm{sh}} \tag{B1}$$

where h_t is the specific stagnation enthalpy, q is the specific heat transfer, and w_{sh} is the specific shaft work transfer to the working fluid

Hence, the specific work associated with any process, is:

$$w_{\mathrm{sh}} = (h_{t,\mathrm{out}} - h_{t,\mathrm{in}}) - q = c_p(T_{t,\mathrm{out}} - T_{t,\mathrm{in}}) - q = c_p T_{t,\mathrm{in}}(\tau - 1 - q^*) \tag{B2}$$

The second law of thermodynamics on the CV is given by:

$$s_{\mathrm{out}} - s_{\mathrm{in}} = \int \frac{\delta q}{T_{\mathrm{wall}}} + s_{\mathrm{gen}} \tag{B3}$$

where the domain of integration includes all walls across which heat transfers take place. The integral expression is general, such that the wall temperature may vary throughout the domain of integration.

In any *reversible* process, s_{gen} equals zero. The entropy constitutive relation for a perfect gas given by the leftmost equality in Eq. (9) allows us to write:

$$\begin{aligned}\frac{(s_{\mathrm{out}} - s_{\mathrm{in}})_{\mathrm{rev}}}{c_p} &= \int \frac{\delta q}{c_p T_{\mathrm{wall}}} = \left(\ln \frac{T_{t,\mathrm{out}}}{T_{t,\mathrm{in}}} - \frac{\gamma - 1}{\gamma} \ln \frac{p_{t,\mathrm{out}}}{p_{t,\mathrm{in}}}\right)_{\mathrm{rev}} \\ &= \left(\ln(\tau) - \frac{\gamma - 1}{\gamma} \ln(\pi)\right)_{\mathrm{rev}}\end{aligned} \tag{B4}$$

The nonadiabatic, reversible work transfer required to achieve a given pressure ratio, π, is then given by:

$$\begin{aligned}(w_{\mathrm{sh}})_{\mathrm{rev}} &= c_p T_{t,\mathrm{in}}(\tau_{\mathrm{rev}} - 1 - q^*) \\ &= c_p T_{t,\mathrm{in}}\left(\pi^{(\gamma-1)/\gamma}\left[e^{\int T_{t,\mathrm{in}}/T_{\mathrm{wall}}\delta q^*}\right] - 1 - q^*\right)\end{aligned} \tag{B5}$$

The "nonadiabatic" efficiency definition is thus:

$$\eta_{\mathrm{na}} = \frac{(w_{\mathrm{sh}})_{\mathrm{na,reversible}}}{(w_{\mathrm{sh}})_{\mathrm{na,actual}}} = \frac{\pi^{(\gamma-1)/\gamma}\left[e^{\int T_{t,\mathrm{in}}/T_{\mathrm{wall}}\delta q^*}\right] - 1 - q^*}{\tau - 1 - q^*} \tag{B6}$$

In Eq. (26), if the ideal process in the *numerator* was assumed to be adiabatic ($q^*=0$), η_{na} would reduce to the definition of η given by Eq. (14). Clearly, then, the efficiencies η and η_{na} only differ by the nature of the reference process. Each definition has its own utility. At the *component* level, the utility of η lies in the fact that it provides the most conventional (adiabatic) reference process against which may be compared the work inputs of an adiabatic and nonadiabatic compressor achieving the same pressure ratio. Taking the compressor as a component whose purpose is to provide a given exit pressure, the definition of η also allows us to compare the exit conditions of two compressors given the same inlet conditions, rotor speed, and work input. This provides the basis for our decision to present the results in the main text of the paper using this efficiency.

At the *system* level the efficiency definition given by η_{na} allows for the bookeeping of lost work that may be recovered in a lossless process with heat transfer. Our discussion on entropy generation mechanisms in the section on 2D blade passage aerodynamics showed that for an aggressive cooling wall temperature ($T_{\mathrm{wall}}/T_{t,\mathrm{in}}=0.5$), cooling introduces additional thermal dissipation to the blade passage with little change in viscous dissipation. This implies that the amount of lost work would likely increase in the nonadiabatic compressor, and the value of η_{na} may be lower for an aggressively cooled compressor versus its adiabatic counterpart. Theoretically, we could conceive of some type of heat engine between the gas path and an on-board heat sink to recover this lost work. A proper determination of the feasibilty of a cooled compressor power plant on a specific vehicle mission may require some type of system-level availability analysis.

References

[1] Hewitt, F. A. and Johnson, M. C., 1991, "Propulsion System Performance and Integration for High Mach Air Breathing Flight," *High Speed Flight Propulsion Systems*, S. N. B. Murthy and E. T. Curran, eds., Vol. 137, AIAA.
[2] Powell, T. and Glickstein, M., 1988, "Precooled Turbojet Engine Cycle For High Mach Number Applications," *AIAA/SAE/ASME/ASEE 24th Joint Propulsion Conference*.
[3] Rudakov, A., and Balepin, V., 1991, "Propulsion Systems With Air Precooling For Aerospaceplane," SAE Paper 911182.
[4] Sreenath, A., 1961, "Studies of Turbojet Engines for Hypersonic Propulsion," Technical Report, McGill University, Department of Mechanical Engineering.
[5] Isomura, K., and Omi, J., 2001, "A Comparative Study of an ATREX Engine and a Turbo Jet Engine," *AIAA/ASME/SAE/ASEE 37th Joint Propulsion Conference*.
[6] Johnson, J., 1995, "Variable Cycle Engine Developments," *Developments in High-Speed-Vehicle Propulsion Systems*.
[7] Shapiro, A., 1953, *The Dynamics and Thermodynamics of Compressible Fluid Flow*. Ronald Press, New York.
[8] Greitzer, E., Tan, C., and Graf, M., 2004, *Internal Flow Concepts and Applications*, Cambridge University Press, Cambridge, UK.
[9] Schlichting, A., 1987, *Boundary Layer Theory*, McGraw-Hill, New York.
[10] Cumpsty, N., 1989, *Compressor Aerodynamics*, Longman, Cambridge, UK.
[11] Shah, P. N., 2006, "Novel Turbomachinery Concepts for Highly Integrated Airframe/Propulsion Systems," Ph.D. thesis, MIT, October.
[12] Reid, L., and Moore, R., 1978, Performance of Single-Stage Axial-Flow Transonic Compressor With Rotor and Stator Aspect Ratios of 1.19 and 1.26, Respectively, and With Design Pressure Ratio of 1.82, Technical Paper 1338, NASA, Cleveland, OH.
[13] Gong, Y., Sirakov, B., Epstein, A., and Tan, C., 2004, "Aerothermodynamics of Micro-Turbomachinery," ASME GT2004-53877.
[14] Kerrebrock, J. L., 1992, *Aircraft Engines and Gas Turbines*, 2nd ed. MIT Press, Cambridge, MA.

Optimization of a Real-Time Simulator Based on Recurrent Neural Networks for Compressor Transient Behavior Prediction

M. Venturini
Engineering Department in Ferrara (ENDIF),
University of Ferrara,
Via Saragat, 1,
44100 Ferrara, Italy

In this paper, feed-forward recurrent neural networks (RNNs) with a single hidden layer and trained by using a back-propagation learning algorithm are studied and developed for the simulation of compressor behavior under unsteady conditions. The data used for training and testing the RNNs are both obtained by means of a nonlinear physics-based model for compressor dynamic simulation (simulated data) and measured on a multistage axial-centrifugal small-size compressor (field data). The analysis on simulated data deals with the evaluation of the influence of the number of training patterns and of each RNN input on model response, both for data not corrupted and corrupted with measurement errors, for different RNN configurations, and different values of the total delay time. For RNN models trained directly on experimental data, the analysis of the influence of RNN input combination on model response is repeated, as carried out for models trained on simulated data, in order to evaluate real system dynamic behavior. Then, predictor RNNs (i.e., those that do not include among the inputs the exogenous inputs evaluated at the same time step as the output vector) are developed and a discussion about their capabilities is carried out. The analysis on simulated data led to the conclusion that, to improve RNN performance, the adoption of a one-time delayed RNN is beneficial, with an as-low-as-possible total delay time (in this paper, 0.1 s*) and trained with an as-high-as possible number of training patterns (at least 500). The analysis of the influence of each input on RNN response, conducted for RNN models trained on field data, showed that the single-step-ahead predictor RNN allowed very good performance, comparable to that of RNN models with all inputs (overall error for each single calculation equal to 1.3% and 0.9% for the two test cases considered). Moreover, the analysis of multi-step-ahead predictor capabilities showed that the reduction of the number of RNN calculations is the key factor for improving its performance over a significant time horizon. In fact, when a high test data sampling time is chosen (in this paper,* 0.24 s*), prediction errors were acceptable (lower than 1.9%).* [DOI: 10.1115/1.2437232]

Introduction

The interest shown in recent years with respect to the potential contributions that artificial intelligence techniques can provide to the modeling of energy systems and turbomachines mainly lies in the fact that the relative improvement that such techniques offer usually appears to be more pronounced as the complexity of a problem increases [1]. This effort is demonstrated by the great amount of work reported in recent literature dealing with the development of a particular type of tools based on artificial intelligence techniques, such as neural network (NN) models, for different fields of applications of gas turbines.

A first example is that of gas turbine diagnostics in steady-state conditions, for which neural network models have been employed alone [2–6], in combination with other techniques [7], or coupled with alternative artificial intelligence-based methods, such as expert systems [8], genetic algorithms [9], and fuzzy logic systems [10].

Another field of interest is that of sensor fault detection since a system model is usually required and implies a system identification process: this traditionally proves to be one of the preferred areas of expertise of neural networks [11]. Moreover, a demonstration of NN capabilities in detecting sensor faults, through the prediction of the complete engine operating parameters with few variables and the estimation of some nonmeasurable parameters, is shown in [12]. Furthermore, neural networks are still demonstrating their rich potential in the simulation of transient data.

The traditional approach to develop a dynamic simulation code is usually based on the use of the laws of conservation and of the performance maps of the considered machine [13–22]. Though the physics-based approach offers some strong points, such as the possibility to correctly explain the results by analyzing the physics of the considered processes, the development of physics-based dynamic simulation models may present some problems [23]. In fact, the capability of the model to reproduce the real machine is affected by the quality of the calibration process, which may be difficult to perform with a high level of accuracy, since some model parameters have to be estimated and/or the machine performance maps may not be available [20,21]. Moreover, computational times for complex systems may be so high as to limit their use in on-line applications, though some solutions were proposed in [24,25].

Thus, neural networks offer an alternative solution for developing dynamic models because of the capability of easily modeling an even very complex system due to their self-adapting characteristics. Moreover, they usually present good generalization capabilities even with a reduced set of identification data, robustness in

---

Contributed by the International Gas Turbine Institute of ASME for publication in the Journal of Turbomachinery. Manuscript received May 26, 2006; final manuscript received May 31, 2006. Review conducted by David Wisler. Paper presented at the ASME Turbo Expo 2006: Land, Sea and Air (GT2006), May 8, 2006–May 11, 2006, Barcelona, Spain. Paper No. GT2006-90117.

the presence of poor and/or noisy input data [26], and high computational speed, which proves crucial mainly when they are used for real-time simulations.

Neural networks also have the ability to incorporate system aging effects by performing their own on-line training [27]. Finally, NNs have also demonstrated their effectiveness for control purposes in cases in which the traditional control techniques were not accurate enough to ensure precise or even safe control [28].

The well-known limit of these models is high prediction error when they operate outside the field in which they were trained, i.e., they are not able to extrapolate. Therefore, great attention has to be paid to selecting NN training data correctly, in order to (i) cover all the possible range of variation of the considered process variables and (ii) set up a system model that is accurate enough in the operating region of interest, since inaccuracies can negatively influence the model reliability.

Hence, NN models for energy system simulation in unsteady conditions have been developed and some examples of their application are reported below in chronological order:

- prediction of the most significant quantities on a heat exchanger used as steam generator [1,29],
- simulation of the response of a combined cycle power plant during a slow transient [30],
- development of a nonlinear gas turbine model [31],
- setup of an observer to predict the air-fuel ratio for a spark ignition engine [32],
- development of a fault detection and diagnosis system for a turbofan engine through “nested NNs” [33] and for a field-operated propulsion engine through “echo state networks” [34], and
- simulation of transient behavior of a small-size axial-centrifugal compressor [23].

In this paper, NN models (feed-forward NNs with a single hidden layer, trained by using a back-propagation learning algorithm) for the simulation of compressor behavior under unsteady conditions are studied and developed. In order to develop a NN model capable of reproducing time-dependent data, neural networks in a so-called recursive computational structure, which makes use of one feedback loop (recurrent neural networks (RNNs), are usually adopted in practice [1,23,29,32,35]. Thus, they are also investigated in this paper.

The data used for training and testing the NNs were obtained by means of a nonlinear modular model for compressor dynamic simulation [21] (simulated data) and also measured on a multistage axial-centrifugal small-size compressor running in the test facility of the University of Ferrara [36] (field data). In particular, note the following:

- The nonlinear model, developed through a physics-based approach, was calibrated on the axial-centrifugal compressor for which the field data were available and was validated through the same experimental data [21]. The generated data represent different variations in the compressor operating condition and are the same as already used in [23].
- The field data are the same as already used for the physics-based dynamic model validation [21] and also for testing the capabilities of the RNN models developed in [23].

The first step of the analysis is the completion of the sensitivity analyses conducted in [23] on simulated data. In particular, starting from the best model setup in that same paper, the influence of (i) the number of training patterns and (ii) each RNN input on model response is evaluated both on data that are uncorrupted and corrupted with measurement errors. Different RNN configurations and total delay time values are analyzed in the current paper as before [23].

Then, RNN capabilities are tested against measured values by training the RNN models directly on field operating data. First, the analysis of the influence of each RNN input on model response is repeated for models trained on field data as previously done for models trained on simulated data in order to evaluate real system dynamic behavior.

Second, predictor RNNs (i.e., those that do not include among the inputs the vector of exogenous inputs evaluated at the same time step as the output vector) are developed and a discussion about their capabilities is carried out by taking into account the main factors that affect their overall performance.

Thus, with respect to [23], which represented the first step developed by the author in applying blackbox models for the simulation of transient data, the current paper investigates two novel aspects in the same field of dynamic simulation by means of neural networks, i.e., the development of RNNs (i) trained on field data and (ii) that act as predictors, in the same way as in [29]. In fact, the use of experimental dynamic data for RNN training and testing is reported in few papers (three years of operating data obtained from a three-spool RB211 driven compressor station in [12]; real data collected from a field-operated propulsion engine during 15 separate takeoffs in [34]; measured variables on a Rolls Royce turbofan engine in [31]). This is because NN dynamic models are usually applied to artificial problems by means of data obtained through system simulation models [23,28–30,34].

The last remark deals with the considered compressor and the dynamic model calibrated on it. It was highlighted in [21] that the deviation of system dynamics from its stationary behavior is small since the physical system is characterized by small size volumes and, thus, small time constants. This feature does not affect the validity of the results presented in the paper, which instead can be useful for applying, for instance, to turbomachines characterized by small size volumes (e.g., microturbines). In fact, such turbines, which are becoming very widespread, usually run under unsteady-state conditions and operate in energy systems that can be quite complex, due to the presence of several additional system components (such as external burners, fuel cells, etc.) [37,38]. Since a dynamic simulation model is always required in practice (for purposes of modeling, control, performance evaluation, etc.), system dynamic models based on RNNs can represent an interesting solution for modeling this kind of energy system.

Recurrent Neural Networks

Artificial neural networks (NNs) are mathematical structures that are able to link, in a nonlinear way through several interconnected simple units (the artificial neurons), a multidimensional input space with a multidimensional output space, allowing very high computational speed. A detailed description of NN features and capabilities can be found in specific literature, such as, among others, [35], and in papers illustrating NN applications to different fields [1,6,10–12,23,26,28–34]. For this reason, only the assumptions adopted in the paper for the NN model setup will be outlined, with particular reference to the development of recurrent neural networks.

The problem of developing a NN model capable of reproducing time-dependent data consists on the fact that the NN model has to take into account the time variable by means of a memory process. This can be done through NN architectures characterized by feedback connections among the neurons. An exhaustive review of different NN dynamic models structures can be found in [31,32,35].

In the paper, feed-forward neural networks, which approximate a nonlinear dynamic system by means of a static mapping, are developed, as also adopted in [1,23,28]. However, they can perform an inherently nonlinear dynamic mapping by using local (i.e., in the recurrent hidden layer nodes) and/or global (use of time-delayed variables as inputs) feedbacks, which ensure model dynamics.

According to [23,29–32], recurrent neural networks (RNNs) with one global feedback loop in a recursive computational structure are considered. Recurrent networks are also referred to as

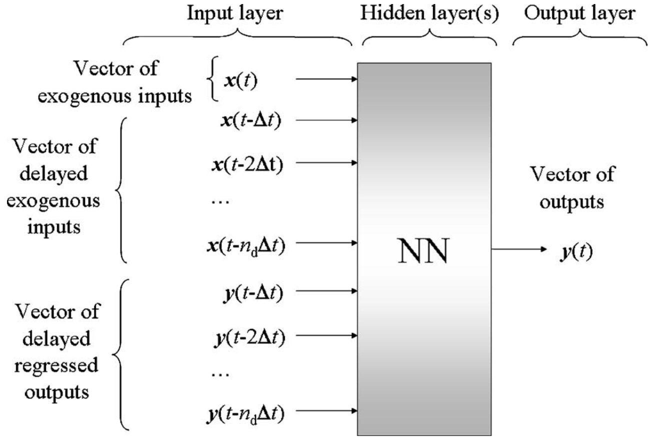

Fig. 1 Scheme of a recurrent neural network (RNN) model

nonlinear autoregressive with exogenous inputs models (NARX). In fact, it can be demonstrated that the role of the delay number in a delay feedback model is similar to that of the system order in a NARX model.

The basic topology of an RNN is shown in Fig. 1, where Δt is the time delay unit. From the scheme reported in Fig. 1, it can be observed that:

- the kernel of the model is the "classical" neural network, the only conceptual difference being (i) the presence of delayed values of the inputs and (ii) the regression of the outputs.
- the vector of exogenous inputs is evaluated at time t (the same as output vector $\boldsymbol{y}$). This condition is not necessary, since RNNs in which the output vector is ahead of the input vector by at least one time unit are presented in [29,35] and are also investigated in the paper. It should be remembered that all the models developed in [23] include the exogenous inputs evaluated at the current time step among the inputs.
- the total delay time of the vector of delayed exogenous inputs and, similarly, of the vector of delayed regressed outputs is $n_d\Delta t$. The condition that RNN regressed outputs (i) start from the time step just before the current time step (t-Δt) and (ii) are delayed up to the same time step as the delayed exogenous inputs (t-$n_d\Delta t$), is not a general requirement. For a discussion about this aspect, the reader is referred to [23,35]. In any case, this represents the most common solution [23,29].

Thus, as seen in Fig. 1, the input layer of the RNN usually consists of two main classes of inputs: (i) exogenous inputs, i.e., originating from outside the network and (ii) delayed values of outputs. Exogenous inputs can be evaluated both at the same time step as the outputs and at antecedent time steps with respect to the outputs. On the other hand, the delayed values of outputs can be either taken from outside the RNN (for example, measured observations or data estimated through a different model) or estimated through the RNN itself at antecedent time steps. In such a way, model outputs are *regressed*. In particular, neural networks, for which the vector of inputs is composed of (i) the exogenous inputs evaluated at antecedent time steps with respect to the outputs and (ii) delayed values of outputs estimated through the RNN itself at antecedent time steps, are identified as predictors and are of great interest since, due to the high computational speed of RNNs, they can be employed as real-time simulators.

Because of the above-mentioned considerations, the dynamic behavior of the RNN model is described by the following equation, where F is a nonlinear function of its arguments:

$$\boldsymbol{y}(t) = F[\boldsymbol{x}(t),\boldsymbol{x}(t-\Delta t), \ldots ,\boldsymbol{x}(t-n_d\Delta t),\boldsymbol{y}(t-\Delta t), \ldots ,\boldsymbol{y}(t-n_d\Delta t)] \tag{1}$$

The transfer function F depends on the chosen activation function (in this paper, sigmoidal) and on the network parameters (i.e., number of inputs, number of neurons in the hidden layers, and connection weights among the neurons). In particular, the proper connection weights can be identified through the optimization of the training process. Thus, according to Eq. (1), the RNN model implicitly takes into consideration the time variable by means of the dependence-with-time of all variables [1,23,29,32,34,35].

The architecture chosen in the paper is the typical *feed-forward multilayer perceptron* (also adopted in [21,28,29]). In particular, NNs with one hidden layer and a continuous sigmoid activation function are used, since it has been shown that this type of NN architecture is able to represent any type of multidimensional nonlinear function, if a suitable number of neurons in the hidden layer is chosen [35,39]. The use of multiple hidden layers usually requires a great computational effort, while it only allows a small improvement of performance [35], and thus architectures with only one hidden layer are usually adopted in practice [23,26,29,31].

With regard to the choice of the suitable training algorithm for RNN models, a good overview is reported in [40]. In the paper, a traditional *back-propagation* algorithm was used and the TRAINSCG algorithm was adopted. in fact, this algorithm appeared to be effective with a low computational effort [23,26,30] and, above all, it was available in the MATLAB® Neural Network toolbox.

The adopted stopping criterion for the NN training phase is the minimization of a performance function that was chosen to be the mean-square error (MSE) on the whole training set between the target outputs and the corresponding NN computed outputs:

$$\mathrm{MSE} = \frac{1}{n_\mathrm{o} n_\mathrm{patt}} \sum_{j=1}^{n_\mathrm{o}} \sum_{i=1}^{n_\mathrm{patt}} [t_{ij} - y_{ij}]^2 \tag{2}$$

where n_o is the number of NN outputs, n_patt is the number of patterns used for the NN training, t_{ij} are the target outputs, and y_{ij} the NN computed outputs.

In this paper, only off-line NN training is performed. This means that a set of training data is collected and the NN model is constructed from this set of data by computing the best-fitting weight parameter combination that minimizes a cost function (in the paper, the MSE). However, a system that is subject to time-varying disturbance or drifting can never generate the same trajectory twice. In this case, it would be advisable to perform an on-line training: this results in a neural network that can be tuned as the system runs, i.e., whose hidden weights are adjustable. This solution is studied, also theoretically, in [27]. In any case, the commonly adopted solution for RNN training is the off-line training [23,28,29].

Data for NN Training and Testing

The test facility in which the compressor under consideration is installed has been widely addressed in [21,23,36] and, thus, is only briefly described in this paper. The experimental apparatus is composed of an inlet duct (in which an orifice plate is mounted to perform the inlet mass flow measurement), a compressor (which is part of the Allison 250-C18 turboshaft engine and is composed of six axial stages and one centrifugal stage), and an outlet duct, which plays the role of a small-volume plenum in which a butterfly valve is inserted for compressor mass flow rate control. Thus, the compressor operates in an open circuit and can be driven by an electric motor up to 30,000 rpm, by means of a step-up gear box.

Compressor Physics-Based Dynamic Model for Data Generation. A nonlinear modular model for dynamic simulation of compressors was set up and implemented in MATLAB environment by means of the Simulink tool [21]. The model was devel-

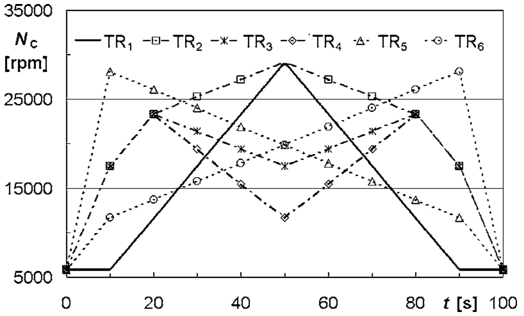

Fig. 2 Compressor rotational speed trend versus time for simulated data used for RNN training (TR_1) and testing (TR_2–TR_6)

oped through a physics-based approach by using the laws of conservation and heat balances, and by using the performance maps of the considered compressor. The model reproduces the test facility by means of three modules: the intake duct (sections 0-1), the compressor (sections 1-2), and the exhaust duct (sections 2-3). The model has three inputs (ambient pressure p_0 and temperature T_0 and compressor rotational speed N_C), and estimates the variables for all model sections, among which the ones considered in the paper are compressor inlet mass flow rate M_1 and pressure p_1 and compressor outlet pressure p_2 and temperature T_2.

The physics-based dynamic model was calibrated on the considered compressor and validated through experimental data [21]. It was observed that, though the approach adopted for developing the physics-based model is general, the deviation of system dynamics from its stationary behavior is small since (i) the model only captures dynamic effects deriving from mass storage and thermal exchange phenomena (in fact, the shaft dynamics is not taken into account in the model, though it can be easily implemented as shown in [22]) and, above all, (ii) the physical system is characterized by small size volumes.

Simulated Data Generation. The physics-based dynamic model has been used to generate different transients that have already been presented in [23]. The simulated maneuvers reproduce accelerations and decelerations, all taken at ISO conditions ($T_0 = 15°C$; $p_0 = 101.3$ kPa): some of them were used for RNN training, while the rest were used to verify the generalization capabilities of the trained RNNs. One of the results obtained through [23] was the identification of the optimal maneuver for RNN training; thus, this curve (triangular shaped, symmetrical with respect to the total time interval, and with a stationary phase at the beginning and at the end) is adopted here for training all the developed RNNs trained on simulated data. For the sake of readability, the simulated curves are also reported in this paper: TR_1 is the curve used for RNN training, while TR_2 through TR_6 are used to verify the generalization capabilities of the trained RNNs.

In Fig. 2, the trend over time of the compressor rotational speed (which is the only input for the compressor dynamic model, once ambient conditions T_0 and p_0 are fixed) is plotted for a time interval of 100 s for each transient TR. All the considered curves cover a range of variation for compressor rotational speed from ~5,000 rpm up to ~30,000 rpm.

The curves used for RNN testing (TR_2–TR_6) differ from each other, since compressor rotational speed varies:

- quite slowly and symmetrically with respect to the total time interval (TR_2–TR_4) and
- quite rapidly, as a fast ramp-shaped curve, and in an asymmetrical way (TR_5 and TR_6).

Finally, it should be specified that for all the generated data, the sampling time Δt_s was equal to 0.1 s; this means that (i) the time delay unit Δt reported in Eq. (1) has also been considered equal to 0.1 s and (ii) each curve contains 1000 data patterns. Furthermore, it should be noted that the developed RNNs have all been tested on patterns (derived from TR_2–TR_6) that do not include the patterns used for training (derived from TR_1).

Table 1 Measurement uncertainty values

Quantity	Absolute uncertainty	Value at $N_C = 28{,}948.0$ rpm	Percentage uncertainty (%)
N_C	30.0 rpm	28 948.0 rpm	0.10
p_1	0.636 kPa	98.36 kPa	0.65
p_2	1.817 kPa	165.83 kPa	1.10
M_0	0.012 kg/s	0.526 kg/s	2.28
T_2	1.0 K	374.3 K	0.27

Simulated Data Corruption Through Measurement Errors. To take into account the presence of measurement errors, the generated data were corrupted with random errors included in the measurement uncertainty intervals reported in Table 1. The estimation of the absolute uncertainties for the measured quantities, reported in the second column of Table 1, was performed by using the results of the uncertainty analysis conducted in [36], which was also adopted in [23]. The percentage uncertainty values (fourth column of Table 1) are calculated with respect to the values of the quantities in correspondence to the rotational speed for which the uncertainty analysis was conducted (i.e., 28,948 rpm).

Available Measured Data. The available measured data consist of two test cases (TC1 and TC2), both taken at quasi-ISO conditions ($T_0 \approx 17°C$; $p_0 \approx 102$ kPa), which represent acceleration and deceleration maneuvers for the compressor on which the physics-based model was calibrated [21].

The same two curves were also adopted in [23] for testing the developed RNNs trained on simulated data. The two curves are reported in Fig. 3 and differ from each other since TC1 curve covers a wider range of variation for compressor rotational speed (N_C ranges from ~13,000 up to 23,000 rpm), while TC2 curve covers a more restricted region of N_C values (from ~20,000 up to 26,000 rpm). In any case, the rotational speed gradient is comparable for both curves (i.e., ~200 rpm/s).

With respect to simulated data, it can be observed that (i) the range of variation for measured compressor rotational speed N_C lies within the range of variation of compressor rotational speed values in the simulated data (assumed to be in the range of 5000–30,000 rpm) and (ii) the rotational speed gradient for field data is lower than that of the TR_1 curve (~600 rpm/s).

The available field data are characterized by a sampling time equal to 0.0067 s and, thus, by a number of patterns equal to 27,150 (TC1) and to 9450 (TC2). The patterns that will be used in

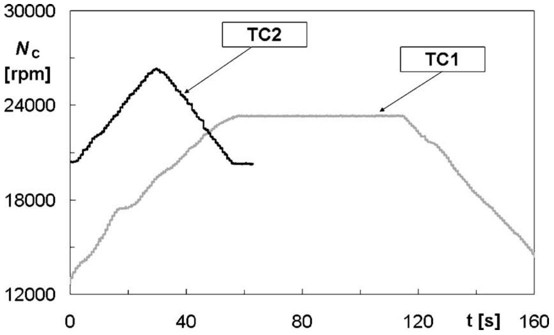

Fig. 3 Rotational speed trend versus time (measured data) for the two test cases TC1 and TC2

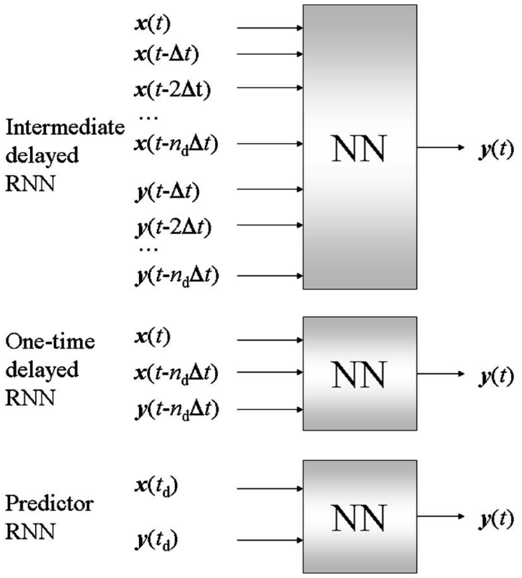

Fig. 4 Scheme of the recurrent neural network models adopted in the paper

the next section for training the RNNs on field data were derived from the available measured data, by uniformly sampling all the originally available 36,600 patterns.

RNN Model Identification

RNN Inputs and Outputs. The RNN models developed in the paper are characterized by a single exogenous input (compressor rotational speed N_C) and four outputs (compressor inlet and outlet pressure p_1 and p_2, compressor inlet mass flow rate M_1 and compressor outlet temperature T_2). Thus, the exogenous input vector $\boldsymbol{x}$ is composed of only one element (i.e., $\boldsymbol{x}(t)=[(N_C(t)]$, and thus, the dimension of the vector is $d_x=1$), while the output vector $\boldsymbol{y}$ is made up of four elements, i.e., $\boldsymbol{y}(t)=[p_1(t),p_2(t),M_1(t),T_2(t)]$ and, thus, $d_y=4$. The choice of adopting a multiinput-multioutput architecture was made in accordance with [23].

RNN Architecture. Two different types of RNNs are developed from the general scheme presented in Fig. 1, as done in [23], and are sketched in Fig. 4:

- "Intermediate delayed" RNN: Inputs and outputs are regressed to the RNN input layer for all intermediate time steps up to the time $n_d\Delta t$. Thus, the total number of inputs is $n_i=d_x+n_d^*(d_x+d_y)$.
- "One-time delayed" RNN: the values of exogenous inputs and of the regressed outputs are both supplied to the RNN input layer only delayed of time $n_d\Delta t$. Thus, the total number of inputs is $n_i=(2d_x+d_y)$, i.e., six.

In this paper, different values of the total delay time for both intermediate delayed RNNs and one-time delayed RNNs are tested.

A third typology of RNNs can be obtained from both intermediate delayed and one-time delayed RNNs, i.e., the predictor RNN, for which an extensive survey can be found in [29]. A predictor RNN is characterized by the fact that it does not include among the inputs the vector of exogenous inputs evaluated at the same time step as the output vector, and thus, its output vector is ahead of the input vector by at least one time unit. For the predictor sketched in Fig. 4, a concise notation is adopted: $\boldsymbol{x}(t_d)$ identifies the vector of exogenous inputs evaluated at antecedent time steps, and $\boldsymbol{y}(t_d)$ represents the vector of delayed regressed outputs. The two vectors obviously differ if an intermediate delayed architecture or a one-time delayed architecture is considered.

Then, as a function of the forecasting horizon, two types of predictors can be distinguished:

- single-step-ahead (SS) predictor. The SS predictor RNN estimates the vector of outputs for one time step following the current time step of the inputs. In the paper, the vector of delayed regressed outputs $\boldsymbol{y}(t_d)$ is not calculated by the RNN, but is always supplied from outside (estimated through the physics-based model in the case of simulated data and measured in the case of experimental data).
- multi-step-ahead (MS) predictor. The MS predictor RNN estimates the vector of outputs for many time steps ahead and reaches the desired forecasting time step through a recursive use of an SS predictor. With the exception of the first time step, for which the predictor is obviously fed by a vector of delayed regressed outputs $\boldsymbol{y}(t_d)$ supplied from outside the RNN (estimated through the physics-based model in the case of simulated data and measured in the case of experimental data), the MS predictor is always fed by a vector of delayed regressed outputs $\boldsymbol{y}(t_d)$ estimated through the SS predictor at antecedent time steps. For this reason, the accuracy of the SS predictor is of utmost importance, since even small SS prediction errors at the beginning of the horizon accumulate and propagate, thus resulting in poor prediction accuracy [29].

Comments on Data Sampling Time, RNN Delay Time, and Number of RNN Calculations. The sampling time for training and test data (respectively, $(\Delta t_s)_{\mathrm{tr}}$ and $(\Delta t_s)_{\mathrm{test}}$) can be different. The only constraint is that the adopted delay time $n_d\Delta t$ must be the same for both training and test data, since the RNN needs to be fed with consistent data. Moreover, for an intermediate delayed RNN, the choice of the appropriate total delay time also has to take into account the availability of data in correspondence with the intermediate time steps. The relation between RNN total delay time and the sampling time of training and test data can be expressed as in Eq. (3), where k_{tr} and k_{test} are multiplicative factors,

$$n_d\Delta t = k_{\mathrm{tr}}(\Delta t_s)_{\mathrm{tr}} = k_{\mathrm{test}}(\Delta t_s)_{\mathrm{test}} \tag{3}$$

On the other hand, no relation exists between the time interval $(\Delta t_{\mathrm{tot}})_{\mathrm{tr}}$ available for extracting the training data and the time interval $(\Delta t_{\mathrm{tot}})_{\mathrm{test}}$ to be simulated. Available data sampling time may be recommended to have low values, since data with a higher sampling time (i.e., lower sampling frequency) can be obtained by performing a subsequent data postprocessing. In the paper, quite low sampling times are considered ($\Delta t_s=0.1$ s and $\Delta t_s=0.0067$ s for simulated and field data, respectively), while relatively higher sampling times can be found in literature ($\Delta t_s=5.0$ s in [29] and $\Delta t_s=0.25$ s in [34] for simulated and field data, respectively).

In order to maximize RNN accuracy at each time step (i.e., for a single-step-ahead predictor), an improvement of RNN performance can be obtained by a proper setup of the RNN architecture and configuration, as shown later in the paper through the sensitivity analyses conducted on both simulated and field data.

On the other hand, if an MS predictor RNN is considered, another possibility is offered through resetting the propagated error at fixed time steps. This can be done by supplying "good" data in correspondence with the selected reset time step. Thus, in this manner, the vector of delayed regressed outputs is no longer estimated by the RNN itself, but is provided from outside the RNN, as, for example, measured observations or data estimated through a different model. This possibility is investigated below in Fig. 8 for different values of the reset time step.

For an assigned time interval and a given sampling time Δt_s, the number of available patterns can be obtained as the ratio between the total time interval and the sampling time Δt_s. In particular, if one or more resets are performed during the time interval to be simulated $(\Delta t_{\mathrm{tot}})_{\mathrm{test}}$, the following relation can be written, by using Eq. (3),

$$(\Delta t_{\mathrm{tot}})_{\mathrm{test}} = \left[(n_{\mathrm{patt}})_{\mathrm{test}} \left(\frac{n_{\mathrm{d}} \Delta t}{k_{\mathrm{test}}} \right) \right] (n_{\mathrm{reset}} + 1) \tag{4}$$

where n_{reset} is the number of resets performed in the given time interval to be simulated ($n_{\mathrm{reset}}=0,1,2,\ldots$) and $(n_{\mathrm{patt}})_{\mathrm{test}}$ represents the number of patterns (and also the number of RNN calculations) between two subsequent resets.

Performance Evaluation of RNN Models. The parameter used for the comparison of the RNNs is the root-mean-square error RMSE, which is frequently adopted for this kind of RNN applications [23,26,29].

Such a parameter represents the error RMSE made by the RNN on the whole set of test data in the calculation of each jth output (p_1, p_2, M_1, and T_2) for any given kth transient used for RNN testing (TR_2–TR_6 for simulated data and TC1 or TC2 for field data),

$$\left(\mathrm{RMSE} = \sqrt{\frac{1}{n_{\mathrm{patt}}} \sum_{i=1}^{n_{\mathrm{patt}}} \left(\frac{t_i - y_i}{t_i} \right)^2} \right)_{jk} \qquad \begin{matrix} j = 1, \ldots, n_{\mathrm{o}} \\ k = 1, \ldots, n_{\mathrm{TR}} \end{matrix} \tag{5}$$

where t_i are the target outputs, y_i the computed outputs, n_{patt} is the number of patterns for each transient used for RNN testing, n_{o} is the number of RNN outputs (i.e., four) and n_{TR} is the number of transients used for RNN testing (i.e., five in the case of simulated data and two in the case of field data).

Two different concise indices are then derived:

- $\mathrm{RMSE}_{\mathrm{ov}}$, which represents the overall RMSE made by the RNN on all outputs for each transient used for RNN testing and is defined as

$$\left(\mathrm{RMSE}_{ov} = \sqrt{\frac{1}{n_{\mathrm{o}}} \sum_{j=1}^{n_{\mathrm{o}}} (\mathrm{RMSE})_j^2} \right)_k, \qquad k = 1, \ldots, n_{\mathrm{TR}} \tag{6}$$

- $\mathrm{RMSE}_{\mathrm{m}}$, which represents the RMSE made by the RNN on all transients used for testing. In this case, the "mean" is referred to all transients and, thus, the parameter can be calculated for any jth single output, as in Eq. (7), and also as an overall value, as in Eq. (8), as

$$\left(\mathrm{RMSE}_{m} = \sqrt{\frac{1}{n_{\mathrm{TR}}} \sum_{k=1}^{n_{\mathrm{TR}}} (\mathrm{RMSE})_k^2} \right)_j, \qquad j = 1, \ldots, n_{\mathrm{o}} \tag{7}$$

$$(\mathrm{RMSE}_{m})_{ov} = \sqrt{\frac{1}{n_{\mathrm{o}}} \sum_{j=1}^{n_{\mathrm{o}}} (\mathrm{RMSE}_{m})_j^2} \tag{8}$$

RNN Sensitivity Analyses on Simulated Data

The starting point of the analyses that are developed in the paper is represented by the results obtained in [23]. In particular, all the RNNs developed for the analyses on simulated data are (i) characterized by 15 neurons in the hidden layer and by a multi-output architecture and (ii) are trained on TR_1 curve data. Two types of analyses are performed on simulated data: (i) determination of the proper number of RNN training patterns n_{patt} and, thus, of the associated data sampling time, and (ii) evaluation of the influence of each input on RNN response.

All the analyses, summarized in Table 2, are carried out for both intermediate delayed and one-time delayed RNNs. The analyses consider different values of the total delay time and different combinations of inputs. In all cases, the presence of measurement errors is taken into account.

Table 2 RNN models developed for the sensitivity analyses on simulated data

RNN architecture	Total delay time (s)	Number of training patterns	RNN inputs
Intermediate delayed	1.0 1.0, 0.5	100, 250, 500, 1000 1000	All Variable
One-time delayed	1.0, 0.2 1.0, 0.5, 0.1	100, 250, 500, 1000 1000	All Variable

Number of Training Patterns. The influence of the number of training patterns $(n_{\mathrm{patt}})_{\mathrm{tr}}$ on RNN performance is established by comparing the response of three different RNN models: one intermediate delayed RNNs ($n_d=10$, i.e., total delay time equal to 1.0 s) and two one-time delayed RNNs ($n_d=2,10$, i.e., total delay time equal to 0.2 s and to 1.0 s).

All the developed RNNs are compared by means of the parameter RMSE_m for different values of the number of training patterns: 100, 250, 500, and 1000, this latter being the reference case as reported in [23]. When less than 1000 patterns are used, it was decided to uniformly sample the training curve, which was originally composed of 1000 patterns. The results are reported for two different cases: (i) absence of measurement errors, so that both training and test patterns are not corrupted with measurement errors, and (ii) presence of measurement errors both in training and test patterns, i.e., both training and test patterns are corrupted with measurement errors.

From Fig. 5, it can be noted that:

- for all RNN models, errors decrease as the number of training patterns increases, which depends on the chosen sampling time once the total time interval considered for training data is fixed. However, the solution of adopting 500 (or even 250 for one-time delayed networks) training patterns seems not to affect errors noticeably, while 100 training patterns should not be considered as a viable solution.
- independent of the number of training patterns, it is confirmed that the one-time delayed RNN with the lowest total delay time (i.e., 0.2 s) represents the best solution [23]. Moreover, for this latter RNN, the dependence of its performance with $(n_{\mathrm{patt}})_{\mathrm{tr}}$ becomes less evident.

Influence of RNN Inputs. The interest in evaluating the influence of RNN inputs on RNN performance lies in two aspects. First, the analysis allows the identification of which input is more significant so that the model with the best combination of inputs (i.e., the one that allows the lowest errors) can be adopted for further analyses. Second, it allows the user to understand which is the "order" of system dynamics. For instance, if the most signifi-

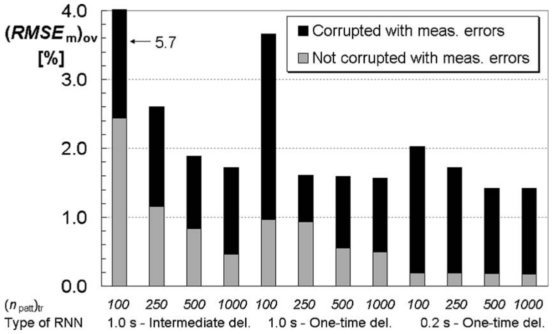

Fig. 5 Influence of the number of training patterns for intermediate delayed and one-time delayed RNNs in the absence of and in the presence of measurement uncertainty

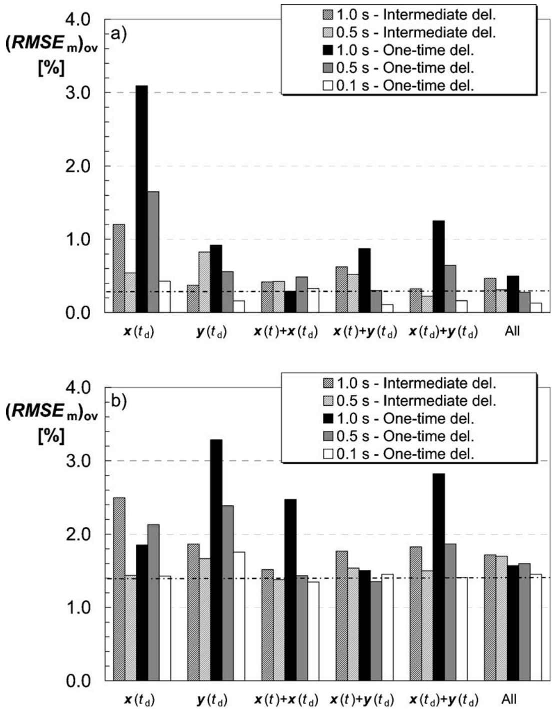

Fig. 6 Influence of RNN inputs for one-time delayed and intermediate delayed RNNs (*a*) in the absence of and (*b*) in the presence of measurement uncertainty; the dashed-dotted line stands for the $(\mathrm{RMSE}_m)_{ov}$ value for the RNN with the only input $\boldsymbol{x}(\boldsymbol{t})$

cant input proves to be the vector of exogenous inputs evaluated at the current time step, then it means that the system is characterized by poor dynamic effects since in this case a pseudostatic model should be adopted.

The influence of RNN inputs on RNN performance was established by comparing the response of five different RNN models: two intermediate delayed RNNs (n_d=5, 10, i.e., total delay time equal to 0.5 s and 1.0 s) and three one-time delayed RNNs (n_d =1, 5, 10, i.e., total delay time equal to 0.1 s, 0.5 s, and 1.0 s). Then, for each of the five RNNs, seven different models with all the possible combinations of inputs have been considered ($\boldsymbol{x}(t)$, $\boldsymbol{x}(t_d)$, $\boldsymbol{y}(t_d)$, $\boldsymbol{x}(t)+\boldsymbol{x}(t_d)$, $\boldsymbol{x}(t)+\boldsymbol{y}(t_d)$, $\boldsymbol{x}(t_d)+\boldsymbol{y}(t_d)$, and $\boldsymbol{x}(t)+\boldsymbol{x}(t_d)+\boldsymbol{y}(t_d)$, this latter solution with all the possible inputs identified as "All"), where $\boldsymbol{x}(t)$ is the vector of exogenous inputs evaluated at the current time step and $\boldsymbol{x}(t_d)$ and $\boldsymbol{y}(t_d)$ are the vectors of exogenous inputs and of delayed outputs, respectively, evaluated at antecedent time steps. It is worth remembering that (i) vectors $\boldsymbol{x}(t_d)$ and $\boldsymbol{y}(t_d)$ are different if a one-time delayed RNN instead of an intermediate delayed RNN is considered and (ii) all the developed RNNs are trained by adopting 1000 training patterns.

The results of the analysis are reported in Fig. 6, in the case both of absence (Fig. 6(*a*)) and of presence (Fig. 6(*b*)), of measurement errors. In the Fig. 6, a dashed-dotted line is inserted to indicate the overall RMSE_m in the case that the vector of exogenous inputs evaluated at the current time step $\boldsymbol{x}(t)$ is the only RNN input. In fact, such error is independent of the considered type of RNN and is equal to 0.3% or 1.4% when measurement errors are absent or present, respectively.

Some general considerations can be highlighted as follows:

- The overall results obtained in the case that both training and test patterns are not corrupted with measurement errors and in the case that both training and test patterns are corrupted with measurement errors substantially agree. In fact, the case in which both training and test patterns are not corrupted with measurement errors can be regarded as a lower limit for RNN simulation error and, thus, the presence of measurement errors can be taken into account through an additive term which only depends on the measurement noise level.
- The choice of the optimal architecture between one-time delayed RNNs and intermediate delayed RNNs depends on the considered combination of inputs. In any case, independent of the considered combination of inputs, the one-time delayed RNN with as low as possible total delay time (i.e., 0.1 s) almost always allows the lowest RMSE_m overall values both for data that are corrupted or uncorrupted with measurement errors, independent of the considered combination of inputs, as already shown in [23,29]. Thus, since the difference between the various RNN models decreases as the number of inputs increases, the adoption of the proper total delay time proves to be the key factor to set up the optimal RNN model.
- In the case that both training and test patterns are corrupted with measurement errors (Fig. 6(*b*)), if a low delay time is adopted (i.e., 0.1 s), the model with the combination of inputs $\boldsymbol{x}(t_d)$ and $\boldsymbol{y}(t_d)$ (i.e., the one-time delayed predictor RNN) allows quite good RNN performance, with an overall prediction error of ~1.4%.

Table 3 One-time delayed RNNs trained and tested on field data

Predictor RNN	Total delay time (s)	Number of training patterns	RNN inputs	Reset time step (s)
SS	0.24 0.0067	1017 1017,2034	Variable	-
MS	0.24 0.0067	509,1017,2034	All and $\boldsymbol{x}(t_d)+\boldsymbol{y}(t_d)$	1,30

A final remark has to be made about the model with $\boldsymbol{x}(t)$ (exogenous inputs evaluated at the current time step) as the only input. In fact, this model often proves to be preferable, both for uncorrupted (Fig. 6(*a*)) and corrupted (Fig. 6(*b*)) data. Such behavior can be attributed to the particular problem considered, since the deviation of system dynamics from its stationary behavior is small: in fact, as partially anticipated, (i) the model only captures dynamic effects deriving from mass storage and thermal exchange phenomena and, above all, (ii) the physical system is characterized by small size volumes.

RNN Application to Field Data

The analyses performed in the previous paragraphs and in [23] on simulated data allow the selection of the parameters to be tuned in order to set up the best RNN model. In this section, RNN capabilities are tested against measured values obtained from the compressor under investigation: the difference between the analyses developed through this paper and through [23] is that in [23] the RNN models were trained on simulated data, while here the RNN models are trained directly on field operating data.

All the RNN models developed in this section, which are summarized in Table 3, are characterized by one-time delayed configuration (with two different values of the total delay time), by 15 neurons in the hidden layer and by a multioutput architecture.

Influence of RNN Inputs. Three different one-time delayed RNNs are considered: (i) total delay time equal to 0.24 s and n_{patt} equal to 1017, (ii) total delay time equal to 0.0067 s and n_{patt} equal to 1017, and (iii) total delay time equal to 0.0067 s and n_{patt} equal to 2034. It should be remembered that the training patterns have been derived by uniformly sampling the available patterns

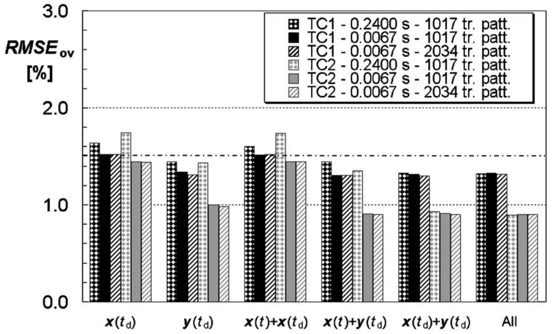

Fig. 7 Influence of RNN inputs for one-time delayed RNNs for TC1 and TC2 curves; the dashed-dotted line stands for the RMSE_{ov} value for the RNN with the only input $\boldsymbol{x}(t)$

from both TC1 and TC2 curves.

On these three RNN models, the analysis of the influence of RNN inputs on RNN performance is performed, as previously conducted on simulated data, by testing the developed RNNs on all the patterns included in the two test cases. In any case, it has been verified that, if the patterns used for training were not used for testing, the results are in practice the same; this can be explained by considering that the considered training patterns represent a small fraction of all the 36,600 available patterns (2.8% or 5.6% when 1017 or 2034 patterns are used for RNN training, respectively).

The results of the analysis are reported in Fig. 7, with the above-introduced notation ($\boldsymbol{x}(t_d)$, vector of exogenous inputs evaluated at antecedent time steps; $\boldsymbol{y}(t_d)$, vector of delayed regressed outputs; "All," solution with all the possible inputs). The dashed-dotted line in Fig. 7 indicates the overall RMSE in the case where the vector of exogenous inputs evaluated at the current time step $\boldsymbol{x}(t)$ is the only RNN input; such error is equal to 1.5% for both TC1 and TC2 curves.

The following comments can be made about the analysis of the influence of inputs conducted on field data:

- It is once again confirmed that, independent of the considered combination of inputs, the lowest RMSE overall values can be obtained with an as low as possible total delay time (0.0067 s) and with an as high as possible number of training patterns (2034). In particular, the reduction of the total delay time seems to be much more effective than the increase of the number of training patterns in reducing the overall error.
- Differently from the case of corrupted simulated data in Fig. 6(*b*), the model with the vector of exogenous inputs evaluated at the current time step $\boldsymbol{x}(t)$ as the only input is almost never preferable. The behavior in the case of field data can be attributed to the fact that, though the dynamic content of real system data is probably still poor (due to small size volumes), some "inertial" effects exist, and thus, the delayed values of exogenous inputs and of regressed outputs have to be both adopted as RNN inputs.
- The combination of inputs $\boldsymbol{x}(t_d)$ and $\boldsymbol{y}(t_d)$, which does not take into account the vector of exogenous inputs evaluated at the current time, allows very good RNN performance, comparable to that of RNN models with "All" inputs. In particular, for the best predictor RNN model (delay time of 0.0067 s and n_{patt} equal to 2034), which uses both $\boldsymbol{x}(t_d)$ and $\boldsymbol{y}(t_d)$ as inputs, the overall prediction error on each single calculation is 1.3% and 0.9% for TC1 and TC2 curve, respectively.

This latter consideration is very important because, by comparing directly the results obtained through the physics-based dynamic model developed in [21] and through the optimal RNN model trained on simulated data developed in [23], it is possible to ascertain that the optimized single-step predictor (total delay time equal to 0.0067 s and n_{patt} equal to 2034), trained on field data, allows better performance than both models. In fact, the detailed results reported in Table 4 for all the quantities show that, independent of the considered quantity and of the maneuver, the RMSE values obtainable through the best SS predictor RNN developed in this paper are the lowest (except p_2 for TC1 curve). The main reason for this result can be attributed to RNN training data, which, in the current paper, are taken experimentally on the compressor under investigation, whereas in [23] they were generated by means of the physics-based model. Finally, it can be noted that RMSE values are all lower (with the only exception of M_1 for TC1 curve) than the percentage uncertainty values reported in Table 1; thus, the SS predictor may be considered validated.

Table 4 RMSE values for the physics-based model for an RNN trained on simulated data and for a predictor RNN trained on field data

	RMSE [%]				
	p_1	p_2	M_1	T_2	Overall
TC1 curve					
Physics-based model [21]	0.23	0.79	3.96	0.47	2.04
RNN trained on simulated data [23]	0.74	0.34	5.93	0.22	3.00
SS predictor RNN trained on field data	0.09	0.51	2.54	0.20	1.30
TC2 curve					
Physics-based model [21]	0.21	0.95	1.69	0.60	1.02
RNN trained on simulated data [23]	1.07	1.65	1.98	0.66	1.43
SS predictor RNN trained on field data	0.09	0.60	1.69	0.19	0.90

Multi-Step-Ahead Predictor RNN. The setup of an MS predictor has been performed by developing an on-purpose simulation program in MATLAB environment. Once the chosen RNN, previously trained off line and acting as an SS predictor, is selected, the program allows the choice of (i) the maneuver to be simulated, (ii) the total time interval to be covered, (iii) data sampling time, and (iv) the time step from which the simulation should start. At each time step, the program estimates the whole vector of RNN inputs by arranging together the vector of exogenous inputs evaluated at antecedent time steps (measured) and the vector of delayed regressed outputs (estimated through the RNN model itself). Thus, the program allows estimation of the outputs for the desired time horizon.

Six different multi-step-ahead predictor RNNs were considered, with a different number of training patterns (509, 1017, and 2034) and with different values of the total delay time (0.24 s and 0.0067 s). With regard to the delay time, it has to be stressed that the available data have been sampled so that 0.24 s and 0.0067 s do not only represent RNN total delay time, but also data sampling time (equal to data "discretization"), i.e., $t_d = \Delta t_s$. This means that, for an assigned time horizon to be simulated, the number of calculations performed by the RNN obviously varies.

The results are presented in Fig. 8 only for the most interesting predictor, i.e., the one with the combination of inputs $\boldsymbol{x}(t_d)$ and $\boldsymbol{y}(t_d)$, while the results for the RNN model with "All" inputs are also reported for comparison purposes only. It should be remembered that the delayed regressed values of outputs $\boldsymbol{y}(t_d)$ used as inputs are estimated through the RNN itself at antecedent time steps.

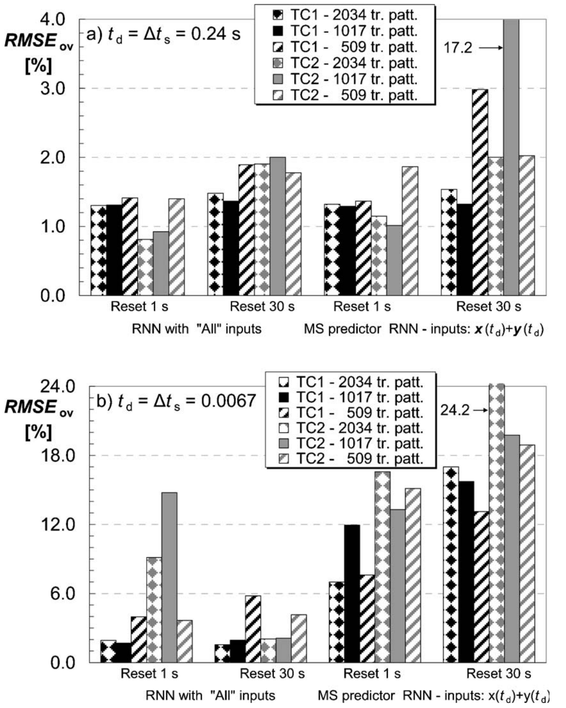

Fig. 8 Overall prediction error for an MS predictor RNN for TC1 and TC2 curve as a function of the reset time step (1 s and 30 s), of the number of training patterns (509, 1017, and 2034) and of data sampling time: (*a*) 0.24 s and (*b*) 0.0067 s

The predictor capabilities are tested over two different time horizons: 1 s and 30 s. This means that the delayed values of outputs $\boldsymbol{y}(t_d)$, which, for an MS predictor RNN are estimated through the RNN itself, are replaced with actual values (measured data) in correspondence with the selected reset time step (1 s or 30 s) to avoid the propagation of the predictor error as the simulation proceeds. As a function of the reset time step, the number of RNN calculations between two subsequent resets varies, as reported in Table 5. However, the calculation of the RMSE_{ov} is performed over the entire curve (TC1 or TC2).

From Fig. 8, it can be observed that the results are approximately independent of the considered test case (TC1 or TC2). As regards the choice of the proper data sampling time and reset time step, it can be observed that:

- for a total delay time of 0.24 s (Fig. 8(*a*)), the performance of the MS predictor is almost comparable to that of the RNN model with "All" inputs, with the exception of two cases (RNN trained on 509 patterns, simulation of TC1 curve and reset after 30 s; RNN trained on 1017 patterns, simulation of TC2 curve and reset after 30 s).
- when a high test data sampling time is chosen (0.24 s, as in Fig. 8(*a*)), prediction errors made by the predictor RNN are acceptable. In fact, if the worst case is excluded (RNN trained on 1017 patterns, simulation of TC2 curve and reset after 30 s), they are in the range of 1.0–1.9% or 1.3–3.0% over a time horizon of 1 s or 30 s, respectively, as a function of the adopted number of training patterns. It is worth noting that this result has been obtained in spite of the fact that the considered RNN is not optimized, since it is characterized by a relatively high total delay time (i.e., 0.24 s), assumed to be equal to the sampling time only for convenience.
- on the other hand, when a low test data sampling time is chosen (0.0067 s), the prediction error is clearly not acceptable, and thus the prediction accuracy can be very poor (Fig. 8(*b*)). In fact, even the comparison of RNN performance for a similar number of calculations performed by the MS predictor (125 for the RNN with total delay time of 0.24 s in Fig. 8(*a*) and 150 for the RNN with total delay time of 0.0067 s in Fig. 8(*b*)) shows that the key factor is represented by the sampling time, which has to be high so that a significant time ahead can be predicted with acceptable errors;
- the comparison of MS predictor performance for the same number of patterns (i.e., 2034) and the same reset time step (i.e., 1 s) also confirms that errors for the MS predictor with total delay time of 0.24 s are acceptable (1.5% or 2.0% for TC1 or TC2 curve, respectively), while errors for the MS predictor with total delay time of 0.0067 s are very high (7.0% or 16.6% for TC1 or TC2 curve, respectively).

Table 5 Number of calculations performed by MS predictor RNNs trained on field data for two values of the reset time step

	Number of RNN calculations	
Reset time step (s)	1	30
$t_d=\Delta t_s$=0.0067 s	150	4500
$t_d=\Delta t_s$=0.24 s	4	125

Discussion on the Capabilities of the Multi-Step-Ahead Predictor RNN. The evaluation of the best single-step-ahead predictor RNN can be done according to the results found in [23] and in the previous section of this paper. In particular, a one-time delayed RNN (i) with as-low-as-possible total delay time $t_d=n_d\Delta t_s=k_{\text{tr}}(\Delta t_s)_{\text{tr}}$ and (ii) trained with an as-high-as-possible number of patterns $(n_{\text{patt}})_{\text{tr}}=(\Delta t_{\text{tot}})_{\text{tr}}/(\Delta t_s)_{\text{tr}}$ proved to be the best solution.

Thus, if t_d is kept low in order to achieve a good RNN performance on the single calculation, the number of calculations $(n_{\text{patt}})_{\text{test}}$ must be high, once the total time interval to be simulated is fixed, in accordance with Eq. (4). This finally leads to ever increasing errors on the delayed values of outputs, since the number of RNN calculations increases.

Another possibility, implicitly suggested by Eq. (4), is the increase of the number of resets. This operation presents two weak points because the use of data from outside the RNN (i) limits the use of the RNN model as a predictor and, mainly, (ii) cannot be applied if the system under investigation is fast varying over time. In fact, in this case, the acquisition system may not have enough time to feed the RNN model. Moreover, the solution of adopting high test data sampling time (as in Fig. 8(*a*)) can be recommended only in the case that the dynamics of the system is slow enough that fast-acting events are not expected to happen.

Thus, the final result of the investigation conducted in this paper is that the best solution in setting up the RNN model can be found by properly weighting the following factors: (i) number of calculations performed by the RNN between two subsequent resets, (ii) data sampling time, (iii) RNN delay time, (iv) number of training patterns, (v) desired RNN model discretization over time, and (vi) system dynamics. Items i–iv (arranged in order of importance) only deal with the set up of the RNN, items v and vi deal with the particular problem under consideration. In fact, if the system is characterized by high "inertia," sampling frequencies can be low since its variations are slow; on the other side, if the system is characterized by low inertia, sampling frequencies must be high if the process (and its fast variations) is to be captured.

In any case, as a general conclusion, the reduction of the number of RNN calculations seems to be the key factor for improving the capabilities of multi-step-ahead predictor RNNs, as also evidenced in [29].

Conclusions

In the paper, recurrent feed-forward neural networks (RNNs) with one feedback loop were set up and tested in order to evaluate their capability in reproducing compressor behavior under unsteady conditions. The data used for training and testing the RNNs have been obtained both by means of a nonlinear physics-based model for compressor dynamic simulation (simulated data) and measured on a multi-stage axial-centrifugal small-size compressor (experimental data).

The analysis on simulated data led to the conclusion that errors decrease as the number of training patterns (which depends on the chosen sampling time once the total time interval considered for training data is fixed) increases, though good performance can be obtained by using at least 500 (or even 250 for the best networks) training patterns. Moreover, the evaluation of the influence of each input on RNN response showed that, independent of the considered combination of inputs, the lowest errors can be obtained by adopting a one-time delayed RNN with an as low as possible total delay time. Thus, the combined action of an increase in the number of training patterns and of a decrease in the RNN total delay time is beneficial to improve RNN performance, mainly in the case that the exogenous inputs evaluated at the current time step are not supplied, since in this manner the increase in errors can be limited.

The analysis of the influence of each input on RNN response, conducted for RNN models trained directly on field operating data, confirmed that, independent of the considered combination of inputs, the lowest overall errors can be obtained with an as-low-as-possible total delay time (in this paper, 0.0067 s) and by increasing the number of training patterns (in this paper, 2034). In particular, the RNN model, which does not include the vector of exogenous inputs evaluated at the current time step among the inputs, allowed very good RNN performance, comparable to that of RNN models with all inputs (overall error for each single calculation equal to 1.3% and 0.9% for the two test cases considered). Since errors were all lower (with only one exception) than the percentage measurement uncertainty values, the RNN model may be considered validated. Moreover, the optimized single-step predictor allowed better performance than both the physics-based dynamic model and the optimal RNN model trained on simulated data.

The analysis of multi-step-ahead predictor capabilities showed that prediction errors were acceptable when a high test data sampling time was chosen (in this paper, 0.24 s). In fact, with the exception of only one case, they were in the range of 1.0–1.9% or 1.3–3.0% for the two considered values of the reset time step (1 s and 30 s, respectively), as a function of the adopted number of training patterns. This result was obtained in spite of the fact that the considered RNN was not optimized, since it was characterized by a relatively high delay time (0.24 s), assumed equal to the sampling time only for convenience. On the other hand, when a low test data sampling time is chosen (in this paper, 0.0067 s), the prediction error was clearly not acceptable.

Thus, in order to set up the optimal multi-step-ahead predictor RNN model, the best solution can be found by properly setting up the best single-step-ahead predictor (through the choice of the proper number of calculations performed by the RNN between two subsequent resets, data sampling time, RNN delay time and number of training patterns) and by taking into account the particular problem under consideration (i.e., desired RNN model discretization over time and system dynamic content). In any case, as a general conclusion, the reduction of the number of RNN calculations seems to be the key factor for improving the capabilities of multi-step-ahead predictor RNNs over a significant time horizon.

Future developments of the present study will be aimed at evaluating the capabilities of such predictors for dynamic process systems characterized (i) by more considerable inertial effects (e.g., higher-size volumes and effect of spool dynamics) and (ii) by more complex configurations, which, for instance, take into consideration the whole energy system, with the interaction of several machines and pipelines.

Acknowledgment

The work was carried out with the support of the M.i.U.R. (Italian Ministry of Education, University and Research). The author gratefully acknowledges Prof. Roberto Bettocchi, Prof. Pier Ruggero Spina, Michele Pinelli, Ph.D., and Dr. Mirko Morini for the suggestions.

Nomenclature

d = vector dimension
F = RNN transfer function
k = multiplicative factor for data sampling time
M = mass flow rate
MS = multi-step-ahead
MSE = mean square error
n_{d} = number of time delay units
n_{i} = number of inputs
n_{o} = number of outputs
n_{patt} = number of patterns
n_{reset} = number of resets
n_{TR} = number of transients used for RNN testing
N_{C} = compressor rotational speed
p = pressure
RMSE = root-mean-square error
SS = single-step-ahead
t = time, expected target output
t_{d} = total delay time ($=n_{\mathrm{d}}\Delta t$)
T = temperature
TC = test case curve (field data)
TR = transient curve (simulated data)
$\boldsymbol{x}$ = vector of exogenous inputs
$\boldsymbol{y}$ = vector of delayed outputs
y = computed output
Δt = time delay unit
Δt_{s} = sampling time
Δt_{tot} = total time interval

Subscripts and Superscripts

0,1,2,3 = compressor physics-based model sections
m = mean on all transients used for testing
ov = overall
tr = training
test = test
$\boldsymbol{x}$ = input vector $\boldsymbol{x}$
$\boldsymbol{y}$ = output vector $\boldsymbol{y}$

References

[1] Parlos, A. G., Chong, K. T., and Atiya, A. F., 1994, "Application of the Recurrent Multilayer Perceptron in Modeling Complex Process Dynamics," IEEE Trans. Neural Netw., **5**(2), pp. 255–266.
[2] Torella, G., and Lombardo, G., 1996, "Neural Networks for the Diagnostics of Gas Turbine Engines," ASME Paper No. 96-TA-39.
[3] Kanelopoulos, K., Stamatis, A., and Mathioudakis, K., 1997, "Incorporating Neural Networks Into Gas Turbine Performance Diagnostics," ASME Paper No. 97-GT-35.
[4] Bettocchi, R., Spina, P. R., and Torella, G., 2002, "Gas Turbine Health Indices Determination by Using Neural Networks," ASME Paper No. GT-2002-30276.
[5] Arriagada, J., Genrup, M., Loberg, A., and Assadi, M., 2003, "Fault Diagnosis System for an Industrial Gas Turbine by Means of Neural Networks," *Proc. of International Gas Turbine Congress 2003 (IGTC'03)*, Tokyo, Nov. 2–7, GTSJ, Tokyo, Paper No. IGTC2003Tokyo TS-001.
[6] Bettocchi, R., Pinelli, M., Spina, P. R., and Venturini, M., 2005, "Artificial Intelligence for the Diagnostics of Gas Turbines. Part I: Neural Network Approach," ASME Paper No. GT2005-68026.
[7] Volponi, A. J., DePold, H. R., Ganguli, R., and Daguang, C., 2000, "The Use of Kalman Filter and Neural Networks Methodologies in Gas Turbine Performance Diagnostics: A Comparative Study," ASME Paper No. 2000-GT-0547.
[8] DePold, H. R., and Gass, F. D., 1999, "The Application of Expert Systems and Neural Networks to Gas Turbine Prognostics and Diagnostics," ASME J. Eng. Gas Turbines Power, **121**, pp. 607–612.
[9] Sampath, S., and Singh, R., 2004, "An Integrated Fault Diagnostics Model Using Genetic Algorithm and Neural Networks," ASME Paper No. GT-2004-53914.
[10] Bettocchi, R., Pinelli, M., Spina, P. R., and Venturini, M., 2005, "Artificial

Intelligence for the Diagnostics of Gas Turbines. Part II: Neuro-Fuzzy Approach," ASME Paper No. GT2005-68027.

[11] Simani, S., Fantuzzi, C., and Spina, P. R., 1998, "Application of a Neural Network in Gas Turbine Control Sensor Fault Detection," *Proc. of 1998 IEEE International Conference on Control Applications*, Trieste, Italy, IEEE, New York, pp. 182–186.

[12] Botros, K., K., Kibria, G., and Glover, A., 2000, "A Demonstration of Artificial Neural Networks Based Data Mining for Gas Turbine Driven Compressor Stations," ASME Paper No. 2000-GT-0351.

[13] Fink, D. A., Cumpsty, N. A., and Greitzer, E. M., 1992, "Surge Dynamics in a Free-Spool Centrifugal Compressor System," ASME J. Turbomach., **114**, pp. 321–332.

[14] Hale, A. A., and Davis, M. W., 1992, "DYNamic Turbine Engine Compressor Code DYNTECC—Theory and Capabilities," AIAA Paper No. AIAA-92-3190.

[15] Blotemberg, W., 1993, "A Model for the Dynamic Simulation of a Two-Shaft Industrial Gas Turbine With Dry Low No_x Combustor," ASME Paper No. 93-GT-355.

[16] Bettocchi, R., Spina, P. R., and Fabbri, F., 1996, "Dynamic Modeling of Single-Shaft Industrial Gas Turbine," ASME Paper No. 96-GT-332.

[17] Bianchi, M., Peretto, A., and Spina, P. R., 1998, "Modular Dynamic Model of Multi-Shaft Gas Turbine and Validation Test," *Proc. of The Winter Annual Meeting of ASME*, ASME, New York, Vol. AES-38, pp. 73–81.

[18] Camporeale, S. M., Fortunato, B., and Mastrovito, M., 2002, "A High-Fidelity Real-Time Simulation Code of Gas Turbine Dynamics for Control Applications," ASME Paper No. GT-2002-30039.

[19] Theotokatos, G., and Kyrtatos, N. P., 2003, "Investigation of a Large High-Speed Diesel Engine Transient Behaviour Including Compressor Surging and Emergency Shutdown," ASME J. Eng. Gas Turbines Power, **125**, pp. 580–589.

[20] Tveit, G. B., Bjorge, T., and Bakken, L. E., 2005, "Impact of Compressor Protection System on Rundown Characteristics," ASME Paper No. GT2005-68436.

[21] Venturini, M., 2005, "Development and Experimental Validation of a Compressor Dynamic Model," ASME J. Turbomach., **127**(3), pp. 599–608.

[22] Morini, M., Pinelli, M., and Venturini, M., 2006, "Development of a One-Dimensional Modular Dynamic Model For The Simulation of Surge in Compression Systems," ASME Paper No. GT2006-90134.

[23] Venturini, M., 2006, "Simulation of Compressor Transient Behavior Through Recurrent Neural Network Models," ASME J. Turbomach., **128**(4), pp. 1–11.

[24] Bozzi, L., Crosa, G., and Trucco, A., 2003, "Simplified Simulation Block Diagram of Twin-Shaft Gas Turbines," ASME Paper No. GT-2003-38679.

[25] Ohanian, S., and Kurz, R., 2001, "Series or Parallel Arrangement in a Two-Unit Compressor Station," ASME J. Eng. Gas Turbines Power, **124**, pp. 936–941.

[26] Bettocchi, R., Pinelli, M., Spina, P. R., Venturini, M., and Zanetta, G. A., 2006, "Assessment of the Robustness of Gas Turbine Diagnostics Tools Based on Neural Networks," ASME Paper No. GT2006-90118.

[27] Jiang, D., and Wang, J., 2000, "On-Line Learning of Dynamical Systems in the Presence of Model Mismatch and Disturbances," IEEE Trans. Neural Netw., **11**(6), pp. 1272–1283.

[28] Plett, G. L., 2003, "Adaptive Inverse Control of Linear and Nonlinear Systems Using Dynamic Neural Networks," IEEE Trans. Neural Netw., **14**(2), pp. 360–376.

[29] Parlos, A. G., Rais, O. T., and Atiya, A. F., 2000, "Multi-Step-Ahead Prediction in Complex Systems Using Dynamic Recurrent Neural Networks," Neural Networks, **13**(7), pp. 765–786.

[30] Desideri, U., Fantozzi, F., Bidini, G., and Mathieu, P., 1997, "Use of Artificial Neural Networks for the Simulation of Combined Cycles Transients," ASME Paper No. 97-GT-442.

[31] Chiras, N., Evans, C., and Rees, D., 2002, "Nonlinear Gas Turbine Modeling Using Feedforward Neural Networks," ASME Paper No. GT-2002-30035.

[32] Arsie, I., Pianese, C., and Sorrentino, M., 2002, "Recurrent Neural Network Based Air-Fuel Ratio Observer for SI Internal Combustion Engines," *Proc. of ESDA 2002*, Istanbul, ASME, New York, Paper No. ESDA2002/APM038 ACC008.

[33] Ogaji, S. O. T., Li, Y. G., Sampath, S., and Singh, R., 2003, "Gas Path Fault Diagnosis of a Turbofan Engine From Transient Data Using Artificial Neural Networks," ASME Paper No. GT2003-38423.

[34] Menon, S., Uluyol, O., and Gupta, D., 2004, "Turbine Engine Modeling Using Temporal Neural Networks for Incipient Fault Detection and Diagnosis," ASME Paper No. GT2004-53649.

[35] Haykin, S., 1999, *Neural Networks—A Comprehensive Foundation*, 2nd ed., Prentice-Hall, Englewood Cliffs, NJ.

[36] Bettocchi, R., Pinelli, M., and Spina, P. R., 2005, "A MultiStage Compressor Test Facility: Uncertainty Analysis and Preliminary Test Results," ASME J. Eng. Gas Turbines Power, **127**(1), pp. 170–177.

[37] Traverso, A., Scarpellini, R., and Massardo, A., 2005, "Experimental Results and Transient Model of an Externally Fired Micro Gas Turbine Technology," ASME Paper No. GT2005-68100.

[38] Stiller, C., Thorud, B., and Bolland, O., 2005, "Safe Dynamic Operation of a Simple SOFC/GT Hybrid System," ASME Paper No. GT2005-68481.

[39] Cybenko, G., 1989, "Approximation by Superimposition of a Sigmoidal Function," Math. Control, Signals, Syst., **2**, pp. 303–314.

[40] Atiya, A., F., and Parlos, A., G., 2000, "New Results on Recurrent Network Training: Unifying the Algorithm and Accelerating Convergence," IEEE Trans. Neural Netw., **11**(3), pp. 697–703.

Engine Design Studies for a Silent Aircraft

Cesare A. Hall

Daniel Crichton

Department of Engineering,
Whittle Laboratory,
Madingley Road,
Cambridge, U.K

The Silent Aircraft Initiative is a research project funded by the Cambridge-MIT Institute aimed at reducing aircraft noise to the point where it is imperceptible in the urban environments around airports. The propulsion system being developed for this project has a thermodynamic cycle based on an ultrahigh bypass ratio turbofan combined with a variable area exhaust nozzle and an embedded installation. This cycle has been matched to the flight mission and thrust requirements of an all-lifting body airframe, and through precise scheduling of the variable exhaust nozzle, the engine operating conditions have been optimized for maximum thrust at top-of-climb, minimum fuel consumption during cruise, and minimum jet noise at low altitude. This paper proposes engine mechanical arrangements that can meet the cycle requirements and, when installed in an appropriate airframe, will be quiet relative to current turbofans. To reduce the engine weight, a system with a gearbox, or some other form of shaft speed reduction device, is proposed. This is combined with a low-speed fan and a turbine with high gap-chord spacing to further reduce turbomachinery source noise. An engine configuration with three fans driven by a single core is also presented, and this is expected to have further weight, fuel burn, and noise benefits. [DOI: 10.1115/1.2472398]

Introduction

The Silent Aircraft Initiative is a multidisciplinary project that is developing a concept aircraft with noise emission as the primary design driver. The aircraft is aimed at entry into service in about 20 years, and the ambitious objective is to reduce the noise generated to the point where it would be imperceptible above background noise in a typical urban environment outside an airport. Such an aircraft could be deemed as "silent," and this would represent a reduction in aircraft noise greater than that achieved over the last fifty years. Figure 1 illustrates the scale of this challenge, showing the Silent Aircraft noise target relative to the component noise levels for a current passenger aircraft. Note that to reach this noise level requires an aircraft that is less than half as noisy as the target identified by the ACARE vision for 2020 [1].

In order to reach the Silent Aircraft noise goal, large reductions, relative to current technology, are required for all components of engine and airframe noise. To make such large reductions, several methods must be employed simultaneously (see [2,3]). For example, to reduce jet noise, a very large, low-velocity exhaust flow is required combined with a power-management departure procedure. To make adequate turbomachinery noise reductions, the source noise can be reduced with improved component design and new engine configurations, but further attenuation of the noise is also needed using acoustic liners and shielding by the airframe [4].

In addition to the aggressive noise target, the new aircraft must be economical relative to other aircraft of the future. This requires a propulsion system that has competitive fuel burn as well as acceptable development, acquisition, and maintenance costs. Prior to the work in this paper, several trade studies were completed to determine the potential noise reductions possible for various engine configurations and to understand their implications for weight and performance [2]. This work found that a propulsion system embedded into the rear upper surface of an all-lifting body was best suited to meeting the project objectives. Furthermore, a turbofan system with a variable exhaust was shown to have the potential to have lower fuel consumption for a given noise level.

Several previous research projects have also studied advanced UHBR engine configurations aimed at significant improvements in noise and/or fuel consumption. For example, the NASA study of advanced engines for high efficiency [5] looked at several configurations, including geared fans and contra-fan designs, aimed at weight and fuel burn reductions. Another system study of engine concepts carried out by NASA [6] investigated the optimum engine parameters for low noise with acceptable operating costs. The design considerations for a new UHBR engine, aimed at reduced fuel burn, are clearly outlined in [7], and Ref. [8] gives a good overview of future technology required to further reduce noise from conventional aircraft engines. This proposes the use of geared turbofans to give a large improvement in noise emission.

A study of more radical propulsion concepts for a functionally silent aircraft is also presented in [9], which proposes distributed engine systems integrated with a blended-wing-body type aircraft.

What is new in the present study is that the off-design performance of the engine has been considered from the start of the design process. This is key since the engine conditions when low noise is essential are far from the design point (typically top-of-climb or cruise). In addition, the engine cycle in this project has been optimized for operation with a variable exhaust system and for an installation embedded within an all-lifting wing type airframe. Previous studies have tended to focus on engine designs intended for conventional tube-and-wing aircraft.

The current paper, therefore, aims to extend the previous work [2], which was based on quite simple analyses, to create more detailed designs of propulsion systems. In doing so, the off-design operation of a UHBR turbofan is examined and a design process for an advanced low-noise propulsion system is demonstrated. The designs are developed to the point where they can be assessed in terms of their performance, weight, and noise, and several possible engine arrangements are presented. Overall, this paper makes a contribution to the field of future engine designs for low noise and demonstrates the potential of UHBR engines with variable exhaust systems.

Propulsion System Requirements

The Silent Aircraft is expected to use an "all-lifting body" style of airframe [10]. The baseline design has a payload of 250 pas-

---

Contributed by the International Gas Turbine Institute of ASME for publication in the JOURNAL OF TUROBMACHINERY. Manuscript received July 13, 2006; final manuscript received July 23, 2006. Review conducted by David Wisler. Paper presented at the ASME Turbo Expo 2006: Land, Sea and Air (GT2006), Barcelona, Spain, May 8–11, 2006. Paper No. GT2006-90559

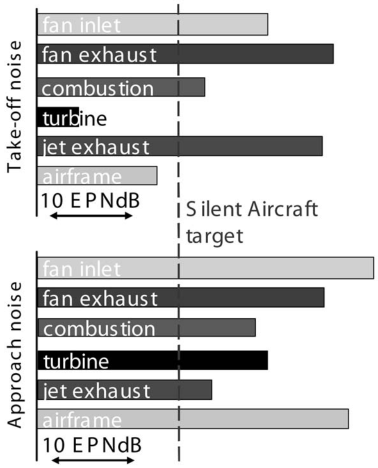

Fig. 1 Noise levels for a current 250 passenger aircraft compared with the Silent Aircraft target

sengers and a design range of 4000 nautical miles. This mission was chosen to give the lowest weight aircraft that would be economically competitive with other civil airlines. A 3-D view of a CAD representation of a possible airframe and propulsion system is shown in Fig. 2.

Studies with an airframe design tool were used to determine the thrust requirements at different points in the mission with corresponding altitudes and Mach numbers. The flight mission profile was chosen to give the lowest aircraft take-off weight (MTOW), with the assumption that this would minimize the noise radiated at take-off and approach. The methodology and analysis used to optimize the airframe design is described in detail within [12]. Table 1 summarizes the resulting requirements of the propulsion system at key operating conditions in the flight envelope.

For the purposes of this paper, the noise target of the Silent Aircraft is expressed as a peak dBA value that cannot be exceeded at any point on the ground outside the airport boundary during take-off and landing in normal operating conditions. This peak dBA limit was imposed because this can be linked to both World Health Organization guidelines on community noise and data on average traffic noise levels in urban areas [13,14]. Normal operating conditions are taken as an atmospheric temperature of below ISA+12 K and a runway length of 3000 m. This allows the aircraft to operate in a "nonsilent" mode for any remaining extreme conditions ("short & steep," "very hot," and "hot & high" take-off).

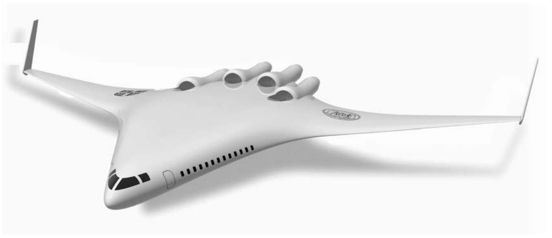

Fig. 2 A 3-D rendering of a candidate Silent Aircraft airframe and propulsion system, taken from [11]

Table 1 Propulsion system mission requirements

Condition	Altitude (m)	Mach number	Total thrust (kN)	SFC (g/sN)	Noise target (peak dBA)
Sideline	180	0.23	316.8	—	<57.0
Flyover	195	0.24	172.8	—	<57.0
Top-of-climb	12,192	0.80	82.4	—	—
Mid cruise	12,570	0.80	65.4	<15.0	—
Approach	120	0.23	<72.0	—	<57.0

For take-off, an optimized departure profile was used in which the thrust was managed to achieve the maximum climb rate without exceeding the noise target in terms of jet noise. This procedure is demonstrated in [3], and it was found that a total exhaust area of 13.2 m^2 would be required to enable an acceptable departure profile. The sideline and flyover conditions represent two points in the departure profile that are critical in terms of noise. At sideline, the aircraft is still inside the airport boundary and the climb rate is highest. At flyover, the aircraft is closest to the population on the ground. The sideline lateral position is the same as the ICAO certification distance of 450 m, but the flyover point used is closer to the runway (4048 m rather than 6500 m after brakes off).

Top-of-climb (TOC) is the condition that determines the size of the engine. This is where high thrust is required to keep climbing and the atmosphere is thin. For an economically viable aircraft of the future, the installed engine specific fuel consumption (SFC) at cruise was specified to be at least as competitive with the next generation high bypass ratio podded turbofan engines (15 g/sN =0.53 lb/lbh). Note that improvements in SFC are beneficial in terms of total noise because they reduce the weight of fuel that needs to be carried, and thus the MTOW.

For the approach condition, a maximum net thrust target was specified in order to limit the airframe drag required. A greater drag leads to higher airframe noise through the dissipation of turbulent kinetic energy in the wake. The minimum thrust specified was chosen to be as low as possible while enabling an engine spool-up time (the time required for the engine to accelerate to maximum thrust) that would be comparable to current turbofans.

Note that all the engine design studies in this paper are matched to the same all-lifting body airframe and flight mission. The methodology applied to develop the engine cycle and the mechanical designs should be equally applicable to the propulsion systems for other airframe configurations. However, a different airframe or installation would have a large impact on the values of many of the engine characteristics.

Engine Installation Considerations

Before the parameters of the engine cycle can be specified some characteristics of how the propulsion system is packaged with the airframe need to be considered. For the Silent Aircraft design, the engines are positioned on the upper surface of the airframe, towards the trailing edge (as illustrated in Fig. 2). This location was adopted to take advantage of the performance benefits of boundary layer ingestion and to maximize the shielding of forward arc engine noise [4]. It also offers airframe control and safety advantages, because the engines are positioned well behind the passenger bays [12].

A target S-shaped inlet performance was assumed based on results in the open literature; for example [15,16], and preliminary CFD studies [17]. Several calculations were completed at the cruise condition for different numbers of engines and various intake configurations. The current baseline design has 4 separate engine units (Fig. 2), which gives an acceptable fan diameter and good installation performance. The mesh geometry and Mach number contours, from a calculation of this configuration, are as shown in Figs. 3 and 4, respectively. Figure 4 shows how a large region of high loss flow builds up at the bottom of the inlet duct as the engine face is approached, and this is typical for an S-shaped duct.

The final propulsion system for the Silent Aircraft is expected to use boundary layer ingestion (BLI) to give a fuel burn benefit, as mentioned above, and as discussed in [2]. BLI introduces significant challenges to both the engine and airframe design. In particular, BLI generates additional nonuniform flow distortion in both the radial and circumferential directions, which is present at

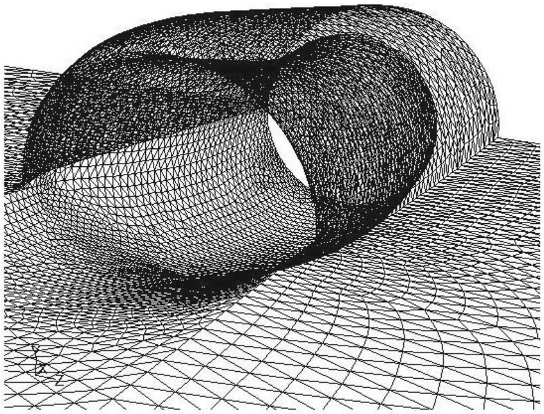

Fig. 3 View of the surface mesh for a four-engine installation, taken from [17]

all flight conditions. BLI also changes the engine thrust requirements because any boundary layer fluid that passes through the engine and contributes to thrust would have otherwise contributed to airframe drag. Thus, to progress the engine design for the studies in this paper, the engine inlets were temporarily assumed to be boundary layer diverting (BLD). This enables the engine thrust requirements to stay as per Table 1. The impact of BLI on the engine performance and the airframe requirements will be included in future work.

CFD results for S-shaped inlet ducts all show significant separated regions at the fan-face. From the inlet highlight to the fan-face, a typical S-shaped inlet was found to have a pressure recovery (p_{02}/p_{01}) of about 0.96. This value can be applied to both BLI and BLD cases, and it was used in the following engine design studies as a target performance for the engine inlet. Overall, it is expected to be a lower-bound estimate because design improvements and flow control should be able to reduce the losses. The level of circumferential distortion was also determined from the predictions, and in terms of DC60 (an industry measure of the severity of flow nonuniformity), the S-duct gave values of around 20%. The impact of this distortion on the system design will be explored in detail in future research, because it is mainly a consequence of BLI. The designs presented in this paper are therefore intended to tolerate this level of distortion, but are not optimized for performance with it present.

The engine exhaust is considered as a long cylindrical duct in which the core and bypass streams are mixed completely, followed by a loss-free variable nozzle. The exhaust duct pressure losses were determined using simple compressible pipe flow analysis (Fanno line flow) with skin friction coefficients appropriate for the surface of a perforated acoustic liner. The exhaust duct size was set to match the maximum nozzle area required for a quiet take-off. This size of duct was used to avoid a “diffusing nozzle” being necessary at any point in the aircraft flight envelope. The length of mixer duct was set at 2 fan diameters to accommodate a large area of downstream acoustic liners. This led to an exhaust pressure recovery (p_{08}/p_{064}) of 0.98 for the designs in this paper.

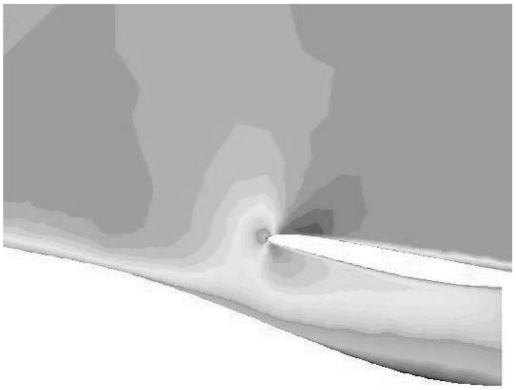

Fig. 4 Contours of Mach number through a four-engine installation, taken from [17]

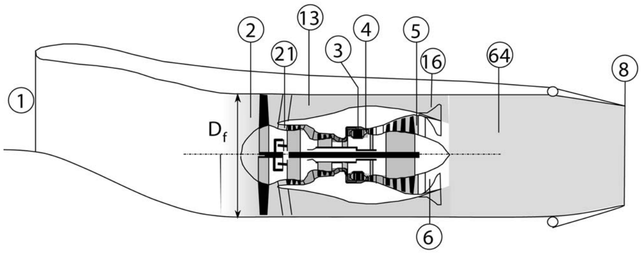

Fig. 5 Schematic of engine layout showing station numbering, adapted from [18]

Engine Cycle Design

The engine configurations developed in this paper are ultrahigh bypass ratio (UHBR) turbofans combined with variable area exhaust nozzles. This configuration was identified in [2], and for the aircraft mission requirements it was expected to be more suitable than other possible variable cycle systems such as bypass stream ejectors or a system with auxiliary fans. The optimum solution for a different mission requirement may be quite different. The engine station numbering used for the thermodynamic cycle is as shown in Fig. 5.

To allow for technological advances, 2025 estimates of peak component efficiencies and metallurgical limits were made by extrapolating historical trends. These were imposed as limits on the engine cycle temperatures and component efficiencies that could not be exceeded at any point in the engine operation. It was expected that a future quiet engine would have a similar maximum fan capacity to today’s turbofan designs, but that this could be achieved at a lower fan pressure ratio and tip speed (see [2]). A maximum fan capacity was therefore imposed as a constraint and combined with a generic low pressure ratio fan characteristic to estimate off-design performance variations. It was also predicted that advances in mechanical properties would allow the hub-to-tip radius ratio of a future fan to be lower than current designs. A value of 0.25 was used to minimize the fan diameter (current designs are typically in the range 0.3–0.35).

In order to develop an engine cycle, a design condition is chosen to fix the engine size and key parameters. For this study, the top-of-climb point was used and the thermodynamic cycle was optimized to minimize the fan diameter and fuel consumption at this condition. The top-of-climb point was then considered with the other off-design conditions and some iteration was employed to optimize the performance for every engine operating condition in Table 1.

Cycle Optimization at Top-of-Climb. The engine design cycle was developed using GasTurb10 [18] with the aim of producing the most compact and fuel-efficient engine that would satisfy the requirements in Table 1. Figure 6 shows how an engine cycle appropriate for the future Silent Aircraft was evolved from a current conventional turbofan. Each bar in the figure represents a redesign of the engine in which the fuel consumption has been minimized and the net thrust and temperature limits have been constrained. The relative heights of the adjacent bars show the impact of each design change on engine fuel consumption and engine size. The aim of such a chart is to show that the final

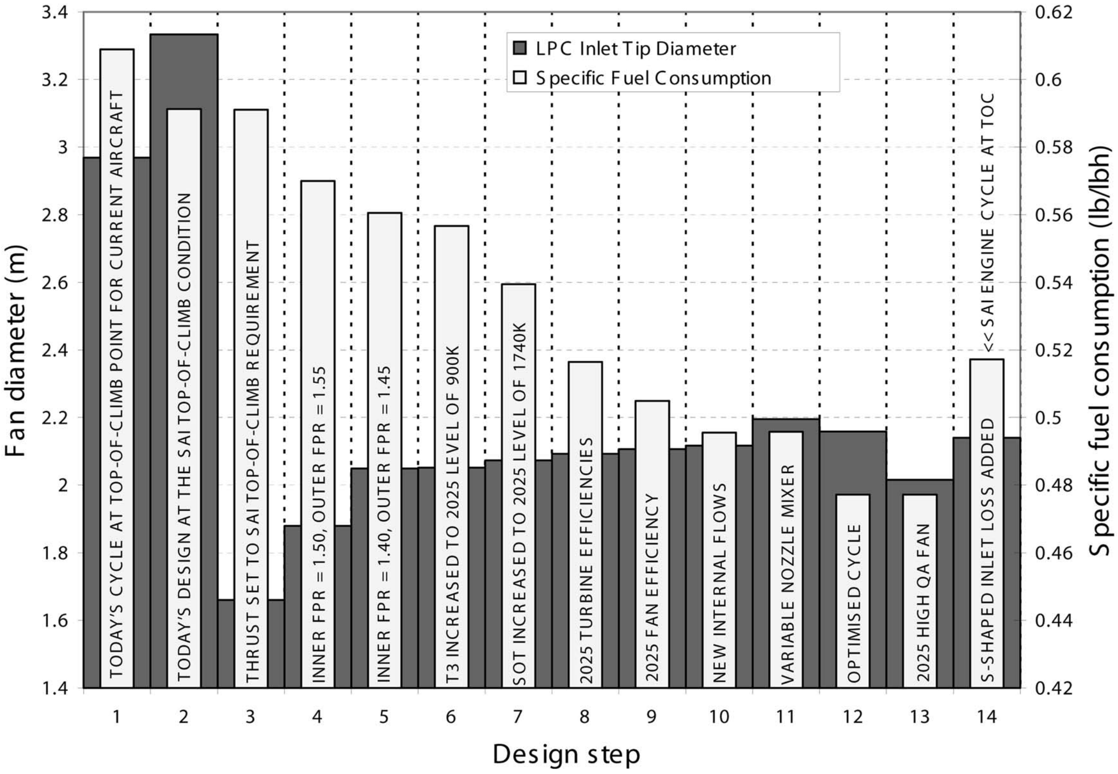

Fig. 6 Evolution of the Silent Aircraft engine cycle at top-of-climb assuming a four-engine system

design cycle is feasible. The changes in the height of the bars between each design show the incremental effects of changing the design cycle parameters.

The first three steps shown in Fig. 6 represent the design changes necessary to match today's turbofan engine to the top-of-climb condition in Table 1. The two subsequent changes indicate how a large performance benefit can be attributed to the low fan pressure ratio that is specified (steps 4 and 5). A drawback of this is that the fan diameter increases significantly as FPR is reduced. Higher temperature limits and improved turbine performance contribute significantly to improving core efficiency (steps 6, 7, and 8). However, as the engine efficiency is improved, the fan diameter has to increase to maintain the same net thrust. This effect is also seen when the fan efficiency is increased and the losses due to internal air systems are reduced (steps 9 and 10). The exhaust duct that is specified is larger than optimum to match the variable area nozzle (step 11) and this also leads to a slightly larger fan. The cycle was then optimized for best thermodynamic performance (step 12). This involved iterating to determine the bypass-to-core total pressure ratio (p_{016}/p_{06}) that gave the minimum SFC. The use of the high capacity, low hub-tip-ratio fan (step 13) gives further improvements. However, the introduction of the S-duct inlet total pressure loss (step 14) increases the fan diameter and significantly worsens the overall performance.

Note that the design cycle used in this paper has a fan pressure ratio of 1.45, and for a four-engine case, a fan diameter of 2.16 m. The choice of design FPR is a compromise that is driven by several factors. A lower value leads to higher propulsive efficiency at the cost of a larger engine size, which increases the total installed drag. In terms of noise, as FPR reduces it becomes easier to meet the jet noise target, and the nozzle area change needed between take-off and top-of-climb is minimized [19]. Fan source noise also tends to reduce with FPR, as shown later in this paper in Fig. 14. Unfortunately, a lower FPR design is heavier and more sensitive to inlet distortion and to installation pressure losses, as shown in [2].

A top-of-climb FPR of 1.45 was therefore chosen as the lowest possible value that would be achievable with a robust mechanical design. The corresponding engine bypass ratio is 15.5, which clearly makes it a UHBR. However, BPR is not a good design parameter to characterize the engine because it changes significantly between operating conditions (see Table 2, later). The SFC at top-of-climb is 14.7 g/sN, which is slightly better than the best turbofans operating today. This seems realistic for a UHBR engine in 2025 within an S-type inlet.

Off-Design Operation. Using the final cycle design developed above, the engine parameters at other points in the flight mission were determined. With the engine size fixed and the thrust constrained, the main degree of freedom available is the nozzle setting. At each of the flight conditions in Table 1, the fan can operate anywhere along a characteristic of constant thrust. Figure 7 shows scaled constant-speed fan characteristics based on [20] with constant-thrust characteristics overlaid (dashed) for each of the key operating conditions. The optimum operating points used for the final design are marked as small circles. The precise perfor-

Table 2 Cycle parameters for the Silent Aircraft engine design in this paper

Parameter	Sideline	Top-of-climb	Cruise	Unit
FPR	1.27	1.45	1.40	—
$N_f/\sqrt{T_{02}}$	90	100	99	%
ΔA_8	+35	0	+8	%
M_{a2}	0.64	0.66	0.70	—
η_{fan}	94.5	90.4	93.4	%
T_{03}	910	900	840	K
T_{04} (TET)	1730	1880	1700	K
OPR	41.0	57.4	53.9	—
BPR	19.0	15.5	16.8	—
SFC	8.8	14.7	14.2	g/sN

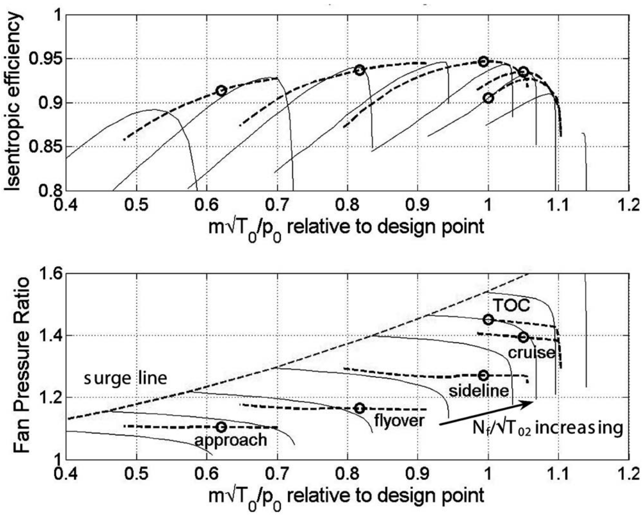

Fig. 7 Operation of the Silent Aircraft engine fan for a variable nozzle design

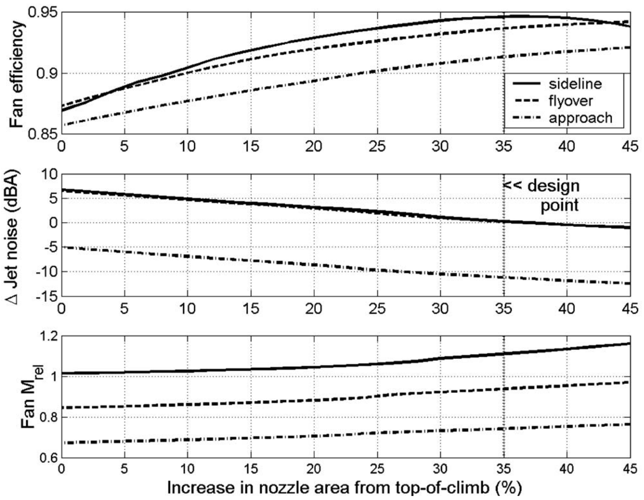

Fig. 9 Variation in fan efficiency, jet noise, and fan tip relative Mach number with nozzle area.

mance depends on the shapes of the fan characteristics, so these plots can be viewed as an example case. Improved fan characteristics for a full 3-D fan design are developed in the companion paper [19].

The characteristics in Fig. 7 have been scaled around the design FPR of 1.45 (top-of-climb) and a peak rotor isentropic efficiency of 94.5% (the maximum possible expected in 2025). By varying the nozzle exit area while maintaining the net thrust constant-thrust lines could be produced. These were further constrained by shaft speed and temperature limits. The optimum top-of-climb point is positioned towards the stability margin on the 100% speed characteristic. This was done primarily so that the exhaust nozzle could be opened sufficiently at sideline to give higher fan capacity at this condition (and thus low jet noise), while keeping high efficiency. The design condition can be positioned further down the maximum speed characteristic, but this reduces the operating range available at other conditions. The fan capacity at cruise is allowed to increase slightly without exceeding the design fan shaft speed to give improved efficiency.

Figure 8 shows the fan characteristics if the same mission requirements and design engine cycle are assumed for a fixed nozzle engine. In this case, the fan is constrained to work at a single working point for each flight condition. The top-of-climb point is positioned so that the cruise condition is at peak efficiency. The sideline, flyover, and approach points are thus fixed at lower flow rates, which are at higher fan pressure ratios and closer to instability than for the case with a variable nozzle.

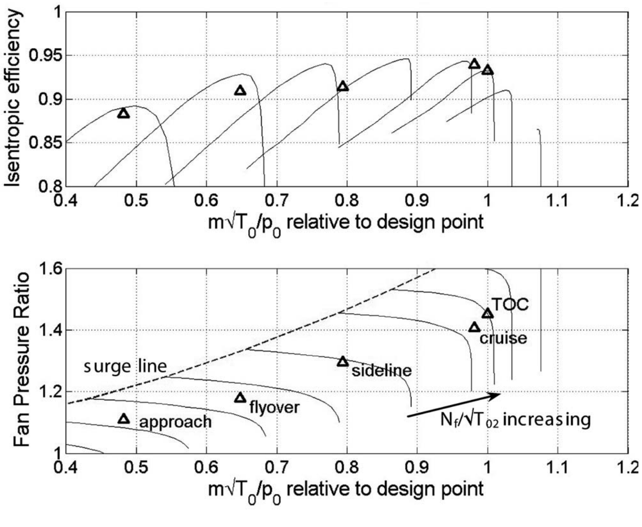

Fig. 8 Operation of the Silent Aircraft engine fan for a fixed nozzle design

Table 2 details the key cycle parameters at sideline, top-of-climb, and cruise corresponding to the operating points in Fig. 7. This illustrates the component performances and the cycle temperatures that are required to achieve the design requirements. It is important to emphasize that the operation of the Silent Aircraft engine with a variable area nozzle differs significantly from that of an engine with a fixed nozzle operated for a conventional aircraft. Firstly, the fan pressure ratio at take-off is much lower than at cruise or top-of-climb. The principal reason is that only a fraction of the available thrust at take-off is needed. The total sea level static thrust available from the propulsion system (all engines) is about 570 kN, and less than 60% of this is needed at the sideline condition. The low thrust requirement at sideline is key to minimizing the jet noise, and this is further exploited with an optimized take-off procedure that is described in [3].

Another unusual aspect of the design is that the fan speed is similar at all the three conditions in Table 2, and the fan-face Mach number is consistently high. Previous studies [2] showed that a high fan capacity at take-off leads to lower jet noise and Figs. 7 and 9 demonstrate how this can be achieved with a variable exhaust nozzle.

The variations in cycle temperatures and pressures are also different from a conventional turbofan. Usually the cycle temperatures are all highest at take-off, and it is this condition that is most demanding in terms of the mechanical stresses. For the design developed here the compressor outlet temperature is highest at take-off, but only slightly above the top-of climb and cruise points. The turbine entry temperature is a maximum at top-of-climb, where the overall pressure ratio is also much greater than the sideline condition. This occurs because the thrust requirement of the engine during take-off is only a fraction of the total thrust available.

The variable nozzle has the potential to reduce fuel consumption. It should be possible to carefully control the nozzle position to maximize the fan efficiency at all flight conditions, as indicated in Fig. 7. For a fixed nozzle design, a fan is constrained to operate on a working line that might not be at peak efficiency. In addition, the fan characteristics of an engine operating in-service may not be exactly as predicted. A variable nozzle enables performance discrepancies to be corrected during flight, ensuring the optimum

Table 3 Principal mechanical parameters for the engine designs presented

	Design A	Design B	Design C	Design D
Configuration	Three-spool turbofan	Two-spool geared fan	Two-spool, slower fan	Multiple fan system
D_f (m)	2.16	2.16	2.18	1.28
l_{eng} (m)	3.46	2.42	2.70	2.70
n_{eng}	4	4	4	12
Number of fan rotor blades	20	20	18	18
Max. U_{tip} (m/s)	380	380	350	350
IPC/booster stages	7	7	8	8
HPC stages	10	5	5	5
HPC min. blade height (mm)	10	22	22	22
LP turbine stages	9	4	4	4
W_{eng} (%)	100	99.2	91.4	81.3

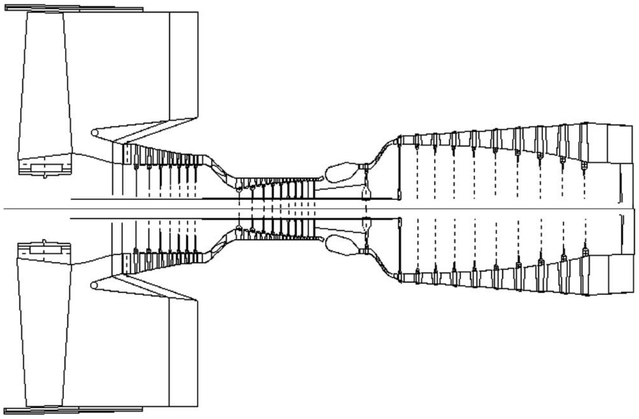

Fig. 10 Design A: 3-spool conventional turbofan design for the Silent Aircraft

efficiency is achieved.

A variable exhaust nozzle can also improve the engine operability. During take-off, with the nozzle fully opened, the fan operates well away from the stability line. This is particularly helpful for a low FPR fan at this point in the flight mission because the engine is at risk of crosswind induced inlet separation. A carefully controlled variable nozzle could enable other aeromechanical problems such as flutter to be avoided at other key conditions in the flight envelope.

The variations in fan efficiency, tip relative Mach number, and exhaust jet noise (relative to the target level), along the constant-thrust characteristics in Fig. 7, are shown in Fig. 9 for the three noise critical operating conditions. A design fan tip speed of 350 m/s (at top-of-climb) has been assumed for this figure. The plots illustrate that as the exhaust nozzle is opened, the performance of the fan is improved. The jet noise, as computed using the Stone jet noise model [21], decreases as the nozzle is opened because the jet velocity reduces substantially. However, the fan tip speed and axial flow velocity have to increase to maintain the same thrust. Fan broadband noise is typically correlated against tip relative Mach number (ESDU 98080, [22]) and other fan noise sources increase with tip speed. Thus, there is a trade-off between fan source noise and jet noise, which demands careful attention. This aspect is explored further in the companion paper [19], which shows that by positioning the fan operating condition at a point of high efficiency during take-off, it is possible to reduce fan source noise while still meeting the jet noise target.

Preliminary Engine Mechanical Designs

A preliminary mechanical design system provided by Rolls-Royce plc was used to create engine architectures that could achieve the engine thermodynamic cycle detailed in the previous section. A mechanical design is driven by the flight condition where the engine temperatures and pressures are highest because this creates the highest stresses. However, the component designs must also satisfy the aerodynamic loadings required at all points in the flight envelope. For the Silent Aircraft engine, a maximum sea level thrust condition was used to create the most mechanically demanding condition, and this was combined with the top-of-climb point for the peak aerodynamic loadings and peak non-dimensional flow rates.

To complete a mechanical design, the cycle conditions are input and these are combined with design rules for each of the engine components: fan, compressors, combustor, turbines, ducts, shafts, and bearings. The rules applied specify geometric, stress, and aerodynamic limits that are used to determine an acceptable engine layout. Within the software it is possible to vary the engine components that are included within the engine design and also to modify how they are linked together.

Table 3 summarizes the parameters of the four engine designs presented in this paper. All the configurations satisfy the cycle parameters shown in Table 2 and the mission requirements in Table 1.

Design A is a conventional three-shaft turbofan architecture. The general arrangement for this design (Fig. 10) was obtained using current design levels of aerodynamic loading and stress, and typical geometrical constraints for the turbomachinery annulus. There are several problems with this design that make it an unrealistic solution. Firstly, the LP turbine has nine stages, making it very bulky, heavy, and noisy. This is necessary in order to drive the relatively large fan at low rotational speed. The low shaft speed also leads to high torque, demanding very thick shafts. The core annulus is quite convoluted and S-ducts with dramatic changes in radius between the IP and HP turbines are required. Ten stages of HP compressor are required to achieve the cycle OPR and this demands a blade height in the final stage of less than 10 mm. This size of blade would suffer significant losses from Reynolds number effects and tip clearance flows, and it would be very difficult to manufacture accurately with current tools.

Design B, illustrated in Fig. 11, was developed in order to address the problems identified in Design A. To reduce the LP turbine size a 3:1 reduction gearbox has been placed between the fan

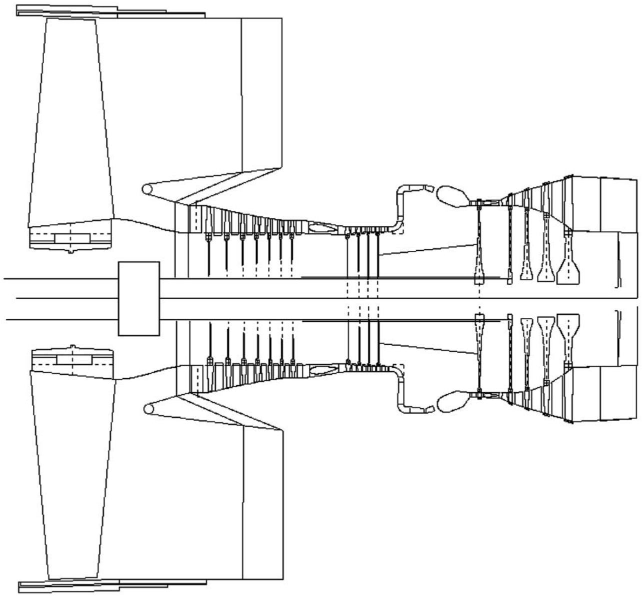

Fig. 11 Design B: Geared turbofan for the Silent Aircraft with axial-radial HP compressor

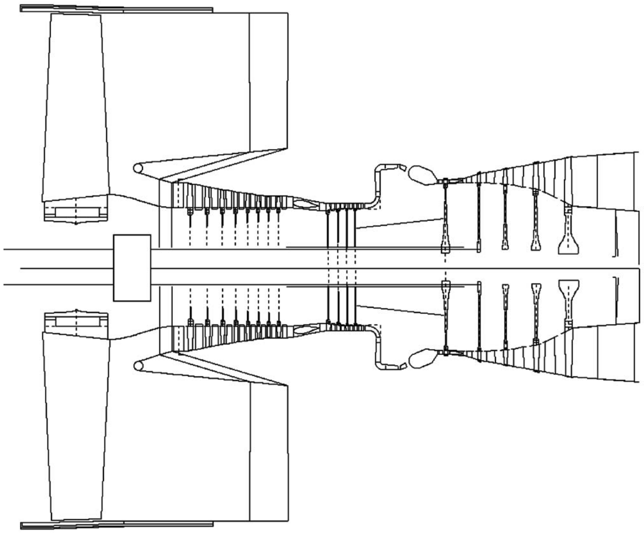

Fig. 12 Design C: Geared turbofan for the Silent Aircraft modified for lower noise

and compressor. The engine is thus a two-shaft design with what previously were the IP compressor (now booster) and the IP turbine all on the same LP shaft and spinning at three times the speed of the fan. The torque in the LP shaft is therefore reduced and the stage loadings in the LP turbine are kept at an acceptable level, despite there only being four stages driving both the fan and booster compressor. The gearbox weight for this engine was estimated as 8% of the total engine weight, which is significant, but much smaller than the weight of the original LP turbine. However, the engine weight is not greatly reduced from that of Design A because of the introduction of a heavy centrifugal HP compressor stage. This was added to remove the S-shaped ducts in the annulus and to increase the minimum blade height in the HP compressor, thus making the engine easier to manufacture. Overall, the engine is much more compact and it appears to be more viable than Design A. However, it had not been optimized for low noise, and initial estimates predicted that the source noise levels from this design would be too high.

Design C (Fig. 12) was created as a quieter and lighter version of Design B. The main changes were to reduce the fan tip speed and to increase gap-to-chord ratios in the turbine. All sources of fan noise tend to increase with fan tip speed. Supersonic noise sources also appear if the relative blade Mach number exceeds unity. The control of blade tip speed for minimum noise is explored further in the companion paper [19]. For the purposes of this paper, it was assumed that the aerodynamic loading of the fan could be significantly increased without reducing the efficiency. The fan in Design C therefore has a design tip speed of 350 m/s with only 18 rotors. If the same 3:1 gearbox is assumed, the loadings on the LP turbine and booster compressor increase leading to more aerofoils and an extra stage of compressor.

To minimize the turbine source noise during approach the gap-to-chord ratios in all stages of the LP turbine were increased to above 100%, whereas in Design B the spacing was as small as possible for low weight and size. Despite Design C being larger than Design B, the overall weight of the fan system and the containment is reduced significantly, giving a reduction in the total bare engine weight of about 8%.

Design D is shown in Fig. 13. It was developed to study the effects of having multiple fans driven by a single core, which is a configuration expected to give noise and fuel consumption benefits. In this case there would be a total of 12 fans and 4 engine cores in the propulsion system. Although this is a radically different approach to the previous designs, it still satisfies the same engine cycle and mission requirements. The core design is identical to Design C. Each of the fans also has the same hub-tip ratio as the previous designs and the overall mass flow rates are identical. The results from the design tool show that Design D is 11% lighter than Design C in terms of bare engine weight (Table 2). A formula relating engine weight to fan diameter is proposed in [2] (eq. (11)), which would suggest a weight reduction closer to 20%. However, the actual change is expected to be smaller because only the fan system weight is reduced, rather than scaling all components down, which is assumed in [2].

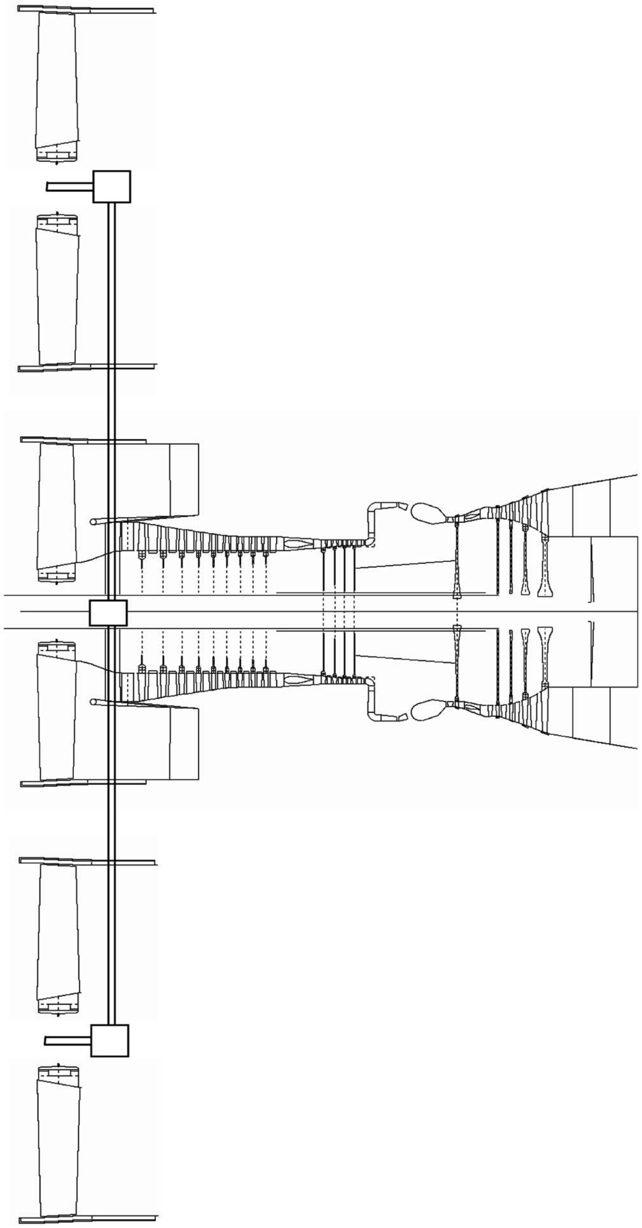

Fig. 13 Design D: Multiple fan version of a geared turbofan for the Silent Aircraft

The layout of Design D is thought to have two advantages in terms of noise. Firstly, the length-to-diameter ratio of the exhaust ducts can be extended to increase the attenuation from acoustic liners [2]. Secondly, if the fan tip speed is maintained, as has been done in this design, the fan shaft speed must increase, and therefore the blade passing frequency increases. Higher frequencies are more readily attenuated by liners and are more effectively shielded by the airframe [4], leading to lower noise transmission. Design D is also expected to have potential fuel burn benefits

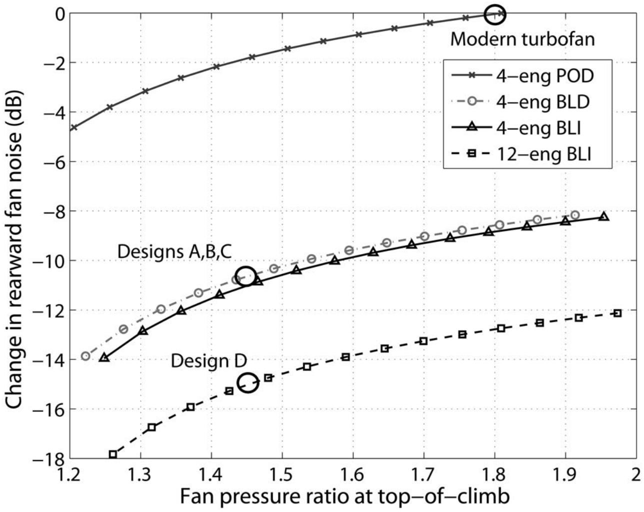

Fig. 14 Variation in rearward fan noise with design fan pressure ratio based on ESDU 98008 [22]

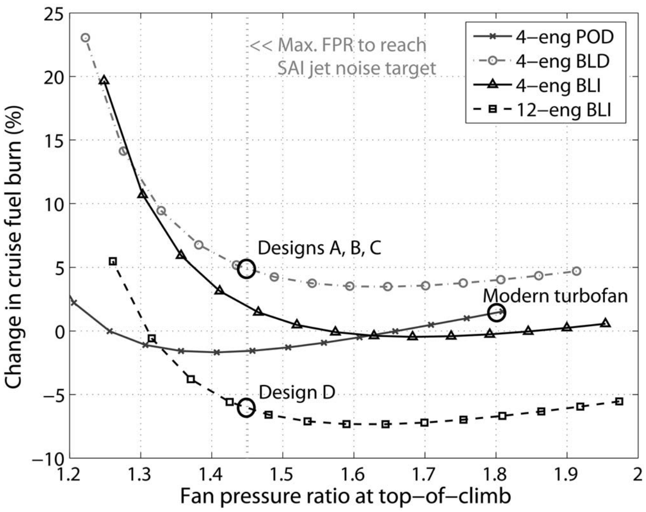

Fig. 15 Variation in cruise fuel burn with design fan pressure ratio and installation configuration

because it enables the propulsion system to be better packaged into the airframe, reducing the installation drag contribution and also increasing the total amount of airframe boundary layer that can be swallowed by the engine inlets [2]. These effects on noise and fuel consumption are explored further in the section below. The added mechanical complexity of the additional shafts and gearboxes required for this design is not considered further here, although this is expected to create additional design challenges. There are also safety issues, such as the greater risk of containment failures impacting on adjacent systems, which also need to be accounted for.

Installation Trade Studies. A simple analysis is presented in [2] that allows different engine configurations to be readily compared in terms of noise, weight, and fuel consumption. This section applies a similar analysis to examine the relative merits of the different engine designs presented and to see how noise and fuel burn would change were a different design FPR value chosen.

Using the thrust requirements at take-off and top-of-climb, once the installation configuration is fixed, the fan diameter and the exhaust flow conditions can be determined for a given design FPR. This enables variations in jet and fan noise to be estimated from correlations such as those in [21,22]. Figure 14 shows the expected trends in rearward fan broadband noise for different possible installation options. The changes are shown relative to a reference level, which is the noise from a two-engine podded turbofan propulsion system with a design FPR typical of today's technology. This reference level was chosen because it is representative of a current conventional design.

Each of the configurations considered in the plots satisfies the mission requirements in Table 1, and in all cases a variable exhaust nozzle is assumed in which the fan capacities at top-of-climb and sideline are matched. Podded, BLD, and BLI cases are included in order to show the expected improvement in noise reduction from a longer installation. The plots indicate how fan noise reduces continuously with design FPR. This occurs because at a fixed thrust level, design fan tip speed reduces to maintain the same aerodynamic stage loading. This effect outweighs the increase in noise caused by the increased fan diameter. The results suggest that Design D, with exhaust ducts of a high length-to-diameter ratio, will be much quieter than a podded equivalent and a few dB quieter than the equivalent four-engine embedded system.

The fuel burn effects of different installation options were explored with a similar trade study. The results are shown in Fig. 15, which shows fuel burn variation relative to a two-engine podded turbofan propulsion system with a design FPR typical of today's technology. The analysis includes several factors that are calculated using the formulae in [2]: (i) the increase of wetted area drag with engine size, (ii) the increase in propulsive efficiency with reduced jet velocity, (iii) the reduction in overall efficiency with losses in the intake and exhaust, and (iv) the drag reduction of the airframe produced by boundary layer ingestion. Again, the aircraft mission requirements in Table 1 were used, and all the engines were assumed to be turbofans fitted with a variable area exhaust nozzle in which the values of fan capacity at take-off and top-of-climb were matched to the design value. For the embedded configurations, the installation pressure recovery factors were the same as used for the engine cycle design described previously. With BLI, an extra inlet total pressure loss of 2% was included to account for the lower total pressure of the ingested boundary layer flow.

Note that the SFC values calculated for the engine cycle design study (Table 2) do not account for differences in installation drag. Furthermore, SFC cannot be used to follow the effects of boundary layer ingestion, and therefore the rate of fuel consumption is a better measure of overall performance.

Figure 15 shows that there is an optimum design FPR in terms of fuel burn, which differs depending on the type of installation and the number of engines. Although the podded design is found to have greater installation drag, it benefits from having a simple inlet and a short exhaust with low total pressure losses. Thus, the lowest fuel burn occurs at a low design FPR and thus at a high fan diameter. The fans in the embedded systems (BLI and BLD) are very susceptible to installation duct losses, and the effect of these is larger at low fan pressure ratios. This leads to higher fan pressure ratios being preferable for embedded systems. However, as shown by Fig. 14 and the studies described in [19], as fan pressure ratio increases, the jet and fan source noise will increase.

This study shows that Design D, at a design fan pressure ratio of 1.45, could offer a potential 12% reduction in fuel consumption relative to a four-engine system without boundary layer ingestion. Relative to a podded design, the fuel burn benefit is lower, around 5%. If a higher design FPR could be used the benefit of BLI could be greater. This may make the jet noise target more difficult to reach, but as indicated by Fig. 14, an embedded propulsion system with multiple ducts should be quieter in terms of turbomachinery noise.

Conclusions

An optimized cycle for an embedded UHBR turbofan operating with a variable exhaust nozzle has been devised. Realistic estimates of the performance of an S-type inlet and the technological limits in 2025 have been included, and these lead to a feasible thermodynamic cycle for the Silent Aircraft propulsion system. The cycle used as a basis of further design studies has a top-of-climb fan pressure ratio of 1.45.

The off-design operation of a UHBR turbofan with a variable exhaust nozzle can be optimized for low noise, during approach and take-off, and for performance at cruise. The benefits relative to a fixed nozzle design have been demonstrated and the engine cycle variations for the Silent Aircraft design have been determined. For the design study described in this paper, the nozzle required has a maximum area variation of 35%. This enables the jet noise target to be reached and also improves the fan efficiency and stability margin during take-off.

Preliminary mechanical designs have been completed for the Silent Aircraft engine thermodynamic cycle. A two-spool geared turbofan with a gearbox between the fan and booster compressor and an axial-radial HP compressor gives a compact, low-weight design. This has been modified by reducing the fan tip speed and by increasing the turbine spacing; this is expected to lower component source noise, while further reducing engine weight.

The mechanical design of a multiple-fan engine system has also been considered. Neglecting the more complicated transmission system, this is expected to be lighter than the other designs, and it is easier to package into an all-lifting wing airframe. Simple trade studies suggest that this can offer significant noise and fuel burn benefits provided boundary layer ingestion can be successfully implemented.

Acknowledgment

The authors are grateful to the other members of the Silent Aircraft Initiative team. Particular thanks to Matthew Sargeant, Steve Thomas, and Patrick Freuler for their input. Technical advice and assistance with the preliminary engine design software was provided by experts from Rolls-Royce plc, and the authors would like to acknowledge this contribution that made the present paper possible. This work has been financially supported by the Cambridge-MIT Institute.

Nomenclature

Symbols

A = area
D_f = fan tip diameter
l = length
$\dot{m}$ = mass flow rate
n_{eng} = number of engine fan units in the propulsion system
M_a = axial Mach number
M_{rel} = relative Mach number
N = rotational shaft speed
p = pressure
Q_a = fan flow capacity, $Q_a = \dot{m}\sqrt{c_p T_{02}}/A_f p_{02}$
T = temperature
U_{tip} = fan rotor blade tip speed
W = weight
X_N = net thrust
η_f = fan isentropic efficiency

Subscripts

0 = total, stagnation value
1 = conditions at engine inlet entry
13 = conditions at fan exit (bypass stream)
2 = conditions at the engine face
3 = conditions at compressor exit
8 = condition at the nozzle exit
eng = engine parameter
f = fan parameter

Abbreviations

BLD = boundary layer diversion
BLI = boundary layer ingestion
BPR = engine bypass ratio
CFD = computational fluid dynamics
FPR = fan total pressure ratio (p_{013}/p_{02})
HPC = high pressure compressor
IPC = intermediate pressure compressor
LP = low pressure compressor
MTOW = maximum take-off weight of aircraft
OPR = overall core cycle pressure ratio (p_{03}/p_{02})
SFC = thrust specific fuel consumption
TET = turbine entry temperature (T_{04})
UHBR = ultrahigh bypass ratio

References

[1] ACARE, 2000, “European Aeronautics: A Vision for 2020,” Advisory Council for Aeronautics Research in Europe.

[2] Hall, C., and Crichton, D., 2005, “Engine And Installation Configurations For A Silent Aircraft, ISABE-2005–1164,” presented at International Symposium on Air Breathing Engines, Munich, Germany.

[3] Crichton, D., Tan, D., and Hall, C., 2004, “Required Jet Area for a silent aircraft at take-off,” presented at 8th ASC-CEAS Workshop, Budapest University of Technology and Economics, Hungary.

[4] Agarwal, A., and Dowling, A. P., 2005, “Low Freqency Acoustic Shielding of Engine Noise by the Silent Aircraft Airframe, AIAA 2005–2996,” presented at 11th AIAA/CEAS Aeroacoustics Conference, Monterey, California.

[5] Gliebe, P. R., and Janardan, B. A., 2003, “Ultra-High Bypass Engine Aeroacoustic Study,” NASA-2003-212525, Oct.

[6] Daggett, D. L., Brown, S. T., and Kawai, R. T., 2003, “Ultra-Efficient Engine Diameter Study,” NASA CR-2003-212309.

[7] Borradaile, J. A., 1998, “Towards the Optimum Ducted UHBR Engine,” Paper No. AIAA-88–2954.

[8] Crow, D. E., 2001, “A Comprehensive Approach to Engine Noise Reduction Technology,” Paper No. ISABE-2001.

[9] Manneville, A., Pilczer, D., and Spakovszky, Z., 2004, “Noise Reduction Assessments and Preliminary Design Implications for a Functionally-Silent Aircraft.,” presented at 10th AIAA/CEAS Aeroacoustics Conference, Manchester, UK.

[10] Liebeck, R., 2004, “Design of the Blended Wing Body Subsonic Transport,” J. Aircr., **41**, pp. 10–25.

[11] The Silent Aircraft Initiative, “Silent Aircraft Initiative … A New Approach,” http://silentaircraft.org.

[12] Diedrich, A., Hileman, J., Tan, D., Willcox, K., and Spakovszky, Z., 2006, “Multidisciplinary Design and Optimization of the Silent Aircraft,” Paper No. AIAA 2006-1323.

[13] Berglund, B., Lindvall, T., and Schwela, D. H., 1999, “Guidelines for Community Noise,” World Health Organization.

[14] “Noise Mapping England: The London Road Traffic Noise Map,” 2004, Department for Environment, Food and Rural Affairs (Defra), London.

[15] Anabtawi, A. J., Blackwelder, R. F., Lissaman, P. B. S., and Liebeck, R. H., 2001, “An Experimental Study of Vortex Generators in Boundary Layer Ingesting Diffusers With a Centerline Offset,” University of Southern California, Los Angeles, CA.

[16] Berrier, B. L., and Allan, B. G., 2004, “Experimental and Computational Evaluation of Flush-Mounted, S-Duct Inlets,” Paper No. AIAA 2004-0764.

[17] Freuler, P., 2004, “Boundary Layer Ingesting Inlet Design for a Silent Aircraft,” Master’s thesis, Massachusetts Institute of Technology, Cambridge, MA.

[18] Kurzke, J., 2004, “Gas Turbine 10: A Program for Gas Turbine Performance Calculations.”

[19] Crichton, D., Xu, L., and Hall, C. A., 2006, “Preliminary Fan Design for a Silent Aircraft,” Paper No. GT2006-90564.

[20] Freeman, C., and Cumpsty, N. A., 1992, “Method for the Prediction of Supersonic Compressor Blade Performance,” J. Propul. Power, **8**, pp. 199–206.

[21] Stone, J. R. and Montegani, F. J., 1980, “An Improved Prediction Method for the Noise Generated in Flight by Circular Jets,” Paper No. NASA TM-81470.

[22] Engineering Science and Data Unit, 2003, “ESDU 98008: Prediction of Noise Generated by Fans and Compressors in Turbojet and Turbofan Engines,” ESDU International Plc, London.

An Approach to Integrated Multi-Disciplinary Turbomachinery Design

Jerome P. Jarrett[1]
e-mail: jpj1001@cam.ac.uk

William N. Dawes

P. John Clarkson

Department of Engineering,
University of Cambridge,
Trumpington Street,
Cambridge CB2 1PZ,
United Kingdom

Aeroengines are designed using fractured processes. Complexity has driven the design of such machines to be subdivided by specialism, customer, and function. While this approach has worked well in the past, with component efficiencies, current material performance, and the possibilities presented by scaling existing designs for future needs becoming progressively exhausted, it is necessary to reverse this process of disintegration. Our research addresses this aim. The strategy we use has two symbiotic arms. The first is an open data architecture from which existing disparate design codes all derive their input and to which all send their output. The second is a dynamic design process management system known as "SignPosting." Both the design codes and parameters are arranged into complementary multiple level hierarchies: fundamental to the successful implementation of our strategy is the robustness of the mechanisms we have developed to ensure consistency in this environment as the design develops over time. One of the key benefits of adopting a hierarchical structure is that it confers not only the ability to use mean-line, throughflow, and fully 3D computational fluid dynamics techniques in the same environment, but also to cross specialism boundaries and to insert mechanical, material, thermal, electrical, and structural codes, enabling exploration of the design space for multi-disciplinary nonlinear responses to design changes and their exploitation. We present results from trials of an early version of the system applied to the redesign of a generic civil aeroengine core compressor. SignPosting has allowed us to examine the hardness of design constraints across disciplines which has shown that it is far more profitable not to strive for even higher aerodynamic performance, but rather to improve the commercial performance by maintaining design and part-speed pressure ratio stability and efficiency while increasing rotor blade creep life by up to 70%.

[DOI: 10.1115/1.2472416]

Introduction

The complexity of the modern jet engine has led to the fragmentation of the process by which it is designed. In part this is due to the modular nature of the product, i.e., engines are often described in terms of compressors, turbines, combustors, nacelles, and is in part due to the specialists involved in the design of each module: aerodynamic, mechanical, structural, material, stress, and thermal designers, business administrators, and cost analysts, to name but a few.

In order for this type of organization to function adequately, it is necessary to fix various key parameters, attributes, and design constraints early in the design process in order that each module specialist may proceed with more detailed design work. This information, such as overall engine layout, cycle temperatures and pressures, stage numbers, and shaft speeds, is the output of the Preliminary Design. These parameters fundamentally determine the performance of the final design, yet the decisions upon which their selection is based relies on experience gained with previous designs via correlations [1]. These facts, and the commercial risks involved, encourage both conservatism in engine designers and evolutionary design.

Evolutionary design has much to commend it: risks are minimized, large engine families can be constructed offering a wide thrust range due to their modularity, and designers can stay close to, if not within, the bounds of reliability of the correlations and empiricism deployed in the Preliminary Design. Furthermore, it has worked well in the past: there have been significant improvements in the areas of SFC, noise, and emissions over the last three decades by incremental advances with conceptually similar designs.

The principal disadvantage of evolutionary design is that it strongly discourages design outside of "known territory": novel architectures necessarily involve moving into areas of the design space in which a company has little or no experience, with huge attendant risk.

While the law of diminishing returns has been felt increasingly for some time [2], the situation has recently been brought into sharp focus. In October 2002 the Advisory Council for Aeronautics Research in Europe published its Strategic Research Agenda, which contains, among others, the following design challenges to be achieved by the year 2020:

- Reduce CO_2 by 50% per passenger kilometer (assuming kerosene remains the main fuel in use)
- Reduce perceived noise to one-half of current average levels
- Reduce NOX emissions by 80%

Evolutionary development along the current trend lines will not result in these goals being reached [3]. Indeed, it is felt that, in many areas, developing existing designs to their full potential will fail to attain even half of the required performance improvement. A step change is required that necessitates the accurate determination of trade-offs within the design of both the aircraft and the engines and also a better understanding of the controlling features of step changes in performance.

---

[1] Lead and Corresponding Author: Tel: +44-1223-332552

Contributed by the International Gas Turbine Institute of ASME for publication in the JOURNAL OF TURBOMACHINERY. Manuscript received February 10, 2006; final manuscript received August 18, 2006. Review conducted by David Wisler. Paper presented at the ASME Turbo Expo 2004: Land, Sea and Air (GT2004), Vienna, Austria, June 14–17, 2004, Paper No. GT2004-53852.

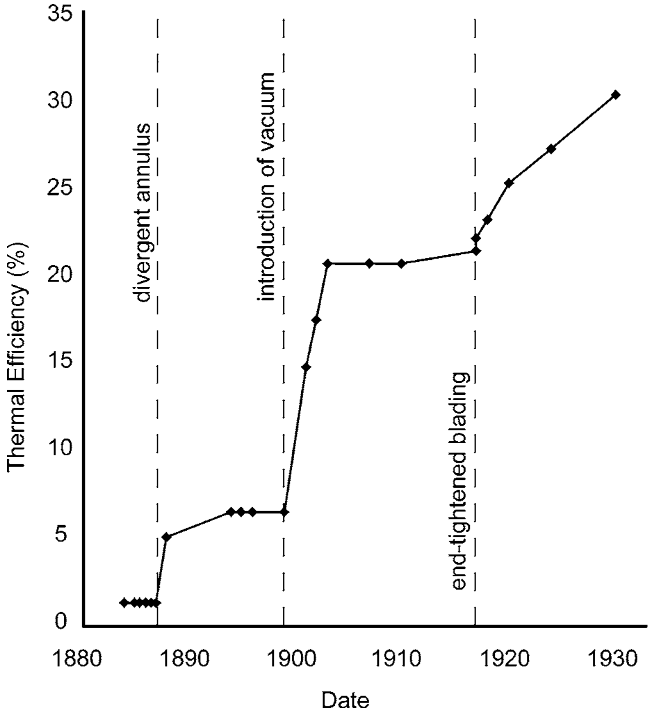

Fig. 1 The development of non-compounded steam turbines, 1884–1930 [4]

The Surge-Stagnate Model

We have previously reported a new model of the complex design process that provides insight into the factors controlling its shape: the Surge-Stagnate Model [4]. A turbomachinery example of this is our study of noncompounded steam turbines [5]. The performance gains, in terms of thermal efficiency, over their early development may be plotted with time, as illustrated in Fig. 1.

This study showed that the performance changes over time in a series of diminishing returns controlled cycles. The step changes result from fundamental alteration of the Preliminary Design, the subsequent exponentially decaying improvement is from evolutionary refinement in the Detailed Design of the new concept: progress stagnates as the optimum detail conditions are established [6].

Our earlier work has indicated how this knowledge of the controlling features of the complex design process may be used to manipulate its shape: to shorten stagnations and boost surges. Laboratory experiments applying our method to the preliminary design of a commercial high pressure steam turbine revealed the ability to enhance the isentropic efficiency of the design by 1.3 percentage points while reducing the design cycle time by an order of magnitude.

The shortening of the design time was due to two reasons. The first was reducing the time wasted in the existing process by automating data handling and better integration of the design tools. This is consistent with reported improvements with commercial design integration systems: for example compressor preliminary design cycle time reductions of 85% have been achieved with the use of iSIGHT from Engineous [7], one of the most widely used of such systems in the turbomachinery world.

The second reason we found for the greatly reduced design time was the assistance our method provides to the designer and his decision making process. Indeed, one of the key pieces of insight which our steam turbine study gave was that much time was spent by the designer learning the shape of the local design space. The designer first had to learn what the appropriate issue to fix was before he could begin to tackle it; second he had to learn the response of the design to changes well enough to proceed in the most effective manner. We have developed the technique we refer to as "Quasi-Optimization" to assist this two-stage learning process.

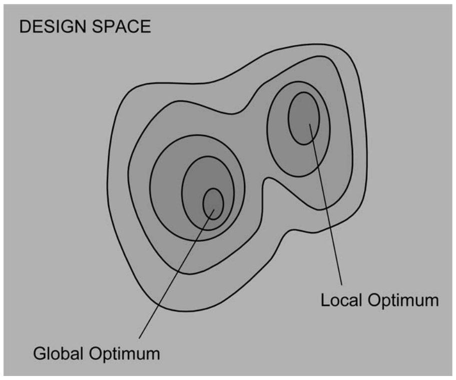

Fig. 2 The classic optimization problem

Quasi-Optimization

The "classic" optimization problem, of finding the global optimum despite local optima, is sketched in Fig. 2.

This design space is, in reality and particularly for turbomachinery, made more complicated by "cliff-edge effects:" discontinuities in the design space due to the discrete nature of some of the key parameters such as the number of stages.

Numerous methods have been applied to this classic design problem: gradient-based approaches, guided searches such as Tabu and methods that mimic natural processes such as genetic algorithms and simulated annealing.

Our own experience and work with industry have indicated that gradient-based methods are perhaps the most intuitive, particularly when performance parameters and design variables are directly linked, i.e., all-other-things-being-equal a 10% increase in shaft speed will change the design point pressure rise of the compressor by *x*% and adiabatic efficiency by *y*%.

Alas, of course, situations are rarely this straightforward and many real design problems are complex, non-linear and most often multi-objective. Powerful techniques have been developed in response to these challenges such as Multi-Objective Genetic Algorithms, which are fielded by later versions of systems like iSIGHT. While such techniques can be effective at their aim of producing pareto optimal solutions, the more complex the problem the greater the likelihood that the designer feels detached from the "real" design; trying to determine *why* one turbine geometry is "better" than another when the designs are presented as two nondominated solutions on a pareto curve plotted against compound objective functions is far from trivial.

This encouraged us to look once again at gradient-based methods. One of the fundamental limitations of such methods when applied to the classic "optimum search" problem is, of course, the dependence on proximity of the starting point to the global optimum. If a simple gradient-based optimiser starts too close to a local optimum that is where it will end up: it will not find its global goal.

However, the "optimum search" problem is often not that faced by the aeroengine module detailed designer. They are more likely to be charged with producing a design with a performance specified by the Preliminary Design (which is in turn heavily influenced by airframe requirements). Therefore, whereas the "classic" problem is to locate the end point of the design process, the detailed designer *knows* the desired outcome: the question is *how to get there*, as is depicted in Fig. 3.

Now it is possible to define the end point of the design process, within given tolerances, in M-dimensional space (where there are M parameters defined by the specification) by a position vector $\mathbf{S}$.

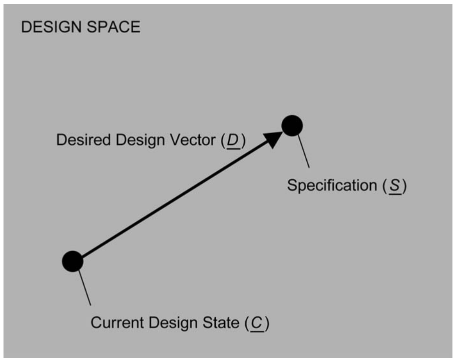

Fig. 3 The jet engine detailed design problem

Similarly, the predicted performance of the current design can be so defined as position vector **C**, with a varying degree of certainty. It is therefore simple to deduce the desired design vector **D**, as indicated below

$$\mathbf{D} = \mathbf{S} - \mathbf{C}$$

Naturally, as the design progresses, **C** changes and so therefore does **D**. If the designer has control over *N* variables, then *N* vectors ($\mathbf{U}_N$) can be defined, where $\mathbf{U}_N$ indicates the effect on predicted performance of a known, small perturbation in variable *N*.

Each of these user variable vectors may be plotted in *M*-dimensional space and compared with the desired design vector **D**. For ease of visualization, the case for $N=2$, $M=2$ is plotted in Fig. 4.

Assuming that $\mathbf{U}_1$ and $\mathbf{U}_2$ are independent, the best single change that can be made to the design shown in Fig. 4 is to proceed in the direction of $\mathbf{U}_1$ by the magnitude necessary to reach the point of closest approach to **D**, defined by vector $\mathbf{C}^*$, as shown in Fig. 5.

This selection of which user variable to modify may be made by dividing both $\mathbf{U}_N$ and **D** by their respective moduli and taking the scalar product of the resulting vectors. *N* "scores" of magnitude between zero and unity result. These represent the degree to which each of the vectors $\mathbf{U}_N$ lies parallel to **D**. Thus, the $\mathbf{U}_N$ with the score closest to unity is the most favorable and is therefore recommended to the designer

$$\left(\frac{\mathbf{U}_N}{|\mathbf{U}_N|}\right) \cdot \left(\frac{\mathbf{D}}{|\mathbf{D}|}\right) = (\text{score})_N$$

The point of closest approach may be determined by simple comparison of the relative magnitudes of the selected $\mathbf{U}_N$ with that of **D**, enabling the system to recommend by how much the selected $\mathbf{U}_N$ should be changed.

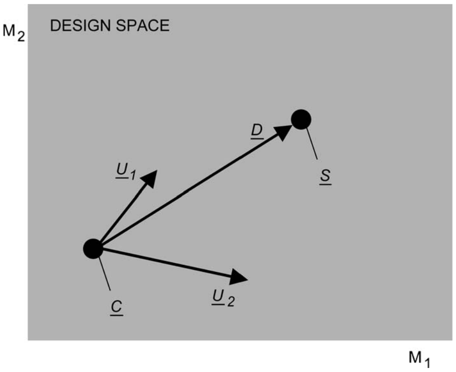

Fig. 4 Plotting user variable vectors

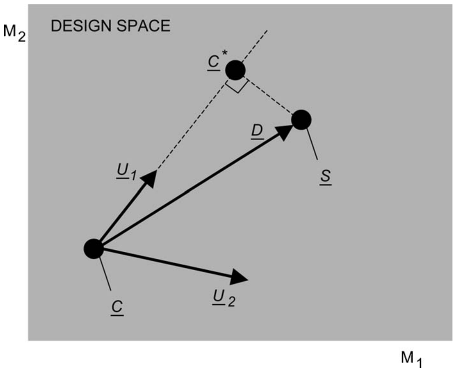

Fig. 5 Choosing the direction in which to move

Thus, the design system is able to provide the designer with guidance as to the best next move in the design process. The designer is at liberty to seek this advice (or not) at any point of the design process and is under no obligation to heed it. The technique lends itself to automation, whereby the system can be set to take its own advice and to repeat the procedure either a predetermined number of times, until a convergence limit is reached, or for a desired period of time.

While this is an undeniably crude approach, it has the advantage that it is independent of both *M* and *N*. Not only does this mean that a specification may be drawn up with any number of requirements, it makes no demands that any of these parameters be from the same specialism: cost factors may be mixed with aerothermal and mechanical properties together with metrics for preparing a Total Care Package for the engine. In addition, *M* and *N* may be either Preliminary Design parameters or Detailed Design factors, or a combination thereof.

Furthermore, it enables *M* and *N* to vary throughout the design process: either because more information becomes available with time, or due to fundamental topological changes to the product architecture (such as the addition or removal of stages: the "cliff-edge effects" noted above). This capability arises from temporarily holding static the dimensionality of the design space while the above analysis is undertaken. It is due to this technique, and the ability to operate on sparse data, that we describe this method as quasi-optimization.

In reality, it is highly unlikely that $\mathbf{U}_1$ and $\mathbf{U}_2$ are independent: another vulnerability of conventional gradient-based methods. However, the adverse effects of dependent variables can to an extent be mitigated by exploiting nonlinear trade-offs inherent in many real design problems, particularly across disciplines. These offer opportunities to make changes that have minimal impact on those performance parameters with which the designer is content, but strongly influence those over which he would like control. Ideally, one would have a truly orthogonal set of design variables; as a simple example, it would be desirable to be able to identify a vector $\mathbf{U}_N$ that would improve SFC with no change in cost.

We have developed a two-stage process in response to this challenge. First, the set of design vectors $\mathbf{U}_N$ is recomputed as the design changes (i.e., as **C** moves to new areas of the design space) such that the most favorable direction can be continuously re-evaluated. Second, as different vectors $\mathbf{U}_N$ are used to produce a composite vector closer to the desired vector **D**, the single vector **D** may be deduced. Now, if **S** is so defined as to allow a range of, say, increased blade life but constrained to not tolerate any change in efficiency, then if **S** is reached, the "ideal" vector $\mathbf{U}_N$ may be generated. This vector $\mathbf{U}_N$ will therefore behave (in this simple example) thus

$$\frac{\partial(\text{efficiency})}{\partial \mathbf{U}_N} = 0 \qquad \frac{\partial(\text{blade life})}{\partial \mathbf{U}_N} = +\max$$

Now, $\mathbf{U}_N$ is defined in terms of variables familiar to the turbomachinery designer, rather than compound objective functions. Thus, the designer is aided in understanding how to change geometry, shaft speeds, loading distributions, etc., to achieve the desired result. Furthermore, this assists him in understanding the *rationale* of the optimization process: not only does he have a better design, *he knows what has made it better*.

Naturally, this approach falls down if **S** is unreachable. Yet, this is where our method enables a deeper understanding of the design problem at hand: if **S** truly is unreachable, the system can be interrogated to discover which design constraints have been hit first. Thus, if we cannot create vector **D** to get to **S**, despite how we move **C**, then we can determine the most effective way to alter **S** so that we can. This enables us to ask whether we are fundamentally trying to solve the wrong problem: there may be far richer commercial rewards attainable by modifying **S** than desperately trying to approach a suboptimal specification.

We thus have a two-part method of achieving our aim of moving from evolutionary refinement in the Detailed Design to step changes in performance resulting from fundamental alteration of the Preliminary Design. One part is to exploit nonlinearity and deduce orthogonal design vectors. The other is to interrogate the Specification to identify the most limiting constraints, examine the hardness of each, and modify the Preliminary Design accordingly.

SignPosting

We have embodied the above technique in our SignPosting design process management system [8]. SignPosting is a method of dynamically generating a design process by decomposing the process into its constituent tasks. The quantity and quality of the data required to execute and produced by each task are then assessed. As confidence in the design builds with time, so different tasks become available and others redundant.

Provided that this task decomposition can be performed, there is no theoretical limit to the number and type of tasks which may be added to the system. The key to making the system function in a design arena as complex as turbomachinery is its hierarchical data store.

This is necessary to be able to store data simultaneously at multiple levels of granularity. Take, for example, a measure of efficiency. This may be defined for a section of a blade, a whole blade, a row, a stage, a module, the engine, and the engine/airframe combination. Different tasks will interface with this data store at a variety of levels: it is vital that, at all times, the information contained in the store is internally consistent, i.e., that all the stage efficiencies combine to the value stored for that module, and so on.

Multi-disciplinary Design

We have integrated a suite of analysis tools into the SignPosting architecture in order to conduct cross-disciplinary design as illustrated in Fig. 6. The system, with which the designer interacts via a simple textual interface, is implemented in FORTRAN77.

Three proprietary preliminary aerothermal codes are combined with in-house material and mechanical models. Proprietary post-processing is incorporated. We have found the use of proprietary tools important: if the industrial designer is using familiar codes in a new way he is far more likely to "buy-in" to the process than with completely new tools.

A most important feature of our system is the geometry handling. Even in the Preliminary Design, the geometry of the design may be defined by hundreds of data points, which complicates the optimization problem due to the very large number of dependent variables. Taking the example of the meridional view of an axial turbomachine, we read in the detailed geometry from the proprietary codes, snap Bezier curves to the hub and casing lines, each with two control variables along their length to give control over the geometry. Thus, the designer may make sweeping changes to the geometry at a high level; the geometry handler then converts the Bezier functions back into the detailed geometry expected by the analysis codes. All of this is achieved automatically and essentially instantaneously.

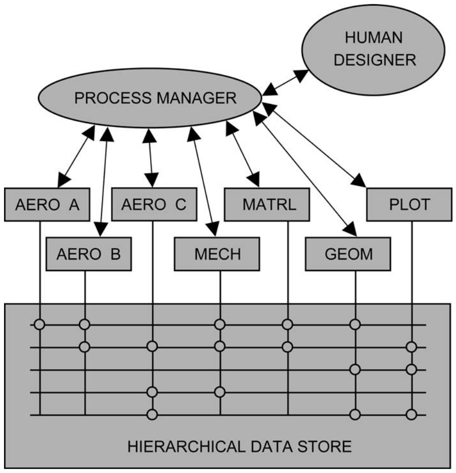

Fig. 6 The SignPosting system for turbomachinery

All data are transferred to and from the data store via text files. The FORTRAN process manager source code contains scripted calls to run the modules (such as "AERO A" in Fig. 6) from the command line, thus permitting modules to be written in languages other than FORTRAN if that is required (for example one of our modules is written in C).

As can be seen, the system is primarily designed to be operated as a man-in-loop process. Thus, the designer instructs the system as to which task to execute next and can, at any point, seek guidance from the system by instructing it to indicate the best variable to change, and by how much. It is entirely at his discretion whether or not to act on this advice.

However, as outlined above, the system can be instructed to operate in a fully automatic mode where it will alternately estimate the magnitude and direction of the next move and execute those changes. This it will repeat either a predetermined number of times, until a convergence limit is reached, or for a desired period of time. In other words, it can be run a set number of design iterations, or until it has come close enough to the specification, or (in arguably a more commercially relevant way) produced the best design it can in a given time.

To determine whether the design is close enough to the specification, SignPosting refers to a user-defined specification document that details both the design requirements and constraints, together with their associated permitted tolerances; for example, the overall length and the inlet plane of a compressor may be fixed, but its outlet allowed to move radially over a certain number of inches. There may be minimum permitted values for required part-speed pressure rise and design point efficiency. If the design strays outside the tolerance bounds of either requirements or constraints, this is flagged to the designer via the textual interface.

These permitted values and tolerances are complemented by our tracking of the uncertainty of the current design values and predicted performance: as mentioned above, a key feature of SignPosting is its knowledge not only of the quantity of data needed to run the design process but also its *quality*.

This system as described has been applied to a generic civil core engine compressor, the geometry of which we have used as the starting point of a redesign using SignPosting. The aerodynamic performance, as predicted by the analysis codes included in the system, is already good: it is a moderately loaded design with a polytropic efficiency in excess of 90%.

Though the performance could undoubtedly be improved by evolutionary design, the gains in efficiency at least will not be

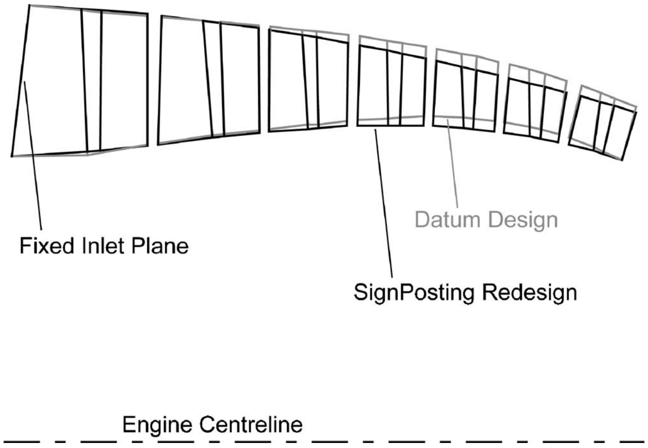

Fig. 7 SignPosting redesign overlaid on the datum main gas path geometry

large: the evolutionary detailed aerodynamic design is already well into diminishing returns. We therefore chose to set SignPosting the task of deploying quasi-optimization to see if changes affecting other specialisms while holding the aerodynamic performance constant might lie more parallel to the direction of producing a "better" design.

Thus, the design problem we posed SignPosting was to employ our two-part method to move from evolutionary refinement in the Detailed Design to step changes in commercial performance resulting from fundamental alteration of the Preliminary Design. Thus, SignPosting had first to identify and exploit nonlinearity, then deduce orthogonal design vectors, and modify the Preliminary Design accordingly.

The conditions of the test were to match the aerodynamic performance of the datum design with the same part count and in the same overall length (with fixed inlet plane and axial positions of the disks), but improve the commercial performance by searching for nonlinear cross-disciplinary trade-offs, deducing orthogonal design vectors, and embodying them in a new Preliminary Design.

The results of this test are shown below: the principal changes to the meridional geometry occur in stages four, five, and six, made clear in Fig. 7.

SignPosting has modified the geometry in response to the coupling between the mechanical and material attributes of the design. The material model encourages the reduction of rotor root stress in favor of increased creep life. The mechanical model produces estimates for the blade root stresses based upon the equation [9]

$$\sigma_r = \frac{\rho_b \omega^2}{a_r} \int_r^t a r \mathrm{d}r$$

Taking the simplified case of constant section blade, this expression becomes

$$\sigma_r = \frac{\rho_b}{2}(2\pi\Omega)^2(r_t^2 - r_r^2)$$

Given that the blade tip speed is given by

$$U_t = 2\pi\Omega r_t$$

substituting gives

$$\sigma_r = \frac{\rho_b}{2}U_t^2\left[1 - \left(\frac{r_r}{r_t}\right)^2\right]$$

Thus, it can be seen that, for blades of the same material, the root stress is a function of tip speed and hub-to-tip ratio. Given that SignPosting was permitted to alter the shaft speed, it is interesting to note that it found geometric changes to be preferable. Since Ω is therefore the same in both cases, it follows that SignPosting has reduced the root stress by reducing the tip speed and increasing the hub-to-tip ratio of the later stages. The root stress changes are detailed in Table 1.

Table 1 Comparison of rotor root stress in compressor preliminary designs

Stage number	Change in root stress (%)
1	Negligible
2	Negligible
3	−1
4	−6
5	−8
6	−10
7	−11

Though these changes are noticeable, they do not appear to have made a great impact on the design. However, SignPosting was tasked to identify and exploit nonlinearities, and the response of the steady-state tensile strain rate due to creep (and hence the creep life of the rotor blades) is far from linear. The strain rate is given by [10]

$$\dot{\varepsilon}_{ss} = A\sigma^n e^{-Q/\bar{R}T}$$

Since in this case we have the same stagewise temperature profile and have not changed the material from which the rotor blades are made, this reduces to

$$\dot{\varepsilon}_{ss} \propto \sigma^n$$

Given that n is approximately 5 for the titanium alloys likely to be found in this type of compressor, the changes to the blade creep life are as detailed in Table 2.

The nonlinear response of the system is made clear in Fig. 8, which shows how modest are the geometric changes to produce such a dramatic change in the creep life of the rotor. It also demonstrates the effect of fixing the inlet plane (the tip, but neither the hub radius of the exit plane nor axial position of the last stage disk was free to move).

This only represents part of the challenge we set SignPosting. The other requirement was to hold constant the aerodynamic performance of the machine and explore the design space for orthogonal design vectors.

In addition to the changes detailed above which have so dramatically improved the creep life, SignPosting has affected a number of aerodynamic modifications in terms of re-cambering and re-staggering both the rotor and stator of each stage, as shown in Fig. 9.

SignPosting has made these modifications such that, for a given stage pressure rise, it has changed both the Flow Coefficient and Stage Loading Coefficient such that the stage efficiency remains unaltered. In essence, it has modified each stage (particularly the rear stages) by tracking around a contour on the Smith Chart, as depicted in Fig. 10.

Table 2 Comparison of rotor blade creep life in compressor preliminary designs

Stage number	Change in creep life (%)
1	Negligible
2	Negligible
3	+5
4	+35
5	+50
6	+60
7	+70

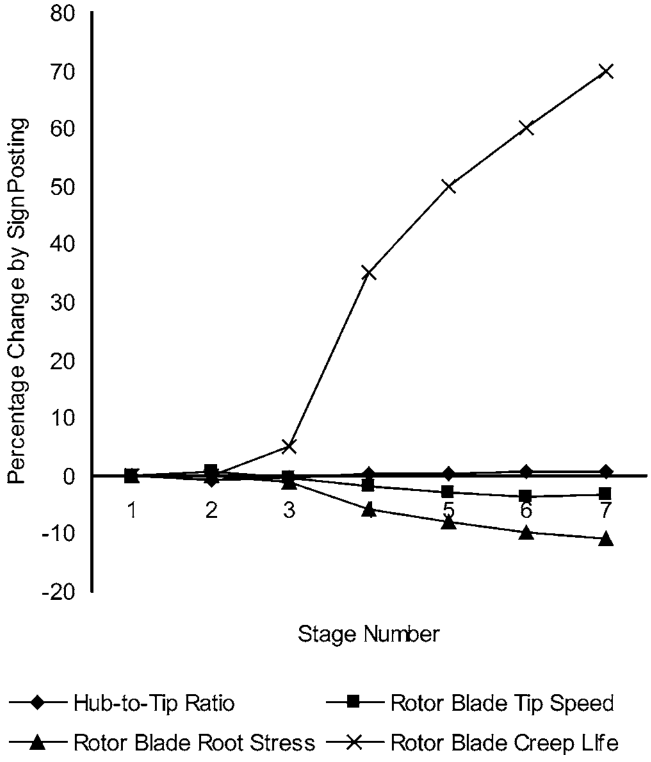

Fig. 8 Mechanical redesign

As demanded, the SignPosting redesign also has the same predicted design performance (to the accuracy of the tools used) in terms of design speed pressure ratio, part-speed performance, surge margin, adiabatic and polytropic efficiency, and number of blades.

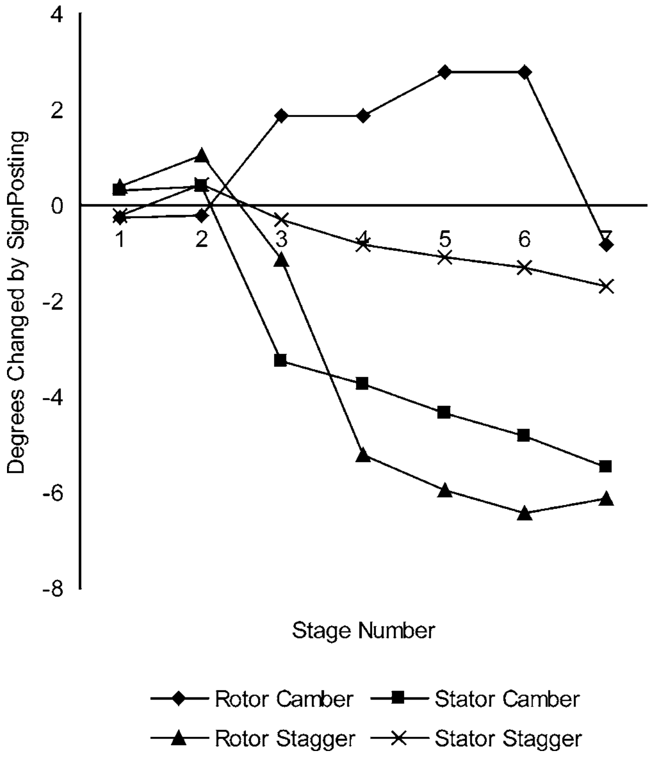

Fig. 9 Aerodynamic redesign

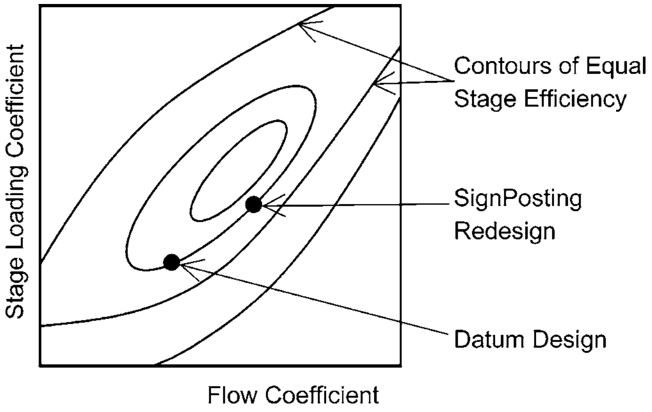

Fig. 10 Illustrative Smith Chart

One of the key constraints in the Preliminary Design emerged as the distribution of stage exit Mach number: SignPosting pushed this towards (but did not reach) limits set by downstream components; further examination of the hardness of this constraint is now under way.

Figure 11 shows how the stagewise distributions of some of the key aerodynamic design parameters have been altered by SignPosting.

The increase in stage loading in the rear stages has enabled the creep life advantages conferred by reducing the tip speed of the rotors to be had without reducing the pressure rise performance of the design. The simultaneous increase of Flow Coefficient has enabled this to be achieved without efficiency penalty for the reasons outlined in Fig. 10.

Thus, it is evident that SignPosting has indeed achieved what was asked of it: it has identified multi-disciplinary nonlinearities and deduced orthogonal design vectors. This is demonstrated in Fig. 12, which shows that the design been modified in such a way that creep life has been dramatically improved with no measurable change in efficiency.

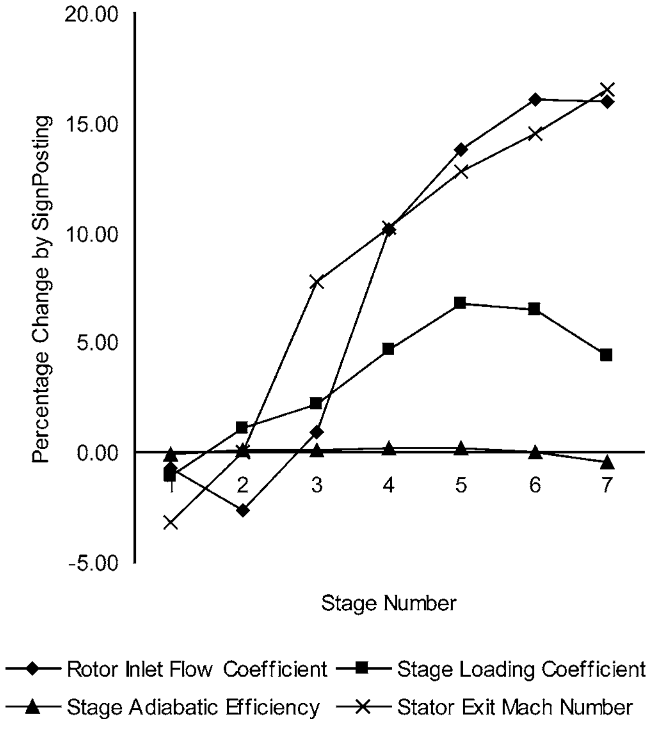

Fig. 11 Effect on aerodynamic performance

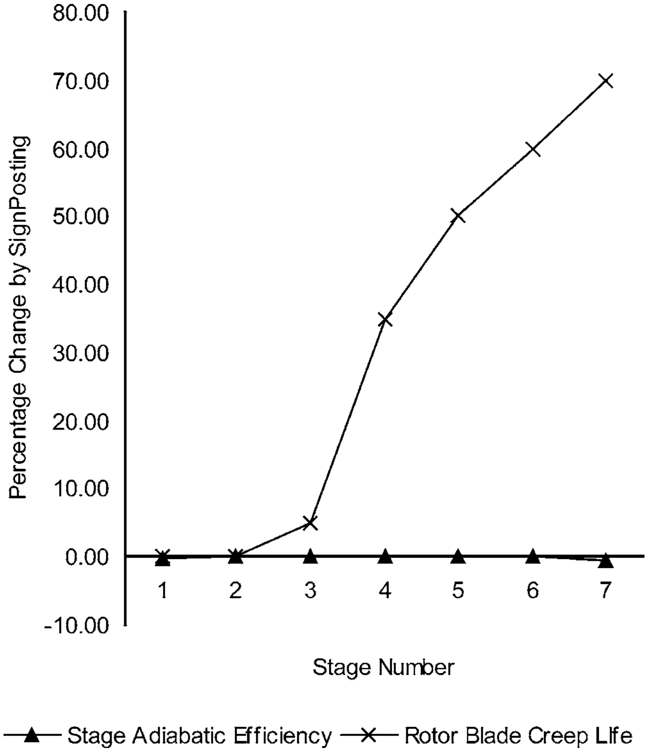

Fig. 12 Evidence of orthogonal design

This redesign was completed with SignPosting in its automatic quasi-optimization mode and required 3-1/2 minutes of run-time on a desktop PC.

We have used this very simple example for illustrative purposes: it is not necessarily a design change that the designer might aim for. For instance, it would not be especially beneficial to have parts of the same module with a wide spread of predicted life from a maintenance viewpoint.

This example also ignores many other effects, such as changes in weight, part count, cost, and the fact that reduced disk stresses may lead, in a real design, to the use of different materials. An alternative to extending the life of some of the rotors may be to exploit the less hostile conditions by blading the rear stages in a lighter alloy (which should increase the nonlinear benefits since it would further reduce the root stresses) or by increasing the pressure ratio and running the rear stages hotter (i.e., boost the cycle performance of the whole engine by trading some of the life saved by the root stress reduction against temperature activated creep).

Despite these limitations, however, our example is indicative of the sort of questions it is possible to ask of the SignPosting design system and of the performance gains possible by crossing specialism boundaries, exploring the design space to find and exploit nonlinear trade-offs and orthogonal design vectors.

Having begun to reap the rewards of crossing specialism boundaries, we are examining the breaking down of the "silo walls" between engine modules; to this end we have recently begun work on extending the SignPosting tool to handle the simultaneous design of a compressor and the turbine that drives it.

The next major steps in our research are to incorporate weight, cost (design, build, and through-life) and maintenance modules into SignPosting and to explore methods by which we can include metrics to couple the physical design to the design of the engine Total Care Package.

Conclusions

Jet engines are designed using fractured process since they are designed in detail as separate modules by a multitude of different specialists. To function adequately, the detailed design relies on the correct decisions being made at the Preliminary Design Stage where the performance of the final product is fundamentally determined.

This process strongly discourages anything but evolutionary design, since the Preliminary Design is heavily based on past engines. Future engines will require a step change in performance, which the current design process cannot provide with acceptable risk.

We have presented a method by which rotor blade creep life has been increased by up to 70%: a step change. This has been achieved without measurable detriment to the aerodynamic performance by using our SignPosting design system to explore the multi-disciplinary design space for, and then exploit, nonlinear trade-offs and orthogonal design vectors.

Acknowledgment

The authors would like to express their thanks to the UK Engineering and Physical Sciences Research Council, the UK Department of Trade and Industry, and Rolls-Royce plc. for jointly funding this work.

Nomenclature

a = cross-sectional area of blade at radius r
A = constant in power-law creep
$\dot{\varepsilon}_{ss}$ = steady-state tensile strain rate in creep
n = creep exponent
Q = activation energy per mole
$\bar{R}$ = universal gas constant
T = absolute temperature
M = number of dimensions of the design space
N = number of user variables
$\mathbf{D}$ = desired design vector
$\mathbf{S}$ = product specification vector
$\mathbf{C}^*$ = vector of next-step point of closest approach
$\mathbf{C}$ = current predicted design performance vector
$\mathbf{U}_N$ = design vector due to a perturbation in N
ρ_b = blade material density
σ = true stress
U_t = rotor blade tip speed
r = blade section radius
SFC = specific fuel consumption
σ_r = rotor blade root stress
ω = blade angular velocity
x_r = value of parameter x at blade root
x_t = value of parameter x at blade tip
Ω = shaft speed

References

[1] Gallimore, S., 1998, "Axial Flow Compressor Design," IMechE, The Successful Exploitation of CFD in Turbomachinery Design, March 1998, London, UK.
[2] Rubbert, P. E., 1994, "CFD and the Changing World of Airplane Design," AIAA Wright Brothers Lecture, Sept. 1994, Anaheim, CA.
[3] Advisory Council for Aeronautics Research in Europe, 2002, "The Challenge of the Environment," Strategic Research Agenda, Vol 2.
[4] Jarrett, J., and Clarkson, P. J., 2002, "The Surge-Stagnate Model for Complex Design," J. Eng. Design, **13**(3), pp. 189–196.
[5] Jarrett, J. P., Dawes, W. N., and Clarkson, P. J., 2002, "Accelerating Turbomachinery Design," ASME Paper No. GT-2002-30618.
[6] Jarrett, J. P., Clarkson, P. J., and Dawes, W. N., 2002, "Improving Turbomachinery Design Process Management," in ASME 2002 Design Engineering Technical Conferences and Computers and Information in Engineering Conference, Sept. 2002, Montreal, Canada, DETC2002/DTM-34015.
[7] Trevino, J., "Design Cycle Time Improvement Using iSIGHT," 2000 International iSIGHT's Users' Conference, October 2000, Chapel Hill, NC.
[8] Clarkson, P. J., and Hamilton, J. R., 2000, "'Signposting,' A Parameter-Driven Task-Based Model of the Design Process," Res. Eng. Des., **12**, pp. 18–38.
[9] Cohen, H., Rogers, G. F. C., and Saravanamuttoo, H. I. H., 1987, *Gas Turbine Theory*, Longman Scientific and Technical, Harlow, UK, ISBN: 058230539X.
[10] Ashby, M. F., and Jones, D. R. H., 1980, *Engineering Materials: An Introduction to Their Properties and Applications*, Elsevier, Oxford, ISBN: 0080261388.

Direct Parametric Analysis of Resonance Regimes for Nonlinear Vibrations of Bladed Disks

E. P. Petrov
Centre of Vibration Engineering,
Mechanical Engineering Department,
Imperial College London,
South Kensington Campus,
London SW7 2AZ, UK
e-mail: y.petrov@imperial.ac.uk

A method has been developed to calculate directly resonance frequencies and resonance amplitudes as functions of design parameters or as a function of excitation levels. The method provides, for the first time, this capability for analysis of strongly nonlinear periodic vibrations of bladed disks and other structures with nonlinear interaction at contact interfaces. A criterion for determination of major, sub-, and superharmonic resonance peaks has been formulated. Analytical expressions have been derived for accurate evaluation of the criterion and for tracing resonance regimes as function of such contact interface parameters as gap and interference values, friction and contact stiffness coefficients, and normal stresses. High accuracy and efficiency of the new method have been demonstrated on numerical examples including a large-scale nonlinear bladed disk model and major types of contact interfaces including friction contact interfaces, gaps, and cubic nonlinearities. [DOI: 10.1115/1.2720487]

Introduction

The bladed disk assemblies have many contact interfaces such as at blade–disk joints, at contact surfaces between interlocking blade shrouds and at contact surfaces of friction dampers. Forces occurring at these interfaces are essentially nonlinear due to the friction mechanics and unilateral interaction (due to the impossibility to transfer tensile normal stresses) at contact interfaces, which have major effects on forced response of bladed disk assemblies. Design parameters, including the parameters of the friction contact interfaces, alter resonance frequencies, levels of the resonance forced response, spectrum of the forced response, and its other characteristics. The resonance forced response levels, and values of the resonance frequencies, are of primary interest in the majority of practical investigations. An appropriate choice of the parameters for friction dampers and other friction contact interfaces allows dangerous resonance regimes to be avoided by changing the resonance frequencies to values desired and/or by decreasing the resonance amplitudes to acceptable levels through introducing damping or through exploring nonlinear properties of the contact interfaces.

The resonance forced response levels are conventionally determined (see e.g., Refs. [1–9]) by calculation of the dependency for the forced response level on excitation frequency over a frequency range where the resonance regimes are expected. There is usually a need to understand how parameters of a structure affect forced response and, moreover, how to choose a set of contact interface or other design parameters that provide minimum resonance forced response levels or that allow moving the resonance frequency outside of some operational frequency range. In order to do this a simple calculation of frequency-dependent forced response characteristics is usually not satisfactory. Hence, numerous forced response calculations are performed sometimes for different parameter values in order to understand the effect of the parameters on the resonance frequency and response levels.

Because of this, there is a need in the development of methods facilitating parametric analysis of gas–turbine structures to provide information additional to customary forced response analysis which would allow avoiding or significantly reducing multivariant forced response calculations. A method for calculation of first- and second-order sensitivity coefficients sensitivity of the steady-state nonlinear forced response to variation of the parameters of contact interfaces was developed in Ref. [10]. The sensitivity coefficients allow construction of good approximations for the forced response levels as a function of contact interface parameters when variations of the contact parameter values are small or moderate. A concept of the direct parametric analysis for bladed disks with friction and gaps and a method for effective parametric studies was developed in Ref. [11]. This method allows periodic forced response levels to be calculated as functions of contact parameters in large ranges of parameter variation which may be needed in practical design. However, forced response–contact parameter dependency was calculated in Ref. [11] for a given excitation frequency and the problem of determination and tracing of the resonance peak frequencies and response levels has not been solved there or in any other publication available.

In this paper, an effective method for direct parametric analysis of resonance regimes is proposed for highly nonlinear periodic vibrations of bladed disks and other structures with contact interfaces.

The new method, which is believed to be developed here for the first time, provides capabilities to calculate resonance frequencies and resonance forced response levels directly as functions of parameters of friction contact interfaces.

Owing to these capabilities the multivariant calculations of the forced response for different sets of the contact interface parameters, which have necessarily been performed hitherto, can now be avoided and the optimum values for these parameters can in many cases be determined directly from results of calculations. The new method is highly computationally efficient, robust, and accurate.

The resonance regimes of steady-state periodic forced response are analyzed in the frequency domain using multiharmonic expansion of periodic motion of a structure. A special criterion is formulated here, which allows determination of major, super-, and subharmonic resonance frequencies simultaneously with determination of the coefficients of the multiharmonic displacements at these resonances.

Contributed by the International Gas Turbine Institute of ASME for publication in the Journal of Turbomachinery. Manuscript received July 24, 2006; final manuscript received July 25, 2006. Review conducted by David Wisler. Paper presented at the ASME Turbo Expo 2006: Land, Sea and Air (GT2006), Barcelona, Spain, May 8–11, 2006. Paper No. GT2006-90147.

The analytical expressions have been derived allowing highly accurate and fast evaluation of the criterion and of all matrices necessary for solution of the formulated equations and its tracing with design parameter variation.

The capabilities of the method proposed to analyze structures with different types of nonlinearities have been demonstrated by numerical examples for structures with different types of the nonlinear interaction: (i) cubic nonlinearity; (ii) gap nonlinearity; and (iii) friction dampers. An example of application of the new approach to the large-scale finite-element model of a bladed disk with underplatform dampers has been considered.

The dependencies of the resonance frequencies and resonance amplitudes to parameters of friction contact interfaces and on excitation levels are calculated. The numerical examples demonstrate the high efficiency of the method developed.

Formulation of the Problem

A level of forced response, a, is generally dependent on forcing conditions such as excitation frequency, ω, and level and distribution of excitation forces, $\mathbf{p}$. Moreover, it is dependent on a set of values of design parameters for a structure analyzed, $\mathbf{b}$, i.e.,

$$a = a(\omega,\mathbf{p},\mathbf{b}) \tag{1}$$

where the vector of design parameters can include sets of friction contact parameters for every jth contact interface: $\mathbf{b} = \{\mathbf{b}_1,\mathbf{b}_2,\ldots,\mathbf{b}_l\}^T$. A vector of contact parameters at each interface, $\mathbf{b}_j$, can include values of friction coefficient μ; normal and tangential contact stiffness coefficients k_n and k_t; normal load N_0 gap g; and other design parameters, i.e., $\mathbf{b}_j = \{\mu,k_t,k_n,N_0,g,\cdots\}^T$.

Usually forced response levels are customarily calculated for variable excitation frequency and for some chosen fixed set of design parameter values, $\hat{\mathbf{b}}$, and excitation forces, $\hat{\mathbf{p}}$, i.e.,

$$a(\omega) = a(\omega,\mathbf{p}=\hat{\mathbf{p}},\mathbf{b}=\hat{\mathbf{b}}) \tag{2}$$

In design practice there is usually a need to understand how design parameters affect the maximum forced response level and therefore forced response calculation has to be repeated over a frequency range of interest for different parameter sets. Such parametric studies of the forced response can require large computational expense, especially for cases of strongly nonlinear nature of the vibration and a large number of parameters studied. Moreover, due to the high sensitivity of nonlinear forced response to design parameters values, in many cases there is a problem obtaining reliable approximations that would allow interpolation or/and extrapolation of behavior of the structure with variation of design parameters when forced response is determined only for several parameter values.

The highest forced response levels are of interest in most industrial applications. Because of this analysis of resonance regimes is suggested here by calculation of resonance frequencies, ω^{res}, and resonance amplitudes, a^{res}, directly as functions of design parameters, i.e.,

$$\begin{aligned}\omega^{\mathrm{res}}(\lambda) &= \omega^{\mathrm{res}}(\mathbf{p}(\lambda),\mathbf{b}(\lambda))\\ a^{\mathrm{res}}(\lambda) &= a^{\mathrm{res}}(\mathbf{p}(\lambda),\mathbf{b}(\lambda))\end{aligned} \tag{3}$$

where λ is a variable which is called here "a tracing variable." It is used here to describe variation of design parameters and excitation when operational conditions are changed (i.e., rotational speed, temperature, excitation forces, etc.). Such variation can be simultaneous for all contact interface parameters and excitation forces (for example, when this variation is owing to variation of the rotation speed or temperature), it can be applied to one chosen interface parameter, or it can be a level of excitation forces. Examples of use of the direct parametric analysis in some practical applications are given in the "Numerical Results" section of this paper.

Method for Direct Parametric Analysis of Resonance Regimes

Frequency Domain Equation of Motion. The equation for motion for a structure with nonlinear interfaces can be written in the following form.

$$\mathbf{K}\mathbf{q}(t) + \mathbf{C}\dot{\mathbf{q}}(t) + \mathbf{M}\ddot{\mathbf{q}}(t) + \mathbf{f}(\mathbf{q}(t),\mathbf{b}(\lambda)) - \mathbf{p}(t,\lambda) = \mathbf{0} \tag{4}$$

where $\mathbf{q}(t)$ is a vector of displacements; and $\mathbf{K}$, $\mathbf{C}$, and $\mathbf{M}$ are stiffness, viscous damping, and mass matrices used for description of linear forces. For a bladed disk rotating with speed ω, the stiffness matrix, $\mathbf{K}$, can also include terms accounting for the rotations effects, such as geometric stiffness matrix reflecting stiffening effects of the centrifugal forces; and a spin-softening-matrix describing stiffness softening due to the changing direction of the centrifugal forces under vibration. $\mathbf{f}(\mathbf{q}(t),\mathbf{b}(\lambda))$ is a vector of nonlinear interface forces, which is dependent on the displacements and on parameters of the contact interfaces. $\mathbf{p}(t,\lambda)$ is a vector of periodic external excitation forces, which can be dependent on the tracing variable, λ.

For a search of the steady-state periodic vibration response, the displacements' variation in time can be represented by a restricted Fourier series

$$\mathbf{q}(t) = \mathbf{Q}_0 + \sum_{j=1}^{n} (\mathbf{Q}_j^{(c)} \cos m_j\omega t + \mathbf{Q}_j^{(s)} \sin m_j\omega t) \tag{5}$$

where $\mathbf{Q}_j^{(c)}$ and $\mathbf{Q}_j^{(s)}$ $(j=1\ldots n)$ are vectors of cosine and sine harmonic coefficients for system degree of freedoms (DOFs), marked by superscripts $^{(c)}$ and $^{(s)}$ accordingly; $\mathbf{Q}_0$ is a vector of constant components of the displacements; and m_j $(j=1\ldots n)$ are specific numbers of harmonics that are kept in the displacement expansion. The multiharmonic representation of the forced response allows determination of major types of periodic vibration which are possible for strongly nonlinear structures including: (i) major resonances; (ii) superharmonic resonances; (iii) subharmonic resonances; and (iv) combination resonances. This determination can be made by an appropriate choice of values for m_j in the multiharmonic expansion of Eq. (5). In the case of a search for major and superharmonic resonances, m_j can be integer numbers corresponding to those harmonics that can contribute significantly to the forced response. For a search of subharmonic and combination resonances, m_j can be appropriately selected fractional numbers.

Application of the multiharmonic balance method and condensation techniques developed in Refs. [12,13] gives an equation of motion in the frequency domain with respect to the harmonic coefficients of the multiharmonic expansion in the form

$$\mathbf{R}(\mathbf{Q},\omega,\lambda) = \mathbf{Q} + \mathbf{A}(\omega)(\mathbf{F}(\mathbf{Q},\mathbf{b}(\lambda)) - \mathbf{P}(\lambda)) = \mathbf{0} \tag{6}$$

where $\mathbf{Q}=\{\mathbf{Q}_0,\mathbf{Q}_1^{(c)},\mathbf{Q}_1^{(s)},\ldots,\mathbf{Q}_n^{(s)}\}^T$ is a vector of harmonic coefficients of displacements; $\mathbf{P}=\{\mathbf{P}_0,\mathbf{P}_1^{(c)},\mathbf{P}_1^{(s)},\ldots,\mathbf{P}_n^{(s)}\}^T$ is a vector of harmonic components of the excitation forces; $\mathbf{F}(\mathbf{Q},\mathbf{b}(\lambda)) = \{\mathbf{F}_0,\mathbf{F}_1^{(c)},\mathbf{F}_1^{(s)},\ldots\mathbf{F}_n^{(s)}\}^T$ is a vector of harmonic components of nonlinear forces; and $\mathbf{A}(\omega)$ is a multiharmonic frequency response function (FRF) matrix of the linear part of the system, i.e.,

$$\mathbf{A}(\omega) = \mathrm{diag}[\mathbf{A}_0,\mathbf{A}_1(\omega),\ldots,\mathbf{A}_n(\omega)] \tag{7}$$

where FRF matrices, $\mathbf{A}_j(\omega)$, can be generated from mode shapes and natural frequencies obtained for a linear structure when contact interactions are neglected. For each harmonic number this matrix can be obtained in the following form

$$\mathbf{A}_j(\omega) = \begin{bmatrix} \mathrm{Re}(\tilde{\mathbf{A}}_j(\omega)) & \mathrm{Im}(\tilde{\mathbf{A}}_j(\omega)) \\ -\mathrm{Im}(\tilde{\mathbf{A}}_j(\omega)) & \mathrm{Re}(\tilde{\mathbf{A}}_j(\omega)) \end{bmatrix} \tag{8}$$

$$\begin{aligned}\tilde{\mathbf{A}}_j &= [(1 + i\eta)\mathbf{K}(\omega) + (m_j\omega)^2\mathbf{M}]^{-1} \\ &\simeq \sum_{r=1}^{N_m} \frac{\phi_r(\omega)\phi_r^T(\omega)}{(1 - i\eta_r(\omega))(\omega_r(\omega))^2 - (m_j\omega)^2}\end{aligned} \tag{9}$$

where $\omega_r(\omega)$, $\boldsymbol{\phi}_r(\omega)$, and $\eta_r(\omega)$ are natural frequencies, mode shapes, and modal damping factors for the linear part of a structure. The fact that all modal characteristics can be dependent on the rotation speed, ω, is allowed for here. N_m is the number of modes used in Eq. (9) for the FRF matrix generation. The expression for FRF matrix is written above for a common case of structural, frequency-independent damping. Expressions for a case of viscous damping and for a general case of combination of frequency-dependent and frequency-independent damping are given in Ref. [12].

Criterion for Resonance Determination. Nonlinear Eq. (6) allows determination of the harmonic components of displacement, $\mathbf{Q}$, for a given rotation speed/excitation frequency, ω, a design parameter set, $\mathbf{b}(\lambda)$, and excitation forces, $\mathbf{P}(\lambda)$. To determine a resonance frequency, ω^{res}, it has to be considered as a new unknown value. Therefore, a special additional criterion has to be formulated in order to calculate $\mathbf{Q}^{\mathrm{res}}$ and ω^{res} for resonance peaks. For this purpose a condition that the amplitude of displacements for a selected harmonic number and for a selected DOF takes its extreme value at a resonance frequency is proposed. This condition can be expressed in the form

$$r = \frac{1}{2}\frac{\partial}{\partial\omega}((q_{jk}^c)^2 + (q_{jk}^s)^2) = \mathbf{Q}^T\mathbf{I}_{jk}\frac{\partial\mathbf{Q}}{\partial\omega} = 0 \tag{10}$$

where q_{jk}^c and q_{jk}^s are coefficients for cosine and sine accordingly for jth harmonic of kth DOF selected from the vector of coefficients, $\mathbf{Q}$, and $\mathbf{I}_{jk}$ is a diagonal matrix which has the only two units at the main diagonal which correspond to sine and cosine coefficients for jth harmonic of kth DOF. It should be noted that nonlinear structures can have not only major, but also subharmonic, superharmonic, or combination resonances. The choice of the corresponding harmonic number and a DOF where the resonance peak can be observed allows direct parametric analysis of any of those types of resonances.

Calculation and Tracing of Resonance Regimes. In order to calculate vector of harmonic coefficients, $\mathbf{Q}^{\mathrm{res}}$, at a resonance and the corresponding resonance frequency, ω^{res}, Eqs. (6) and (10) have to be combined and solved simultaneously. The combined nonlinear equation takes the form

$$\mathbf{R}^{\mathrm{res}}(\mathbf{Q},\omega,\lambda) = \begin{Bmatrix} \mathbf{R}(\mathbf{Q},\omega,\lambda) \\ r(\mathbf{Q},\omega,\lambda) \end{Bmatrix} = \mathbf{0} \tag{11}$$

the solution of this nonlinear equation with respect to a vector of unknowns $\mathbf{X}=\{\mathbf{Q},\omega\}^T$ gives a resonance frequency, $\omega^{\mathrm{res}}(\lambda)$ and a vector of harmonic coefficients $\mathbf{Q}^{\mathrm{res}}(\lambda)$ at a resonance for a set of parameter values given by the tracing variable, λ. The solution of Eq. (11) is performed iteratively by the Newton–Raphson method

$$\frac{\partial\mathbf{R}^{\mathrm{res}}(\mathbf{X}^{(k)})}{\partial\mathbf{X}}(\mathbf{X}^{(k)} - \mathbf{X}^{(k+1)}) = \mathbf{R}^{\mathrm{res}}(\mathbf{X}^{(k)}) \tag{12}$$

where k is a number of iterations. The rate of the convergence is usually very dependent on the choice of the initial value, $\mathbf{X}^{(0)}$, for a solution. To ensure efficient calculations special methods (see Ref. [11]) are used for tracing the resonance solutions when the tracing variable is varied. These methods require calculation of the extended Jacobian, which for our case has the form

$$\mathbf{J} = \begin{bmatrix} \dfrac{\partial\mathbf{R}^{\mathrm{res}}}{\partial\mathbf{X}} & \dfrac{\partial\mathbf{R}^{\mathrm{res}}}{\partial\lambda} \end{bmatrix} = \begin{bmatrix} \dfrac{\partial\mathbf{R}}{\partial\mathbf{Q}} & \dfrac{\partial\mathbf{R}}{\partial\omega} & \dfrac{\partial\mathbf{R}}{\partial\lambda} \\ \dfrac{\partial r}{\partial\mathbf{Q}} & \dfrac{\partial r}{\partial\omega} & \dfrac{\partial r}{\partial\lambda} \end{bmatrix} \tag{13}$$

The extended Jacobian includes the Jacobian matrix of Eq. (6) $\partial\mathbf{R}/\partial\mathbf{Q}$, and a vector $\partial\mathbf{R}/\partial\lambda$. Analytical expressions for these matrices have been derived in Refs. [9,12,13].

In order to ensure robustness, high accuracy, and efficiency of the resonance regime calculations, additional components of the extended Jacobian, $\mathbf{J}$, which are necessary for resonance regime determination, are also derived analytically. Moreover, to evaluate the formulated resonance criterion a vector of $\partial\mathbf{Q}/\partial\omega$ has to be determined. Such expressions have not been reported in the literature before and they are given below.

The expressions for submatrices of the extended Jacobian, $\mathbf{J}$, are obtained by taking derivatives of Eqs. (6) and (10) with respect to independent variables, $\mathbf{Q}$, ω, and λ. From Eq. (6) we obtain the following expressions

$$\frac{\partial\mathbf{R}}{\partial\mathbf{Q}} = \mathbf{I} + \mathbf{A}(\omega)\frac{\partial\mathbf{F}}{\partial\mathbf{Q}} \tag{14}$$

$$\frac{\partial\mathbf{R}}{\partial\omega} = \frac{\partial\mathbf{A}(\omega)}{\partial\omega}(\mathbf{F} - \mathbf{P}) \tag{15}$$

$$\frac{\partial\mathbf{R}}{\partial\lambda} = \mathbf{A}(\omega)\left(\frac{\partial\mathbf{F}}{\partial\lambda} - \frac{\partial\mathbf{P}}{\partial\lambda}\right) \tag{16}$$

where $\mathbf{I}$ is an identity matrix. Expressions for the tangent stiffness matrix of contact interactions, $\partial\mathbf{F}/\partial\mathbf{Q}$, and for a vector of sensitivity of the nonlinear interaction forces to the tracing variable, $\partial\mathbf{F}/\partial\lambda$, used in these equations are obtained exactly using the analytical expressions developed in Ref. [9] for a case of a general model of a friction contact interface. A vector of rates of variation of the excitation forces, $\partial\mathbf{P}/\partial\lambda$, is calculated from a dependency of the excitation forces on the tracing variable, λ, which is prescribed for the forced response analysis. A frequency derivative of the FRF matrix, $\partial\mathbf{A}/\partial\omega$, is obtained by differentiating Eq. (9)

$$\begin{aligned}\frac{\partial\tilde{\mathbf{A}}_j}{\partial\omega} &= \sum_{r=1}^{N_m} \frac{2m_j^2\omega + 2(1 + i\eta_r)\omega_r\dfrac{\partial\omega_r}{\partial\omega} + i\omega_r^2\dfrac{\partial\eta_r}{\partial\omega}}{((1 + i\eta_r)\omega_r^2 - (m_j\omega)^2)^2}\boldsymbol{\phi}_r\boldsymbol{\phi}_r^T \\ &\quad + \sum_{r=1}^{N_m} \frac{2}{(1 - i\eta_r)\omega_r^2 - (m_j\omega)^2}\boldsymbol{\phi}_r\frac{\partial\boldsymbol{\phi}_r^T}{\partial\omega}\end{aligned} \tag{17}$$

Differentiating Eq. (10) with respect to $\mathbf{Q}$, ω, and λ, we have

$$\frac{\partial r}{\partial\mathbf{Q}} = \mathbf{I}_{jk}\frac{\partial\mathbf{Q}}{\partial\omega} + \mathbf{Q}^T\mathbf{I}_{jk}\frac{\partial}{\partial\mathbf{Q}}\left(\frac{\partial\mathbf{Q}}{\partial\omega}\right) \tag{18}$$

$$\frac{\partial r}{\partial\omega} = \mathbf{Q}^T\mathbf{I}_{jk}\frac{\partial}{\partial\omega}\left(\frac{\partial\mathbf{Q}}{\partial\omega}\right) \tag{19}$$

$$\frac{\partial r}{\partial\lambda} = \mathbf{Q}^T\mathbf{I}_{jk}\frac{\partial}{\partial\lambda}\left(\frac{\partial\mathbf{Q}}{\partial\omega}\right) \tag{20}$$

A vector of sensitivity of harmonic coefficients to frequency variation, $\partial\mathbf{Q}/\partial\omega$, included in these equations is obtained by taking a full derivative of Eq. (6), which gives the following equation for determination of $\partial\mathbf{Q}/\partial\omega$

$$\frac{\partial\mathbf{R}}{\partial\mathbf{Q}}\frac{\partial\mathbf{Q}}{\partial\omega} = -\frac{\partial\mathbf{R}}{\partial\omega} \tag{21}$$

Derivatives of $\partial\mathbf{Q}/\partial\omega$ with respect to $\mathbf{Q}$, ω, and λ are calculated from equations obtained by differentiating Eq. (21) with respect to these variables.

Numerical Results

Capabilities of the developed method for the direct parametric analysis of resonance regimes were explored on a set of test cases. Some of the numerical examples studied are discussed below.

Nonlinear Single-Degree-of-Freedom System. For initial exploration of the method, a single DOF (SDOF) oscillator was considered. The equation of motion of the oscillator has the following form

$$\ddot{x} + 1.6\omega^{-1}\dot{x} + 40x + f(x) = a \sin \omega t \tag{22}$$

where $f(x)$ is a nonlinear force and the damping coefficient $1.6/\omega$ is represented in the form allowing modeling of structural, frequency-independent damping. Three major types of the nonlinear forces are studied, which occur in practical bladed disks at contact interfaces:

(i) Nonlinear interaction of friction damper type with the friction model which was developed in paper Ref. [9];

(ii) Gap nonlinearity described by the following expression for the nonlinear force

$$f(x) = \begin{cases} kx, & \text{for } x \geqslant g \\ 0, & \text{for } x < g \end{cases} \tag{23}$$

(iii) Cubic nonlinearity, i.e., $f(x)=kx^3$, where k is a stiffness coefficient. This type of nonlinearity can be used for modeling Hertzian contacts at contact interfaces

It is assumed that a consistent system of units is used for displacements, excitation forces, and parameters of the nonlinearities. Such system of units can be chosen arbitrarily, and hence they are not specified in the results obtained for the SDOF system.

Friction Damper Nonlinearity. A friction damper model developed in Ref. [9] has four parameters which characterize contact of rough surfaces: (i) static normal load N_0; (ii) tangential stiffness coefficient k_t; (iii) friction coefficient μ; and (iv) normal stiffness coefficient k_n. For the SDOF system considered here the effects of variation of the first two parameters are studied explicitly. The latter two parameters are not analyzed because for the case of constant normal load considered here: (i) the friction coefficient has an effect on the forced, which is similar to that of the normal, since they involved in calculations as limiting friction force value, μN_0, and variation of either parameter can give the same effect; and (ii) due to the absence of motion in the normal direction to the friction contact k_n does not affect the vibration levels. Friction coefficient was assumed in calculation to be fixed $\mu=0.3$ and the excitation level is $a=100$. The first ten integer harmonic numbers are kept in the multiharmonic expansion.

In Fig. 1 effects of the normal load variation on the resonance frequency and amplitude are studied for a fixed value for $k_n=30$. The normal load is varied from the value of -10^4 (when there is no contact between damper and the oscillator), to 10^4 (when the damper is fully stuck).

In Fig. 1(*a*) and further in this paper maximum values of multiharmonic displacements (which are also referred to in the paper as response levels) are determined over a period of vibration, i.e., $x_{\max}=\max_{t\in[0,2\pi/\omega]}(x(t))$. Comparison with conventional forced response curves plotted in Fig. 1(*a*) shows that the direct parametric analysis really finds the resonance peaks with continuous variation of N_0. The calculated dependency of the resonance response level as a function of the normal load shown in Fig. 1(*b*) indicates that the response level has a minimum located within the range of the normal load variation. A value of $N_0=475.3$, which provides the lowest resonance amplitudes, can be selected directly from the plot.

Effects of variation of the tangential stiffness coefficient from 0 to 10^4 are shown in Fig. 2 (the normal load $N_0=2000$ is accepted for these calculations). One can see from Fig. 2(*b*) that k_t has a significant effect on the resonance frequency and the resonance peak response level. Its growth increases the resonance frequency and, for the system considered, it can decrease the resonance re-

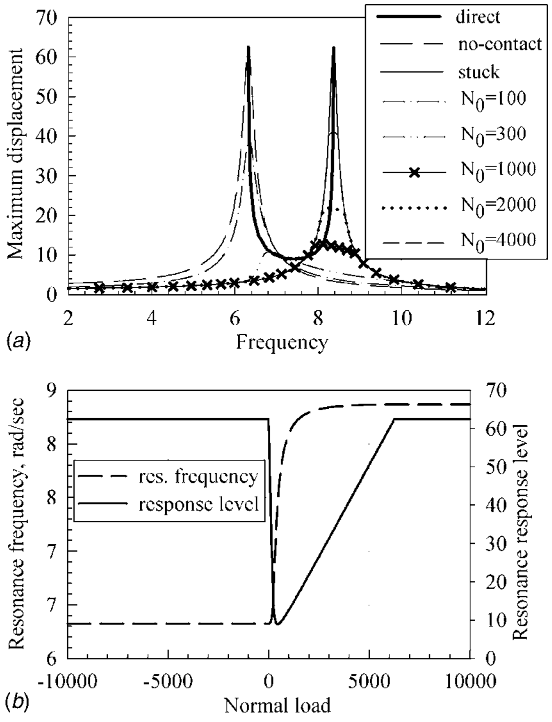

Fig. 1 A system with friction damper: (*a*) comparison of direct parametric analysis and the conventional approach; and (*b*) resonance frequency and response level

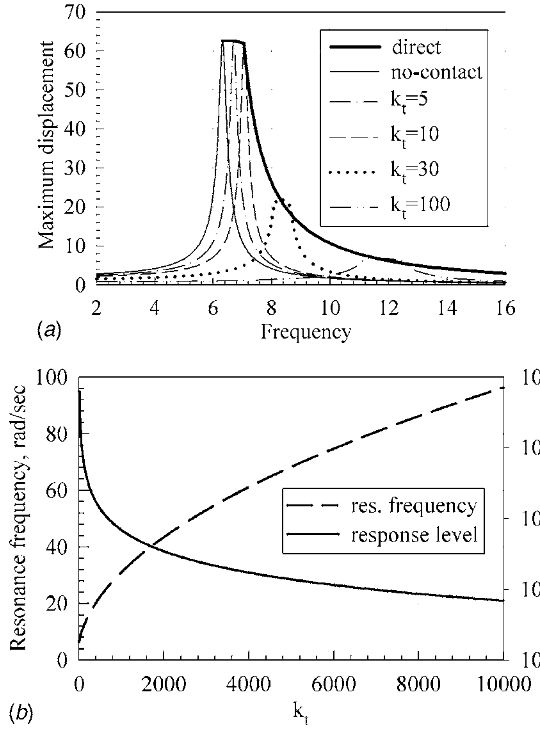

Fig. 2 Effect of the tangential stiffness on a system with friction damper: (*a*) comparison of direct parametric analysis and the conventional approach; and (*b*) the resonance frequency and response level

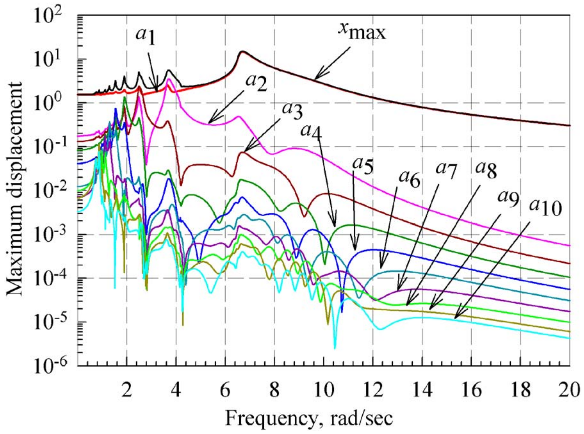

Fig. 3 Maximum displacement and harmonic amplitudes of its multiharmonic expansion

sponse level by several orders of magnitude.

For the cases of the constant normal load considered above, the major, first harmonic was dominant in the forced response. In order to demonstrate applicability of the new method for essentially multiharmonic forced response, a case was considered with the oscillating normal load applied to the friction damper, i.e.,

$$N_0 = \begin{cases} 300 + 320 \sin \omega t, & \text{for } N_0 \geqslant 0 \\ 0, & \text{otherwise} \end{cases} \tag{24}$$

For this case, the damper is subjected to temporarily separation, and the forced response becomes essentially multiharmonic. In Fig. 3 maximum displacement of the multiharmonic response, $x_{\max}$, is shown together with amplitudes, a_j, of ten harmonics included in the multiharmonic representation of displacements. One can observe not only a major resonance at the frequency 6.68 rad/s, but also superharmonic resonances (e.g., at frequencies 3.68 rad/s, 2.48 rad/s, and others). One can also see that amplitudes of second and third harmonics are close to amplitudes of first harmonic even at the frequencies corresponding to the superharmonic resonances. Results of the direct parametric analysis for major and superharmonic resonances of second and third orders are shown in Fig. 4 for a case when amplitude, a, of the excitation force is varied from 10 to 400. These results are validated here by comparison with the conventional calculation of the forced response performed for several different values of excitation force.

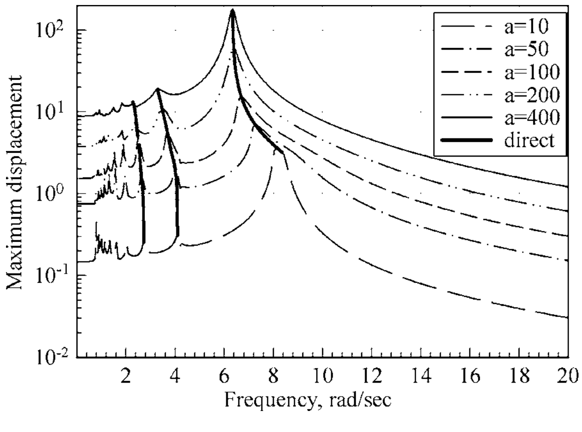

Fig. 4 Tracing of major and superharmonic resonances by the direct parametric analysis for a varying level of excitation

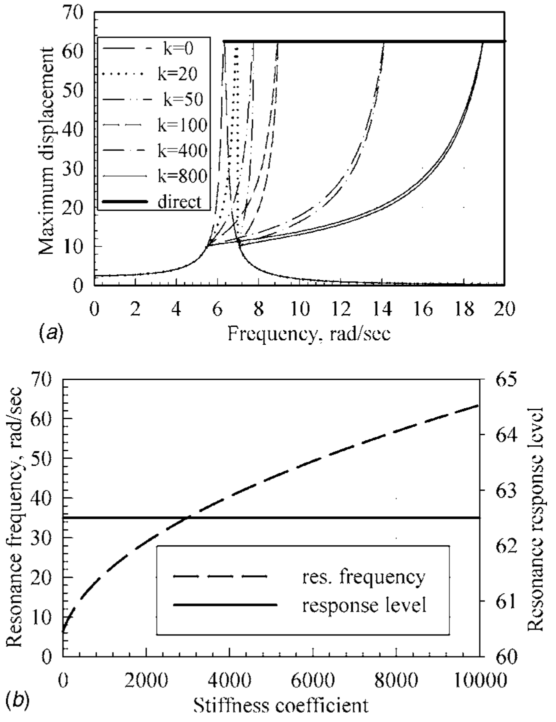

Fig. 5 Effects of stiffness for a system with gap nonlinearity: (*a*) direct parametric analysis and the conventional approach; and (*b*) resonance frequency and response level

Gap Nonlinearity. For a case of the gap nonlinearity there are two parameters that affect the nonlinear force: (i) a value of the stiffness coefficient k; and (ii) a gap value g. Results of calculation of resonance frequencies and amplitudes for the stiffness coefficient variation from 0 to 10^4 are shown in Fig. 5. The gap value was assumed to be 10 in these calculations and the excitation amplitude, $a=100$. Resonance peak amplitudes and frequencies calculated for a case of variation of the gap value from negative to positive values in the range-100–100 are shown in Fig. 6 (for a case of stiffness coefficient value equal to 100).

In Figs. 5(*a*) and Fig. 6(*a*) forced response levels calculated as a function of frequency for several values of parameter of the gap nonlinearity are also plotted. One can see that the direct parametric analysis again allows very accurate determination of the resonance peaks. One can see that resonance response level is independent of both parameters of the gap nonlinearity. The resonance frequency increases monotonically with increase of the stiffness coefficient in the range of values studied and this increase can be approximated by a power function. Variation of the gap value changes the resonance frequency from a value of a system without the gap nonlinearity (when gap is large and never closed under the given level of the excitation) to a resonance frequency value for a system with a linear spring with stiffness coefficient equal to the gap nonlinearity stiffness (when initial interference is large and the gap is never opened). Between these two limiting values the resonance frequency varies almost linearly with variation of the gap value.

Cubic Nonlinearity. For a case of cubic nonlinearity the stiffness coefficient, k, was chosen as a varied parameter. Hence the resonance frequencies and maximum displacements found over the vibration period are calculated as a function of this stiffness coefficient. Amplitude of excitation, a, in Eq. (22) was assumed to be 50. Results of the application of the method developed to this system are shown in Fig. 7.

In Fig. 7 the maximum displacement over vibration period calculated by the direct parametric analysis method at resonance

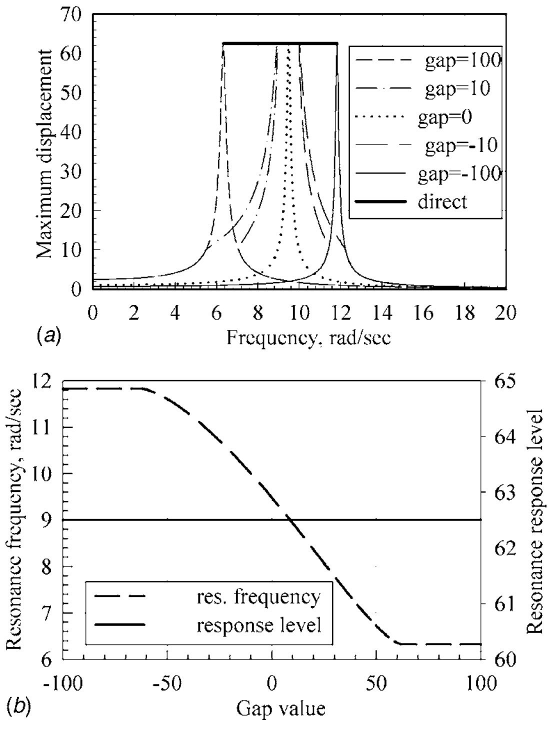

Fig. 6 A system with gap nonlinearity: (*a*) comparison of direct parametric analysis and the conventional approach; and (*b*) resonance frequency and response level

peaks is plotted by a red line. For comparison the maximum displacements were also calculated and plotted as functions of excitation frequency for different values of the stiffness coefficient using a conventional approach. The stiffness coefficient is varied from 0.01 to 30. For comparison, forced responses are also calculated as a function of excitation frequency and plotted here for a several values of *k*. One can see that the direct parametric analysis finds very accurately the resonance peaks. In Fig. 7 the resonance frequency and the resonance response level are plotted—as they were calculated—with respect to variation of the stiffness coefficient. Analysis of the results shows that dependency of the resonance frequency with respect to the stiffness coefficients is well approximated by a square root function, i.e., $\omega^{\mathrm{res}} \simeq 27.4\sqrt{k}$, and the response amplitude is constant.

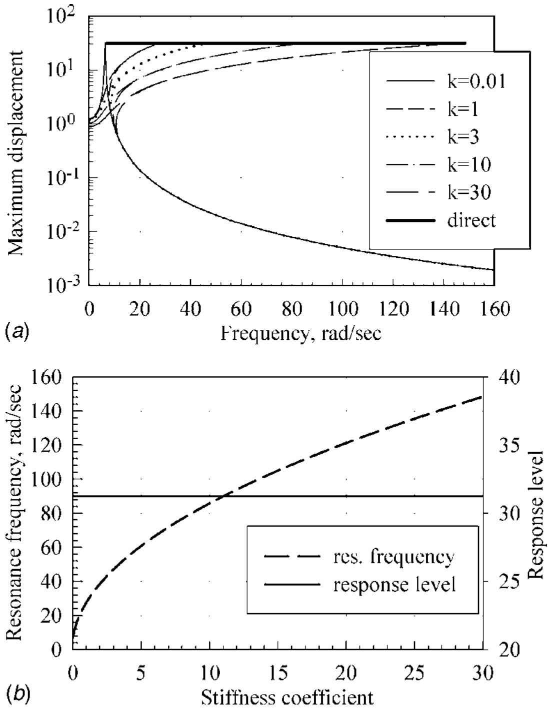

Fig. 7 A system with cubic nonlinearity: (*a*) comparison of direct parametric analysis and the conventional approach; and (*b*) resonance frequency and response level

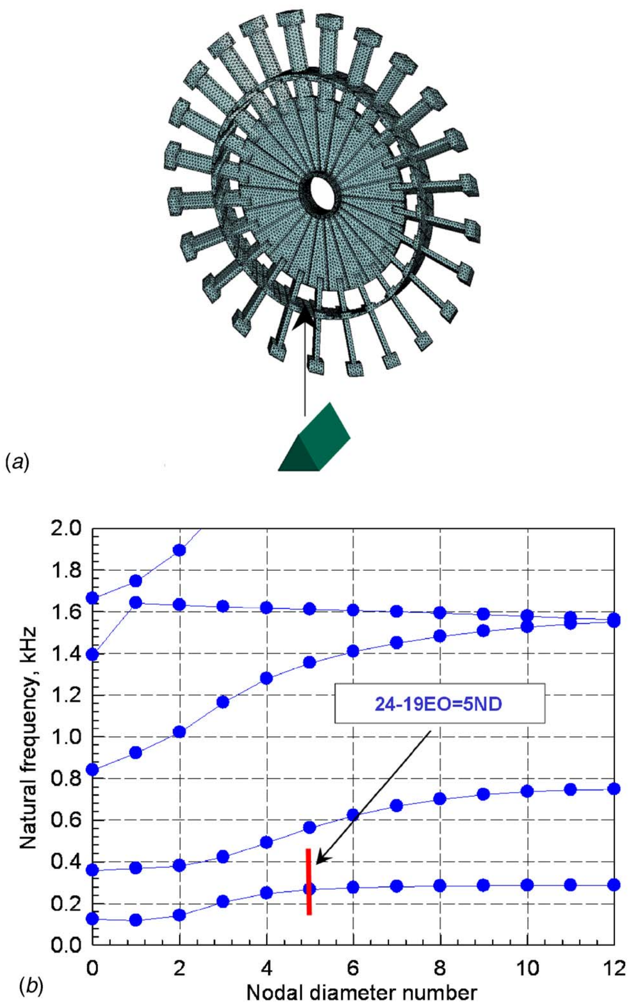

Fig. 8 A FE model of the test-rig bladed disk and natural frequencies of the assembly (obtained without UPDs)

Large-Scale Model of a Bladed Disk. A blisk of 24 blades, which is analyzed here, was manufactured for a test rig built at Imperial College London in the framework of the EU project "Aeroelastic Design of Turbine Blades II" (ADTurbII) (see Ref. [14]). A finite-element model of this blisk is shown in Fig. 8(*a*). The model of one sector of the blisk used in calculation here contains 21,555 DOFs.

Natural frequencies of the tuned bladed disk without underplatform dampers are plotted for all nodal diameters (NDs) from 0 to 12 in Fig. 8(*b*).

By making use of cyclic symmetry properties, as in the method developed in paper Ref. [12] accurate calculations of strongly nonlinear vibrations of a whole bladed disk can be performed using only one of its sector. Nonlinear interaction occurs at contact interfaces between blade platforms and cottage–roof underplatform dampers (UPDs). A traveling wave excitation by 19th

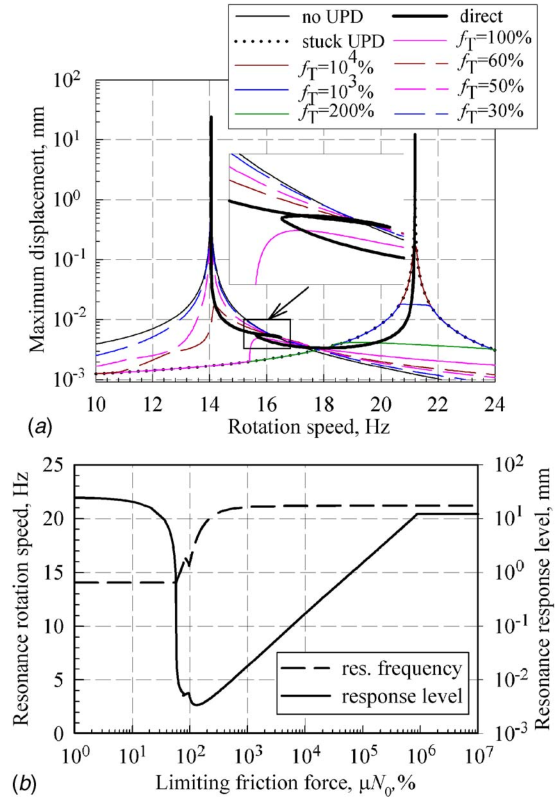

Fig. 9 Effects of limiting friction force for a bladed disk with UPDs: (*a*) direct parametric analysis and the conventional approach; and (*b*) the resonance frequency and response level

engine order is considered which excites modes of the tuned assembly with $24-19=5$ ND. Since there is no root or other contact interfaces in the blisk the modal damping is due solely to damping in material of the blisk and the damping loss factor is assumed relatively low: $\eta=7.5e-05$. Dissipation of vibration energy due to friction forces produced by UPDs is calculated together with the forced response calculation. The resonance frequency and resonance forced response level calculated for the bladed disk as functions of the limiting friction force, $f_T=\mu N_0$, are shown in Fig. 9. The forced response was determined at a node located at the blade tip.

The limiting friction force was varied from 1% to 10^7% of its initial value. The wide range of the limiting friction force variation was selected to include the direct parametric analysis determination of resonance frequencies of the system with fully stuck dampers and with negligible effect of the dampers.

In real conditions the limiting friction forces can vary in rather wide ranges since it is dependent not only on the friction coefficient, μ, but also on the normal load proportional to damper mass, m_d, distance from the damper to the rotation axis, r_d, the rotation speed, Ω, and others, i.e., $f_T=c\mu m_d r_d \Omega^2$ (where c is a coefficient depending on geometric shape of the underplatform damper). Comparison of results obtained by the method developed and by the conventional forced calculations for different values of the parameter analyzed is shown in Fig. 9(*a*).

A small region of the plot is zoomed in order to demonstrate a complex shape of the resonance curve in this region. The direct parametric analysis can significantly facilitate choice of the optimal parameters for UPDs. From Fig. 9(*b*) one can easily find that the resonance response level has its minimum value, 3.3874 μm, for $f_T=131\%$ of its initial value. One can also see that the resonance frequency changes largely when the limiting friction force varies from 60% to 250%.

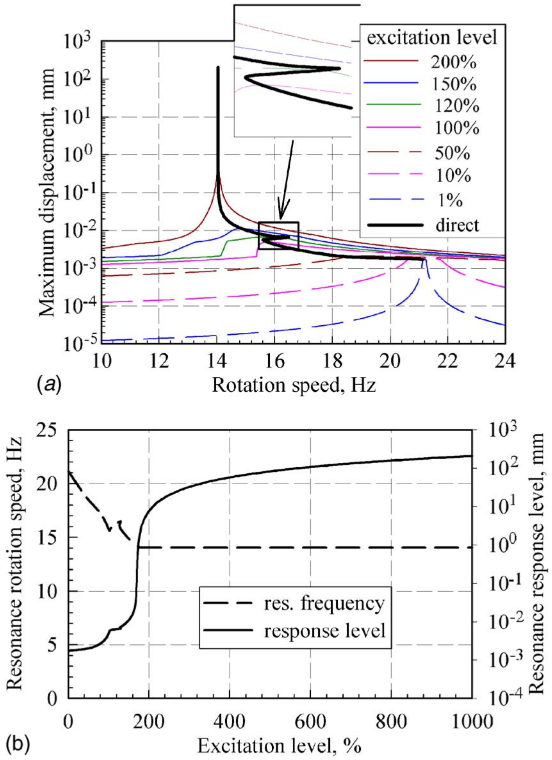

Fig. 10 Effects of excitation level for a bladed disc with UPDs: (*a*) comparison of direct parametric analysis and the conventional approach; and (*b*) the resonance frequency and response level

It is important to know how the UPDs will reduce resonance response levels under different forcing conditions. Examples of results of such study obtained by the new method are shown in Fig. 10.

For this case, the parameters of the UPDs are assumed to be fixed to have $f_T=100\%$ and the excitation level is varied from 1% to 1000% of its nominal value. Highly nonlinear character of the forced response for the structure studied is evident from Fig. 10(*b*), where one can see that resonance response level is a nonlinear function of the level of excitation, which contrasts with one of the basic features characteristic of linear systems. The steepest increase of the resonance amplitude is observed when the excitation level is increased from 160% to 200%. Variation of the excitation level in the range from 1 to 200% affects significantly the resonance frequency. For all higher levels of excitation the resonance frequency remains almost unchanged and is very close to the resonance frequency of the bladed disk without UPDs.

Numerical Efficiency of the Direct Parametric Analysis. In the conventional approach, the forced response calculation is required over some frequency range, in order to determine the resonance amplitude and, moreover, these calculations have to be repeated for every set of values of the design parameter that are of interest. The direct parametric analysis allows search of the resonance frequencies and amplitudes directly from a solution of multiharmonic equations of motion with the resonance criterion added (see Eq. (11)).

Moreover, the method tracing the resonance regimes allows determination of the resonance characteristics of the essentially nonlinear systems for design parameters varied in wide ranges, while automatically selecting step size for the parameter value variation. The parameter step is selected to allow: (i) capturing dependency of resonance amplitude and frequency variation on design parameter, even when they are very sensitive to parameter variation and change sharply, and (ii) avoiding small steps when the resonance

Table 1 Computational time for the parametric analysis

Parameter	Variation range (%)	CPU time (s)
Limiting friction force	1–1,000,000	4.7
Excitation level	1–10,000	116

characteristics are not sensitive to the parameter variation.

The direct parametric analysis of the resonance frequencies is very computationally effective and in many cases requires even less time than a single conventional forced response calculation for a given set of design parameters.

Examples of computational time required for the analysis of the large-scale finite-element (FE) model of the bladed disk are given in Table 1 for both cases considered above: (i) a case of limiting force variation, and (ii) a case of excitation level variation. A standard PC was used in these calculations. A conventional forced response analysis, performed for only one set of the parameter values over the frequency range selected, required 10–20 s.

Conclusions

A method for direct parametric analysis of resonance regimes of strongly nonlinear vibration of bladed disks has been developed for the first time.

The new method allows calculation of resonance frequencies and forced response levels at resonance peaks directly as functions of design parameters of interest or as functions of excitation levels. It facilitates extensively a choice of the optimal parameters aimed at such objectives as maximum reduction of the resonance levels, a specially selected resonance frequency value, or others. In many cases the optimal parameter value can be obtained directly as a result of a single direct parametric calculation.

Steady-state periodic vibrations are analyzed in frequency domain using multiharmonic representation for displacements of a structure.

A criterion for the resonance peak determination has been formulated. Analytical expressions have been derived for exact evaluation of the criterion for a general case of nonlinear vibrations and for the extended Jacobian, which is necessary for solution of the nonlinear equations of motion and for tracing of the resonance characteristics as functions of design parameters.

Capabilities of the new method to analyze structures with different types of nonlinearities, encountered in most practical applications, have been demonstrated, namely for: (i) cubic nonlinearity; (ii) gap nonlinearity; and (iii) friction dampers.

High accuracy achieved by the direct parametric analysis method in calculation of the resonance forced response characteristics is proved by comparison with the results obtained by the conventional forced response analyses and by computational expense data.

An example of application of the new approach to the large-scale FE model of a bladed disk with underplatform dampers has been considered.

Acknowledgment

The author is grateful to Rolls-Royce Plc. for providing the financial support for this project and for giving permission to publish this work.

References

[1] Griffin, J. H., and Labelle, R. F., 1996, “A Rational Method for Optimizing Shroud Damping,” ASME Paper No. 96-GT-402, pp. 1–8.
[2] Yang, B.-D., and Menq, C.-H., 1997, “Modeling of Friction Contact and its Application to the Design of Shroud Contact,” ASME J. Eng. Gas Turbines Power **119**, pp. 958–963.
[3] Szwedowicz, J., Sextro, W., Visser, R., and Masserey, P., 2003, “On Forced Vibration of Shrouded Turbine Blades,” ASME Paper No. GT-2003-38808, pp. 1–10.
[4] Sanliturk, K. Y., Ewins, D. J., and Stanbridge, A. B., 2003, “Underplatform Dampers for Turbine Blades: Theoretical Modeling, Analysis, and Comparison with Experimental Data,” J. Eng. Gas Turbines Power, **123**, pp. 919–929.
[5] Cameron, T., and Griffin, J., 1989, “An Alternating Frequency/Time Domain Method for Calculating the Steady-State Response of Nonlinear Dynamic Systems,” Trans. ASME, J. Appl. Mech., **56**, pp. 149–154.
[6] Nacivet, S., Pierre, C., Thouverez, F., and Jezequel, L., 2003, “A Dynamic Lagrangian Frequency-Time Method for the Vibration of Dry-Friction-Damped Systems.” J. Sound Vib., **265**, pp. 201–219.
[7] Wang, J. H., and Chen, W. K., 1993, “Investigation of the Vibration of a Blade with Friction Damper by HBM,” J. Eng. Gas Turbines Power, **115**, pp. 294–299.
[8] Berthillier, M., Dupont, C., Mondal, R., and Barrau, R. R., 1998, “Blades Forced Response Analysis with Friction Dampers,” Trans. ASME, J. Vib. Acoust., **120**, pp. 468–474.
[9] Petrov, E. P., and Ewins, D. J., 2003, “Analytical Formulation of Friction Interface Elements for Analysis of Nonlinear Multi-Harmonic Vibrations of Bladed Discs,” ASME J. Turbomach., **125**, pp. 364–371.
[10] Petrov, E. P., 2005, “Sensitivity Analysis of Nonlinear Forced Response for Bladed Discs with Friction Contact Interfaces,” Proceedings of ASME Turbo Expo 2005, Reno–Tahoe, NV, June 6–9, Paper No. GT2005-68935.
[11] Petrov, E. P., 2005, “Method for Direct Parametric Analysis of Nonlinear Forced Response of Bladed Discs with Friction Contact Interfaces,” J. Turbomach., **126**, pp. 654–662.
[12] Petrov, E. P., 2003, “A Method for Use of Cyclic Symmetry Properties in Analysis of Nonlinear Multiharmonic Vibrations of Bladed Discs,” J. Turbomach., **126**, pp. 175–183.
[13] Petrov, E. P., and Ewins, D. J., 2004, “Method for Analysis of Nonlinear Multiharmonic Vibration of Bladed Discs Mistuned by Scatters in Characteristics of Friction Contact Interfaces and Blades,” J. Turbomach., **127**, pp. 128–136.
[14] Elliott, R., Green, J. S., and Seinturier, E., 2005, “Aeroelastic Design of Turbine Blades-ADTurB II Overview,” Proceedings 6th European Turbomachinery Conference, Lille, France. 7–11 March, Paper No. AMP-105_01/62.

Unsteady Aerodynamic Blade Excitation at the Stability Limit and During Rotating Stall in an Axial Compressor

Ronald Mailach
e-mail: ronald.mailach@tu-dresden.de

Konrad Vogeler
e-mail: konrad.vogeler@tu-dresden.de

Technische Universität Dresden,
Institut für Strömungsmechanik,
01062 Dresden, Germany

The stable operating range of axial compressors is limited by the onset of rotating stall and surge. These flow conditions endanger the reliability of operation and definitely have to be avoided in compressors of gas turbines. However, there is still a need to improve the physical understanding of these flow phenomena to prevent them while utilizing the maximum available working potential of the compressor. This paper discusses detailed experimental investigations of the rotating stall onset with the main emphasis on the aerodynamic blade excitation in the Dresden four-stage low-speed research compressor. The stall inception, which is triggered by modal waves, as well as the main flow features during rotating stall operation are discussed. To investigate the unsteady pressure distributions, both the rotor and the stator blades of the first stage were equipped with piezoresistive pressure transducers. Based on these measurements the unsteady blade pressure forces are calculated. Time-resolved results at the stability limit as well as during rotating stall are presented. For all operating conditions rotor–stator interactions play an important role on the blade force excitation. Furthermore the role of the inertia driven momentum exchange at the stall cell boundaries on the aerodynamic blade force excitation is pointed out. [DOI: 10.1115/1.2720486]

Keywords: axial compressor, rotating stall, modal waves, rotor-stator-interaction, unsteady profile pressure, unsteady aerodynamic blade force

1 Introduction

The stable operating range of axial compressors for low mass flow is limited by the rotating stall (RS) inception. This flow regime can trigger the formation of surge, particularly for high rotational speed and large downstream plenum. In gas turbines and jet engines these dangerous flow conditions must be avoided because of the excitation of high-amplitude vibrations and high thermal loading of the blades and other machine components, which can result in a reduction of fatigue life or even a destruction of these machine parts. In practice this is done by maintaining a surge margin, which can amount to 20–25% of the compressor pressure rise. As a consequence the attainable efficiency of the machine is strongly reduced. Therefore, several control mechanisms for extending the usable operating range of axial compressors were discussed within recent years. A potential practical application of such methods requires a further improvement of the physical understanding of the stall and surge inception and development process.

There are different flow patterns that precede the RS inception. The first one is the modal wave stall inception [1]. Modal waves are a typical stall precursor in low-speed compressors but have also been observed in high-speed compressors [2,3]. Often this flow disturbance occurs only a short time before exceeding the stability limit of the compressor. Modal waves are a long-lengthscale wavelike disturbance of the pressure and velocity field rotating around the circumference. The breakdown of the flow field at the stability limit is initiated in a velocity minimum of the modal wave.

The second pattern is a short-lengthscale disturbance, which is known as a "spike." It is a small cell of stalled flow, which in its initial phase is typically limited to the blade tip region of only one or a few blade passages. It grows within a few rotor revolutions to a full-span RS cell. Camp and Day [4] give a detailed overview of the recent work on these two stall inception patterns.

Other flow patterns, which can already be found in the stable operating range of compressors and can be regarded as precursors for full-span RS, are short-lengthscale multicell configurations. These flow conditions can especially appear in blade rows with higher loading, e.g., in the front stages of high-speed compressors at part speed, in miss-staggered blade rows, or in blade rows with relative large tip clearance. This is discussed in Refs. [5,6].

The stall inception process in the Dresden four-stage axial low-speed research compressor (LSRC) will be discussed in this paper. An important aspect for a reliable operation of the compressor is the aerodynamic blade excitation at operating points near the stability limit and especially for unstable flow conditions, where a clear difference to the design conditions can be expected. Within recent years an increasing number of both experimental and numerical investigations on unsteady aerodynamic blade forces in turbomachinery became available. A literature survey on this topic is given by Mailach et al. [7,8]. However, to the best knowledge of the authors up to the present only stable operating points of compressors are discussed in open literature. Experimental data about unsteady aerodynamic blade pressure forces for unsteady flow conditions in compressors are not available yet.

The aim of this paper is therefore to gain insight into the complex physics of aerodynamic blade excitation for unsteady flow conditions in compressors. On the basis of the time-resolved pressure measurements on the rotor and stator blade rows the unsteady pressure forces of the blades are calculated. Results will be presented for exceeding the stability limit and the developing RS

Contributed by the International Gas Turbine Institute of ASME for publication in the JOURNAL OF TURBOMACHINERY. Manuscript received July 18, 2006; final manuscript received July 25, 2006. Review conducted by David Wisler. Paper presented at the ASME Turbo Expo 2006: Land, Sea and Air (GT2006), Barcelona, Spain, May 8–11, 2006. Paper No. GT2006-90214.

Table 1 Design parameters of Dresden LSRC

IGV+4 identical stages			
Reynolds number, rotor inlet, MS[a], DP[b] (related to rotor chord length)	5.7×10^5		
Mach number, rotor inlet, MS[a], DP[b]	0.22		
Design speed	1000 rpm		
Mass flow, DP[b]	25.35 kg/s		
Mean flow coefficient, DP[b]	0.553		
Enthalpy coefficient Ψ_{is}, DP[b]	0.794		
Hub diameter	1260 mm		
Hub to tip ratio	0.84		
Axial gaps between all blade rows, MS[a]	32 mm		
	IGV	rotor	stator
Blade number	51	63	83
Chord length, MS[a] (mm)	80	110	89
Stagger angle, MS[a] (versus circumference) (deg)	82.8	49.3	64.0
Solidity, MS[a]	0.941	1.597	1.709

[a] MS=midspan.
[b] DP=design point.

regime. The excited pressure forces are quantified and compared to the results for stable operating points, which are available from previous investigations of the authors [7,8].

2 Experimental Setup, Data Acquisition, and Post-Processing

The Dresden LSRC consists of four identical stages, which are preceded by an inlet guide vane (IGV) row. Table 1 gives a summary of the main design parameters while Fig. 1 shows a sectional drawing of the compressor. The blading of the compressor was developed on the basis of the profiles of a middle stage of a high-pressure compressor of a gas turbine. More detailed descriptions of the compressor are given by Sauer et al. [9], Müller et al. [10], and Boos et al. [11].

For the experiments described in this paper, the operating point of the compressor was shifted on the design speed line from a stable operating point toward the RS onset by closing the throttle slowly. When the stability limit was exceeded, the compressor was operated during RS for a maximum of 10 s while keeping the throttle position unchanged.

A single rotor blade and a single stator blade were equipped altogether with 36 time-resolving piezoresistive pressure transducers (Kulite LQ47). To minimize the influence on the flow the sensors and the wires were fitted into the blade surfaces. They are equally distributed along the midspan on the pressure side (PS) and the suction side (SS). On both blades the sensors are positioned from 10% to 90% chord with steps of 10% chord. The leading edge and the trailing edge regions could not be equipped with pressure transducers without noticeably disturbing the flow. As an example the rotor blade is shown in Fig. 2.

The investigations of the unsteady blade pressure forces at the stability limit and during rotating stall were performed on Rotor 1 and Stator 1, since the stall inception appears in the first stage. Both the steady and the unsteady part of the pressure were measured with the piezoresistive transducers. The zero point offset of the sensors was corrected before starting the short-duration measurements. The signals from the transducers were amplified 125 times. This was done using a separate miniature amplifier for each sensor. For the measurements on the rotor blades the amplifier card was mounted within the rotor drum. The amplified signals are transmitted via slip rings into the fixed frame of reference.

The pressure force components F_x and F_y are referred to the blade coordinate system (Fig. 3). They were calculated by integrating the measured unsteady pressure distributions along the PS and the SS with respect to the blade contour. The pressure in the leading edge and the trailing edge region was extrapolated to improve the accuracy of the results. Based on the time-resolved force components F_x and F_y further parameters were determined. These are the resulting pressure force F and the turning moment M_{CG}, which is referred to the center of gravity (CG) of the blade. Eventually the angle α between the abscissa and the direction of the resulting force F was determined (Fig. 3).

A simple approach was made for the extrapolation of the pressure toward the leading and trailing edges. The pressure at the

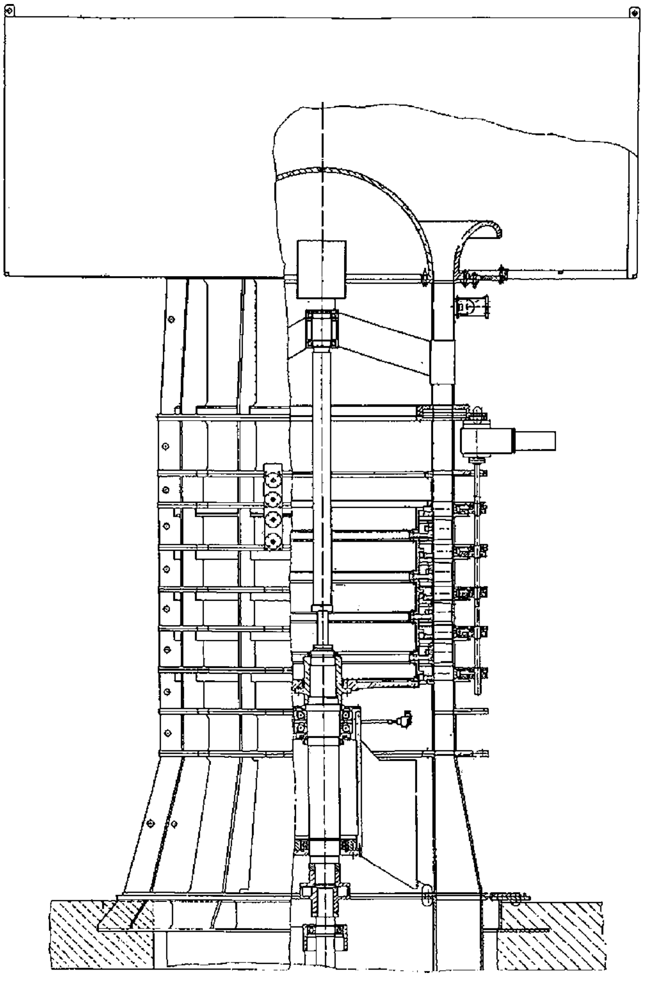

Fig. 1 Sectional drawing of Dresden LSRC

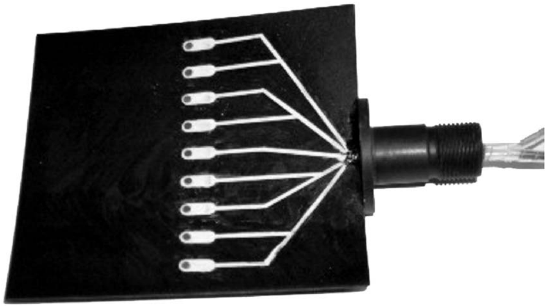

Fig. 2 Rotor blade equipped with piezoresistive pressure transducers on PS and SS (view on PS)

leading edge was estimated by averaging the pressure values at the 10% chord positions on PS and SS, while the pressure at the trailing edge was determined by averaging the pressures at the 90% chord positions. Certainly this approach is only nearly correct for design conditions, when the stagnation points are very close to the leading edge and trailing edge, respectively. To verify the approach the extrapolated pressure distribution of the piezoresistive sensors was compared with the results of the pressure taps. The pressure taps had a minimum distance of only 2.5% chord length from the leading edge and trailing edge, respectively. This comparison was done for different stable operating points. In every case the extrapolated pressures from the piezoresistive sensors are consistent with the measured values of the pressure taps at the positions close to the leading edge and trailing edge, respectively.

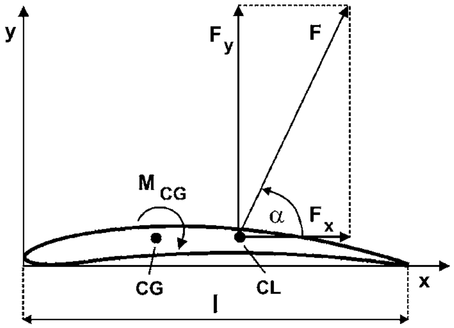

Fig. 3 Force definitions in blade coordinate system

For operating conditions close to the stability limit the point of maximum loading is shifted toward the leading edge of the blades. Using the extrapolation the pressures between the leading edge and the first sensor positions on the PS and SS are possibly under- or overestimated. Indeed it was verified for the investigated blades that these errors are nearly compensated for when calculating the dominant force component F_y by integrating the pressure distribution. On the other hand the force component F_x would clearly be underestimated if the extrapolation was not used. This is because the largest portion of this force component is induced near the leading edge and the trailing edge. The tests therefore confirmed that the extrapolation improves the accuracy of the force calculation from the measured pressure distributions. Eventually, the recent numerical investigations of Jia et al. [12] showed a good agreement of the time-averaged and the time-resolved blade pressure forces with the experimental results.

A restriction of the experimental setup is that local changes of the time-resolved pressure at the leading or trailing edge can certainly not be realized with the extrapolation. These changes can possibly appear due to small separation bubbles during rotating stall operation, for instance. Furthermore the spanwise variation of the unsteady aerodynamic force cannot be determined with the current experimental setup. However, it is pointed out by other researchers that there are no major radial variations of the full-span RS structure (e.g., Ref. [13]). Thus we can regard the pressure forces determined at the midspan as a good approximation for the pressure forces of the whole blade.

The sampling rate for the measurements was set to 32.77 kHz. The pressure force calculation is done for each individual time step of the measurement data. No averaging of the data is done. The rotor blade passing frequency (BPF) is 1.05 kHz for design speed. Viewed from the rotating frame of reference the passing frequencies of the stator blades and the IGVs are 1.38 kHz and 0.85 kHz, respectively. Thus the blade passing signals are well resolved. As a result, the time-resolved pressure force parameters for a single rotor and a single stator blade are obtained. The contribution of shear forces to the overall aerodynamic blade force cannot be taken into account.

Eventually, the data obtained with two casing-mounted piezoresistive pressure sensors (Kulite XT190) were used to discuss the stall inception and development process.

3 Stall Inception Process and Fundamental Stall Cell Structure

The stability behavior of the Dresden LSRC was extensively investigated by Mailach [5]. A short summary of this previous

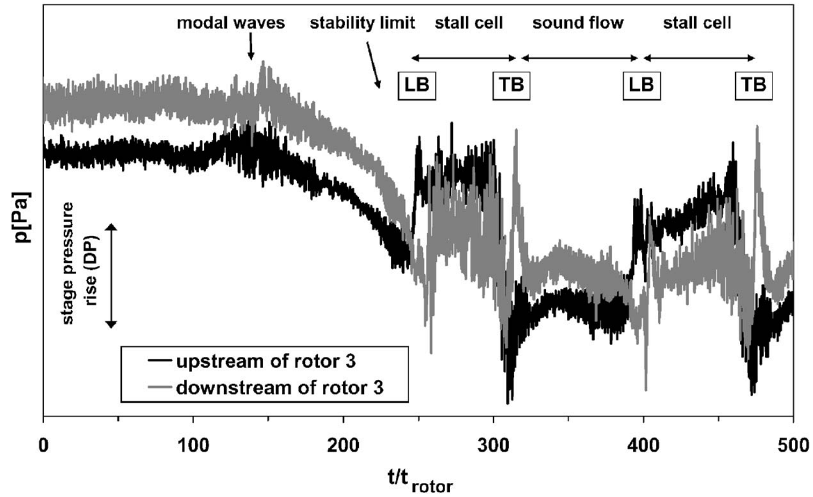

Fig. 4 Casing wall pressure within axial gaps up- and downstream of rotor 3

work will be provided below to give insight into the flow structure at the stability limit and during RS operation. As an example the stall inception in the third compressor stage is shown in Fig. 4. In this diagram the casing wall pressures in the middle of the axial gaps up- and downstream of the rotor blade row are presented. The arbitrary time scale is related to the rotor blade passing period t_{rotor}.

Two independent modal waves can be found in the stable operating range of the Dresden LSRC. The modal disturbances can be described by the 1 and 2 mode order. This corresponds to a circumferential wavelength of 360 deg and 180 deg, respectively. The modal waves are associated with wavelike variations of the flow properties (pressure, velocity, blade incidence, etc.) and propagate in circumferential and axial directions. Axially reversed flow does not appear to be due to these disturbances [5]. The circumferential propagation speed of the two different modal waves is about 25–30%, but differs from each other.

Just before the stability limit the two modal waves superimpose, while their amplitudes increase. In Fig. 4 the last appearance of the modal waves can be seen in the time period $t/t_{\mathrm{rotor}}=120-160$. They can be identified by a rise of the pressure and its fluctuations. Simultaneously the blade incidence increases until the critical incidence angle of the blading is exceeded. As a result of this a single-cell full-span RS develops directly from the modal waves in the first compressor stage. From there it expands very fast to all compressor stages. In Fig. 4 a rapid pressure drop indicates that stall is reached ($t/t_{\mathrm{rotor}}=160-250$). Surge does not appear in the Dresden LSRC, because of the comparably low flow velocities and the small downstream plenum.

At about $t/t_{\mathrm{rotor}}=250$ the stall cell arrives at the measuring positions considered in the third stage (Fig. 4). This boundary of the stall cell is denoted as leading boundary (LB). Within the stall cell the axial velocity component is negative (deep stall). The fluid is therefore transported from the compressor exit toward the inlet. This is verified by the results of hot-wire measurements [5]. The mean pressure level as well as the pressure fluctuations within the stall cell are higher than in the region of sound flow between the cells (Fig. 4).

At the trailing boundary (TB) of the stall cell the flow changes from a stalled to unstalled condition. The subsequent period with sound flow is visible between $t/t_{\mathrm{rotor}}=320-390$. The sound forward flow shows comparable characteristics to the flow field of the normally operating compressor, but at a lower pressure level. This is in accordance with the observations of Palomba et al. [13].

At $t/t_{\mathrm{rotor}}=390$ the stall cell again appears at the measurement position considered. After this first revolution of the stall cell it is already fully developed and does not change its size, pattern, and circumferential speed remarkably. The stalled flow region covers about 160 deg of the circumference. For design speed the stall cell rotates 6.5 times/s with respect to the fixed frame (40% of rotor turning speed) and about 10 times/s with respect to the rotating frame of reference (60% of rotor speed).

An important characteristic during RS operation is the pressure peaks and valleys appearing at the cell boundaries (LB and TB, Fig. 4). This feature has already been observed by Cumpsty and Greitzer [14], Gyarmathy [15], and Saxer-Felici et al. [16]. It is discussed by those authors that the fluid inertia is responsible for a momentum exchange of the fluid of adjacent blade rows at the stall cell boundaries.

The stall cell moves relatively to both the fixed and the rotating frame of reference with a velocity below the rotor speed. Therefore at the TB of the cell the flow within the rotor blade channels changes from an unstalled to a stalled flow condition, while in the stator blade channels the flow goes from stalled to unstalled. Due to the fluid inertia the sound flow within the rotor blade channels meets the stagnant flow within the stator blade channels for a short duration at the TB of the stall cell. According to Cumpsty and Greitzer [14] this inertia effect concerns only one or two blade channels. So the flow through the rotor blade channels changes very fast from a large velocity to near zero or even axially reversed flow at the TB of the stall cell considered. This results in a local positive peak of the pressure rise across the rotor blade row and a negative one across the stator blade rows. In other words, at the TB a sharp pressure drop (valley) can be found in the axial gap upstream of a rotor blade row and a sharp pressure increase (peak) appears downstream of the rotor blade row.

At the LB of the cell the opposite effect appears, since the flow within the rotor blade channels changes from stalled to unstalled flow condition, while in the stator blade channels the flow goes from unstalled to stalled. As a result of this at the LB, a sharp pressure peak can be found upstream of the rotor blade row and a distinct pressure valley downstream of it. These observations are confirmed by the work of Gyarmathy [15], who further improved the understanding of the momentum exchange process at the stall cell boundaries. The role of this momentum exchange on the stall cell propagation is clearly pointed out there. The appearance of these pressure peaks in a single-stage axial compressor is confirmed by Saxer-Felici et al. [16].

Clear signs of this momentum exchange process at the stall cell boundaries can also be observed in the Dresden LSRC (Fig. 4). At the cell boundaries (LB and TB) spiky pressure peaks and valleys appear. Upstream of the rotor blade row a pressure peak at the LB and a pressure valley at the TB are dominant. Downstream of the rotor blade row, considered the opposite pressure excursions, can be found at the cell boundaries. This generally confirms the observations in Refs. [14–16].

Indeed these pressure excursions due to the momentum exchange are superimposed on the fundamental flow field, which is determined by the influence of the wakes and the potential effects of the blades. Therefore the momentum exchange effects can sometimes be masked. Furthermore in a multistage compressor an aerodynamic interaction of several up- and downstream blade rows takes place, which makes the flow field much more complex. So the different pressure peaks in the time-resolved data in Fig. 4 cannot be clearly interpreted in every case. However, several pressure peaks and valleys can be identified at the cell boundaries and will have a remarkable influence on the unsteady pressure forces of the blades. In contrast to the assumptions of Cumpsty and Greitzer [14] the strong peaks due to the momentum exchange cover not only one or two blade passages but a larger circumferential flow region corresponding to a maximum of 10–15 passing blades (Fig. 4, LB and TB of stall cell).

As discussed by Cumpsty and Greitzer [14] the axial velocity discontinuity at the LB is less abrupt than at the TB of the stall cell. As a result the peaks at the TB are more evident. Gyarmathy [15] observed the same tendency. This trend is also confirmed by our results. It can be seen in Fig. 4 that the peak-to-peak value of the pressure signals up- and downstream of the rotor blade row is clearly larger at the TB than at the LB. The short-duration pressure difference at the TB of the cell has an order of magnitude of up to two times the compressor stage pressure rise.

In the next section the influence of the observed flow patterns on the unsteady pressure forces on the rotor and stator blades of the first stage will be discussed.

4 Time-Resolved Blade Pressure Forces at the Stability Limit and During Rotating Stall

4.1 Stator 1. Figure 5 shows the results of the time-resolved pressure force calculations at midspan of Stator 1 at the stability limit and during RS. In these diagrams the time is related to the rotor blade passing period t_{rotor} (identical rotor blade number in all stages). A period of 700 rotor blade passings is shown, which corresponds to about 0.67 s and 11.1 rotor revolutions, respectively.

For comparison the time-resolved pressure on PS and SS at 50% chord at midspan are depicted in Fig. 5(*a*). The profile pressures on Stator 1 show a qualitatively comparable behavior like

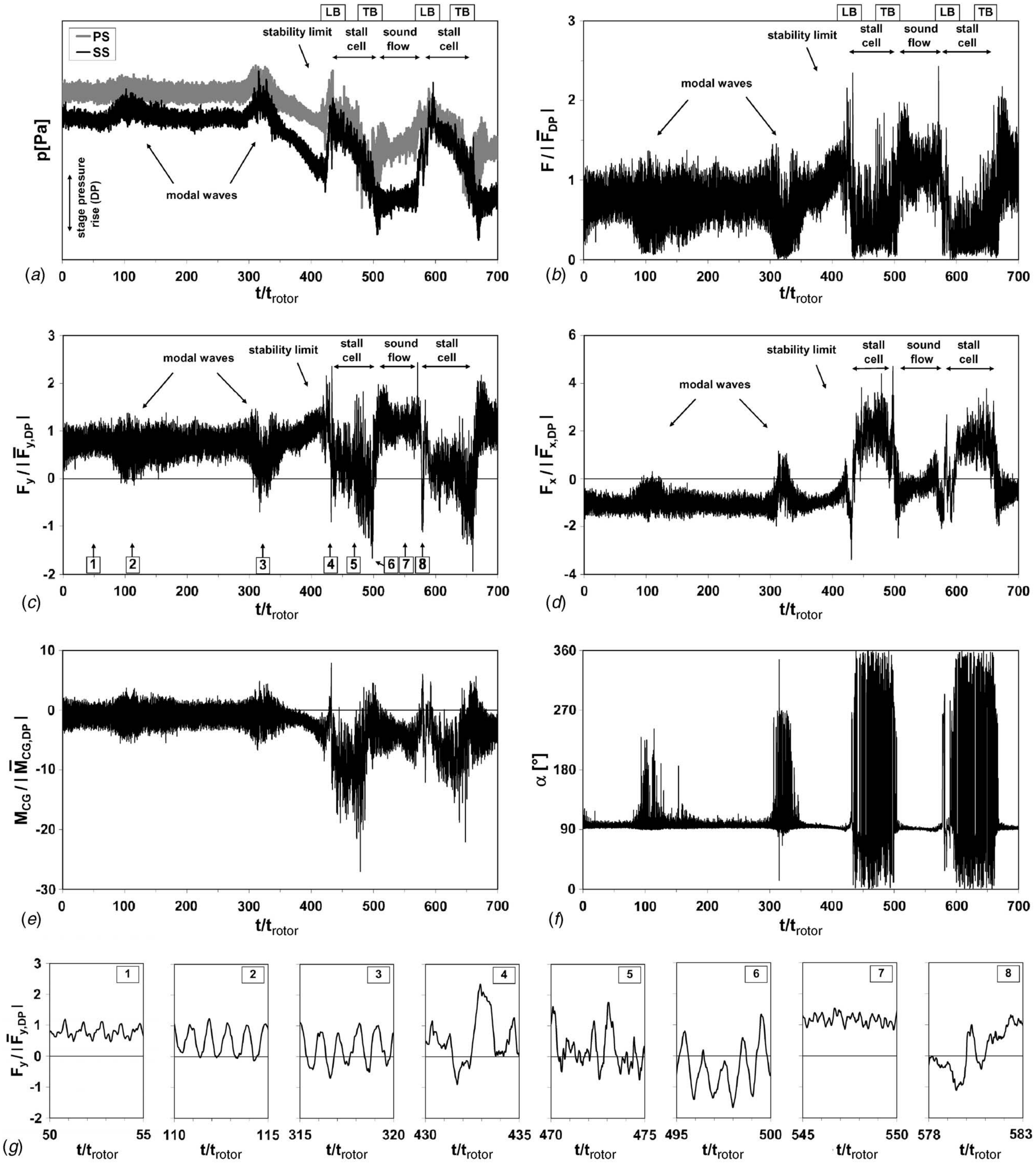

Fig. 5 Stator 1: profile pressures at 50% chord and blade pressure force parameters at the stability limit and during rotating stall (midspan, design speed)

the casing wall pressures discussed by means of Fig. 4. The modal wave influence is stronger in the first stage and leads to the RS inception, denoted as the stability limit in Fig. 5(*a*). Subsequently the change between stalled and sound flow is indicated by these data. The momentum exchange process at the cell boundaries, discussed in the previous section, obviously also has a strong influence on the profile pressures. The pressure excursions at the stall cell boundaries are clearly seen in Fig. 5(*a*). Furthermore both before and after the stability limit the passing blades are responsible for high-frequency fluctuations of the profile pressures.

Figure 5(*b*) shows the resulting blade pressure force. It seems not to be useful to relate the force to its mean value of the time period considered or to calculate a force coefficient, since after passing the stability limit a permanent change between sound and stalled flow appears at the blade considered. For comparison the time-resolved force is therefore related to the absolute value of the mean pressure force at the design point (DP) of the compressor. The mean coefficients of force, force components, and torque for the design point are given in Ref. [8].

In Figs. 5(*c*)–5(*e*) the force components and the torque are depicted. These parameters are again related to its absolute mean value at DP. So the sign of this related force component and the force component itself are identical. (Please note that the mean F_x and M_{CG} are negative at DP.) Furthermore Fig. 5(*f*) shows the angle between the blade chord direction and the resulting force F. The definitions of these parameters are given in Fig. 3.

To show the details at the most interesting points of time, eight shorter time periods (five rotor blade passings) are marked in Fig. 5(*c*) and depicted in separate diagrams (Fig. 5(*g*)/1–8). The ordinate of the left diagram is valid for all diagrams in Fig. 5(*g*). The parameter considered is the dominating force component F_y. The amount of this component is nearly identical to that of the resulting force F because of the small contribution of F_x. However, it is useful to consider F_y instead of F in more detail, since it additionally indicates the change of the flow direction.

The main source of unsteadiness of the profile pressures and the blade pressure forces within the stable operating range are rotor–stator interactions due to the viscous wakes and the potential effects of the blades. For the Dresden LSRC this topic is extensively discussed by Mailach et al. [7,8].

Approaching the stability limit the influence of the long-lengthscale modal waves on the excited force increases (Fig. 5(*b*)). The low-frequency influence of the modal waves superimposes to the high-frequency wake and potential effects. For stable operating points already near the stability limit the amplitudes of the low-frequency modal waves can be in the same order of magnitude as those of the fluctuations with the BPF's (compare Fig. 7 in Mailach et al. [8]).

It becomes obvious at Points 1–3 (Figs. 5(*c*) and 5(*g*) 1–3), that substantial differences of the blade excitation arise from the superposition of the blade passing events and the modal waves. At Point 1 the fluctuations due to the blade passing are somewhat increased compared to stable operating points. The peak-to-peak value is now about ±40%, while this value was at the most ±35% for stable operating points [8]. However, at Points 2 and 3 the stator blade under consideration is inside a region of larger blade incidence provoked by the long-lengthscale modal waves. As a result of this a remarkable increase of the fluctuation amplitudes of the blade pressure force can be observed. At Point 2 the force F and its dominant component F_y periodically changes between maximum values of up to 130% and zero. This process is triggered with the passing rotor blades. During the last revolution of the modal waves its influence further increases (Point 3, Fig. 5(*g*)/3). Pulsed by the rotor blade passing now the force components F_y and F_x change between positive and negative values with very large amplitudes. This is probably the first sign of the short-duration appearance of flow separations (axially reversed flow) leading to RS inception during the next revolution of the modal waves. As a result the force angle of attack α very strongly changes between 90 deg and 270 deg during the last appearance of the modal waves (about $t/t_{\mathrm{rotor}}=310-340$ in Fig. 5(*f*)). That means the "normal" direction of the resulting force from PS toward the SS is changing to the opposite direction and back for each passing rotor blade.

After the last passing of the modal wave a rotating stall cell directly develops from it. Because of the blockage of the growing stall cell the flow is turned in a circumferential direction. Just before the first appearance of the stall cell this leads to a higher blade incidence and consequently an increase of the blade pressure force at the stator blade considered (Figs. 5(*b*) and 5(*c*)).

The stability limit is reached at about $t/t_{\mathrm{rotor}}=420-430$ (LB of first stall cell appearance). An extreme increase of the force amplitudes appears at this transition point from the stable flow regime to the reversed flow region of RS. Spiky fluctuations of the force parameter can be found due to the momentum exchange process between the blade rows discussed before. The peak amplitudes of the force F are up to nearly 250% of the mean force at DP. The force fluctuations show a stochastic pattern, and the influence of the passing blades is not dominant at the stall inception point (Figs. 5(*b*) and 5(*g*)/4).

The first passing of the stall cell, which is coupled with axial reversed flow, appears between $t/t_{\mathrm{rotor}}=430-500$. The mean values of the force F within the stall cell are somewhat below those just before the stability limit. Considerable fluctuations of the force and its direction occur with high frequencies. However, stochastic events predominate versus the periodic signal of the rotor blade passing. The component F_y strongly fluctuates between positive and negative values (Figs. 5(*c*) and 5(*g*)/5). Furthermore the force direction strongly fluctuates within the stall cell, which points out the high unsteady mechanical loading of the blades (Fig. 5(*f*)). The component F_x is positive due to the axial reversed flow within the stall cell (Fig. 5(*d*)). Also the turning moment around the center of gravity strongly fluctuates (Fig. 5(*e*)). This can be explained by the fluctuations of the force as well as the strong shift of the center of lift along the blade chord.

At the TB of the stall cell the flow conditions change from axial reversed to forward flow. The strong periodic changes of the pressure forces are linked to the effect of the passing blades, leading to a high amplitude aerodynamic blade excitation (Fig. 5(*g*)/6). This is an explicit difference from the behavior at the LB and within the stall cell (compare to Fig. 5(*g*), Points 4 and 5). The momentum exchange process at the considered TB—superimposed with the blade passing events—covers a time period of about 10–15 passing rotor blades (only a part of it is visible in Fig. 5(*g*)/6). The amplitudes of the fluctuations due to the passing blades at the TB are much larger than in the stable operating range (compare to Fig. 5(*g*), Points 1 and 2).

After the passing of the cell the blade under consideration is located in an area of sound forward flow (Fig. 5, $t/t_{\mathrm{rotor}}=520-570$ and Fig. 5(*g*)/7). The mean aerodynamic force is in the same order of magnitude as that for stable operating points. Also the fluctuations are low compared to those within the stall cell and especially at the stall cell boundaries.

At $t/t_{\mathrm{rotor}}=570$ the LB of the stall cell again arrives at the blade considered (e.g., Fig. 5(*g*)/8). In accordance with the first appearance of the cell (LB, identical to stability limit), the fluctuations cover only a few blade passages and appear more stochastically than at the TB of the cell.

4.2 Rotor 1. The data for Rotor 1 are presented in Figs. 6(*a*)–6(*g*) in the same way as for Stator 1 (compare Fig. 5). In the stable operating range the unsteady pressure force of Rotor 1 is dominated by the potential effects of the downstream stator blades, which move relatively to the rotor blades considered [8]. The IGV wakes play only a secondary role. This is why the time base in Fig. 6 is referred to as the passing period of the downstream stator blades t_{stator} in all cases. The dominance of the stator potential flow field propagating upstream on the unsteady pressure force excitation of Rotor 1 is obvious in Fig. 6(*g*), Points 1–3.

As already discussed for Stator 1 the modal waves are responsible for a periodical change of the flow properties covering a larger sector of the circumference. The influence of this disturbance just before the stability limit can clearly be seen in the traces of the profile pressures and the force parameters of the rotor blades, depicted in Fig. 6. The passing of the modal waves at a given position again leads to a modulation of the pressure force amplitudes due to the passing blades. The rotor blade considered is located in a region of larger incidence due to the modal waves at the points of Times 2 and 3 (Figs. 6(*g*)/2 and 6(*g*)/3). As a result a significant increase of the peak-to-peak amplitudes due to the stator blade potential effect appears (compared to Point 1 for instance, Fig. 6(*g*)/1). The main features of the parameters discussed before the stability limit for Rotor 1 and Stator 1 are comparable.

The stability limit is indicated by a sharp pressure force peak, visible at $t/t_{\mathrm{rotor}}=380-385$ in Fig. 6. At this point of time the force increases very fast to about 2.5 times the design value (Fig.

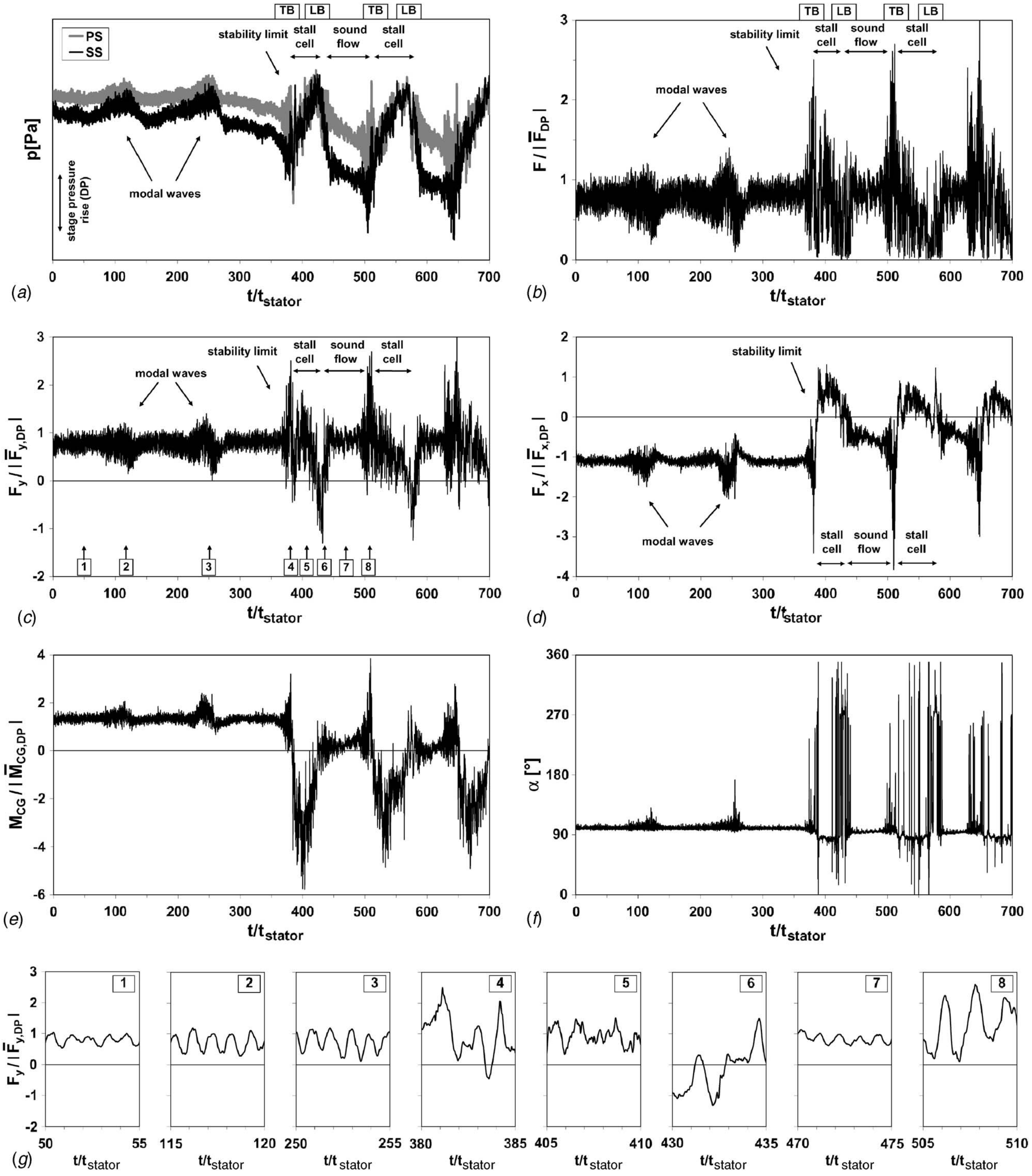

Fig. 6 Rotor 1: profile pressures at 50% chord and blade pressure force parameters at the stability limit and during rotating stall (midspan, design speed)

6(*g*)/4). In the rotor frame of reference, the slip between the stall cell propagation velocity and the rotor turning speed leads to a stall cell propagation in the opposite direction from that of the rotor turning direction itself. Thus the rotor blades traverse the stall cell in the opposite direction than the stator blades. This can be seen in Figs. 5(*a*) and 6(*a*), for example, in the signals of the sensors on the SS during the first cell passing: The stator blades enter the cell at the LB, after that the pressure decreases during cell passing, and finally the stator blades leave the stall cell at the TB. In contrast the rotor blades enter the cell at the TB, and after that the pressure increases until the rotor blades leave the cell at the LB.

The change between stalled and unstalled flow is indicated by the rotor blade force parameters in a qualitatively comparable form like for the stator blades (Figs. 6(*b*)–6(*f*)). As already discussed for Stator 1, the maximum force fluctuations during the RS operation appear at the stall cell boundaries. Although the rotor blades traverse the stall cell in opposite direction than the stator

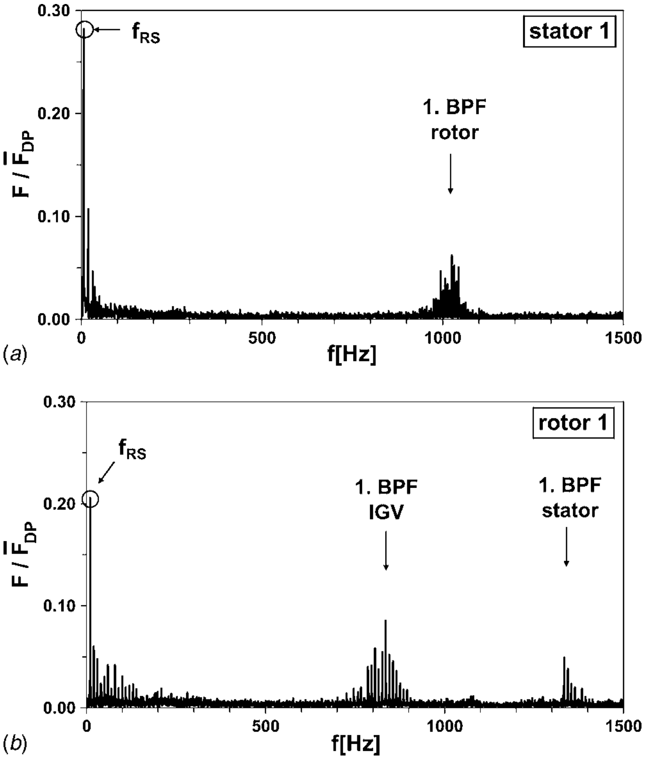

Fig. 7 Frequency spectra of pressure force of stator and rotor blades during rotating stall (first stage, midspan, design speed)

blades the same fundamental features can be observed at the cell boundaries: these are high-amplitude fluctuations with the frequency of the passing blades at the TB and a more diffuse change of the flow properties at the LB (Fig. 6).

At the stall cell boundaries—especially at the TB—the IGV passing is responsible for high-frequency large-amplitude pressure force fluctuations (Fig. 6(*g*)/8). This points out the different flow mechanism at the cell boundaries compared to the behavior within the stall cell and within the region of sound flow between the cells. In these flow regions (as well as during stable compressor operation) the IGV passing plays only a minor role in the unsteady blade excitation.

The mean force during axial reversed flow within the cell is again comparable to that for the sound flow conditions before stall inception (Figs. 6(*b*), 6(*c*), and 6(*g*)/5). However, the fluctuations of the pressure force are stronger during reversed flow conditions. As already observed for the stator blades, stochastic fluctuations dominate within the stall cell. An indication of the reversal of the flow direction is again given by the change of the sign of the F_x component (Fig. 6(*d*)).

For the sound flow conditions outside the stall cell the potential effect of the downstream stator blades periodically changes the unsteady profile pressure distribution, and consequently the blade pressure forces (e.g., Fig. 6(*g*)/7). The IGV blade passing events are not visible. This is a comparable behavior to that observed before the stability limit (e.g., Fig. 6(*g*)/1).

Thus a comparable development of the unsteady blade pressure forces concerning its fundamental features and amplitudes can be found on the rotor and stator blades at the stability limit and during RS.

5 Frequency Contents of Blade Pressure Forces During Rotating Stall

In the following section the frequency contents of the aerodynamic blade forces during RS will be discussed. (Appropriate results for a stable operating point near the stability limit can be found in Ref. [8].) A consideration of the periodic portions of the force is useful for an estimation of the excited blade vibrations and a comparison to the natural frequencies of the blades. The frequency spectra of the pressure force of the stator and rotor blades are shown in Figs. 7(*a*) and 7(*b*). For comparison the force is again divided by the mean force at DP.

In both cases the dominant influence on the unsteady blade pressure forces appears due to the stall cell. The single stall cell propagates with 40% of rotor turning speed in the fixed frame and 60% of rotor speed with respect to the rotor blades. This leads to a RS frequency of $f_{RS}=6.5$ Hz on the stator blade and $f_{RS}=10.0$ Hz on the rotor blades (marked with circles in Fig. 7). Several higher harmonics of the RS frequency are visible in both cases because of the complex RS structure. In particular on the rotor blades these multiples of the fundamental RS frequency cover a large frequency range of up to 140 Hz (14th harmonic of f_{RS}), Fig. 7(*b*). However, this upper frequency is clearly below the first natural frequencies of the blades (first bending mode at 200 Hz, first torsion mode at 440 Hz).

The BPFs of the IGV and the stator appear on the rotor blades at 850 Hz and 1380 Hz, respectively (Fig. 7(*b*)). Both frequencies are modulated with the RS frequency, leading to a broadband aerodynamic blade excitation. Although the IGV passing is only dominant during the short time periods at the stall cell boundaries (especially at the TB, compare Fig. 6(*g*)/8), the amplitudes in the frequency spectrum are somewhat higher than those due to the downstream located stator blade. This is in contrast to the observations for stable operating points, where the upstream potential influence of the stator blades was much stronger than that of the IGV wakes (Fig. 6(*g*)/1, more details in Ref. [8]). Higher harmonics of the BPFs are of less influence.

On the stator blades the rotor BPF is again modulated with the RS frequency (Fig. 7(*a*)). Because of the same rotor blade numbers in all stages the effects from up- and downstream cannot be distinguished in this case.

Since the frequency spectra reflect periodic events, the amplitudes at the frequencies, which can be attributed to the RS cell and the blade passing, are clearly lower than visible in the time-resolved force traces (compare for instance to Figs. 5(*b*) and 6(*b*)). This is also due to the fact that the flow structure during RS permanently changes between stalled and unstalled flow. Thus the dominating effects and their amplitudes always change and they are not strongly periodic for the time period used to determine the frequency spectra.

6 Conclusions

In this paper experimental investigations of the unsteady aerodynamic blade excitation in the Dresden four-stage low-speed compressor are presented. Results are shown for the rotor and stator blades of the first stage for operating conditions at the stability limit and during rotating stall. To the authors' best knowledge these are the first experimental data on time-resolved blade pressure forces for rotating stall operation in axial compressors, available in the open literature.

The stall inception process and the fundamental features of the stall cell structure and propagation are discussed. It was found that rotor–stator interactions play an important role in the aerodynamic blade force excitation for stable compressor operation as well as during rotating stall. Just before the stability limit modal waves are responsible for low-frequency fluctuations of the unsteady profile pressures and the pressure forces with comparable large amplitude. The modal wave influence superimposes to the high-frequency blade passing events. This leads to a periodic change of the unsteady blade excitation amplitudes.

A single-cell full-span rotating stall cell directly develops from the modal waves. At the stall inception point a strong short-duration increase of the blade pressure forces appears. Within the stall cell large stochastic fluctuations of the blade pressure forces and its direction have been found. For sound flow conditions outside the stall cell a comparable development of the time-resolved blade pressure forces such as for stable operating points have been observed.

The theory of the momentum exchange between adjacent blade rows at the stall cell boundaries, where the stalled and the sound flow meet for short time durations, is confirmed by the investigations presented. Due to the momentum exchange the maximum blade pressure force fluctuations appear at the stall cell boundaries. New features found for the momentum exchange process are that it covers several blade passing events and is triggered by the passing blades. In particular at the trailing boundary of the stall cell the blade passing plays a dominant role for the aerodynamic blade excitation. The peak force amplitudes during rotating stall operation amount to 2.5 times the mean force at the design point.

The frequency spectra of the blade pressure forces are dominated by the rotating stall frequency and its harmonics. Further periodic force fluctuations appear with the blade passing frequencies of the adjacent blade rows, which are modulated with the rotating stall frequency.

Acknowledgment

The work reported in this paper was performed within the project "Unsteady Forces and Boundary Layer Behaviour on the Blades of a Low-Speed Axial Compressor," which is part of the joint project "Periodical Unsteady Flow in Turbomachines" funded by the Deutsche Forschungsgemeinschaft (DFG, German Research Society).

Nomenclature

f = frequency (Hz)
F = blade pressure force (N)
l = chord length (m)
M = torque (N m)
p = pressure (Pa)
t = time (s)
x = chordwise position (m)
y = position perpendicular to chord (m)
α = angle between resulting force and tangent at the profile contour (x direction), see Fig. 3 (deg)
– = mean value

Abbreviations and Subscripts

BPF = blade passing frequency
CG = center of gravity
CL = center of lift
DP = design point
IGV = inlet guide vane
LB = leading boundary of the stall cell
LSRC = low-speed research compressor
MS = midspan
PS = pressure side
RS = rotating stall
SS = suction side
TB = trailing boundary of the stall cell
x = component in blade chord direction
y = component perpendicular to the blade chord

References

[1] McDougall, N. M., Cumpsty, N. A., and Hynes, T. P., 1990, "Stall Inception in Axial Compressors," ASME J. Turbomach., **112**, pp. 116–125.

[2] Day, I. J., Breuer, T., Escuret, J., Cherett, M., and Wilson, A., 1999, "Stall Inception and the Prospects for Active Control in Four High-Speed Compressors," ASME J. Turbomach., **121**, pp. 18–27.

[3] Höss, B., Leinhos, D., and Fottner, L., 2000, "Stall Inception in the Compressor System of a Turbofan Engine," ASME J. Turbomach., **122**, pp. 32–44.

[4] Camp, T. R., and Day, I. J., 1998, "A Study of Spike and Modal Stall Phenomena in a Low-Speed Axial Compressor," ASME J. Turbomach., **120**, pp. 393–401.

[5] Mailach, R., 2001, "Experimentelle Untersuchung von Strömungsinstabilitäten im Betriebsbereich zwischen Auslegungspunkt und Stabilitätsgrenze eines vierstufigen Niedergeschwindigkeits-Axialverdichters," Doctoral thesis, TU Dresden, Dresden, Germany.

[6] Mailach, R., Lehmann, I., and Vogeler, K., 2001, "Rotating Instabilities in an Axial Compressor Originating from the Fluctuating Blade Tip Vortex," ASME J. Turbomach., **123**, pp. 453–463.

[7] Mailach, R., and Vogeler, K., 2004, "Rotor-Stator Interactions in a Four-Stage Low-Speed Axial Compressor, Part I: Unsteady Profile Pressures and the Effect of Clocking," ASME J. Turbomach., **126**, pp. 507–518.

[8] Mailach, R., Müller, L., and Vogeler, K., 2004, "Rotor-Stator Interactions in a Four-Stage Low-Speed Axial Compressor, Part II: Unsteady Aerodynamic Forces of Rotor and Stator Blades," ASME J. Turbomach., **126**, pp. 519–526.

[9] Sauer, H., Bernstein, W., Bernhard, H., Biesinger, T., Boos, P., and Möckel, H., 1996, "Konstruktion, Fertigung und Aufbau eines Verdichterprüfstandes und Aufnahme des Versuchsbetriebes an einem Niedergeschwindigkeits-Axialverdichter in Dresden," Abschlußbericht zum BMBF-Vorhaben 0326758A, Dresden, Germany.

[10] Müller, R., Mailach, R., and Lehmann, I., 1997, "The Design and Construction of a Four-Stage Low-Speed Research Compressor," *Proceedings of the IMP '97 Conference on Modelling and Design in Fluid-Flow Machinery*, J. Badur, Z. Bilicki, J. Mikielewicz, and E. Sliwicki, eds., Gdansk, Poland, Nov. 18–21, pp. 523–530.

[11] Boos, P., Möckel, H., Henne, J. M., and Selmeier, R., 1998, "Flow Measurement in a Multistage Large Scale Low Speed Axial Flow Research Compressor," ASME Paper No. 98-GT-432.

[12] Jia, H., Vogeler, K., Müller, L., and Mailach, R., 2006, "Numerical Investigation of Rotor-Stator-Interactions in a 1.5-Stage Low-Speed Axial Compressor," *Conference Proceedings on Modelling Fluid Flow (CMFF'06), Budapest, Hungary*, Sept. 6–9.

[13] Palomba, C., Puddu, P., and Nurzia, F., 2003, "Experimental Investigation of Rotating Stall Cell Structure Variation During Recovery," *Proceedings of the 5th European Conference on Turbomachinery—Fluid Dynamics and Thermodynamics*, M. Stastny, G. H. Sieverding, and G. Bois, eds., Prague, Czech Republic, March 18–21, pp. 187–195.

[14] Cumpsty, N. A., and Greitzer, E. M., 1982, "A Simple Model for Compressor Stall Cell Propagation," J. Eng. Power, **104**, pp. 170–176.

[15] Gyarmathy, G., 1996, "Impeller-Diffuser Momentum Exchange During Rotating Stall," ASME Paper No. 96-WA/PID-6.

[16] Saxer-Felici, H. M., Saxer, A. P., Inderbitzin, A., and Gyarmathy, G., 1999, "Prediction and Measurement of Rotating Stall Cells in an Axial Compressor," ASME J. Turbomach., **121**, pp. 365–375.

Kevin P. Nolan
e-mail: kevin.nolan@ul.ie

Edmond J. Walsh

Stokes Research Institute,
Department of Mechanical and Aeronautical Engineering,
University of Limerick,
Limerick, Ireland

Donald M. McEligot
Idaho National Laboratory (INL),
P.O. Box 1625,
Idaho Falls, ID 83415-38;
University of Arizona,
Tuscon, AZ 85721;
and IKE,
Universität Stuttgart,
D-70550 Stuttgart, Germany

Ralph J. Volino
Department of Mechanical Engineering,
United States Naval Academy,
Annapolis, MD 21402

Predicting Entropy Generation Rates in Transitional Boundary Layers Based on Intermittency

Prediction of thermodynamic loss in transitional boundary layers is typically based on time-averaged data only. This approach effectively ignores the intermittent nature of the transition region. In this work laminar and turbulent conditionally sampled boundary layer data for zero pressure gradient and accelerating transitional boundary layers have been analyzed to calculate the entropy generation rate in the transition region. By weighting the nondimensional dissipation coefficient for the laminar conditioned data and turbulent conditioned data with the intermittency factor, the entropy generation rate in the transition region can be determined and compared to the time-averaged data and correlations for laminar and turbulent flow. It is demonstrated that this method provides an accurate and detailed picture of the entropy generation rate during transition in contrast with simple time averaging. The data used in this paper have been taken from conditionally sampled boundary layer measurements available in the literature for favorable pressure gradient flows. Based on these measurements, a semi-empirical technique is developed to predict the entropy generation rate in a transitional boundary layer with promising results. [DOI: 10.1115/1.2720488]

Introduction

The increases in turbomachinery efficiency over the years have come in part from a continued elevation of turbine inlet temperatures and increased pressure ratios. However, these strategies are becoming increasingly difficult due to material limitations. The continuance of improved turbomachinery efficiency requires that sources of loss be better understood. Entropy generation minimization (EGM) is a method of thermodynamic optimization of real systems that owe their thermodynamic imperfections to heat transfer, fluid flow, and mass transfer irreversibilities [1].

Denton [2] noted that it is the inner part of the boundary layer where most of the entropy generation occurs especially with turbulent boundary layers due to higher near wall velocity gradients. The understanding and prediction of the origins of loss in laminar and turbulent boundary layers has found some success. Truckenbrodt [3] integrated the Pohlhausen [4] family of velocity profiles to show an inversely proportional relationship between the nondimensional entropy generation rate and momentum thickness Reynolds number. For turbulent boundary layers, Schlichting [5] demonstrated that the nondimensional entropy generation rate is only weakly dependent on the Reynolds number of the flow. Both of these correlations have performed well with good agreement found with measurements [6].

Understanding loss mechanisms in the transition region where intermittent turbulent spot passage will result in an increased local entropy generation rate is particularly important. Walsh and Davies [7] demonstrated through hot film measurements in a linear cascade that the transition region extends over a relatively large region of the turbine blade suction surface. Extensive study of boundary layer transition, notably work by Mayle [8], Walsh and Davies [9], Gostelow et al. [10], and Abu-Ghannan and Shaw [11], has endeavored to predict transition onset and length in both compressible and incompressible regimes. Also direct numerical simulations of bypass transition by Jacobs and Durbin [12] have provided valuable insight into the mechanics of transition. However, no prediction method for the entropy generation rate within a transitional boundary that considers the unsteadiness due to turbulent spot passage has been developed to date.

Correlations and theories to predict intermittent nature of transitional boundary layers has also been described, notably by Emmons [13] and Dhawan and Narasimha [14]. Many researchers have developed transition models based on the linear combination method where laminar and turbulent quantities in the transition region are averaged weighted by the intermittency level. A review by Narasimha and Dey [15] discusses many of these models in detail. More recently, work on conditional-sampling and intermittency has focused on the effects of free stream turbulence intensity on transition and the resulting structures of the transitional boundary layers, Kim and Simon [16], Wang and Zhou [17], Sohn and Reshotko [18], and Volino et al. [19]. However, very limited experimental or theoretical work has been devoted to the entropy generation rate within the transition region, and to the authors' knowledge no work has been presented where the transitional entropy generation rate has been calculated based on the intermittency factor at discrete locations.

Using a conditionally sampled method weighted on intermittency we find a prediction of the rate of entropy generation in the transition region becomes possible. This provides significant advantages over the time-averaged method where switching between laminar-like and turbulent-like flow can result in measurements not indicative of actual flow conditions [20]. In this paper we develop a technique to predict the entropy generation rates within a transitional boundary layer. The technique is tested against existing data and reasonably good agreement is found. As the technique is an extension of existing semi-empirical approaches to

---

Contributed by the International Gas Turbine Institute of ASME for publication in the Journal of Turbomachinery. Manuscript received July 24, 2006; final manuscript received July 25, 2006. Review conducted by David Wisler. Paper presented at the ASME Turbo Expo 2006: Land, Sea and Air (GT2006), Barcelona, Spain, May 8–11, 2006. Paper No. GT2006-91027.

Table 1 Favorable pressure gradient data by Volino et al. [19]

Station	x (m)	U_∞ (m/s)	Re_x $\times 10^3$	$\frac{\bar{u}'_\infty}{U_\infty}$ (%)	K $\times 10^6$	γ_{pk} (%)	$\delta_{99.5}$ (mm)
1	0.1182	6.22	49	6.4	5.32	4.1	4.04
2	0.1895	7.12	90	4.9	4.04	3.0	3.99
3	0.2677	7.99	143	3.9	3.25	4.7	4.52
4	0.3449	9.13	210	3.2	2.53	8.9	5.16
5	0.4231	10.35	293	2.7	1.97	17.0	4.72
6	0.5033	11.38	383	2.4	1.63	34.4	5.28
7	0.5805	12.49	485	2.1	1.33	56.0	5.67
8	0.6587	13.63	600	1.9	1.13	71.4	5.80
9	0.7353	14.62	719	1.7	0.97	86.2	6.58
10	0.8165	15.89	867	1.5	0.83	93.2	7.92

boundary layer modeling, its inclusion in a predictive code should be simplified. Although it generally remains to be proved as the number of available data sets was limited.

Data

Two sets of conditionally sampled boundary layer data available in the literature were analyzed. The data are hot wire measurements for a zero pressure gradient transitional boundary layer by Kim and Simon [16], and a favorable pressure gradient transitional boundary layer subject to a stream-wise velocity gradient of 13.9 s^{-1} by Volino et al. [19]. Measured parameters are summarized in Tables 1 and 2. The zero pressure gradient case is subjected to a free-stream turbulence intensity of 1.5% while for the favorable pressure gradient case the turbulence intensity drops from 8% at the test section inlet to 2% at the last measurement station.

Analysis of the zero pressure gradient data was hampered by the low stream-wise resolution with just five measurement locations, one of which is located in the transition region; hence, only the favorable pressure gradient case is presented in this paper.

Theoretical Analysis

Entropy Generation. Calculating the volumetric entropy generation rate given by Hughes and Brighton [21] for a two-dimensional (2D) incompressible adiabatic flow

$$\dot{S}'''_{\mathrm{gen}} = \underset{\text{VISCOUS}}{\frac{\mu}{T}\left[\frac{\partial u}{\partial y}\right]^2} - \underset{\text{REYNOLDS STRESS}}{\frac{\rho\overline{u'v'}}{T}\left[\frac{\partial u}{\partial y}\right]} \tag{1}$$

For laminar flow the Reynolds shear stress term may be neglected. Denton [2] gives the entropy generation rate per unit area in the form of the dimensionless dissipation coefficient C_D where

$$C_D = \frac{T}{\rho u_e^3}\int_0^\delta \dot{S}'''_{\mathrm{gen}}dy \tag{2}$$

For laminar boundary layers Denton [2] details a method by Truckenbrodt [3] based on an inverse relationship between dissipation coefficient and momentum thickness Reynolds number, given in Eq. (3)

$$C_{D_{\mathrm{LAM}}} = \beta\,\mathrm{Re}_\theta^{-1} \tag{3}$$

where β is obtained by integrating the Pohlhausen family of velocity profiles giving

$$\beta = 0.1746 + 0.0029\Lambda + 0.000076\Lambda^2 \tag{4}$$

The quantity β has a range of $0.151 \leqslant \beta \leqslant 0.22$ for the Pohlhausen pressure gradient shape factor $-12 \leqslant \Lambda \leqslant 12$. Using methods for predicting the laminar boundary layer thickness Λ can be predicted with knowledge of the fluid properties and the free-stream velocity distribution.

Denton [2] noted that for turbulent boundary layers the dissipation coefficient is much less dependent on the state of the boundary layer than the more widely used skin friction coefficient, C_f, with about 90% of entropy generation occurring within the inner part of the boundary layer. Schlichting [5] reports a correlation for turbulent boundary layers with a shape factor H_{12} between 1.2 and 2, and a Re_θ between 10^3 and 10^5

$$C_{D_{\mathrm{TURB}}} = 0.0056\,\mathrm{Re}_\theta^{-1/6} \tag{5}$$

Denton [2] also noted reasonable agreement between Eq. (5) and data for Re_θ between 500 and 1000 for accelerating, constant pressure, and diffusing boundary layers.

For the transition region no correlation exists to describe the distribution of the dissipation coefficient with varying Re_θ. Emmons [13] presumed that since the flow in the transition region is part of the time laminar ($\gamma=0$) and part of the time turbulent ($\gamma=1$), the average flow at any stream-wise position is given by

$$f = (1-\gamma)f_{\mathrm{LAM}} + \gamma f_{\mathrm{TURB}} \tag{6}$$

Here f is any boundary layer flow related quantity such as the skin friction coefficient C_f with f_{LAM} and f_{TURB} its local laminar and

Table 2 Conditionally sampled quantities by Volino et al. [19]

	Re_θ	H	Re_θ	H	Re_θ	H
Station	Unconditioned		Laminar		Turbulent	
1	136	1.96	136	1.97	90	1.97
2	149	1.98	149	1.99	135	1.72
3	169	1.94	168	1.94	186	1.59
4	196	1.87	193	1.89	244	1.51
5	221	1.82	212	1.86	293	1.48
6	263	1.76	239	1.86	366	1.46
7	324	1.66	264	1.86	432	1.46
8	372	1.58	278	1.82	474	1.43
9	457	1.49	297	1.81	580	1.39
10	580	1.43	364	1.69	745	1.35

turbulent values. Dhawan and Narasimha [15] showed that this equation gives reasonable approximations for the boundary layer thicknesses and shape factor. They also showed that the skin friction coefficient C_f may be substituted into Eq. (6) to give good agreement with experimental data. Here Eq. (6) is applied to the distribution of the dissipation coefficient C_D in a similar manner giving

$$C_D = (1-\gamma)C_{D_{\mathrm{LAM}}} + \gamma C_{D_{\mathrm{TURB}}} \tag{7}$$

This equation will be used to determine the intermittency-weighted entropy generation rate in the transition region from the conditionally sampled data.

Prediction Method. The laminar and turbulent dissipation coefficient correlations, Eqs. (3) and (5), are functions of the momentum thickness Reynolds number. In order to sum these correlations weighted on a predicted stream-wise intermittency distribution using Eq. (6) and for the purposes of a practical predictive method, it is necessary to predict the boundary layer momentum thickness in relation to the free-stream condition. This is achieved by introducing two empirical correlations to estimate the boundary layer momentum thickness. For laminar flow Thwaites' method [22] is employed, Eq. (8). Derived from the momentum integral equation this method, although relatively simple, is quite accurate, is widely used in the literature. The method requires knowledge of fluid properties and the free-stream velocity distribution only to yield the momentum thickness

$$\theta^2 = \frac{0.45\nu}{Ue^6}\int_0^x Ue^5\,dx \tag{8}$$

For turbulent flow Schlichting [5] details Buri's momentum method [23] to calculate the Re_θ distribution from free-stream conditions where

$$[\mathrm{Re}_\theta(x)]^{1+a} = \frac{1}{\nu'}\frac{E_2(x)}{[U(x)]^e} \tag{9}$$

where

$$E_2(x) = E_2(x_s) + \int_{x1}^{x} U^n\,dx \tag{10}$$

and

$$E_2(x_s) = \nu'[U(x_s)]^e[\mathrm{Re}_{\theta s}]^{1+a} \tag{11}$$

with the modified viscosity ratio

$$\frac{\nu'}{\nu} = \frac{1}{(1+a)\alpha} \tag{12}$$

and

$$\alpha = 0.0245(1-2.007\log H_{12})^{1.705} \tag{13}$$

Here α is dependent on the shape factor H_{12} taken to be 1.4 for turbulent boundary layers [5]. The constants a, e, and n are dependent on the flow regime under consideration, the subscript s denotes the point of transition onset. For a turbulent boundary layer Schlichting [5] gives $a=0.268$, $e=2.92$, and $n=3.92$. This method is favored over more common, simpler correlations for turbulent boundary layers, such as Head's method as better agreement is found with measurements in the transition region. Buri's method requires an input of parameters at transition onset, the free-stream velocity, and the momentum thickness Reynolds number, $\mathrm{Re}_{\theta s}$ is predicted using the correlation proposed by Mayle [8]

$$\mathrm{Re}_{\theta s} = 400\mathrm{Tu}^{-5/8} \tag{14}$$

Inserting $\mathrm{Re}_{\theta s}$ into the prediction obtained using Thwaites' method, a value of Re_{xs} and hence the free-stream velocity at transition onset can be obtained for a given free-stream velocity distribution. Figure 1 shows the predicted momentum thickness Reynolds number distributions for the conditionally sampled data in the transition region with surprisingly good agreement being found for the undeveloped turbulent flow.

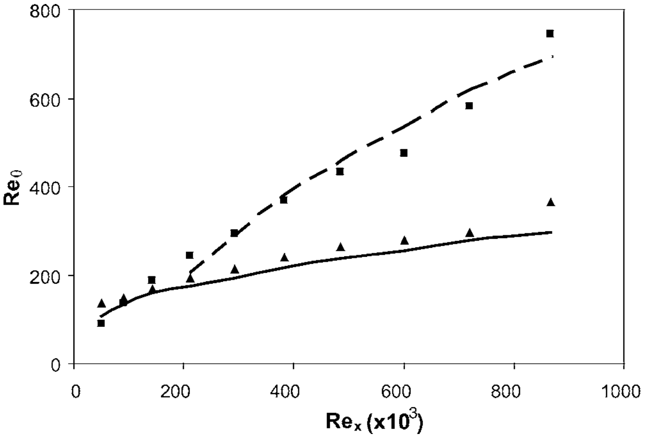

Fig. 1 Re$_\theta$ predictions for favorable pressure gradient case: (▲) laminar conditioned data; (■) turbulent conditioned data; (—) Thwaites' method; and (- -), Buri's method

The stream-wise intermittency distribution of Dhawan and Narasimha [14] for a transitional boundary layer is shown in its nondimensional form in Eq. (15)

$$\gamma = 1 - \exp[-\hat{n}\sigma(\mathrm{Re}_x - \mathrm{Re}_{xs})^2] \tag{15}$$

For zero pressure gradient flow Mayle [8] suggests a correlation for predicting the turbulent spot growth parameter based on the free-stream turbulence intensity as

$$\hat{n}\sigma_{\mathrm{ZPG}} = 1.25\times 10^{-11}\mathrm{Tu}^{7/4} \tag{16}$$

For a favorable pressure gradient flow Steelant and Dick [24] propose a correlation based upon the data of Mayle [8] to predict the spot growth parameter normalized by Eq. (16)

$$\frac{\hat{n}\sigma}{\hat{n}\sigma_{\mathrm{ZPG}}} = 10^{-3227K^{0.5985}} \tag{17}$$

Equations (15)–(17) can be employed to predict the intermittency distribution in favorable pressure gradient flows. The prediction requires knowledge of the fluid properties, the stream-wise velocity distribution, and the free-stream turbulence intensity. Figure 2 shows a comparison of the measured intermittency distribution with the prediction. Good agreement is found.

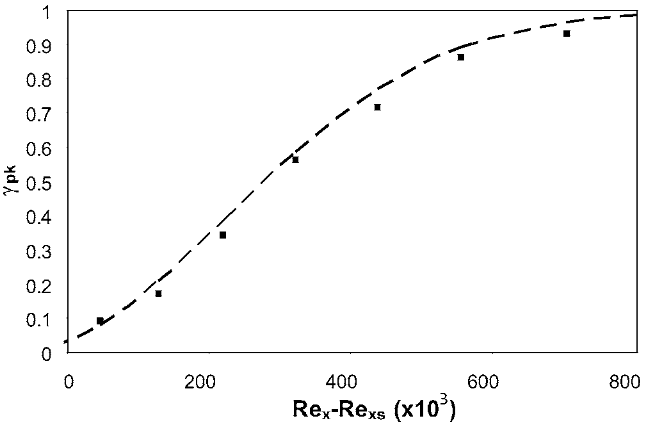

Fig. 2 Predicted intermittency distribution: (■) experimental data, Volino et al. [19]; and (- -) prediction, Eqs. (16)–(18)

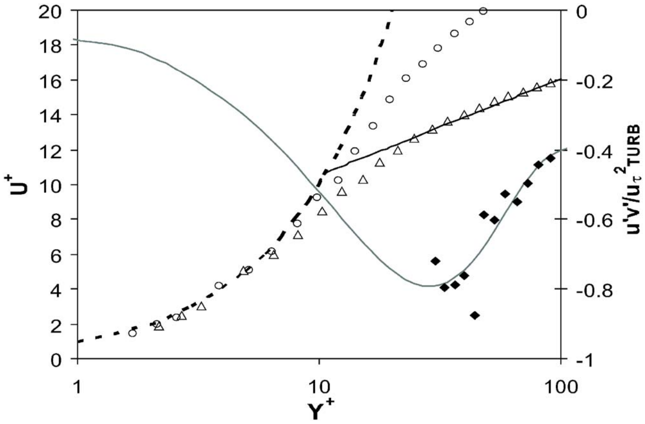

Fig. 3 Boundary layer data at Station 5: (∘) laminar-conditioned data; (△) turbulent-conditioned data; (◆), turbulent-conditioned Reynolds shear stresses; (- -), $Y^+=U^+$; (—), von Kármán turbulent correlation; and (—, solid grey line) polynomial fit of turbulent-conditioned Reynolds shear stress data

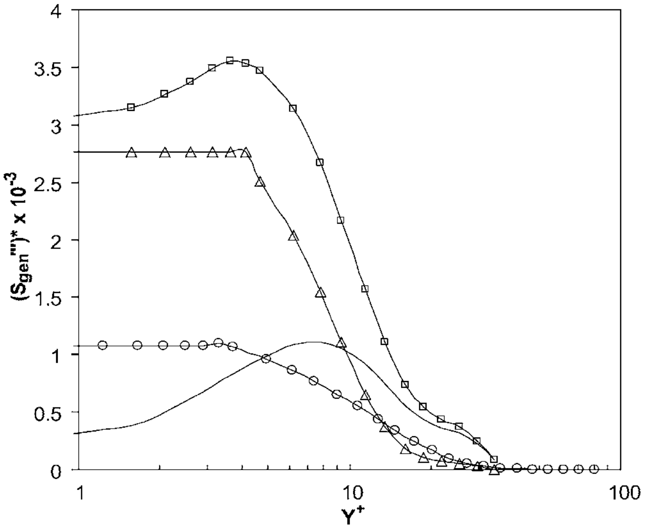

Fig. 4 Entropy generation rate profiles at Station 5: (∘) laminar-conditioned data; (△) viscous contribution to turbulent conditioned data; (—) Reynolds shear stress contribution to turbulent conditioned data; and (□) turbulent-conditioned data

Data Analysis

The exact magnitude of the dissipation coefficient cannot be calculated without knowing full details of the boundary layer [2]. In order to accurately represent the velocity profiles the data were fit with a linear approximation in the near wall region where the data obey $Y^+ \approx U^+$ with a polynomial approximation fitted to the remainder of the data. The overlap between the linear and the polynomial fit was found to be generally within $Y^+ \approx 5(\pm 2)$ in broad agreement with the behavior for fully turbulent flow. Both curve fits were set to zero at the wall due to the zero slip condition. This method gives confidence that the near wall velocity gradient is accurately represented as this is where the majority of the entropy generation occurs. The linear curve fit can be forecasted back to the wall exploiting the law of the wall. The Reynolds shear stresses are fit with a sixth-order polynomial set to zero at the wall. Only the unconditioned and turbulent conditioned Reynolds shear stresses were approximated. The laminar conditioned data $\overline{-u'v'}$ fluctuations are neglected. Figure 3 shows boundary layer data from Station 5 plotted in wall coordinates.

Figure 4 shows the $\dot{S}'''_{\text{gen}}$ plots generated from the curve fits of the laminar and turbulent conditioned data. The turbulent conditioned data are separated into the viscous and Reynolds shear stresses components of Eq. (1) while only the viscous contribution of the laminar conditioned data is calculated.

Results and Discussion

High entropy generation rates in the near wall region are observed in Fig. 4. The entropy generation rate is significantly higher for the turbulent conditioned data which represent the average entropy generation within the turbulent spots. A constant level of viscous entropy generation is found in the near wall region with the Reynolds shear stress contribution resulting in a peak in total turbulent entropy generation away from the wall.

Figure 5 shows the dissipation coefficient data calculated at each measurement station plotted against Re_θ. Also shown are the laminar and turbulent correlations, Eqs. (3) and (5). The Re_θ values for intermittency-weighted data are calculated simply by implementing Emmons' [13] linear combination of the conditionally sampled Re_θ, Eq. (6). Dey [25] has shown that the momentum imbalance due to such a linear combination is small and may be considered negligible. A difference between the calculated intermittency-weighted and nonconditionally sampled Re_θ is observed. This may be due to the variation of the intermittency across the boundary layer profile since the peak value of γ is used in the calculations.

The laminar conditioned data show good agreement with the trend of Truckenbrodt's correlation, but it is consistently 25% higher than the upper limit of β. Calculating β from Eq. (4) using experimental data results in an average value of $\beta=0.27$.

While this value of β is outside the upper limit of the Pohlhausen velocity profiles and results in a somewhat distorted curve in the outer portion of the predicted boundary layer profile, the near wall velocity gradient is well represented as seen in Fig. 6. This approximation appears to be sufficient as the high velocity gradient in the near wall region is where the majority of entropy is generated [2]. Inserting $\beta=0.27$ into Eq. (3) results in excellent agreement with the data with an average deviation of less than 5%.

Comparing the nonconditionally sampled data with the intermittency-weighted data in Fig. 5, one sees a significant difference. The nonconditionally sampled data shows a somewhat erratic transition from laminar to turbulent with two distinct peaks visible which is similar to those observed by Stieger [6] and

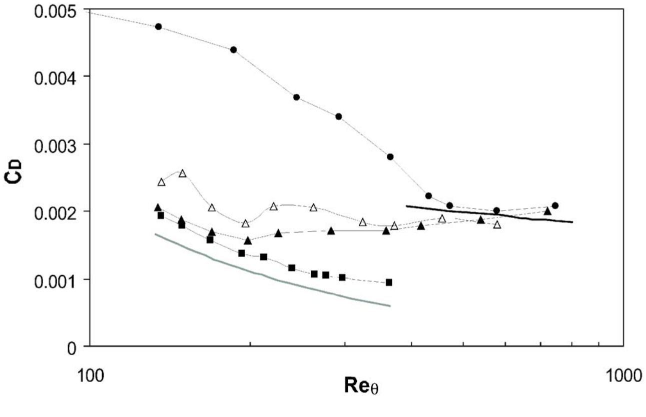

Fig. 5 Dissipation coefficient versus Re_θ or experimental data: (■) laminar-conditioned data; (•) turbulent-conditioned data; (▲) intermittency-weighted data; (△) nonconditionally-sampled data; (—, solid grey line) laminar correlation; and (—) turbulent correlation

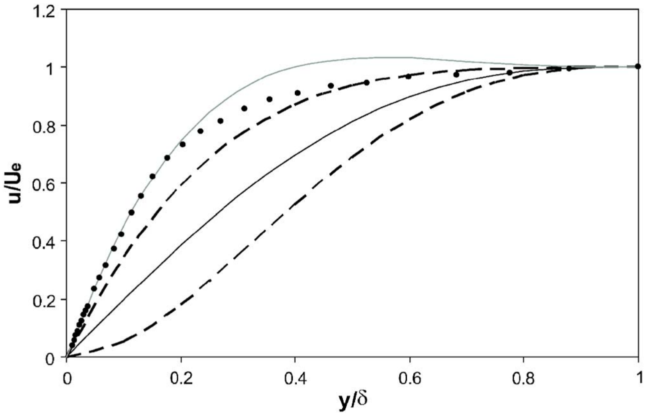

Fig. 6 Pohlhausen velocity profiles for laminar conditioned data: (•) laminar data, Volino et al. [19]; (—) zero pressure gradient, β=0.173 (Λ=0); (- -), limits of Pohlhausen (Λ±12); and (—, solid grey line) β=0.27 (Λ=21)

O'Donnell [26]. This is due to the inclusion of large velocity fluctuations in the transition region that cannot be simply time averaged. These fluctuations do not contribute to the entropy generation as they are short-term temporal events which are due to the intermittent nature of transition and not local Reynolds shear stresses as noted by Kim et al. [20].

Figure 5 shows that the data exhibit higher turbulent conditioned dissipation coefficient levels at low Reynolds numbers than predicted by the turbulent correlation. However, at $\mathrm{Re}_\theta > 500$ ($\mathrm{Re}_x > 5 \times 10^5$) good agreement is found and is generally in line with the observations of Denton [2] for turbulent boundary layers. Figure 7 displays the dissipation coefficient prediction obtained for the favorable pressure gradient case by inserting the laminar correlation (β=0.27) Eq. (3) and turbulent correlation Eq. (6) into Eq. (8) and weighting them with the predicted intermittency distribution. Reasonable agreement is found, however, an accurate prediction of the intermittency-weighted dissipation coefficient for $\mathrm{Re}_\theta < 500$ is hindered by the absence of a correlation for the turbulent dissipation coefficient at low Reynolds numbers. The turbulent flow in this region is not fully developed and is not characteristic of fully developed turbulent flow. The following correlation is proposed, however further experimentation is required to verify and refine its accuracy

$$C_{D_{\mathrm{TURB}}} = 0.0066 e^{-0.0024\,\mathrm{Re}_\theta}, \mathrm{Re}_{\theta < 500} \qquad (18)$$

Equation (18) for $\mathrm{Re}_\theta < 500$ is also shown in Fig. 7 for illustrative purposes only as it cannot be included in the present prediction.

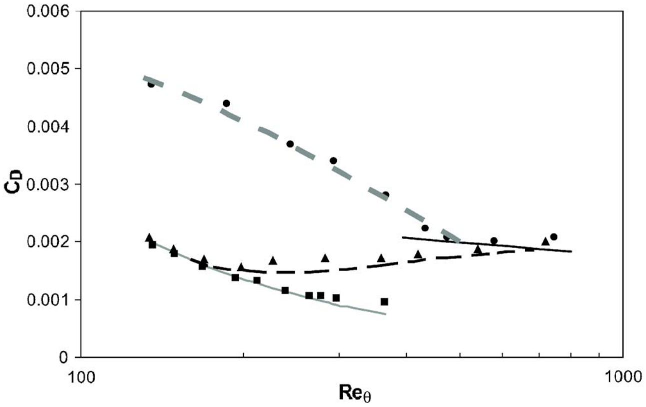

Fig. 7 Comparison of predicted and measured intermittency-weighted dissipation coefficient for favorable pressure gradient case: (■) laminar-conditioned data; (▲), intermittency-weighted measurements; (•), turbulent-conditioned data; (—, solid grey line) laminar correlation, β=0.27 (Λ=12); (—) turbulent correlation; (- -, broken grey line) prediction; (– –) Eq. (18).

The prediction of the intermittency distribution for the favorable pressure gradient is good and it is shown that empirical correlations of Thwaites [22] and Buri [23] perform well and allow the laminar and turbulent dissipation distributions to be represented in terms of free-stream conditions. In the favorable pressure gradient case when the laminar correlation is modified to use the deduced value of β=0.27, the accuracy of the prediction is further improved. Since many empirical and semi-empirical methods have been implemented in commercial codes before to predict transition, as shown by Roux et al. [27], it should be relatively straightforward to utilize the prediction method proposed here based upon intermittency distributions, turbulence intensities, and velocity distributions predicted by such codes.

The development of a predictive method for the entropy generation rate in boundary layer transition requires accurate predictions of the laminar and turbulent dissipation coefficient distributions. The data presented in this paper show that such accurate predictions are indeed possible, however the limited number of conditionally sampled data sets available is a significant difficulty.

Conclusions

Entropy generation rate calculations in conditionally sampled transitional boundary layers have been performed for the first time. A significant difference is seen between the intermittency-weighted data and the nonconditionally sampled data. A more gradual and smooth transition to turbulent flow for the intermittency-weighted dissipation coefficient data is found. It behaves in a similar manner to the more commonly used skin friction coefficient C_f. A tentative correlation is proposed for the turbulent dissipation coefficient for momentum thickness Reynolds numbers less than 500. Both Thwaites' method and Buri's momentum method give good predictions of the laminar and turbulent momentum thicknesses within the transition region, allowing predictions of laminar and turbulent dissipation coefficients based on free-stream parameters. These correlations may be coupled with the predictions of the intermittency distribution of Dhawan and Narasimha [14] to provide the basis of a predictive method for the entropy generation rate in transitional boundary layers, accounting for the intermittent nature of such flows.

Acknowledgment

This paper has emanated from research conducted with the financial support of Science Foundation Ireland. The INL contribution was partly supported via DOE Idaho Operations Office Contract No. DE-AC07-05ID14517.

Nomenclature

C_D = dissipation coefficient, $T/(\rho u_e^3)\int_0^\delta \dot{S}'''_{\mathrm{gen}} dy$
C_f = skin friction coefficient, $\tau_w/(1/2\rho U_\infty^2)$
H_{12} = boundary layer shape factor, (δ^*/θ)
K = acceleration parameter, $(\nu/U_\infty^2)(dU_\infty/dx)$
$\hat{n}$ = dimensionless turbulent spot production rate
Re_θ = momentum thickness Reynolds number
Re_x = stream-wise coordinate Reynolds number
$\dot{S}'''_{\mathrm{gen}}$ = entropy generation rate per unit volume
$(\dot{S}'''_{\mathrm{gen}})^*$ = nondimensional $\dot{S}'''_{\mathrm{gen}}$, $(\dot{S}'''\mathrm{gen}\theta T)/(\rho U_\infty^3)$
T = absolute temperature
Tu = free-stream turbulence intensity
u = mean stream-wise velocity
U_e = boundary layer edge velocity, $(0.99U_\infty)$
U_∞ = free-stream velocity
u' = instantaneous stream-wise fluctuating velocity

$\bar{u}'$ = rms stream-wise fluctuating velocity
$\overline{u'v'}$ = time averaged turbulent shear stress
U^+ = local mean stream-wise velocity in wall coordinates
u_τ = friction velocity
v' = instantaneous cross-stream fluctuating velocity
x = stream-wise coordinate, distance from leading edge
y = cross-stream coordinate, distance from wall
Y^+ = distance from wall in wall coordinates
δ = boundary layer thickness
δ^* = displacement thickness
γ = intermittency factor
Λ = Pohlhausen pressure gradient shape factor, $\Lambda = (\delta^2/\nu)(dU/dx)$
θ = momentum thickness
μ = dynamic viscosity
ν = kinematic viscosity, μ/ρ
ρ = density
σ = turbulent spot propagation parameter

Subscripts

COMP = nonconditionally sampled condition
PK = peak value
TURB = turbulent condition
s = transition onset
ZPG = zero pressure gradient

References

[1] Bejan, A., 1982, *Entropy Generation Through Heat and Fluid Flow*, Wiley, New York.

[2] Denton, J. D., 1993, “Loss Mechanisms in Turbomachines,” ASME J. Turbomach., **115**, pp. 621–656.

[3] Truckenbrodt, E., 1952, “A Method of Quadrature for the Calculation of Laminar and Turbulent Boundary Layers in Plane and Rotational Symmetric Flow,” NACA TM 1379 (Translated from Ing.-Arch., **20**(4), 1952, pp. 211–228).

[4] Pohlhausen, K, 1921, “Zur Näherungsweisen Integration der Differentialgleichung der Laminaren Reibungsschicht,” Z. Angew. Math. Mech., **1**, pp. 252–268.

[5] Schlichting, H., 1979, *Boundary Layer Theory*, 7th ed., Mc–Graw Hill, New York.

[6] Stieger, R. D., 2002, “The Effects of Wakes on Separating Boundary Layers in Low Pressure Turbines,” Ph.D. dissertation, Cambridge University, Cambridge, UK.

[7] Walsh, E. J., and Davies, M. R. D., 2005, “Measurements in the Transition Region of a Turbine Blade Profile Under Compressible Conditions,” ASME J. Fluids Eng., **127**, pp. 400–403.

[8] Mayle, R. E., 1991, “The Role of Laminar-Turbulent Transition in Gas Turbine Engines,” ASME J. Turbomach., **113**, pp. 509–537.

[9] Walsh, E. J., and Davies, M. R. D., 2003, “Measurement and Prediction of Transition on the Suction Surface of Turbine Blade Profiles,” *Proceedings of the 5th European Conference on Turbomachinery – Fluid Dynamics and Thermodynamics*, Prague, Czech Republic, ASI, Prague, Paper No. TT01–201, pp. 889–900.

[10] Gostelow, J. P., Blunden, A. R., and Walker, G. J., 1994, “Effects of Free Stream Turbulence and Adverse Pressure Gradients on Boundary Layer Transition,” ASME J. Turbomach., **116**, pp. 392–404.

[11] Abu-Ghannam, B. J., and Shaw, R., 1980, “Natural Transition of Boundary Layers- The Effect of Turbulence, Pressure Gradient and Flow History,” J. Mech. Eng. Sci., **22**, pp. 213–228.

[12] Jacobs, R. G., and Durbin, P. A., 2001, “Simulations of Bypass Transition,” J. Fluid Mech., **428**, pp. 185—212.

[13] Emmons, H. W., 1951, “The Laminar-Turbulent Transition in a Boundary Layer,” J. Aeronaut. Sci., **18**, pp. 490–498.

[14] Dhawan, S., and Narasimha, R., 1958, “Some Properties of Boundary Layer Flow During the Transition from Laminar to Turbulent Motion,” J. Fluid Mech., **3**, pp. 418–436.

[15] Narasimha, R., and Dey, J., 1989, “Transition Zone Models for 2-Dimensional Boundary Layers: A Review,” Sadhana: Proc., Indian Acad. Sci., **14**, pp. 93–120.

[16] Kim, J., and Simon, T. W., 1991, “Free-Stream Turbulence and Concave Curvature Effects on Heated, Transitional Boundary Layers,” Volume I, NASA CR 187150 and Volume II, NASA CR 187151, Final Report to Minnesota University, Department of Mechanical Engineering, Minnesota University, Minneapolis, MN.

[17] Wang, T., and Zhou, D., 1998, “Conditionally-sampled Flow and Thermal Behaviour of a Transitional Boundary Layer at Elevated Free-stream Turbulence,” Int. J. Heat Fluid Flow, **19**, pp. 348–357.

[18] Sohn, K. H., and Reshotko, E., 1991, “Experimental Study of Boundary Layer Transition with Elevated Freestream Turbulence on a Heated Flat Plate,” NASA Paper No. CR 187068.

[19] Volino, R. J., Schultz, M. P., and Pratt, C. M., 2003, “Conditional Sampling in a Transitional Boundary Layer under High Free-stream Turbulence Conditions,” ASME J. Fluids Eng., **125**, pp. 28–37.

[20] Kim, J., Simon, T. W., and Kestoras, M., 1994, “Fluid Mechanics and Heat transfer Measurements in Transitional Boundary Layers Conditionally-sampled on Intermittency,” ASME J. Turbomach., **116**, pp. 405–416.

[21] Hughes, W. F., and Brighton, J. A., 1967, *Fluid Dynamics – Schaums Outline Series*, McGraw–Hill, New York.

[22] Thwaites, B., 1987, “*Incompressible Aerodynamics*,” Clarendon, Oxford, UK.

[23] Buri, A., 1931, “Eine Berechnungsgrundlage für die turbulente Grenzschicht bei Beschleunigter und Verzögerter Strömung,” dissertation, ETH, Zürich, Switzerland

[24] Steelant, J., and Dick, E., 1996, “Modelling of Bypass Transition with conditioned Navier-Stokes Equations Coupled to an Intermittency Transport Equation,” Int. J. Numer. Methods Fluids, **23**, pp. 193–220.

[25] Dey, J., 2000, “On the Momentum Balance in Linear-Combination Models for the Transition Zone,” ASME J. Turbomach., **122**, pp. 587–588.

[26] O’Donnell, F. K., 2000, “The Measurement of Aerodynamic Entropy Generation in a Turbine Blade Boundary Layer,” Ph.D. thesis, University of Limerick, Limerick, Ireland, UK.

[27] Roux, J. M., Mahé, P., Sauthier, B., and Duboué, J. M., 2001, “Aerothermal Predictions with Transition Models for High-pressure Turbine Blades,” Proc. Inst. Mech. Eng., Part A: J. Power and Energy, **215**, pp. 735–742.

Investigation of Velocity Profiles for Effusion Cooling of a Combustor Liner

J. J. Scrittore
Mechanical Engineering Department,
Virginia Polytechnic Institute and State University,
Blacksburg, VA 24061

K. A. Thole
Department of Mechanical and Nuclear Engineering ,
Pennsylvania State University,
University Park, PA 16802-1412

S. W. Burd
Pratt & Whitney,
United Technologies,
East Hartford, CT 06108

Effusion cooling of combustor liners for gas turbine engines is quite challenging and necessary to prevent thermal distress of the combustor liner walls. The flow and thermal patterns in the cooling layer are affected by the closely spaced film-cooling holes. It is important to fully document how the film layer behaves with a full-coverage cooling scheme to gain an understanding into surface cooling phenomena. This paper discusses experimental results from a combustor simulator tested in a low-speed wind tunnel. Engine representative, nondimensional coolant flows were tested for a full-coverage effusion plate. Laser Doppler velocimetry was used to measure the flow characteristics of the cooling layer. These experiments indicate that the full-coverage film cooling flow has unique and scaleable velocity profiles that result from the closely spaced effusion holes. A parametric study of the cooling flow behavior illustrates the complex nature of the film flow and how it affects cooling performance. [DOI: 10.1115/1.2720492]

Introduction

Component cooling technologies play an increasingly important role as the firing temperatures of gas turbine combustors are raised higher than ever to meet the demand for higher turbine power. As combustor gas temperatures are well above the incipient melting temperature of the component metal, methods such as coating applications, film-cooling (also referred to as effusion cooling), slot cooling, backside impingement, and backside pin fin cooling become necessary. Effusion cooling, which contains an array of closely spaced discrete film cooling holes, is widely used to cool the liner walls of gas turbine combustors. This cooling method forms a layer of cooling flow on the combustor liner to isolate the component metal from the hot mainstream flow. As such, high mass flow with little mixing is desired.

A large-scale recirculating wind tunnel was used to simulate a typical combustor where full-coverage film-cooling flows were tested. The film cooling blowing ratios used in this study were typically higher than those presented for turbine applications and higher than most found in the open literature. The study presented in this paper did not include reacting flow; thereby effects attributed to the heat release due to combustion were not represented in this study. From these large scale tests, however, it was possible to understand the effects of film flow on combustor liner cooling.

The objective for the work reported in this paper was to compare the development of the film-cooling effectiveness to the developing flowfield. A prediction of the cooling effectiveness based on the behavior of the film cooling flow would allow insight as to where a full-coverage cooling scheme becomes fully developed as defined by self-similar velocity profiles. After describing the characteristics of the combustor simulator facility, this paper describes results from the experiments conducted using the effusion plate.

Relevant Past Studies

Many studies have documented both experimental and computational data for film cooling flows. The large number prevents a full discussion of all of the results in our paper, but rather a subset will be discussed that is relevant to full-coverage, high momentum-flux ratio cooling flows.

A series of papers by Andrews et al. [1–3] have compared the influence of cooling hole size, pitch, and inclination angle through a number of experimental studies. In combustor designs, the amount of coolant flow per surface area is considered in the selection of the cooling hole diameter and pattern to ensure that the intended pressure loss across the combustor is met. Andrews et al. [1] investigated 90 deg cooling holes for a number of different arrays and found that there was a significant improvement in the overall cooling effectiveness for a larger hole relative to a smaller hole, which they attributed primarily to the fact that there were lower external heat transfer coefficients for the larger holes. Since they conducted these tests at high temperatures, they also found significant radiation effects. Andrews et al. [2] found that the heat transfer coefficients scaled well using a Nusselt number based on distance along the externally film-cooled plate and Reynolds number based on the cooling hole characteristics (diameter and jet velocity). Andrews et al. [3] also compared normal (90 deg) and inclined film holes (30 deg and 150 deg) for an array of effusion holes and found that cooling effectiveness improved with inclined holes. The counterflow holes (150 deg) resulted in reverse flow and good cooling performance at low coolant flows but not at high coolant flows. Lin et al. [4] also investigated a number of effusion cooling hole designs. They found that the hole injection angle and hole spacing are the primary parameters affecting adiabatic film cooling effectiveness. Interestingly, they also found for co-flowing jet injection that there was little effect of blowing ratio, but for counterflow injection they found that blowing ratio had a large effect. This is consistent with work cited by Andrews et al. [3].

Martiny et al. [5] used a very low injection angle of 17 deg for an effusion, film-cooled plate in which they measured adiabatic effectiveness levels for a range of blowing ratios. Their results indicated significantly different flow patterns depending on the cooling jet blowing ratio. It is important to recognize that their study used only four rows of cooling holes and as will be shown in this paper, this small number of rows did not allow for a fully developed condition to occur.

Sasaki et al. [6] examined if it were possible to use a superposition method with a full-coverage film-cooling array. They found that, in fact, there was an additive nature of multirow film-cooling that allowed the use of the superposition method. In a later study,

---

Contributed by the International Gas Turbine Institute of ASME for publication in the Journal of Turbomachinery. Manuscript received July 13, 2006; final manuscript received August 2, 2006. Review conducted by David Wisler. Paper presented at the ASME Turbo Expo 2006: Land, Sea and Air (GT2006), Barcelona, Spain, May 8–11, 2006. Paper No. GT2006-90532.

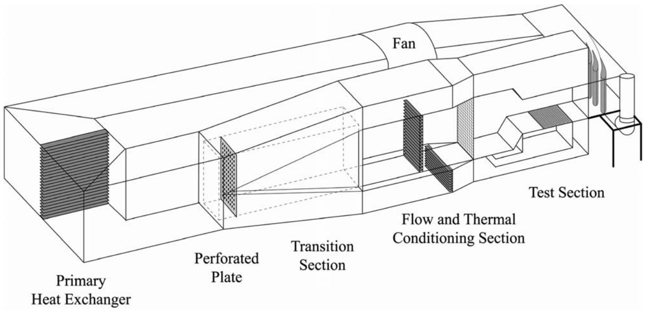

Fig. 1 Illustration of the wind tunnel facility used for film-cooling experiments

Table 1 Description of effusion plate geometry

d	5.7 mm
L/d	8.9
t/d	4.4
S_s/d	4.9
S_p/d	
α	30 deg

however, Harrington et al. [7], who also studied a full-coverage film cooling array with normal jet injection, found that the superposition prediction of the full-coverage cooling effectiveness based on single row measurements tended to overpredict adiabatic effectiveness. They found that eight rows of cooling holes were required to reach an asymptotic "fully developed" adiabatic effectiveness level. These researchers also measured jet separations for their normal (90 deg) holes at blowing ratios greater than 0.65.

Fric et al. [8] used flow visualization techniques to detect cooling jet separations and coalescence as a function of blowing ratio. They found that the film coverage is minimum for the blowing ratios from 1.7 to 3.3 and film coverage improves above this range. Bazdidi-Tehrani et al. [9] found that there was little effect of the density ratio on the film heat transfer coefficient for a given coolant mass flow per unit surface area, which was similar to their cooling effectiveness results. Pietrzyk et al. [10] found that higher density jets had higher penetration distances and lower velocities in the near wall region. It was also found that high and low density jets had similar maximum turbulence values, but there was a significantly lower turbulence relaxation rate for the high-density jets.

In summary, there is little data presented in the literature studying full-coverage, high momentum flux ratio cooling focusing on flow fields related to cooling effectiveness. While there is a wealth of film-cooling literature, much of this data is not applicable because of the high blowing ratios and densely spaced cooling holes required for most aeroengine combustors.

Facilities and Measurement Methods

The focus of this study was to obtain flow field measurements for a densely-spaced full-coverage array of film cooling holes. The characteristics of the flow and how they relate to the adiabatic cooling effectiveness for a realistic combustor cooling design are of interest to designers and the focus of this work. To achieve good spatial resolution, it is beneficial to use large-scale models while matching the relevant nondimensional parameters. The primary measurement techniques used were laser Doppler velocimetry to quantify the flow field and an infrared camera to measure surface temperatures. This section describes the experimental facility in which these measurements were made, the instrumentation that was used, and the corresponding estimates of measurement uncertainty.

Experimental Facilities. The geometric scaling factor for the test section is approximately nine times that of an actual combustor, which permitted good measurement resolution in the experiments. Figure 1 illustrates the wind tunnel containing the test section and effusion plate.

Flow is supplied by a 50 hp axial fan as shown in Fig. 1. Downstream of a primary heat exchanger is a transition section that divides the flow into three channels including a heated primary channel, representing the main gas path and two symmetric secondary outer channels, representing the coolant flow paths. Within the transition section of the primary channel, the flow immediately passes through a perforated plate that provides the necessary pressure drop to control the flow splits between the primary and secondary passages. At a distance 2 m downstream of the perforated plate, the flow passes through a bank of heaters followed by a series of screens and flow straighteners. The heater section is comprised of three individually controlled banks of electrically powered, finned bars supplying a maximum total heat addition of 55 kW.

The cross-sectional area of the test section at this location is 1 m in height (H_{in}) and 1.1 m in width (W). At a distance of 0.85 m downstream of the flow straighteners, the heated primary flow is accelerated via a reduction in the flow area due to a 45 deg contraction. At a distance 0.46 m downstream of the contraction the secondary coolant flow is injected into the primary flow passage through film-cooling holes in the effusion plate located on the bottom wall of the test section. At this location, the cross-sectional area is 0.55 m in height (96 z/d) and 1.1 m in width giving an inlet to exit area ratio of 1.8.

In addition to heat being removed from the flow by a primary heat exchanger, the flow in the secondary passages pass through a second heat exchanger to further reduce the coolant flow temperature. The flow in the secondary passages is then directed into a 0.61 m^3 plenum that supplies the test plate coolant. To ensure the correct coolant flow is supplied to the coolant plenum, an adjustable valve was used to meter the flow. The mass flow exiting the film-cooling holes was set by applying the appropriate pressure ratio between the total supply plenum pressure and the exit static pressure. Using the documented discharge coefficient $C_d=0.73$ for this particular cooling hole and flow configuration where the ratio of coolant total supply pressure to mainstream static pressure is 1.0015 (Barringer et al. [11]), the mass flows through the test plate were established. The effusion plate was constructed of 2.54 cm thick urethane foam with a low thermal conductivity ($k=0.029$ W/mK resulting in a maximum conduction loss of 1.1×10^{-3} W/cm^2) to allow for adiabatic surface temperature measurements. The dense pattern of 730 cylindrical film-cooling holes was cut into the urethane foam using a five-axis water jet. The holes were arranged into 20 rows in the streamwise direction. The cooling hole pattern on the test plate is described in Table 1 and shown schematically in Fig. 2.

For this study, the film cooling characteristics were studied at four different blowing ratios: $M=3.2$, 3.8, 4.4, and 5.0. One parameter that is not representative is the coolant-to-mainstream density ratio, which is typically quite high in combustors. Typical operating conditions for the film cooling flow tests consisted of a matched coolant and mainstream temperature of 30°C. For the cooling effectiveness measurements, the mainstream temperature was nominally 45°C with a coolant flow temperature of 26°C. These conditions resulted in density ratios for all of the unheated cases of 1.0 (jet-to-mainstream) and 1.08 for all of the heated cases that were investigated. Adiabatic effectiveness data were taken for the blowing ratios: $M=3.2$ and 5.0. For the cases presented in this paper, 9–13% of the total flow was directed through the secondary coolant passages for the effusion cooling while the remaining flow was directed through the primary passage of the test section. The flow accelerated 9–15% through the test section as a result of the mass flow addition. These flow conditions re-

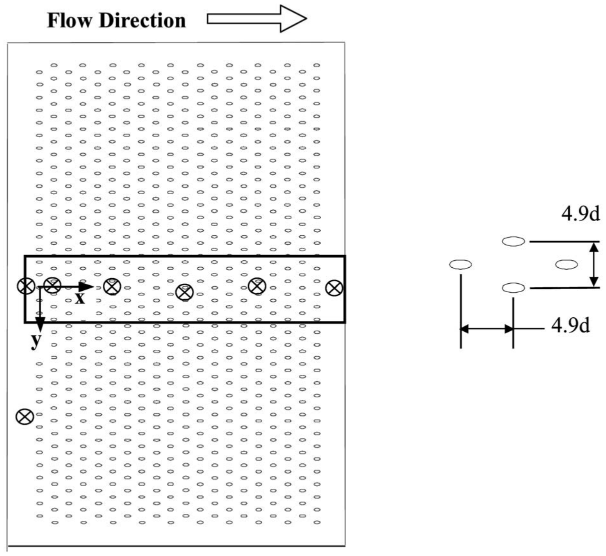

Fig. 2 Illustration of the test plate schematic showing surface temperature measurement region and locations for measurements of velocity profiles

sulted in a test section exit Reynolds number of $8.2-8.6 \times 10^4$. The film cooling jet Reynolds number varied from 2.4 to 3.8×10^3.

Instrumentation and Measurement Uncertainty. A single fiberoptic laser Doppler velocimeter (LDV) probe capable of measuring two components was used to take flow measurements. To allow the measurement volume of the probes to reach the center of the test plate, data was taken with a 750 mm focusing lens equipped with a 2.6 magnification beam expander. This setup had a measurement volume of 73 μm in diameter and 1.3 mm in length. The flow was seeded with olive oil particles that were nominally 1 μm in diameter. The plane was acquired with the probe perpendicular to the flow direction. This allowed for the direct measurement of the local streamwise velocity component, u. However, in order to take measurements near the surface of the liner panel, the probe was slightly tilted at 8 deg, whereby there was little effect on the true wall-normal component measurements. The nominal sampling time for each measurement location was 20 s whereby 10,000 data points were acquired for each component. The probability of obtaining a sample was proportional to the speed of the flow; therefore, statistical particle bias corrections were applied to the data by weighting each individual sample based on the residence time of a particle in the probe volume. Multiple flow measurements at different locations showed good repeatability.

A Flir Systems P20 infrared camera was used to take measurements of the effusion test plate to calculate the adiabatic effectiveness at the plate surface. The camera captured the temperature of the surface at each image pixel location by measuring the total electromagnetic radiation emitted from the black painted foam plate surface. Two type E thermocouples measuring temperatures at the surface of the plate were used to calibrate the images to assure that the correct surface emissivity and ambient temperatures were being used to report the actual surface temperatures. Five pictures were averaged at each image location to reduce uncertainty in the measurements. The infrared camera was mounted above the top endwall of the test section 0.53 m from the test plate. The proximity of the camera to the test plate allowed a spatial resolution of 0.49 mm^2/pixel, with a maximum image size of 410 cm^2. However, the size of the test plate required five image locations and the additional step of assembling the infrared images into a correctly dimensioned composite image. Thermocouples were used to monitor the inlet and coolant temperatures. All of the temperature measurements were made using 30-gauge, type E thermocouples that were connected to a data acquisition system through 20-gauge thermocouple extension wire.

The partial derivative and sequential perturbation methods, described by Moffat [12], were used to estimate the uncertainties of the measured values. The precision uncertainty for the highest streamwise velocities was 0.8% based on a 95% confidence interval while the bias uncertainty for the mean velocity measurements was 1%. Precision uncertainties were calculated using the deviation of five images for each of the five measurement sets of IR camera images. The precision uncertainty of the measurements was $\pm 0.086^\circ\text{C}$. The bias uncertainty was $\pm 0.47^\circ\text{C}$ based on the calibration of the image. The bias uncertainty of the thermocouples was $\pm 0.2^\circ\text{C}$. The total uncertainty was then calculated as $\pm 0.47^\circ\text{C}$ for the images and $\pm 0.22^\circ\text{C}$ for the thermocouples. Uncertainty in effectiveness, η, was found based on the partial derivative of η with respect to each temperature in the definition and the total uncertainty in the measurements. An uncertainty of $\partial\eta = \pm 0.017$ at $\eta = 0.5$ and $\partial\eta = \pm 0.019$ at $\eta = 0.9$ were calculated. The precision uncertainty for the highest streamwise velocities was 0.77% while the bias uncertainty for the mean velocity measurements was 1%.

Results

As was discussed, one of the objectives of this work was to determine how the film cooling flowfield develops for an effusion film-cooled plate. Prior to measuring this flow development, the incoming boundary layer was measured to characterize the inlet conditions. Static pressure measurements were also made along the plate to determine the local momentum flux ratios as a function of streamwise distance along the plate. To determine the flowfield development, velocity profiles were acquired at a number of locations, as indicated in Fig. 2. These locations were chosen to chart the development of the film flow as it progressed down the test plate for the flow conditions $I = 10.6$ and 25.5 ($M = 3.2$ and 5.0) and a density ratio of 1.0. Velocity profiles were also measured downstream of row 20 for $I = 10.6$, 14.8, 19.7, and 25.5 to understand the effect of the momentum flux ratio. After it was found that the film flow became fully developed after the 15th row of cooling holes, lateral and streamwise planes were measured at row 15 to describe how the film cooling was interacting with mainstream and upstream film flow.

The following section will describe the results of this study by first describing the inlet flow conditions approaching the first row of cooling holes, results of the flow field measurements and then adiabatic effectiveness results for the entire streamwise extent of the test plate.

Inlet and Cooling Flow Conditions. The inlet conditions were measured at two locations upstream of the first row of cooling holes. To ensure inlet flow uniformity, the measurements were located at the center of the test plate and at 25% of the width as shown in Fig. 2. These measurements were made of five cooling hole diameters upstream of the first row of cooling holes. Note that all profiles are normalized to the local mainstream velocity. The maximum percent difference based on the mainstream velocity between the two inlet locations was 1.6% for the streamwise component and 0.29% for the turbulence level. The inlet mainstream streamwise velocity was 2.3 m/s with a freestream turbulence level of 1.3%. The displacement thickness of the inlet boundary layer was found to be 0.86 z/d with a momentum thickness Reynolds number equal to 451. Figure 3 shows the two boundary layer profiles at the two different pitchwise locations that were measured. As can be seen from Fig. 3, there is good pitchwise uniformity at the start of the plate.

The film cooling flow was established using the discharge coefficient and an inviscid calculation with the knowledge of the cooling plenum's total pressure with respect to the static pressure

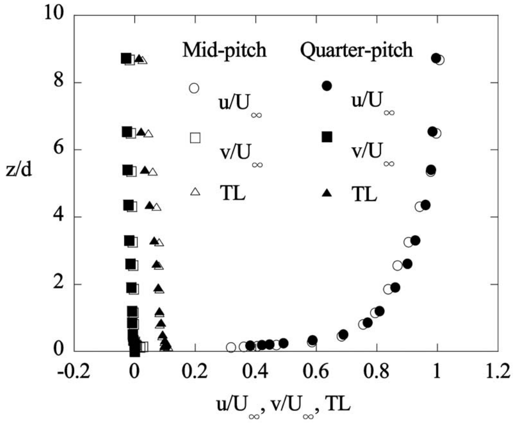

Fig. 3 Inlet flow conditions measured at mid-pitch and quarter-pitch

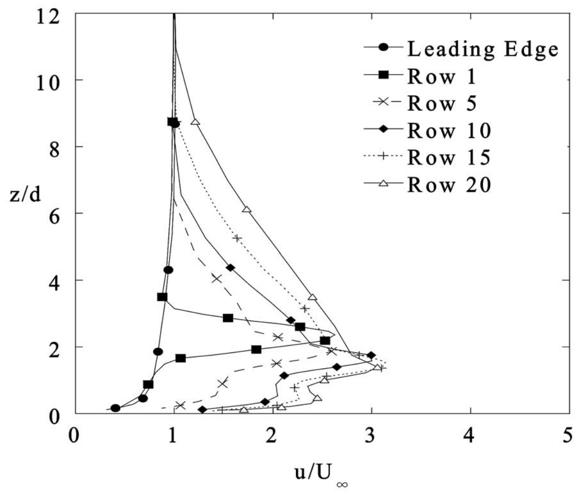

Fig. 5 Streamwise velocity profiles measured for $I=10.6$

at the hole exits. The static pressures were measured at the test plate centerline between every other row of cooling holes to accurately deduce the coolant discharge rate and local momentum flux ratios. It was found that the coolant plenum total pressure and surface static pressure difference remained constant within 3% indicating that there was a constant coolant supply in the streamwise direction. However, the accumulation of cooling flow increased the local freestream velocity, thereby decreasing the local momentum-flux ratio as shown in Fig. 4. The local momentum-flux ratio of the cooling jets was found to decrease by about 20% from the first to 20th hole row.

Development of the Velocity Profiles. Velocity profiles were measured downstream of the cooling hole rows 1, 5, 10, 15, and 20 to determine how the film-cooling effusion flow develops and whether the flow becomes fully developed. These profiles were taken one cooling row downstream of the respective hole rows as shown in Fig. 2. Measurements were made for the blowing ratios $M=3.2$ and 5.0 ($I=10.6$ and 25.5).

Figure 5 shows the mean velocity profiles as the flow develops along the effusion plate for the lowest momentum flux ratio case. As the flow is injected from the first row to the 15th row, there is a continual decrease in the penetration height of the jet, as defined by the maximum streamwise velocity. The peak occurs at 2.4 *d* for row 1 and at 1.4 *d* for row 15 and row 20. It is also interesting to note that the continuous injection results in an increase in velocity for the outer portion of the flow (above the peak velocity).

Figure 6 also shows that the streamwise velocities have two distinct local velocity maxima that emerge at row 10 and remain further downstream. This phenomenon was consistent at both high and low blowing ratios, as will be discussed. The most important information that can be gleaned from Figs. 5 and 6 is that for both momentum flux ratios the data indicate that the flow becomes fully developed at nominally row 15 in terms of a peak velocity, while the outer portion of the flow continues to accelerate from the mass addition.

Pietrzyk [13] formulated a physical model describing the flow field behind a high velocity ratio jet ($V_j/U_\infty=0.5$). This researcher identified a wall-jet layer generated by longitudinal vortexes created at the lateral edges of the cooling hole. This layer was attributed to generating the secondary velocity peak at the near-wall. It was concluded that the longitudinal vortices were the most detrimental flow structures affecting film cooling performance. Pietrzyk et al. [14] found that there was an influx of higher speed fluid into the wake region below the jet core causing a negative velocity gradient near the wall. It was also found that the strength of the longitudinal vortices scaled with the velocity ratio, which was essentially the main scaling parameter in this study. Lee et al. [15] also measured double peaked streamwise velocity profiles in

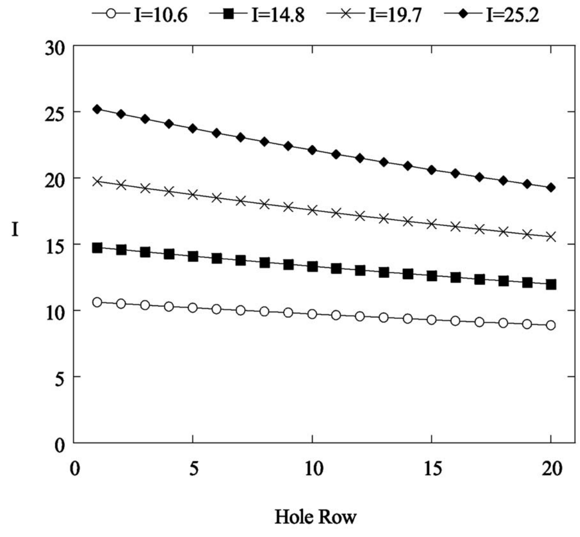

Fig. 4 Streamwise dependence on the local momentum-flux ratios of film cooling jets

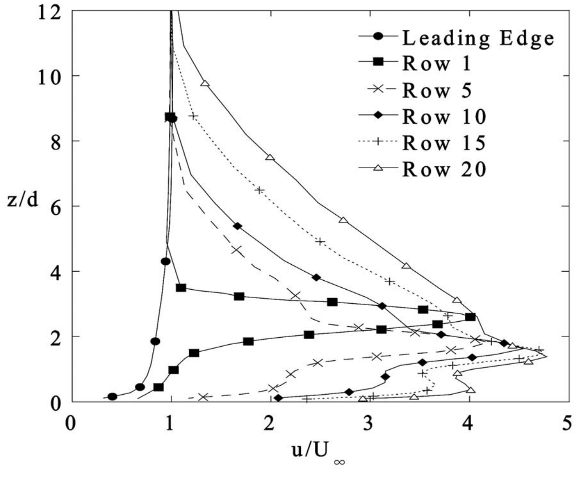

Fig. 6 Streamwise velocity profiles measured for $I=25.5$

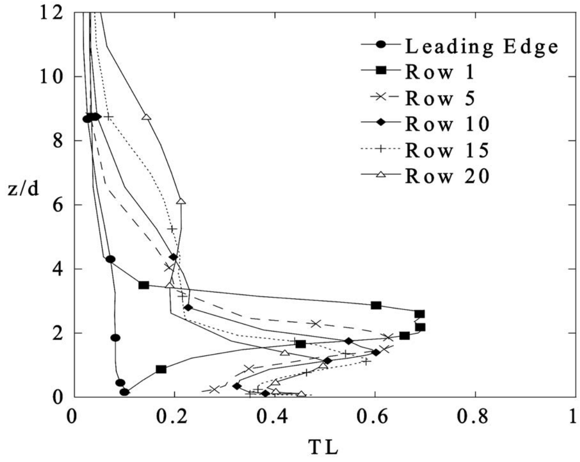

Fig. 7 Turbulence level profiles for $I=10.6$

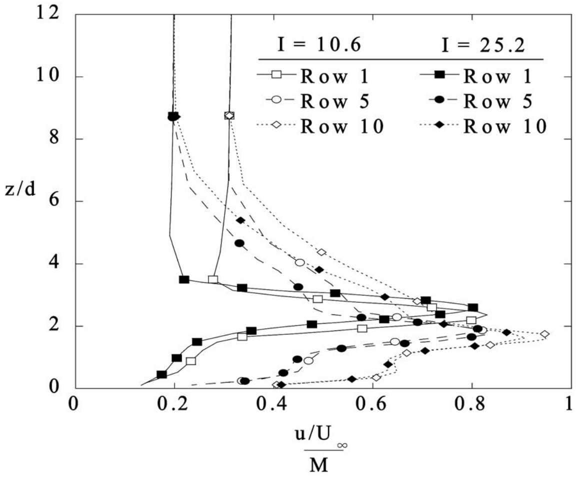

Fig. 9 Streamwise velocity profiles measured one row downstream of rows 1, 5, and 10 for $I=10.6$ and 25.5 using the blowing ratio, M, to normalize the profiles

the flowfield downstream of streamwise inclined jets in the crossflow. These researchers found that inclined jets induce a much higher wall-normal velocity in the jet wake region than normal jets, due to stronger secondary motion and a larger pressure drop gradient. Both of these studies considered only a single row of holes.

As was discussed, the location of the peak streamwise velocity was found to be dependent on the hole row as shown in Fig. 5 for $I=10.6$. A similar result occurred as shown in Fig. 6 for $I=25.5$. For row 1, the peak velocity occurred only slightly further off the wall for the $I=25.5$ case relative to the $I=10.6$ case. As the flow further developed, the location of the peak for the two flow cases occurred at nearly the same vertical location at $z/d=1.4$. But, the velocity values for the $I=25.5$ case were much higher than for the $I=10.6$ case.

Turbulence levels were also compared for the two momentum flux ratios and can be seen in Figs. 7 and 8. Note that these turbulence levels are the rms of the streamwise and wall-normal velocity fluctuations normalized by the local mean velocities external to the film-cooled layer. The data in Figs. 7 and 8 indicate that higher turbulence levels occur at higher momentum flux ratios, which is expected given the larger shear in the boundary layer. Similar to the mean velocities, however, the wall-normal location of the peak turbulence levels is relatively insensitive to the momentum flux ratio.

Similar to the mean velocities that were shown in Figs. 5 and 6, the turbulence profiles become self-similar in terms of peak values downstream of the 15th row. In the near wall region, the peak turbulence levels for both cases decrease with increasing streamwise distance while the levels continue to increase with downstream distance in the outer flow region (above the peak). The turbulence levels in the near wall region also start to increase very close to the wall and become self-similar at nominally the 15th cooling row.

In analyzing these results, it became evident that both the mean velocity profiles and the turbulence levels at a given film-cooling hole row scaled with the injection levels. As a result, an attempt was made to analyze the results by using the momentum flux and the mass flux ratios as scaling parameters in plotting the profiles. Figures 9 and 10 show several row locations whereby the mass flux ratio was placed in the denominator of the velocity scaling parameter. These figures indicate a very good scaling of the velocity profiles using the mass flux ratio at each row considered. Momentum flux ratios were also used to scale the velocity fields, but did not indicate good scaling characteristics.

To further evaluate whether the mass flux ratio was a good scaling parameter, a number of velocity profiles were measured one hole row spacing downstream of the last row of cooling holes to gain an understanding of how the blowing ratio affects the

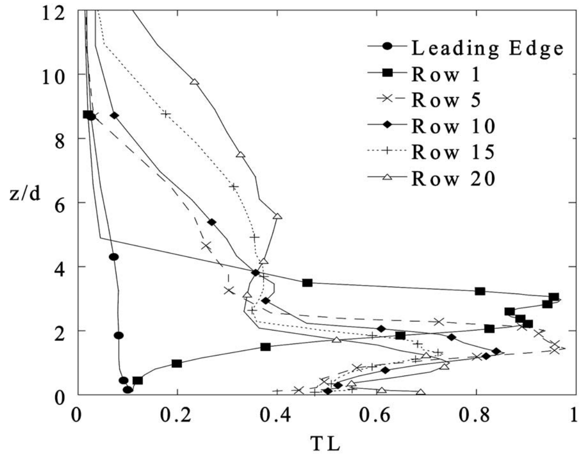

Fig. 8 Turbulence level profiles for $I=25.5$

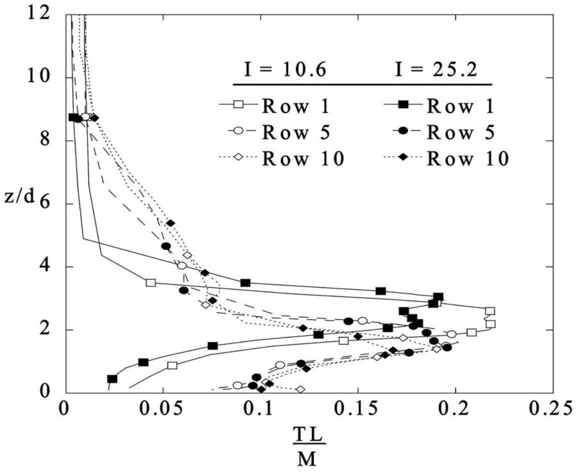

Fig. 10 Turbulence level profiles measured one row downstream of rows 1, 5, and 10 for $I=10.6$ and 25.5. Profiles normalized to the blowing ratio, M.

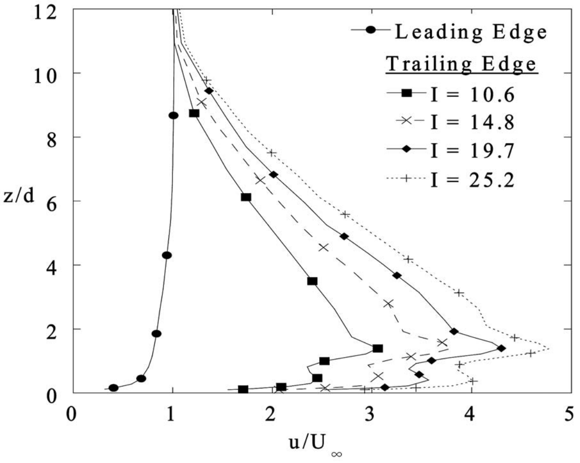

Fig. 11 Streamwise velocity profiles measured one row downstream of row 20

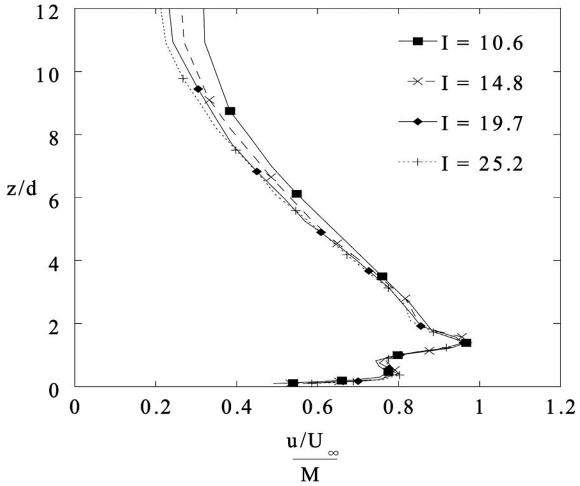

Fig. 13 Streamwise velocities profiles measured one row downstream of row 20. Profiles normalized to the blowing ratio, *M*.

accumulated flow characteristics. The motivation was to establish if the flow profile retained its shape, if the thickness of the film layer was affected, and how the different flow rates affected turbulence transport.

Profiles for a range of momentum flux ratios are shown in Fig. 11 with the corresponding turbulence levels shown in Fig. 12. These profiles were measured downstream of the 20th row of holes, which was considered to be in the fully developed region. The streamwise velocity and turbulence levels scale very well to the mass flux ratio as shown in Figs. 13 and 14 for both the mean velocity as well as for the turbulence levels. Progressing from the wall, the velocity profiles begin to diverge, because of the effects due to interactions with the freestream.

Forth et al. [16] studied film cooling heat transfer parameter scaling for different geometries and flow and thermal conditions. They found that the cooling flow could be divided into “weak injection” and “strong injection” regimes. Strong injection indicated the presence of jet liftoff occurring at $I \approx 0.1$. These researchers found that the velocity ratio best scales heat transfer data in the strong injection regime. The velocity ratio directly corresponds to mass flux ratio with unity density ratio and agrees with the results presented in this paper.

Each blowing ratio creates a velocity profile with a double-peaked nature that the authors believe is an inherent characteristic of the full-coverage effusion plate operating at high blowing ratios. However, this profile shape is highly dependent on the measurement location with respect to the cooling hole. The double-peaked, profile is seen most readily in the range from $x/d=3$ to 5 downstream of the hole center.

The turbulence level profiles indicate complex trends that correspond to distinct regions with respect to the cooling jet. Three peaks in turbulence level can be observed between two adjacent minima. The minima that occurs at $z/d=3$ corresponds to a near-zero streamwise velocity gradient at that location. The peak in turbulence level at $z/d=1$ is consistent with the shear layer at the bottom of the coolant jet and the drop in turbulence in the near wall region at $z/d=0.37$ corresponds to the secondary velocity peak at that location.

Two planes of velocities were measured downstream of the fifteenth row of cooling holes for $I=25.5$. The streamwise velocity plane shown in Fig. 15 gives u and w velocity vectors superimposed on a streamwise velocity contour. Figure 15 shows good streamwise periodicity evidenced by the $z/d=2$ jet penetration height of the row 15 jet as well as the upstream (row 13) jet. It is clear that the cooling jet separated from the test plate surface as it created a recirculation zone extending no farther than one hole diameter from the cooling hole trailing edge. The flow quickly reattached to the wall which caused the second velocity peak that

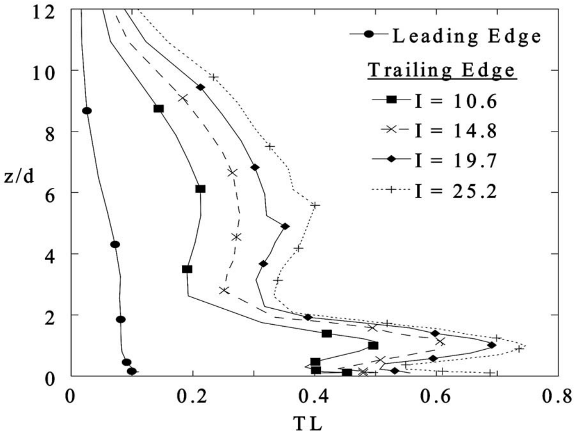

Fig. 12 Turbulence level profiles measured one row downstream of row 20

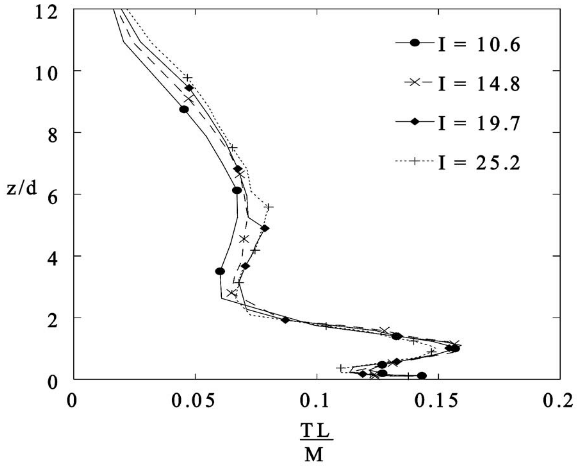

Fig. 14 Turbulence level profiles measured one row downstream of row 20. Profiles normalized to the blowing ratio, *M*.

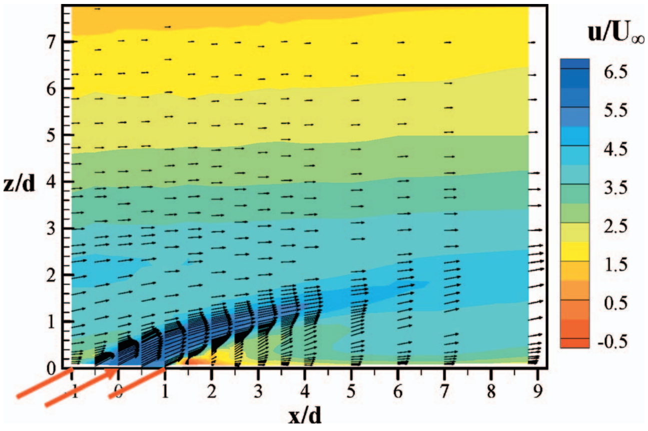

Fig. 15 Streamwise velocity contours downstream of row fifteen for $I=25.5$. Vectors show streamwise and wall-normal velocity components. Arrow indicates row 15 cooling hole.

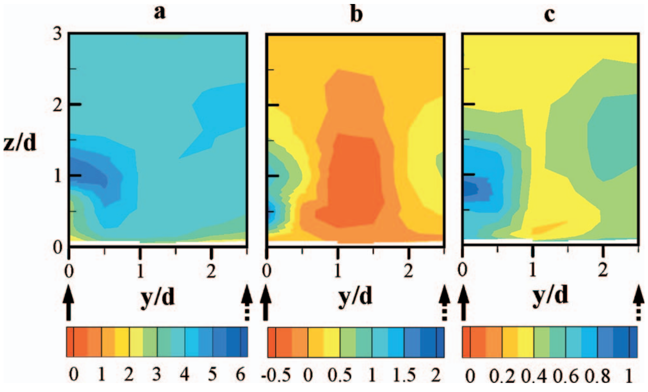

Fig. 17 Cross-sectional, plane $x/d=3$ downstream of row 15 showing (*a*) streamwise velocity, u/U_∞; (*b*) wall-normal velocity, v/U_∞; and (*c*) turbulence levels. Solid arrows indicate row 15 hole location and dashed arrows indicate row 14 hole location.

appears in the mean velocity profiles shown in Fig. 13.

Shown in Fig. 16, the highest turbulence level in the flow field was 115%, found downstream of the location in the jet shear layer where the local velocity was 3.2 times the local mainstream velocity. It should be noted that the extremely high turbulence levels were due to the higher streamwise mean and fluctuating velocities in the cooling layer being normalized to the much lower local freestream velocity. As shown in Fig. 16, the turbulence levels in the bottom shear layer of the jet were generally higher than the top shear layer indicating higher velocity gradients near the wall. The coolant jet core exiting the hole had turbulence levels between 45% and 50%.

Figures 17(*a*)–17(*c*) show a plane normal to the streamwise direction with contours of streamwise velocity, wall-normal velocity, and turbulence levels. The appearance of a counter-rotating vortex is shown through the contours of the streamwise and wall-normal velocities. The primary peak in the streamwise velocity is formed into a kidney shape near the outer edges of the jet. Figure 17(*c*) clearly shows that the peak turbulence is located below the highest streamwise velocity gradients. Also seen in Fig. 17(*c*) is the turbulence convecting downstream from the adjacent cooling holes.

Cooling Effectiveness Results. Adiabatic effectiveness measurements were made on the effusion test plate for cases $I=10.6$ and 25.5 in the region shown in Fig. 2. This region was chosen to capture the cooling characteristics of all 20 rows of cooling holes. The measurement region captured six columns of cooling holes located at the midpitch of the test plate. Conditions were found to be pitchwise periodic over the measurement region as shown in Fig. 18.

Contours of the adiabatic effectiveness shown in Fig. 18 show a slight improvement in cooling effectiveness at $I=25.5$ relative to $I=10.6$. The cooling effectiveness trends showed similarities to the film flow profiles. Since there was a difference in effectiveness levels at the 19th and 20th rows, however, it is evident that a thermally fully-developed condition is not reached at the same location the velocity field becomes fully developed. This is in spite of the asymptotic behavior of the adiabatic effectiveness for both blowing ratios.

Lateral averages of the adiabatic effectiveness show the exact same cooling behavior for the first three rows of holes. Similar trends for both blowing ratios were seen downstream of the third cooling row, with a slightly improved cooling effectiveness at $I=25.5$, shown in Fig. 19.

It can also be seen from the contours and the lateral averages that there is conduction upstream of the test plate, evidenced by

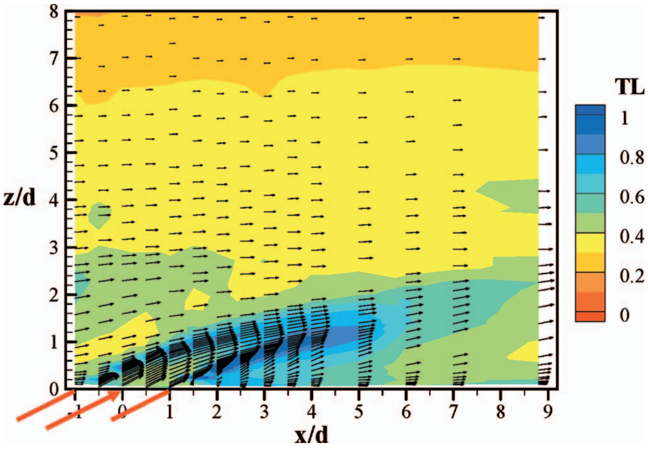

Fig. 16 Turbulence levels with vectors for $I=25.5$ showing streamwise and wall-normal velocity components. Arrow indicates row 15 cooling hole.

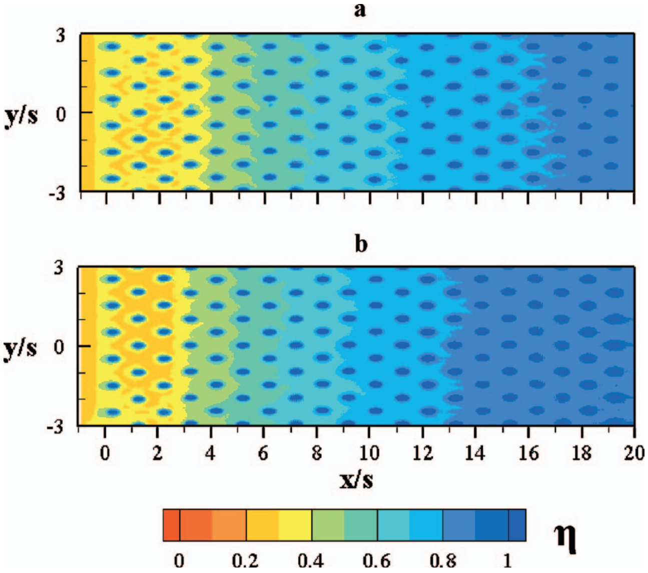

Fig. 18 Adiabatic effectiveness contours of the effusion panel from rows 1 to 20 for (*a*) $I=10.6$ and (*b*) $I=25.5$

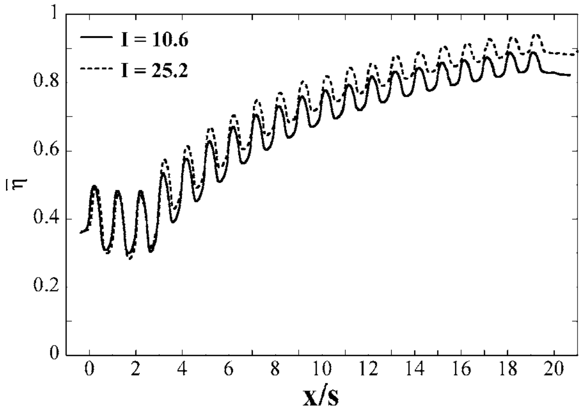

Fig. 19 Lateral average of adiabatic effectiveness of the effusion panel from rows 1 to 20 for I=10.6 and I=25.5. Note that x/s=0 is the leading edge of the first hole row.

the nonzero effectiveness levels at the leading edge. This conduction can be explained by the fact that the cooling holes are cooling the plate through convection within the holes. Also interesting about the contours and the lateral averages is the fact that there is an actual decrease in the adiabatic effectiveness levels near $x/D = 10$ before an increase can be seen. The reason for this decrease is because the jet penetration heights were very high at the leading edge of the plate, as was indicated by the velocity profiles. Moreover, these jets entrained hot mainstream flow to the surface by the longitudinal vortices, resulting in negative wall-normal velocities, revealed in Fig. 17(*b*). Furthermore, the rate of hot mainstream entrainment for the first three hole rows was the same for both blowing ratios, indicated by the identical cooling behavior shown in Fig. 19. The penetration heights at the leading edge did not allow the coolant to effectively cool the plate until further downstream where the peak velocities moved closer to the wall.

Conclusions

An effusion cooling scheme was investigated through flow-field measurements and adiabatic wall temperatures. A range of blowing ratios were considered for the given cooling scheme for a design that contained 20 rows of cooling holes with equally spaced holes in both the streamwise and pitchwise directions.

The results of this study indicate that full-coverage effusion cooling develops into a fully-developed velocity profile at a nominal location of 15 film-cooling hole rows. The jet penetration for the first few rows of film-cooling holes was much higher than that which occurred for the fully-developed condition. The penetration height for the cooling hole rows was independent of the momentum flux ratio for the range that was considered at the fully-developed condition.

The most interesting aspect of the results was the indication that for an effusion cooling hole design, such as that considered in these tests, the streamwise velocity, and turbulence level profiles scale exactly with the blowing ratio. This scaling effect was found to hold at all measurement locations and all blowing ratios. This finding allows the profile shape and magnitude to be readily determined.

The velocity planes that were measured indicated jet separation just downstream of the hole trailing edge and the existence of the commonly reported counter-rotating vortex which serves to entrain hot mainstream flow toward the surface at the plate leading edge. Downstream, however, this effect serves to mix the accumulated coolant flow and provide a more uniform surface temperature across the pitch.

The cooling effectiveness of the film layer increased asymptotically at the same rate for both blowing ratios with only little improvement for the higher blowing ratio relative to the lower blowing ratio.

Acknowledgment

The authors gratefully acknowledge United Technologies—Pratt & Whitney for their support of this work.

Nomenclature

C_d = discharge coefficient
d = film cooling hole diameter
H_{in} = combustor inlet height
I = momentum flux ratio, $I = \rho_c U_c^2 / \rho_\infty U_\infty^2$
L = film cooling hole length
$\dot{\mathbf{m}}$ = mass flow rate
M = mass flux ratio, $M = \rho_c U_c / \rho_\infty U_\infty$
S_s, S_p = streamwise, pitchwise film cooling hole spacing
t = test plate wall thickness
T = temperature
TL = turbulence level, $\text{TL} = \sqrt{0.5((u_{\text{rms}}^2 + w_{\text{rms}}^2))} / U_\infty$
u, v, w = local, mean velocity components
U_{in} = test section inlet velocity
x, y, z = coordinate system shown in Fig. 2
W = test section inlet width

Greek symbols

α = inclination angle of cooling hole
∂ = uncertainty
ρ = density
ν = kinematic viscosity
η = adiabatic effectiveness, $h = (T_\infty - T_{\text{adiabatic}}) / (T_\infty - T_c)$

Subscripts

adiabatic = adiabatic surface
c = coolant conditions (secondary flow)
∞ = local freestream conditions (primary flow)
rms = root mean square of fluctuating velocity
s = test plate surface

Superscripts

$\bar{\eta}$ = laterally averaged adiabatic effectiveness

References

[1] Andrews, G. E., Asere, A. A., Gupta, M. L., and Mkpadi, M. C., 1985, "Full Coverage Discrete Hole Film Cooling: The Influence of Hole Size," ASME 85-GT-47.
[2] Andrews, G. E., Alikhanizadeh, M., Tehrani, F. B., Hussain, C. I., and Azari, M. S. K., 1987, "Small Diameter Film Cooling Holes: Influence of Hole Size and Pitch," ASME 87-HT-28.
[3] Andrews, G. E., Khalifa, I. M., Asere, A. A., and Bazdidi-Tehrani, F., 1995, "Full Coverage Effusion Film Cooling with Inclined Holes," ASME 95-GT-274.
[4] Lin, Y., Song, B., Li, B., Liu, G., and Wu, Z., 2003, "Investigation of Film Cooling Effectiveness of Full-Coverage Inclined Multihole Walls with Different Hole Arrangements," ASME GT2003-38881.
[5] Martiny, M., Schulz, A., and Witting, S., 1995, "Full-Coverage Film Cooling Investigations: Adiabatic Wall Temperatures and Flow Visualization," ASME 95-WA/HT-4.
[6] Sasaki, M., Takahara, K., Kumagai, T., and Hamano, M., 1979, "Film Cooling Effectiveness for Injection from Multirow Holes," ASME J. Eng. Power **101**, pp. 101–108.
[7] Harrington, M., McWaters, M., Bogard, D., Lemmon, C., and Thole, K. A., 2001, "Full-Coverage Film Cooling with Short Normal Injection Holes," J. Turbomach. **123**, pp. 798–805.
[8] Fric, T., Campbell, R., and Rettig, M., 1997, "Quantitative Visualization of Full-Coverage Discrete-Hole Film Cooling," ASME 97-GT-328.
[9] Bazdidi-Tehrani, F., and Andrews, G., 1997, "Full Coverage Discrete Hole Film Cooling: Investigation of the Effect of Variable Density Ratio (Part II)," ASME 97-GT-341.
[10] Pietrzyk, J. R., Bogard, D. G., and Crawford, M. E., 1990, "Effects of Density Ratio on the Hydrodynamics of Film Cooling," J. Turbomach. **112**, pp. 437–443.

[11] Barringer, M. D., Richard, O. T., Walter, J. P., Stitzel, S. M., and Thole, K. A., 2002, "Flow Field Simulations of a Gas Turbine Combustor," J. Turbomach. **124**, pp. 508–516.
[12] Moffat, J. R., 1988, "Describing the Uncertainties in Experimental Results," Exp. Therm. Fluid Sci. **1**, pp. 3–17.
[13] Pietrzyk, J. R., 1989, "Experimental Study of the Interaction of Dense Jets With a Crossflow for Gas Turbine Applications," Ph.D. dissertation, University of Texas at Austin, Austin, TX.
[14] Pietrzyk, J. R., Bogard, D. G., and Crawford, M. E., 1989, "Hydrodynamics Measurements of Jets in Crossflow for Gas Turbine Film Cooling Applications," J. Turbomach. **111**(2), pp. 139–145.
[15] Lee, S. W., Lee, J. S., and Ro, S. T., 1994, "Experimental Study on the Flow Characteristics of Streamwise Inclined Jets in Crossflow on Flat Plate," J. Turbomach. **116**, pp. 97–105.
[16] Forth, C. J. P., and Jones, T. V., 1986, "Scaling Parameters in Film-Cooling," Proceedings of the 8th International Heat Transfer Conference, pp. 1271–1276.

Y. B. Suzen
Assistant Professor
Department of Mechanical Engineering and
Applied Mechanics,
North Dakota State University,
Fargo, ND 58105

P. G. Huang
Professor and Chair
Mechanical and Materials Engineering
Department,
Wright State University,
Dayton, OH 45435

D. E. Ashpis
Aerospace Engineer
Mem. ASME
NASA Glenn Research Center at Lewis Field,
Cleveland, OH 44135

R. J. Volino
Associate Professor
Mem. ASME
Department of Mechanical Engineering,
United States Naval Academy,
Annapolis, MD 21402-5042

T. C. Corke
Clark Chair Professor
Fellow ASME

F. O. Thomas
Professor
Mem. ASME

J. Huang
Graduate Assistant

Department of Aerospace and Mechanical
Engineering,
Center for Flow Physics and Control,
University of Notre Dame,
Notre Dame, IN 46556

J. P. Lake
Special Projects Flight Commander,
586th FLTS/DON,
Holloman AFB, NM 88330

P. I. King
Professor
Mem. ASME
Department of Aeronautics and Astronautics,
Air Force Institute of Technology,
Wright-Patterson AFB, OH 45433

A Computational Fluid Dynamics Study of Transitional Flows in Low-Pressure Turbines Under a Wide Range of Operating Conditions

A transport equation for the intermittency factor is employed to predict the transitional flows in low-pressure turbines. The intermittent behavior of the transitional flows is taken into account and incorporated into computations by modifying the eddy viscosity, μ_t, with the intermittency factor, γ. Turbulent quantities are predicted by using Menter's two-equation turbulence model (SST). The intermittency factor is obtained from a transport equation model which can produce both the experimentally observed streamwise variation of intermittency and a realistic profile in the cross stream direction. The model had been previously validated against low-pressure turbine experiments with success. In this paper, the model is applied to predictions of three sets of recent low-pressure turbine experiments on the Pack B blade to further validate its predicting capabilities under various flow conditions. Comparisons of computational results with experimental data are provided. Overall, good agreement between the experimental data and computational results is obtained. The new model has been shown to have the capability of accurately predicting transitional flows under a wide range of low-pressure turbine conditions.
[DOI: 10.1115/1.2218888]

1 Introduction

The process of transition from laminar to turbulent flow is a major unsolved problem in fluid dynamics and aerodynamics. One area where the transition process plays an important role and is even more complicated due to the diverse flow conditions encountered is the low-pressure turbine applications. Transitional flows in these applications are affected by several factors such as varying pressure gradients, wide range of Reynolds number and freestream turbulence variations, flow separation, and unsteady wake-boundary layer interactions. Accurate simulation and prediction of transitional flows under these diverse conditions is key

---

Contributed by the Turbomachinery Division of ASME for publication in the JOURNAL OF TURBOMACHINERY. Manuscript received February 14, 2004; final manuscript received February 13, 2006. Review conducted by R. L. Davis.

to design of more efficient jet engines.

In low-pressure turbine applications, flow over the blades is mostly turbulent at the high Reynolds number conditions encountered at takeoff and the efficiency is at its design maximum. However, at lower Reynolds number conditions which correspond to high altitudes and cruise speeds the boundary layers on the airfoil surface have a tendency to remain laminar; hence, the flow may separate on the suction surface of the turbine blades before it becomes turbulent. This laminar separation causes unpredicted losses, substantial drops in efficiency, and increase in fuel consumption [1–3].

In order to calculate the losses and heat transfer on various components of gas turbine engines, and to be able to improve component efficiencies and reduce losses through better designs, accurate prediction of development of transitional boundary layers is essential [1].

One approach proven to be successful for modeling transitional flows is to incorporate the concept of intermittency into computations. This can be done by multiplying the eddy viscosity obtained from a turbulence model, μ_t, used in the diffusive parts of the mean flow equations, by the intermittency factor, γ (Simon and Stephens [4]). This method can be easily incorporated into any Reynolds averaged Navier-Stokes solver. In this approach, the intermittency factor, γ, can be obtained from an empirical relation such as the correlation of Dhawan and Narasimha [5], or it can be obtained from a transport model.

Dhawan and Narasimha [5] correlated the experimental data and proposed a generalized intermittency distribution function across flow transition. Gostelow et al. [6] extended this correlation to flows with pressure gradients under the effects of a range of freestream turbulence intensities. Solomon et al. [7], following the work of Chen and Thyson [8], developed an improved method to predict transitional flows involving changes in pressure gradients. These empirical methods led to development of transport equations for intermittency.

Steelant and Dick [9] proposed a transport equation for intermittency, in which the source term of the equation is developed such that the γ distribution of Dhawan and Narasimha [5] across the transition region can be reproduced. Steelant and Dick used their model, coupled with two sets of conditioned Navier-Stokes equations, to predict transitional flows with zero, favorable, and adverse pressure gradients. However, since their technique involved the solution of two sets of strongly coupled equations, the method is not compatible with existing computational fluid dynamics (CFD) codes, in which only one set of Navier-Stokes equations is involved. Moreover, the model was designed to provide a realistic streamwise γ behavior but with no consideration of the variation of γ in the cross-stream direction.

Cho and Chung [10] developed a k-ε-γ turbulence model for free shear flows. Their turbulence model explicitly incorporates the intermittency effect into the conventional k-ε model equations by introducing an additional transport equation for γ. They applied this model to compute a plane jet, a round jet, a plane far wake, and a plane mixing layer with good agreement. Although this method was not designed to reproduce flow transition, it provided a realistic profile of γ in the cross-stream direction.

Suzen and Huang [11] developed an intermittency transport equation combining the best properties of Steelant and Dick's model and Cho and Chung's model. The model reproduces the streamwise intermittency distribution of Dhawan and Narasimha [5] and also produces a realistic variation of intermittency in the cross-stream direction. This model has been validated against European Research Community On Flow Turbulence And Combustion (ERCOFTAC) benchmark T3-series experiments reported by Savill [12,13], low-pressure turbine experiments of Simon et al. [14], and separated and transitional boundary layer experiments of Hultgren and Volino [15] with success [11,16–21].

In this paper we concentrate on prediction of three recent low-pressure turbine experiments on the Pratt and Whitney's Pack B blade under low Reynolds number conditions using the transport model for intermittency. Due to the fact that the Pack B blade is very sensitive to changes of flow conditions, it is an ideal test blade for validating the transition/turbulence models. The three sets of experiments considered are conducted by Lake et al. [3,22], Huang et al. [23], and Volino [24] at three independent facilities. These experiments provide an extensive database for investigating transitional flows under low-pressure turbine conditions and are employed as benchmark cases for further testing of the predicting capabilities of the current intermittency model. A summary of the experiments are given in the next section. In Sec. 3, the intermittency transport model is presented and implementation of the model and the empirical correlations employed for the onset of transition are described. In Sec. 4, the predictions of the new intermittency model are compared against the experimental data. Conclusions are provided in Sec. 5.

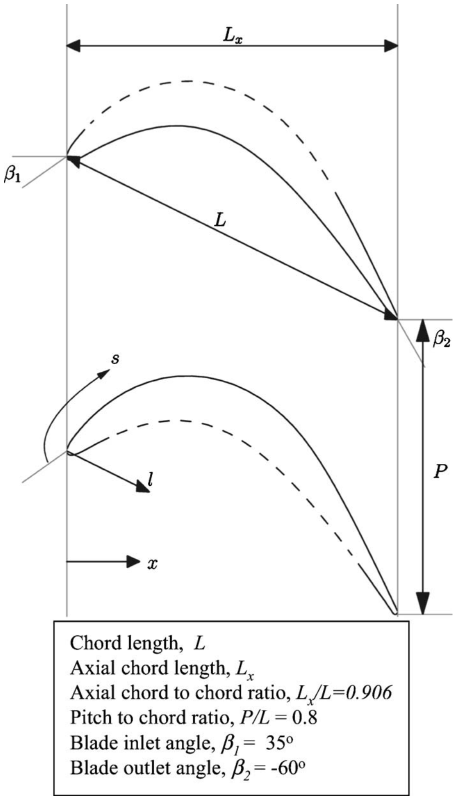

Fig. 1 P&W Pack B blade cascade details

2 Low-Pressure Turbine Experiments

In this paper, we concentrate on computation of three sets of low-pressure turbine experiments using the intermittency transport model. These experiments are conducted by Lake et al. [3,22], Huang et al. [23], and Volino [24]. In these experiments Pratt and Whitney's Pack B blade is used; the details of the blade are shown in Fig. 1. Overall, these experiments cover a Reynolds number range from 10,000 to 172,000 and the freestream turbulence intensity ranges from 0.08% to 4%. The cases and data used for comparison in this paper are summarized in Table 1. In the following sections details of these experimental efforts are given.

2.1 Pack B Blade Cascade Experiments of Lake et al. [3,22]. Lake et al. [3,22] conducted experiments on the Pack B blade in order to identify methods for reducing separation losses on low-pressure turbine blades under low Reynolds number conditions. In the experiments, they investigated flows at low Reynolds numbers of 43,000, 86,000, and 172,000 based on inlet

Table 1 Details of the experiments used for comparison with computations

Source	Test Section	C_x (m)	Re ($U_{\text{in}}C_x/\nu$)	FSTI (%)	Data used for Comparison
Lake et al. [3,22]	P&W Pack B cascade	0.1778	86,000	1 & 4	C_p distribution
			172,000	1 & 4	C_p distribution
Huang et al. [23]	P&W Pack B cascade	0.1595	10,000	0.08	C_p distribution
			25,000	0.08	C_p distribution
			50,000	0.08, 1.6, 2.85	C_p distribution, velocity profiles[a]
			75,000	0.08, 1.6, 2.85	C_p distribution, velocity profiles[a]
			100,000	0.08, 1.6, 2.85	C_p distribution, velocity profiles[a]
Volino [24]	P&W Pack B single passage	0.1537	10,291	0.5	C_p distribution, velocity profiles
			20,581	0.5	C_p distribution, velocity profiles
			41,162	0.5	C_p distribution, velocity profiles
			82,324	0.5	C_p distribution, velocity profiles

[a] Velocity profiles are available for FSTI=0.08% and 2.85% from experiments.

velocity and axial chord and freestream turbulence intensities (FSTI) of 1% and 4%. These conditions are similar to those encountered at high-altitude, low-speed flight of reconnaissance unmanned aerial vehicles used by USAF.

In Lake's experiments, surface pressure coefficients, boundary layer velocity, and turbulence profiles, total pressure loss data were obtained at FSTI=1% and FSTI=4%. The test setup shown in Fig. 2 included eight blades with axial chord of 0.1778 m (7 in.), and blade spacing of 0.1575 m (6.2 in.). The blades were numbered 1 through 8 starting from the inside bend. Boundary layer measurements were taken on blade 5 and surface pressures were measured around blades 4 and 6. In this paper, the Pack B blade experiments with Reynolds numbers of 86,000 and 172,000 and freestream turbulence intensities of 1% and 4% are computed and comparison of pressure distributions between experiments and computations are performed.

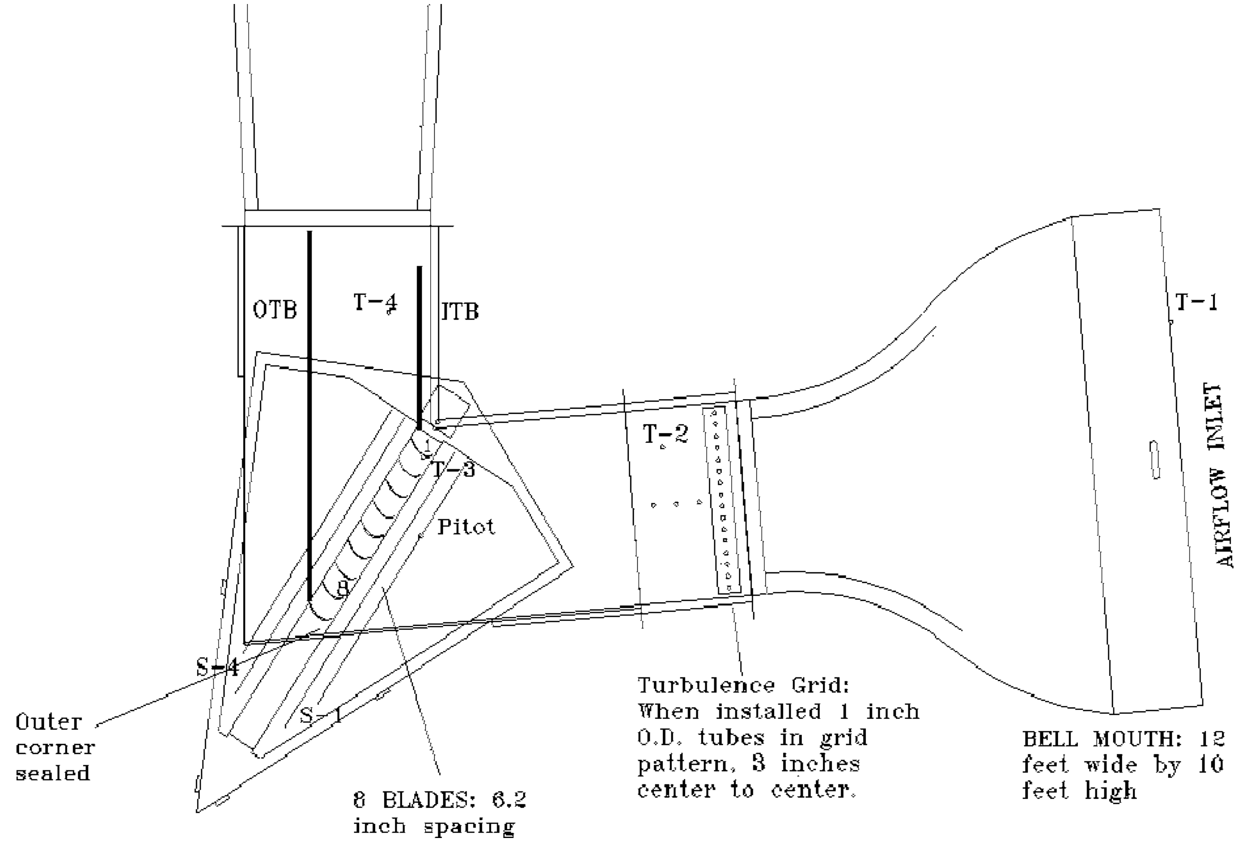

Fig. 2 Experimental setup used by Lake et al. [3,22]

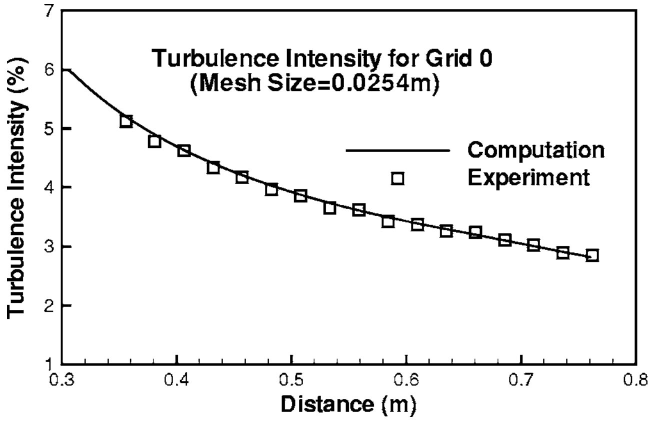

Fig. 3 Comparison of computed and experimental decay of turbulence for experiments of Huang et al. [23], with grid 0

2.2 Pack B Blade Cascade Experiments of Huang et al. [23]. Huang et al. [23] conducted experiments on Pack B blade cascade for a range of Reynolds numbers and turbulence intensities. The Reynolds numbers range from 10,000 to 100,000 based on inlet velocity and axial chord as listed in Table 1. In their experiments the blades had an axial chord length of 0.1595 m (6.28 in.). The freestream turbulence intensity in the tunnel was measured as 0.08%. In order to increase the turbulence intensity, two grids with different mesh sizes were used. One of the grids had the mesh size of 0.0254 m (denoted as grid 0) and the other had 0.008 m (denoted as grid 3). The decay of turbulence after the grids was measured using crosswire and they are shown in Figs. 3 and 4 along with the computed results for grid 0 and grid 3, respectively. The grids were movable in the tunnel so that the turbulence level of the flow that reaches the blades could be controlled by moving the grid that is, by increasing or decreasing the distance between the grid and the blade. Experiments were performed for Reynolds numbers 50,000, 75,000, and 100,000, with grids placed 0.762 m (30 in.) away from the blade leading edge, corresponding to turbulence intensities of 2.85% and 1.6% at the leading edge for grid 0 and grid 3, respectively. For Re $=100{,}000$, grid 0 is placed at 0.5588 m (22 in.) and 0.3556 m (14 in.), corresponding to turbulence intensities of 3.62% and 5.2%, respectively. Pressure coefficient data are available for all cases and detailed boundary layer measurements are available for Re=50,000, 75,000, and 100,000 with FSTI=0.08% and 2.85% cases. The cases and data used for comparisons in this paper are listed in Table 1.

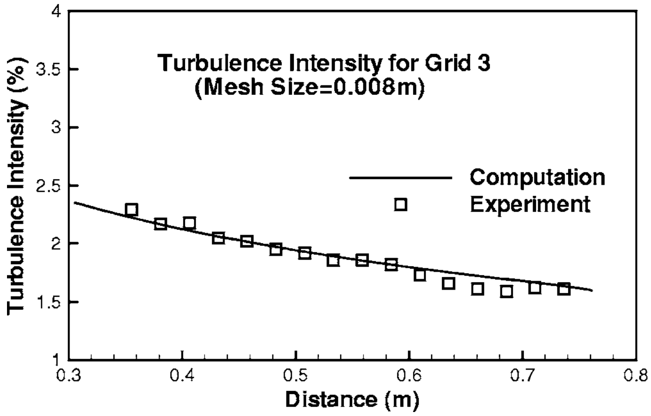

Fig. 4 Comparison of computed and experimental decay of turbulence for experiments of Huang et al. [23], with grid 3

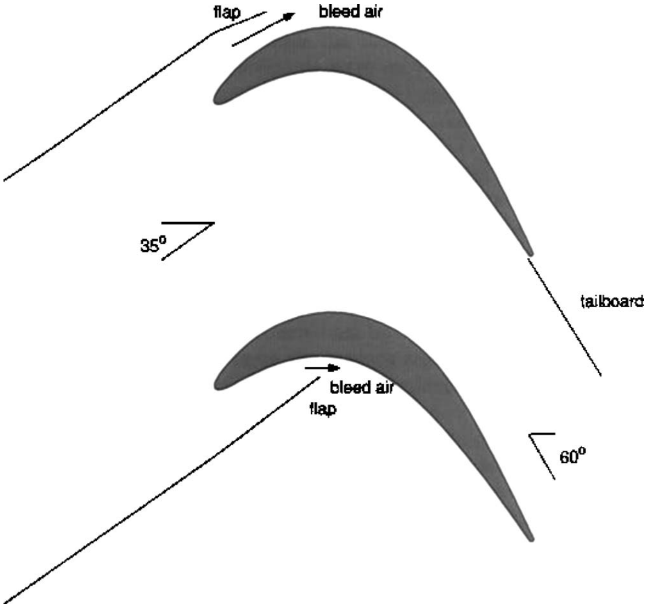

Fig. 5 Schematic of the test section for experiments of Volino [24]

2.3 Pack B Experiments of Volino [24]. Volino [24] investigated the boundary layer separation, transition, and reattachment under low-pressure turbine airfoil conditions. The experiments included five different Reynolds numbers ranging between 10,291 and 123,492 and freestream turbulence intensities of 0.5% and 9%. The test section consisted of a single passage between two Pack B blades as shown in Fig. 5. The axial chord length of the blades was 0.1537 m (6.05 in.). There are flaps located upstream of each blade to control the amount of bleed air allowed to escape from the passage. These flaps were adjusted by matching measured pressure distribution for a high Reynolds number with the inviscid pressure distribution on the blade. In addition to the upstream bleed flaps, a tailboard on the pressure side was used to set the pressure gradient. The compiled data include pressure surveys, mean and fluctuating velocity profiles, intermittency profiles, and turbulent shear stress profiles. It was observed that the effect of high Reynolds number or high freestream turbulence level was to move transition upstream. Transition started in the shear layer over the separation bubble and led to rapid boundary layer reattachment. At the lowest Re case, transition did not take place before the trailing edge and the boundary layer did not reattach. The beginning of transition corresponded to the beginning of a significant rise in the turbulent shear stress. These experimental results provide detailed documentation of the boundary layer and extend the existing database to lower Reynolds numbers. The cases used for comparisons with computations in this paper are listed in Table 1 along with the type of data used for comparisons.

3 Intermittency Transport Model

In this section, the transport model for intermittency is presented. The model combines the transport equation models of Steelant and Dick [9] and Cho and Chung [10]. Details of the development and implementation of the transport model are given in Suzen and Huang [11,16,17], and in Suzen et al. [18].

The model equation is given by

$$\frac{\partial \rho\gamma}{\partial t}+\frac{\partial \rho u_j\gamma}{\partial x_j} = (1-\gamma)\left[\begin{array}{l}(1-F)2C_0\rho\sqrt{u_k u_k} f(s) f'(s) \\ +F\left(\dfrac{C_1\gamma}{k}\tau_{ij}\dfrac{\partial u_i}{\partial x_j}-C_2\gamma\rho\dfrac{k^{3/2}}{\varepsilon}\dfrac{u_i}{(u_k u_k)^{1/2}}\dfrac{\partial u_i}{\partial x_j}\dfrac{\partial \gamma}{\partial x_j}\right)\end{array}\right] + C_3\rho\frac{k^2}{\varepsilon}\frac{\partial \gamma}{\partial x_j}\frac{\partial \gamma}{\partial x_j} + \frac{\partial}{\partial x_j}\left(((1-\gamma)\gamma\sigma_{\gamma l}\mu+(1-\gamma)\sigma_{\gamma t}\mu_t)\frac{\partial \gamma}{\partial x_j}\right) \tag{1}$$

The distributed breakdown function, $f(s)$ has the form

$$f(s)=\frac{as'^4+bs'^3+cs'^2+ds'+e}{gs'^3+h} \tag{2}$$

where $s'=s-s_t$, and s is the distance along the streamline coordinate, and s_t is the transition location. The coefficients are

$$a=50\sqrt{\frac{n\sigma}{U}} \quad b=-0.4906$$

$$c=0.204\left(\frac{n\sigma}{U}\right)^{-0.5} \quad d=0.0 \quad e=0.04444\left(\frac{n\sigma}{U}\right)^{-1.5}$$

$$h=10e \quad g=50 \tag{3}$$

The shear stresses are defined as

$$\tau_{ij}=\mu_t\left[\frac{\partial u_i}{\partial x_j}+\frac{\partial u_j}{\partial x_i}-\frac{2}{3}\frac{\partial u_k}{\partial x_k}\delta_{ij}\right]-\frac{2}{3}\rho k\delta_{ij} \tag{4}$$

The blending function F is constructed using a nondimensional parameter $k/W\nu$, where k is the turbulent kinetic energy and W is the magnitude of the vorticity. The blending function has the form

$$F=\tanh^4\left[\frac{k/W\nu}{200(1-\gamma^{0.1})^{0.3}}\right] \tag{5}$$

The model constants used in Eq. (1) are

$$\sigma_{\gamma l}=\sigma_{\gamma t}=1.0 \quad C_0=1.0 \quad C_1=1.6$$

$$C_2=0.16 \quad C_3=0.15$$

The intermittency is incorporated into the computations simply by multiplying the eddy viscosity obtained from a turbulence model, μ_t, by the intermittency factor, γ. Simon and Stephens [4] showed that, by combining the two sets of conditioned Navier-Stokes equations and making the assumption that the Reynolds stresses in the nonturbulent part are negligible, the intermittency can be incorporated into the computations by using the eddy viscosity, μ_t^* which is obtained by multiplying the eddy viscosity from a turbulence model, μ_t, with the intermittency factor, γ. That is

$$\mu_t^*=\gamma\mu_t \tag{6}$$

is used in the mean flow equations. It must be noted that γ does not appear in the generation term of the turbulent kinetic energy equations.

Computations of the experiments are performed using a recently developed multiblock Navier-Stokes solver, called GHOST. The code was developed at the University of Kentucky, by Huang, and is a pressure-based code based on the SIMPLE algorithm with second-order accuracy in both time and space. Advection terms are approximated by a QUICK scheme and central differencing is used for the viscous terms. The "Rhie and Chow" momentum interpolation method [25] is employed to avoid checkerboard oscillations usually associated with the nonstaggered grid arrangement. This code is capable of handling complex geometries, moving, and overset grids and includes multiprocessor computation capability using message passing interface (MPI). Since multiple processors are used during the computations, it is more efficient to divide the computational domain into several smaller pieces with very fine grids and distribute the zones to processors with the consideration of load balancing. This code has been used extensively in a recent turbulence model validation effort (Hsu et al. [26]) and computations of unsteady wake/blade interaction (Suzen and Huang [27]) conducted at the University of Kentucky.

The multiblock grid systems used in the computations are obtained by conducting a series of grid refinement studies in order to ensure that the details of the flow field are captured accurately and the results are grid independent. All grid systems have first y^+ less than 0.5 near solid walls.

In using this intermittency approach, the turbulence model selected to obtain μ_t must produce fully turbulent features before transition location in order to allow the intermittency to have full control of the transitional behavior. Menter's [28] SST model satisfies this requirement. It produces almost fully turbulent flow in the leading edge of the boundary layer and therefore is used as a baseline model to compute μ_t and other turbulent quantities in the computations [18].

The value of $n\sigma$ used in evaluating the constants given by Eq. (3) is provided by the following correlation for zero-pressure gradient flows [18]

$$\hat{n}\sigma=(nv^2/U^3)\sigma=1.8\times10^{-11}Tu^{7/4} \tag{7}$$

When flows are subject to pressure gradients, the following correlation is used

$$\frac{\hat{n}\sigma}{(\hat{n}\sigma)_{\mathrm{ZPG}}}=\begin{cases}M^{[1-\exp(0.75\times10^6 K_t Tu^{-0.7})]}, & K_t<0\\ 10^{-3227K_t^{0.5985}}, & K_t>0\end{cases} \tag{8}$$

with M defined as

$$M=(850Tu^{-3}-100Tu^{-0.5}+120)$$

where $(\hat{n}\sigma)_{\mathrm{ZPG}}$ is the value for flow at zero pressure gradient and can be obtained from Eq. (7), and $K_t=(\nu/U_t^2)(dU/dx)_t$ is the flow acceleration parameter. The favorable pressure gradient part of the above correlation (for $K_t>0$) is from Steelant and Dick [9]. The portion of the correlation for adverse pressure gradient flows for $K_t<0$ is formulated using the transition data of Gostelow et al. [6] and Simon et al. [14] (Suzen et al. [18]).

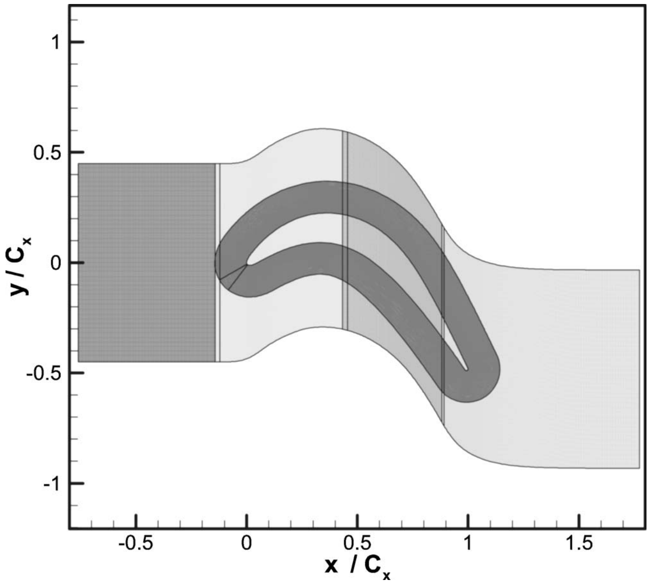

Fig. 6 Multiblock grid used for computations of experiments of Lake et al. [3,22] and FSTI=0.08% experiments of Huang et al. [23]

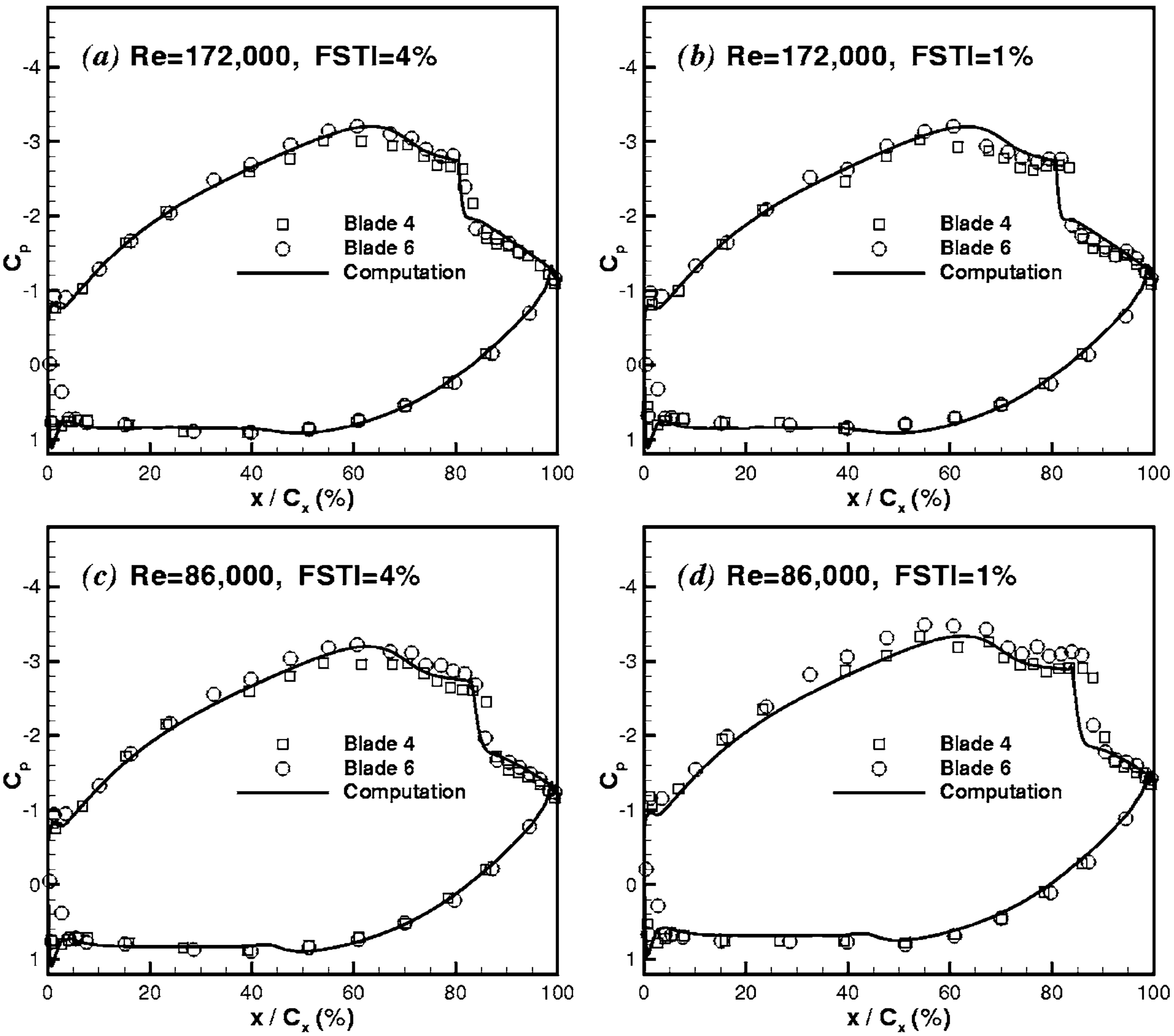

Fig. 7 Comparison of computed pressure coefficient with experiments of Lake et al. [3,22]

The current approach uses the intermittency transport model to obtain the intermittency distribution for the transitional flows, while the onset of transition is defined by correlations.

The onset of attached flow transition is determined by the following correlation in terms of turbulence intensity, Tu, and the acceleration parameter, K_t,

$$\mathrm{Re}_{\theta t} = (120 + 150Tu^{-2/3})\coth[4(0.3 - K_t \times 10^5)] \qquad (9)$$

where K_t was chosen as the maximum absolute value of that parameter in the downstream deceleration region [18]. This correlation maintains the good features of Abu-Ghannam and Shaw [29] correlation in the adverse pressure gradient region, and in addition reflects the fact that the flow becomes less likely to have transition when subject to favorable pressure gradients by rapidly rising as K_t becomes positive.

In order to determine the onset of separated flow transition Re_{st} is expressed in terms of the turbulence intensity (Tu) and the momentum thickness Reynolds number at the point of separation ($\mathrm{Re}_{\theta s}$) in the form [19]

$$\mathrm{Re}_{st} = 874\mathrm{Re}_{\theta s}^{0.71}\exp[-0.4Tu] \qquad (10)$$

This correlation provides a better representation of the experimental data than Davis et al. [30] correlation and is used to predict onset of separated flow transition in the present computations.

4 Results and Discussion

4.1 Simulations of Experiments of Lake et al. [3,22]. The intermittency model is applied to predict the Pack B blade experiments of Lake et al. [3,22]. In the computations, flows at Reynolds numbers of 86,000 and 172,000 based on inlet velocity and axial chord with freestream intensities of 1% and 4% were investigated.

The computations were performed using the grid system shown in Fig. 6 consisting of five zones obtained as a result of a grid refinement study. In the grid refinement study computations were performed on a series of successively finer grids and the variations in the results were observed. The grid shown in Fig. 6 was chosen to be adequate for obtaining grid-independent solutions for all cases. The four zones on which the blade grid is superposed each have 125×225 grid points and the O-type grid around the blade has 401×101 points with first y^+ less than 0.5.

The comparisons of computed and experimental pressure coefficient distributions are shown in Figs. 7(*a*)–7(*d*). In these figures, the experimental distributions correspond to the measurements made on test blades 4 and 6.

The computed results compare well with the experiments for high turbulence intensity, FSTI=4%, cases shown in Figs. 7(*a*) and 7(*c*). However, for FSTI=1% cases shown in Figs. 7(*b*) and

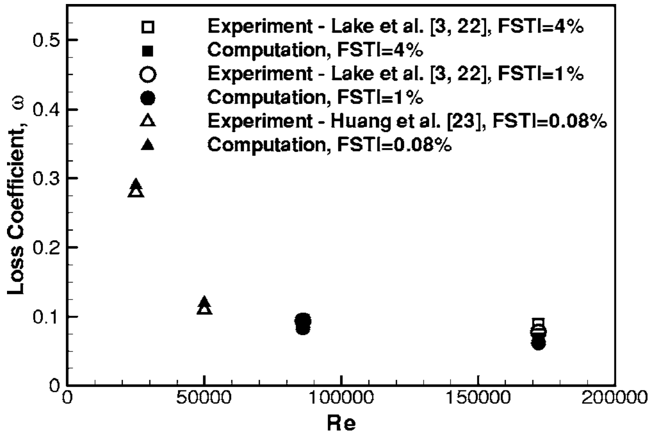

Fig. 8 Comparison of computed total pressure loss coefficients with experiments of Lake et al. [3,22] and Huang et al. [23]

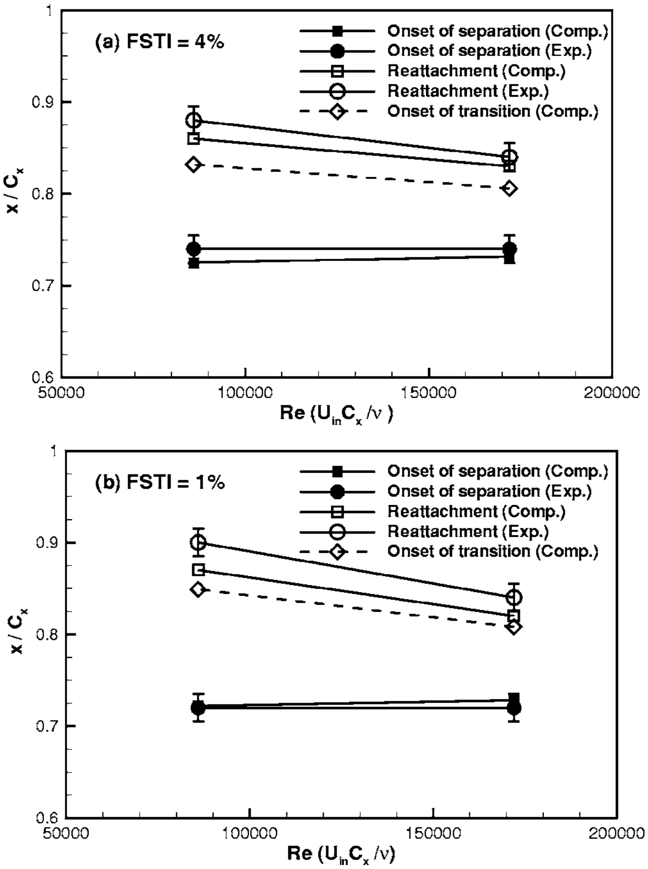

Fig. 9 Comparison of separation, reattachment, and transition locations for experiments of Lake et al. [3,22]

7(*d*), the extent of the separation bubbles is underpredicted in the computations. For example, for Re=86,000, FSTI=1%, shown in Fig. 7(*d*), the flow reattaches earlier in computations than it does in the experiment, as can be observed from the difference in the pressure coefficient distributions between x/C_x=80 to 85%.

The comparison of computed total pressure loss coefficients with experiments is shown in Fig. 8. For the Re=86,000 case, the computed loss coefficient is in good agreement with the experiments for both FSTI levels. However, for the Re=172,000 case the computations underpredicted the loss coefficient compared to experiments for both FSTI=1% and FSTI=4%. From Fig. 8 it is evident that the cascade losses decrease as the Reynolds number increases. This reduction in cascade losses with increasing Reynolds number is due to the decrease in size of the separated flow region on the suction side of the blades.

The onset of separation locations, reattachment locations, and onset of transition locations on the suction surface are summarized in Table 2 for these cases, along with the corresponding values from experiments. In the experiments, the onset of transition locations and the reattachment locations are not reported. The experimental onset of separation and reattachment points are extracted from the experimental pressure coefficient data. The onset of separation is taken to be the axial location where the plateau in the pressure coefficient distribution of the suction side begins, and the reattachment point is taken to be the axial location after the sharp change in C_p following the plateau. This procedure may lead to an error of approximately ±1.5% of axial chord in the estimated onset locations.

The onset of separation, reattachment, and onset of transition locations are plotted against Reynolds number in Figs. 9(*a*) and 9(*b*) for FSTI=4% and 1%, respectively. The uncertainty in the estimated experimental values is indicated by error bars in the figures. For the high turbulence intensity case, computation predicts onset of separation and reattachment slightly upstream of the experiment. For the low FSTI case shown in Fig. 9(*b*), the separation zone is predicted smaller than the experiments. The onset of transition is predicted over the separated flow region in the shear layer. From comparison of these figures it is evident that, with decreasing freestream turbulence intensity, the separation zone becomes larger, and for a given FSTI condition, the separated flow region gets smaller with increasing Reynolds number.

4.2 Simulations of Experiments of Huang et al. [23].

In this set of experiments, first the cases with no grid in tunnel corresponding to FSTI=0.08% are computed. In these computations, the same grid system used for the computations of experiments of Lake et al. [3,22] shown in Fig. 6 is used.

The comparisons of the computed and the experimental pressure coefficients are shown in Figs. 10(*a*)–10(*e*) for Re=100,000, 75,000, 50,000, 25,000, and 10,000 based on inlet velocity and axial chord. The agreement between the experiments and computations is very good for all cases.

The computed total pressure loss coefficients are compared to the available data for Re=25,000 and 50,000 in Fig. 8. The loss coefficients predicted in the computations are 2% to 3% higher compared to the experiments for both Reynolds numbers.

The onset of separation, transition, and reattachment locations are tabulated in Table 3 for all cases and plotted against Reynolds number in Figs. 11(*a*)–11(*c*) for FSTI=0.08%, 1.6%, and 2.85%,

Table 2 Separation, reattachment, and transition locations for cases of Lake et al. [3,22]

Re ($U_{\text{in}}C_x/\nu$)	FSTI (%)	x_s/C_x (Computation)	x_s/C_x (Experiment)	x_r/C_x (Computation)	x_r/C_x (Experiment)	x_{tr}/C_x (Computation)
172,000	4	0.732	0.74	0.83	0.84	0.806
86,000	4	0.725	0.74	0.86	0.88	0.832
172,000	1	0.728	0.72	0.82	0.84	0.808
86,000	1	0.722	0.72	0.87	0.90	0.849

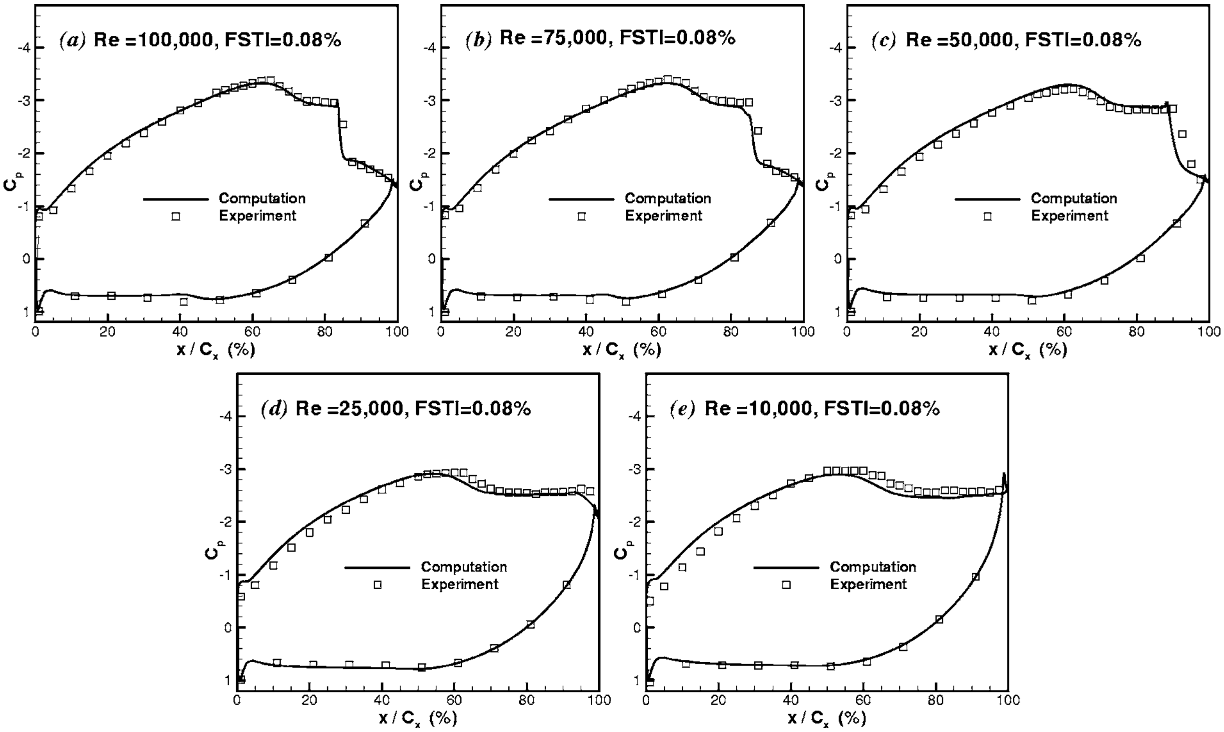

Fig. 10 Comparison of computed pressure coefficients with experiments of Huang et al. [23] for FSTI=0.08% cases

respectively.

Computed velocity profiles at seven axial stations along the suction surface of the blade are compared to the experiments for Re=100,000, 75,000, and 50,000 in Figs. 12–14, respectively.

For the Re=100,000 case, the computed velocity profiles compare very well with the experiment as shown in Figs. 12(*a*)–12(*g*). At the first three measurement stations, flow is laminar and attached as shown in Figs. 12(*a*)–12(*c*). Flow separation takes place at x/C_x=0.725 and the separated flow region is visible in Figs. 12(*d*) and 12(*e*), corresponding to axial locations of x/C_x=0.75 and 0.80. The flow transition and reattachment takes place around x/C_x=0.84 in the computation. Reattachment location is earlier than the experiment which takes place at x/C_x=0.875. In Fig. 12(*f*) corresponding to axial station of x/C_x=0.85 the computed flow field has already attached, although the experimental profile indicates a very small separation zone close to wall. At x/C_x =0.9 the flow is completely attached as shown in Fig. 12(*g*).

When the Reynolds number is reduced to 75,000, the size of the separation bubble increases as can be observed from the comparison of the velocity profiles shown in Figs. 13(*a*)–13(*g*). At this Reynolds number the flow separates around $x/C_x \approx 0.72$ and reattaches around $x/C_x \approx 0.87$. The transition onset location is predicted at x/C_x=0.854. The size of the separation bubble is larger than the Re=100,000 case from comparison of Figs. 13(*d*)–13(*f*) and 12(*d*)–12(*f*).

Next, the Reynolds number is reduced to 50,000 and the comparison of computed and experimental velocity profiles is shown in Figs. 14(*a*)–14(*g*). For this case the separation bubble is much larger from the previous cases and extends until $x/C_x \approx 0.975$ in the experiment and $x/C_x \approx 0.93$ in the computations, as can be seen in Figs. 14(*d*)–14(*g*). Computations predicted the transition onset location at x/C_x=0.89. In the computations, the onset of separation is predicted well in agreement with experiment; however, the reattachment point is earlier, making the size of the separation bubble smaller when compared to experiment. This is evident from the comparison of velocity profiles at the last two stations shown in Figs. 14(*f*) and 14(*g*).

The onset of separation and reattachment points for FSTI =0.08% cases is predicted upstream of the experiments as shown in Fig. 11(*a*).

Next, the high FSTI cases are computed using the six zone multiblock grid system shown in Fig. 15. The computational domain is extended upstream of the blade in order to specify the correct turbulence intensity at the inlet and to match the decay of

Table 3 Separation, reattachment, and transition locations for cases of Huang et al. [23]

Re ($U_{\text{in}}C_x/\nu$)	FSTI (%)	x_s/C_x (Computation)	x_s/C_x (Experiment)	x_r/C_x (Computation)	x_r/C_x (Experiment)	x_{tr}/C_x (Computation)
10,000	0.08	0.661	0.725	⋯	⋯	⋯
25,000	0.08	0.656	0.725	0.980	⋯	0.936
50,000	0.08	0.714	0.725	0.925	0.975	0.890
75,000	0.08	0.718	0.725	0.860	0.870	0.854
100,000	0.08	0.725	0.725	0.840	0.875	0.840
50,000	1.6	0.722	0.728	0.900	0.900	0.854
75,000	1.6	0.728	0.730	0.867	0.875	0.834
100,000	1.6	0.732	0.730	0.860	0.877	0.821
50,000	2.85	0.728	0.722	0.887	0.900	0.837
75,000	2.85	0.732	0.729	0.840	0.870	0.816
100,000	2.85	0.735	0.734	0.842	0.850	0.806

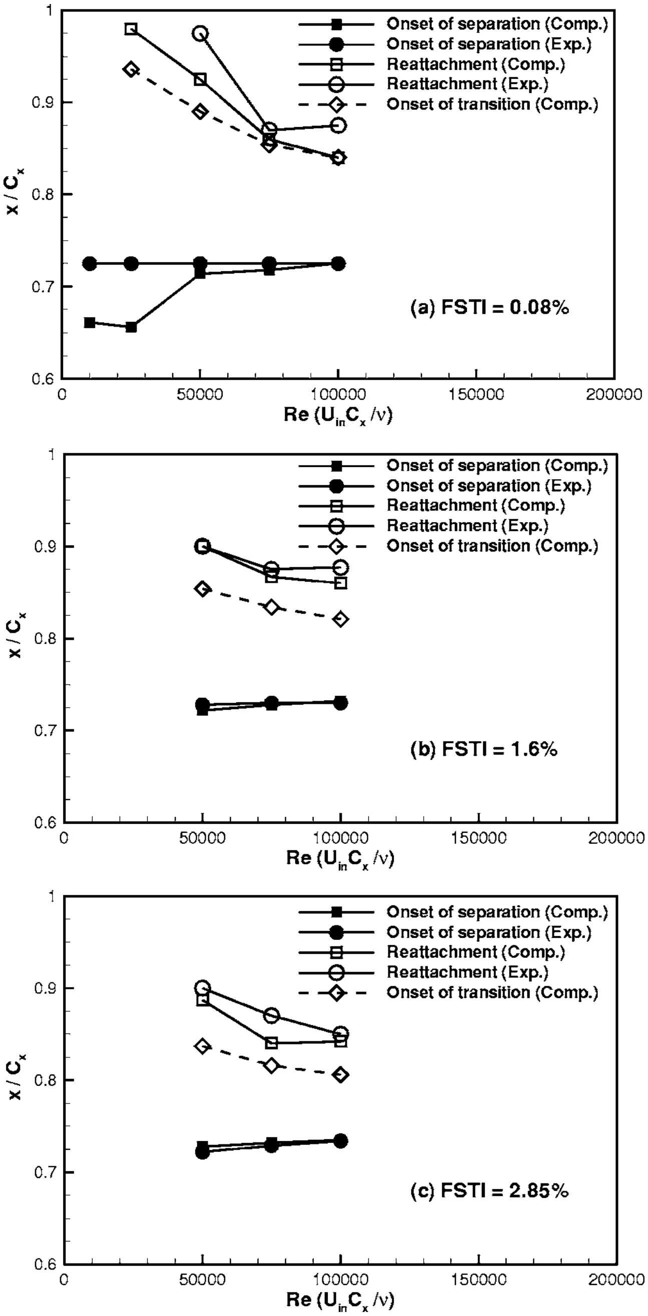

Fig. 11 Comparison of separation, reattachment, and transition locations for experiments of Huang et al. [23]

turbulence that reaches the blade. The matched computed and experimental turbulence decays are shown in Figs. 3 and 4 for grid 0 and grid 3, respectively. The cases considered have the grids placed 0.762 m (30 in) upstream of the blade, corresponding to turbulence intensities of 2.85% and 1.6% for grid 0 and grid 3, respectively.

The comparison of the computed and the experimental pressure coefficient distributions for Re=50,000, 75,000, and 100,000 for FSTI=2.85% cases is shown in Fig. 16. The agreement is very good between computations and experiments.

Comparisons of computed velocity profiles with the experiments for Re=100,000 are given in Figs. 17(*a*)–17(*g*). In this case, the flow separates around $x/C_x \approx 0.74$ and reattaches at $x/C_x \approx 0.85$. The onset of transition is predicted at $x/C_x = 0.806$. The computed size and extent of the separation bubble is in good agreement with the experiment as tabulated in Table 3 and as can be seen in Figs. 11(*c*) and 16(*d*)–16(*f*).

For the lower Reynolds number of 75,000, computed velocity profiles are compared with the experiments in Figs. 18(*a*)–18(*g*). The agreement between experiment and computation is good prior to the reattachment as shown in Figs. 18(*a*)–18(*e*). There is a discrepancy in the reattachment region. The flow separation takes place around $x/C_x \approx 0.73$ and reattaches at $x/C_x \approx 0.87$ according to the experiment, whereas computation predicts reattachment earlier at around $x/C_x \approx 0.84$ with the onset of transition predicted at $x/C_x = 0.816$. The difference in reattachment points is evident in the comparison of the computed and experimental velocity profiles shown in Fig. 18(*f*). At this station the experimental profile indicates separated flow and the computed profile shows an already attached flow.

The next case considered has the same FSTI=2.85% but with Reynolds number being reduced to 50,000. The comparison of velocity profiles is shown in Figs. 19(*a*)–19(*g*). The computations agree well with the experiment, and the size and extent of the separation bubble are well predicted as can be seen from Fig. 11(*c*). The onset of separation is around $x/C_x \approx 0.72$ and the flow reattaches around $x/C_x \approx 0.9$, with transition onset at $x/C_x = 0.837$.

In Fig. 20, computed and experimental pressure coefficient distributions for grid 3 case which correspond to FSTI=1.6% are compared for Re=50,000, 75,000, and 100,000. Again, very good agreement between computations and experiments is obtained. The onset of separation and reattachment locations shown in Fig. 11(*b*) compares well with the experiments.

Overall, Figs. 11(*a*)–11(*c*) indicate that, as FSTI increases, the separated flow region decreases, and at a given FSTI, increasing Reynolds number has the same effect on the separated flow region.

4.3 Simulations of Pack B Experiments of Volino [24].

In computation of experiments of Volino [24] the flow field is modeled with the 31-zone multiblock grid shown in Fig. 21 obtained as a result of a series of grid refinement studies. The bleed flaps below the lower blade and above the upper blade are defined by fitting third-order polynomials through the available points obtained from experimental setup; these curves are used as the flap shapes in generating the computational grid. Initial computations indicated that the shape of the bleed flaps and the orientation of the tailboard behind the upper blade greatly affect the computed results, especially the onset of separation and reattachment points on the lower blade's suction surface. In order to select the most accurate orientation for the tailboard and the shape of the bleed flaps, several test computations were performed for the case with Re=41,162 and FSTI=0.5% using different tailboard orientations and bleed flap shapes. In these computations the main goal was to match the experimental velocity profiles in the laminar flow part and to capture the correct onset point of separation. Once an acceptable geometry is obtained, the final bleed flap shapes and tailboard orientation are used for computation of all other Reynolds number cases.

Computed pressure coefficient distributions are compared to experiments in Figs. 22(*a*)–22(*d*) for Re=82,324, 41,162, 20,581, and 10,291, and the separation onset, reattachment, and transition onset information is summarized in Table 4. The C_p comparison for Re=82,324 shown in Fig. 22(*a*) indicates that the computation predicts early reattachment of the flow; in the recovery region following reattachment the pressure coefficient distribution is overpredicted.

The computed pressure coefficient distributions for the lower Reynolds number cases shown in Figs. 22(*c*) and 22(*d*) compare well with experiments. For the Re=41,162 case shown in Fig. 22(*b*), the onset of separation and reattachment locations matches the experiment as given in Table 4; however, in the recovery re-

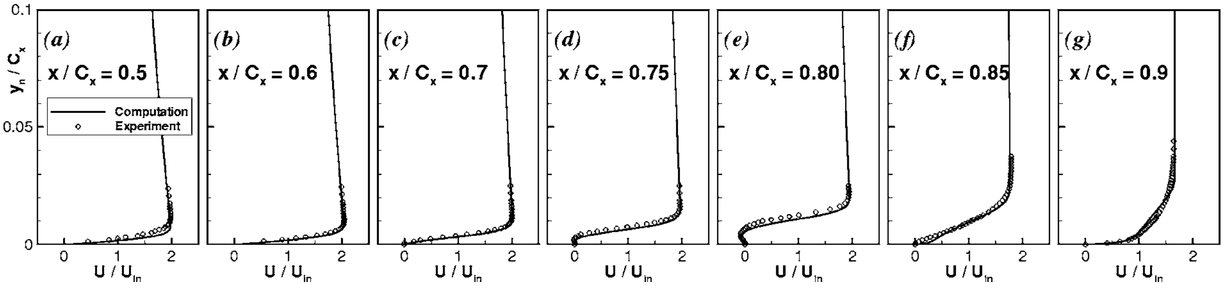

Fig. 12 Comparison of computed velocity profiles with experiments of Huang et al. [23], Re=100,000, FSTI=0.08% case

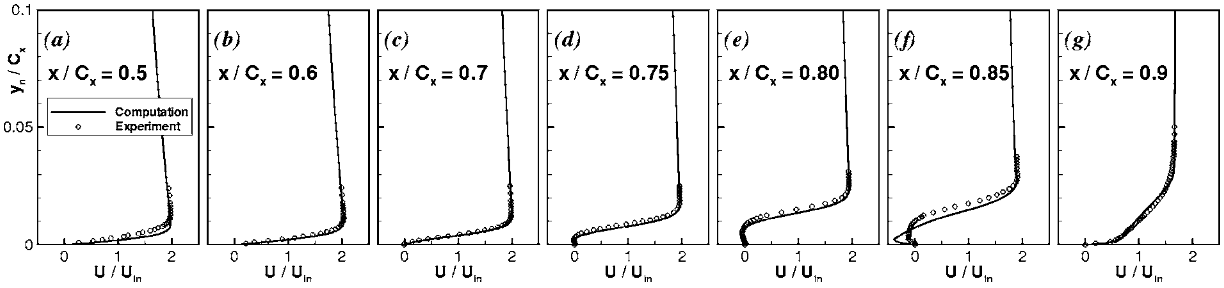

Fig. 13 Comparison of computed velocity profiles with experiments of Huang et al. [23], Re=75,000, FSTI=0.08% case

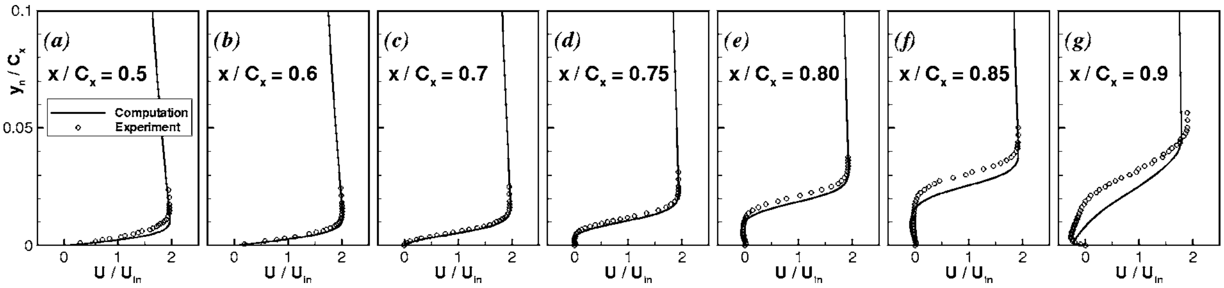

Fig. 14 Comparison of computed velocity profiles with experiments of Huang et al. [23], Re=50,000, FSTI=0.08% case

gion the pressure coefficient distribution is overpredicted.

Computed velocity profiles are compared to experiment at 11 stations along the suction surface of the blade in Figs. 23(*a*)–23(*k*) for Re=82,324 and FSTI=0.5%. The results compare well with the experiment up to x/C_x=0.732 shown in Figs. 23(*a*)–23(*g*). After this station flow separation takes place. Separation onset and reattachment are slightly earlier in the computations compared to experiment as given in Table 4. This also can be observed from the velocity profiles at stations x/C_x=0.798 to 0.912 shown in Figs. 23(*h*)–23(*j*). Overall computations compare well with the experimental measurements.

Next the Reynolds number is reduced to 41,162 and the computed and experimental velocity profiles are compared in Figs. 24(*a*)–24(*k*). The computed profiles agree well with experiments except at x/C_x=0.912 shown in Fig. 24(*j*). At this station the computation indicates a smaller separated flow region close to reattachment in contrast to the experiment. However, the flow reattaches around x/C_x=0.95 both in computation and experiment, and in the next measurement station the agreement is well.

The next case considered has a Reynolds number of 20,581. Computed velocity profiles are shown along with the experimental data at 11 axial stations in Figs. 25(*a*)–25(*k*). In this case flow separates around $x/C_x \approx 0.76$ and does not reattach in experiment; however, computations indicated reattachment at $x/C_x \approx 0.98$. This discrepancy is evident from the comparison of velocity pro-

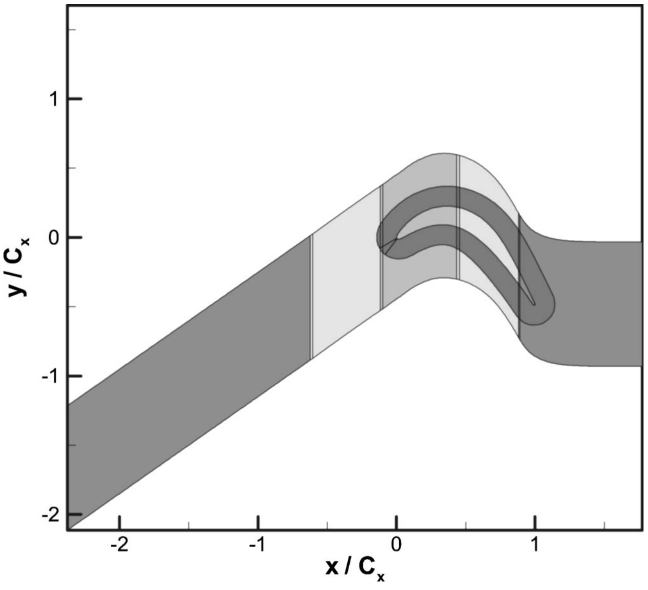

Fig. 15 Grid used for computation of experiments of Huang et al. [23] with FSTI=1.6% and 2.85%

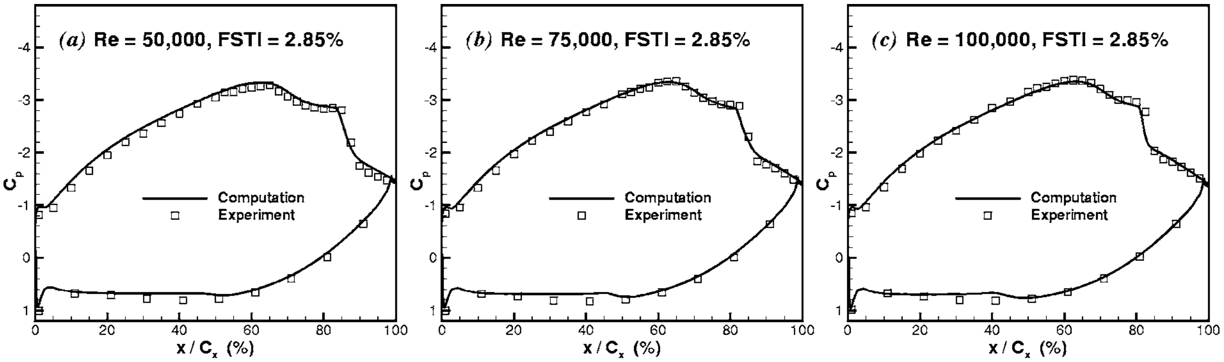

Fig. 16 Comparison of computed pressure coefficients with experiments of Huang et al. [23] for FSTI=2.85% cases

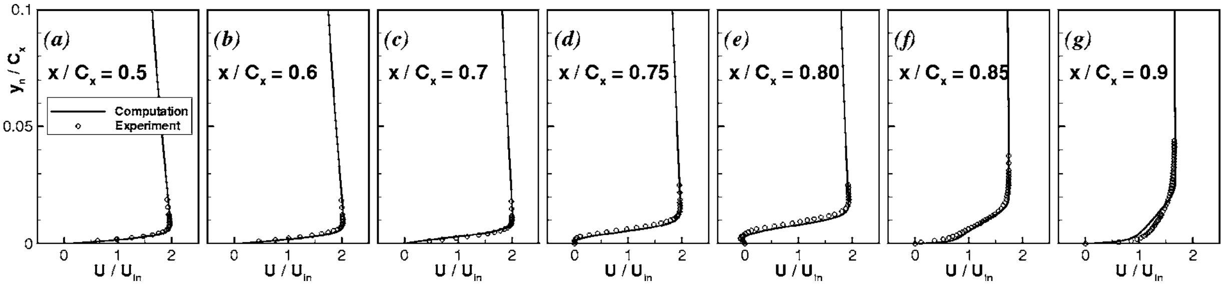

Fig. 17 Comparison of computed velocity profiles with experiments of Huang et al. [23], Re=100,000, FSTI=2.85% case

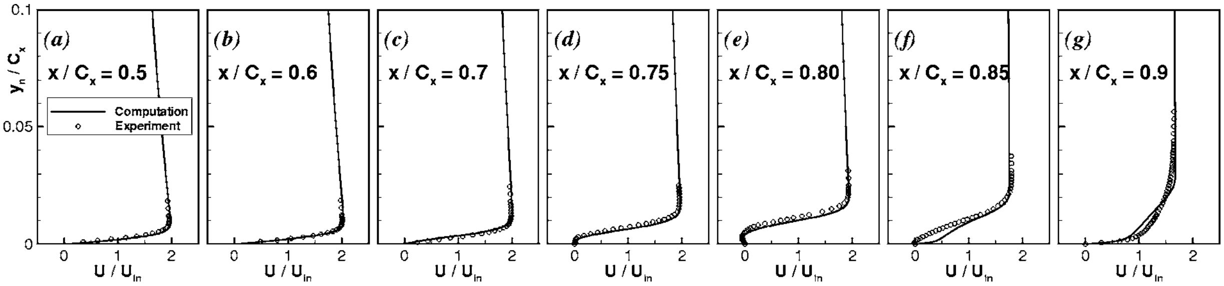

Fig. 18 Comparison of computed velocity profiles with experiments of Huang et al. [23], Re=75,000, FSTI=2.85% case

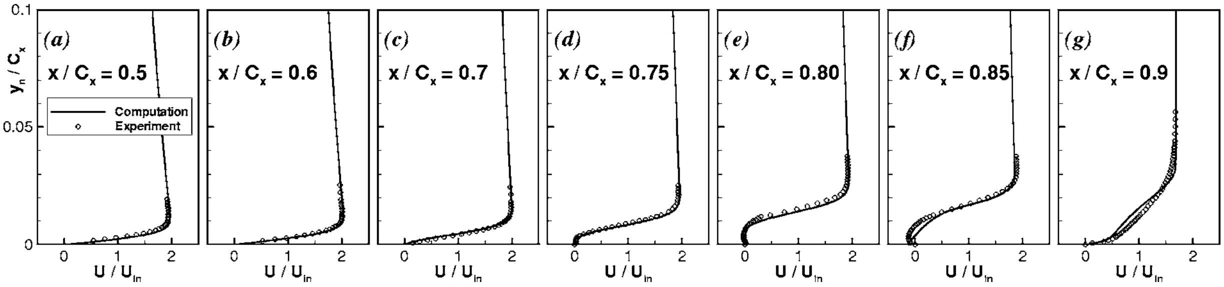

Fig. 19 Comparison of computed velocity profiles with experiments of Huang et al. [23], Re=50,000, FSTI=2.85% case

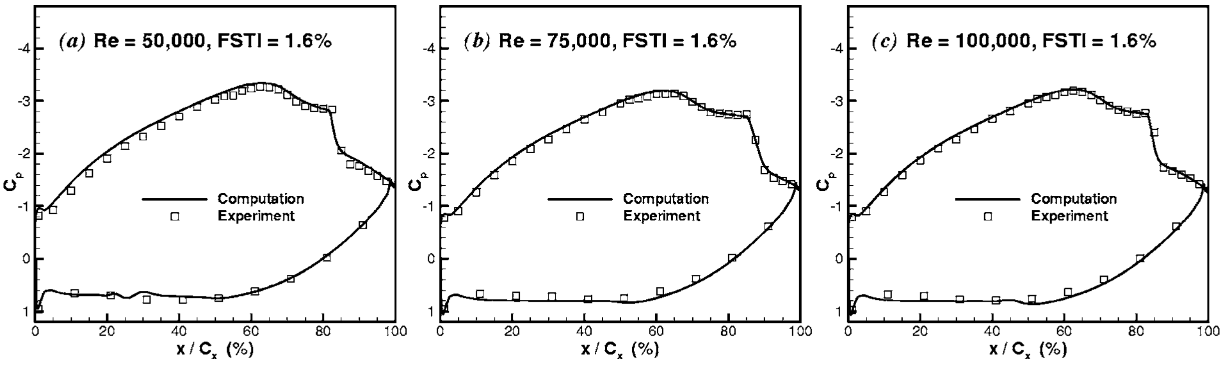

Fig. 20 Comparison of computed pressure coefficients with experiments of Huang et al. [23] for FSTI=1.6% cases

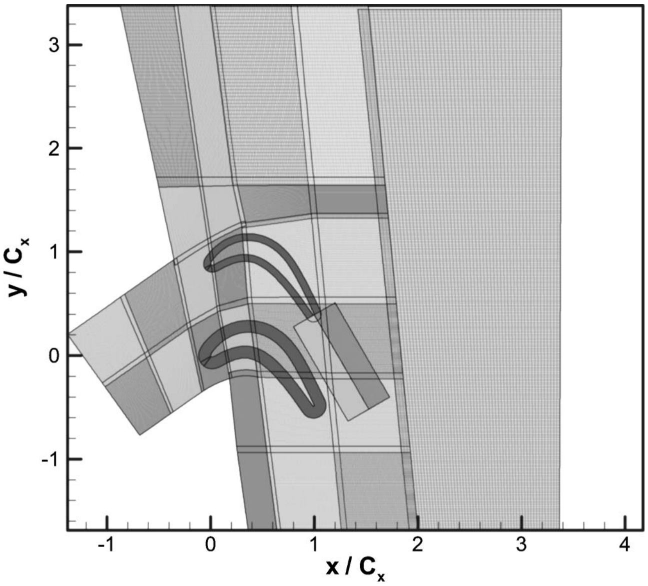

Fig. 21 Thirty-one zone multiblock grid used for computation of experiments of Volino [24]

files at the last two measurement stations shown in Figs. 25(*j*) and 25(*k*). The computation indicates a smaller separated region in these stations and finally reattaches very close to the trailing edge. Onset of transition was predicted at $x/C_x = 0.978$.

The final case in this set of experiments is the one with Re = 10,291. The computed velocity profiles compare very well with the experimental data as shown in Figs. 26(*a*)–26(*k*). In this case the flow separates around $x/C_x \approx 0.76$ and does not reattach. The flow is completely laminar; transition was not predicted on the blade.

5 Concluding Remarks

A transport equation for the intermittency factor is employed to predict three sets of recent low-pressure turbine experiments on the Pack B blade. The intermittent behavior of the transitional flows is taken into account by modifying the eddy viscosity with the intermittency factor. Comparisons of the computed and experimental data are made and overall good agreement with the experimental data is obtained. The predicting capabilities of the current intermittency approach and the intermittency transport model in prediction of transitional flows under a wide range of low-pressure turbine conditions is demonstrated.

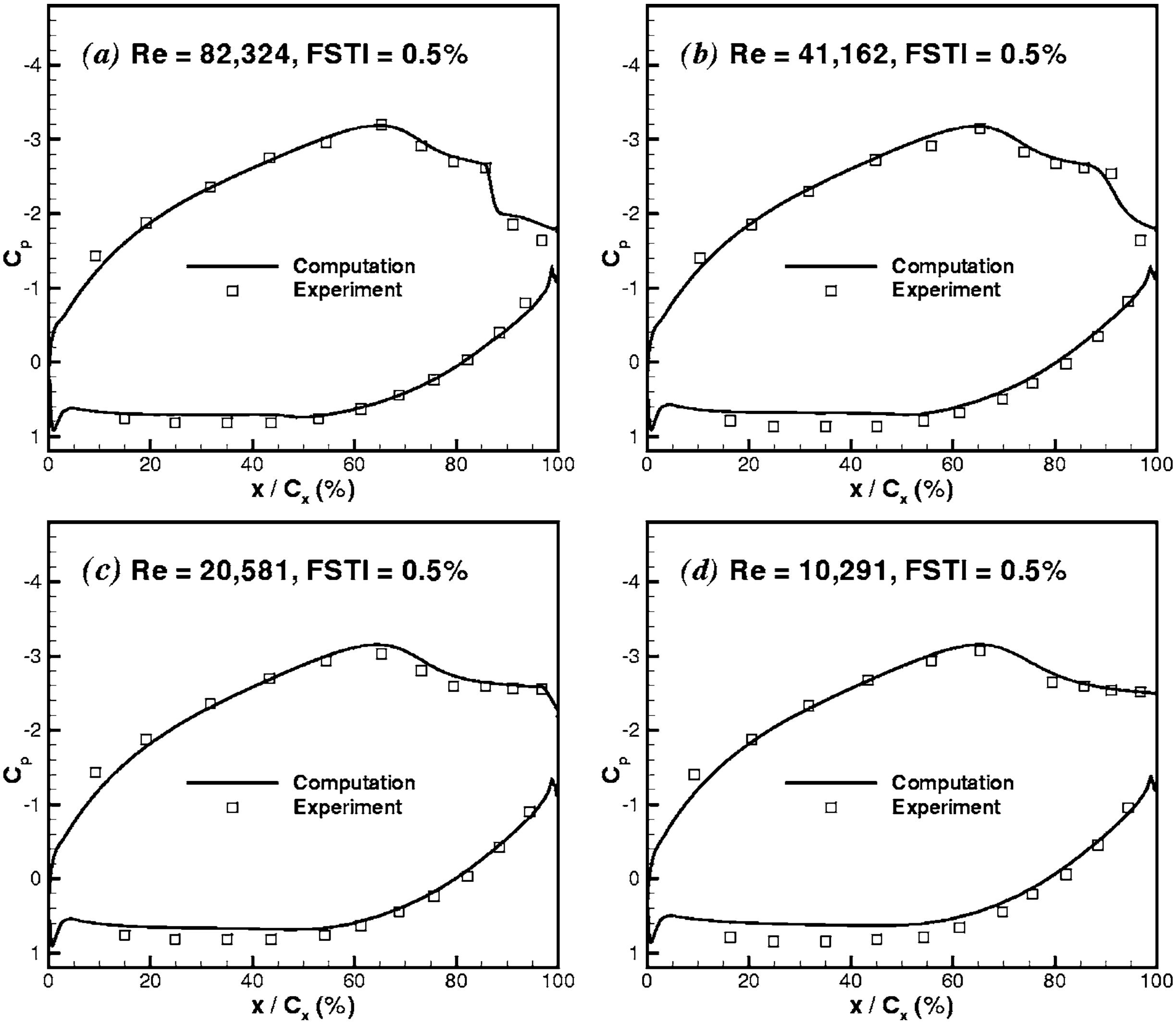

Fig. 22 Comparison of computed pressure coefficient distributions with experiments of Volino [24], FSTI=0.5%

Table 4 Separation, reattachment, and transition locations for cases of Volino [24]

Re ($U_{\mathrm{in}}C_x/\nu$)	FSTI (%)	x_s/C_x (Computation)	x_s/C_x (Experiment)	x_r/C_x (Computation)	x_r/C_x (Experiment)	x_{tr}/C_x (Computation)
10,291	0.5	0.760	0.750	⋯	⋯	⋯
20,581	0.5	0.765	0.760	0.980	⋯	0.978
41,162	0.5	0.760	0.770	0.950	0.950	0.840
82,324	0.5	0.757	0.767	0.890	0.900	0.857

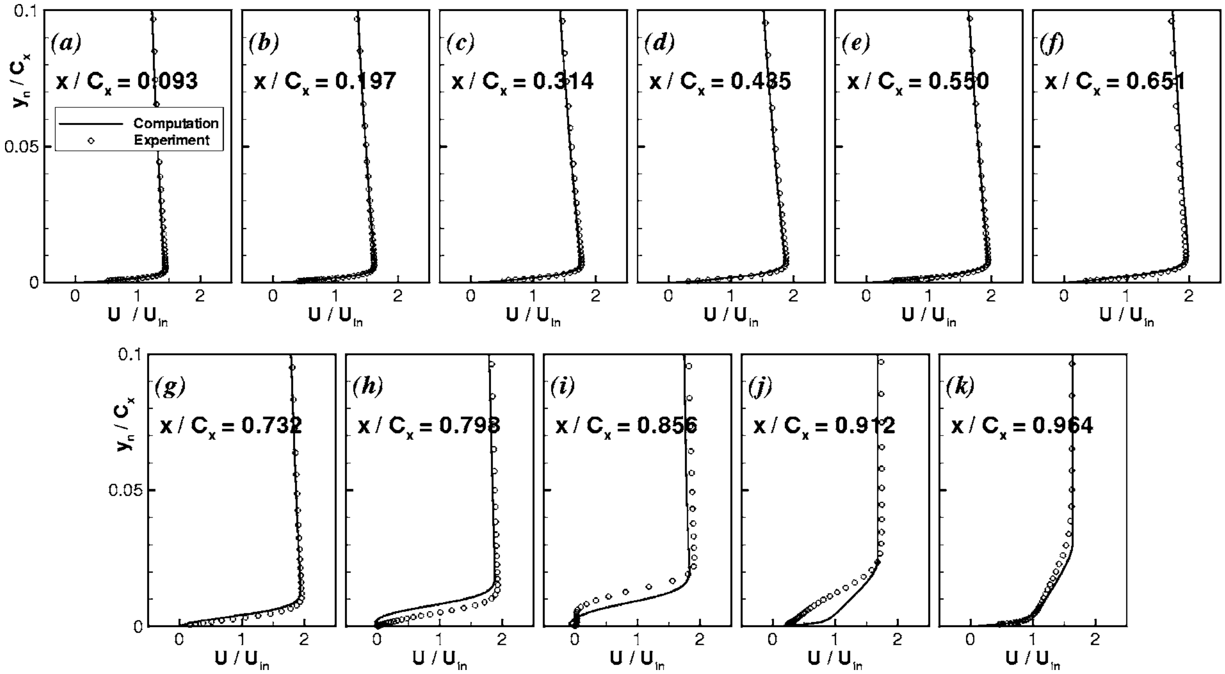

Fig. 23 Comparison of computed velocity profiles with experiments of Volino [24], Re=82,324, FSTI=0.5%

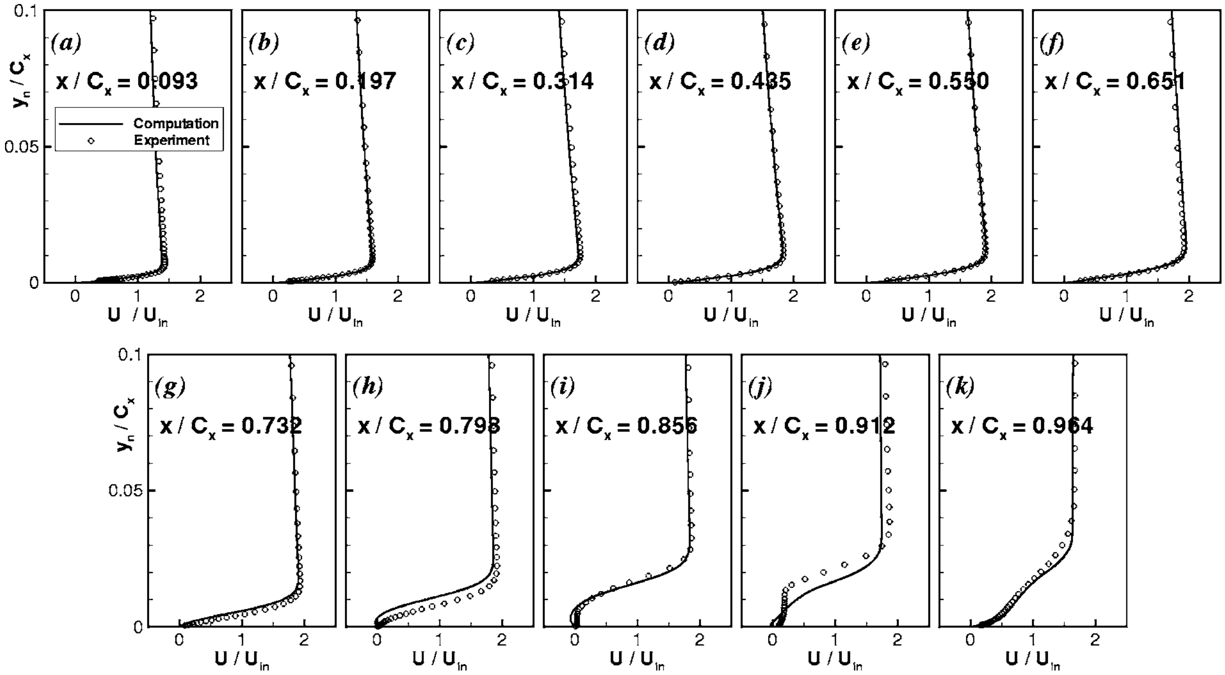

Fig. 24 Comparison of computed velocity profiles with experiments of Volino [24], Re=41,162, FSTI=0.5%

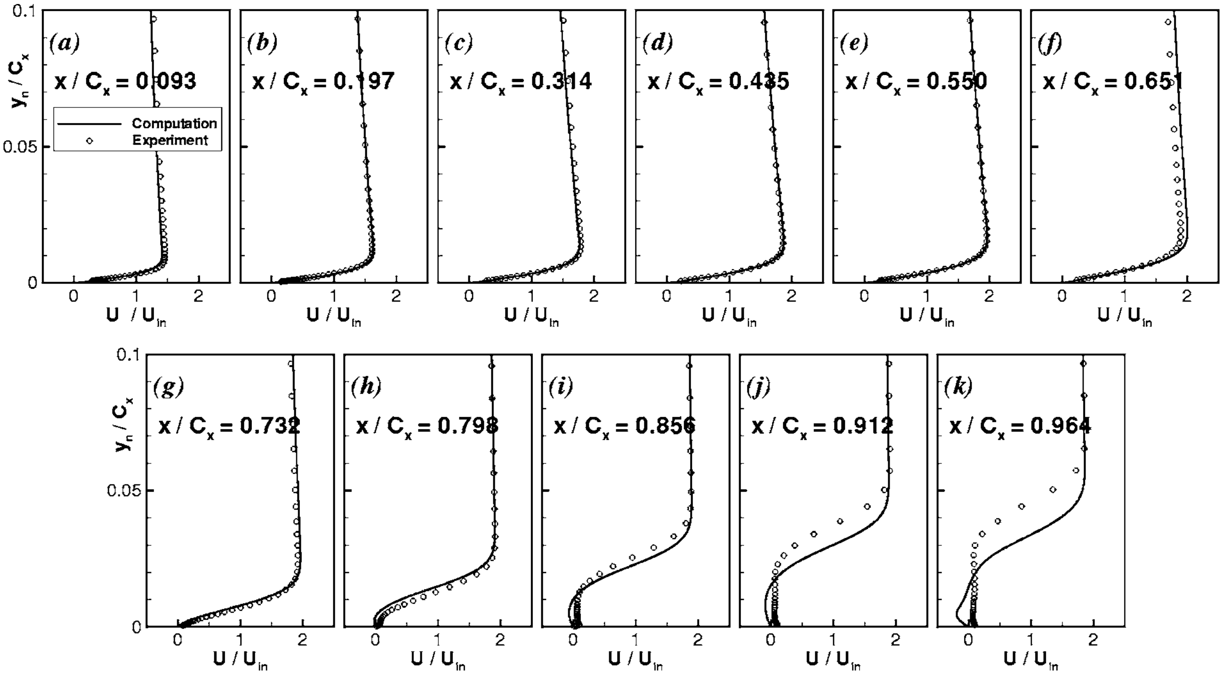

Fig. 25 Comparison of computed velocity profiles with experiments of Volino [24], Re=20,581, FSTI=0.5%

Acknowledgment

This work is supported by NASA Glenn Research Center under Cooperative Agreement NCC3-590 and followed by NCC3-1040. The project is part of the Low Pressure Turbine Flow Physics Program of NASA-Glenn.

The experimental efforts at University of Notre Dame are supported by Cooperative Agreement NCC3-935 and Cooperative Agreement NCC3-775 and the research at U.S. Naval Academy is supported by Contract C-31011-K. This paper was originally published as AIAA Paper 2003-3591.

Nomenclature

C_p = pressure coefficient, $2(P-P_\infty)/(\rho_\infty U_{in}^2)$
C_x = axial chord
FSTI = freestream turbulence intensity (%)
K_t = flow acceleration parameter $(\nu/U_e^2)(\mathrm{d}U_e/\mathrm{d}s)$
k = turbulent kinetic energy
L_x = axial chord
N = nondimensional spot breakdown rate parameter, $n\sigma\theta_t^3/\nu$

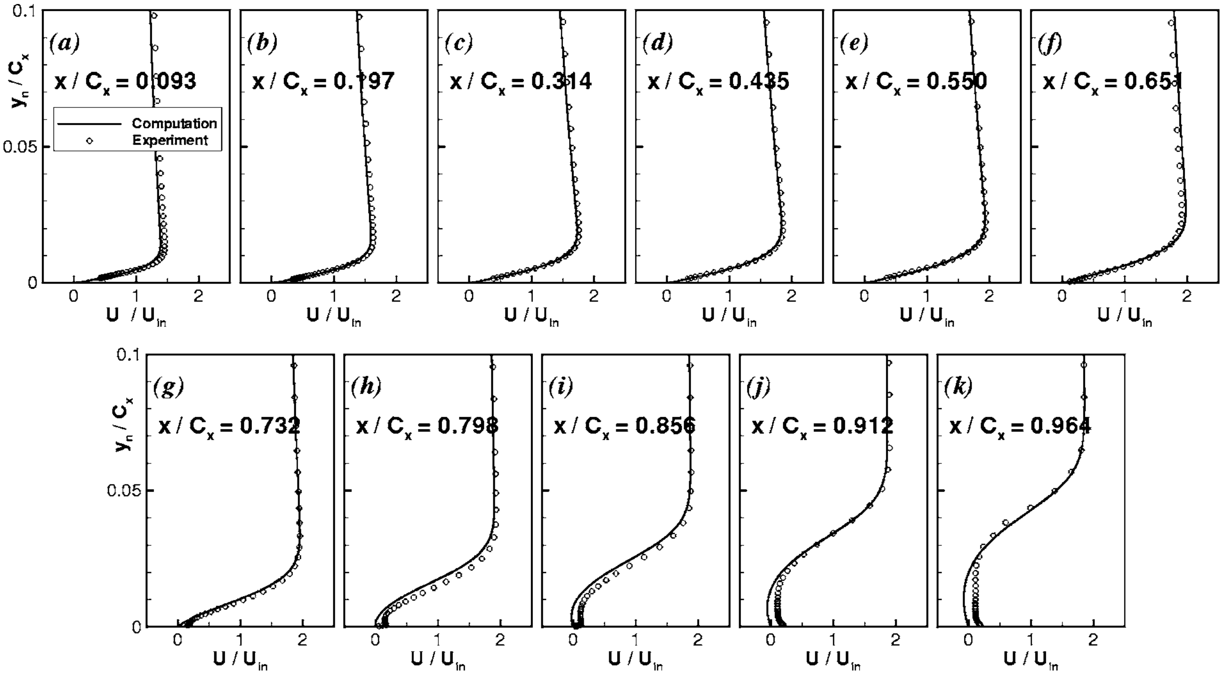

Fig. 26 Comparison of computed velocity profiles with experiments of Volino [24], Re=10,291, FSTI=0.5%

n = spot generation rate
P = static pressure
P_{total} = total pressure
Re = Reynolds number
$\text{Re}_{st} = (s_t - s_s)U_e/\nu$
$\text{Re}_{\theta t} = \theta_t U_e/\nu$
s = streamwise distance along suction surface
Tu = turbulence intensity (%), u'/U
U = boundary layer streamwise velocity
U_e = local freestream velocity
U_{in} = inlet freestream velocity
u_τ = friction velocity
W = magnitude of vorticity
y_n = distance normal to the wall
$y^+ = y_n u_\tau/\nu$
γ = intermittency factor
θ = momentum thickness
λ_θ = pressure gradient parameter $(\theta^2/\nu)(\mathrm{d}U/\mathrm{d}s)$
μ = molecular viscosity
μ_t = eddy viscosity
$\nu = \mu/\rho$
$\nu_t = \mu_t/\rho$
ω = total pressure loss coefficient, $2(P_{\text{total}_{\text{inlet}}} - P_{\text{total}_{\text{exit}}})/(\rho_\infty U_{\text{in}}^2)$
ρ = density
σ = spot propagation parameter

Subscripts

e = freestream
s = onset of separation
t = onset of transition

References

[1] Mayle, R. E., 1991, "The Role of Laminar-Turbulent Transition in Gas Turbine Engines," ASME J. Turbomach., **113**, pp. 509–537.
[2] Rivir, R. B., 1996, "Transition on Turbine Blades and Cascades at Low Reynolds Numbers," AIAA Paper No. 96–2079.
[3] Lake, J. P., King, P. I., and Rivir, R. B., 2000, "Low Reynolds Number Loss Reduction on Turbine Blades With Dimples and V-Grooves," AIAA Paper No. 00–0738.
[4] Simon, F. F., and Stephens, C. A., 1991, "Modeling of the Heat Transfer in Bypass Transitional Boundary-Layer Flows," NASA Technical Paper No. 3170.
[5] Dhawan, S., and Narasimha, R., 1958, "Some Properties of Boundary Layer During the Transition from Laminar to Turbulent Flow Motion," J. Fluid Mech., **3**, pp. 418–436.
[6] Gostelow, J. P., Blunden, A. R., and Walker, G. J., 1994, "Effects of Free-Stream Turbulence and Adverse Pressure Gradients on Boundary Layer Transition," ASME J. Turbomach., **116**, pp. 392–404.
[7] Solomon, W. J., Walker, G. J., and Gostelow, J. P., 1995, "Transition Length Prediction for Flows With Rapidly Changing Pressure Gradients," ASME Paper No. 95-GT-241.
[8] Chen, K. K., and Thyson, N. A., 1971, "Extension of Emmons' Spot Theory to Flows on Blunt Bodies," AIAA J., **9**(5), pp. 821–825.
[9] Steelant, J., and Dick, E., 1996, "Modelling of Bypass Transition With Conditioned Navier-Stokes Equations Coupled to an Intermittency Transport Equation," Int. J. Numer. Methods Fluids, **23**, pp. 193–220.
[10] Cho, J. R., and Chung, M. K., 1992, "A k-ε-γ Equation Turbulence Model," J. Fluid Mech., **237**, pp. 301–322.
[11] Suzen, Y. B., and Huang, P. G., 1999, "Modelling of Flow Transition Using an Intermittency Transport Equation," NASA Contractor Report, NASA-CR-1999–209313, Cleveland, OH.
[12] Savill, A. M., 1993, "Some Recent Progress in The Turbulence Modeling of By-pass Transition," in *Near-Wall Turbulent Flows*, R. M. C. So, C. G. Speziale, and B. E. Launder, eds., Elsevier Science Publishers B.V., Amsterdam, pp. 829–848.
[13] Savill, A. M., 1993, "Further Progress in The Turbulence Modeling of By-pass Transition," *Engineering Turbulence Modeling and Experiments 2*, W. Rodi and F. Martelli, eds., Elsevier Science Publishers B.V., Amsterdam, pp. 583–592.
[14] Simon, T. W., Qiu, S., and Yuan, K., 2000, "Measurements in a Transitional Boundary Layer Under Low-Pressure Turbine Airfoil Conditions," NASA Contractor Report, NASA-CR-2000–209957, Cleveland, OH.
[15] Hultgren, L. S., and Volino, R. J., 2000, "Separated and Transitional Boundary Layers Under Low-Pressure Turbine Airfoil Conditions," in preparation.
[16] Suzen, Y. B., and Huang, P. G., 2000, "Modeling of Flow Transition Using an Intermittency Transport Equation," AIAA Paper AIAA-2000–0287.
[17] Suzen, Y. B., and Huang, P. G., 2000, "Modeling of Flow Transition Using an Intermittency Transport Equation," ASME J. Fluids Eng., **122**, pp. 273–284.
[18] Suzen, Y. B., Xiong, G., and Huang, P. G., 2000, "Predictions of Transitional Flows in Low-Pressure Turbines Using an Intermittency Transport Equation," AIAA Paper AIAA-2000–2654.
[19] Suzen, Y. B., Huang, P. G., Hultgren, L. S., and Ashpis, D. E., 2001, "Predictions of Separated and Transitional Boundary Layers Under Low-Pressure Turbine Airfoil Conditions Using an Intermittency Transport Equation," AIAA Paper AIAA-2001–0446.
[20] Suzen, Y. B., Huang, P. G., Hultgren, L. S., and Ashpis, D. E., 2003, "Predictions of Separated and Transitional Boundary Layers Under Low-Pressure Turbine Airfoil Conditions Using an Intermittency Transport Equation," ASME J. Turbomach., **125**(3), pp. 455–464.
[21] Suzen, Y. B., Xiong, G., and Huang, P. G., 2002, "Predictions of Transitional Flows in Low-Pressure Turbines Using an Intermittency Transport Equation," AIAA J., **40**(2), pp. 254–266.
[22] Lake, J. P., King, P. I., and Rivir, R. B., 1999, "Reduction of Separation Losses on a Turbine Blade With Low Reynolds Number," AIAA Paper AIAA-99–0242.
[23] Huang, J., Corke, T. C., and Thomas, F. O., 2003, "Plasma Actuators for Separation Control of Low Pressure Turbine Blades," AIAA Paper AIAA-2003–1027.
[24] Volino, R. J., 2002, "Separated Flow Transition Under Simulated Low-Pressure Turbine Airfoil Conditions: Part 1-Mean Flow and Turbulence Statistics," ASME Paper ASME-GT-30236.
[25] Rhie, C. M., and Chow, W. L., 1983, "Numerical Study of the Turbulent Flow Past an Airfoil With Trailing Edge Separation," AIAA J., **21**, pp. 1525–1532.
[26] Hsu, M. C., Vogiatzis, K., and Huang, P. G., 2003, "Validation and Implementation of Advanced Turbulence Models in Swirling and Separated Flows," AIAA Paper AIAA 2003–0766.
[27] Suzen, Y. B., and Huang, P. G., 2005, "Numerical Simulation of Unsteady Wake/Blade Interactions in Low-Pressure Turbine Flows Using an Intermittency Transport Equation," ASME J. Turbomach., **127**(3), pp. 431–444.
[28] Menter, F. R., 1994, "Two-Equation Eddy-Viscosity Turbulence Models for Engineering Applications," AIAA J., **32**(8), pp. 1598–1605
[29] Abu-Ghannam, B. J., and Shaw, R., 1980, "Natural Transition of Boundary Layers—The Effects of Turbulence, Pressure Gradient, and Flow History," J. Mech. Eng. Sci., **22**(5), pp. 213–228.
[30] Davis, R. L., Carter, J. E., and Reshotko, E., 1987, "Analysis of Transitional Separation Bubbles on Infinite Swept Wings," AIAA J., **25**(3), pp. 421–428.

Experimental Measurements and Modeling of the Effects of Large-Scale Freestream Turbulence on Heat Transfer

A. C. Nix[1]
Department of Mechanical and Aerospace Engineering,
West Virginia University,
Morgantown, WV 26506-6106
e-mail: andrew.nix@mail.wvu.edu

T. E. Diller
Fellow ASME

W. F. Ng
Fellow ASME

Department of Mechanical Engineering,
Virginia Polytechnic Institute and State University,
Blacksburg, VA 24061

The influence of freestream turbulence representative of the flow downstream of a modern gas turbine combustor and first stage vane on turbine blade heat transfer has been measured and analytically modeled in a linear, transonic turbine cascade. High-intensity, large length-scale freestream turbulence was generated using a passive turbulence-generating grid to simulate the turbulence generated in modern combustors after passing through the first stage vane row. The grid produced freestream turbulence with intensity of approximately 10–12% and an integral length scale of 2 cm ($\Lambda_x/c=0.15$) *near the entrance of the cascade passages. Mean heat transfer results with high turbulence showed an increase in heat transfer coefficient over the baseline low turbulence case of approximately 8% on the suction surface of the blade, with increases on the pressure surface of approximately 17%. Time-resolved surface heat transfer and passage velocity measurements demonstrate strong coherence in velocity and heat flux at a frequency correlating with the most energetic eddies in the turbulence flow field (the integral length scale). An analytical model was developed to predict increases in surface heat transfer due to freestream turbulence based on local measurements of turbulent velocity fluctuations and length scale. The model was shown to predict measured increases in heat flux on both blade surfaces in the current data. The model also successfully predicted the increases in heat transfer measured in other work in the literature, encompassing different geometries (flat plate, cylinder, turbine vane, and turbine blade) and boundary layer conditions.* [DOI: 10.1115/1.2515555]

Introduction

Gas turbine engine designers continually strive to improve engine performance by increasing overall engine efficiency and thrust-to-weight ratio. With turbine blades operating near their thermal limits, it is critical to the designer to have accurate predictions of hot mainstream gas to blade surface heat transfer rates. One of the main unknowns in the heat transfer prediction capability is the effect of the freestream turbulence generated in the combustor. The intensity and length scale of the turbulence impacting the first stage turbine are large [1]. Even after the turbulence intensity decrease through the first stage vane row [2,3], the intensity is on the order of 10% with integral length scales of several centimeters ($\Lambda_x/c\sim 0.10–0.30$).

Many studies have been performed in the last 25 years to quantify the effects of freestream turbulence on heat transfer. These have focused on developing correlations for the increase in time-average heat transfer as a function of the turbulence intensity for particular geometries. More recently the effect of the length scale of the turbulence has been documented to also be important.

Flat plate experiments present the most basic geometry, with the absence of curvature and pressure gradient effects. Blair [4] demonstrated that increases in freestream turbulence induce upstream boundary layer transition. Maciejewski and Moffat [5] observed a linear relationship between measured heat transfer coefficient (h) and turbulent fluctuations in the freestream (u') for a turbulent boundary layer with high freestream turbulence. Later work [6–8] revised this by using the value of $u'_{\mathrm{rms,max}}$ in the inner wall region as a correlating parameter. Barrett and Hollingsworth [9] attempted to add the effects of length scale. Thole and Bogard [10] concluded that at higher levels of turbulence, large-scale eddies penetrate the boundary layer.

Cylinder heat transfer experiments are of particular importance because the stagnation point is typically the region of highest heat transfer on turbine vanes and blades except for regions of transitional and turbulent flow. Because of the thin boundary layer and high flow acceleration, the stagnation region boundary layer is laminar in nature with freestream flow unsteadiness superimposed by the turbulence. Van Fossen et al. [11] studied the influence of turbulence length scale on heat transfer on a cylinder. A correlation was developed which included the ratio of the integral length scale to the leading edge diameter. Dullenkopf and Mayle [12] presented a correlation that introduced the idea of an "effective" turbulence level. Fluctuations at high frequencies (small scale) are viscously damped, while disturbances at low frequency (large scale) are seen as quasi-steady similar to bulk flow pulsations, which in the mean do not affect heat transfer. Only a small frequency band around a dominant frequency is effective at increasing heat transfer.

Cascade experiments were performed by several groups to document the effects of large-scale freestream turbulence in low-speed turbine vane cascades (see Ames [13,14], Radomsky and Thole [2,3,15], and Wang et al. [16]). Freestream turbulence was shown to significantly augment heat transfer in the laminar flow regions of the blade (stagnation point, pressure surface, and favorable pressure gradient region of the suction surface). Heat transfer augmentation was reported to be highest in the stagnation region and on the pressure surface. Stagnation region increases agreed well with cylinder stagnation point correlations. Comparisons of

---

[1] Corresponding author.

Contributed by the International Gas Turbine Institute of ASME for publication in the JOURNAL OF TURBOMACHINERY. Manuscript received March 3, 2006; final manuscript received October 5, 2006. Review conducted by David Wisler. Paper presented at the ASME Turbo Expo 2004: Land, Sea and Air (GT2004), Vienna, Austria, June 14–17, 2004, Paper No. GT2004-53260.

Stanton number demonstrated that turbulence has a much greater effect on the pressure surface of the vane as compared to the suction surface.

Only a few time-resolved heat flux experiments with simultaneous velocity measurements have been published. Moss and Oldfield [17,18] traversed a hot-wire probe above a flat plate with thin-film heat flux gauges on the surface. They performed time-domain analyses of the time-resolved signals, comparing raw signals and cross correlations between the velocity and heat flux signals and between heat flux signals of different gauges. They identified effects of large-scale fluctuations in heat flux from the freestream turbulence and small-scale fluctuations from the boundary layer turbulence. Through correlations of velocity and heat flux and spatial correlations between heat flux gauges they concluded that the turbulent eddy structure of the boundary layer is dominated by the freestream turbulence. Holmberg [19,20] performed measurements of unsteady surface heat flux with a hot wire collocated with the heat flux gauge. Coherence between freestream velocity and surface heat flux was found to be useful in determining the scale and frequency range of turbulent structures interacting with surface heat flux. Holmberg and Pestian [21] measured u' and v' velocity components and fluctuating surface temperature (t') and heat flux (q') in a low-speed wall-jet facility. Surface heat flux was shown to be dominated by the u' fluctuating velocity field primarily by large eddies which reach deep into the boundary layer. These results are consistent with the observations of Moss and Oldfield [17,18].

The present work reports detailed time-resolved measurements of heat flux and velocity at three locations on the pressure and suction surfaces of a transonic turbine blade in a linear cascade. Measurements of the baseline (low turbulence) time-averaged heat transfer and the increases in heat transfer due to the generated freestream turbulence field are also reported. All of the measurements are taken at engine representative flow conditions of Reynolds and Mach number for a modern high turning rotor blade in a stationary cascade. Engine combustor turbulence was simulated to match the measured conditions of Van Fossen and Bunker [1]. Analytical modeling of a mechanism by which freestream turbulence affects surface heat transfer is presented. The model is directly applied to the time-averaged heat transfer results measured in the current work, as well as to results reported by other research groups.

Experimental Facility and Instrumentation

The experiments for the data reported in this work were conducted in the Virginia Tech transonic blowdown wind tunnel facility. The wind tunnel test section consists of a linear cascade of high turning transonic turbine blades with one blade at the center of the cascade instrumented with heat flux sensors. The wind tunnel and test section have been documented in detail in previous work [22]. Test conditions were regulated to match both engine Reynolds and Mach numbers and turbulence conditions are representative of the flow downstream of the first stage stator row of modern gas turbine engines as summarized in Table 1.

Wind Tunnel and Cascade. Experiments were performed in a blowdown cascade wind tunnel that is capable of heated runs with run times up to 30 s. Heated runs are achieved by passing the mainstream flow through a passive heat exchanger that provides temperatures of up to 120°C entering the turbine cascade test section.

The test section and cascade used in this investigation, including the turbulence grid, are shown in Fig. 1. The cascade consists of four full and two half blades forming five passages. The blade design is a generic, high turning, first stage turbine geometry. The blade is scaled up three times to accommodate the instrumentation. The geometric design and nondimensional conditions of the cascade are shown in Table 1. The Mach number distribution was shown to correspond to design conditions.

Table 1 Summary of experimental conditions

Nondimensional conditions	Engine	Experiment
Mach No. exit	Transonic	1.2
Reynolds No. inlet	5×10^5	1×10^6
Temperature ratio (T_∞/T_b)	1.4	1.4
Cascade Conditions and Geometry		
Inlet Mach	0.4	
Exit Mach	1.2	
Turbulence intensity	10%	
Length scale	2 cm	
Inlet total pressure	164 kPa (10 psig)	
Inlet total temperature	100°C	
Reynolds No. exit (Re_{ex})	5×10^6	
Blade chord (c)	13.6 cm	
Suction surface chord (c_{ss})	24.8 cm	
Pressure surface chord (c_{ps})	14.9 cm	
Blade span (sp)	15.3 cm	
Blade pitch (p)	12.2 cm	
sp/c	1.12	
p/c	0.9	

Turbulence Grid. Turbulence was generated in the facility using a passive turbulence grid placed upstream of the cascade test section inlet. The grid consists of three 5.08 cm (2 in.) wide bars spaced 7.62 cm (3 in.) apart. Each bar is 2.54 cm (1 in.) thick. The design was based on results obtained by Polanka and Bogard [23] and uses large bars and high-flow blockage to generate high turbulence. Details of the development and performance of the grid in this facility and the methods for determining the intensity and length scale of the turbulence are discussed in Nix et al. [22]. The turbulence grid generates an acceptable level of turbulence with intensity of 15% and 2 cm length scale $(\Lambda_x/c=0.15)$ near the cascade test section inlet. The turbulence intensity decays to approximately 10% near the entrance to the cascade passages with a length scale of 2 cm. This level is representative (if not slightly higher) than the levels believed to exist in the core flow following the first stage vane row. Total pressure probe and hot-wire surveys performed in the cascade test section demonstrated good flow uniformity [22].

Instrumented Turbine Blade. One blade near the center of the cascade (shown in Fig. 1) was instrumented with an array of sensors. Measurements were made at locations on both the pressure and suction surfaces of the blade to compare the effects of turbu-

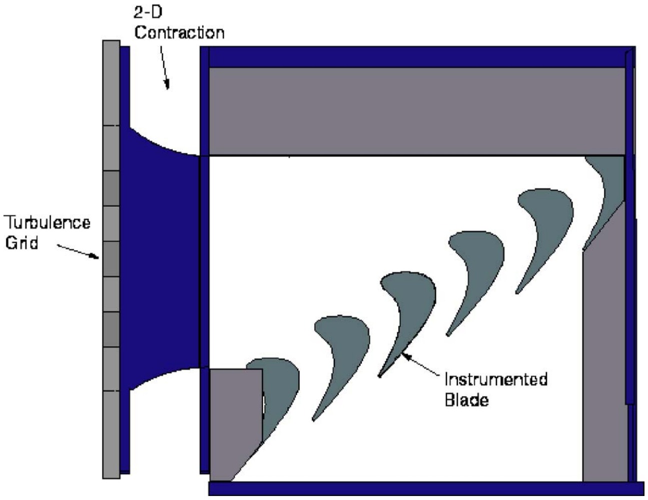

Fig. 1 Cascade test section and turbulence grid

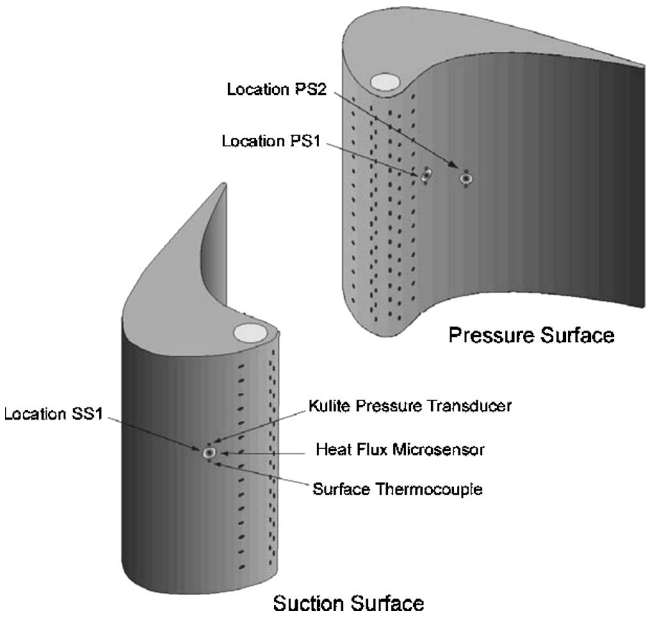

Fig. 2 Instrumented turbine blade

lence on heat transfer under different flow conditions (mean velocity, pressure gradient, curvature and velocity fluctuations). For the results presented in this work, one location on the suction surface (SS1) was used and two locations on the pressure surface (PS1 and PS2). Each measurement location consists of an array of three sensors, as shown in Fig. 2. Each triplet of sensors includes a Vatell HFM-7 heat flux microsensor, a Kulite XCQ-062-50a pressure transducer, and a K-type thermocouple. The cooling holes illustrated in the figure were not used in this particular study and were plugged.

Table 2 details the gauge locations and summarizes the conditions at each location. The chord length of the blade on each surface is denoted as c_{ss} for the suction surface and c_{ps} for the pressure surface. It should be noted that the two locations on the pressure surface are located in regions of different curvature and pressure gradient.

Instrumentation and Data Acquisition. Steady upstream total pressure and static pressure were measured with a pitot-static probe, blade pressure measurements were measured with the surface Kulite, and total temperature was measured using a total temperature probe. Time-averaged heat flux was measured with the HFM heat flux sensors mounted on the surface of the blade. The data were sampled at 100 Hz and recorded through a 64-channel National Instruments AMUX 64T multiplexer and data acquisition card and recorded with LABView. The methodology for determining steady heat transfer coefficients in the transient conditions of the transonic wind tunnel has been described by Smith et al. [24], using 1000 data points per run.

Unsteady measurements in the passage were performed to measure time-resolved velocity near the surface of the instrumented blade, simultaneous with the heat flux sensors. It should be noted that the unsteady data runs with the hot-wire in place were performed without heated flow, but with a precooled turbine blade for the driving temperature difference for heat transfer. This eliminates temperature fluctuations from the reduction of hot-wire data. The passage hot-wire probes were designed with the prongs supporting the wire at a 90 deg angle to the probe body so that the wire could be oriented parallel to the surface of the turbine blade. The sensor was designed such that the probe body provides as little disturbance of the passage flow as possible. Figure 3 shows a picture of the passage hot-wire mounted such that the prongs are above the heat flux gauge.

Table 2 Summary of blade measurement locations

Location	$x/c_{\mathrm{ss\ or\ ps}}$	x/c	Approximate Mach number	Pressure gradient (+/−)
SS1	0.20	0.36	0.55	+ Favorable
PS1	0.18	0.20	0.22	− Adverse
PS2	0.40	0.43	0.25	+ Favorable

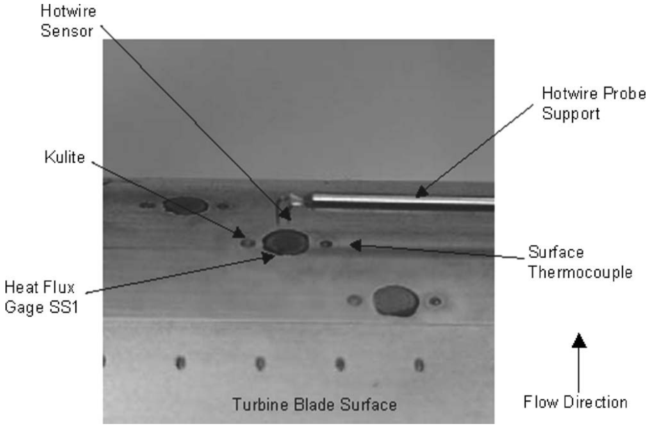

Fig. 3 Blade surface gauges and passage hot-wire probe

In this configuration, the wire was approximately 5 mm above the surface of the turbine blade. This distance is outside of the boundary layer and far enough from the blade surface to ensure the probe will not impact the blade surface. The boundary layer thickness on the current blade was estimated based on previous measurements [25,26] to be approximately 0.3 mm over most of the suction surface and between 0.3 and 1.5 mm on the pressure surface. Consequently, the 5 mm distance is outside of the boundary layer, but close enough to measure mean and fluctuating velocities near the edge of the boundary layer. The hot wire was controlled using a Dantec 55M01 hot-wire anemometer. The anemometer was set to provide a frequency response of approximately 50 kHz at the tunnel velocity.

Measurements of time-resolved heat transfer and velocity were recorded with a LeCroy 6810 high-speed data acquisition system. Data were recorded at 100 kHz for a short duration of 1.3 s and filtered at 40 kHz. The sampling period gives a sufficient sample size for statistical analysis while limiting the output file sizes.

The dynamic response and spatial resolution of the heat flux sensors and hot-wire anemometer was of importance when analyzing the time-resolved data. The heat flux sensors are sufficiently small compared to the blade chord and span to provide reasonably good spatial resolution to minimize the effects of spatial averaging. The ratio of the turbulence integral length scale to the sensor diameter is approximately $\Lambda_x/D_s=5.5$. Using the sensor diameter and a convective velocity of approximately 100 m/s, the frequency resolution of the gauges is estimated as approximately 20 kHz. This is well above the frequency range of interest, since it will be shown that there is no coherence between velocity and heat flux above 5 kHz. The scales of interest discussed later are all on the order of the gauge diameter or larger. This provides a wide enough frequency band for sampling time-resolved heat flux data for correlation with high-frequency velocity data.

Experimental Results

Steady Heat Transfer. Heat transfer coefficients were measured with and without high freestream turbulence. The methodology for determining steady heat transfer coefficients in the transonic facility is described in Smith et al. [24]. The technique uses

Table 3 Summary of heat transfer coefficients with low- and high-freestream turbulence

Location	Heat transfer coefficients ($W/m^2 K$) SS1	 PS1	 PS2
Low turbulence HTC	719	652	566
High turbulence HTC	779	764	662
% Increase over low Tu	8.3%	17.1%	16.9%
Uncertainity in increase in *h*	2.9%	3.2%	2.5%

an experimental determination of the freestream recovery temperature and wall temperature and measured heat flux to determine the local heat transfer coefficient. Background or "low turbulence" levels in the facility are less than 1%. With the turbulence grid installed, the flowfield near the entrance to the cascade passages has a turbulence intensity of approximately 10% with a length scale of 2.0 cm [22]. These conditions are heretofore referred to as "high turbulence."

Table 3 reports the results of measurements at each gauge location for low- and high-freestream turbulence cases including measurement uncertainty. The uncertainty in the increase in heat transfer coefficient due to freestream turbulence is predominantly a function of precision uncertainty (measurement repeatability). Because the same calibration factor is used for all of the measurements from each heat flux gauge, the bias uncertainty for the change in heat transfer coefficient is very small. The uncertainty in the measured increase is an average of 2.9% (much lower than the measured percentage increase).

The results shown in Table 3 indicate that there is a more significant increase in heat transfer coefficient on the pressure surface due to high-freestream turbulence as compared to the suction surface. The increase in heat transfer on the pressure surface (17%) is approximately two times greater than that measured on the suction surface (8%). The results of suction versus pressure side heat transfer are in good agreement with work by previous researchers on both turbine blades and vanes. The increase in heat transfer on the pressure surface gauges is similar in terms of percentage increase, but the absolute increase in heat transfer coefficient is larger at location PS1 (closer to the leading edge) than at location PS2. As noted earlier, the two gauges are located in regions of relatively similar velocity; however, the flow at PS1 experiences a slightly adverse pressure gradient while location PS2 sees a favorable pressure gradient.

Time-Resolved Heat Transfer. A major goal of this work is to investigate the time-resolved surface heat flux and the interaction of unsteady velocity of the mainstream flow near the blade surface with surface heat flux. Analysis of the time-resolved signals provides insight into the mechanism by which freestream turbulence affects surface heat transfer.

As discussed earlier, measurements of time-resolved velocity were performed with a hot-wire probe located approximately 5 mm above the surface of the three instrumented locations of the turbine blade (see Fig. 3). The turbulence characteristics on the pressure and suction surfaces are shown in Table 4. The intensity of turbulent fluctuations (independent of normalization by the local mean velocity) is shown to be very low on the suction surface and much higher on the pressure surface. The turbulent fluctuations on the pressure surface are shown to decrease slightly as the flow progresses from PS1 to PS2. Measurements of cross-stream (or pitch-wise) variations of turbulence intensity downstream of the grid showed little variation in intensity [22], so differences in suction surface versus pressure surface turbulence is not due to nonuniformity of inlet turbulence. The higher intensity of fluctuations on the pressure side versus the suction surface qualitatively agrees with the data from Holmberg [19,20] and Radomsky and Thole [2].

Table 4 Measured local turbulence parameters

Location	u'_{rms} (m/s)	Tu (%)	Λ_x (cm)
SS1	9.31	4.5	3.46
PS1	20.97	18.8	2.39
PS2	17.47	12.5	2.51

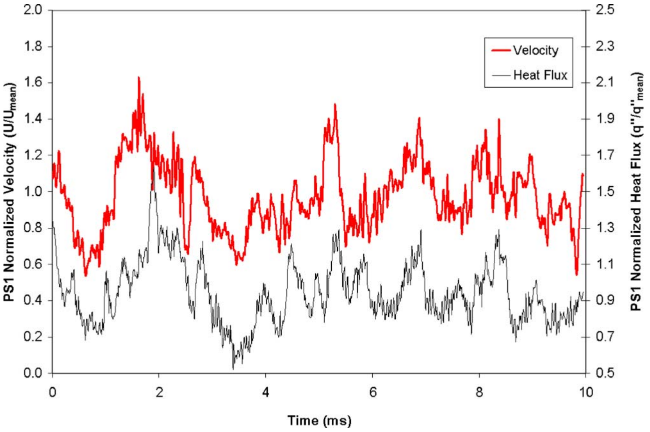

Fig. 4 Comparison of velocity and heat flux time signals. Velocity (top line); heat flux (bottom line).

Figure 4 shows a section of the time-resolved velocity and heat flux signals normalized by their mean values for one representative measurement location (PS1). The traces of velocity and heat flux demonstrate that there is low-frequency correlation between the two signals, as peaks in velocity show corresponding peaks in heat flux. The low-frequency energy of the velocity signal appears to be in phase with the corresponding energy in the heat flux signal. It is apparent from the figures that higher frequency fluctuations in the signals do not appear to be correlated. These results are qualitatively similar to data reported in work by Moss and Oldfield [18].

Comparison of the data in the frequency domain was performed to further investigate the relationship between freestream velocity fluctuations and surface heat transfer fluctuations. Figure 5 shows the power spectral density of velocity and heat flux at one representative blade location. It can be seen that the velocity and heat flux spectra have very similar shapes and have significant energy at low frequencies which attenuates at frequencies of approximately 5 kHz and above.

To quantify the correlation of the heat flux and velocity signals, the coherence function was applied to the time-resolved data in the frequency domain. The results for each gauge location are shown in Fig. 6. The figure demonstrates that significant coherence at all three gauge locations is limited to a relatively narrow band of frequencies below 2 kHz with zero coherence at frequencies starting at about 5 kHz.

Shown on the figure is a band of frequencies corresponding to the integral length scale range at the three gauge locations ±10%. The most energetic frequency (corresponding to the integral length scale) at each location was determined by

$$f = \frac{3 \cdot U}{8\pi\Lambda_x} \tag{1}$$

For location SS1, this frequency is approximately 650 Hz, and 570 Hz and 700 Hz at locations PS1 and PS2, respectively.

The frequency range and magnitude of significant coherence agrees qualitatively with data reported by Holmberg et al. [19,20].

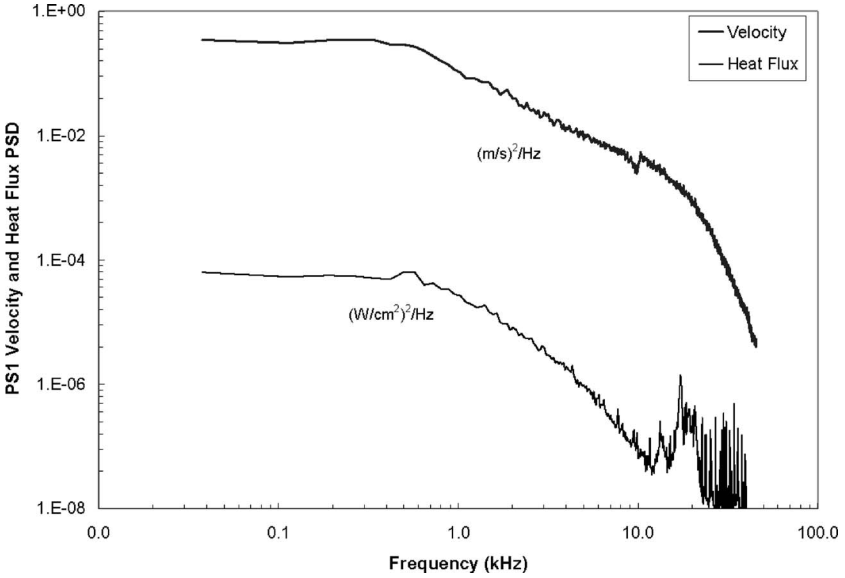

Fig. 5 Comparison of velocity and heat flux spectra. Velocity (top line); heat flux (bottom line).

The coherence measured on the pressure surface at PS1 and PS2 shows no "preferential frequencies," rather a broad spectrum of frequencies centered on the integral scale, out to approximately 2 kHz, show significant coherence. On the suction surface, the coherence shows a peak at approximately 550 Hz. This peak is well correlated with the frequency of the integral scale. The comparison of the coherence on the two surfaces may indicate that a much smaller range of coherent structures in the freestream penetrate the boundary layer on the suction surface to affect surface heat transfer. On the pressure surface, the range of turbulent vortices in the freestream which show significant coherence with surface heat transfer is broader, possibly indicating the ability of lower energy scales to penetrate into the boundary layer to affect surface heat transfer.

Analytical Model

The experimental results indicate several key things about the mechanism of how large-scale freestream turbulence affects boundary layer heat transfer. The large coherence between the u' velocity and the surface heat flux for the most energetic frequencies suggests that the large-scale turbulent eddies penetrate through the boundary layer with little alteration or abatement. The several centimeter length scale of the freestream turbulence is so much larger than the boundary layer thickness that the lack of interaction between the two appears reasonable. Time-resolved heat flux and pressure measurements by Popp et al. [27] during shock passing events also are instructive to understand the details of the heat flux. The resulting temporary increase in heat flux was

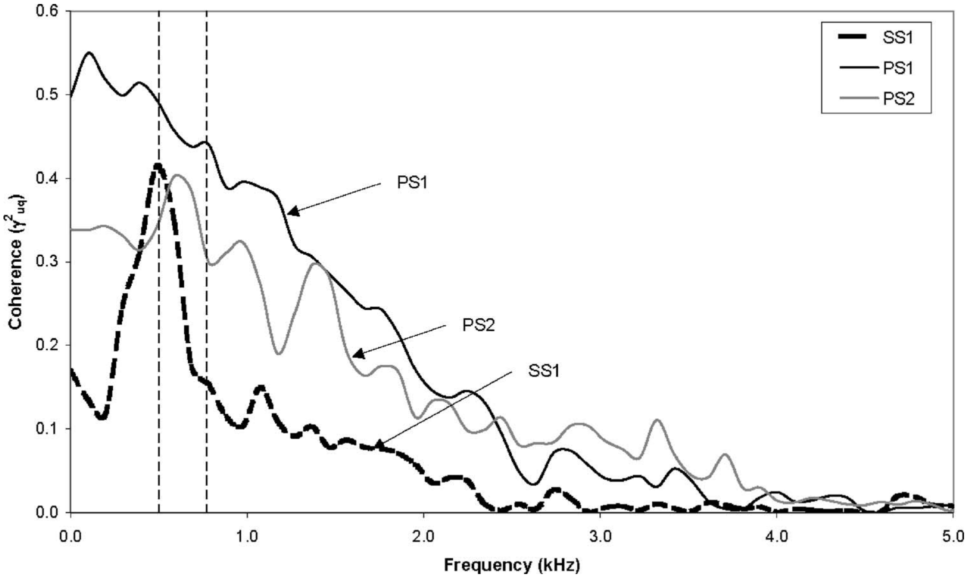

Fig. 6 Coherence between velocity and heat flux signals

Table 5 Model application to transonic tunnel data

Location	Measured u'_{rms} (m/s)	Measured Λ_x (cm)	Δh_t (W/m^2 K)	Low FST h (W/m^2 K)	High FST predicted h (W/m^2 K)	High FST measured h (W/m^2 K)
SS1	9.31	3.81	57	719	776	779
PS1	20.97	2.34	116	652	768	764
PS2	17.47	2.54	101	566	667	662

correlated directly with the increased temperature and was superimposed onto the normal heat flux through the boundary layer. Moss and Oldfield [18] also concluded that the enhancement from freestream turbulence was due to the large vortices that penetrated deep into the turbulent boundary layer.

Therefore, the basic tenet of the model is that the mechanism for the enhanced heat transfer is due to the large-scale motion of hot fluid from the freestream through the boundary layer to the surface. This has similarities to simple theories of turbulent heat transfer, such as the Prandtl mixing length model, for application within a turbulent boundary layer where a length scale is multiplied by a gradient of the velocity. The present model is entirely different, however, because the motion is not within the gradient region of the boundary layer, but goes directly from the freestream to the surface entirely through the boundary layer.

Consequently, the heat transfer consists of two independent portions—that due to the normal transfer through the boundary layer and that due to the turbulent motions from the freestream to the surface. They are treated independently. The model for the effect of the turbulent motions is surface renewal. The thermal energy is exchanged during the time of the contact of the hot freestream fluid with the surface. It is assumed that the surface itself has a much higher conductivity than the fluid, which in this case is air. The heat transfer into the air can be characterized by the semi-infinite solution, with air as the medium

$$\Delta q_t = k \cdot \frac{(T_\infty - T_w)}{\sqrt{\pi \alpha t}} \tag{2}$$

The characteristic time for this event is the integral length scale of the local turbulence divided by the unsteady turbulent velocity, $\Lambda_x / u'_{\mathrm{rms}}$. The corresponding heat flux at the end of this time period is

$$\Delta q_t = k \cdot \frac{(T_\infty - T_w)}{\left(\pi \alpha \dfrac{\Lambda_x}{u'_{\mathrm{rms}}}\right)^{1/2}} \tag{3}$$

This quantity is added to the heat flux without freestream turbulence. In terms of the heat transfer coefficient

$$\Delta h_t = \frac{k}{\left(\pi \alpha \dfrac{\Lambda_x}{u'_{\mathrm{rms}}}\right)^{1/2}} \tag{4}$$

where

$$h = h_o + \Delta h_t \tag{5}$$

It should be noted that the model results are only a function of the local conditions of the fluid in the freestream outside of the boundary layer. There are no parameters of the geometry, state of the boundary layer, or thickness of the boundary layer. There also are no empirical coefficients or parameters to fit the results to the experiments. The simplicity of this mechanistic model in superposing the turbulence effect clearly shows how the freestream turbulence adds to the surface heat flux.

Comparisons

The analytical model developed from the time-resolved data was applied to the steady heat transfer results from the current work as well as to data from the work of other researchers to test its validity against other data sets. Requirements for application of the model were that the experiments measured surface heat transfer coefficients with and without turbulence and included local measurements (i.e., collocated with the surface heat transfer measurements) of time-resolved velocity to determine u'_{rms} and Λ_x.

Application of Model to Current Data Set. Using the measured turbulence data presented in Table 4 and determining the freestream static temperature at each gauge location from the measured test section total temperature and the blade Mach number distribution, the analytical model was applied at each gauge location on both the pressure and suction surfaces of the transonic turbine blade. The results are presented in Table 5.

The ratio of length scale compared to the boundary layer thickness estimate (Λ_x / δ) is approximately 100 on the suction surface and 20–30 on the pressure surface. The results demonstrate very good agreement between the model predicted and measured heat transfer coefficients on both blade surfaces. In addition, the analytical model closely predicts the observed differences in heat transfer augmentation between the suction surface and pressure surface. It is estimated that the boundary layer is laminar at all of these locations [25,26].

The application of other models and correlations in the open literature was performed on the current data set including the Dullenkopf and Mayle effective turbulence correlation [12], Maciejewski and Moffat St' correlation [6], and the Van Fossen et al. Frossling number correlation [11]. These other correlations predicted the pressure surface heat transfer augmentation well, but did not perform well on the suction surface data point or in predicting the differences in the heat transfer augmentation between the suction and pressure surfaces. The present model uses local turbulence characteristics rather than upstream turbulence measurements, which may account for its ability to accurately predict the current data set.

Application of Model to Other Data Sets. The model application to other cases spans cylinder stagnation point data, flat plate data, turbine vane, and turbine blade data, and includes both laminar and turbulent boundary layers on different geometries.

Cylinder Stagnation Point Data. The effects of freestream turbulence on stagnation point heat transfer, measuring time-resolved velocity and heat flux, were studied in unpublished work by Diller and Van Fossen. The measurements were performed in the same facility as used by Van Fossen et al. [11], using the same turbulence grids. The heat transfer model was a cylinder with a wedge shaped afterbody extending downstream to eliminate vortex shedding. The heat transfer model was placed in a low-speed wind tunnel with a freestream velocity of approximately 45 m/s. The cylinder model had an HFM high-frequency heat flux microsensor mounted in the stagnation region and a hot-wire anemometer probe mounted such that it could be traversed in the streamwise direction to measure time-resolved velocity approaching the stag-

Table 6 Results of model applied to cylinder stagnation point data (Diller and Van Fossen)

Case	Distance (in.)	Measured u'_{rms} (m/s)	Measured Λ_x (cm)	Δh_t (W/m^2 K)	Predicted high FST h (W/m^2 K)	Measured high FST h (W/m^2 K)
G4201	1.89	2.43	0.86	52.6	233	262
G4202	0.27	2.39	0.65	60.0	240	267
G4203	0.22	2.59	0.98	50.8	231	272
G4204	0.17	2.75	0.77	59.1	239	271
G4205	0.12	2.62	0.42	78.2	258	274
G4206	0.07	2.27	0.24	96.1	276	273

nation region. The results of the heat transfer tests for Grid G4 in the work of Van Fossen et al. [11] are presented in Table 6. The reported data represent six cases where the hot-wire probe was located at different streamwise locations (distance in second column) upstream of the stagnation region of the heat transfer model.

The analytical model was applied to these data as shown in Table 6. The mean heat transfer coefficient at low turbulence (less than 0.5% for this facility) was approximately 180 W/m^2 K. Uncertainty in the model predictions is likely of the same order as the model predictions from the current research work (±4.5% on the value of Δh_t). The model predictions of the heat transfer coefficient are quite good at the location where the turbulence characteristics are measured closest to the stagnation region (1.8 mm or 0.07 in.).

Low-Speed Turbine Vane Data. The effect of freestream turbulence intensity and length scale on turbine vane heat transfer in a low-speed facility was studied in detail by Radomsky and Thole [2]. An active turbulence-generating grid was placed upstream of the test section. Three-component laser Doppler velocimetry (LDV) measurements were performed, mapping the turbulence intensity in the blade passages. The turbulent length scale was measured using a single-sensor hot wire. In order to accurately apply the analytical model, the measurements nearest to the vane surface (near the edge of the boundary layer) were used as input data. Two inlet turbulence conditions (10% and 20%) were compared. The integral length scale of the inlet turbulence was 4.6 cm for the 10% turbulence case and 5.0 cm for the 20% turbulence case. The results of the model application to the 20% turbulence case are shown graphically in Fig. 7 with uncertainty bars of ±4.5% added to selected data points.

The results shown in Fig. 7 demonstrate that the model is good at predicting the increases in heat transfer due to freestream turbulence in the region where the boundary layer is laminar. The freestream turbulence also moves the transition region closer to the front of the blade, which causes a large discrepancy between the model and experiments for this region. Of course, this effect is not covered by this simple model. The model also does not match as well in the regions toward the trailing edge of the blade that appear to have a turbulent or transitional boundary layer. Similar results were obtained for the 10% freestream turbulence case.

Turbulent Flat Plate Data. Measurements of the effect of freestream turbulence and length scale on heat transfer to a flat plate with a turbulent boundary layer were reported by Moss and Oldfield [17]. Heat transfer was measured at three streamwise locations on the surface of the plate with and without freestream turbulence. Fluctuating velocity was measured with a hot-wire probe near the edge of the boundary layer at the surface of the plate. The flat plate boundary layer was tripped to create a turbulent boundary layer at downstream locations. The grids with the highest intensity were used (Grids D and E in Moss and Oldfield [17]) for the comparisons. The results of the modeling are presented in Table 7. Uncertainty in the modeled values of Nu/Nu$_0$ was estimated through the perturbation method to be ±2.4% (±0.03 Nu/Nu$_0$).

For Grid D, the model slightly overpredicts the measured increases in heat transfer. The model does not predict the heat transfer for Grid E as well, overpredicting the measured heat transfer at all three streamwise locations. This is similar to the results re-

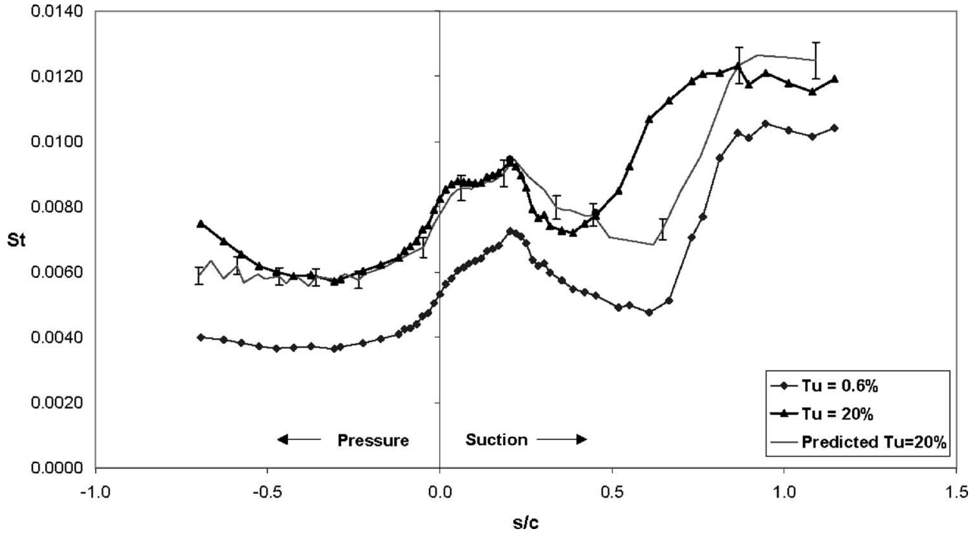

Fig. 7 Comparison of model predicted and measured Stanton numbers (St) from Radomsky and Thole [2]

Table 7 Model results compared to data from Moss and Oldfield[a]

Dist. x (mm)	Tu (%)	u'_{rms} (m/s)	Λ_x (cm)	Δh_t ($\mathrm{W/m^2\,K}$)	h_{o} ($\mathrm{W/m^2\,K}$)	Calc. $\mathrm{Nu/Nu_0}$	Reported $\mathrm{Nu/Nu_0}$
Grid D							
100	16.0	11.2	1.46	86.6	210.4	1.41	1.30
180	15.0	10.5	1.53	82.0	182.6	1.45	1.39
300	11.7	8.2	1.66	69.5	157.8	1.44	1.41
Grid E							
100	12.1	8.5	0.85	98.8	210.4	1.47	1.30
180	9.4	6.6	0.97	81.5	182.6	1.45	1.30
300	6.9	4.8	1.21	62.5	157.8	1.40	1.30

[a] See Ref. [17].

ported earlier in comparison with the work of Radomsky and Thole [2] where heat transfer in the regions of the turbine vane where the boundary layer was turbulent was overpredicted by the model.

The length scale for the Grid E case is smaller than for the Grid D case. The discrepancy between the model results and the measured heat transfer is larger for the smaller length scale case. This may indicate that the primary assumption of the model that large-scale eddies penetrate to the surface to affect heat transfer does not hold as well for smaller scale turbulence.

Conclusions

Measurements of the effect of large-scale freestream turbulence on time-averaged heat transfer on transonic turbine blades showed twice the increase on the pressure surface as that on the suction surface (17% on the pressure surface versus 8% on the suction surface). This corresponds to an increases in blade surface temperature of 4–10% (between 50°C and 100°C). Increases in temperature of 25°C or more can significantly decrease the life of turbine materials. The corresponding unsteady measurements of local velocity and heat flux demonstrated that there is a small band of frequencies for which free stream velocity fluctuations affect surface heat transfer, roughly centered around the frequency of the integral length scale (most energetic eddies) of the free stream turbulence. The analytical model that was developed based on the assumption of large-scale eddies penetrating the boundary layer and superimposing their thermal energy in the form of heat flux increases on the mean heat flux appears to be reasonable. Using the integral length scale and rms of the velocity, a mechanistic model of the effect of large-scale freestream turbulence matched experimental data quite well for a range of geometries. The difference in pressure and suction side heat transfer increases were explained in addition to the augmentation of heat transfer at the stagnation point of cylinders, on turbine vanes and flat plates. The model predicted the effect of freestream turbulence for a range of intensities from 5% to 20% and integral length scales from 0.25 cm to 5 cm. The model overpredicts the effect of freestream turbulence on turbulent boundary layers and does not include the effect of high-freestream turbulence on early boundary layer transition. With these limitations, the justification has been presented for a realistic physical model of how large-scale freestream turbulence affects surface heat transfer.

Acknowledgment

This work was sponsored by the Air Force Office of Scientific Research (AFOSR) under Grant/Contract No. F49620-01-1-0177, monitored by Dr. Tom Beutner.

Nomenclature

c = chord length
c_{ps} = pressure surface chord length
c_{ss} = suction surface chord length
D_s = HFM gauge sensing diameter
f = frequency
h = convection heat transfer coefficient
h_{o} = low freestream turbulence heat transfer coefficient
k = thermal conductivity of freestream air
Nu = Nusselt number
Nu_0 = low freestream turbulence Nusselt number
p = blade pitch
q' = heat flux fluctuations
q'' = heat flux
$\mathrm{Re}_{\mathrm{ex}}$ = Reynolds number $\rho U_{\mathrm{ex}} c/\mu$
sp = blade span
St = Stanton number
t' = temperature fluctuations
T_b = blade surface temperature
T_w = wall temperature
T_∞ = freestream temperature of air
Tu = turbulence intensity u'_{rms}/U
u', v' = velocity fluctuations
u'_{rms} = rms of streamwise velocity fluctuations
U = freestream velocity
U_{ex} = blade passage exit velocity
x = distance along blade chord
α = thermal diffusivity of freestream air
δ = boundary layer thickness
Δq_t = modeled increase in heat flux due to freestream turbulence
Δh_t = modeled increase in heat transfer coefficient due to freestream turbulence
γ^2_{uq} = coherence function between velocity and heat flux
Λ_x = turbulent length scale
ρ = density of freestream air
μ = viscosity of freestream air

References

[1] Van Fossen, G. J., and Bunker, R. S., 2002, "Augmentation of Stagnation Region Heat Transfer Due to Turbulence From an Advanced Dual-Annular Combustor," Paper No. ASME GT-2002-30184.

[2] Radomsky, R. W., and Thole, K. A., 1998, "Effects of High Freestream Turbulence Levels and Length Scales on Stator Vane Heat Transfer," Paper No. ASME 98-GT-236.

[3] Radomsky, R. W., and Thole, K. A., 2000, "Flowfield Measurements for a Highly Turbulent Flow in a Stator Vane Passage," ASME J. Turbomach., **122**, pp. 255–262.

[4] Blair, M. F., 1983, "Influence of Free-Stream Turbulence on Turbulence Boundary Layer Heat Transfer and Mean Profile Development, Parts I and II," ASME J. Heat Transfer, **105**, pp. 33–47.

[5] Maciejewski, P. K., and Moffat, R. J., 1989, "Heat Transfer with Very High Free Stream Turbulence," Stanford University Report No. HMT-42, Stanford University, Stanford, CA.

[6] Maciejewski, P. K., and Moffat, R. J., 1992, "Heat Transfer with Very High Free Stream Turbulence: Parts I & II," ASME J. Heat Transfer, **114**, pp. 827–839.

[7] Maciejewski, P. K., and Anderson, A. M., 1996, "Elements of a General Correlation for Turbulent Heat Transfer," ASME J. Heat Transfer, **118**, pp. 287–293.

[8] Denninger, M. J., and Anderson, A. M., 1999, "An Experimental Study on the Relationship Between Velocity Fluctuations and Heat Transfer in a Turbulent

Air Flow," ASME J. Turbomach., **121**, pp. 288–294.
[9] Barrett, M. J., and Hollingsworth, D. K., 2003, "Correlating Friction Velocity in Turbulent Boundary Layers Subjected to Free-Stream Turbulence," AIAA Paper No. J-26247.
[10] Thole, K. A., and Bogard, D. G., 1995, "Enhanced Heat Transfer and Shear Stress Due to High Free-Stream Turbulence," ASME J. Turbomach., **117**, pp. 418–424.
[11] Van Fossen, G. J., Simoneau, R. J., and Ching, C. Y., 1995, "Influence of Turbulence Parameters, Reynolds Number, and Body Shape on Stagnation Region Heat Transfer," ASME J. Heat Transfer, **117**, pp. 597–603.
[12] Dullenkopf, K., and Mayle, R. E., 1995, "An Account of Free-Stream-Turbulence Length Scale on Laminar Heat Transfer," ASME J. Turbomach., **117**, pp. 401–406.
[13] Ames, F. E., 1995, "The Influence of Large-Scale High-Intensity Turbulence on Vane Heat Transfer," ASME J. Turbomach., **119**, pp. 23–30.
[14] Ames, F. E., 1997, "Aspects of Vane Film Cooling with High Turbulence—Part I: Heat Transfer," Paper No. ASME 97-GT-239.
[15] Radomsky, R. W., and Thole, K. A., 2002, "Detailed Boundary Layer Measurements on a Turbine stator Vane at Elevated Freestream Turbulence Levels," ASME J. Turbomach., **124**, pp. 107–118.
[16] Wang, H. P., Goldstein, J., and Olson, R. J., 1999, "Effect of High Freestream Turbulence with Large Scale on Blade Heat/Mass Transfer," ASME J. Turbomach., **121**, pp. 217–224.
[17] Moss, R. W., and Oldfield, M. L. G., 1992, "Measurements of the Effect of Free-Stream Turbulence Length Scale on Heat Transfer," Paper No. ASME 92-GT-244.
[18] Moss, R. W., and Oldfield, M. L. G., 1996, "Effect of Free-Stream Turbulence on Flat-Plate Heat Flux Signals: Spectra & Eddy Transport Velocities," ASME J. Turbomach., **118**, pp. 461–467.
[19] Holmberg, D. G., Diller, T. E., and Ng, W. F., 1998, "A Frequency Domain Analysis: Turbine Pressure Side Heat Transfer," Paper No. ASME 98-GT-152.
[20] Holmberg, D. G., Diller, T. E., and Ng, W. F., 1997, "A Frequency Domain Analysis: Turbine Leading Edge Region Heat Transfer," Paper No. ASME 97-WA/HT2.
[21] Holmberg, D. G., and Pestian, D. J., 1996, "Wall-Jet Turbulent Boundary Layer Heat Flux, Velocity, and Temperature Spectra and Time Scales," Paper No. ASME 96-GT-529.
[22] Nix, A. C., Smith, A. C., Diller, T. E., Ng, W. F., and Thole, K. A., 2001, "High Intensity, Large Length-Scale Freestream Turbulence Generation in a Transonic Cascade," Paper No. ASME GT-2002-30523.
[23] Polanka, M. D., 1999, "Detailed Film Cooling Effectiveness and Three Component Velocity Field Measurements on a First Stage Turbine Vane Subject to High Freestream Turbulence," Ph.D. dissertation, The University of Texas at Austin, Austin, TX.
[24] Smith, D. E., Bubb, J. V., Popp, O., Grabowski, H. C., Diller, T. E., Schetz, J. A., and Ng, W. F., 2000, "Investigation of Heat Transfer in a Film Cooled Transonic Turbine Cascade, Part I: Steady Heat Transfer," Paper No. ASME 2000-GT-202.
[25] Wesner, A., 1996, "A Single-Plate Interferometric Study of the Unsteady Density Field in a Transonic Cascade," Ph.D dissertation, Virginia Tech., Blacksburg, VA.
[26] Holmberg, D. G., 1996, "A Frequency Domain Analysis of Surface Heat Transfer/Freestream Turbulence Interactions in a Transonic Turbine Cascade," Ph.D dissertation, Virginia Tech., Blacksburg, VA.
[27] Popp, O., Smith, D. E., Bubb, J. V., Grabowski, H. C., Diller, T. E., Schetz, J. A., and Ng, W. F., 2000, "Investigation of Heat Transfer in a Film Cooled Transonic Turbine Cascade, Part II: Unsteady Heat Transfer," Paper No. ASME 2000-GT-203.

Stephen Rashid
Advanced Turbomachine, LLC,
261 N. Main Street,
Wellsville, NY 14895
e-mail: srashid@advancedturbomachine.com

Matthew Tremmel
ProAero Technology,
641 Nightingale Drive,
Indialantic, FL 32903

John Waggott

Randall Moll
Steam Advanced Engineering,
Dresser-Rand Company,
37 Coats Street,
Wellsville, NY 14895

Curtis Stage Nozzle/Rotor Aerodynamic Interaction and the Effect on Stage Performance

Curtis, or velocity compounded, stages commonly don't achieve the same accuracy of performance prediction expected of most other turbine stages. A review of Curtis stage design practices, field wear, and dirt patterns, in conjunction with performance testing and computational fluid dynamics (CFD) modeling, determined that the nozzle/rotor aerodynamic interaction is far more complex than typical design and performance calculations assume. Understanding this nozzle/rotor interaction is key to obtaining both improved performance, and a more accurate performance prediction. This paper discusses the nature of this interaction, and it's implications to Curtis stage performance prediction. [DOI: 10.1115/1.2720481]

Introduction

Curtis, or velocity compounded, stages are a subgroup of impulse turbine stages. They are typically applied when the velocity ratio, U/C_0, is below 0.25, resulting in very low wheel speed compared to the overall expansion energy. The low relative wheel speed means that not all of the fluid energy can be extracted in the initial rotor row, thus, Curtis stages have at least one additional stator row, or reversing ring, combined with a second rotor row. Some Curtis stages have as many as four rotor rows in total, with reversing rings between each rotor pair, however, the two row Curtis stage is by far the most commonly used. These succeeding reversing ring/rotor combinations provide the velocity compounding for the stage by capturing the remaining velocity energy in the fluid. Since Curtis stages are impulse stages, it is assumed that all of the stage pressure drop occurs across the stage nozzle. A typical flowpath layout for a two row Curtis stage is provided in Fig. 1.

Curtis stages are usually used in applications where very high work levels are required from a single stage. The typical efficiency of a Curtis stage is 40–50%, so they tend to be applied in single stage machines where low cost and raw power are the key requirements. Curtis stage design practices reflect their utilitarian application, and are based on empirical data gathered over many years.

Due to the nature of these machines, and the applications they serve, there is very little published information regarding the performance prediction of Curtis stages beyond general text books on turbomachinery. Some information on these stages is provided in Salisbury [16] and Church [17], but this information is very general in nature.

However, even in this environment, where cost tends to outweigh efficiency, there is a need to predict the final unit performance so that the turbine can be sized with reasonable accuracy to it's intended usage. This is where the Curtis design systems fall short. Performance predictions for Curtis stages are an order of magnitude less precise than what is commonly achieved on Rateau impulse or reaction stages.

Curtis stage builders have conducted numerous test programs in an attempt to tighten the performance prediction tolerance, with only limited success. This paper will discuss the causes of this performance prediction inaccuracy, with supporting information from aerodynamic theory, testing, turbine dirt and wear patterns, and CFD analysis.

Finally, the test data presented in the following sections are the result of performance tests conducted by the authors under the auspices of a performance testing program carried out by Dresser–Rand Company.

Curtis Stage Performance Variability

As noted previously, Curtis stages are not used where efficiency is a design requirement. Typical Curtis stage efficiencies range between 40% and 50%, and can be as low as 25% at very low values of U/C_0. However, being able to predict efficiency, with some degree of accuracy, is necessary, even in low-efficiency applications. In Curtis stage designs, the increased error associated with efficiency prediction generally translates to increased nozzle area to provide a flow margin in case output power becomes an issue. While this approach does ensure that the design power is attained, in can further reduce turbine efficiency through increased throttling losses if the flow margin is not required, making the poorer performance a self-fulfilling prophecy.

Curtis stage builders have spent a fair amount of effort to understand the variability in Curtis stage performance. This variability is shown in Fig. 2(*a*), along with Rateau stage designs for comparison. Figure 2(*b*) presents the efficiency differential between measured test and predicted efficiency versus predicted efficiency. Predicted efficiencies were obtained using the same design/performance calculation tools used to design the turbines in question. The primary design tool used to predict efficiency is a meanline calculation with a calibrated loss model.

As can be seen in Figs. 2(*a*) and 2(*b*), the variation in final tested efficiency relative to the predicted design value is significantly greater for Curtis stages than it is for Rateau stages. Even if the Curtis stage performance expectation is lowered to the average of the test data (the dashed black line in Figs. 2(*a*) and 2(*b*)), the variation from the new standard is still much greater than that for Rateau stages. Thus, the Curtis stage performance prediction issue is not just a matter of simply over predicting efficiency, it is to a large extent the greater error band associated with that performance prediction.

It is not uncommon for final tested Curtis stage performance to vary by 2–3% relative to the predicted value, and discrepancies of more than 5% occur in about 25% of Curtis installations. This means that the final efficiency may vary by several points relative to the predicted value. By contrast, the tested efficiency of Rateau

---

Contributed by the International Gas Turbine Institute of ASME for publication in the JOURNAL OF TURBOMACHINERY. Manuscript received June 12, 2006; final manuscript received June 16, 2006. Review conducted by David Wisler. Paper presented at the ASME Turbo Expo 2006: Land, Sea and Air (GT2006), Barcelona, Spain, May 8–11, 2006. Paper No. GT2006-91115.

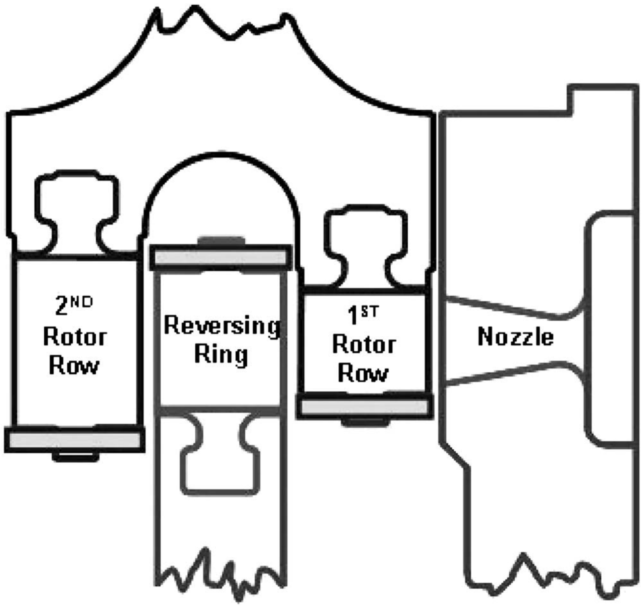

Fig. 1 Typical two row Curtis stage flowpath layout

machines seldom varies by more than a fraction of a percent from the design prediction, which generally translates to efficiency discrepancies of less that a point, and usually within 0.5 points.

Finally, while there is significant data scatter, there appears to be a trend with U/C_0. Performance prediction for Curtis stages, as imprecise as it is, tends to be better at lower values of U/C_0, as shown in Fig. 3.

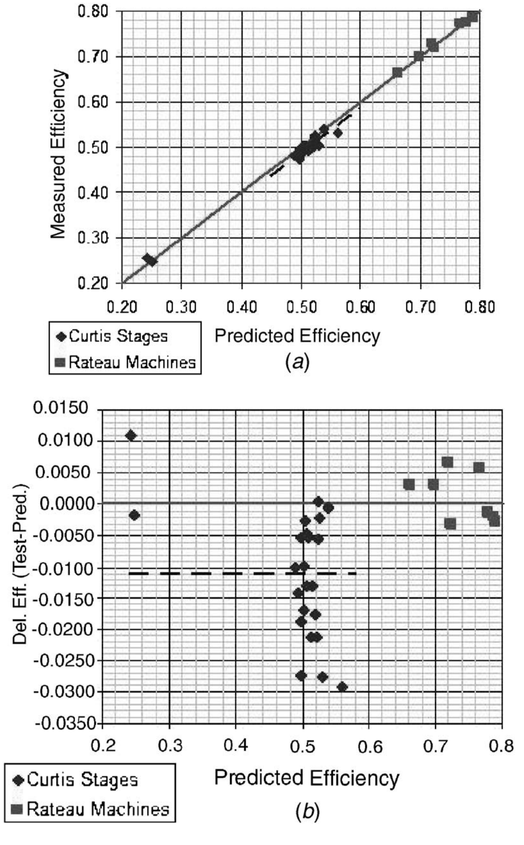

Fig. 2 (*a*) test versus predicted efficiency comparison; and (*b*) $\Delta\eta$ (test-predicted) versus predicted efficiency for Curtis and Rateau machines

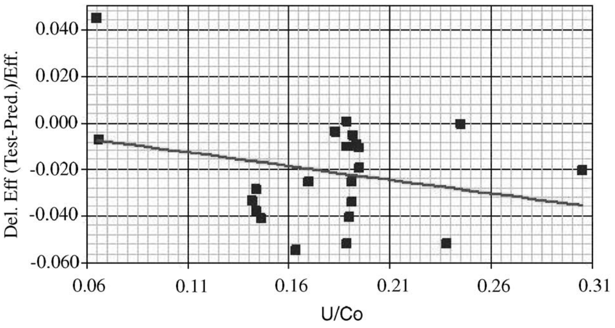

Fig. 3 Normalized Curtis efficiency variation versus U/C_0

Since, in a two row Curtis stage, nearly 80% of the stage power is provided by the first row, and noting that the nozzles and rotor blades are typically not aerodynamically challenging to design in their own rights, it is assumed that the interaction between the nozzle and first rotor row is the primary design area key to the understanding of Curtis stage performance variability.

Velocity Triangles

The basic nozzle/rotor interaction issue can be seen in a typical Curtis stage nozzle exit/rotor inlet velocity triangle. The low U/C_0 ensures that the first rotor row inlet flow vector is very close in magnitude and direction to the nozzle exit flow vector. While Curtis stages may be characterized by low U/C_0 due to low wheel speed, generally they operate in this regime as a result of the high stage energies at which they are applied. This results in a rotor inlet Mach number, in the relative reference frame, that is nearly as high as the Mach number leaving the nozzle in the absolute reference frame. Figure 4 provides a graphical representation of the nozzle to rotor velocity triangle, with the nozzle absolute exit velocity (labeled "V"), and variations in the rotor relative inlet velocity (for Curtis and Rateau stages, as labeled) as wheel speed, and U/C_0, increase.

The Curtis stage regime shown in Fig. 4 encompasses U/C_0 values of 0.04–0.20, while the Rateau stage spans values of 0.40–0.55. In both cases, these are typical design ranges for U/C_0. The dotted lines in Fig. 4 highlight these relative velocity regimes as a fraction of the absolute velocity, *V*. This fundamental velocity triangle comparison can be extended to obtain quantitative insight. In Fig. 5, the ratio of nozzle exit absolute Mach number to the rotor inlet relative Mach number is presented as a function of U/C_0 and nozzle exit flow angle. This plot essentially depicts the required nozzle exit Mach number to retain a sonic rotor inlet.

The curves in Fig. 5 are derived from a simple trigonometric relationship based on the nozzle exit/rotor inlet velocity triangle

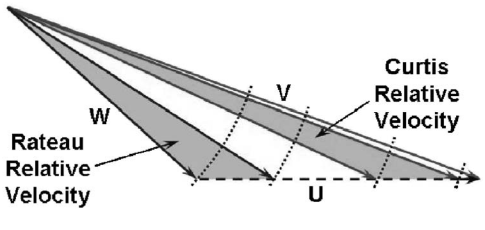

Fig. 4 Nozzle/rotor velocity triangle comparison between Curtis and Rateau stages

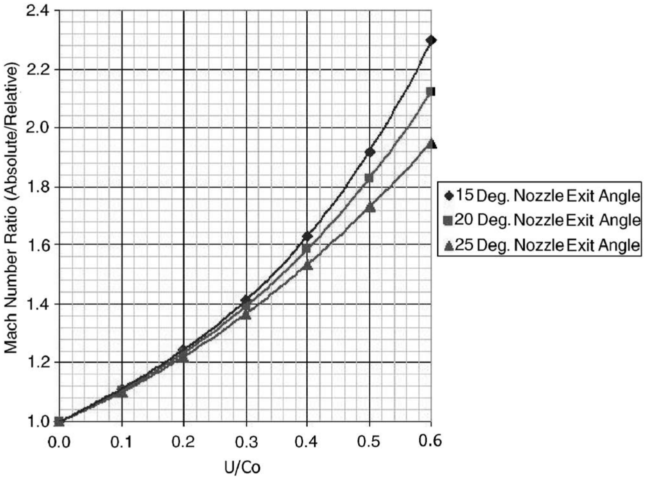

Fig. 5 Absolute/relative Mach number ratio as a function of U/C_0 and nozzle exit flow angle

$$\frac{M_{\mathrm{ABS}}}{M_{\mathrm{REL}}} = \frac{1}{\sqrt{\left(\cos(\alpha) - \left(\frac{U}{(\phi)C_0}\right)\right)^2 + \sin^2(\alpha)}} \tag{1}$$

where ϕ^2 represents the energy coefficient of the nozzle, or the square of the velocity coefficient, ϕ, and was assumed to be 0.95 (the resulting value of ϕ being 0.9747) for the curves of Fig. 5.

It can be seen that, at the low U/C_0 values typically associated with Curtis stages, the rotor inlet relative Mach number will remain sonic, or even supersonic, for relatively modest nozzle exit velocities. However, as the U/C_0 increases, it takes an ever increasing nozzle exit Mach number to retain a sonic rotor inlet condition. Therefore, Curtis stages have an aerodynamic constraint, a supersonic rotor inlet, which is not common to other impulse turbine stages, or for that matter, other turbine stages in general, simply due to the low U/C_0 regime in which they operate and the high nozzle exit Mach number associated with high stage energy.

Supersonic Nozzle Exit Condition

The nozzle exit condition for a Curtis stage, as noted in the previous section is nearly always supersonic. As with other turbine rows, this supersonic exit condition results in Prandtl–Meyer expansion on the uncovered portion of the nozzle, with the accompanying supersonic flow angle deviation. While Prandtl–Meyer expansion is the mechanism for this deviation, the best results for calculating the final supersonic flow angle have typically been achieved through the use of isentropic A/A^* relationships [1]

$$\sin(\alpha_2) = \sin(\alpha_2^*)\left(\frac{A}{A^*}\right) \tag{2}$$

where α_2 and α_2^* are measured from tangential. This is due to the complexity of the shock/expansion fan structure which greatly complicates the Prandtl–Meyer analysis.

This condition must be satisfied regardless of any other boundary conditions that may exist. Therefore, the inlet relative flow angle to the first rotor row will be a function of the nozzle geometry, the nozzle pressure ratio, and the wheel speed.

Unique Rotor Incidence

As noted in the previous sections, the velocity triangle into the first rotor row of a Curtis stage is very likely to result in a supersonic relative velocity. While this condition is common in certain axial compressors and fans, as noted by Cumpsty [6], it is only encountered occasionally in turbines.

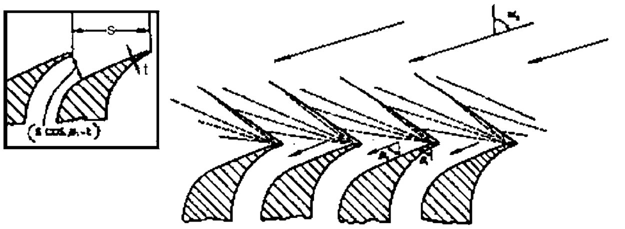

Fig. 6 Rotor blades with a leading edge chamfer operating at a fixed incidence [3]

The significance of the supersonic inlet condition to the first rotor row is the accompanying unique incidence [2]. A turbomachinery row with a supersonic inlet velocity can only accept flow at a specific flow angle. In order to establish a periodic flow field, the bow shock and the succeeding expansion fans must exactly counteract each other so that each blade will see the same conditions as the adjacent blade. This is shown in Fig. 6, which has been reprinted from Ref. [3].

Methods for determining the unique inlet angle of a supersonic blade row depend on the leading edge geometry of the airfoil in question.

As seen in Fig. 6, Stratford and Sansome [3,4] defined a method for calculating the unique incidence based on a Prandtl–Meyer relationship between the upstream flow angle, the blade metal angle, the leading edge thickness, and the relative stream segment areas between Stations 2 and 2′ (shown in Fig. 7)

$$F_{P\text{-}M}(\beta_2 - \beta_{2'}) = (\tau(\sin\beta_{2'}) - t) - \tau(\sin\beta_2) \tag{3}$$

or in the nomenclature of Stratford and Sansome

$$F_{P\text{-}M}(\alpha_1 - \beta_1) = (s(\cos\beta_1) - t) - s(\cos\alpha_1) \tag{4}$$

where $F_{P\text{-}M}(\theta)$ is the Prandtl–Meyer function defined as

$$F_{P\text{-}M}(\theta) = \sqrt{\frac{\gamma+1}{\gamma-1}}\tan^{-1}\sqrt{\frac{\gamma-1}{\gamma+1}(M^2-1)} - \tan^{-1}\sqrt{M^2-1} \tag{5}$$

If it is assumed, on an overall basis, that the Mach number at Station 2′, as shown in Fig. 7, must equal the Mach number at Station 2, the areas of these two stations must be essentially the same in the absence of significant losses through the shock/expansion fan system (which is reasonable for an oblique shock). Therefore, the upstream relative flow angle, β_2, can be defined by

$$\beta_2 = \sin^{-1}\left(\frac{\lambda_{\mathrm{LE}}}{\tau}\right) \tag{6}$$

Under these conditions, the Prandtl–Meyer function, $F_{P\text{-}M}(\beta_2 - \beta_{2'})$, (or $F_{P\text{-}M}(\alpha_1 - \beta_1)$ in the nomenclature of Stratford and Sansome), is set equal to zero and the relationship defined by Stratford and Sansome simplifies to the equation for β_2 illustrated by Fig. 7.

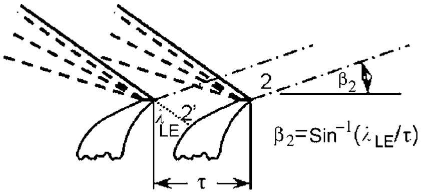

Fig. 7 Determination of unique incidence based on A/A^* or constant flow area

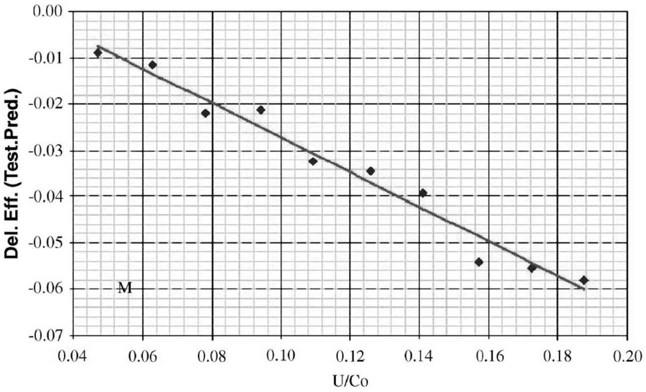

Fig. 8 Normalized efficiency variation versus U/C_0 for an individual turbine

Finally, in order for the supersonic rotor inlet condition to exist, the flow area at the rotor inlet must be correct, not only with respect to the flow angle, but in terms of the overall flow area as well. Simple continuity and two-dimensional (2D) potential flow calculations verify that the streamtube required to satisfy the overall rotor inlet flow area is significantly less than the full leading edge height. If this is not the case, if the full height is involved in passing the flow, then the entire flowfield must shock down to a subsonic solution at the rotor leading edge. The resulting static pressure increase at the rotor leading edge would represent significant stage reaction.

Curtis Stage Performance Testing

As can be seen in Fig. 3, there is an apparent effect of U/C_0 on the performance of a Curtis stage which is not accounted for in the performance models. In order to ascertain the basis of this U/C_0 effect, a series of performance tests were carried out. These tests sought to verify the apparent trend in performance prediction accuracy with U/C_0 shown in Fig. 3.

Test instrumentation consisted of three inlet flange pressures and temperatures, one nozzle bowl pressure, four nozzle exit pressures (as described in Fig. 9), and three exhaust flange pressures and temperatures. In addition, speed, flow rate, and torque were also measured. All instruments (pressure transducers and resistance temperature detectors (RTDs)) were calibrated before and after each test to verify data accuracy. Pressure transducers of appropriate range were used at each measurement location. The data presented are the results of numerous individual tests. Test uncertainty varies slightly from test to test, but the typical test uncertainty is approximately ±3%, with the largest component of this uncertainty being spatial uncertainty (the uncertainty associated with how well an array of instruments can accurately measure the average condition). Finally, repeat test points were taken after each test program, and entire test programs rerun, to verify the repeatability of the data.

This series of tests consisted of running a single Curtis stage unit, at constant pressures and temperatures, over a range of velocity ratios by varying the turbine speed. The results of these tests are provided in Fig. 8.

In addition to overall performance instrumentation, this test series also included static pressure taps at various locations around the nozzle exit. Fig. 9 illustrates the positioning of these static pressure taps at the nozzle trailing edge.

This added nozzle instrumentation was intended to assist in the determination of stage reaction, and how the pressure just inside the nozzle (P_{SHORT}, P_{MID}, and P_{LONG}) compared to the pressure between the nozzle and rotor (P_{FACE}).

Studies on a supersonic Rateau stage carried out by Kurzrock [5] note that reaction varies with U/C_0, with the reaction being

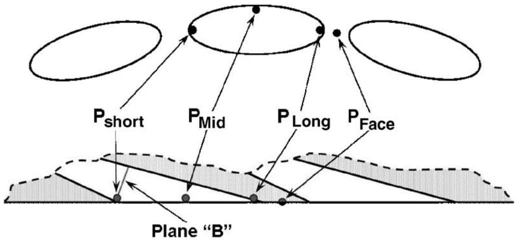

Fig. 9 Nozzle exit static pressure tap locations

negative at the low boundary of his published data, U/C_0 of 0.2. Data from the Curtis stage testing, as noted in Fig. 8, were carried out at U/C_0 values below the range of Kurzrock's published work, but the trend toward negative reaction in this regime was confirmed, as presented in Fig. 10.

While Fig. 10 shows virtually constant reaction over the entire U/C_0 range, the nozzle static pressure taps reveal significant variation in pressure with changes in wheel speed. In Fig. 11, nozzle long, mid, and short side pressures are plotted as ratios to the nozzle face pressure.

As Fig. 11 shows, the short side pressure has almost no variation relative to the face pressure. Since the short side pressure represents the last point at which the nozzle is a full passage, it demonstrates a well behaved relationship with the face pressure. The mid and long side pressures, however, vary considerably relative to the face pressure. These pressures, in the "uncovered" portion of the nozzle are subject to the after expansion as flow leaves the "covered" portion of the passage, showing the effects of flow angle variation, and/or streamtube height variation, with speed,

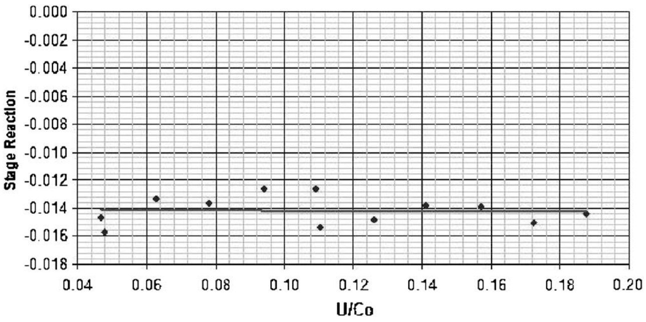

Fig. 10 Measured stage pressure reaction for Curtis stage testing

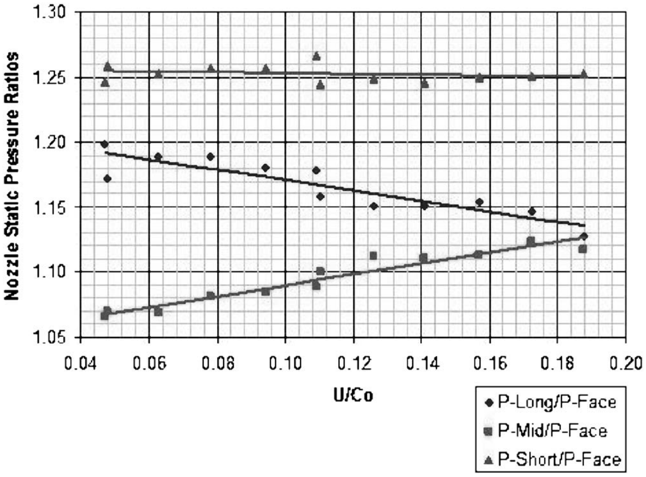

Fig. 11 Nozzle static pressure data versus U/C_0

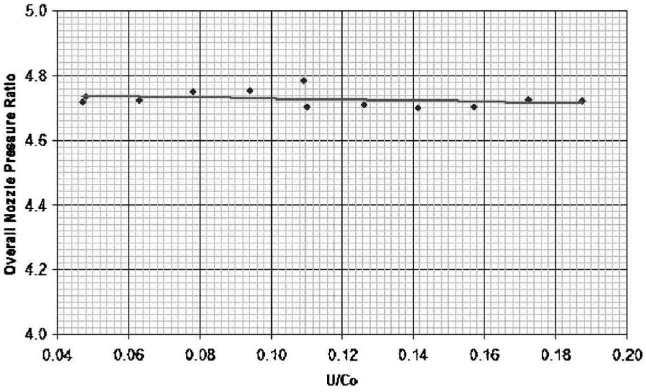

Fig. 12 Overall nozzle pressure ratio versus U/C_0

and thus U/C_0. This angle/streamtube height variation occurs even though the overall nozzle pressure ratio remains essentially constant, as seen in Fig. 12.

Dirt and Wear Patterns

As discussed in the previous sections, the supersonic flowfield of the first rotor inlet dictates that the leading edge flow area be significantly less than the full leading edge span would provide. While this conclusion appears to be difficult to substantiate, there is evidence in field units that this is indeed the case.

Figure 13 presents a mapping of first rotor row dirt patterns observed by the authors during a field inspection of a single stage Curtis unit. These are superimposed on a clean, single blade for clarity. For the most part, there was a nearly uniform coating of deposits over the entire flowpath portion of the blade. However, the most striking feature of the observed deposits is the virtually clean area on the midspan region of the suction surface leading edge. This clean portion stopped abruptly at the point where the suction surface became covered by the adjacent blade. Figure 14 provides dimensions, taken at the time of the inspection, of the radial extent and location of the clean area.

When these dirt patterns are compared to typical first rotor row blade wear on long running units, as diagrammed in Fig. 15, there is a clear correspondence between the areas of highest blade wear, and the cleanest portions of the dirt patterns.

Finally, a comparison of the axial nozzle breakout area to an annular streamtube of the same area was made, and is depicted in Fig. 16(*a*). When the height of the respective areas are compared to the noted clean area on the first rotor row suction surface, it is found that the exposed nozzle height of 11.84 mm is significantly larger than the apparent 7.95 mm height of the stream entering the rotor.

The calculated annular streamtube height of 8.13 mm is very close to the 7.95 mm value. This leads to the conclusion that the flow is indeed coalescing from discrete nozzle streams into a coherent uniforn stream, and at the time it enters the rotor, it has virtually completely made the transition. The actual streamtube entering the rotor is probably not perfectly annular, but similar to the shaded area shown in Fig. 16(*a*).

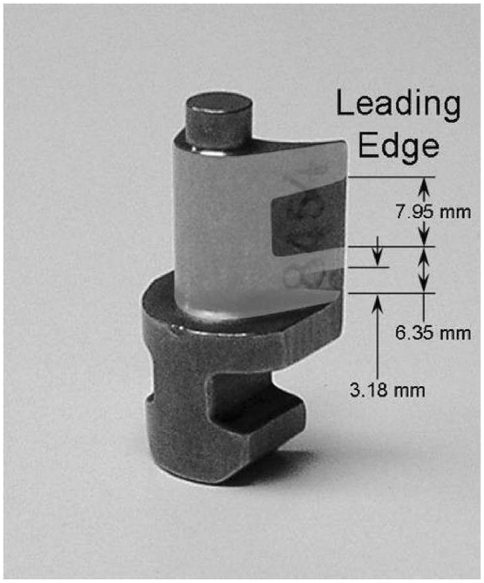

Fig. 14 Radial location and extent of clean suction surface leading edge

With an axial spacing between the nozzle exit and the first rotor row leading edge on the order of 1.27 mm, it doesn't seem likely that the flow could make the transition. However, the data presented in Figs. 10–12 indicate that the transition actually begins in the nozzle. Figures 10 and 12 show that the nozzle exit Mach number is essentially constant with U/C_0. This constant Mach number, combined with the requirement for unique rotor incidence, implies that the axial flow area and absolute flow angle must compensate to achieve these conditions. Therefore, A_{AX} and α_2 are a function of M_2

$$A_{\mathrm{AX}}(\sin(\alpha_2)) = F(M_2) \tag{7}$$

and

$$\beta_2 = \tan^{-1}\left(\frac{\sin(\alpha_2)}{\cos(\alpha_2) - \left(\dfrac{U}{\phi C_0}\right)}\right) \tag{8}$$

where β_2 is equal to 24.05 deg for the hardware tested based on Eq. (6). From Eqs. (7) and (8), it can be seen that as U/C_0 in-

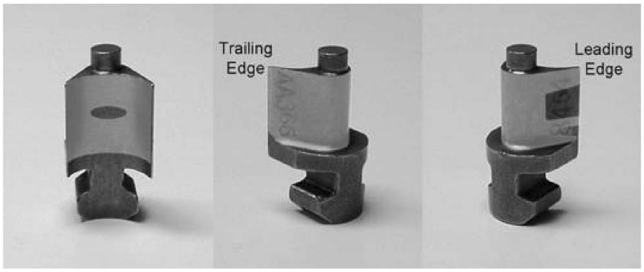

Fig. 13 First rotor dirt patterns observed during a field inspection (mapped on a new blade for clarity)

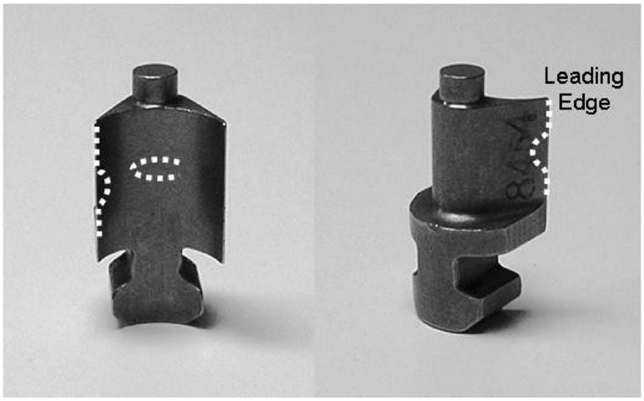

Fig. 15 Typical areas of first rotor blade wear for long service units

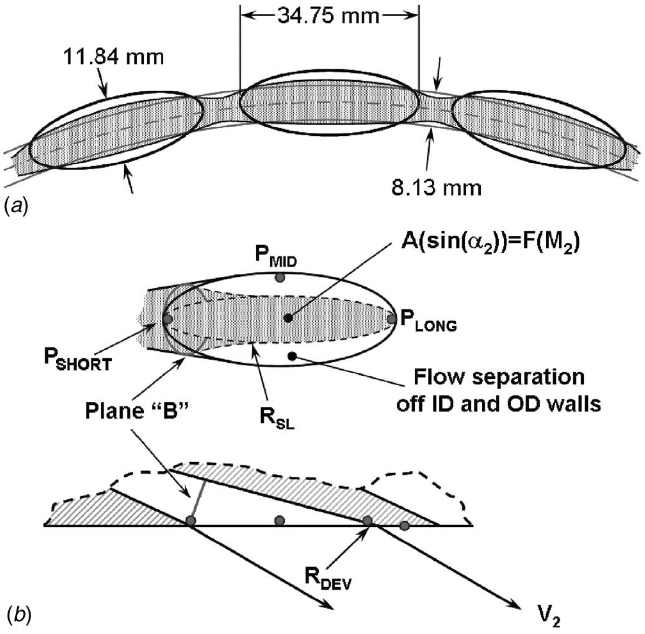

Fig. 16 (*a*) **Comparison of axial nozzle breakout area to equivalent annular height; and** (*b*) **streamtube and angle variation at the nozzle exit to maintain constant Mach number and unique rotor incidence with varying U/C_0**

creases, α_2 decreases, and A_{AX} compensates to hold the Mach number. This is depicted in Fig. 16(*b*), where R_{SL} represents the streamline curvature in the meridional plane due to the variation in A_{AX}, and R_{DEV} denotes the streamline curvature in the tangential plane due to deflection of the exit flow angle.

The data presented in Fig. 11 show the static pressure at P_{SHORT} is constant with U/C_0, indicating that the streamtube at plane "*B*" is not changing as U/C_0 varies. Plane "*B*" is the last point in the nozzle where the nozzle is fully enclosed. As U/C_0 increases, P_{LONG} decreases, indicating reduced streamtube curvature due to the deflection of α_2. As the axial flow area compensates with increasing U/C_0, the streamtube curvature, R_{SL}, is also reduced, resulting in higher pressures at P_{MID}.

Note that P_{MID} and P_{LONG} have opposite responses to reduced streamtube curvature in their respective planes. This is due to the difference in their locations relative to the streamtube curvatures that drive them. P_{LONG} is at the outer diameter (OD) of R_{DEV} causing pressure to increase with increased curvature. P_{MID} is inboard of the outer diameter (OD) of R_{SL} which results in reduced pressure for an increase in curvature.

For the test unit, operating at the design condition, the U/C_0 is 0.17, and the resulting streamtube height is 9.98 mm. This height is much closer to the 7.95 mm height noted in the dirt patterns than the full nozzle exit height of 11.84 mm. Thus, the transition to the 7.95 mm flow height begins at the last "covered" portion of the nozzle, or plane "*B*."

CFD Modeling

To gain some insight into the nature of the complicated flow through a Curtis stage, an unsteady CFD calculation was performed for a representative geometry and running condition.

As reflected Table 1 a complete quantitative analysis comparing the experimental results to the CFD simulation would be difficult to perform, due to the difference in nozzle arrangement and annulus shape. Therefore, the CFD simulation focused on uncovering and detailing the complicated interaction of the nozzle/rotor aerodynamic wake/shock interactions and respective flow complexity.

Table 1 Comparison of features of actual Curtis stage to CFD simulation

Feature	Curtis stage machine	CFD simulation
Stages	2	1
P_{01}/P_3	4.1	4.1
U/C_0	0.18 (based on meanline)	—
Nozzle arrangement	3-port, 180-deg arc Gov port: 12 nozzles Port 1: 2 nozzles Port 2: 2 nozzles	Full annulus with 40 nozzles
Rotor count	108	108
Nozzle type	Drilled hole	Blade passage
Annulus shape	Stepped	Smooth
Leakage	Unknown	None

Numerical Method. Simulation of the flowfield through the nozzle and first rotor row was performed with the parallel code TURBO [13,14]. It was developed by Dr. Jen Ping Chen with support from NASA, Department of Defense, and the turbomachinery industry. TURBO is a compressible flow code that solves the unsteady RANS equations within the rotating reference frame. The code uses an implicit finite volume scheme with a NASA/CMOTT-developed two-equation k-ε turbulence model [15]. For efficient use of computing resources, a phase-lag approximation is available to enable use of only one blade passage per blade row in the simulation. Recent applications of the TURBO code have shown its usefulness for multistage, time accurate CFD [9,10].

Geometry and Grids. The grid for the simulation was created by TCGRID [12] developed by Dr. Roderick Chima at NASA Glenn. A custom code was then developed to convert the grids to the necessary formats for use with TURBO. Due to the difficulty in modeling the drilled-hole nature of the stationary nozzle in the Curtis stage, a representative blade model was developed. Throat position and location were kept as close as possible to the original hole-based design while blade height was varied to match throat and exit areas. Figure 17 shows the midspan comparison between the blade-to-blade passage of the nozzle hole and resulting blade passage.

The nontapered nature of the blading used in Curtis stages presented an issue regarding the smoothness of the annulus contour for the simulation. The nozzle exit height is 9.96 mm while the rotor height is 17.78 mm. The axial gap is only 1.27 mm. The sudden step in height could not be adequately handled. Therefore, the nozzle exit height was reduced to compensate for the additional area created by using a blade "passage" rather than the drilled hole. The height of the nozzle at the throat location was also slightly reduced. The end result was throat area and nozzle exit plane area that corresponded to the drilled-hole geometry. Based on the dirt pattern evidence that the nozzle basically jets the flow into the rotor, the upper and lower 6.35 mm of the inlet rotor does not appear to be "seen" by the flow. Therefore, a blending of the nozzle and rotor flowpaths using linear interpolation between nozzle throat and rotor exit was implemented. The resulting meridional flowpath is shown in Fig. 18.

The simulation consisted of the first nozzle and the subsequent

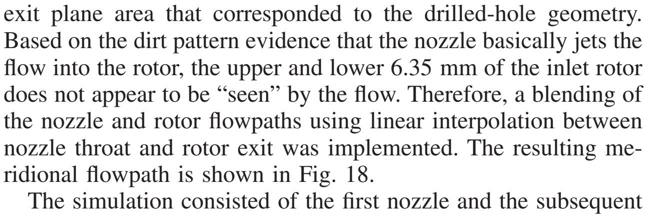

Fig. 17 Comparison of nozzle shape based on actual drilled-hole (left) and simulation-based adjustment (right)

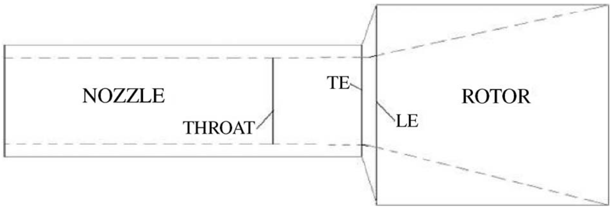

Fig. 18 Actual flowpath (solid lines) versus modifications for CFD simulation (dashed lines)

first rotor only. The grid dimensions (axial × circumferential × radial) for the nozzle were $111 \times 61 \times 51$ and for the rotor $255 \times 67 \times 51$. Initial analysis mesh sizes were somewhat smaller but results from these simulations indicated significant interaction between the supersonic flow and the severe separation encountered on the suction side. Smoothing of the mesh near the suction side to reduce possible nonphysical oblique shock effects from coarse grids was deemed necessary. Figure 19 illustrates the midspan section of the computational grids showing the general arrangement of the Curtis stage. Figure 20 is a closeup of the trailing edge of the nozzle and leading edge of the rotor. The total number of grid points used in the simulation was 1,216,656. It is recognized that the mesh in the region of the trailing edge of the nozzle is very coarse due to the flat configuration. When coupled with the very small axial gap and denser mesh of the rotor, numerical uncertainty is certainly an issue in this simulation.

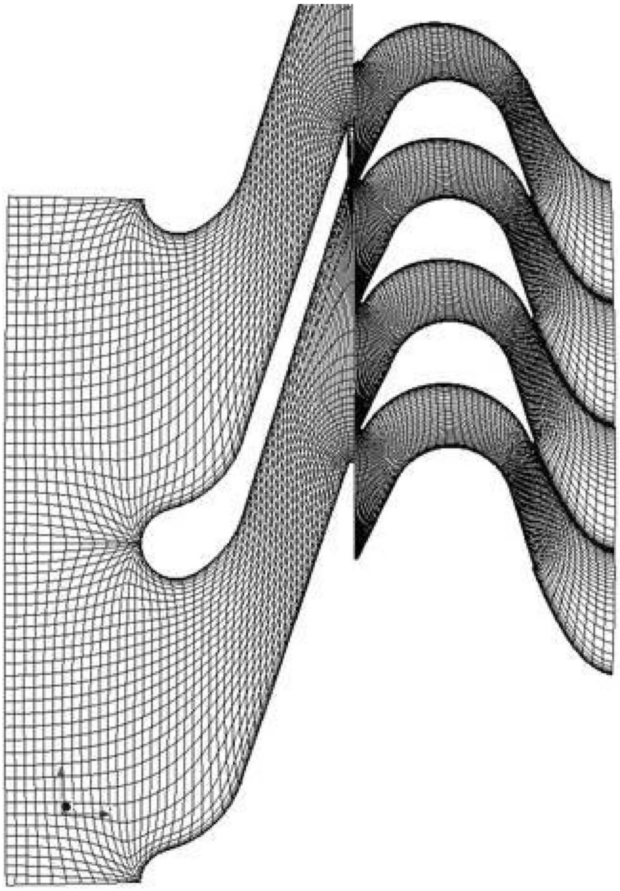

Fig. 19 TCGRID-based smoothed *H* meshes used for TURBO (coarsened for clarity)

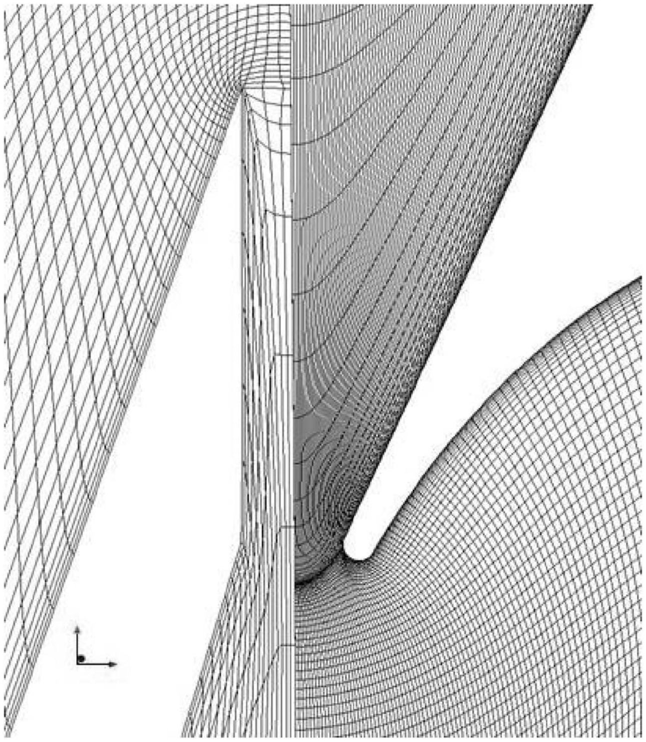

Fig. 20 Mesh details at interface plane

Numerical Results

Simulation Details. The simulation was run on 12 2.2 GHz AMD Opteron 64-bit processors of a "Beowulf" type commodity compute cluster. The simulation was run until mass flow periodicity was achieved in the inlet, interface, and exit planes. One hundred fifty time steps were used for each rotor passing which equates to 405 for each stator passing. Each iteration required approximately 9 s of computation time. The design pressure ratio of 4.09:1 was used and the simulation was started using the results from a steady-state simulation (though not converged). Time periodicity was determined by plotting pressure traces near the leading edge and trailing edge of the rotor airfoil. In Fig. 21, the variation of the blade surface pressure near the leading edge and the trailing edge is plotted versus time for two nozzle-passing cycles at 50% span. The flow periodicity, in general, is in good agreement through two nozzle passings. The largest differences occur near the leading edge on the pressure side. Trailing edge nonperiodicity is usually attributed to vortex shedding, and in this case, is impacted by the flow separation. For the leading edge, the interaction of the thick trailing edge from the nozzle and bow shock interaction with the wake is a likely cause of the slight variation.

Unsteady Flowfields. Figure 22 shows the unsteady flowfield in the rotor passage at nine time instants during a nozzle passing. The two most obvious flow features in these results are the large separation on the rotor suction side and the migration of the large nozzle wake through the passage ($0.0 < t/T < \sim 0.4$). One result of the "cookbook" approach to the design of Curtis stage turbines by the application of fixed blade shapes and stagger angles is the risk of a misengineered stage. It is clear that for the design conditions of this turbine, the suction side leading "flat" to circular arc occurs too early and, for this solidity, results in the flow separating from the suction surface.

Some additional interesting features include the following:

1. disruption of the bow shock of the rotor ($0.0 < t/T < 0.2$) by the nozzle wake. Figure 23 shows the bow shock near the

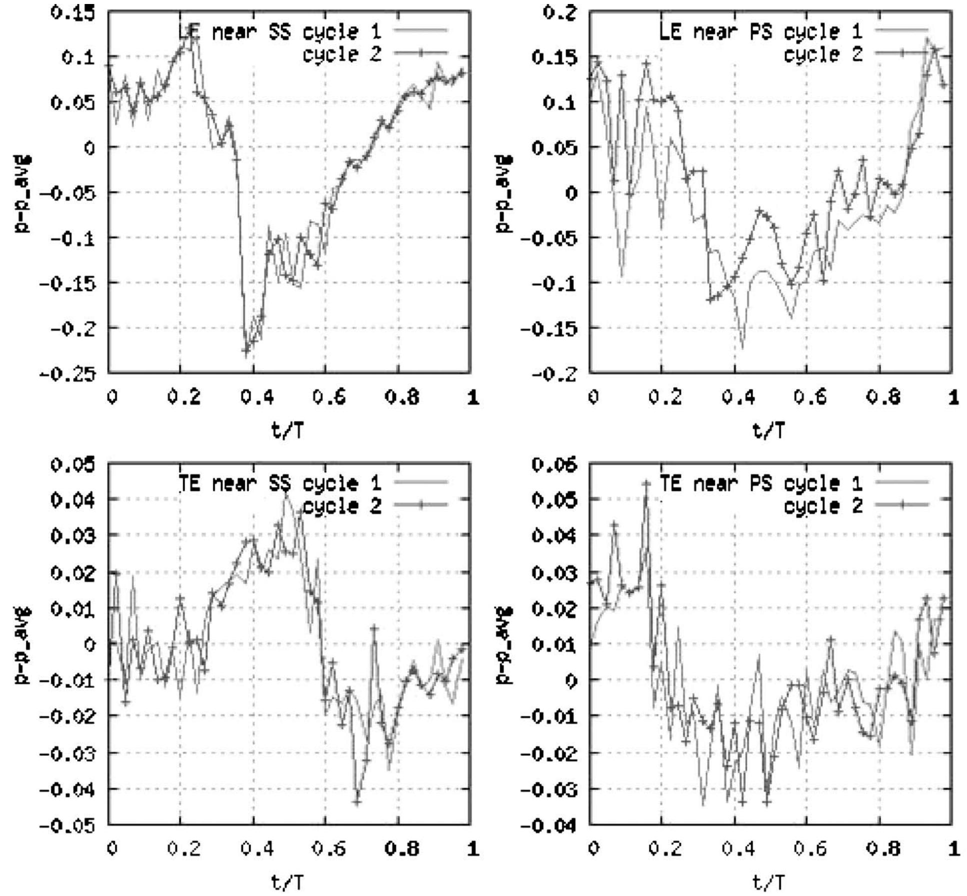

Fig. 21 Periodicity of unsteady blade surface pressure

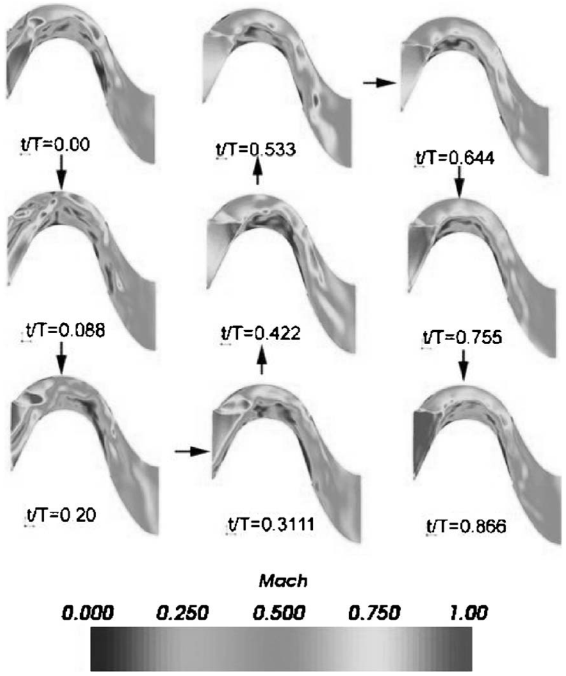

Fig. 22 Rotor Mach contours at 50% span

leading edge of the rotor at a time where the nozzle has not yet passed (lower airfoil) and subsequently, when the leading edge of the rotor is enveloped by the nozzle wake (upper airfoil). The bow shock system is completely disrupted and it takes several more time steps before the flow reestablishes itself; and

2. interaction of the bow wake with the edge of the separation region ($0.4 < t/T < 1$). Rather than a shock pattern being set up between the blade surfaces it is established between the separation edge and the rotor pressure surface. Figure 24 shows Mach contours with the upper limit set to 1.0. Seen are a series of oblique shocks and expansions reflecting off of the edge of the separation layer. There is also a shock set up on the pressure side just downstream of the leading edge that intersects with the bow shock.

Surface Pressure Distributions. The surface pressure distributions from the time-averaged results of both the nozzle and rotor are shown in Figs. 25 and 26. The supersonic acceleration of the flow through the nozzle past the throat is clearly seen. The loading along the span of the rotor blade is fairly uniform, with slightly less near the hub.

Radial Distributions. Working with the time averaged results of the unsteady flowfield allows for the investigation of the steady-state type results with little additional effort. Typical design-oriented plots of flow angle and Mach number are presented in Figs. 27 and 28 for the nozzle and rotor, respectively. Despite an approximately 2.5 deg variation in exit flow angle from the nozzle, the corresponding rotor inlet flow angle is constant for the 25–75% span, due to the unique incidence effects described earlier.

Figure 29 shows the radial distribution of the time averaged

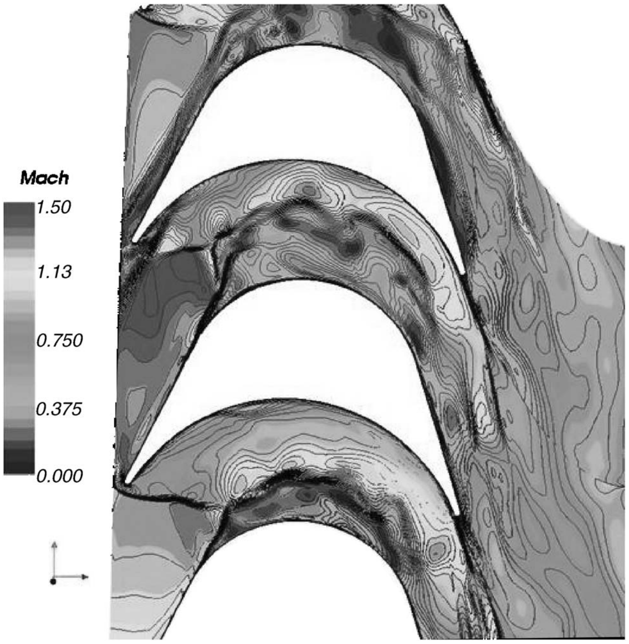

Fig. 23 Rotor/nozzle wake interaction

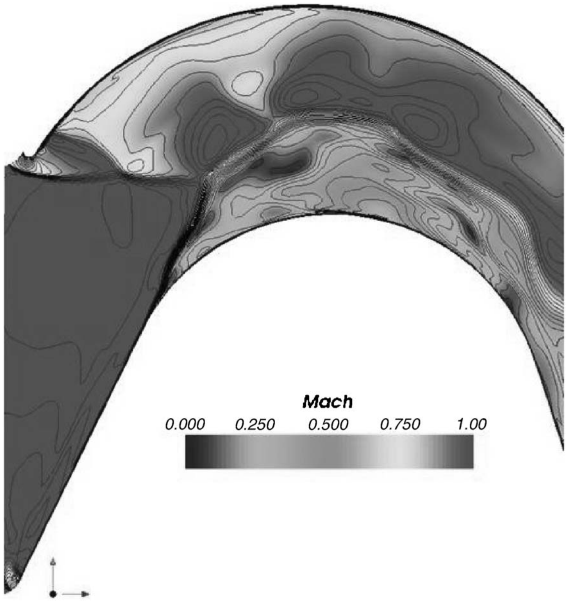

Fig. 24 Mach contours interaction with separation region

total pressure and temperature ratio across the simulated stage. The large flow separation dominates the majority of the span causing a large total pressure loss, and corresponding poor work extraction. Efficiency is actually higher in the endwall regions where the flow separation does not completely extend.

Figure 30 shows the three-dimensional streamlines for flow starting near the leading edge pressure (light grey) and suction surfaces (dark grey). Most notable is the presence of a vortex just aft of the bow shock on the pressure side of the airfoil. The hub vortex proceeds to fill in the void left by the separated flow from the suction side. Also note how the suction side flow does not expand to fill the full height of the airfoil. The flow on the surface of the suction side in the aft portion of the blade is entirely made up of the flow from the cross passage vortices. It is doubtful that present design codes take these kinds of losses into account. Secondary flow correction, shock loss correction, and standard profile losses would need to be carefully measured over the application range of such airfoils [7,8,11].

Conclusions

The high error band in Curtis stage performance prediction is due mainly to the complexity of the interaction between the nozzle and the first rotor row. The first rotor row of a Curtis stage has a supersonic inlet, and resulting unique incidence, due to low U/C_0 and high stage energy. In order to maintain the supersonic inlet, the rotor leading edge streamtube must be considerably smaller in height than the blade trailing edge (and thus, the provided blade leading edge height), or the flowfield will shock down to a subsonic inlet, with the attending high positive stage reaction. Dirt and wear patterns confirm the streamtube contraction into the first rotor row.

Maintaining the rotor's unique incidence requires that the nozzle angle, and/or streamtube height, must adjust as wheel speed changes, and this was noted in the behavior of nozzle static pressure taps during Curtis stage testing. Stage reactions, measured on these Curtis stage tests confirm the low, actually negative, reaction noted on other supersonic rotor tests.

The nozzle to rotor streamtube contraction and geometric expansion is very aggressive, and the drilled-hole nozzle type was challenging to model in CFD. However, CFD did confirm the

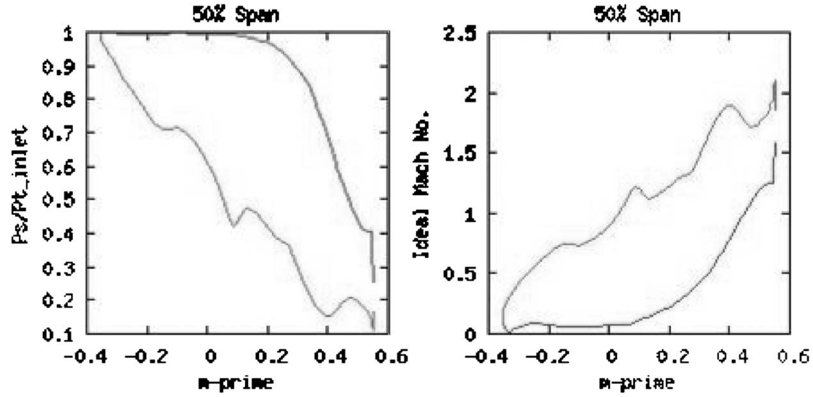

Fig. 25 Time-averaged nozzle static pressure (left) and ideal Mach number (right)

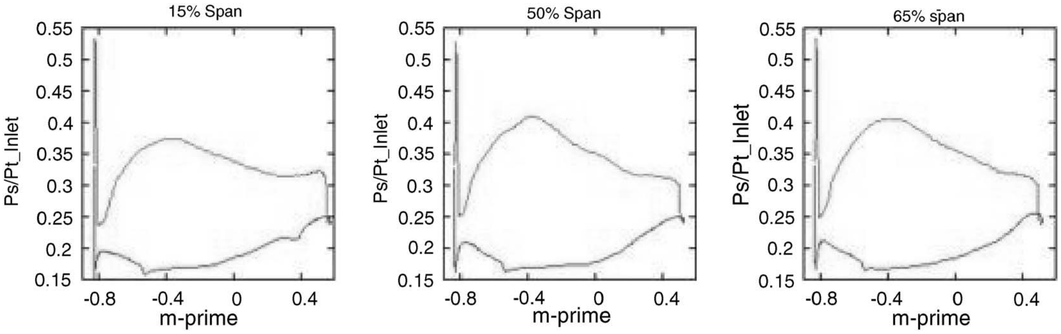

Fig. 26 Time averaged rotor surface static pressure distributions at 15%, 50%, and 85% span

separation of flow off the leading edge suction surface (as seen in the dirt patterns), and the resulting impingement of that high-energy flow stream on the pressure surface of the adjacent blade (observed in both dirt and wear patterns). The unsteady flow behavior caused by the thick “trailing edge” of the nozzle was also shown to significantly influence the behavior of the rotor flow well past what traditional Curtis stage design methodologies account for.

Acknowledgments

The authors would like to thank Dr. Jen Ping Chen for his generous assistance with running TURBO, Dr. Mark Turner for the use of his TURBO post-processing capabilities, and Dresser-Rand Energy Systems for providing support, equipment, and testing facilities for this study.

Nomenclature

a = speed of sound (m/s)
A = flow area (mm^2)
C_0 = isentropic stage energy (m/s)
Ma = Mach number
P = static pressure (MPa)
P_0 = total pressure (MPa)
R = radius of curvature (mm)

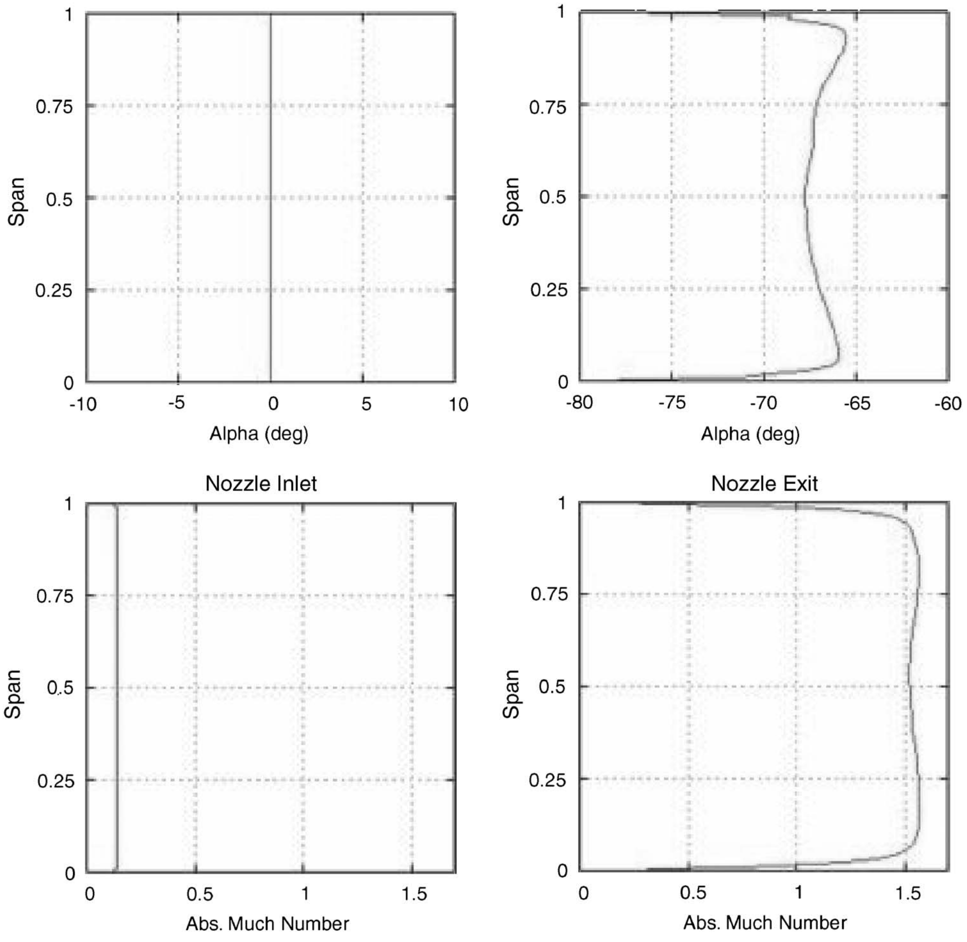

Fig. 27 Time-averaged nozzle inlet and exit flow angle and Mach number

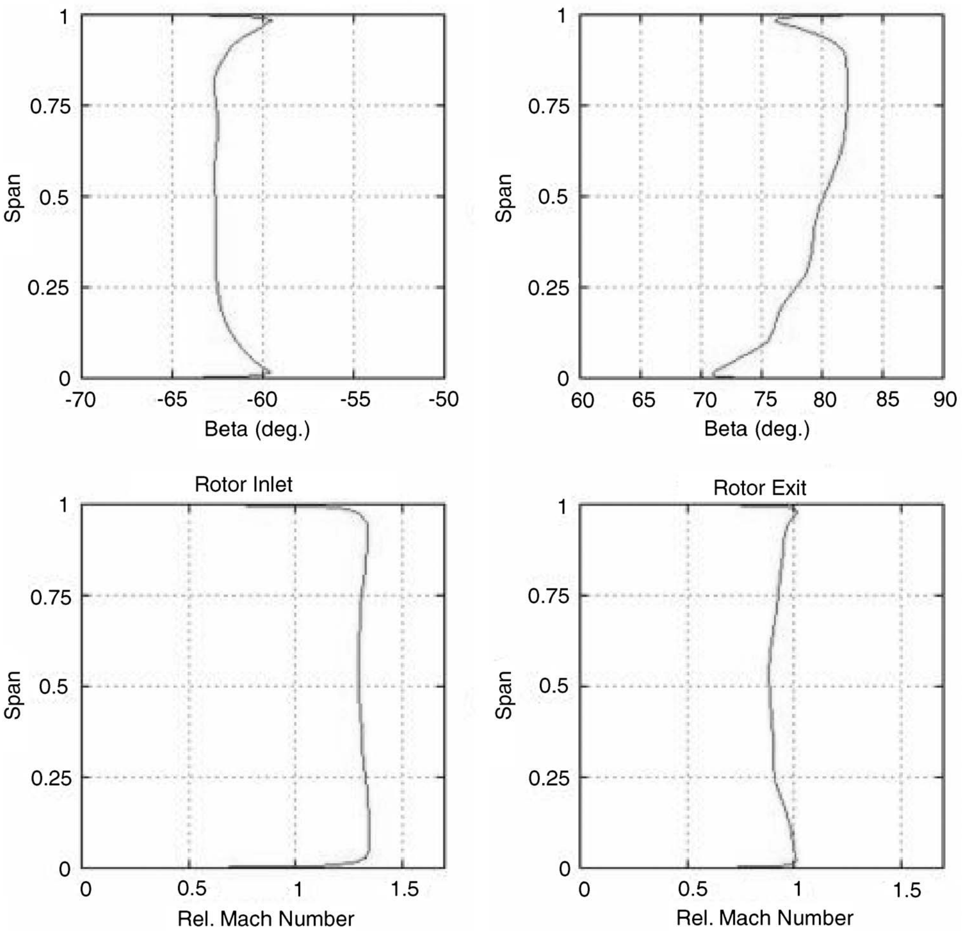

Fig. 28 Time-averaged rotor inlet and exit flow angle and Mach number

t = blade thickness (mm)
U = mean wheel speed (m/s)
V = absolute velocity (m/s)
W = relative velocity (m/s)
α = absolute flow angle (deg)
β = relative flow angle (deg)
γ = ratio of specific heats
λ = passage width or throat (mm)
τ = blade or vane pitch (mm)
ϕ = velocity coefficient
ϕ^2 = energy coefficient

Subscripts

1 = nozzle inlet
2 = nozzle exit/rotor first row inlet
3 = rotor first row exit
ABS = absolute reference frame
AX = axial
DEV = deviation
FACE = nozzle exit face P tap
LE = leading edge
LONG = long side nozzle P tap
MID = midline nozzle P tap
REL = relative reference frame
SHORT = short side nozzle P tap
SL = streamline
TE = trailing edge

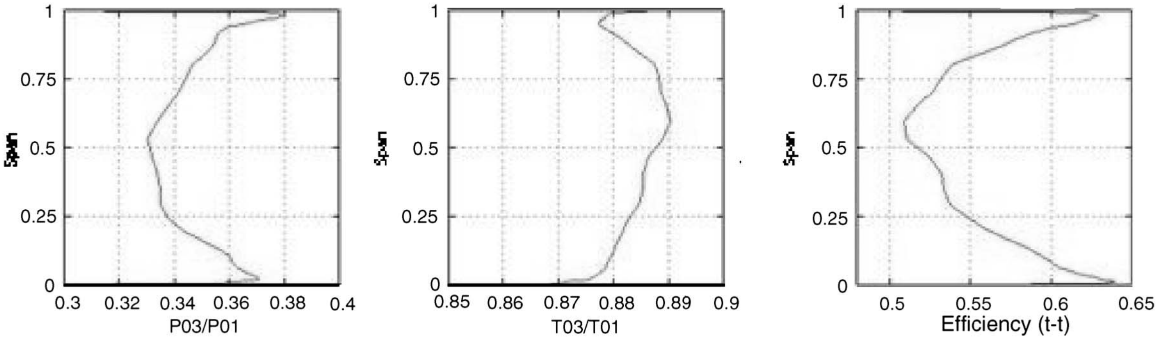

Fig. 29 Time-averaged stage total pressure, total temperature, and efficiency distribution

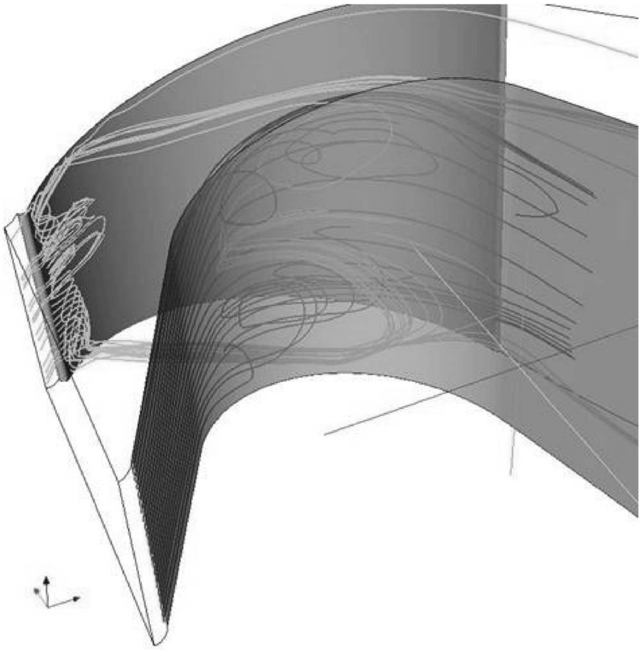

Fig. 30 Time-averaged streamlines of the rotor

Superscripts

$*$ = condition at Mach 1.0

References

[1] Horlock, J. H., 1966, *Axial Flow Turbines, Fluid Dynamics and Thermodynamics*, Robert E. Krieger Pub. Co., Malabar, FL, Sec. 3.3.3, pp. 81–84.

[2] Horlock, J. H., 1966, *Axial Flow Turbines, Fluid Dynamics and Thermodynamics*, Robert E. Krieger Pub. Co., Malabar, FL, Sec. 7.3.2, pp. 201–208.

[3] Stratford, B. S., and Sansome, G. E., 1959, “The Performance of Supersonic Turbine Nozzles,” R & M No. 3273, Aeronautical Research Council.

[4] Stratford, B. S., and Sansome, G. E., 1960, “Theory and Tunnel Tests of Rotor Blades for Supersonic Turbines,” R & M No. 3275, Aeronautical Research Council.

[5] Kurzrock, J. W., 1989, “Experimental Investigation of Supersonic Turbine Performance,” ASME Paper No. 89-GT-238.

[6] Cumpsty, N. A., 1989, *Compressor Aerodynamics*, Robert E. Krieger Pub. Co., Malabar, FL, Secs. 5.2 and 5.3, pp. 198–209.

[7] Wang, X., and Chen, J. P., 2004, “A Post-Processor to Render Turbomachinery Flow Using Phase-Lag Simulations,” AIAA Paper No. 2004-0615.

[8] Dorney, D. J., Griffin, L. W., Huber, F., and Sondak, D. L., 2002, “Unsteady Flow in a Supersonic Turbine With Variable Specific Heats,” Journal of Propulsion, **18**(2), 493–496.

[9] Gorrell, S. E., Car, D., Puterbaugh, S. L., Estevadeordal, J., and Okiishi, T. H., 2005, “Investigation of Wake-Shock Interactions in a Transonic Compressor With DPIV and Time-Accurate CFD,” ASME Paper No. GT2005-69107.

[10] Bakhle, M. A., Liu, J. S., Panovsky, J., Kieth, T. G., and Mehmed, O., 2002, “Calculation and Correlation of the Unsteady Flowfield in a High Pressure Turbine,” NASA Paper No. NASA/TM-2002-211475.

[11] Rashid, S., 1997–2001, personal notes.

[12] Chima, R. V., 2003, *TCGRID 3-D Grid Generator for Turbomachinery: User’s Manual and Documentation*, Version 300.

[13] Chen, J. P., and Whitfield, D. L., 1993, “Navier-Stokes Calculations for the Unsteady Flowfield of Turbomachinery,” AIAA Paper No. 93-0676.

[14] Chen, J. P., Celestina, M., and Adamczyk, J. J., 1994, “A New Procedure for Simulating Unsteady Flows Through Turbomachinery Blade Passages,” ASME Paper No. 94-GT-151.

[15] Zhu, J., and Shih, T. H., 1997, “CMOTT Turbulence Model for NPARC,” NASA Paper No. NASA CR 204143.

[16] Salisbury, J. K., 1950, *Steam Turbines and Their Cycles*, Robert E. Krieger Pub. Co., Malabar, FL, Chap. 6, pp. 177–179.

[17] Church, E. F., 1950, *Steam Turbines*, McGraw-Hill, New York, Secs. 5.9 and 5.10, pp. 154–158.

Influence of Loading Distribution on the Off-Design Performance of High-Pressure Turbine Blades

D. Corriveau
Defence R&D Canada (DRDC Valcartier),
Quebec City,
Quebec Canada G3J 1X5t
e-mail: daniel.corriveau@drdc-rddc.gc.ca

S. A. Sjolander
Professor
Department of Mechanical and Aerospace Engineering,
Carleton University,
Ottawa, ON K1S 5B6, Canada
e-mail: ssjoland@mae.carleton.ca

Linear cascade measurements for the aerodynamic performance of a family of three transonic, high-pressure (HP) turbine blades have been presented previously by the authors. The airfoils were designed for the same inlet and outlet velocity triangles but varied in their loading distributions. The previous papers presented results for the design incidence at various exit Mach numbers, and for off-design incidence at the design exit Mach number of 1.05. Results from the earlier studies indicated that by shifting the loading towards the rear of the airfoil an improvement in the profile loss performance of the order of 20% could be obtained near the design Mach number at design incidence. Measurements performed at off-design incidence, but still at the design Mach number, showed that the superior performance of the aft-loaded blade extended over a range of incidence from about −5.0 deg *to* +5.0 deg *relative to the design value. For the current study, additional measurements were performed at off-design Mach numbers from about 0.5 to 1.3 and for incidence values of* −10.0 deg, +5.0 deg, *and* +10.0 deg *relative to design. The corresponding Reynolds numbers, based on outlet velocity and true chord, varied from roughly* 4×10^5 *to* 10×10^5*. The measurements included midspan losses, blade loading distributions, and base pressures. In addition, two-dimensional Navier–Stokes computations of the flow were performed to help in the interpretation of the experimental results. The results show that the superior loss performance of the aft-loaded profile, observed at design Mach number and low values of off-design incidence, does not extend readily to off-design Mach numbers and larger values of incidence. In fact, the measured midspan loss performance for the aft-loaded blade was found to be inferior to, or at best equal to, that of the baseline, midloaded airfoil at most combinations of off-design Mach number and incidence. However, based on the observations made at design and off-design flow conditions, it appears that aft-loading can be a viable design philosophy to employ in order to reduce the losses within a blade row provided the rearward deceleration is carefully limited. The loss performance of the front-loaded blade is inferior or at best equal to that of the other two blades for all operating conditions.* [DOI: 10.1115/1.2464145]

Keywords: turbine aerodynamics, transonic, incidence, losses

Introduction

Aircraft engine turbine blades must be designed such that an acceptable level of losses is generated within the blade passages for a wide range of flow conditions encountered during the various phases of a flight (idling, takeoff, cruising). Among the flow conditions of interest to the turbine designer are the air inlet angle, the flow Mach number, and the flow Reynolds number. The individual and combined influence of these aerodynamic parameters on the performance of a turbine blade must be well understood in order to accurately predict the performance of a gas turbine engine.

Several studies have been published over the years in the open literature regarding the effects of off-design incidence on the profile losses as measured in turbine cascades. However, a significant portion of these studies were performed at low-speed conditions and for low-pressure (LP) turbine blades. This is partly explained by the fact that subsonic cascade wind tunnels are much more common and much less expensive to operate. Furthermore, it is much more common for a LP turbine stage, where the Mach number encountered is usually subsonic, to operate at significant off-design values of incidence than a high-pressure (HP) turbine stage. Among the studies performed at subsonic Mach numbers in which the effect of incidence on losses was examined, those of Vijayaraghavan and Kavanagh [1], Goobie et al. [2], and Tremblay et al. [3] are worth mentioning.

The effects of exit Mach number on losses at off-design incidence have been studied by a few researchers. However, the data presented in the open literature are limited. Graham and Kost [4] examined the performance of two airfoils over a range of outlet Mach numbers from 0.7 to 1.4. They varied the incidence from −20 deg to +8 deg. Their results show the sensitivity of the blade performance to both incidence and the suction side curvature aft of the throat. The study of Šťastný et al. [5] on the rotor blade of a steam turbine presents detailed loss measurements for a wide range of both the outlet Mach numbers and incidence. Finally, a significant amount of data from Carleton University have been published by Jeffries [6] and Jouini [7]. The various studies generally show that, at high values of Reynolds number, the effects of incidence on losses change relatively little as the exit Mach number increases.

The current study examined the effect of alternative loading distributions on the off-design performance of transonic HP turbine blades. A few previous experimental studies exist on the effect of loading distribution on the performance of turbine blades. However, the conclusions of these studies are often contradictory. Patterson and Hoeger [8] studied the effect of both the velocity distribution and Reynolds number on the performance of three LP turbine vanes. Their results were obtained mainly at low

---

Contributed by the International Gas Turbine Institute of ASME for Publication in the Journal of Turbomachinery. Manuscript received June 13, 2006; final manuscript received August 12, 2006. Review conducted by David Wisler. Paper presented at the ASME Turbo Expo 2006: Land, Sea and Air (GT2006), Barcelona, Spain, May 8–11, 2006. Paper No. GT2006-90849.

transonic Mach numbers. They concluded that the aft-loaded profile yielded the worst performance for the conditions investigated. The performance of the first and second stage stator vanes of an LP turbine was tested for both front and aft-loaded profiles by Hashimoto and Kimura [9]. It was found that the front-loaded designs yielded lower losses and a wider range of usable incidence for high subsonic Mach numbers. Hoheisel et al. [10] looked at the effect of free-stream turbulence and blade pressure gradient on the losses for three turbine cascades. They studied a front-loaded profile together with two aft-loaded ones. The three designs had the same overall aerodynamic loading. Tests performed at low Mach numbers showed that lower losses can be obtained with an aft-loaded pressure distribution, provided that the rearward diffusion is carefully controlled. More recently, Howell et al. [11] presented results for high-lift and aft-loaded LP turbine profiles with unsteady incoming wakes. They showed that aft-loaded LP blades tend to have lower losses due to a reduction in the extent of turbulent boundary layer on the suction surface. It was concluded that the aft-loaded profile offered this advantage mainly in unsteady flow.

As mentioned previously, the present study examines the effect of loading distribution on the off-design performance of HP turbine airfoils. Three profiles having different loading distributions were considered. The baseline airfoil is the midspan section of the HP rotor of a small gas turbine engine of recent design. The three airfoils were designed for the same inlet and outlet velocity triangles and have the same Zweifel loading coefficients. The performance of the cascades was assessed based on loss and base pressure measurements. Loading measurements were also used to assist in the interpretation of the results. Measurements were made for a wide range of Reynolds numbers and transonic Mach numbers.

Experimental Apparatus and Procedures

High Speed Wind Tunnel. The measurements were obtained in the Pratt & Whitney Canada high-speed wind tunnel at Carleton University. A schematic of the wind tunnel is shown in Fig. 1. The wind tunnel is of the blow-down type. Run times of 30–60 s are achieved, depending on the cascade outlet Mach number. During a run, the test section total pressure is maintained nearly constant, yielding essentially a constant outlet Mach number. On the other hand, the total temperature decreases during a run, by a maximum of 20°C. As a result, the Reynolds number increases during the run. However, the effect of the Reynolds number variation on the losses was shown by Jouini [7] to be less than the overall estimated uncertainty in the losses. The turbulence intensity at the cascade inlet is about 4%. The outlet of the cascade test section is fitted with an ejector–diffuser system. This system allows the static pressure downstream of the cascade to be controlled and thus permits the cascade outlet Mach number to be varied independently of the Reynolds number. The diffuser outlet exhausts to the laboratory at atmospheric conditions. A more detailed description of the wind tunnel is given by Jeffries [6].

Test Cascades. The airfoil and cascade geometries are summarized in Fig. 2. The cascades were manufactured with a common axial chord of 37.3 mm. The baseline blade (HS1A) is the midspan section of a high-pressure turbine from a Pratt & Whitney Canada (PWC) engine and is considered to be a midloaded profile. Starting from the baseline profile, two other blades were designed by the first author using PWC design tools. The objective was to obtain front-loaded and aft-loaded profiles with the same overall loading (as measured by the Zweifel coefficient) as the baseline profile. In addition, the metal areas were kept constant so that the new profiles would be structurally compatible with the existing baseline airfoil.

The aft-loaded airfoil (HS1C) was obtained from HS1A by modifying several geometric parameters. The stagger angle was reduced from 25.1 deg to 22.5 deg and the unguided (uncovered) turning angle was increased by 3.0 deg to 14.5 deg. The leading edge ellipse ratio and wedge angle were also modified to reduce the velocity overspeeds on both the pressure and suction surfaces in the vicinity of the leading edge. Finally, the suction-side curvature was modified to adjust the pressure distribution. The front-loaded airfoil (HS1D) was obtained mainly by increasing the stagger angle to 30.5 deg. Some minor modifications were also made to the suction-side curvature.

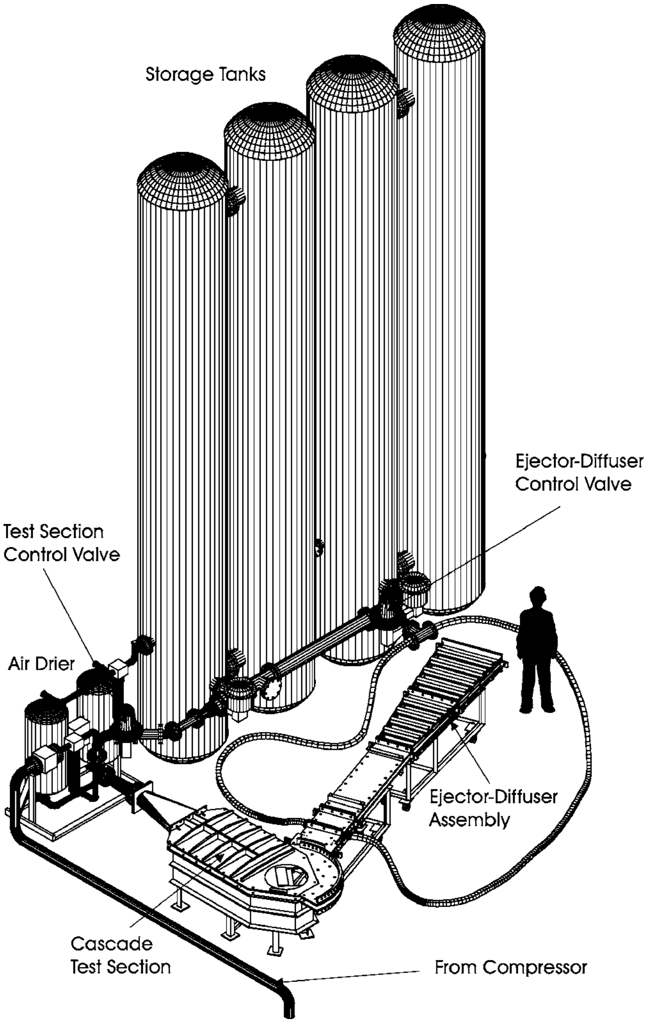

Fig. 1 Pratt & Whitney Canada high-speed wind tunnel

The three cascades consist of seven full blades and eight blade passages. Two of the blades at the center of the cascades were instrumented with static taps for loading measurements. One of the instrumented airfoils included a static tap at the center of the trailing edge to allow the base pressure to be measured. The base-pressure tap has a diameter of 20% of the trailing-edge thickness.

Instrumentation and Experimental Procedures. The downstream flow field measurements were obtained with a three-hole pressure probe used in the non-nulling mode. The probe tip has a width of 1.37 mm, which corresponds to 4.7% of the blade pitch, and a thickness of 0.46 mm. The probe was calibrated in 1 deg steps over a range of ±10 deg of flow misalignment in yaw. Static-pressure probe measurements were also made downstream of the cascade. The cylindrical probe has a tip cone angle of 15 deg and a diameter of 1.02 mm. For the analysis of the results, the static-pressure measurements obtained with the static-pressure probe were combined with the flow angle and total pressure measurements from the three-hole probe. Fully mixed-out loss coefficients and other relevant quantities were calculated from the data using

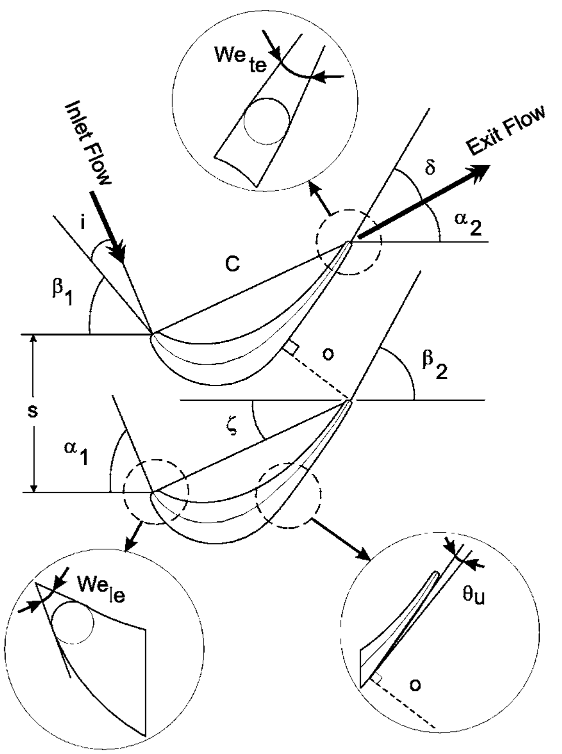

Cascade Parameters	HS1A	HS1C	HS1D
Chord Length, C	41.2mm	40.4mm	43.3mm
Blade Span, H	61.0mm	61.0mm	61.0mm
Blade Pitch, s	29.14mm	29.14mm	29.14mm
Leading Edge Ellipse Ratio, a/b	1.0	2.1	1.0
Leading Edge Ellipse Minor Axis, b	1.02mm	1.02mm	1.02mm
Trailing Edge Thickness, t	1.26mm	1.26mm	1.26mm
Aspect Ratio, H/C	1.481	1.510	1.409
Inlet Metal Angle, β_1	50.5°	50.5°	50.5°
Outlet Metal Angle, β_2	59.0°	59.0°	59.0°
Leading Edge Wedge Angle, We$_{le}$	38.0°	15.0°	38.0°
Trailing Edge Wedge angle, We$_{te}$	6.0°	6.0°	6.0°
Design Incidence, i_{des}	-4.5°	-4.5°	-4.5°
Stagger Angle, ζ	25.1°	22.5°	30.5°
Throat Opening, o	15.9mm	15.9mm	15.9mm
Unguided Turning, θ_u	11.5°	14.5°	11.5°
Zweifel Coefficient, Z	0.856	0.856	0.856

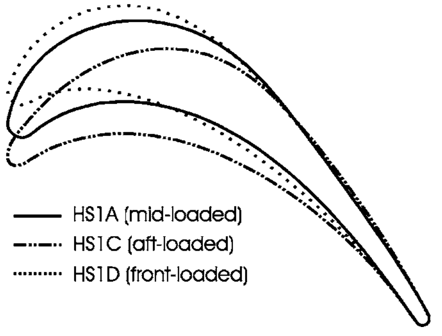

Fig. 2 Summary of the blades' geometry

the procedures of Amecke and Šafařík [12]. The method assumes a mixing process to uniform conditions in a constant area channel with frictionless parallel walls.

The measurement uncertainty for the outlet flow angles is estimated to be 1.0 deg. The uncertainty for the static pressure measurements is ±2% of the local dynamic pressure. The uncertainty in the cascade inlet Mach numbers is ±0.015. The cascade exit Mach number uncertainty is about ±0.005 for Mach numbers greater than 0.8. For lower exit Mach numbers the uncertainty in the Mach number increases due to some drift in the blowing pressure. The uncertainty for the mixed-out total-pressure loss coefficients is estimated as ±0.006 for Mach numbers between 0.85 and 1.1. For higher transonic Mach numbers the uncertainties are higher due to the formation of complex shock structures. The uncertainty values were estimated using the method of Moffat [13] for single-sample uncertainty analysis.

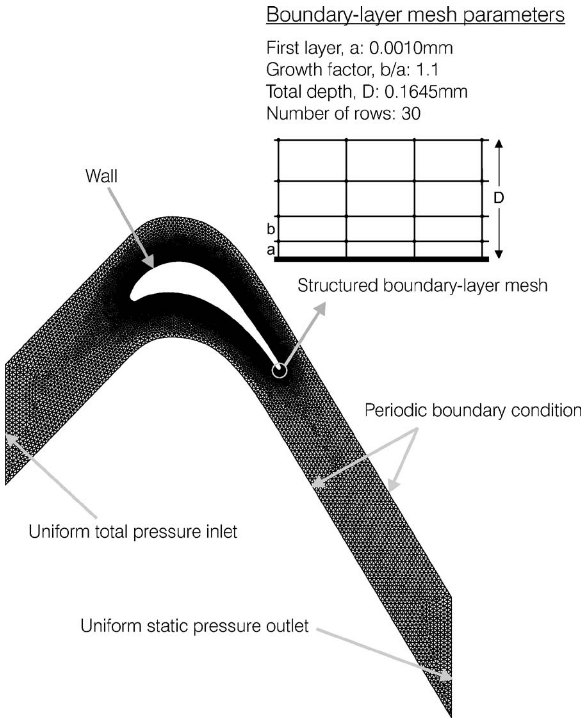

Fig. 3 Unstructured mesh used for the computation

Numerical Procedure. In order to help in the interpretation of the experimental results, two-dimensional computation fluid dynamic (CFD) simulations were performed using Version 6.1 of the commercial code FLUENT. FLUENT uses a control-volume based technique to convert the governing equations into algebraic expressions that are solved iteratively. The two-dimensional steady simulations were performed using the segregated solver of FLUENT. For the particular cascade flow that was solved, the segregated solver was found to yield faster convergence rates over the coupled solver, even for the case where the outlet flow was supersonic. All numerical results presented here were obtained from second-order converged solutions. The second-order upwind scheme was used for the computations performed in the course of this work. A second-order pressure interpolation scheme was used as well in order to obtained the face pressures. The semi-implicit method for pressure-linked equations (SIMPLE) scheme was used to achieve pressure–velocity coupling. The Spalart and Allmaras [14] turbulence model was used to simulate the turbulent characteristics of the flow. The Spalart and Allmaras turbulence model was designed for wall-bounded flows and has been shown to give good results for boundary layers subjected to adverse pressure gradients.

A single blade passage was modeled as shown in Fig. 3. Periodic boundary conditions were used midway into the passage on either side of the blade in order to simulate an infinite blade row. The flow field was meshed using a hybrid grid. The main flow field was meshed using an unstructured grid composed of triangular elements. The boundary-layer region consists of a structured grid of quadrilateral elements. The size of the boundary layer mesh was adjusted such that the dimensionless distance of the first element from the wall, y^+, was about 1.0 everywhere around the blade. Grid independence tests were performed and grids com-

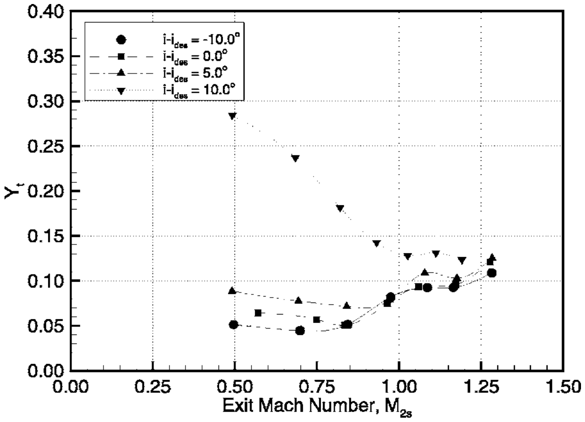

(a) Mid-loaded cascade HS1A

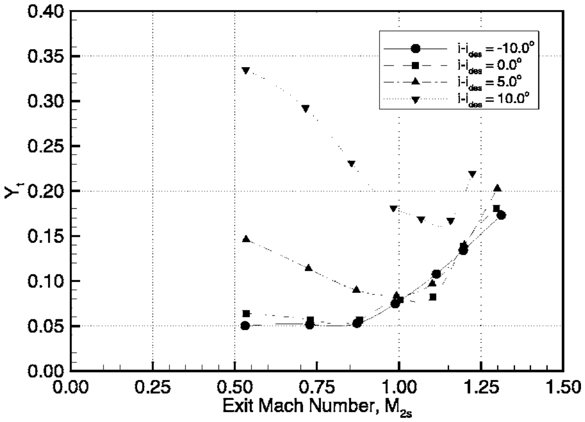

(b) Aft-loaded cascade HS1C

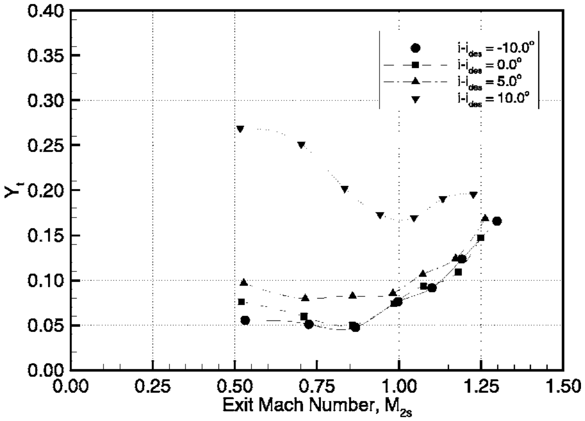

(c) Front-loaded cascade HS1D

Fig. 4 Effect of Mach number on the variation of the total pressure loss coefficient for various incidences

posed of 20,000 nodes or more were found to yield essentially constant losses as well as identical pressure distributions for a given set of boundary conditions.

Results and Discussion

In Figs. 4(*a*)–4(*c*), the variation of the total pressure loss coefficient with Mach number is shown for the three blade profiles. Results are presented for incidence values ($i_{\text{effective}}$) of −10.0 deg, 0.0 deg, +5.0 deg, and +10.0 deg.

Starting with the baseline mid-loaded cascade, HS1A, from Fig. 4(*a*) several differences can be seen in the variation of the losses with Mach number for the different values of incidence. At incidence values of −10.0 deg, 0.0 deg, and +5.0 deg, the trends in the variation of the losses with Mach number are very similar to one another and are consistent with similar measurements made by Mee et al. [15], for example. The losses are essentially constant at low Mach numbers. At transonic Mach numbers, the losses start increasing due to the appearance of shock waves in the blade passages. Among the differences that can be observed at these three incidences, are slight increases in losses at low outlet Mach numbers as the incidence increases from −10.0 deg to 0.0 deg.

Similar trends are observed for the aft-loaded blade, HS1C, and the front-loaded blade, HS1D, for incidence values between −10.0 deg and +5.0 deg.

At an incidence of +10.0 deg, the highest incidence for which measurements were made, the trend in the variation of the losses with Mach number is very different. For the lowest Mach numbers, the losses are high compared to those observed at the lower values of incidence. Such high levels of loss would usually be attributed to extensive boundary layer separation on the suction surface. However, as shown in Corriveau and Sjolander [16], at high values of incidence and low Mach numbers there is little or no region of two-dimensional flow at midspan for cascade HS1A. Therefore, the high losses observed at +10.0 deg and low Mach numbers may be due to some extent to the presence at midspan of secondary losses. The high losses observed at +10.0 deg will be discussed further in conjunction with the discussion of the base pressure measurements.

The results just presented showed the effect of incidence on the variation of the losses with Mach number for the three blade profiles individually. In order to facilitate the comparison between the three blades, and thus see the influence of the loading distribution on the losses at off-design incidence and Mach number, the data were re-plotted as shown in Figs. 5–8 together with the corresponding computational results.

At an incidence of −10.0 deg (Fig. 5), the variation of the profile losses with Mach number is very similar for the three blades except at high Mach numbers where the baseline midloaded blade has significantly better loss performance. For outlet Mach numbers in the range from 0.80 to about 1.05 (the design Mach number), the aft-loaded blade, HS1C, and the front-loaded blade, HS1D, appear to have slightly lower losses compared to the baseline midloaded blade, HS1A. This appears to be due to the fact that the rise in losses due to the appearance of shock waves at transonic Mach numbers ($M_{2s} \approx 0.85$) occurs slightly earlier for HS1A.

As the incidence is increased to its design value (Fig. 6), the performance of the aft-loaded profile becomes superior to that of the other two profiles in the vicinity of the design Mach number, as discussed in detail by Corriveau and Sjolander [17,18]. However, for outlet Mach numbers greater than about 1.10 for HS1C and 1.15 for HS1D, the losses start increasing rapidly and the loss performance of these two blades deteriorates much faster than that of HS1A.

For an incidence of +5.0 deg, the plot of the variation of losses with outlet Mach number (Fig. 7) shows that the losses for the aft-loaded blade, HS1C, are much higher at subsonic Mach numbers than that of HS1A and HS1D. However, as mentioned previously, the losses for the aft-loaded blade appear slightly lower near the design Mach number of 1.05.

At an incidence of +10.0 deg, the variation of losses with Mach number is very different from that observed at lower values of incidence. For operation at this incidence, the baseline midloaded cascade offers the lowest profile losses of the three airfoils at practically all outlet Mach numbers. The aft-loaded blade, HS1C, which showed surprisingly good loss performance at design incidence, has the poorest loss performance over almost the entire Mach number range at an incidence of +10.0 deg.

Comparing the measured and numerical results in Figs. 5 and 6, it can be seen that for −10.0 deg of incidence and design incidence the numerical calculations predict the same trend in the

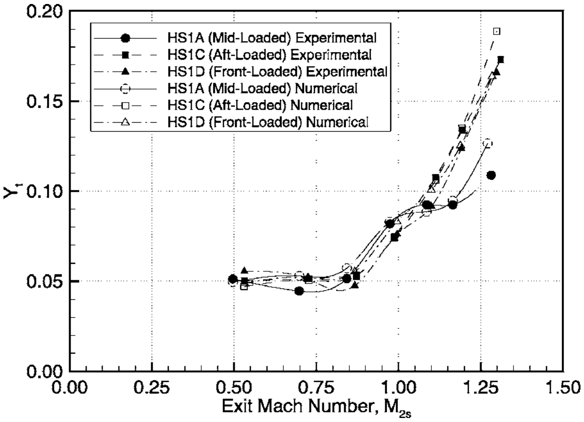

Fig. 5 Comparison of the effect of Mach number on losses measured experimentally and predicted numerically for the three cascades at −10.0 deg incidence

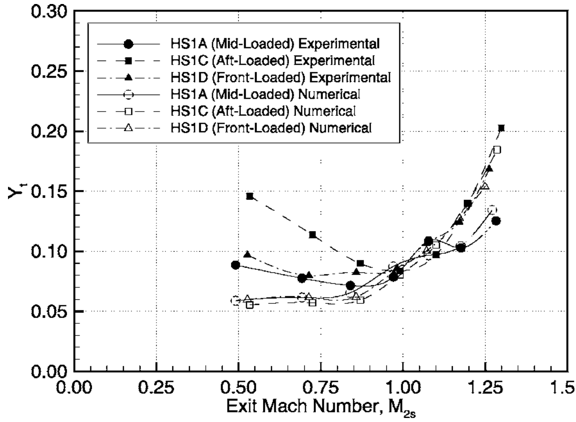

Fig. 7 Comparison of the effect of Mach number on losses measured experimentally and predicted numerically for the three cascades at +5.0 deg incidence

losses with Mach number as were observed experimentally. The magnitude of the predicted losses is also very close to the experimentally measured losses except for a few cases. At +5.0 deg of incidence (Fig. 7), the loss predictions depart slightly from the measurements for outlet Mach numbers lower than about 1.0. However, for outlet Mach numbers greater than 1.0, the predictions are still very good. The poor agreement between the experimental and numerical results at subsonic Mach numbers will be shown at the end of this section to be due to three-dimensional flow at midspan in the cascade test section at these operating conditions.

The trend in loss variation with Mach number and the magnitude of the losses could not be reproduced computationally at an incidence of +10.0 deg. Again, the large discrepancies between the loss measurements and the predictions at +10.0 deg of incidence are explained by the presence of some secondary losses at midspan for the measurements, whereas the computations were strictly two dimensional.

Measurements of the base pressure were performed for all test cases. The effect of incidence on the variation of the base pressure coefficient with Mach number is shown in Figs. 9(*a*)–9(*c*) for the three blade profiles.

For all incidences, the midloaded blade, HS1A, experiences a sharp drop in base pressure for outlet Mach numbers starting at about 0.90, and a subsequent rise beginning at about the design Mach number of 1.05, as shown in Fig. 9(*a*). The drop in base pressure coincides with the point where the losses start to increase at incidences of −10.0 deg, +0.0 deg, and +5.0 deg, as shown in Fig. 4(*a*). Denton [19] has shown using a control volume analysis for incompressible flow that the trailing edge losses can be related to the base pressure coefficient and the boundary layer parameter as follows

$$Y_{\mathrm{te}} = -\frac{C_b t}{o} + \frac{2\theta}{o} + \left(\frac{\delta^* + t}{o}\right)^2 \tag{1}$$

For blade HS1A, the parameter (t/o) equals 0.08 and thus from Eq. (1), the reduction in base pressure of about 0.25 in Fig. 9(*a*) contributes to more or less 0.02 to the increase in Y_{te}. This accounts for roughly a third of the losses observed close to the sonic condition for HS1A, for incidences between −10.0 deg and +5.0 deg. The remainder of the rise in losses is probably mainly due to the direct losses occurring through the shock waves that begin forming at outlet Mach numbers greater than about 0.85.

Above the design Mach number of 1.05, the losses briefly level off for the midloaded blade. This leveling off of the losses coincides with the rising base pressure observed in Fig. 9(*a*) in that range of Mach numbers. As the exit Mach number is increased further, the losses start rising again due to the presence of much higher flow velocity on the rear suction surface of the blade, as seen from the loading distributions in Fig. 10(*a*). Furthermore, stronger trailing edge shocks are present at high exit Mach numbers, thus contributing to the increased losses.

At an incidence of +10.0 deg, the loss variation with Mach number is very much different from that at lower incidences for

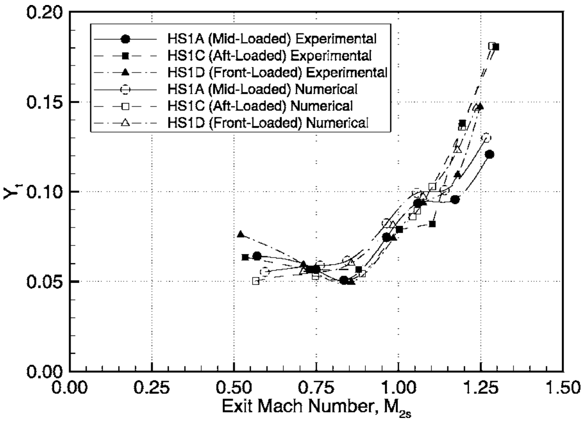

Fig. 6 Comparison of the effect of Mach number on losses measured experimentally and predicted numerically for the three cascades at design incidence

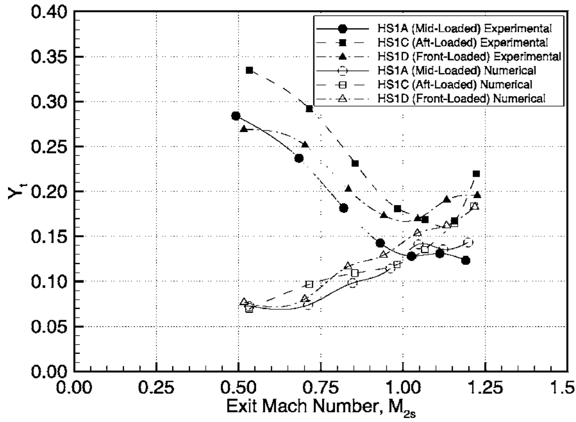

Fig. 8 Comparison of the effect of Mach number on losses measured experimentally and predicted numerically for the three cascades at +10.0 deg incidence

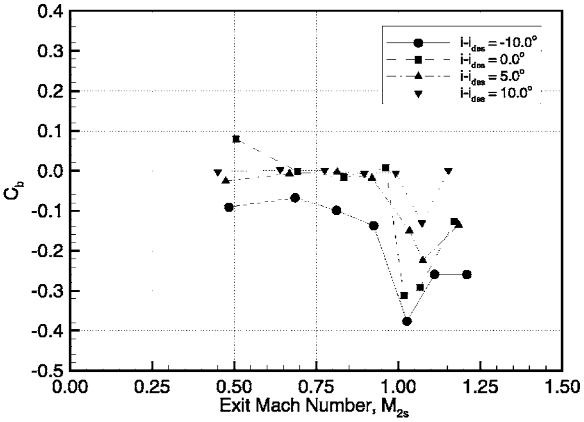

(a) Mid-loaded cascade HS1A

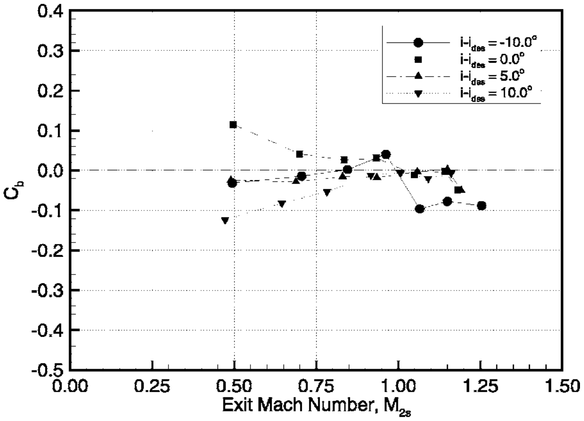

(b) Aft-loaded cascade HS1C

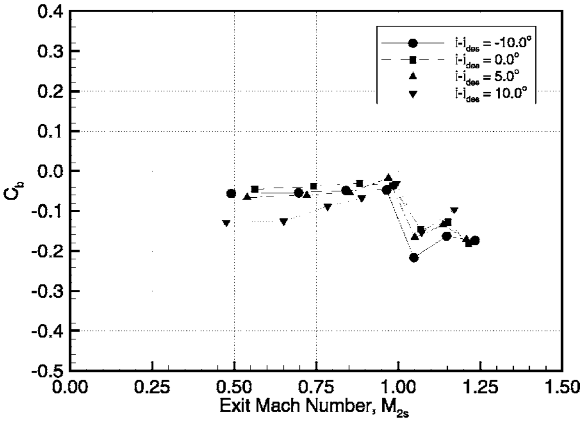

(c) Front-loaded cascade HS1D

Fig. 9 Effect of Mach number on the variation of the base pressure coefficient for various incidences

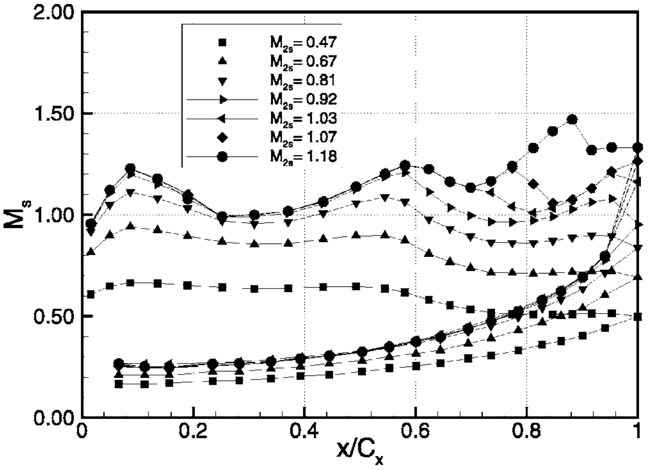

(a) Mid-loaded cascade HS1A

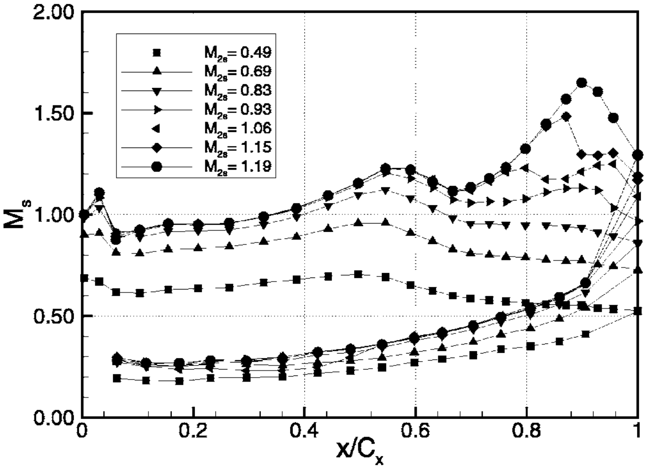

(b) Aft-loaded cascade HS1C

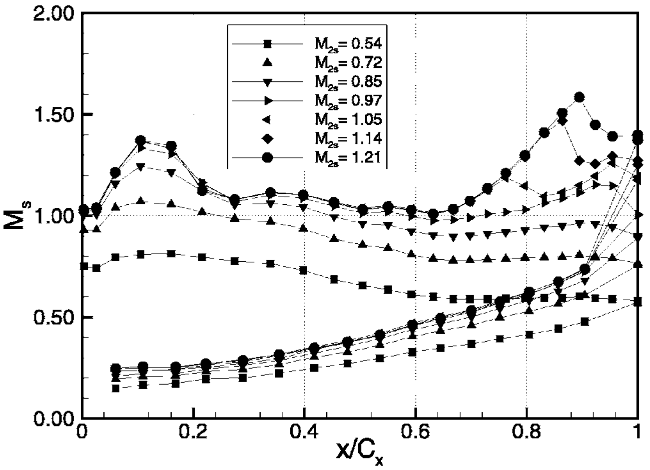

(c) Front-loaded cascade HS1D

Fig. 10 Effect of outlet flow Mach number on the surface Mach number distribution for the three profiles at an incidence of +5.0 deg

the midloaded blade, HS1A, as seen in Fig. 4(*a*). The losses are highest at the lowest Mach number investigated and decrease up to a Mach number of 0.95 where they level off. The presence of high losses at low Mach numbers can have a number of possible origins.

First, the high losses at low Mach numbers could be a Reynolds number effect. As mentioned previously, when the ejector–diffuser is not used in the Pratt & Whitney Canada high-speed wind tunnel, the Reynolds number varies directly with the Mach number. When operating at low Mach numbers, the Reynolds number reaches values on the order of 4×10^5. At low Reynolds number, the transition location on the blade can be delayed significantly, therefore yielding a greater extent of laminar boundary layer on the blade surface. Since laminar boundary layers are more prone to separation in the presence of adverse pressure gradient, losses can be increased significantly through separation. However, the high losses at low Mach numbers seen in Fig. 4(*a*) at an incidence of +10.0 deg do not appear to be due to a Reynolds number effect. This can be seen by comparing the magni-

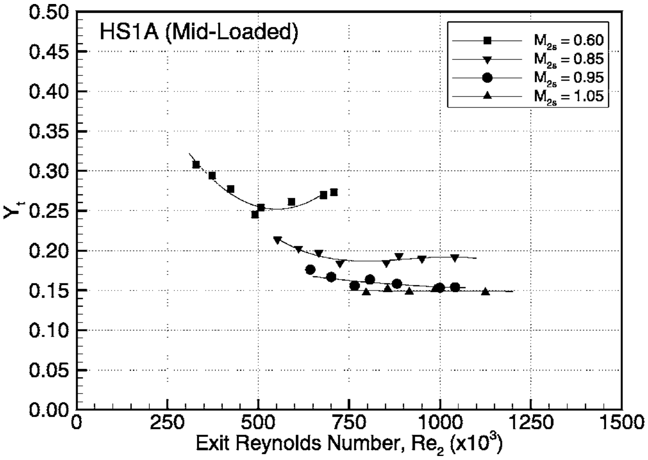

Fig. 11 Reynolds number effect on losses for the baseline midloaded airfoil (HS1A) at several Mach numbers and an incidence of +10.0 deg

tude of the losses at an outlet Mach number of 0.60 in Fig. 4(*a*) with those observed in Fig. 11. In these figures, it can be seen that the magnitude of the losses at a Mach number of 0.60 in Fig. 4(*a*) corresponds essentially to the range where the losses are independent of Reynolds number in Fig. 11.

The main explanation for the high losses observed at low Mach number is the likely presence of secondary flow at midspan. As shown previously in Corriveau and Sjolander [16], the secondary flow through the cascade passage grows in importance with increasing positive incidence. Furthermore, the secondary flow was shown to reach the passage midspan location at lower Mach numbers first. It was shown in Corriveau and Sjolander [16] that at an incidence of +12.0 deg and an outlet Mach number of 0.80 there was essentially no region of two-dimensional flow at midspan. Therefore, it is quite conceivable that the secondary flow had reached midspan even at an incidence of +10.0 deg for subsonic Mach numbers. This seems the most likely explanation for the increased losses measured at midspan for these conditions.

Another indication of the presence of three-dimensional flow at midspan is nonunity values of axial–velocity–density ratio (AVDR). A value of AVDR of 1.0 is a necessary (but not sufficient) condition in order to have two-dimensional flow at midspan. Figure 12(*a*) shows the variation of the AVDR with outlet Mach number for the baseline midloaded blade, HS1A, at the various incidences investigated. From Fig. 12(*a*), it can be seen that the AVDR for HS1A at +10.0 deg of incidence is about 1.12 for Mach numbers below 1.0, indicating the presence of some degree of flow convergence at midspan.

Further evidence of the presence of three-dimensional flows at midspan for HS1A is obtained by comparing the losses measured experimentally with those calculated numerically, as shown in Fig. 13(*a*). As described previously, the numerical computations are strictly two dimensional. Comparison of the loss predictions with the experimental results reveals that the losses calculated numerically are significantly lower than those measured experimentally for the midloaded blade at an incidence of +10.0 deg and outlet Mach numbers below 1.0. For Mach numbers greater than 1.0, the numerical loss predictions compare favorably with the experimental results, as shown in Fig. 13(*a*). This suggests the presence of a reduced amount of three-dimensional flow at midspan. This is corroborated by the fact that with increasing Mach number the AVDR for HS1A decreases and approaches 1.0, as shown in Fig. 12(*a*).

The largest differences between the loss variations with Mach number at off-design incidences for HS1C, HS1D, and HS1A occur at high outlet Mach numbers, except at +10.0 deg of incidence where the three-dimensional flows were shown to play a role.

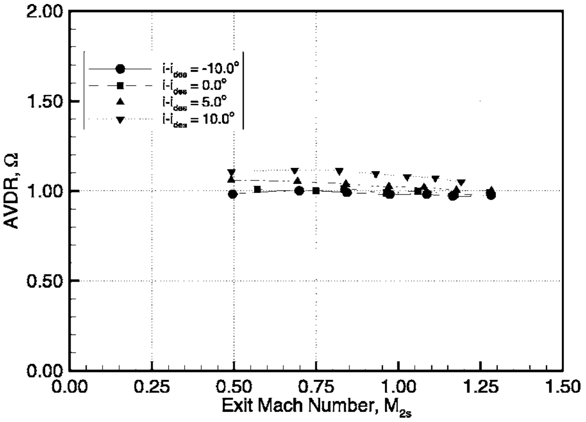

(a) Mid-loaded cascade HS1A

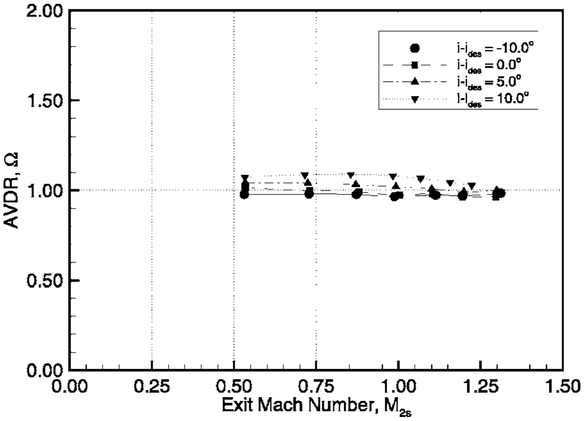

(b) Aft-loaded cascade HS1C

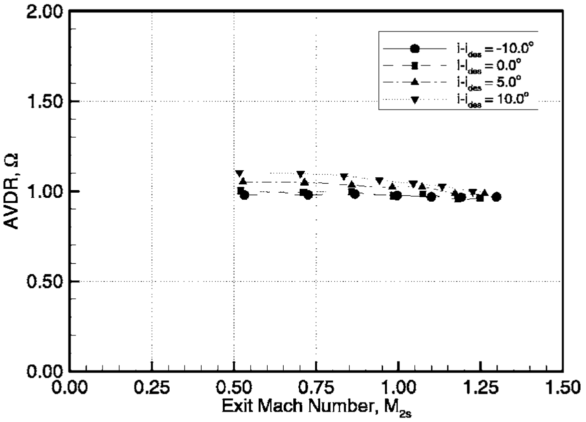

(c) Front-loaded cascade HS1D

Fig. 12 Effect of Mach number on the variation of the axial velocity density ratio for various incidences

It appears that the reason why the losses are much higher at high outlet Mach numbers for HS1C and HS1D compared to HS1A is related to the fact that the losses do not level off for these two blades in the range of Mach numbers from 1.05 to 1.15. This difference can be seen in Figs. 5–7. In these figures, it can be observed that the losses increase at approximately the same rate for the three profiles starting at about an outlet Mach number of 0.85. The fact that the losses do not level off for HS1C and HS1D is consistent with the fact that, unlike for blade HS1A, the base pressure does not rise sharply for HS1C and HS1D at Mach numbers greater than about 1.05, as seen in Figs. 9(*b*) and 9(*c*). As discussed previously, the rapid rise in base pressure at high Mach number for HS1A was shown to contribute to the leveling off of

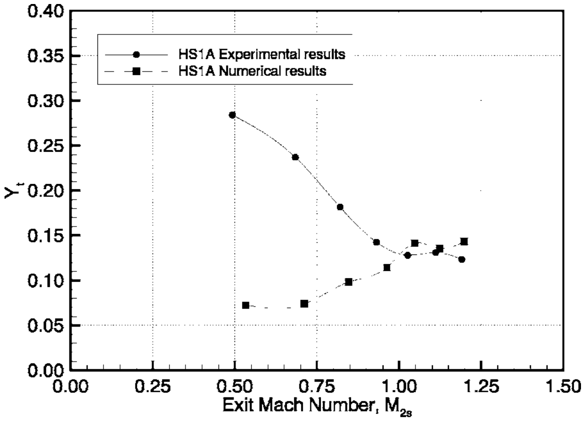

(a) Mid-loaded cascade HS1A

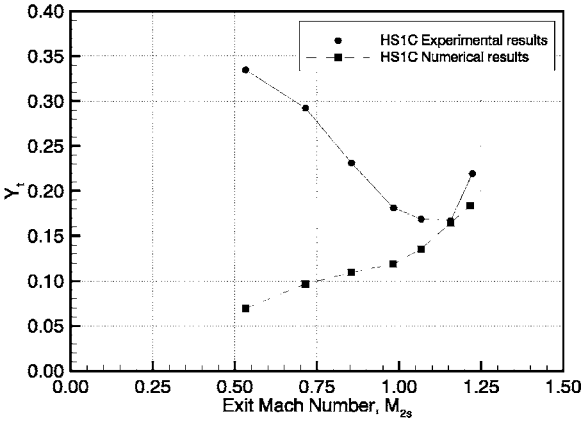

(b) Aft-loaded cascade HS1C

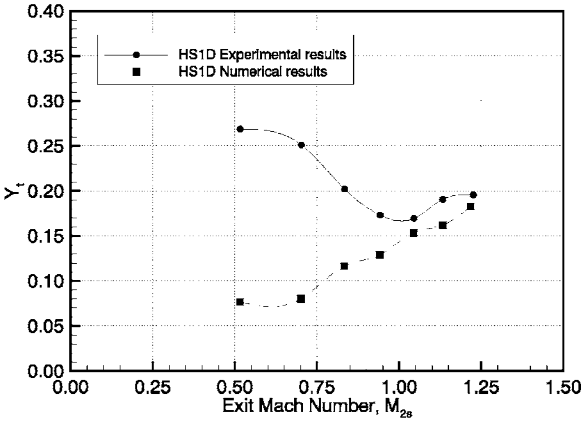

(c) Front-loaded cascade HS1D

Fig. 13 Comparison of loss variation with Mach number for experimental and numerical results at +10.0 deg of incidence

the losses through a direct reduction in the trailing edge losses. The rapid rise in base pressure for HS1A thus contributes to delaying the increase in losses, whereas for blade HS1C and HS1D the base pressure varies only slightly at high outlet Mach number.

The rapid rise in base pressure for HS1A at high outlet Mach numbers can be explained as follows. For higher outlet Mach numbers, the adjacent blade trailing edge shock impingement point shifts to a location closer to the trailing edge on the suction surface, as seen from the loading distributions in Fig. 10(*a*). Thus, at higher Mach numbers, the flow cannot reaccelerate as much following the region of diffusion at the shock impingement point, before reaching the trailing edge. Hence, the fluid momentum in the shear layer is reduced and its entrainment power on the base region fluid is reduced. This results in higher base pressure at the trailing edge.

As mentioned previously, the increase in base pressure for HS1A at high Mach numbers resulted in a relative improvement of its performance when compared to HS1C and HS1D for values of incidence between −10.0 deg and +5.0 deg. As the base pressure increased, the strength of the trailing edge shocks was reduced. This can be seen from Fig. 10(*a*) by comparing the loading distributions for HS1A at exit Mach numbers close to the design Mach number of 1.05 with those for the other airfoils, as given in Figs. 10(*b*) and 10(*c*). As observed from these figures, the amount of diffusion induced on the rear suction surface of the blade by the impinging shock is reduced slightly at the highest outlet Mach number. At high Mach numbers, the aft-loaded blade, HS1C, has a much higher rear suction peak Mach number, which is followed by a large region of diffusion at all values of incidence investigated, compared to the baseline midloaded blade, HS1A. This can be seen in Fig. 10(*b*) for an incidence of +5.0 deg. The presence of high rear suction surface velocity combined with a large amount of diffusion probably explains the rapid rise in losses for HS1C at high Mach numbers. The front-loaded blade, HS1D, also exhibits significant deceleration on the rear suction surface at high Mach numbers. This is in addition to the adverse pressure gradient that extends up to about $x/C_x \approx 0.6$ on the suction surface for most flow conditions as shown in Fig. 10(*c*). These regions of diffusion on the suction surface contribute to the rapid rise in losses for HS1D at high Mach numbers.

At an incidence of +10.0 deg, the secondary flow appears to have a significant influence on the midspan loss performance of blades HS1C and HS1D, as was the case for HS1A. In Fig. 4, it can be observed that the losses are significantly higher at an incidence of +10.0 deg for all three blade profiles. Comparison of the experimentally determined losses with the two-dimensional numerical calculations in Figs. 13(*b*) and 13(*c*) shows that for Mach numbers lower than approximately 1.0 significant discrepancies exist just as for HS1A, due most likely to the presence of some three-dimensional flow at midspan. Again, this interpretation is supported by the fact that the AVDR values for HS1C and HS1D at +10.0 deg are also greater than 1.0 (Figs. 12(*b*) and 12(*c*)).

For the aft-loaded blade, HS1C, it even appears that the three-dimensional flow effect on losses may start at an incidence as low as +5.0 deg for the lowest Mach numbers investigated. This can be seen from Fig. 7, which shows a comparison between the losses measured experimentally and those determined computationally at an incidence of +5.0 deg for the three blades.

As noted, the fact that the losses for HS1C and HS1D are significantly higher, at an incidence of +10.0 deg, is believed to be due partly to the presence of three-dimensional flow at midspan, as was the case for HS1A. However, the magnitude of the losses for HS1C is much higher than those of HS1A over the whole range of outlet Mach numbers. The losses for HS1D are slightly lower than those of HS1A at the lowest Mach number investigated, but as the Mach number is increased, the loss performance for HS1D deteriorates rapidly relative to HS1A.

Conclusions

The paper describes an experimental study on the influence of loading distribution on the performance of HP turbine blades. Measurements have been presented for the midspan aerodynamic performance of three blades at off-design incidence and Mach number. The airfoils tested consist of a midloaded blade (baseline), a front loaded blade, and an aft-loaded blade.

At off-design Mach number and incidence, the loss performance of the aft-loaded (HS1C), and front-loaded (HS1D) airfoils is similar to that of the baseline midloaded airfoil (HS1A) for subsonic outlet Mach numbers, omitting those cases where three-dimensional flow effects are believed to be present. The main weakness of the aft-loaded blade (HS1C) and the front-loaded blade (HS1D), as they are currently designed, is for outlet Mach numbers greater than about 1.10. For all off-design incidences investigated, the baseline midloaded blade, HS1A, had the lowest losses at high outlet Mach numbers.

At high Mach number, the aft-loaded blade, HS1C, has a much higher peak Mach number on the rear suction surface. This is followed by a large region of diffusion at all values of incidence investigated. In order to improve the performance of HS1C at high Mach numbers, this rear suction surface flow deceleration would have to be reduced. Reducing the rear suction surface curvature of HS1C would be one possible solution.

Based on the observations made at design and off-design flow conditions, it appears that aft-loading can be a viable design philosophy to employ in order to reduce the losses within a blade row provided the rearward deceleration is carefully limited.

The front-loaded blade, HS1D, also exhibits significant deceleration on the rear suction surface at high Mach number. This is in addition to the adverse pressure gradient that extends up to about $x/C_x \approx 0.6$ on the suction surface for most flow conditions. The loss performance of the front-loaded blade, HS1D, is inferior or at best equal to that of the other two blades for all operating conditions. As such, it appears that there is no advantage to front loading the airfoil for transonic high-pressure turbine blades.

Acknowledgment

The authors wish to thank Pratt & Whitney Canada Inc. for their advice and assistance in designing blades HS1C and HS1D. Financial support from Pratt & Whitney Canada Inc. is also gratefully acknowledged.

Nomenclature

AVDR = axial velocity density ratio, $=[\int_0^1 (\rho_2 C_{(ax)_2})_{MS} d(y/s) / \int_0^1 (\rho_1 C_{(ax)_1})_{MS} d(y/s)]$
a = leading edge ellipse major axis
b = leading edge ellipse minor axis
C = blade chord length
C_b = base pressure coefficient, $=[(P_b - P_2)/q_2]$
C_x = axial chord length
H = blade span
i = incidence, $(=\alpha_1 - \beta_1)$
$i_{\text{effective}}$ = effective incidence, $(=i - i_{\text{des}})$
Ma = Mach number
o = throat opening
P_b = base pressure
P_0 = total pressure
P = static pressure
q = dynamic pressure, $(1/2 \rho V^2)$
Re = Reynolds number, $(\rho V_2 C/\mu)$
s = blade pitch or spacing
t = trailing edge thickness
V = flow velocity
We = wedge angle
x = axial distance
Y_t = midspan total pressure loss coefficient (pitch-wise averaged), $=[(P_{o1} - P_{o2})/q_2]$
Y_{te} = trailing edge loss coefficient
y^+ = dimensionless distance normal to the wall
Z = compressible Zweifel loading coefficient, $[=s/C_x \cos^2 \alpha_2 (\tan \alpha_1 + \tan \alpha_2) \gamma M_{2s}^2 / (1 + \gamma - 1/2 M_{2s}^2)^{\gamma/(\gamma-1)} - 1]$
a = flow angle measured from the axial direction
b = metal angle measured from the axial direction
d = deviation, $(=\beta_2 - \alpha_2)$
d^* = boundary layer displacement thickness
m = air dynamic viscosity
ρ = air density
θ = boundary layer momentum thickness
θ_u = uncovered turning angle
ζ = stagger angle measured from the axial direction
γ = specific heat ratio

Subscripts

1 = cascade inlet
2 = cascade outlet
ax = axial
des = design
le = leading edge
MS = midspan
s = isentropic
te = trailing edge

References

[1] Vijayaraghavan, S. B., and Kavanagh, P., 1988, "Effect of Free-Stream Turbulence, Reynolds Number, and Incidence on Axial Turbine Cascade Performance," ASME Paper 88-GT-152.

[2] Goobie, S. M., Moustapha, S. H., and Sjolander, S. A., 1989, "An Experimental Investigation of the Effect of Incidence on the Two-Dimensional Flow," *Proceedings of the 9th International Symposium on Air Breathing Engines (ISABE)*, Athens, Greece, Sept. 4-9, pp. 197–204.

[3] Tremblay, B., Sjolander, S. A., and Moustapha, S. H., 1990, "Off-Design Performance of a Linear Cascade of Turbine Blades," ASME Paper 90-GT-314.

[4] Graham, C. G., and Kost, F. H., 1979, "Shock Boundary Layer Interaction on High Turning Transonic Turbine Cascade," ASME Paper 79-GT-37.

[5] Šťastný, M., Šafařík, P., Hořejší, I., and Matas, R., 1997, "Flow Around the Sections of Rotor Blading of a Turbine Stage With Relatively Long Blades at Off-Design Conditions," Proc. Inst. Mech. Eng., Part A, **211**, pp. 207–213.

[6] Jeffries, M. S., 2001, "Initial Investigations of Transonic Turbine Aerodynamics Using the Carleton University High-Speed Wind Tunnel," Ph.D. thesis, Carleton University, Ottawa, Canada.

[7] Jouini, D. B. M., 2000, "Experimental Investigation of Two Transonic Linear Turbine Cascades at Off-Design Conditions," Ph.D. thesis, Carleton University, Ottawa, Canada.

[8] Patterson, D. J., and Hoeger, M., 1986, "The Effect of Reynolds Number and Velocity Distribution on LP Turbine Cascade Performance," ASME Paper 86-GT-271.

[9] Hashimoto, K., and Kimura, T., 1984, "Preliminary Study on Forward Loaded Cascades Designed with Inverse Method for Low Pressure Turbine," ASME Paper 84-GT-65.

[10] Hoheisel, H., Kiock, R., Lichtfuss, H. J., and Fottner, L., 1987, "Influence of Free-Stream Turbulence and Blade Pressure Gradient on Boundary Layer and Loss Behavior of Turbine Cascades," ASME J. Turbomach., **109**, pp. 210–219.

[11] Howell, R. J., Ramesh, O. N., Hodson, H. P., Harvey, N. W., and Schulte, V., 2001, "High Lift and Aft-Loaded Profiles for Low-Pressure Turbines," ASME J. Turbomach., **123**, pp. 181–188.

[12] Amecke, J., and Šafařík, P., 1995, "Data Reduction of Wake Flow Measurements With Injection of Other Gas," Technical Report No. DLR-FB 95-32, DLR.

[13] Moffat, R., 1988, "Describing the Uncertainties in Experimental Results," Exp. Therm. Fluid Sci., **1**, pp. 3–17.

[14] Spalart, P. R., and Allmaras, S. R., 1994, "A One-Equation Turbulence Model for Aerodynamic Flows," Rech. Aerosp., **1**, pp. 5–21.

[15] Mee, D. J., Baines, N. C., Oldfield, M. L. G., and Dickens, T. E., 1992, "An Examination of the Contributions to Loss on a Transonic Turbine Blade in Cascade," ASME J. Turbomach., **114**, pp. 155–162.

[16] Corriveau, D., and Sjolander, S. A., 2002, "Impact of Flow Quality in Transonic Cascade Wind Tunnels: Measurements in an HP Turbine Cascade," *Proceedings 23rd Int. Congress of Aeronautical Science (ICAS)*, Toronto, Canada, Sept. 8-13.

[17] Corriveau, D., and Sjolander, S. A., 2004, "Influence of Loading Distribution on the Performance of Transonic HP Turbine Blades," ASME J. Turbomach., **126**, pp. 288–296.

[18] Corriveau, D., and Sjolander, S. A., 2004, "Experimental and Numerical In*vestigation on the Performance of a Family of Three HP Transonic Turbine Blades," ASME Paper GT2004-53087.

[19] Denton, J. D., 1993, "Loss Mechanism in Turbomachines," ASME J. Turbomach., **115**, pp. 621–656.

Investigation of the Flow Field in a High-Pressure Turbine Stage for Two Stator-Rotor Axial Gaps—Part I: Three-Dimensional Time-Averaged Flow Field

P. Gaetani
e-mail: paolo.gaetani@polimi.it

G. Persico

V. Dossena

C. Osnaghi

Dipartimento di Energetica,
Politecnico di Milano,
Via la Masa 34,
I-20158, Italy

An extensive experimental analysis on the subject of unsteady flow field in high-pressure turbine stages was carried out at the Laboratorio di Fluidodinamica delle Macchine (LFM) of Politecnico di Milano. The research stage represents a typical modern HP gas turbine stage designed by means of three-dimensional (3D) techniques, characterized by a leaned stator and a bowed rotor and operating in high subsonic regime. The first part of the program concerns the analysis of the steady flow field in the stator-rotor axial gap by means of a conventional five-hole probe and a temperature sensor. Measurements were carried out on eight planes located at different axial positions, allowing the complete definition of the three-dimensional flow field both in absolute and relative frame of reference. The evolution of the main flow structures, such as secondary flows and vane wakes, downstream of the stator are here presented and discussed in order to evidence the stator aerodynamic performance and, in particular, the different flow field approaching the rotor blade row for the two axial gaps. This results set will support the discussion of the unsteady stator-rotor effects presented in Part II (Gaetani, P., Persico, G., Dossena, V., and Osnaghi, C., 2007, ASME J. Turbomach., ***129****(3), pp. 580–590). Furthermore, 3D time-averaged measurements downstream of the rotor were carried out at one axial distance and for two stator-rotor axial gaps. The position of the probe with respect to the stator blades is changed by rotating the stator in circumferential direction, in order to describe possible effects of the nonuniformity of the stator exit flow field downstream of the stage. Both flow fields, measured for the nominal and for a very large stator-rotor axial gap, are discussed, and results show the persistence of some stator flow structures downstream of the rotor, in particular, for the minimum axial gap. Finally, the flow fields are compared to evidence the effect of the stator-rotor axial gap on the stage performance from a time-averaged point of view.* [DOI: 10.1115/1.2472383]

Introduction

The periodic flow unsteadiness induced by the relative motion of the stator and rotor rows is one of the leading topics in turbomachinery research. Two guidelines with significantly different approaches have been developed in the study of stator-rotor interaction in turbine stages [1]: low-pressure (LP) and high pressure (HP) turbines.

In the LP turbines the periodic impingement of the stator wakes on the rotor suction surface strongly affects the boundary layer transition on the profile, and for very high lift rotors some advantages can be obtained controlling the unsteady blade-wake interaction, i.e., suppressing the separation bubble on the rotor suction surface. These concepts were used to develop novel ultrahighly loaded profiles [2].

In HP turbines the effects of the periodic impingement of the wakes on the rotor suction surface is less pronounced, basically because of the high chord-based Reynolds numbers. For transonic stages, the interaction of the stator trailing-edge shock wave with the downstream rotor induces complex shock patterns in the stator-rotor spacing and relevant static pressure fluctuations on the rotor [3].

In subsonic stages, the two-dimensional (2D) wake-blade interaction can play only a marginal role if, as usual in HP turbines, low aspect ratio bladings are encountered. In this case, the major loss mechanisms are related to the end-wall secondary vortices induced by the redistribution of incoming vorticity, as a result of the flow turning inside the row of blades. The so-called vortex-blade interaction, i.e., the one between the stator secondary flows and the rotor, is the core of the stator-rotor interaction studies for subsonic HP turbines. Detailed investigations have been published on this topic in the last several years, in terms of time-averaged [4] and time-resolved [5,6] flow field downstream of the rotor, and the persistence of the stator vortex structures downstream of the full stage has been observed.

The basis of the analysis of the vortex-blade interaction is a detailed investigation of the rotor incoming flow because of the different typologies of secondary vortices that can develop in a low aspect-ratio stator. Moreover, with respect to the classical secondary flows in linear turbine cascades [7], some relevant differences have been observed in annular stators: the presence of a radial pressure gradient induces a significant nonsymmetry in the stator loss structures, pulling towards the hub the low-momentum fluid [8,9]. The radial inward flow induced by the radial pressure gradient complicates the definition of a reference flow for the

---

Contributed by the International Gas Turbine Institute of ASME for publication in the Journal of Turbomachinery. Manuscript received July 13, 2006; final manuscript received July 28, 2006. Review conducted by David Wisler. Paper presented at the ASME Turbo Expo 2006: Land, Sea and Air (GT2006), Barcelona, Spain, May 8–11, 2006. Paper No. GT2006-90553.

Table 1 LFM closed-loop test rig: Main operational characteristics

Section	Engine—brake	Max. diam.	Max. rpm
Centrifugal	800 kW, 600 DCV	560 mm	45,000
Axial	400 kW, 54 DCV	400 mm	20,000

calculation of the secondary velocity: as a result the reference flow cannot be derived directly by the measurements and it can only be evaluated theoretically [10].

The three-dimensional (3D) design techniques applied in the design of the modern high-pressure turbine stage discussed in the following also have relevant effects on the downstream flow field. The main feature of the 3D blade design is to modify the spanwise blade load distribution. In the case of "positive" lean (pressure side of the blade forming an acute angle with the hub end-wall), a reduction of the blade load at the hub and an increase at the tip has been found [11], with corresponding effects on the spanwise distribution of discharge flow angle and losses. A "negative" compound leaning (bowing) technique is also widely used in the tip region of turbine rotors to reduce the blade load at the tip and, thus, the tip leakage flow. Both these techniques have been applied in the design of the present turbine stage, and their effects are therefore to be taken into account in the description of the flow field.

Because the aim of the present research program is to assess the role played by the flow unsteadiness in a single stage of modern HP turbines, and considering that the nonuniformity is strongly affected by the stator-rotor spacing, two different axial gaps have been studied in terms of both time-averaged performances and unsteady rotor behavior. In fact, to the knowledge of the authors previous papers concerning the gap effect in turbine stages only presented blade surface measurements [12,13], while the present papers provide a set of detailed measurements on the flow field downstream of the stage for a typical gap and for an unusual larger gap, chosen to limit the stator related effects.

In the present paper, a characterization of the flow field downstream of the stator is reported; the evolution and the mixing of the stator structures in the streamwise direction are also discussed. In this way, a detailed knowledge of the rotor incoming flow for the two stator-rotor axial gaps considered in the paper is achieved.

Even if the capability of a conventional five-hole probe can be dramatically reduced when applied in high-frequency fluctuating flow fields, the time-averaged flow downstream of the full stage is described for the two configurations in order to check the persistence of stator-related structures downstream of the stage; moreover, a discussion on the overall stage performances is also reported. The unsteady flow downstream of the rotor and the unsteady interaction with the stator structures will be described in details in Part II of the paper [14].

Experimental Setup

LFM Closed-Loop Test Rig. For the aim of the already-mentioned research program at the Laboratorio di Fluidodinamica delle Macchine (LFM) of the Politecnico di Milano, a closed-loop test rig for axial and centrifugal turbomachines has been launched in 2001. Table 1 presents the main operational characteristics, while Fig. 1 shows a sketch of the facility.

The test rig is instrumented in order to allow the overall performance evaluation of both installed turbomachines and can be operated under closed conditions or forcing the outlet or the inlet of the axial section to the atmospheric pressure. Both sections are equipped with traversing systems for the measurement of the flow field inside and downstream of the turbomachines; optical accesses for LDV measurements are also provided.

The two reversible dc engines allow a continuous rotational speed regulation and the electrical power generated at the turbine brake is reversed to the centrifugal section engine, leading to significant savings in electrical running costs.

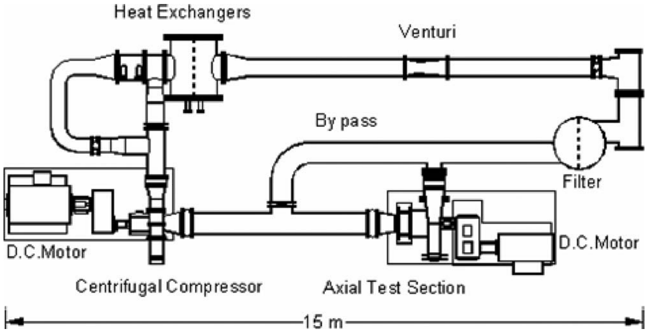

Fig. 1 Sketch of LFM closed-loop test rig

The centrifugal section is now equipped with a centrifugal compressor characterized by a nominal compression ratio of 2.6 at 5 kg/s (inlet at atmospheric condition) at a rotational speed of 18,000 rpm, whereas the axial section is equipped with the axial flow turbine described in the following section. More details about the test rig can be found in [15].

Axial Flow Turbine Stage. For the purposes of the present research program (PRIN 2003), concerning the analysis of unsteady effects in axial flow turbines, a model of a modern HP gas turbine stage was designed, manufactured, and installed in the axial section of the closed-loop test rig. Main geometrical design constraints together with the requirements of a quasi-2D flow at midspan, led the stage design to a positive vane leaning of 12 deg and to a significant blade bowing in the tip region. Table 2 reports on the main geometrical characteristics and operational test condition of the turbine stage.

The axial section was designed to allow different stator-rotor axial gaps by moving the stator row axially. In order to analyze the influence of this parameter on the stage performance and flow field distribution, the paper will present time-averaged measurements performed downstream of the rotor for two different axial gap configurations corresponding to $x/b_s=0.35$ (nominal) and $x/b_s=1.0$ (maximum). The use of this unusually large maximum gap has been applied in order to mostly "switch off" the stator related flow effects downstream the stage.

Table 2 LFM axial flow turbine stage: Main geometrical and operational characteristics

Expansion ratio	1.40					
Inlet temperature	313 K					
Rotational speed	6800 rpm					
Flow rate	3.65 kg/s					
Hub diameter	300 mm					
Tip diameter	400 mm					
	Vanes			**Blades**		
	Vane lean=12 deg			Blade-passing freq.=2.83 kHz		
Blades number	22			25		
Mean out. Mach	0.55			0.2		
Radial clearance (mm)	0.15			0.75		
b (mm)	30.6			46.7		
	Hub	MS	Tip	Hub	MS	Tip
S/b	1.39	1.6	1.86	0.80	0.94	1.07
Inletgeom. Angle (deg)		0		56.9	47.6	25.5
Outlet geom. Angle (deg)	72.5	75.2	77.5		−67.7	

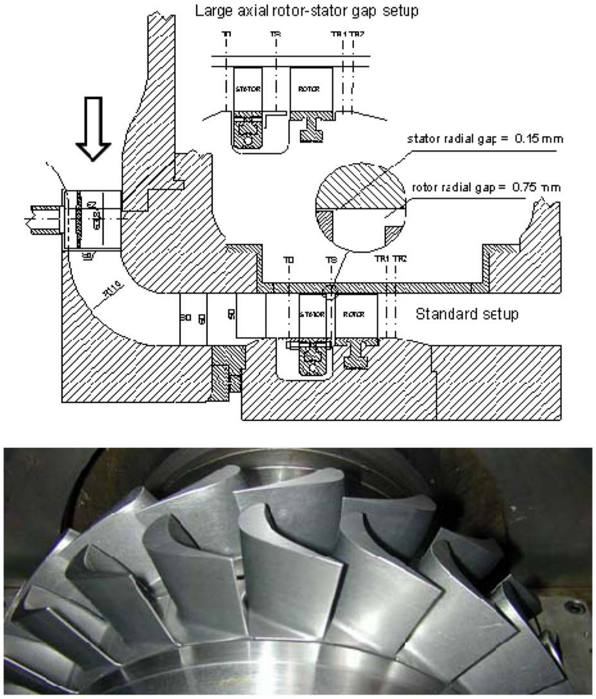

Fig. 2 Meridional view of LFM axial section and axial turbine stage view

Moreover, the evolution of the flow field downstream of the vane row has been performed only for the maximum axial gap, due to the geometrical constraints related to the five-hole probe size.

The measurement grid is obtained by rotating the turbine stator by means of a stepping motor—while the probe is kept at a fixed absolute circumferential position—and by moving the probe in radial direction; thus the measuring plane lies normally to the turbine axis. This methodology implies the vane tip clearance reported in Table 2 and evidenced in Fig. 1 (0.3% of the passage height).

Figure 2 reports a meridional view of the axial section: upstream from the stage, a centripetal flow guide vane deflects the flow from the radial to the axial direction; the yaw angle of the flow entering the stage can be controlled by regulating the stagger angle of the distributor blades. Just upstream from the stator, an annulus contraction accelerates the flow, slightly modifying angle and velocity distribution.

The flow field entering the stage has been characterized on a radial traverse located 30% of b_s upstream of the stator leading edge (T0 in Fig. 2). Because of the centripetal inlet duct, measurements at the stage inlet evidenced a radial total pressure gradient, characterized by the minimum pressure value at the tip and by a total pressure variation of 0.5%. The velocity distribution at the inlet is mostly uniform, and the boundary layer thickness on both walls resulted to be $<4\%$ of the channel height. More details about the upstream flow can be found in [15].

Flow-Field Measurements

Steady Aerodynamic Measurements. Steady flow measurements have been performed by means of a conventional miniaturized five-hole probe at eight axial locations in the stator-rotor axial gap and in a plane located 43% of the rotor axial chord downstream of the stage, for the two considered axial gaps.

The five-hole probe has been calibrated over a range of ±24 deg in yaw and pitch angles and for Mach numbers ranging from 0.2 to 1.0. The measurement accuracy, verified by means of a wide statistical analysis on a calibrated nozzle, is 0.3 deg in terms of flow angles and 0.5% of the kinetic head for total and static pressure.

Steady Temperature Measurements. Time-averaged temperature measurements were performed upstream and downstream of the stage; measurements were taken by means of a thermocouple installed at the same radial position of the pressure probe head but 10 mm displaced in tangential direction. Temperature data have been used to derive the relative total pressure and as a comparison for the qualitative evaluation of the stage work.

3D Measurements Downstream of the Vane

As already mentioned, the measuring grid is defined by traversing the probe in radial direction over the whole blade height and by rotating the vane row. The grid is defined by means of 40 tangential traverses along the blade height and 48 stations along the vane pitch, for a total number of about 2000 measuring points for each plane. Steady measurements between the two rows have been performed in eight planes located from $x/b_s=0.16$ to $x/b_s=0.60$; these boundaries are imposed by the constraints related to the five-hole probe head length.

In order to discuss the mean flow-field features, where the secondary phenomena are still intense and more easily recognizable, the presentation will focus at first on the measurements performed in the plane closer to the vane trailing edge ($x/b_s=0.16$). Then the flow evolution will be followed and discussed by means of two extra measuring planes. The first one is located at $x/b_s=0.35$ and can be considered as representative of the flow field impinging on the rotor leading edge for the case of nominal axial gap. The second plane is the farthest from the vane trailing edge ($x/b_s=0.60$); at this axial distance, the flow has already experienced a developed mixing process so that the measurements can be considered as representative of the flow field impinging on the rotor leading edge for the case of maximum axial gap ($x/b_S=1$).

All considerations reported in the following are also supported by the measurements performed on the other intermediate planes where the flow field evolution evidences good coherence and continuity. Because the definition of secondary velocity suffers the lack of a reference flow, secondary phenomena are evaluated by means of the streamwise vorticity distribution on the measuring planes. Streamwise vorticity has been calculated on the basis of the local velocity vectors together with the application of the Crocco's equation [16].

Traverses at $x/b_s=0.16$. The frames in Fig. 3 offer a general overview of the main flow features on the first measuring plane. Figure 3(*a*) reports the distribution of the local total pressure loss coefficient Y in terms of contour lines; a trace of the vane trailing edge is also reported as a dashed black line in the same plot. Contours clearly evidence the wake, identified by the radial loss region at about $\theta/\Delta\theta_s=1.2$; the wake trace is mostly parallel to the vane trailing edge, evidencing a pitchwise distortion on its suction side while approaching the two end-walls.

Figure 3(*a*) evidences three high-loss regions:

- The first one (I in Fig. 3), located in the upper part of the wake, is characterized by a loss peak of 0.46 at 80% of the blade height.
- The second one (II in Fig. 3), located on the hub side of the wake trace, evidences a loss core corresponding to $Y=0.42$ at ~20% of the blade height.
- The third loss region (III in Fig. 3), showing the highest loss values of the whole measuring plane ($Y=0.50$), is located at the tip and extends for about $\frac{1}{4}$ of the angular pitch from the wake trace toward the passage pressure side. As already remarked, the stator movement leads to a vane tip clearance of ~0.3% of the blade height (Table 2); this feature can

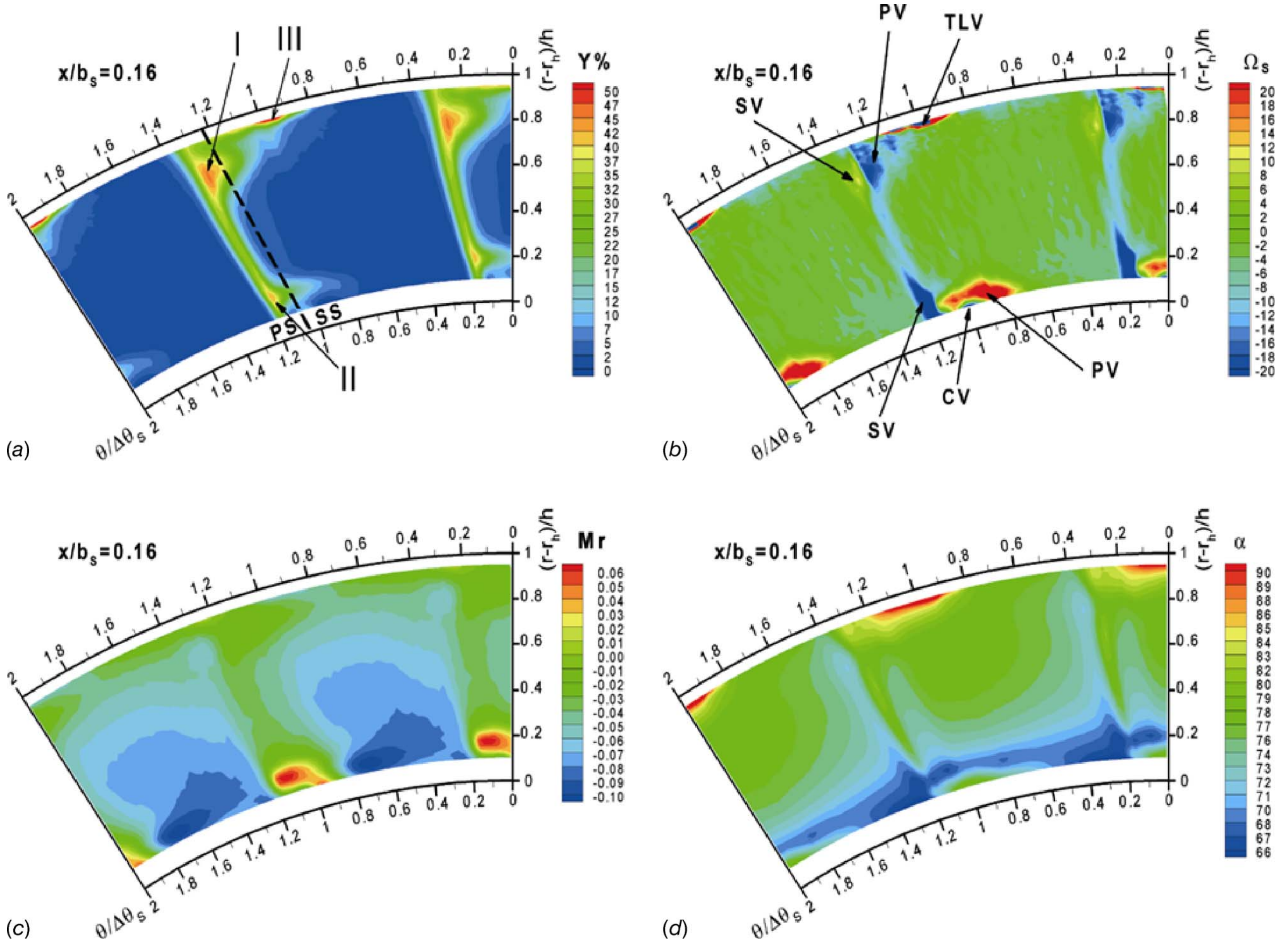

Fig. 3 Contours of (*a*) total pressure loss coefficient, (*b*) streamwise vorticity, (*c*) radial Mach number, and (*d*) blade-to-blade flow angle ($x/b_s=0.16$)

explain the high-loss region III at the vane tip, as the result of the high energy dissipation experienced by the flow leaking over the profile.

Figure 3(*b*) evidences the two passage vortices (PV) characterized by positive Ω_s values (clockwise) at the hub and by opposite values at the tip; both vortices appear very concentrated on the suction side of the channel and close to the end-wall region; these features are consistent with the low thickness of the upstream boundary layer. Furthermore, the two passage vortices are transported toward the hub by the action of the radial velocity component, generally inward directed as reported in Fig. 3(*c*); this centripetal action is the result of the radial pressure gradient imposed by the annular effect and by the leaning of the vane. No traces of the two legs of the horseshoe vortices are found in the measuring plane: the pressure-side leg is merged with the corotating passage vortex, while the suction side leg has probably vanished due to the mixing process.

Moreover, the vorticity contours show on each side of the passage two vortices counterrotating with respect to the associated passage vortex and placed around the wake, which can be identified as the two shed vortices (SV): the first one, centered at 85% of the blade span, is very weak, whereas the second one, centered at 25% of the blade span, is stronger and wider due to the different intensities of the passage vorticies. The identification of the secondary vortices is also supported by the loss distribution reported in Fig. 3(*a*): the two loss cores I and II are exactly located in the region of viscous interaction between the passage and the shed vortex on both sides of the channel.

The vorticity contours reported in Fig. 3(*b*) clearly evidence the presence of another vortical structure located at the outer end wall of the passage and which position is consistent with the loss region previously associated to the tip leakage flow (zone III in Fig. 3(*a*)). The clockwise rotation of the flow in this region suggests that the leaking flow, originally injected in the channel through the radial gap, interacts with the low-energy fluid belonging to the tip boundary layer and characterized by velocity component directed toward the suction side of the passage; as a result, the flow in this region rolls up leading to the positive streamwise vorticity evidenced in Fig. 3(*b*), which can now be identified as a tip leakage vortex (TLV). Moreover, it has to be remarked that the axial velocity in the tip leakage vortex region is near zero, leading to a high overturning as evidenced by the α angle distribution reported in Fig. 3(*d*).

As last feature, Fig. 3(*b*) evidences a vorticity core located at 10% of blade height and at $\theta/\Delta\theta_s=1.0$, just below the hub passage vortex; characterized by negative values (CV); in the same region, Fig. 3(*d*) shows local high overturning angles; this feature can be consistent with a corner vortex, counterclockwise rotating and generated by the hub passage vortex. The underturning region, usually associated to the end-wall side of the corner vortex, is supposed to be confined in the region not covered by the measurements (about 10% of blade height).

Flow-Field Evolution Downstream of the Vane. The flow-field evolution downstream of the vane is presented in order to evaluate the main flow structure entering inside the rotor row.

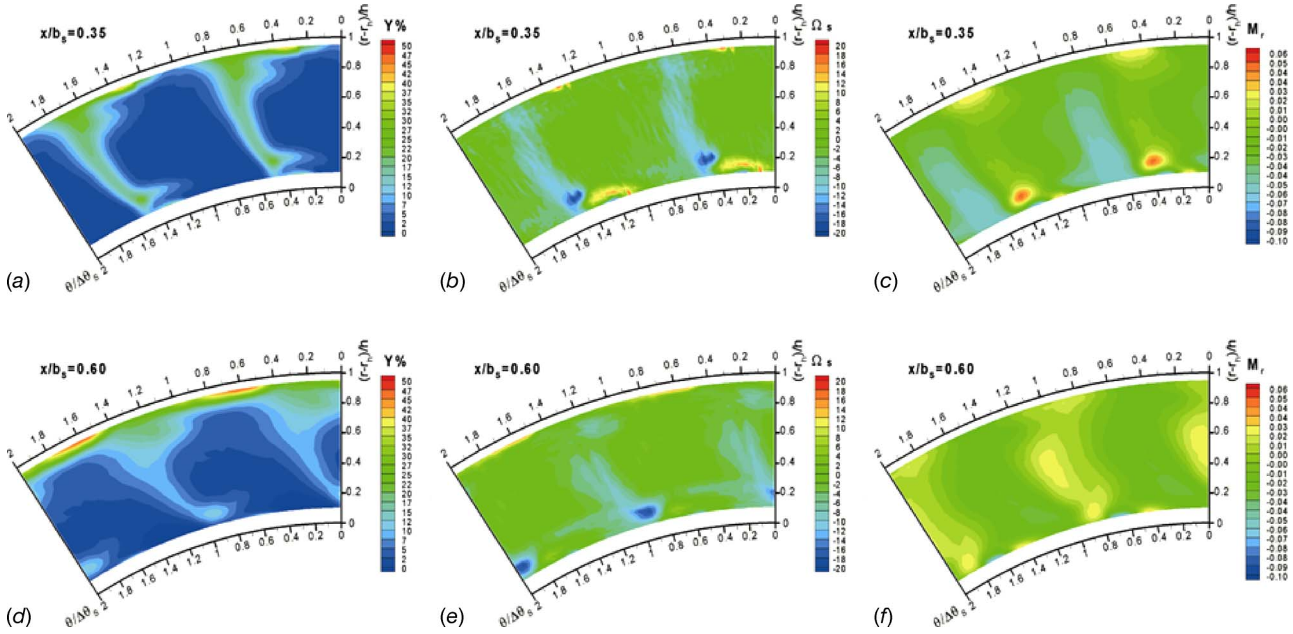

Fig. 4 Total pressure loss coefficient, streamwise vorticity and radial Mach number contours at (*a–c*) $x/b_s=0.35$ and (*d–f*) $x/b_s=0.60$

Figure 4 shows Y, Ω_s, and M_r contours on two measuring planes located at $x/b_s=0.35$ and $x/b_s=0.6$, while Fig. 5 shows the main flow parameters in terms of pitchwise mass-averaged quantities.

The analysis of Figs. 4(*a*) and 4(*d*) evidences, as a main feature, the streamwise evolution of the vane wake: while at $x/b_s=0.16$, the wake trace is parallel with respect to vane trailing edge, moving downstream its leaning increases; at the tip the wake is transported by a more tangential flow as remarked by the α contours shown in Fig. 3(*d*) and supported by the spanwise distribution of $\overline{\alpha}$. At the same time, the action of the strong tangential and axial velocity gradients in the tip region and, in particular, in the zone influenced by the leakage flow—where the flow rate tends to zero—enlarges the wake trace.

Moreover, the above-mentioned effect together with the strong interaction between the tip leakage and the tip passage vortex act to reduce the intensity of the secondary vortices, where trace is quite evanescent on the Ω_s contours at $x/b_s=0.35$ and disappears at $x/b_s=0.60$.

Note the low-energy fluid coming from the tip leakage and from the progressively developing end-wall boundary layer; this latter feature enhanced by the highly tangential flow direction, tends to migrate toward the midspan as also remarked by the spanwise $\overline{Y}$ distribution, evidencing a continuous huge growth of the tip loss moving downstream. This feature is also consistent with the effects typically produced by a positive vane leaning, as already observed in a previous measurement campaign performed on linear leaned cascades [17].

Moving the attention toward the hub side, Fig. 4(*b*) shows the persistence of the three secondary vortices at $x/b_s=0.35$; further downstream, Fig. 4(*e*) still evidences one core of negative vorticity corresponding to the shed vortex, while the passage and the corner vortex almost disappear. It is also interesting to underline that the position of the shed vortex remains radially unchanged due to the action of the passage vortex. In fact, the passage vortex

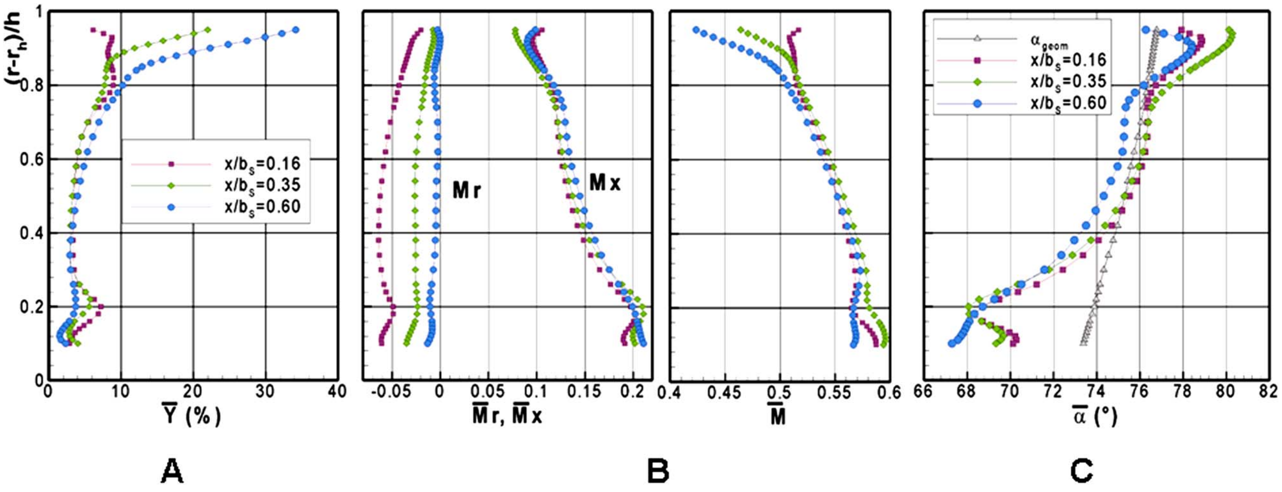

Fig. 5 (*a–c*) Radial distribution of pitchwise mass averaged loss coefficient, Mach number components, and outlet angle

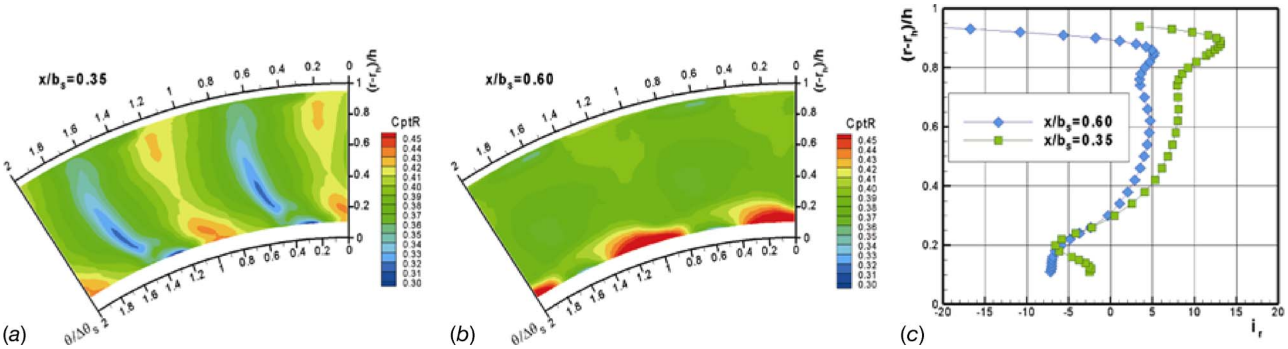

Fig. 6 $C_{pt,R}$ contours upstream of the rotor for the minimum gap (*a*) and the maximum gap (*b*) and radial distribution of pitchwise averaged rotor incidence for both cases (*c*)

region evidences outward directed radial velocities despite the general trend shown all over the measuring plane due to the vane leaning.

Frames reported in Fig. 5 can confirm and summarize some of the above-reported considerations:

- The radial distribution of $\overline{Y}$ (Fig. 5(*a*)) evidences at the tip a strong increase moving downstream, as already remarked. On the contrary, the decrease in loss evidenced at the hub ($h < 20\%$) moving downstream can be related to the high-energy fluid transported toward the hub by the very intense radial velocity. Nevertheless, the overall mass-averaged loss evaluated in the whole measuring plane rises from 5.2% to 6.2% moving downstream.
- Figure 5(*b*) evidences the general centripetal behavior of the radial component, mostly due to the vane leaning. Moving downstream, $\overline{M}_r$ progressively tends to reduce becoming radially uniform and to almost zero on the farthest measuring plane.
- The radial distribution of $\overline{\alpha}$ (Fig. 5(*c*)) evidences a quite linear increase of 12 deg from hub to tip, due to the effect produced by the vane leaning. Moreover, at this general trend, the effects of underturning and overturning produced by the two passage vortices are superimposed. At the hub wall, the underturning observed for three planes remarks the effect of the corner vortex. Near the tip wall, the low values of $\overline{\alpha}$ can be related to the mass-average process between the low flow rate associated to the high turning leakage flow and the higher flow rate of the more axial freestream.

Flow Field in the Relative Frame. Figure 6 reports some features of the relative flow field approaching the rotor for the two different axial gaps; as already mentioned, plane located at $x/b_s = 0.60$ is not coincident with the location of the rotor leading edge for the case of maximum gap, but results can be used as a reference for the flow entering the rotor.

Figures 6(*a*) and 6(*b*) show the contours of $C_{pt,R}$ on the two measuring planes; this parameter will be widely used in the Part II [14] for the analysis of the unsteady flow field downstream of the rotor. It must be remarked that the $C_{pt,R}$ should not be considered as representative of any actual physical quantity upstream of the rotor, but it can be proficiently applied for the analysis of the aerodynamic losses throughout the rotor.

Figure 6(*a*) evidences high $C_{pt,R}$ values in the freestream zone and, on the contrary, very low $C_{pt,R}$ values are associated to the vane wake zone; moreover, the two zones extend radially for most part of the blade height, but deviate towards the pressure side of the passage at the hub, due to the more axial direction of the flow in this region. It is interesting to notice that the low $C_{pt,R}$ region is consistent with the negative Ω_s zone evidenced on the same plane in Fig. 4(*b*). Furthermore, Fig. 6(*a*) evidences another small zone of low $C_{pt,R}$ values centered on $\theta/\Delta\theta_s = 0.3$ at the hub, corresponding to the hub corner vortex.

Moving now to the contours referring to $x/b_s = 0.60$, a general attenuation of all mentioned phenomena can be noted, leading to an almost uniform $C_{pt,R}$ distribution in the whole plane. The only exception is represented by the very high $C_{pt,R}$ rate interesting half vane pitch at the hub: this feature is associated to the very high relative velocity level experienced by the flow in this area.

Figure 6(*c*) allows the comparison of blade incidence radial distribution obtained by means of the computed $\overline{\alpha}$ values on the two planes; at $x/b_s = 0.35$ the incidence rises from −6 deg at the hub to a maximum value of +14 deg at 90% of the blade height. At $x/b_s = 0.60$ the maximum positive incidence reduces to +6. The dramatic reduction of incidence at the tip for the farthest plane is related to the general velocity reduction experienced by the flow in this region due to the tip end-wall boundary layer growth associated to the highly tangential velocity. The pitchwise variation of incidence evaluated on the measuring planes, not shown for sake of brevity, is contained in the band ±10 deg; it is in author's opinion that this variation could only lead to limited effects on the downstream flow field.

3D Measurements Downstream of the Stage

Figure 7 reports about measurements performed at 43% of the blade axial chord downstream of the stage (traverse TR2 in Fig. 2) for both considered axial gaps. Figure 7(*a*) shows the $C_{pt,R}$ distribution for the case of minimum gap; comparing it to the corresponding upstream distribution reported in Fig. 6, it is not possible to note any trace of the original quasi-uniform radial distribution due to the strong action of rotor secondary phenomena. On the contrary, one can note the persistence of a pitchwise nonuniformity. This feature is consistent with an effect coming from the stator due to the fact that all rotor-associated effects are pitchwise averaged by the measurement process.

The same feature can be noted by the δ_r distribution reported in Fig. 7(*b*) and by the radial Mach number distribution reported in Fig. 7(*c*). Even if the detailed analysis of the stator-rotor interaction is demanded to the second part of this paper, a particular effect can be pointed out by means of the steady measurements reported in Fig. 7(*c*). In fact, in the center of the passage, the radial Mach number distribution shows zones of inward- and outward-oriented components, evidencing a counterclockwise rotating vortex: this structure can be associated to the vane hub shed vortex previously evidenced in Fig. 4(*b*). Moreover, the persistence of this vortex is supported by the fact that the rotor hub passage vortex is also counterclockwise rotating and operates in order to lift the hub shed vortex toward the midspan [5]. At the tip of the blade, the general centrifugal tendency of the radial Mach number distribution can be related to the positive blade bowing.

Figure 7(*b*) shows a remarkable overturning centered at 80% of the blade height, probably associated to the upper leg of the tip passage vortex and to the lower leg of the rotor tip leakage vortex;

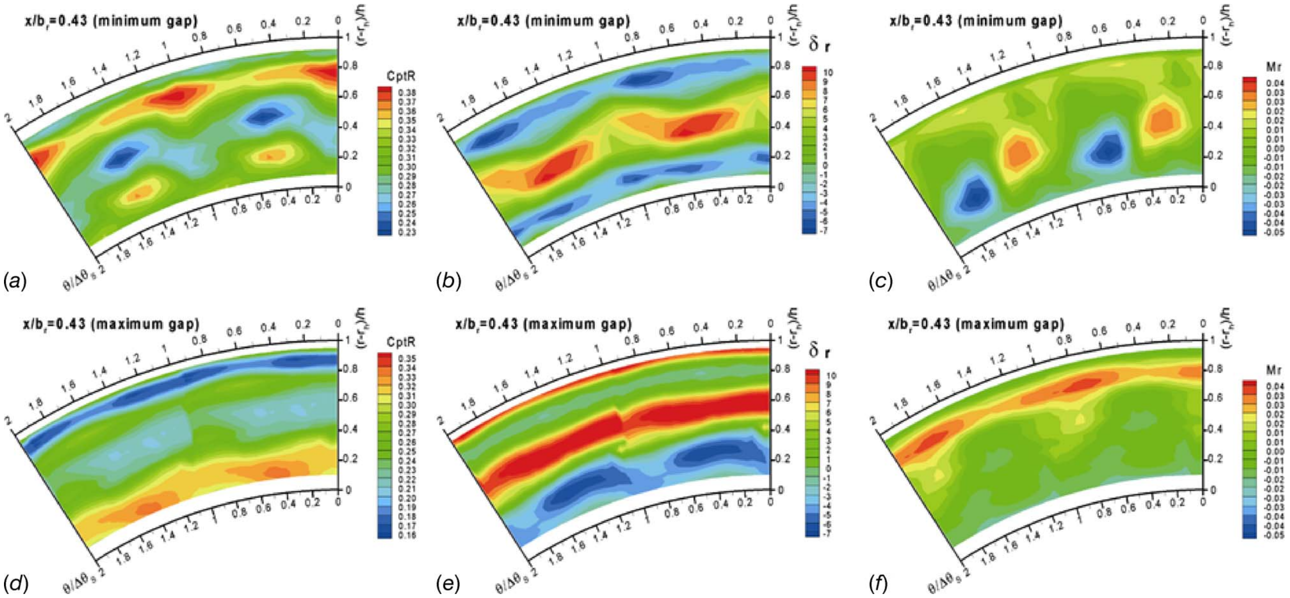

Fig. 7 Relative total pressure coefficient, rotor deviation angle, and radial Mach number contours at the rotor exit for the case of minimum gap (*a–c*) and maximum gap (*d–f*)

the same plot evidences an underturning approaching the endwall, which can be related to the effect of the blade bowing together with the rolling up of the flow coming from the tip leakage.

Referring now to the case of maximum gap reported in Figs. 7(*d*)–7(*f*), it is possible to underline a general reduction of the pitchwise gradients for all the considered quantities, due to the more uniform distribution of the corresponding frames reported in Fig. 4. In particular, no traces of stator vortices are recognizable downstream of the stage on the TR2 plane in this configuration.

Stage Performance

The radial distribution of the stage work for both axial gaps has been computed on the basis of the pitchwise mass-averaged tangential velocities. The same trend has been evidenced also by the work computation evaluated by means of the measured total temperature distribution.

Figure 8 shows the pitchwise mass-averaged radial distribution of the adiabatic stage efficiency $\overline{\eta}$, computed by means of the mass-averaged work at constant radius, made nondimensional with respect to the isentropic enthalpy difference from total upstream to static downstream condition, the last being evaluated at constant P_{ref}.

In order to better understand the above-mentioned trend, Fig. 8 also shows the pitchwise mass-averaged tangential Mach number distribution upstream and downstream the rotating row.

The low work level at the tip, especially for the case of maximum gap is related at first to the low value of Ma_{1t}, particularly in the case of maximum gap due to the high loss level evidenced upstream of the blade, despite the high value of $\overline{\alpha}$, as reported in Fig. 5; at the same time, Ma_{2t} evidences at the tip a positive value, due to the high underturning (Fig. 7(*e*)). Moreover, the higher loss level evidenced at the tip for the case of maximum gap should not be considered as related to the unusual vane tip leakage, but mostly due to the thicker end-wall boundary layer generated by the longer flow path experienced by the high tangential flow in the wider axial annulus.

Referring now to a blade height below 70% span, the trend of work distribution is mainly related to the change in the sign of the tangential velocity component, consistent with the deviation distribution map previously shown in Fig. 7. The higher efficiency for the maximum gap between 20% and 50% of the span is also consistent with the reduction of loss in the hub region from $x/b_s=0.35$ to $x/b_s=0.60$ and inside of the blade row.

The axial Mach number distribution reported in Fig. 5, evidences a low contribution to the overall work production of the tip zone if compared to the hub one (~50%), partly counterbalanced by the growth in peripheral speed. As a consequence the overall mass averaged efficiency results to be 0.79 for the case of maximum gap and 0.83 for the case of minimum (nominal) gap. This difference is also confirmed by the torque-meter measurement data.

Conclusions

For the goals of a large experimental research program addressed to the analysis of unsteady interaction in a HP axial flow turbine stage, the unsteady measurements reported in Part II [14] can be proficiently understood only starting from a detailed characterization of the flow field upstream of the rotor row. For this purpose, the stator-rotor axial gap has been increased up to 100% of the vane chord, in order to allow the detailed measurement of the 3D flow field, starting from a station close to the stator trailing edge and following its mixing process further downstream. Measurements evidenced the presence of a more intense secondary activity on the hub side of the channel; in particular, traces of the hub shed vortex persisted up the $x/b_s=0.6$.

Steady measurements have also been performed downstream of the stage for two different axial gaps corresponding to the values of 35% (nominal) and 100% of the vane axial chord.

For the nominal gap, results show the persistence of some of the secondary features previously detected downstream of the vane row; in particular, the radial velocity field downstream of the stage allows one to evidence the traces of the vane hub shed vortex. For the case of maximum gap, all traces of stator vortex structures vanish downstream of the rotor.

Some conclusions can be drawn also by the analysis of the overall stage performance, evaluated on the basis of the flow-field measurements for both axial gaps. For the considered case, results showed a higher efficiency level for the nominal gap.

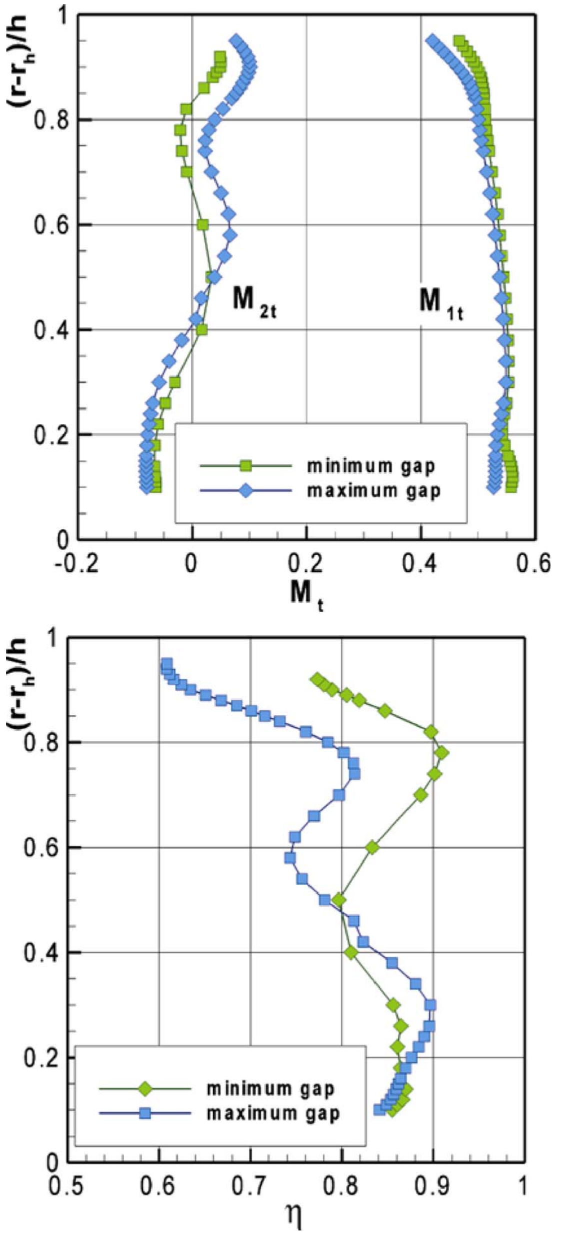

Fig. 8 Pitchwise mass-averaged radial distribution of tangential Mach number upstream and downstream of the rotor and efficiency for both axial gaps

Nomenclature

$C_{pt,R}$ = $(P_{t,R}-P_{\mathrm{ref}})/(P_{t,0}-P_{\mathrm{ref}})$: relative total pressure coefficient
Ma = Mach number
P = pressure
S = pitch
Y = $(P_{t,0}-P_t)/(P_{t,0}-P)$: total pressure loss coefficient
b = axial chord
h = blade/vane height
i = incidence
r = radial coordinate
ref = reference=atmospheric
x = axial direction

Greek

Ω = vorticity
α = absolute flow angle on blade-to-blade plane (from axial)
δ = deviation
θ = pitchwise angular coordinate
$\Delta\theta$ = angular pitch
η = adiabatic stage efficiency (total/static)

Subscripts

R = relative
h = hub
r = rotor, radial
s = stator, streamwise
t = total, tangential
0 = stage upstream
1,2 = rotor upstream/downstream

Overbar

$\bar{\ }$ = pitchwise mass averaged

Acknowledgment

Authors wish to thank the MIUR (Ministero dell'Istruzione, Università e Ricerca) for the support given to the research program "Experimental analysis of the main effects related to the aerodynamic rotor-stator interaction in a high pressure axial flow turbine stage." A particular thank you to A. Spinelli and A. Mora for their valuable contribution.

References

[1] Sharma, O. P., Pickett, G. F., and Ni, R. H., 1992, "Assessment of Unsteady Flows in Turbines," ASME J. Turbomach. **114**, pp. 79–90.
[2] Howell, R., Ramesh, O., Hodson, H., Shulte, V., and Harvey, N., 2001, "High Lift and Aft Loaded Profiles for Low Pressure Turbines," ASME J. Turbomach., **124**, pp. 385–392.
[3] Denos, R., Arts, T., Paniagua, G., Michelassi, V., and Martelli, F., 2001, "Investigation on the Unsteady Rotor Aerodynamics in a Transonic Turbine Stage," ASME J. Turbomach., **124**, pp. 81–89.
[4] Pullan, G., 2006, "Secondary Flows and Loss Caused by Blade Row Interaction in a Turbine Stage," ASME J. Turbomach., **128**, pp. 484–491.
[5] Chaluvadi, V. S. P., Kalfas, A. I., Benieghbal, M. R., Hodson, H. P., and Denton, J. D., 2001, "Blade-Row Interaction in a High-Pressure Turbine," J. Propul. Power, Vol. **17**, pp. 892–901.
[6] Schlienger, J., Kalfas, A. I., and Abhari, R. S., 2005, "Vortex-Wake-Blade Interaction in a Shrouded Axial Turbine," ASME J. Turbomach., **127**, pp. 699–707.
[7] Perdichizzi, A., and Dossena, V., 1993, "Incidence Angle and Pitch-Chord Effects on Secondary Flows of a Turbine Cascade," ASME J. Turbomach., **115**, pp. 383–391.
[8] Sharma, O. P., Butler, T. L., Joslyn, H. D., and Dring, R. P., 1985, "Three-Dimensional Unsteady Flow in an Axial Flow Turbine," J. Propul. Power, **1**, pp. 29–38.
[9] Zaccaria, M. A., and Lakshminarayana, B., 1995, "Investigation of Three-Dimensional Flow Field at the Exit of a Turbine Nozzle," J. Propul. Power, **11**, pp. 55–63.
[10] Sieverding, C. H., Van Hove, W., and Boletis, E., 1984, "Experimental Study of the Three-Dimensional Flow Field in an Annular Nozzle Guidevane," ASME J. Eng. Gas Turbines Power, **106**, pp. 437–444.
[11] Denton, J. D., and Xu, L., 1999, "The Exploitation of Three Dimensional Flow in Turbomachinery Design," Proc. Inst. Mech. Eng., Part C: J. Mech. Eng. Sci., **213**, pp. 125–137.
[12] Dring, R. P., Joslyn, H. D., Hardin, L. W., and Wagner, J. H., 1982, "Turbine Rotor-Stator Interaction," ASME J. Eng. Power, **104**, pp. 729–742.
[13] Venable, B. L., Delaney, R. A., Busby, J. A., Davis, R. L., Dorney, D. J., Dunn, M. G., Haldemann, C. W., and Abhari, R. S., 1999, "Influence of Vane-Blade Spacing on Transonic Turbine Stage Aerodynamics—Part I: Time-Averaged Data and Analysis," ASME J. Turbomach., **121**, pp. 663–672.
[14] Gaetani, P., Persico, G., Dossena, V., and Osnaghi, C., 2007, "Investigation of the Flow Field in a High-Pressure Turbine Stage for Two Stator-Rotor Axial Gaps—Part II: Unsteady Flow Field," ASME J. Turbomach., **129**(3), pp. 580–590.
[15] Persico, G., 2006, "Unsteady Aerodynamic Stator-Rotor Interaction in High Pressure Turbines," Ph.D. thesis, Politecnico di Milano.
[16] Gregory-Smith, D. G., Graves, C. P., and Walsh, J. A., 1987, "Growth of Secondary Losses and Vorticity in an Axial Turbine Cascade," ASME Paper No. 87-GT-114.
[17] Dossena, V., D'Ippolito, G., Persico, G., Mora, A., and Tesini, P., 2004, "On The Effects of Leaning and Bowing Techniques on Turbine Cascades Flow Field: Experimental and Numerical Analysis," *Transactions of 59th ATI Congress, Genova*, SGE, Padova, pp. 1303–1314.

Investigation of the Flow Field in a High-Pressure Turbine Stage for Two Stator-Rotor Axial Gaps—Part II: Unsteady Flow Field

P. Gaetani
e-mail: paolo.gaetani@polimi.it

G. Persico

V. Dossena

C. Osnaghi

Dipartimento di Energetica,
Politecnico di Milano,
Via la Masa 34,
I-20158, Italy

An extensive experimental analysis was carried out at Politecnico di Milano on the subject of unsteady flow in high pressure (HP) turbine stages. In this paper, the unsteady flow measured downstream of a modern HP turbine stage is discussed. Traverses in two planes downstream of the rotor are considered, and, in one of them, the effects of two very different axial gaps are investigated: the maximum axial gap, equal to one stator axial chord, is chosen to "switch off" the rotor inlet unsteadiness, while the nominal gap, equal to 1/3 of the stator axial chord, is representative of actual engines. The experiments were performed by means of a fast-response pressure probe, allowing for two-dimensional phase-resolved flow measurements in a bandwidth of 80 kHz. *The main properties of the probe and the data processing are described. The core of the paper is the analysis of the unsteady rotor aerodynamics; for this purpose, instantaneous snapshots of the rotor flow in the relative frame are used. The rotor mean flow and its interaction with the stator wakes and vortices are also described. In the outer part of the channel, only the rotor cascade effects can be observed, with a dominant role played by the tip leakage flow and by the rotor tip passage vortex. In the hub region, where the secondary flows downstream of the stator are stronger, the persistence of stator vortices is slightly visible in the maximum stator-rotor axial gap configuration, whereas in the minimum stator-rotor axial gap configuration their interaction with the rotor vortices dominates the flow field. A good agreement with the wakes and vortices transport models has been achieved. A discussion of the interaction process is reported giving particular emphasis to the effects of the different cascade axial gaps. Some final considerations on the effects of the different axial gap over the stage performances are reported.*

[DOI: 10.1115/1.2472393]

Introduction

The analysis of the unsteady features of the flow field is one of the leading research topics of turbine aerodynamics. The flow downstream of a turbine blade row is not uniform in space due to potential effects, wakes, secondary flows, and, in transonic stages, trailing-edge shock waves. Because of the relative motion between axially adjacent cascades, the interaction of these flow structures with the downstream blade row is intrinsically unsteady, leading to a complex unsteady three-dimensional flow downstream of a turbine stage.

In subsonic turbine stages, the main aspects of the two-dimensional stator-rotor interaction are related to wake and cascade potential field. In the relative frame, the stator wake velocity defect results in a slip velocity component directed toward the suction side of the rotor blade. The stator wake migration in the rotor suction-side boundary layer and eventually in the rotor wake induces a redistribution of total quantities [1]. The bowing, the shearing and the chopping of the stator wake during its transport inside the rotor channel has been observed by means of LDV measurements at midspan [2]. In highly loaded rotor cascades, the wake fluid recirculation on the blade suction surface induces pressure fluctuations, convected downstream at the freestream velocity [3].

In low aspect ratio turbine stages, the unsteadiness induced by secondary flows plays a relevant role in the rotor aerothermal behavior and in the flow field downstream of the stage. Some early studies [4] and more recent analyses [5] showed that upstream secondary vortices are convected on the rotor blades suction side and tend to migrate toward midspan, modifying the underturning and the overturning of the flow. Despite the number of theoretical models and results achieved in the last two decades, a large number of parametric analyses supported by time-resolved measurements and unsteady numerical simulations are still necessary to set up design methodologies for unsteady flow.

Despite the stator-rotor gap being one of the most influencing parameters in the unsteady turbomachinery performances, only few investigations have been published on this topic for turbines [6,7], and no coherent up-to-date information is available on the gap effect on the efficiency (up to 2% is suggested in [6], $<0.5\%$ is documented in [7] for two-dimensional analysis). Moreover, all these investigations were mainly related to blade surface measurements. For low aspect-ratio turbines, three-dimensional (3D) effects are expected to dominate; according to [8], the variation of axial gap has contrasting effects on wakes and secondary flows and a clear trend in the performances cannot be derived. The aim of the present research program is to assess the role played by stator-rotor interaction on the flow field in a low aspect ratio,

---

Contributed by the International Gas Turbine Institute of ASME for publication in the JOURNAL OF TURBOMACHINERY. Manuscript received July 13, 2006; final manuscript received July 23, 2006. Review conducted by David Wisler. Paper presented at the ASME Turbo Expo 2006: Land, Sea and Air (GT2006), Barcelona, Spain, May 8–11, 2006. Paper No. GT2006-90556.

modern HP turbine stage in single-stage configuration. For this reason, the stator-rotor gap has been modified and the effect of two very different axial gaps has been studied in terms of both time-averaged performances and unsteady flow field. With respect to the previous research available in literature, this paper also provides details on the effects of the stator-rotor gap on the flow field downstream of the rotor.

In the Part I of the paper [9], the time-averaged flow field downstream of the stator and the rotor has been described; in Part II, the unsteady component of the flow field downstream of the turbine rotor is characterized and discussed. At first, the methodology of investigation is described in terms of measurement technique and display schemes. Two traverses downstream of the rotor are considered, TR1 $(x/b_R=0.2)$ and TR2 $(x/b_R=0.43)$, and at TR2 the effects of two axial gaps, nominal $(x/b_S=0.35)$ and maximum $(x/b_S=1)$, are investigated. The very high, unusual value of the maximum gap was chosen in such a way to "switch off" the stator flow features at the rotor inlet. The main features of the stator-rotor interaction are observed and described on the basis of different display schemes. The mixing of the rotor structures and the role of the stator structures downstream of the stage are then discussed in terms of flow features and stage performances.

Unsteady Measurement Technique

Most of the first experimental investigations on unsteady turbine rotor flows were based on the measurements of flow velocity. In the 1990s, significant development was made in design and application of fast-response aerodynamic pressure probes [10–14].

Fast-Response Probe Aerodynamics. At Politecnico di Milano, a cylindrical fast-response aerodynamic pressure probe was developed in the last five years, for application downstream of turbine stages. To limit the probe blockage, the external dimensions were minimized by the use of a single sensor encapsulated inside the probe head. To ensure high reliability, strength, and low costs, a commercial transducer (Kulite XCQ-062) is used; a resulting head diameter of 1.85 mm was obtained.

Since only a single tap (0.3 mm dia) connects the flow environment to the sensor, the two-dimensional (2D) phase-resolved flow can be measured by a pseudo-three-hole operational mode. Total and static pressure, Mach number and flow angle in the blade-to-blade plane are then achieved. The angular range of calibration of the probe, equal to ± 22.5 deg for a defined class of three pressure values (central-maximum pressure, left- and right-side pressure), can be extended by simply rotating the probe of 45 deg steps, making the measurement free from the probe angular calibration range. The aerodynamic calibration was performed on a calibrated nozzle for Mach numbers ranging from 0.15 to 0.6 [15]. The expanded uncertainty of the pressure measurements is $\pm 0.5\%$ of the kinetic head and the one of the yaw angle is ± 0.5 deg.

Probe Dynamic Properties. Since a cylindrical transducer has been allocated inside the probe, a nonstandard configuration of the line-cavity system, connecting the sensor to the pressure tap, has to be adopted. Therefore, detailed numerical techniques were used to define the probe internal geometry, with the aim to enhance the frequency response up to 50 kHz [15]. The dynamic behavior of the probe was verified on a low-pressure shock tube developed at Politecnico di Milano for the dynamic calibration of fast-response probes [16]. The probe showed a step response typical of an underdamped II-order system with a resonance region at 45 kHz. The damping was found to be low enough to extend the operational frequency range up to 80 kHz by means of a proper transfer function.

Once the probe has been installed in the test rig, a dynamic analysis of the unsteady pressure signal acquired by the probe downstream of the turbine rotor at standard operational conditions has been performed [17]. Almost the whole signal harmonic energy is included at the blade-passing frequency ($\sim$2.8 kHz) and its first harmonic. At higher frequencies, a small amplification was found at the line-cavity system resonance frequency. The digital compensation of the pressure signal allows one to correct the amplification in this frequency range, but the effects on the phase-resolved signal in time domain are negligible; anyway, all the data are digitally compensated during the data reduction procedure.

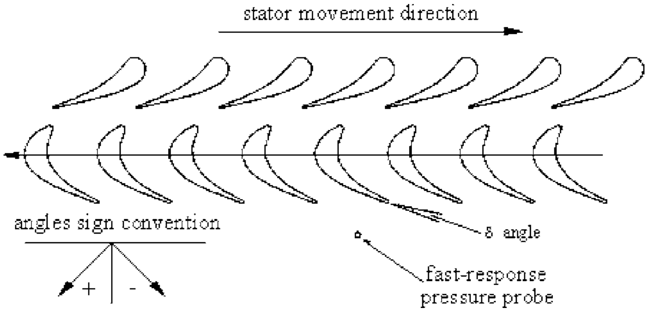

Fig. 1 Measurement scheme (fast-response probe sketched at TR2)

Data Reduction Method and Display Schemes. The instantaneous pressure signals are acquired at 1 MHz for a period of 1 s. The raw pressure data are phase locked to the rotor wheel and then phase averaged to obtain 40 intervals on a single rotor-blade-passing period (BPP); the physical sample rate results at $\sim$100 kHz, according to the probe frequency response. As final step the flow properties are derived by the combination of the different phase averaged pressures.

The unsteady flow quantities, measured in the absolute frame, are extended to the relative frame to enhance the comprehension of the rotor flow structures. To derive relative quantities, the knowledge of the unsteady temperature should be required; since at the Politecnico di Milano no unsteady temperature measuring technique is available at the moment, the time-averaged total temperature was used. Assuming a realistic static temperature fluctuation of 10% of the total temperature drop across the stage, variations of ± 0.002 for $C_{pt,R}$ ± 0.0015 for the relative Mach number and ± 0.1 deg for δ are obtained with respect to the values derived from time-averaged total temperature; these values are of the same order or below the measurement uncertainties.

The results are displayed as snapshots of the rotor passage flow field in the relative frame at different phases with respect to the stator. Since the probe axis is at a fixed position with respect to the key phasor (the stator is rotated with respect to the probe axis to simulate an angular traversing system (see Fig. 1), the reconstructed rotor period starts at the same rotor position for all the relative stator-rotor phases. The stator was rotated in 12 positions to cover one stator pitch.

Because of the vane-blade count $(N_S=22, N_R=25)$, a phase lag exists between consecutive rotor blade passages, defined as $(N_S-N_R)/N_R$, according to [18]; in the present case, the phase lag is 0.12 of the stator BPP. The time averaging of the different channels originates a single rotor channel that allows one to highlight the rotor-related flow structures, even if a mean trace of the stator flow interaction might appear. Then the periodic rms between the instantaneous rotor channels and the mean one is calculated. If the stator flow structures are mixed out, zero rms should be expected in the flow field downstream of the rotor; therefore, the regions of high rms can be considered as markers of the stator flow-field traces downstream of the stage. While in the instantaneous plots the adjacent channels are derived taking into account the phase-lag periodicity, the mean and rms plots are duplicated to aid the comprehension without any phase-lag because the time dependence (stator phase, in the rotor frame) has been suppressed by the averaging technique itself.

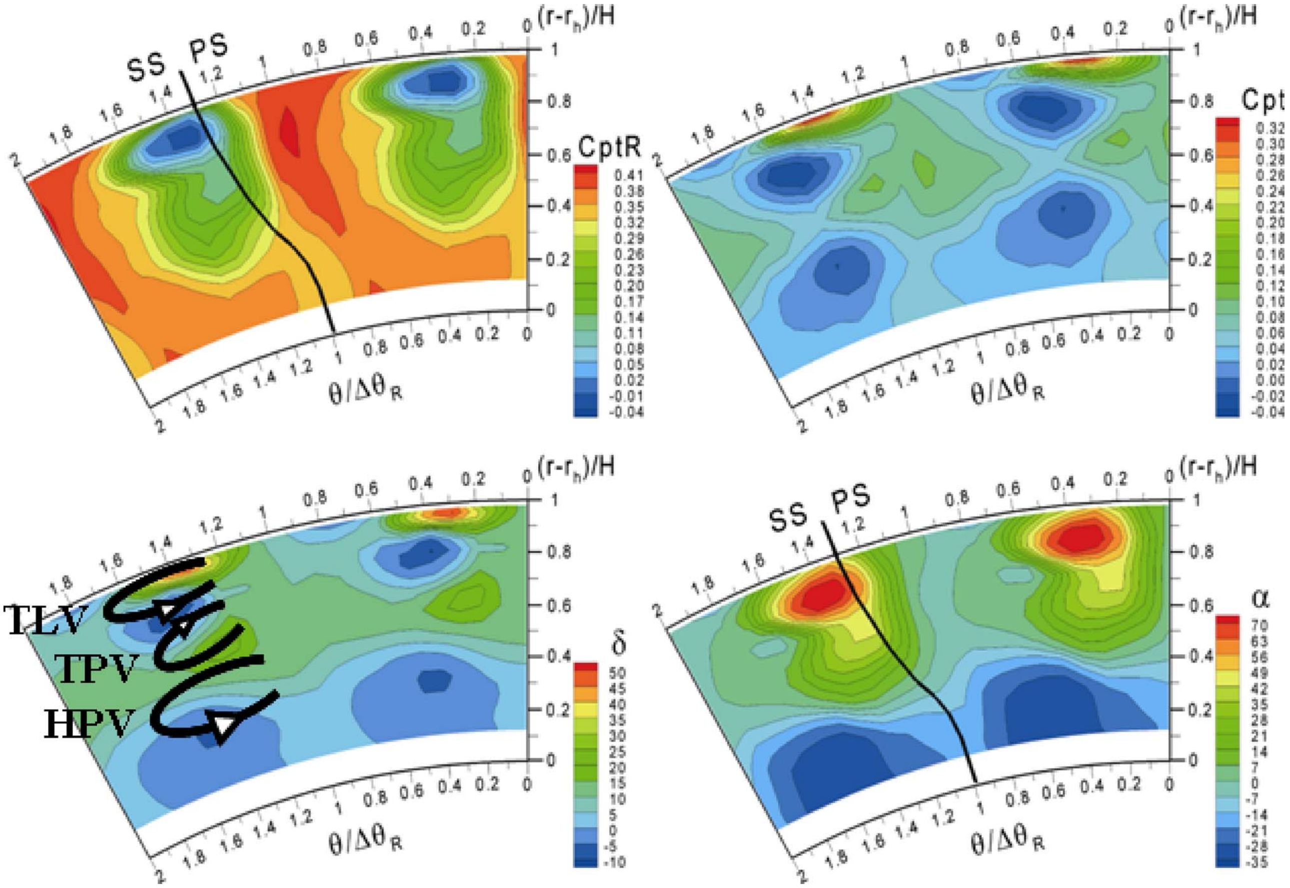

Fig. 2 Mean rotor channel at TR1, maximum stator-rotor gap

Results

In the following, the experimental results downstream of the rotor will be described. In order to improve the comprehension, the analysis starts for the maximum gap configuration (where the effects of the stator are limited) and for the traverse nearest to the rotor trailing edge (x/b_R=0.2, TR1). Then the second traverse (x/b_R=0.43, TR2) for the maximum gap configuration will be discussed, and finally the nominal gap configuration at TR2 is reported.

Relative Flow Upstream of the Rotor

Since in the Part I [9] the steady flow downstream of the stator has been described in detail, only the main features of the rotor inlet flow will be briefly recalled here. At the nominal gap, the relative total pressure shows significant circumferential gradients where the wake and the secondary vortices at the hub are found; in the same area, the minimum of $C_{pt,R}$ occurs. The incidence angle shows a mean negative value at the hub and a positive one at the tip. At the hub, the streamwise vorticity evidences the presence of vortex structures, while at the tip only the effects of the stator tip leakage are visible.

At the maximum gap the $C_{pt,R}$ map shows significant circumferential gradients only in the hub region. The mean incidence angle evidences the same trend of the upstream traverse. The vortical structures are almost completely mixed out with the exception of the shed vortex at the hub. Moreover, the axial Mach number is higher at the hub.

Maximum Stator-Rotor Gap—TR1

Mean Rotor Flow. Figure 2 reports the mean rotor channel in terms of absolute and relative total pressure coefficients (C_{pt} and $C_{pt,R}$) and absolute (α) and rotor deviation (δ) angles. Since the blade discharge angle is constant (−67.7 deg), the δ angle is representative of the relative flow one.

Considering the $C_{pt,R}$ map, three significantly different zones can be identified in spanwise direction. In the tip region (above 80% span), a wide region of low relative momentum affects more than 60% of the pitch; in the center of this region the lowest values of $C_{pt,R}$ are observed. In the remaining part of the rotor pitch, a region of high relative momentum, namely, the freestream, is observed. In the range of 80–30% of the blade span, a similar feature of high/low momentum can be seen, characterized by significantly lower values of loss with respect to that observed at the tip. Below 30% span, an almost uniform distribution of relative total pressure is found, with lower momentum values in the freestream with respect to those at higher spanwise coordinates and with a small trace of losses, weakly moved in circumferential direction, extended for the 25% of the pitch. As general feature, a structure of freestream and loss exists all along the blade span, and a reduction of pitchwise gradients moving from tip to hub is observed. This latter feature is fairly common downstream of axial flow turbomachinery rotors [14,19]: the low relative momentum fluid is pulled toward the tip by the Coriolis force acting in the relative frame (also referred as rotation effect); beside this, the tip leakage provides a relevant contribution in generating higher losses in the outer part of the channel.

The analysis of the rotor deviation can help to discern the vortices from wake in the loss regions. As proposed in [20], an actual vortex can be seen as a combination of a forced vortex in the core contoured by a free vortex. In terms of the blade-to-blade angle, the vortex appears as a succession of straight contour steps in the core contoured by closed contour steps above and below the vortex core. In the δ frame shown in Fig. 2, a wide region according to this scheme is clearly visible in the tip region, with a core region at 90% span between 20% and 50% of the rotor pitch. The underturning (defined with respect to the geometrical angle) in the upper part and overturning in the lower one make this structure a counterclockwise vortex. The vortex core is centered in the minimum of relative total pressure and in the minimum of static pressure (not shown for sake of brevity), while in the upper part the maximum static pressure is detected; moreover, the vortex is characterized by a very high underturning (50 deg) and a limited overturning (10 deg). These features are consistent with the rotor TLV, developed by the rolling up of the tip leakage flow generated in the rotor tip clearance. Underturning higher than 40 deg can be predicted in the leakage vortex core applying the Lakshminarayana's "combined vortex model" to the present rotor cascade. This model, described in [21] and verified against experimental data in turbine cascades, provides also an estimation of the vortex core dimension of 25% of the span, in good agreement with the experimental results depicted in Fig. 2. All of these observations support the identification of this wide loss structure as the TLV.

Below the TLV, other similar structures can be identified. A clockwise rotating vortex has its core around 30% of the pitch and at 70% span, while a counterclockwise vortex is centred at 30% of the pitch and 45% span. These two counterrotating vortices can be identified as the rotor tip and hub passage vortices (TPV and HPV in the following). The high flow turning, the very low aspect ratio of the rotor blades, the effect of the wide tip leakage vortex that pulls the passage vortex toward midspan and the migration of the rotor hub passage vortex toward midspan, also enhanced by the rotation effect, reduce the distance between the two secondary structures that almost interact at midspan.

A more complete description of the rotor relative flow can now be given. The loss region in the $C_{pt,R}$ map can be identified only partially as the rotor wake, which has been sketched as a black trace in the $C_{pt,R}$ frame reported in Fig. 2. At the tip the loss region located near the suction side of the wake is addressed to the tip leakage vortex; the losses between 80% and 30% of the blade span are related to the rotor secondary flows. In the hub region, no clear vortex features can be seen and only the effect of the wake remains.

In the flow regions not affected by vortex structures, the deviation angle remains almost constant in pitchwise direction and it reaches its maximum (~12 deg) between 50% and 60% of the blade span. At the hub, the deviation reduces and slightly negative values are detected.

The information deduced from the relative quantities distribution can now be used to enhance the comprehension of the absolute ones. The α angle, like the $C_{pt,R}$, presents three distinct zones. Near the tip, the highest angle values (up to 80 deg) are related to the low relative momentum region: in the leakage vortex, the relative velocity is very low, resulting in a highly tangential flow in the absolute frame. The same concepts can be applied to explain the high α angle values in the lossy regions all along the blade height. An almost axial discharge flow is detected above midspan in the freestream region. In the hub region, the slightly negative rotor deviation induces high distortion of the flow in opposite direction with respect to the peripheral speed. The result is a very tangential absolute flow in the freestream, meaning that the fluid has to cover a larger streamwise distance to reach the measuring plane: this contributes to explain why a more mixed-out rotor wake is detected at the hub with respect to the other flow regions.

The total pressure map appears in such a way similar to the δ angle one. At the tip (above 90% span) a high absolute momentum fluid is observed between 30% and 40% of the pitch, where the leakage flow in the tip clearance is encountered, as expected. In the remaining part of the map the C_{pt} shows small gradients, but two distinct regions of low C_{pt} are found at 50% of the rotor pitch and at 80% and 40% of the span. It appears that these regions are related to the vortex structures above described; in particular low C_{pt} regions correspond to the zones of maximum α angle gradients in the absolute frame, where relevant loss mechanisms are acting in the absolute frame, and to zones of low axial Mach number. The last feature (not shown for sake of brevity) is connected to the negative δ angle regions, where very low axial Mach number with respect to the freestream is detected; these regions have just been identified as the overturning legs of the rotor vortices. A similar conclusion can be drawn for the high total pressure regions, related to high absolute Mach number and corresponding to the vortex underturning leg.

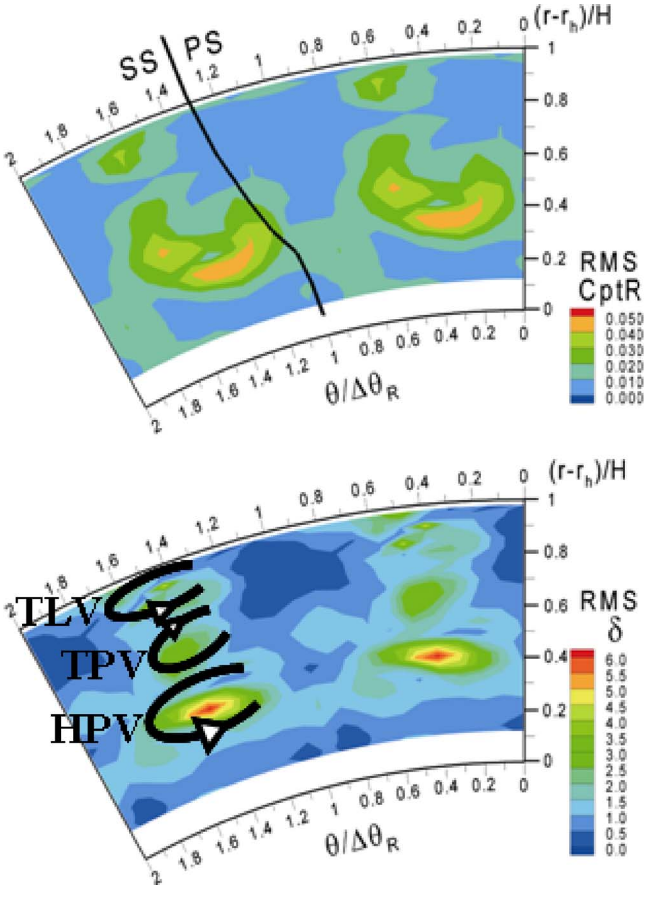

Fig. 3 $C_{pt,R}$ **and** δ **rms at TR1, maximum gap**

Rms. Figure 3 reports the rms of the $C_{pt,R}$ and δ angle. According to the wake transport theoretical models, the low relative total pressure fluid entering the rotor is moved toward the rotor blade suction side by the rotor potential field. During their migration, the low-momentum structures are bowed, stretched and chopped by the rotor blades; similar phenomena are expected in the transport of stator secondary vortices.

Both the rms maps show large regions of almost zero fluctuations. The rms of $C_{pt,R}$ suggests that the regions of higher interactions with upstream stator flow are effectively concentrated on the suction side of the rotor wake/vortex loss regions, all along the blade span. However the region of highest rms is encountered at 40% span, in the boundary between the low momentum fluid near the rotor wake suction side and the freestream below. The rms of δ presents high values near the two vortex cores TPV and HPV. The TLV, even if it is the strongest one, shows very low levels of fluctuations (2–3 deg, to be compared to 50 deg of underturning). The highest rms of δ are detected in the core of the HPV, as already shown in $C_{pt,R}$ frame. This region, characterized by strong

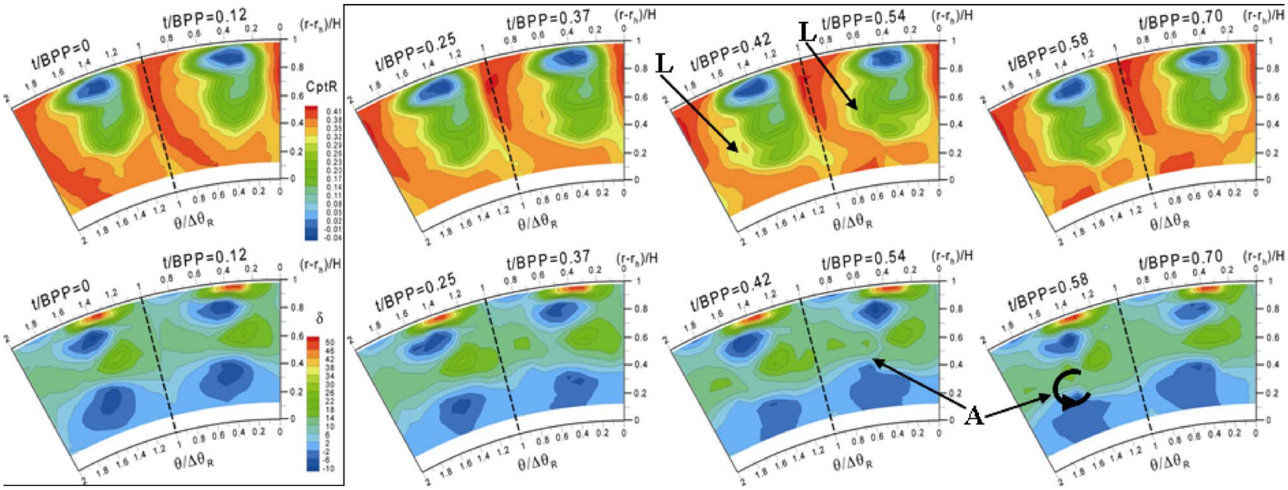

Fig. 4 Instantaneous rotor flow at TR1, maximum stator-rotor gap (phase-lag periodicity applied)

gradients of all the quantities, appears to be the most influenced by the stator exit flow field and will be discussed in detail in the following.

Instantaneous Rotor Flow. Figure 4 reports eight snapshots of the rotor channel in terms of $C_{pt,R}$ and δ, every map containing two consecutive instants.

In the range of $t/\text{BPP}=0$–0.12, different features with respect to the mean rotor flow field are hardly detectable. Later on, at $t/\text{BPP}=0.25$, an interesting effect starts to develop: the low relative total pressure region appears to be more elongated toward the hub and reaches 30% span; in the same instant, a slight spreading (accompanied by an intensity reduction) of the HPV structure centered at 45% span is also observed. It should be recalled that in this region the maximum rms has been found. At $t/\text{BPP}=0.37$, the spreading of the hub vortex continues together with the loss region on the suction side of the wake. At $t/\text{BPP}=0.42$, the intensity of the HPV reaches its minimum, and a low-momentum region (L in Fig. 4) appears near (but being still distinct) the suction side of the loss region at midspan. At later times ($t/\text{BPP}=0.54$), this stator loss flow (L) is merged with the rotor loss structures, and a significant reduction of the freestream region is found. In terms of velocity angle, a small core of high δ is developing near the original one (A in Fig. 4). This process continues and a clear second region of underturning (A in Fig. 4) can be seen at $t/\text{BPP}=0.58$ in the midpart of the channel at 60% span. Then the two regions tend to coalesce and a single underturning zone is visible at $t/\text{BPP}=0.70$. Given its periodic nature, the underturning visible at $t/\text{BPP}=0.58$ seems to be the trace of an inlet vortex. Only negligible effects are detected in the final part of the period: the low-momentum region on the suction side of the rotor wake tends to be mixed out with the rotor wake, and a small trace of this process can be seen at the beginning of the period.

Discussion of the Unsteady Flow. The shape of the rotor mean flow appears similar to what expected in an annular steady-state cascade with tip clearance: three vortices are acknowledged, TLV, TPV, and HPV, like in the results reported in [4] for a HP turbine rotor with very low inlet stator-related gradients. This similarity is due to the very high, unusual axial spacing between the stator and rotor cascade in the present configuration. Despite this fact, following the evolution of the instantaneous rotor flow, only in the first and last parts of the period the effects of the stator flow patterns are completely absent; whereas in the central part of the period some traces of the unsteady inlet gradients affects the wake and the HPV structure. The enlargement of the rotor wake can be explained as the result of the stator wake (region L) transport in the rotor channel by the rotor potential field (wake-blade interaction). The high unsteadiness of the HPV, with respect to the other ones, is a common feature in unsteady turbine studies, as reported in [4,13]. Considering the results downstream of the stator cascade, reported in Part I [9], the tip structures tend to be spread and appears almost mixed out in the last measurement plane ($x/b_s=0.6$). Conversely, in the hub region, the stator structures appear more concentrated and characterised by steeper gradients at the rotor inlet. This explains why the vortex-blade interaction is stronger in the hub region. This interaction mechanism seems to reduce the HPV intensity up to $t/\text{BPP}=0.42$, while a new distinct vortex region (A in Fig. 4), with the same sense of rotation of HPV, appears at $t/\text{BPP}=0.54$ and reaches its maximum at $t/\text{BPP}=0.58$. This new vortex rapidly coalesces and strengthens the HPV vortex. A possible explanation of this behavior can be traced by applying the vortex transport model proposed in [5] to the vorticity field measured in the farthest traverse downstream of the stator: only one region of high vorticity seems to remain at the rotor hub inlet, with the same sign of vorticity of the HPV, previously identified as the SHSV in Part I [9]. A simple flow schematics of a vortex transport inside the rotor channel is sketched in Fig. 5, representing the flow field evolution derived from a 2D numerical simulation of the stator-rotor interaction for the actual turbine. The basic concept is that the incoming vortex tube (the SHSV in the present case) behaves like an incoming low-momentum region (i.e., the stator wake), and it is bowed, stretched, and eventually chopped by the rotor leading edge. Hereafter, it tends to migrate towards the blade suction side, driven by the cross-passage static pressure gradient, and degenerates in two counterrotating legs (black line in Fig. 5). The SS leg keeps the same sense of rotation of the incoming vortex, while the PS leg appears with an opposite one. While the SS leg is progressively pulled toward the blade, the PS leg is significantly stretched inside

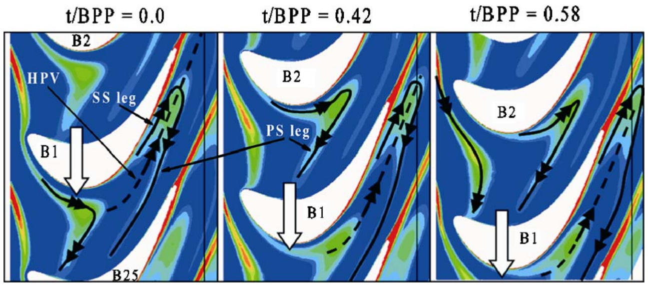

Fig. 5 Simple kinematic model of the wake/vortex transport in a turbine rotor

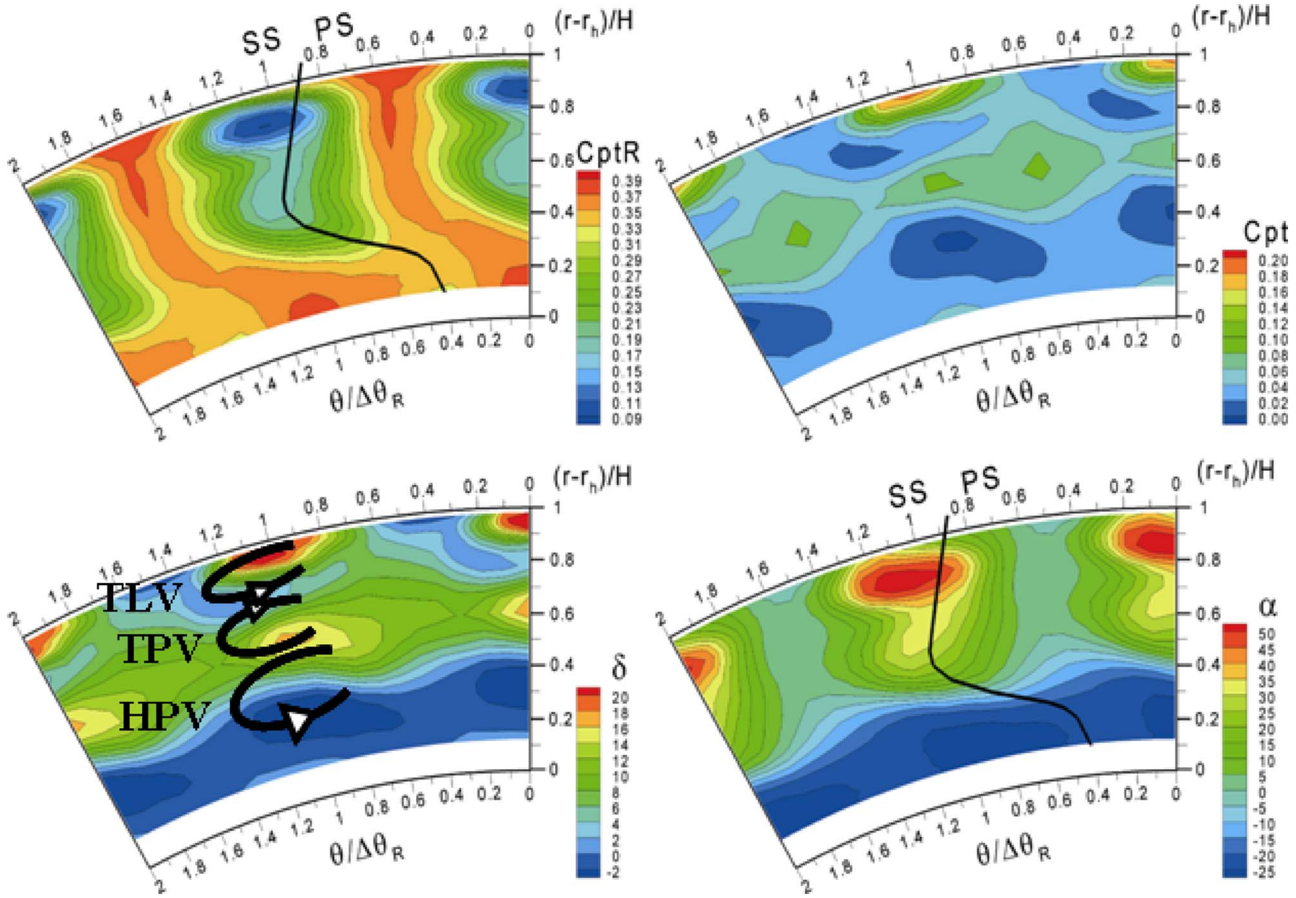

Fig. 6 Mean rotor channel at TR2, maximum stator-rotor gap

the channel. As suggested in [5], this stretching should accelerate the dissipation of this part of the vortex. These vortices interact with the rotor HPV developing inside the channel, sketched as a dashed black line in Fig. 5. An observer in TR1 sees at $t/\mathrm{BPP}=0$ only the effect of the rotor. At $t/\mathrm{BPP}=0.42$, the most advanced part of the low-momentum fluid reaches the measuring plane and the PS leg could appear: the interaction of the HPV with the counterrotating PS leg reduces the intensity of the former. At $t/\mathrm{BPP}=0.58$, when it interacts with the wake, also the SS leg reaches the measuring plane, enforcing the HPV, and appears eventually mixed out. At this time the trace of the PS leg cannot be seen in the measurements probably because of the dissipation. This interaction mechanism is in good agreement with the experimental flow field evolution reported in Fig. 4.

It should be noted that in [22,23] different vortex-blade interaction effects are reported: downstream of turbine rotors a distinct PS leg and an almost mixed out SS leg were observed. The conclusion of these papers was that the result of the interaction is case-sensitive, basically depending on the relative strength of the stator and rotor vortices. Nevertheless, the position of the vortex A (near the rotor SS) and its sense of rotation, the same of the incoming vortex, support the suggested interpretation of the vortex-blade interaction in the present configuration.

Maximum Stator-Rotor Gap—TR2

Mean Rotor Flow. Figure 6 presents the mean rotor flow at TR2. Most of the features observed in TR1 are still present, even if a general reduction of gradients is found. With respect to TR1 measurements, the loss region appears significantly distorted due to the spanwise gradients of δ angle. The wide loss region on the suction side of the rotor wake is visible, but 40% of the rotor pitch displaced in negative circumferential direction with respect to the one observed at TR1, due to the highly negative blade-to-blade relative angle. The shape of the rotor wake is sketched on the $C_{pt,R}$ frame in Fig. 6. Only a small trace of these distortion effects has been seen at TR1, due to the very low streamwise distance covered by the fluid particles to reach the measurement plane.

The loss core related to the tip leakage vortex is significantly spread and values of $C_{pt,R}=0.1$ are found, to be compared to the negative ones detected at TR1. The reduction of vortex magnitude is confirmed by the δ angle gradients reduction in the region above 80% span (variations of 20 deg with respect to 60 deg). As a consequence, the C_{pt} gradient in the tip leakage vortex region is reduced, and the α angle reaches a maximum of 55 deg versus 80 deg at TR1.

Below 80% span, the distribution of δ is similar to that observed at TR1: in the central part of the channel (10–70% of the rotor pitch), a significant underturning is found at and over midspan, while a slight overturning is seen below midspan. Superimposed on this spanwise pattern a region of higher underturning at 60% span and a region of higher overturning at 30% span can be seen at 100% of the pitch. Considering the overturning region at 80% span, two zones of almost straight parallel isoclines can be recognized and two counterrotating vortices can be identified. It is interesting to note that these features, qualitatively identical to the one seen at TR1, are also quantitatively almost unaffected by the mixing process downstream the rotor: 17 deg is the maximum overturning and −4 deg the maximum underturning, to be compared to the corresponding values of 20 deg and −6 deg. A slight difference in the center of the HPV core, now located at midspan, is found, probably due to a further rotation effect as the flow develops in streamwise direction.

The absolute total pressure distribution results similar to that observed at TR1; therefore, the same discussion about the angular

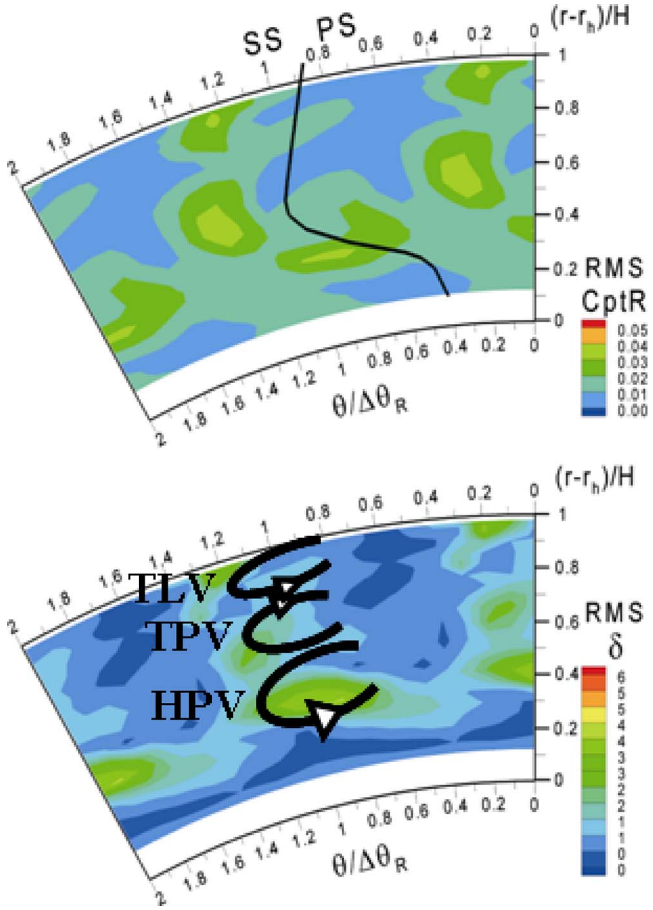

Fig. 7 $C_{pt,R}$ **and** δ **rms at TR2, maximum gap**

gradients and the axial Mach number can be done. Moreover, the C_{pt} dependence on the work is particularly visible here. As presented in Part I [9] (Fig. 8), the work has its maximum at ~30% of the blade span resulting in a low instantaneous C_{pt} in the same region of Fig. 6.

Rms. The mixing out of the rotor loss regions (wake and tip leakage vortex) is expected to affect also the residual traces of the stator structures downstream of the stage. In Fig. 7, which reports the rms of the mean rotor channel at TR2 for $C_{pt,R}$ and δ, the stator-flow affected regions are visible. These regions, even if wider and more diffused, are the same discussed at TR1; quantitatively, a reduction of ~30% of the amplitude of the fluctuations is produced by the streamwise mixing. Given the significantly lower intensity of the fluctuations, and the same shape of the stator-affected regions with respect to TR1, the instantaneous flow at TR2 does not introduce new features and it is not reported.

Nominal Stator-Rotor Gap—TR2

In actual HP turbine stages, gaps of 1/3 or 1/2 stator axial chord are normally applied to reduce the axial extension of the turbomachine. Despite the very large gap of the case presented in the previous sections, some residual traces of the stator loss regions have been observed. The interaction between the stator and rotor flow pattern is therefore expected to play a dominant role in the nominal configuration, where the axial spacing is 0.35 of the stator chord.

Mean Rotor Flow. The main features of the relative flow (Fig. 8) do not really differ from the maximum gap ones: in the tip region (above 80% span), the wide relative loss region related to the TLV is observed, with the expected large gradient in terms of deviation angle. Below the TLV, the common feature of the freestream and wake/vortex loss region can be identified, even if some differences with respect to the previous case are encountered. The rotor freestream is characterized by higher momentum values with respect to the maximum gap case. The rotor wake (sketched in Fig. 8) appears less distorted as a consequence of the lower spanwise gradients of the rotor deviation angle (6–8 deg at the midspan and −2 deg near the hub) in the freestream. Moreover, the loss region appears significantly wider near midspan; this feature is probably the averaged effect of the interaction with the stator structures entering the rotor.

The tip and hub passage vortices can be identified at 65% span and 30% span, respectively, but they appear significantly spread with respect to the maximum gap configuration. Also this feature is believed to depend on the stator-rotor interaction.

Rms. Figure 9 shows the rotor flow rms maps. The periodic unsteadiness level is significantly higher than the one observed at the maximum gap, and relevant differences are encountered. The rms of $C_{pt,R}$ is very high at the suction side of the rotor wake near midspan. Moreover, the wide region of high rms always present below midspan is extended down to the hub end wall (maximum rms at 20% span, 80% of the rotor pitch). The rms of δ shows high unsteadiness between the high rms of $C_{pt,R}$ region and the wake and in the tip leakage vortex region. The rms maps suggest that the distinct effects of wake interaction are present at midspan, and the vortex interaction play a dominant role in the hub region. Also the TLV, even if almost unaffected in terms of momentum losses (as in the maximum gap configuration), results influenced by the incoming flow in terms of relative flow angles. This is probably due to the stator tip leakage flow that still affects the tip region at $x/b_s=0.35$.

Instantaneous Rotor Flow. A detailed description of the rotor unsteady flow evolution is now given by means of instantaneous snapshots (Fig. 10). Since the rotor wake is centered at the borderline between two channels, the flow in the central region will be described in order to improve the comprehension.

At $t/\mathrm{BPP}=0.89$, a rotor-only-dependent flow structure can be observed in the $C_{pt,R}$ map. In the tip region the TLV is similar to the time-mean one; below 80% of the span, an almost straight loss region is observed, with the usual pitchwise gradients reduction at the hub. Large freestream regions can be seen outside the loss region. The deviation angle shows, at 30% span along the wake, isoclines that can be identified as the rotor hub passage vortex (HPV). Referring to the same scheme proposed in the previous section, the rotor TLV and the rotor TPV can be acknowledged, the latter being almost evanescent.

In the next instant ($t/\mathrm{BPP}=0.98$), a clear increase of losses is detected at the hub, as a result of an enlargement of the wake suction side. The HPV intensity decreases, as shown by the lower underturning/overturning peaks in that region. The TLV and TPV seem to be unaffected by this process.

As this process continues ($t/\mathrm{BPP}=0.06$), the low-momentum fluid region enlarges in the rotor channel; two distinct loss zones can be acknowledged at 20% and 30% of the span. Moreover, all along the wake suction side, a region of low $C_{pt,R}$ is visible (marked as A in Fig. 10). The deviation angle shows a reduction in the HPV intensity and the growing of a counterclockwise rotating vortical structure located at 25% of the span (A). Some instants later ($t/\mathrm{BPP}=0.31$), the rotor losses in the hub region are reducing, while a strong loss core appears at midspan about at midpitch (marked as B in Fig. 10). This structure modifies the rotor wake between 30% and 70% of the span, and a corresponding significant reduction of the rotor freestream is induced. The rotor wake appears also slightly distorted in circumferential direction in the hub region. An underturning region, part of a counterclockwise rotating vortical structure centered just below region B and to that related, is observed (marked as C in Fig. 10). The region A is no more visible being mixed out with the rotor wake. The HPV

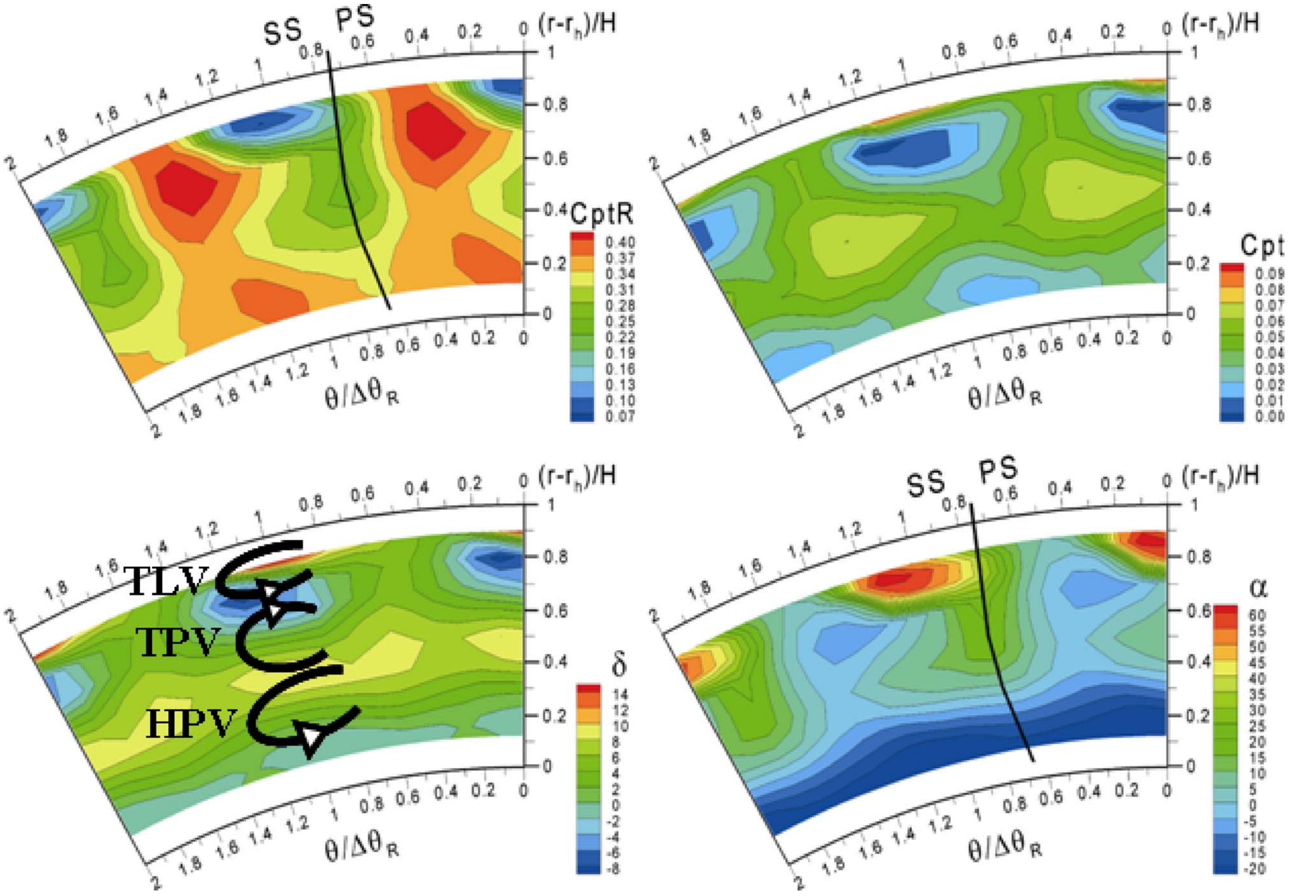

Fig. 8 Mean rotor channel at TR2, nominal stator-rotor gap

looses its intensity and almost disappears in the freestream region (high $C_{pt,R}$). It has to be noted that at this stator-rotor phase the tip leakage losses and the corresponding over-underturning have their minimum.

As time proceeds ($t/\mathrm{BPP}=0.48$), the rotor wake appears much more distorted at the hub and a corresponding very low-loss region can be seen up to 30% span. The loss core B and the vortical structure C migrate toward the wake.

At the last frame ($t/\mathrm{BPP}=0.64$), the trace of the rotor wake almost disappears below 30% span, and the loss core B is almost mixed out with the rotor wake. Region C still exists and moves toward the wake suction side.

Discussion of the Unsteady Flow. The instantaneous features described above show that relevant stator effects influence the rotor flow; most of the observed pulsating structures are in line with the incoming wake/vortex transport models. The relative flow upstream of the rotor (measured at $x/b_s=0.35$ downstream of the stator and presented in Part I [9]) is characterized by a distinct wake, with a higher-momentum defect below midspan. In terms of incoming vortices, at least three zones of high vorticity are present, identified as the stator hub passage vortex (SHPV), the stator hub shed vortex (SHSV), and the stator hub corner vortex (SHCV), the latter being at the measuring grid border. Moreover, the wake at midspan is characterized by low vorticity and low $C_{pt,R}$, but it is just above the SHSV. Since in the relative frame, the SHCV enters the rotor channel before the wake, it is expected to appear downstream of the rotor before the wake if the axial velocity is fairly constant. In the hub region, the distribution of the pitchwise-averaged axial Mach number, α, and the incidence angle support such a conclusion.

It should be remembered that, according to the transport model described in the previous section, the stator wake is bowed in the rotor channel and reaches the measuring plane at different circumferential positions, depending on the transport process and stator-rotor phase. When it reaches the measuring traverse, it is expected to appear slightly distant from the SS and, as time proceeds, it progressively moves toward the rotor wake with which it eventually interacts.

By applying similar considerations on the instantaneous map, some conclusions can be drawn. In particular, the loss core A at $t/\mathrm{BPP}=0.06$ can be identified as the SS leg of the SHCV. Its intensity is lower than the SHSV, but its vorticity has the same rotation direction of the SHSV and of the rotor HPV. As it approaches the rotor wake, it merges with the latter or with the rotor HPV. It has to be noted that some instants before this frame the rotor HPV intensity is lower probably due to the interaction in the rotor passage with the vortical structures belonging to the stator, according to the same vortex interaction scheme described for the maximum gap configuration.

The loss core B at $t/\mathrm{BPP}=0.31$, not directly associated to a vortical structure, can be identified as a trace of the stator wake and its evolution in the next instants is in very good agreement with the wake-blade interaction mechanism described above. In the authors' opinion, region C can be related to the SHSV, which at the rotor inlet was located just below the wake loss core and characterized by a significant vorticity. As the SHSV approaches the rotor wake, its interaction with the corotating rotor HPV increases, merging at an instant between $t/\mathrm{BPP}=0.48$ and $t/\mathrm{BPP}=0.64$. At this time, no significant vorticity is found at midspan except the one related to the SHSV-HPV. The frame at $t/\mathrm{BPP}=0.89$ is the one next to the $t/\mathrm{BPP}=0.64$. As already described,

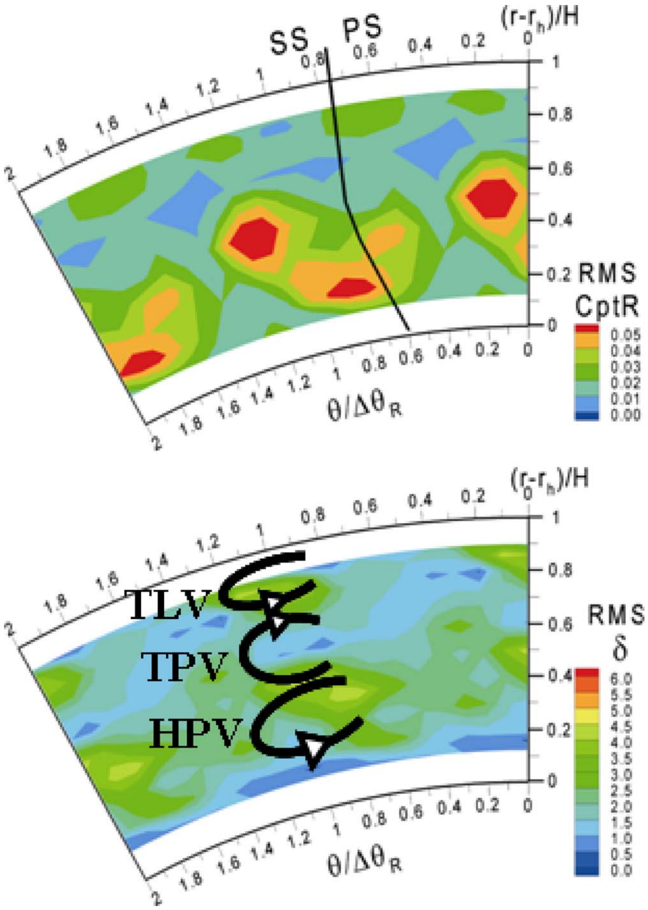

Fig. 9 $C_{pt,R}$ **and** δ **rms at TR2, nominal gap**

the only significant structure is the rotor HPV and a low-intensity underturning region in the freestream (at midspan and $\theta/\Delta\theta_R=1.2$) can be evidenced.

The rotor tip leakage vortex, slightly dependent on the stator-rotor phase, is supposed to be modified essentially by the loss core entering the rotor channel at the tip and depending on the stator tip leakage flow. Note that at the maximum gap, where no circumferential gradient is present at the rotor tip inlet, no significant difference is remarkable on the instantaneous snapshots.

Unsteady Flow Effect on the Stage Efficiency

As shown in Fig. 8 of Part I [9], the stage efficiency is strongly dependent on the blade rows spacing. In particular at the maximum gap, the spanwise distribution of the efficiency presents a significant reduction in the tip region, and a slight increase in the hub one with respect to the nominal gap. As discussed in that section, the efficiency loss at the tip is related both to the high stator losses, resulting in a low inlet tangential Mach number, and to a positive outlet tangential Mach number. Conversely at the hub, the efficiency increase depends on the different outlet tangential velocity, which is lower in the case of minimum gap.

By means of the unsteady measurements, more information can be deduced about the unsteady flow effects on stage efficiency. Focusing on the mean rotor flow at different gaps (Figs. 11(*a*) and 11(*b*)), it can be observed that in the tip region the tangential Mach number acts in such a way to increase the stage work for the nominal gap. Since no significant stator-rotor interaction is visible in that region, this effect is believed to be mainly related to different kinetic energy entering the rotor.

An opposite conclusion can be drawn in the hub region. To get a detailed understanding of the phenomena, the instantaneous tangential Mach number is reported for two significant instants corresponding to the minimum (Fig. 11(*c*), $t/\mathrm{BPP}=0.89$) and maximum trace of the stator flow downstream of the rotor (Fig. 11(*d*), $t/\mathrm{BPP}=0.31$) for the nominal gap. At $t/\mathrm{BPP}=0.89$, negative tangential Mach numbers are visible in wide regions of the rotor passage and in particular in the hub region and in the freestream elsewhere. At $t/\mathrm{BPP}=0.31$, the stator wake and the SHSV appear in the measuring section and are characterized by low $C_{pt,R}$ and an overturning/underturning region, already discussed (marked as region B in Fig. 10). These features result in a positive tangential Mach number (marked as B in Fig. 11), and hence, in a local and time-dependent reduction of the stage work. From a time-average point of view, this effect results in a lower stage work and efficiency.

Conclusion

The unsteady flow downstream of a modern HP turbine stage has been experimentally investigated by means of a single-hole fast-response aerodynamic probe. The stator-rotor interaction has also been studied in detail by varying the stator-rotor axial gap.

In the case of a very high axial gap ($x/b_S=1$), the flow field downstream of the rotor is mainly dominated by the rotor effects. Some regions of stator-related structures are still visible below midspan, where the rotor incoming flow is mainly characterized by a stator shed vortex corotating with the rotor hub passage vortex; the vortex-blade interaction induces periodic fluctuations of the intensity of the rotor HPV.

For the nominal axial gap ($x/b_S=0.35$), very strong pitchwise gradients affect the rotor incoming flow near the hub region and the interaction with the rotor-generated structures dominates the rotor exit flow field at and below midspan. A distinct wake-blade interaction mechanism is detected at midspan, and the mixing between the trace of the stator wake and the rotor one is clearly observed. In the hub region, as a consequence of the vortex-blade interaction, a very complex instantaneous flow field is observed. Only the stator structures corotating with the rotor hub passage vortex seem to persist downstream of the stage. The formation process of the rotor hub passage vortex is therefore dominated by the interaction with the incoming structures becoming highly unsteady.

As a general conclusion, the rotor hub region is the most affected by the stator flow. On the contrary, the rotor flow in the outer part of the channel (above 60% span) remains almost unaffected by the stator incoming flow, since the stator vortices and wake are almost mixed out for both gaps.

Despite relevant stator-rotor interaction phenomena affect more the stage flow in the nominal gap configuration, higher stage performances have been achieved as reported in the Part I [9]. The dependence of the stage performances on the stator-rotor axial gap is the result of a trade-off between the mixing losses downstream of the stator and the rotor performances under unsteady inlet boundary conditions. In the present stage, the result of this trade-off significantly modifies along the blade span as a result of the spanwise variation of the mixing rate upstream of the rotor (higher at the tip, lower at the hub), which is, in turn, a general result of the radial equilibrium. In the tip region, where the stator-rotor interaction is low because of the higher mixing out of the stator wake and the vortical structures within the gap, an increase of the axial gap induces higher losses downstream of the full stage. Conversely in the hub region, the stator-rotor interaction is relevant and in the nominal axial gap configuration it induces lower work and, hence, lower efficiency with respect to the maximum gap one. Since the hub region is the most exposed to the stator-rotor interaction, higher stage efficiency could probably be achieved by an accurate design of the stator blade in such a way to control the secondary flow generation in the hub region.

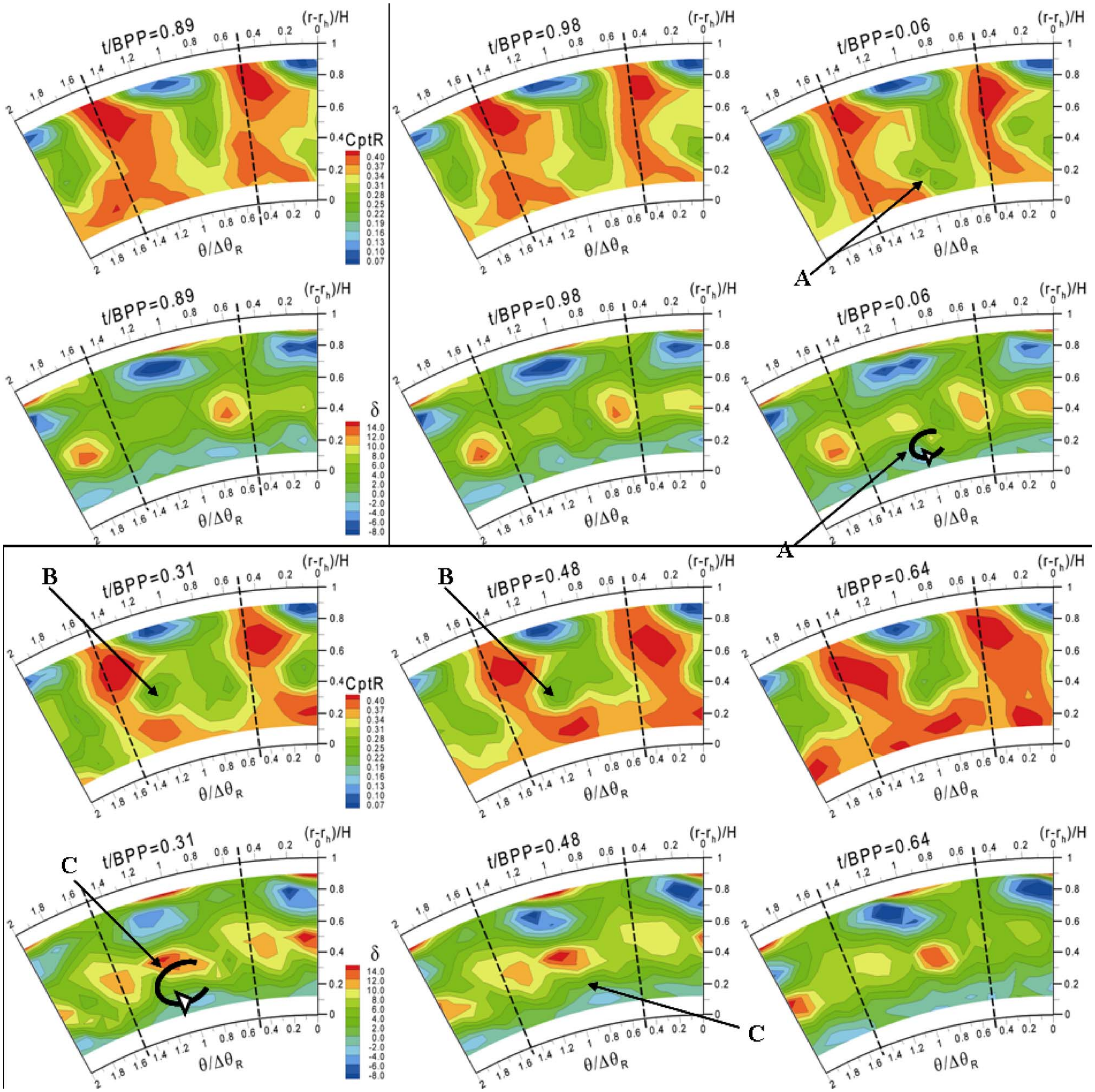

Fig. 10 Instantaneous rotor flow at TR2, nominal stator-rotor gap (phase-lag periodicity applied)

Acknowledgment

Authors wish to thank the MIUR (Ministero dell'Istruzione, Università e Ricerca) for the support given to the research program "Experimental analysis of the main effects related to the aerodynamic rotor-stator interaction in a high pressure axial flow turbine stage."

Nomenclature

b = axial chord
BPP = blade passing period
C_{pt} = $(P_t - P_{\mathrm{ref}})/(P_{t,0} - P_{\mathrm{ref}})$: total pressure coefficient
$C_{pt,R}$ = $(P_{t,R} - P_{\mathrm{ref}})/(P_{t,0} - P_{\mathrm{ref}})$: relative total pressure coefficient
H = blade height
HPV = hub passage vortex
N = number of blades
PS = pressure side
r = turbine radius
SHCV = stator hub corner vortex
SHPV = stator hub passage vortex
SHSV = stator hub shed vortex
SS = suction side
t = time
TLV = tip leakage vortex
TPV = tip passage vortex
α = absolute blade-to-blade angle
δ = rotor deviation angle
θ = rotor angular coordinate
$\Delta\theta_R$ = rotor angular pitch

Subscripts

H = hub
R = rotor, relative

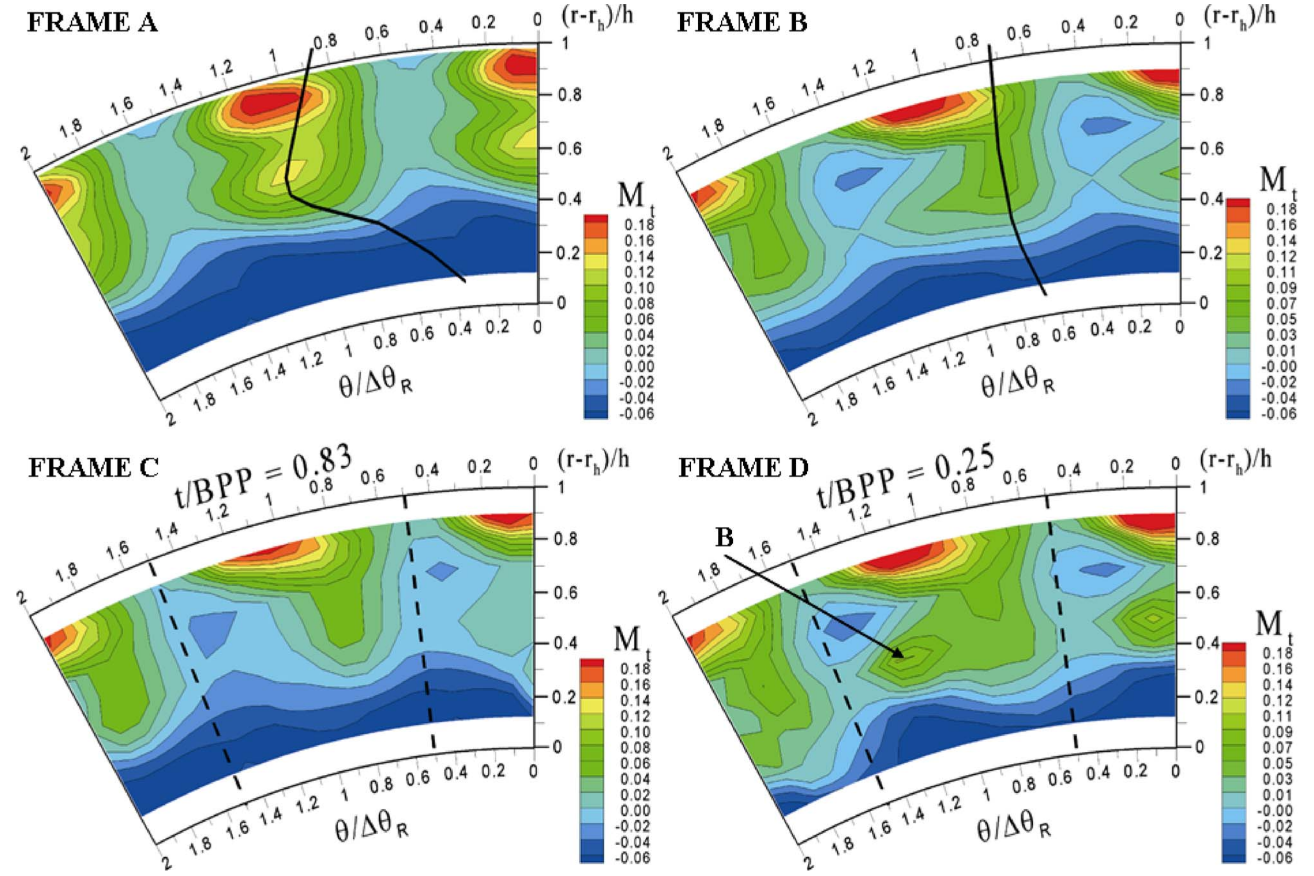

Fig. 11 Tangential Mach number at TR2: (*a*) mean rotor channel–maximum gap, (*b*) mean rotor channel–nominal gap, and (*c,d*) instantaneous rotor flow–nominal gap

S = stator
ref = reference=atmospheric
t = total
0 = stator upstream

References

[1] Funazaki, K., Sasaki, Y., and Tanuma, T., 1997, "Experimental Studies on Unsteady Aerodynamic Loss of a High Pressure Turbine," ASME Paper No. 97-GT-52.

[2] Zaccaria, M. A., and Lakshminarayana, B., 1997, "Unsteady Flow Field Due to Nozzle Wake Interaction With the Rotor in an Axial Flow Turbine—Part I: Rotor Passage Flow Field," ASME J. Turbomach., **119**, pp. 210–222.

[3] Hodson, H. P., and Dowes, W. N., 1998, "On the Interpretation of Measured Profile Losses in Unsteady Wake-Turbine Blade Interaction Studies," ASME J. Turbomach., **120**, pp. 276–283.

[4] Sharma, O. P., Pickett, G. F., and Ni, R. H., 1992, "Assessment of Unsteady Flows in Turbines," ASME J. Turbomach., **114**, pp. 79–90.

[5] Chaluvadi, V. S. P., Kalfas, A. I., Benieghbal, M. R., Hodson, H. P., and Denton, J. D., 2001, "Blade-Row Interaction in a High-Pressure Turbine," J. Propul. Power, **17**, pp. 892–901.

[6] Dring, R. P., Joslyn, H. D., Hardin, L. W., and Wagner, J. H., 1982, "Turbine Rotor-Stator Interaction," ASME J. Eng. Power, **104**, pp. 729–742.

[7] Venable, B. L., Delaney, R. A., Busby, J. A., Davis, R. L., Dorney, D. J., Dunn, M. G., Haldemann, C. W., and Abhari, R. S., 1999, "Influence of Vane-Blade Spacing on Transonic Turbine Stage Aerodynamics: Part I–Time-Averaged Data and Analysis," ASME J. Turbomach., **121**, pp. 663–672.

[8] Pullan, G., 2004, "Secondary Flows and Loss Caused by Blade Row Interaction in a Turbine Stage," ASME J. Turbomach., **128**, pp. 484–491.

[9] Gaetani, P., Persico, G., Dossena, V., and Osnaghi, C., 2007, "Investigation of the Flow Field in a High-Pressure Turbine Stage for Two Stator-Rotor Axial Gaps—Part I: Three-Dimensional Time-Averaged Flow Field," ASME J. Turbomach., **129**(3), pp. 572–579.

[10] Kupferschmied, P., Koppel, P., Gizzi, W., Roduner, C., and Gyarmathy, G., 2000, "Time-Resolved Flow Measurements With a Fast-Response Aerodynamic Probes in Turbomachines," Meas. Sci. Technol., **11**, pp. 1036–1054.

[11] Ainsworth, R. W., Miller, R. J., Moss, R. W., and Thorpe, S. J., 2000, "Unsteady Pressure Measurements," Meas. Sci. Technol., **11**, pp. 1036–1055.

[12] Brouckaert, J. F., 2004, "Development of Fast Response Pressure Probes for Time Resolved Measurements in Turbomachines," Ph.D. thesis Von Karman Institute of Fluid Dynamics Bruxelles.

[13] Schlienger, J., Kalfas, A. I., and Abhari, R. S., 2005, "Vortex-Wake-Blade Interaction in a Shrouded Axial Turbine," ASME J. Turbomach., **127**, pp. 699–707.

[14] Miller, R. J., Moss, R. W., Ainsworth, R. W., and Horwood, C. K., 2003, "Time-Resolved Vane-Rotor Interaction in a High-Pressure Turbine Stage," ASME J. Turbomach., **125**, pp. 1–13.

[15] Persico, G., Gaetani, P., and Guardone, A., 2005, "Design and Analysis of New Concept Fast-Response Pressure Probes," Meas. Sci. Technol., **16**, pp. 1741–1750.

[16] Persico, G., Gaetani, P., and Guardone, A., 2005, "Dynamic Calibration of Fast-Response Probes in Low-Pressure Shock Tubes," Meas. Sci. Technol., **16**, pp. 1751–1759.

[17] Dossena, V., Gaetani, P., and Persico, G., 2004, "Development of High Response Pressure Probes for Time-Resolved 2D and 3D Flow Measurements in Turbomachines," 17th Symposium on Measuring Techniques in Turbomachines, Stockholm.

[18] Gerolymos, G. A., Michon, G. J., and Neubauer, J., 2001, "Analysis and Application of Chorochronic Periodicity in Turbomachinery Rotor/Stator Interaction Computations," J. Propul. Power, **18**, pp. 1139–1152.

[19] Ristic, D., Lakshminarayana, B., and Chu, S., 1999, "Three-Dimensional Flowfield Downstream of an Axial-Flow Turbine Rotor," J. Propul. Power, **15**, pp. 334–344.

[20] Binder, A., Forster, W., Mach, K., and Rogge, H., 1987, "Unsteady Flow Interaction Caused by Stator Secondary Vortices in a Turbine Rotor," ASME J. Turbomach., **109**, pp. 251–257.

[21] Lakshminarayana, B., 1995, "*Fluid Dynamics and Heat Transfer of Turbomachinery*," Wiley, New York, pp. 339–357.

[22] Pullan, G., and Denton, J. D., 2003, "Numerical Simulation of Vortex-Turbine Blade Interaction," 5th European Conference on Turbomachinery, Prague.

[23] Chaluvadi, V. S. P., Kalfas, A. I., Hodson, H. P., Ohyama, H., and Watanabe, E., 2003, "Blade Row Interaction in High-Pressure Steam Turbine," ASME J. Turbomach., **125**, pp. 14–24.

Influence of Sweep on Axial Flow Turbine Aerodynamics at Midspan

Graham Pullan
Whittle Laboratory,
Department of Engineering,
University of Cambridge,
United Kingdom
e-mail: gp10006@cam.ac.uk

Neil W. Harvey
Roll-Royce plc,
Derby, United Kingdom

Sweep, when the stacking axis of the blade is not perpendicular to the axisymmetric streamsurface in the meridional view, is often an unavoidable feature of turbine design. Although a high aspect ratio swept blade can be designed to achieve the same pressure distribution as an unswept design, this paper shows that the swept blade will inevitably have a higher profile loss. A modified Zweifel loading parameter, taking sweep into account, is first derived. If this loading coefficient is held constant, it is shown that sweep reduces the required pitch-to-chord ratio and thus increases the wetted area of the blades. Assuming fully turbulent boundary layers and a constant dissipation coefficient, the effect of sweep on profile loss is then estimated. A combination of increased blade area and a raised pressure surface velocity means that the profile loss rises with increasing sweep. The theory is then validated using experimental results from two linear cascade tests of highly loaded blade profiles of the type found in low-pressure aeroengine turbines: one cascade is unswept, the other has 45 deg *of sweep. The swept cascade is designed to perform the same duty with the same loading coefficient and pressure distribution as the unswept case. The measurements show that the simple method used to estimate the change in profile loss due to sweep is sufficiently accurate to be a useful aid in turbine design.* [DOI: 10.1115/1.2472397]

Introduction

In this paper, sweep (λ) is defined as the deviation of the stacking axis of the blade from a line perpendicular to the axisymmetric streamsurface in the meridional view (Fig. 1). Strictly, we should refer to this as *axial* sweep in order to differentiate it from *true* sweep, which is created by the displacement of blade sections relative to each other in the chordwise direction. In fact, any pair of orthogonal directions can be used to describe the way a blade is stacked. Thus, tangential lean should be used in conjunction with the definition of sweep in Fig. 1, and dihedral (true lean) accompanies true sweep.

It is very common for an axial flow turbine to be designed with some blade rows operating at some level of sweep. This often occurs because the hub or casing are not at constant radius (they are flared), whereas the blading is stacked on a near radial line in the meridional view. For example, the rapidly increasing volume flow in a steam turbine necessitates high casing flare angles and sweep in this region can routinely exceed 40 deg. Sweep is also found in the low-pressure (LP) turbines of large civil turbofans. In these engines, there is a continuing trend to increase the bypass ratio to reduce noise. This, coupled with increases in overall pressure ratio, means a low-radius high-pressure turbine is required to maintain acceptable blade aspect ratios. Unless a gearbox is used, the low rotational speed of the LP shaft (again, to reduce fan noise) means that the LP turbine must be designed at a relatively high radius. This leads to highly flared annulus walls and hence high sweep angles ($\lambda > 40$ deg) in radially stacked blade rows.

Smith and Yeh [1] significantly advanced the understanding of how to design swept blade rows. They first considered a blade row of infinite span and constant section profile. Since such a blade can exert no force on the flow in the spanwise direction, the component of flow velocity in the spanwise direction remains unchanged through the blade row. Smith and Yeh pointed out two important consequences of this result. First, the appropriate section on which to design the two-dimensional blade profile is not the axisymmetric streamsurface but the section in a plane perpendicular to the stacking axis of the blade. Second, since the blade only accelerates the flow in this plane, while the spanwise velocity is preserved, the axisymmetric streamsurface at inlet to the blade will become twisted within the passage and discontinuous at the trailing-edge plane. In a blade row of finite span, the streamsurfaces at the hub and casing must remain parallel to the end walls, however, and Smith and Yeh provide an analytic model for these "end effects" for cascades of thin, low turning airfoils.

Potts [2] used three-dimensional CFD to plot the distortion of the streamsurfaces within swept linear turbine cascades. Comparisons were made between surface pressure distributions calculated with both three-dimensional and two-dimensional (using the section defined by Smith and Yeh [1]) methods and excellent agreement was found except in the region very close to the end walls (within $\approx 15\%$ span).

Hill and Lewis [3] and Bräunling and Lehthaus [4] present experimental investigations of swept turbine blading. Hill and Lewis [3] performed linear cascade tests of a turbine blade profile at three angles of sweep ($\lambda = 0$ deg, 20 deg, 40 deg). The swept blades had the same blade profile (and pitch) when viewed on an axisymmetric streamsurface; they were not redesigned to take into account sweep. The authors show that the swept blades do not achieve the same pressure distribution as the unswept case and that the actual distributions are more closely predicted by applying a two-dimensional calculation method to a section perpendicular to the stacking axis. Bräunling and Lehthaus [4] used an annular transonic test facility. In their experiments (at $\lambda = 0$ deg, 30 deg, 45 deg) the blade profile was unchanged (radially stacked), but the flare angle of the annulus walls was altered instead. The authors tested two blade profiles: a turbine aerofoil and a staggered flat plate. Since the tests were run at a constant inlet angle as projected on to the surface perpendicular to the blade axis ($\alpha_{n1} = \tan^{-1} V_{\theta_1}/V_{n1}$) the swept blades were correctly designed according to the Smith and Yeh [1] approach. As the sweep angle was increased, the meridional velocity also increased and so the exit flow angle α_{m2} was observed to decrease. The effects of the persistence of the spanwise velocity through the blade row were seen on the measured surface pressure distributions.

The purpose of the present work is to contribute to the understanding of the effects of sweep at midspan (away from end ef-

---

Contributed by the International Gas Turbine Institute of ASME for publication in the JOURNAL OF TURBOMACHINERY. Manuscript received July 13, 2006; final manuscript received July 14, 2006. Review conducted by David Wisler. Paper presented at the ASME Turbo Expo 2006: Land, Sea and Air (GT2006), May 8–11, 2006, Barcelona, Spain. Paper No. GT2006-91070.

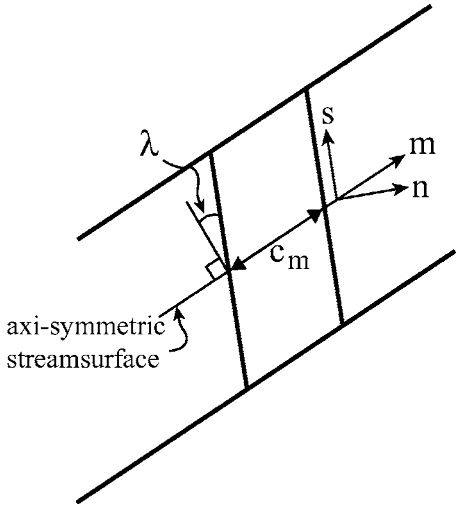

Fig. 1 Definition of sweep

fects) of turbine blading. A modified loading coefficient is derived that takes into account sweep. This allows an optimum pitch-to-chord ratio to be chosen. For the first time, a simple analytical method for estimating the change in blade boundary layer loss due to sweep is then developed. Finally, results from two low-speed linear cascade tests of low-pressure turbine blades are presented. One cascade is unswept, the other has been designed to perform the same duty but at a sweep angle of 45 deg.

Theory

Introduction. In this paper, the effects of sweep on axial flow turbine blade aerodynamics at midspan are described. Before this can be done, we must first establish what is being kept constant as the sweep is varied. In what follows, the meridional velocity V_m and the inlet and exit tangential velocities $V_{\theta 1}$ and $V_{\theta 2}$ (hence the meridional flow angles, e.g., $\alpha_{m1}=\tan^{-1} V_{\theta 1}/V_m$) remain fixed as the sweep angle λ is altered. It is felt that this situation most accurately reflects the common experience of the turbine designer. Referring to Fig. 1, the annulus geometry is largely constrained (as are V_m, α_{m1}, and α_{m2}) but the aerodynamicist has some freedom in the choice of sweep.

Design. Although fully three-dimensional computational methods are common place, the early stages of blade design are still often done on a two-dimensional or quasi-three-dimensional basis. It is usual to choose to design a blade on sections defined by the axisymmetric streamsurfaces generated by a throughflow calculation of the whole machine. For a swept blade, Smith and Yeh [1] have shown that this choice of section is incorrect.

To examine some of the problems caused by designing a swept blade on an axisymmetric streamsurface section, consider a blade with 45 deg of sweep. Fig. 2 shows pressure distributions calculated, as are all the CFD results in this paper, using Multip [5]. The solid line shows the pressure distribution obtained by a two-dimensional simulation of an axisymmetric streamsurface section. The dashed line shows results, at midspan, from a three-dimensional calculation once the two-dimensional profile has been stacked to form the full swept blade, which has an aspect ratio $H/c_n=4$. Two features are apparent. First, the true pressure distribution, as calculated by the three-dimensional simulation of the swept blade, is very poor and suggests that the wrong pitch-chord ratio has been used. Second, the pressure-surface pressure has been reduced (isentropic velocity increased) on the three-dimensional blade. Both of these observations relate directly to the fact that the spanwise velocity, even for a swept blade of finite span, tends to remain unchanged through the blade row. Figure 3 shows contours of spanwise velocity V_s. The constancy of V_s throughout most of the flowfield and the influence of end effects are clear.

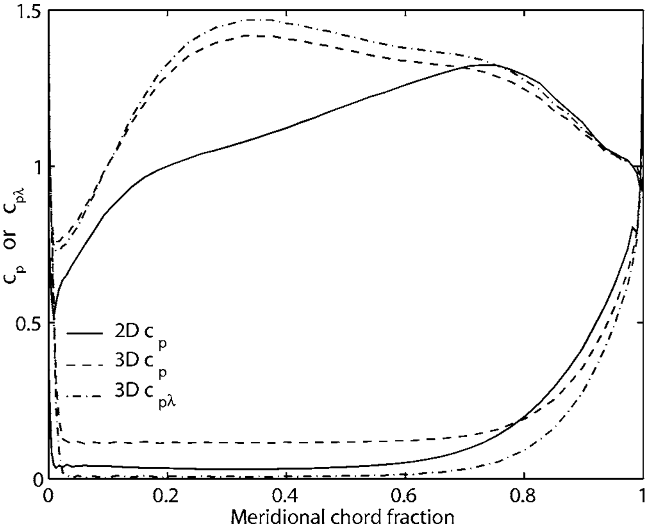

Fig. 2 45 deg swept blade designed on a streamsurface section

Since the spanwise velocity cannot be altered in a swept blade of infinite span, it is useful to redefine the pressure coefficient to take account of this

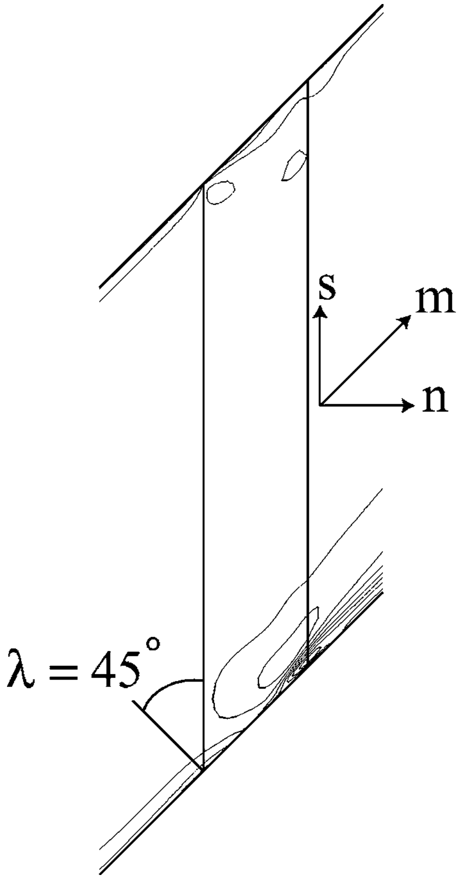

Fig. 3 45 deg swept blade, contours of pitchwise averaged V_s, $\Delta_{con}=0.05V_2$

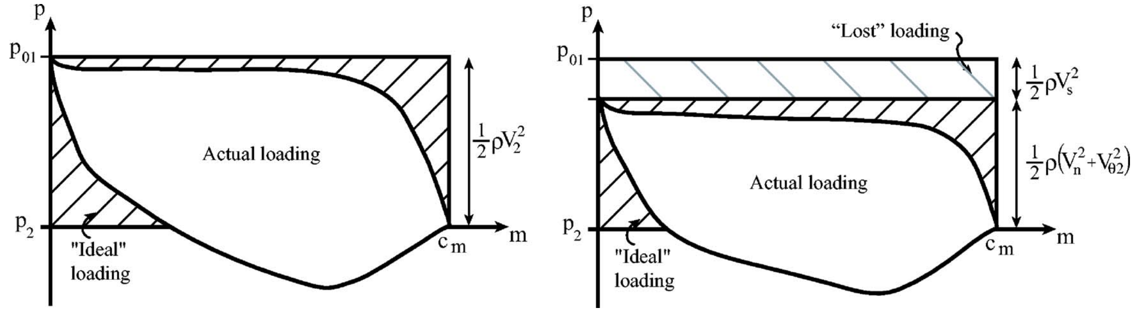

Fig. 4 Schematics of loading coefficient definition, without (left) and with sweep

$$c_p=\frac{p_{01}-p}{p_{01}-p_2};\quad c_{p\lambda}=\frac{p_{01}-\frac{1}{2}\rho V_s^2-p}{p_{01}-\frac{1}{2}\rho V_s^2-p_2} \tag{1}$$

For an incompressible flow, $c_{p\lambda}=0$ in regions where the isentropic velocity is V_s, such as the pressure surface in Fig. 2. Equation (1) therefore allows direct comparisons between the pressure distributions from the two-dimensional section and full three-dimensional blade to be made. Figure 2 shows the $c_{p\lambda}$ distribution for the three-dimensional calculation as a dashed-dotted line.

Since the designer is unable to influence the spanwise velocity, Smith and Yeh [1] determined that the correct choice for a plane on which to employ a two-dimensional approach is the one perpendicular to the stacking axis. In the following two sections, the consequences for the optimum pitch-chord ratio, and for the blade boundary layer loss, of the designer's choice of sweep angle are examined.

Loading Coefficient. Blade loading, or lift, coefficients are often used to characterize how "hard" a particular blade profile is working. A common definition, due to Zweifel, expresses the loading coefficient as the fraction of an "ideal" loading that is present in the actual design. Of course, the definition of "ideal" loading is arbitrary but Zweifel assumes that the pressure-surface pressure is equal to the inlet stagnation pressure, and the suction-surface pressure is that at the exit of the blade row, see the left-hand-side schematic in Fig. 4. Zweifel's loading coefficient Z for flow on a stream surface is then given by

$$Z=\frac{\text{Actual loading}}{\text{Ideal loading}}=\frac{P\rho V_m(V_{\theta 2}-V_{\theta 1})}{c_m(p_{01}-p_2)} \tag{2}$$

Assuming incompressible flow with V_m constant

$$Z=\frac{P\rho V_m^2(\tan\alpha_{m2}-\tan\alpha_{m1})}{c_m\frac{1}{2}\rho V_2^2} \tag{3}$$

Since $V_2=V_m/\cos\alpha_{m2}$, we arrive at the well-known result

$$Z=2\frac{P}{c_m}\frac{\tan\alpha_{m2}-\tan\alpha_{m1}}{\sec^2\alpha_{m2}} \tag{4}$$

We now derive the appropriate definition of loading coefficient for a blade with sweep. The "ideal" loading distribution is now changed because the spanwise component of the inlet velocity remains unchanged through a high aspect ratio (strictly infinite) blade row. This means that the highest pressure that can be achieved on the surface of the blade is not p_{01} but, for an incompressible flow, $p_{01}-(1/2)\rho V_s^2$, see the right-hand-side schematic in Fig. 4. An amount of loading equal to $c_m(1/2)\rho V_s^2$ is "lost" and is unavailable to the designer. We must therefore modify the "ideal" loading of Eq. (2) to reflect this

$$Z_\lambda=\frac{P\rho V_m(V_{\theta 2}-V_{\theta 1})}{c_m\left(p_{01}-\frac{1}{2}\rho V_s^2-p_2\right)} \tag{5}$$

$$=\frac{P\rho V_m^2(\tan\alpha_{m2}-\tan\alpha_{m1})}{c_m\frac{1}{2}\rho(V_n^2+V_{\theta 2}^2)} \tag{6}$$

$$=2\frac{P}{c_m}\frac{\tan\alpha_{m2}-\tan\alpha_{m1}}{\cos^2\lambda+\tan^2\alpha_{m2}} \tag{7}$$

When $\lambda=0$, the denominator of Eq. (7) becomes $\sec^2\alpha_{m2}$ and the expression is identical to Eq. (4) as expected. The importance of Eq. (7) can be illustrated by examining the change in pitch-chord ratio as the sweep angle is changed at constant loading coefficient (and constant V_m, α_{m1}, and α_{m2}). The ratio of pitch-chord ratio for a blade with sweep to that for a blade without sweep is given by

$$\frac{P/c_m|_\lambda}{P/c_m|_{\lambda=0}}=\frac{\cos^2\lambda+\tan^2\alpha_{m2}}{1+\tan^2\alpha_{m2}} \tag{8}$$

Figure 5 shows the reciprocal of Eq. (8) as a function of sweep angle and exit flow angle. Figure 5 therefore shows the factor by which c_m/P, and hence the blade wetted area, must be increased in order to maintain constant loading coefficient for fixed inlet and exit flow angles. The result is intuitive since as the sweep angle increases so too does the amount of loading per unit meridional

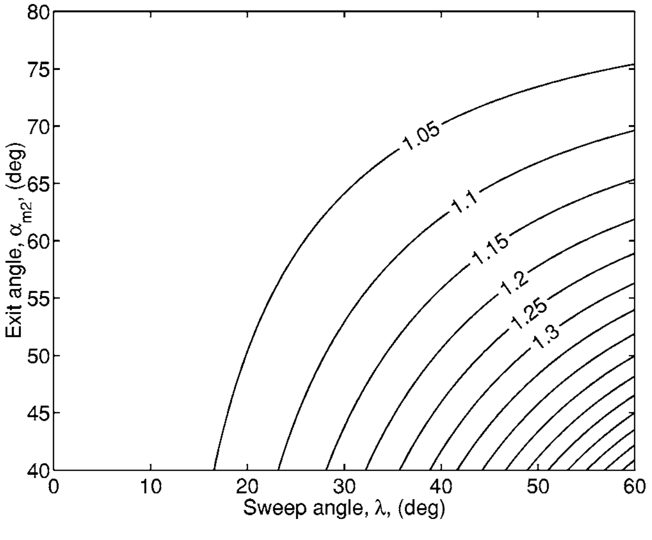

Fig. 5 Area ratio—contours of $(1+\tan^2\alpha_{m2})/(\cos^2\lambda+\tan^2\alpha_{m2})$

chord ($(1/2)\rho V_s^2$), which is unavailable to the blade designer. To maintain the total loading, the blade area must therefore be increased.

Loss. The loss generated by the blade surface boundary layers can be found from the isentropic surface velocity distribution using the following equation [6]:

$$\zeta_s = 2\sum \frac{c_\xi}{P\cos\alpha_{m2}}\int_0^1 c_d\left(\frac{V_0}{V_2}\right)^3 d\left(\frac{x_\xi}{c_\xi}\right) \qquad (9)$$

where ζ_s is the entropy loss coefficient, V_0 is the isentropic surface velocity and the summation is over both blade surfaces. The subscript ξ denotes distance along the blade perimeter on the axisymmetric streamsurface so that c_ξ is the surface length of the blade in this view and $d(x_\xi/c_\xi)$ is an infinitesimal element of surface distance. c_d is the dissipation coefficient and is a function of x_ξ/c_ξ. However, if the boundary layers are turbulent throughout, c_d is approximately constant ($c_d \approx 0.002$) [6].

To evaluate Eq. (9), knowledge of the isentropic surface velocity distribution is needed. As a simple approximation, we assume that the velocity distribution is rectangular with the "ideal" lift distribution for the swept blade in Fig. 4. Therefore,

$$\text{on the suction surface} \quad V_{0,SS} = V_2 = \frac{V_m}{\cos\alpha_{m2}} \qquad (10)$$

$$\text{on the pressure surface} \quad V_{0,PS} = V_s = V_m \sin\lambda \qquad (11)$$

$$\text{and, by definition,} \quad Z_\lambda = 1 \qquad (12)$$

When the blade is unswept, Eqs. (9)–(11), together with the assumption of constant c_d, give

$$\zeta_s|_{\lambda=0} = 2\left.\frac{c_\xi}{P}\right|_{\lambda=0}\frac{c_d}{\cos\alpha_{m2}} \qquad (13)$$

When the blade is swept, the same assumptions lead to

$$\zeta_s|_\lambda = 2\left.\frac{c_\xi}{P}\right|_{\lambda=0}\underbrace{\left(\frac{1+\tan^2\alpha_{m2}}{\cos^2\lambda+\tan^2\alpha_{m2}}\right)}_{\text{area factor}}\frac{c_d}{\cos\alpha_{m2}}\underbrace{(1+\sin^3\lambda\cos^3\alpha_{m2})}_{V_s\ \text{factor}} \qquad (14)$$

The term labeled "area factor" in Eq. (14) is the amount by which c_ξ/P increases as the sweep is varied. It is assumed that the meridional velocity V_m, the flow angles, α_{m1} and α_{m2}, and the loading coefficient Z_λ are all held constant and that the increase in c_ξ/P is approximately the same as the increase in c_m/P determined by Eq. (8). The "V_s factor" term represents the influence of the spanwise velocity on the blade surface loss. The amount by which this term is greater than unity (i.e., $\sin^2\lambda\cos^3\alpha_{m2}$) is the extra loss due to the nonzero pressure-surface velocity.

Figure 6 shows contours of the "V_s factor" term. For high exit angles, the contribution toward loss from the pressure surface is seen to be small, but it becomes significant at moderate exit angles and high sweep angles.

Figure 7 shows contours of loss ratio—the ratio of loss for a swept blade to that of an unswept blade when both operate between the same inlet and exit flow angles and both have the same loading coefficient Z_λ. Although a very simple surface pressure distribution and a constant value of dissipation coefficient have been assumed, the trends are clear. For sweep angles of <20 deg, there is little change in blade boundary layer loss. However, at high sweep angles ($\lambda \approx 40$ deg) and moderate exit angles ($\alpha_{m2} \approx 60$ deg) the loss is estimated to increase by as much as 20%.

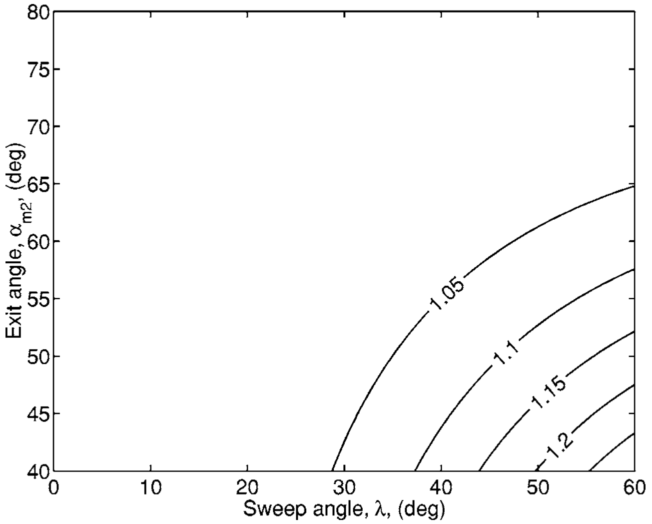

Fig. 6 "V_s factor"—contours of $(1+\sin^3\lambda\cos^3\alpha_{m2})$

Application

Introduction. The theoretical results presented thus far are now applied to the type of blading found in the low pressure (LP) turbines of large modern turbofans. As mentioned in the introduction to this paper, LP turbines (the front stages at least) are likely to be designed with high levels of sweep. A datum, orthogonal blade is first introduced. An equivalent blade, with a sweep angle of 45 deg is then presented. Both blades have been tested in low-speed linear cascades and the results are discussed.

Datum (Unswept) Blade (Blade H). The datum blade was of the thin-solid type that is often employed in LP turbines. Its development and initial testing was described by Curtis et al. [7] where it was designated "Blade H," and results using the same profile have also been reported by Howell et al. [8] and Harvey et al. [9]. Some parameters of the datum blade are listed in Table 1. A measured midspan pressure distribution, along with a CFD prediction using fully turbulent boundary layers, is shown in Fig. 8. The data show that the blade carries a high leading-edge loading and then exhibits continual suction-surface acceleration to the

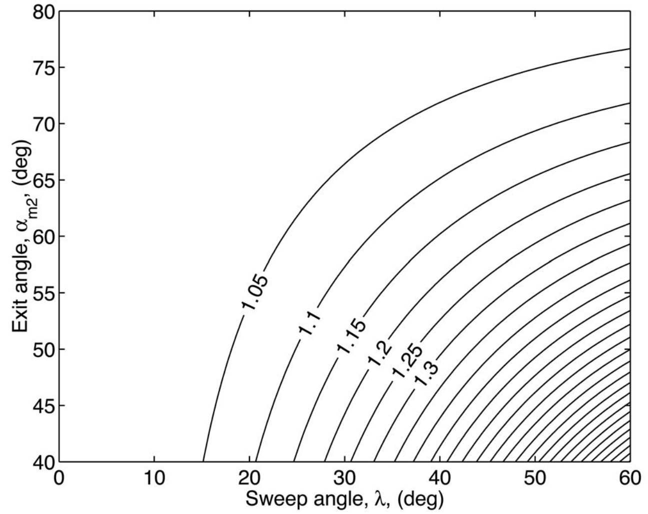

Fig. 7 Loss ratio—contours of $\zeta_s|_\lambda / \zeta_s|_{\lambda=0}$

Table 1 Datum blade parameters

Pitch-meridional chord ratio P/c_m	0.97
Air inlet angle (from axial) α_{m1}	−30.4 deg
Design exit air angle (from axial) α_{m2}	62.8 deg

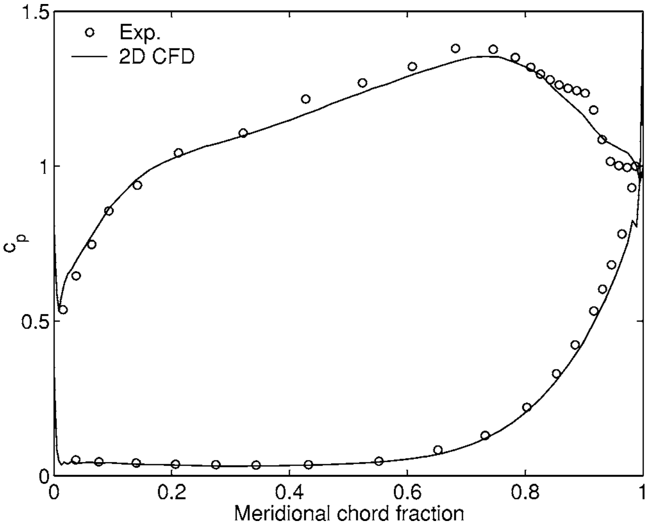

Fig. 8 Measured and predicted midspan pressure distributions, datum blade

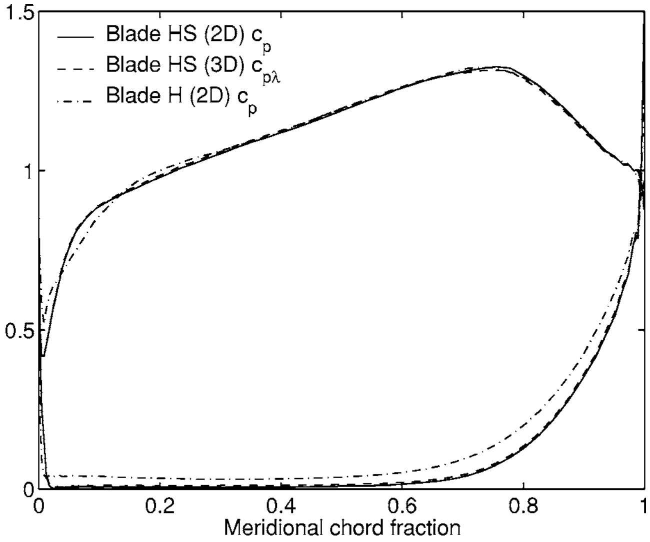

Fig. 10 Predicted pressure distributions, datum and swept blade

point of peak suction. Downstream of this point, the measured and predicted curves deviate as the real (laminar) boundary layer separates and undergoes transition to turbulence before reattaching. On the pressure-surface, the pressure is close to the inlet stagnation value for much of the surface, indicating very low velocities.

Design of Swept Blade (Blade HS). A swept blade was then designed to perform an identical duty to the datum blade. At an exit angle α_{m2}=62.8 deg, Eq. (8) gives the change in wetted area (i.e., change in c_m/P) required to maintain a constant loading coefficient Z_λ as the sweep angle is varied. Also, Eq. (14) provides an estimate for the increase in blade surface boundary layer loss. Figure 9 shows these two curves (at α_{m2}=62.8 deg). For the present blade, a sweep angle of 45 deg was chosen. At such a high value of λ, Fig. 9 shows that the wetted area must increase by 12% and that the blade surface boundary loss is estimated to rise by 16% (the latter is greater than the former due to increased pressure surface velocities).

The blade was designed using a two-dimensional method (fully turbulent) on a plane perpendicular to the stacking axis. The design intent was to achieve the same surface pressure distribution as the datum blade and Fig. 10, which presents results from the two-dimensional CFD, shows that this was closely achieved. Figure 10 also shows the midspan pressure distributions from three-dimensional CFD predictions for the datum and swept blades at the same aspect ratio (H/c_n). The good agreement validates the two-dimensional design process.

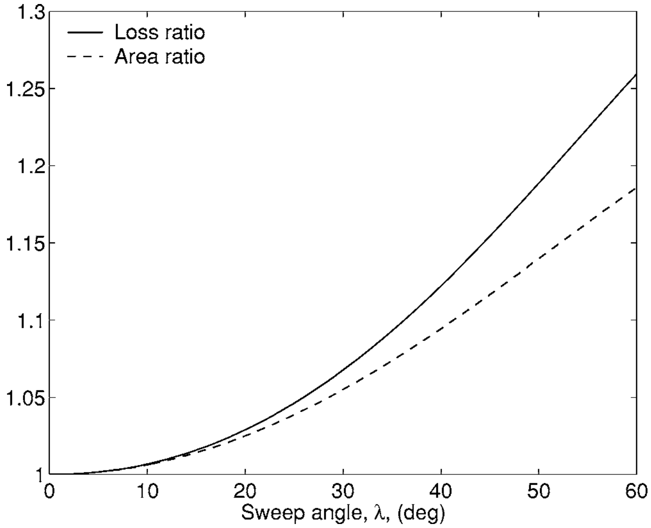

Fig. 9 Loss and area ratio, α_{m2}=62.8 deg

Cascades. A schematic of the datum cascade is shown in Fig. 11. Six blades were used, each with a meridional chord of 94 mm, a pitch of 90 mm, and a span of 375 mm. One of the central two blades was instrumented with 44 surface pressure tappings. A five-hole pneumatic probe was used at a traverse plane 25% c_m downstream of the trailing edges.

For the swept cascade, the chord normal to the stacking axis, c_n, was kept the same as in the unswept case (c_n=94 mm). This resulted in a pitch of 114 mm and a cascade of five blades. Again, the central blade was instrumented with 44 surface pressure tappings. The sweep angle of 45 deg meant that the ends of the blades were displaced a distance of $\Delta m = H$=375 mm in the meridional direction (Fig. 12).

Consider the streamsurface formed by all the stagnation streamlines that hit the leading edge of the bottom blade of the cascade; this stream surface forms the bottom wall of the cascade. The inlet plane to the swept cascade is perpendicular to the meridional direction (Fig. 12). The line formed by the intersection of the inlet plane with the stream surface described is not perpendicular to the endwalls of the cascade. Referring to Fig. 13, $\Delta r\theta$ is the circumferential distance, at the inlet plane, between the stagnation streamlines that arrive at the leading edge of the blade at each end wall

$$\Delta r\theta = \Delta m \tan \alpha_{m1} \qquad (15)$$

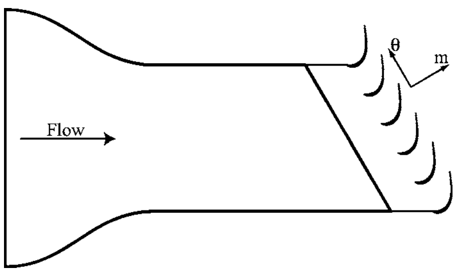

Fig. 11 Schematic of datum, unswept cascade, side view

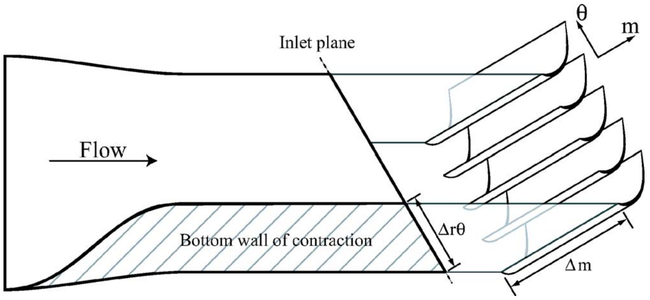

Fig. 12 Schematic of swept cascade, side view

$$=H \tan \lambda \tan \alpha_{m1} \qquad (16)$$

so that

$$\tan \beta = \frac{\Delta r\theta}{H} = \tan \lambda \tan \alpha_{m1} \qquad (17)$$

The common case is that $\lambda=0$ so that $\beta=0$ and the duct at the inlet plane is rectangular. However, for the present swept cascade with $\lambda=45$ deg, $\beta=\alpha_{m1}=30.4$ deg and the inlet duct must be a parallelogram.

The required shape of the duct at the inlet plane necessitates an unusual contraction which is initially "twisted" before entering a duct of constant parallelogram section upstream of the cascade. Figure 14 shows a photograph of the contraction looking downstream toward the cascade. It was thought that the complex asymmetric shape of the contraction may produce end-wall boundary layers which were skewed and of nonuniform thickness. To assess this, an area traverse was made at the inlet plane using a five-hole pneumatic probe. Figure 15 shows contours of total pressure coefficient at this plane. Figure 15 shows that the "natural" tunnel boundary layer (without bleeds) does indeed become highly nonuniform by the time it reaches the cascade inlet. However, Fig. 15 also shows that the situation is greatly improved by bleeding off the boundary layers at two points: upstream and immediately downstream (before the parallelogram duct) of the twisted contraction. The small islands of low total pressure in the bottom-right quadrant of both plots are caused by the wake of an inlet pitot probe. In addition, the measured yaw and pitch angles of the flow were found to be within 1 deg of the axial direction.

Fig. 14 Photograph of the inlet contraction for the swept cascade

Results

Flow Visualization. Figure 16 shows a photograph of oil and dye flow visualization on the suction-surface of the swept blade. The view is almost perpendicular to the suction-surface at the trailing edge (the leading edge is not visible) and the flow is from left to right. The black dotted line is for clarity and follows the direction of the flow visualization. The deviation of the flow from the axi-symmetric streamsurface plane (horizontal in Fig. 16) can be seen. The spanwise velocity remains constant while the flow in the plane perpendicular to the stacking axis is accelerated. As a result, the "streamlines" upstream of the separation bubble are approximately perpendicular to the trailing edge. Immediately upstream of the bubble, the flow is decelerating and the flow visualization turns slightly toward the meridional direction. Downstream of the bubble, the flow is fully aligned again with the axisymmetric streamsurface.

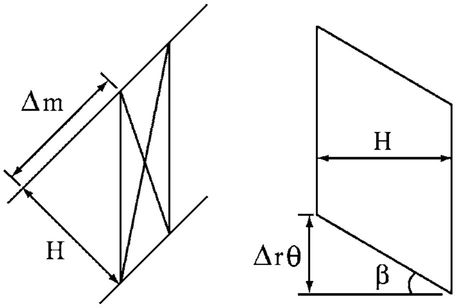

Fig. 13 Swept cascade inlet, meridional (left), and inlet plane views

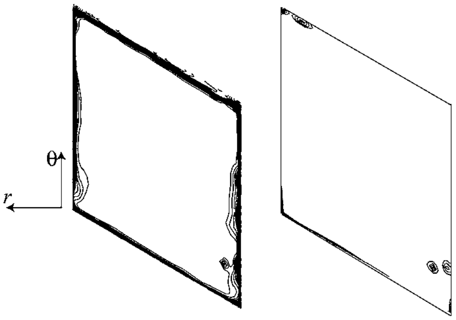

Fig. 15 Measured contours of $(p_{01}-p_0)/(p_{01}-p2)$, inlet plane, $\Delta_{con}=0.01$, without (left) and with bleeds

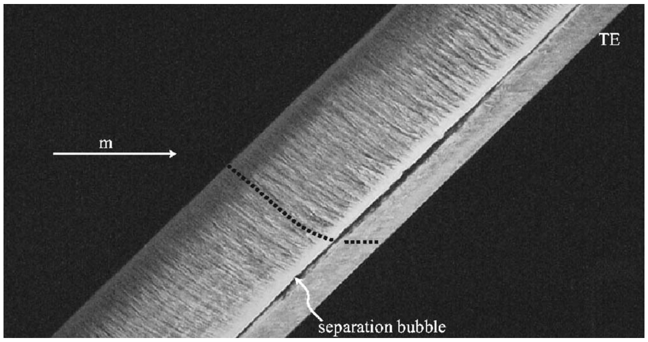

Fig. 16 Suction-surface flow visualization, swept cascade (view perpendicular to suction surface at trailing edge)

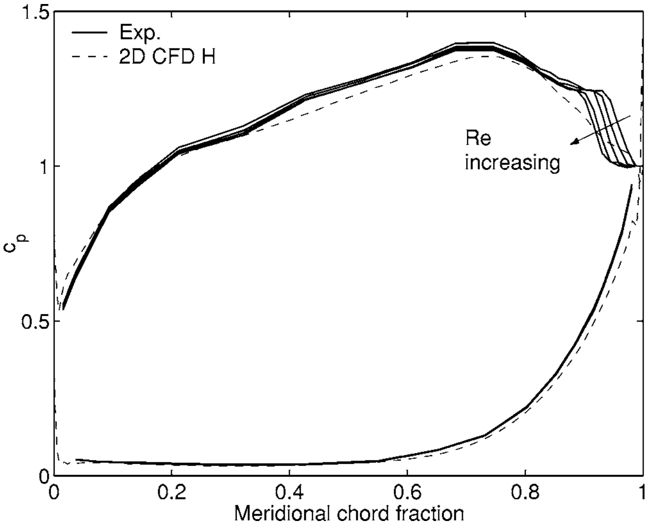

Fig. 17 Measured midspan c_p distributions, unswept blade, $1.7\times10^5<\mathrm{Re}_{c_m}<3.3\times10^5$

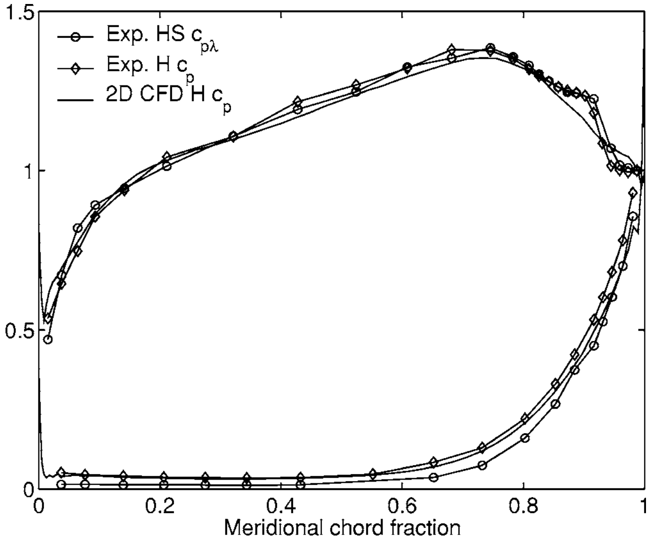

Fig. 19 Midspan pressure distributions for both blades at the same Re_{c_m}

Surface Pressure Distributions. Figures 17 and 18 show midspan surface pressure distributions over a range of Reynolds numbers $(1.7\times10^5<\mathrm{Re}_{c_m}<3.3\times10^5)$ for both blades. The calculated two-dimensional pressure distribution for the unswept blade is shown in both plots as a dashed line. The expected effect of Reynolds number on separation bubble length is seen: increasing the Reynolds number shortens the bubble length. It is clear that the approach used to design the swept blade has worked well. During the design process, the fully turbulent pressure distributions for the swept and unswept blades were matched. It is remarkable how similar the *real* pressure distributions of the two blades, in terms of separation point and bubble length, are given the extreme sweep angle used. To emphasise this, Fig. 19 shows the mid-span surface pressure distribution for both blades at the same Reynolds number. The differences between the two curves are small.

Wake Traverses. To assess the profile loss, area traverses $25\% c_m$ downstream of the trailing edge were made for both blades using a five-hole pneumatic probe. The measurement window extended over one blade pitch (49 points) and had a spanwise extent (perpendicular to the endwalls) of half a blade pitch (25 points) centered at midspan. In effect, 25 separate wake traverses were made in the two-dimensional region close to midspan. A mixed-out loss coefficient was obtained at each spanwise station. The results for the two blades are shown in Figure 20. The error bars indicate ±1 standard deviation (evaluated from the 25 data points). The loss of the swept blade is seen to be higher than the unswept blade at all of the Reynolds numbers tested. Equation (14) predicts a 16% increase in loss. The actual difference between the blades at the lower two Reynolds numbers was close to 30%, and in the range of 19–20% at the other three operating conditions. The simple prediction method assumes a constant dissipation coefficient throughout (i.e., fully turbulent boundary layers). For this blade profile, much of the surface is covered by laminar boundary layers at the Reynolds numbers tested and the actual dissipation coefficient is known to be very sensitive to boundary layer state. It is therefore felt that the discrepancy between the loss increase predicted by the simple theory (16%) and observed experimentally (20% at the higher Reynolds numbers) is satisfactory. It is likely that a closer agreement could be achieved with a profile operating at a Reynolds number where the greater part of the blade surface boundary layers would be turbulent.

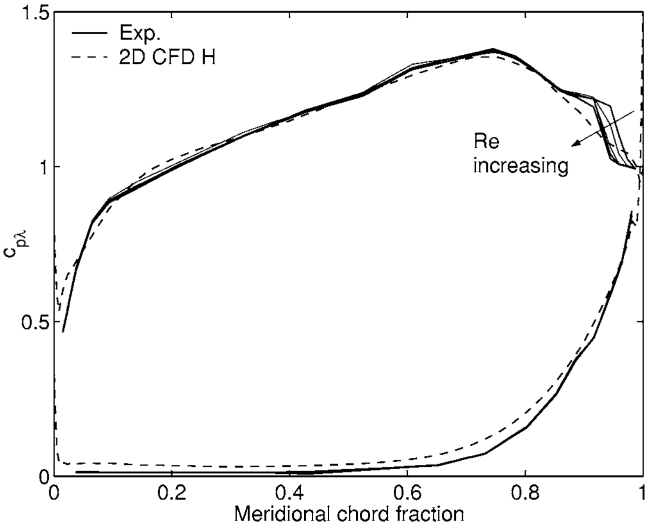

Fig. 18 Measured midspan $c_{p\lambda}$ distributions, swept blade, $1.7\times10^5<\mathrm{Re}_{c_m}<3.3\times10^5$

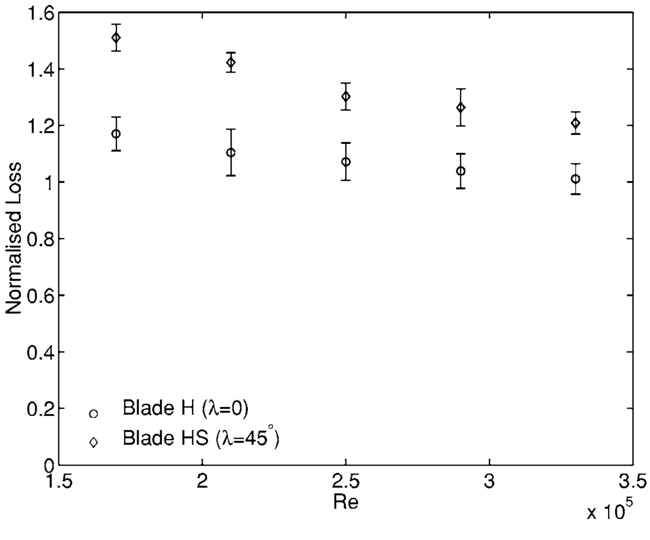

Fig. 20 Measured mixed-out profile loss at midspan

Discussion

The work presented here has confirmed that designing swept aerofoils using a conventional S1/S2 approach will result in the actual surface pressure distributions being significantly different from the design intent. Even though this problem can, relatively simply, be corrected for (using the approach of [1], for example) it is now clear that swept aerofoils incur an unavoidable penalty in terms of increased 2D aerodynamic loss.

There are implications for the turbomachinery designer working with highly swept blade rows. Where consideration of the machine length and weight is not important then the blading, at least the stators, can avoid an increase in profile loss by being stacked with zero sweep. Where such considerations are important, and also where rotating blade rows are required to be near radial to maintain mechanical integrity, then the present work provides the designer with a simple methodology to estimate the cost in terms of aerodynamic loss—at least in 2D (three-dimenasional loss will be the subject of future publications).

This is likely to be an increasingly important issue for the aero engine manufacturer in the future. It is expected that bypass ratios will continue to rise, which will result in smaller engine cores and relatively larger radius changes through the compressor and turbine systems. This will increase radial flow angles and for similar, or shorter, engine lengths the blading will tend to become more swept.

Conclusions

A loading coefficient Z_λ has been developed for the flow on an axisymmetric streamsurface of a swept blade row. The result shows that, at fixed values of meridional velocity (V_m) and flow angles (α_{m1}, α_{m2}) increased sweep requires increased blade wetted area to maintain a constant loading coefficient. A simple method for estimating the change in blade boundary layer loss with sweep (at fixed V_m, α_{m1}, α_{m2}, and Z_λ) has also been described.

These two results have been validated using low-speed linear cascade tests of unswept and swept ($\lambda = 45$ deg) low pressure turbine blades. The swept blade was successfully designed to achieve the same midspan surface pressure distribution as the unswept blade. The mixed-out midspan profile loss was measured to be 20% greater for the swept blade than for the unswept one. The agreement with the 16% increase predicted by the simple theory is felt to be acceptable.

Acknowledgment

The authors are grateful for the numerous discussions that this work has stimulated. In particular, conversations with John Denton, Howard Hodson, and Eric Curtis of the Whittle Laboratory, and Mark Taylor, Adrian White, and Simon Gallimore of Rolls-Royce, have been very helpful. In addition, the authors thank Trevor Chandler, Bill Gurney, and Nick Hooper for the construction of the cascades.

Nomenclature

c = chord
c_d = dissipation coefficient
$c_p(c_{p\lambda})$ = pressure coefficient (with sweep)
p = pressure
r = radius
H = blade height (perpendicular to endwalls)
P = blade pitch
V = velocity
$Z(Z_\lambda)$ = loading coefficient (with sweep)
α = flow angle
ρ = density
λ = sweep angle
ζ_s = entropy loss coefficient
Δ_{con} = contour interval

Subscripts

m = meridional
n = normal to spanwise in meridional plane
s = spanwise
θ = tangential
ξ = along the blade on the axisymmetric streamsurface
0 = stagnation quantity
$1,2$ = inlet, exit

References

[1] Smith, L. H., and Yeh, H., 1963, "Sweep and Dihedral Effects in Axial-Flow Turbomachinery," ASME J. Basic Eng., **85**, pp. 401–416.

[2] Potts, I., 1987, "The Importance of S-1 Stream Surface Twist in the Analysis of Invisvid Flow Through Swept Linear Turbine Cascades," Proc. Inst. Mech. Eng., Part C: Mech. Eng. Sci., **258**(87), pp. 231–248.

[3] Hill, J., and Lewis, R., 1974, "Experimental Investigations of Strongly Swept Turbine Cacades," J. Mech. Eng. Sci., **16**, pp. 32–40.

[4] Bräunling, W., and Lehthaus, F., 1986, "Investigations of the Effect of Annulus Taper on Transonic Turbine Cascade Flow," ASME J. Eng. Gas Turbines Power, **108**, pp. 285–292.

[5] Denton, J., 1992, "The Calculation of Three Dimensional Viscous Flow Through Multistage Turbomachines," ASME J. Turbomach., **114**(1), pp. 18–26.

[6] Denton, J., 1993, "Loss Mechanisms in Turbomachines," ASME J. Turbomach., **115**, pp. 621–656.

[7] Curtis, E., Hodson, H., Banieghbal, M., Denton, J., Howell, R., and Harvey, N., 1997, "Development of Blade Profiles for Low Pressure Turbine Applications," ASME J. Turbomach., **119**, pp. 531–538.

[8] Howell, R., Ramesh, O., Hodson, H., Harvey, N., and Schulte, V., 2001, "High Lift and Aft-Loaded Profiles for Low-Pressure Turbines," ASME J. Turbomach., **123**, pp. 181–188.

[9] Harvey, N., Cox, J., Schulte, V., Howell, R., and Hodson, H., 1999, "The Role of Research in the Aerodynamic Design of an Advanced Low-Pressure Turbine," Proc. Inst. Mech. Eng., Part C: Mech. Eng. Sci., **557**(43), pp. 123–132.

Effects of Surface Deposition, Hole Blockage, and Thermal Barrier Coating Spallation on Vane Endwall Film Cooling

N. Sundaram
Mechanical Engineering Department,
Virginia Polytechnic Institute and State University,
Blacksburg, VA 24061
e-mail: nasundar@vt.edu

K. A. Thole
Department of Mechanical and Nuclear Engineering,
Pennsylvania State University,
University Park, PA 16802-1412
e-mail: kthole@psu.edu

With the increase in usage of gas turbines for power generation and given that natural gas resources continue to be depleted, it has become increasingly important to search for alternate fuels. One source of alternate fuels is coal derived synthetic fuels. Coal derived fuels, however, contain traces of ash and other contaminants that can deposit on vane and turbine surfaces affecting their heat transfer through reduced film cooling. The endwall of a first stage vane is one such region that can be susceptible to depositions from these contaminants. This study uses a large-scale turbine vane cascade in which the following effects on film cooling adiabatic effectiveness were investigated in the endwall region: the effect of near-hole deposition, the effect of partial film cooling hole blockage, and the effect of spallation of a thermal barrier coating. The results indicated that deposits near the hole exit can sometimes improve the cooling effectiveness at the leading edge, but with increased deposition heights the cooling deteriorates. Partial hole blockage studies revealed that the cooling effectiveness deteriorates with increases in the number of blocked holes. Spallation studies showed that for a spalled endwall surface downstream of the leading edge cooling row, cooling effectiveness worsened with an increase in blowing ratio. [DOI: 10.1115/1.2720485]

Introduction

In a typical gas turbine, components in the hot gas path operate under conditions of very high temperature, pressure, and velocity. These hostile conditions cause thermal oxidation and surface deterioration leading to reduced component life. Surface deteriorations are caused from deposits formed by various contaminants present in the combustion gases. With depleting natural gas resources, the focus now is on using alternate fuels like coal derived synthetic gas for gas turbine operation. These alternate fuels are not as clean as natural gas, resulting in deposition, erosion, and/or corrosion on turbine airfoils. Hence, it is important to understand how surface distortions can affect the performance of film cooling.

During engine operation, contaminants in the hot gas path are in a molten state resulting in surface deposition that leads to film cooling hole blockage and oxidation of the metal surface as a result of spallation. The dominant delivery mechanism of the contaminants onto the surface depends on the size or state of the contaminant [1]. Since the region around the film cooling holes are at a relatively lower temperature, deposits tend to adhere to surfaces near the holes. In some cases the deposits on the surface extend into the film cooling holes and end up partially or completely blocking the holes. Also, deposits can detach from the surface peeling the thermal barrier coating (TBC) resulting in spallation.

Higher power outputs from the turbine require higher turbine inlet temperatures and increasing gas temperatures in turn increase the rate of deposition. This study is aimed at understanding which of these effects is more detrimental to film cooling adiabatic effectiveness levels. With the knowledge of which of these effects are more detrimental, cooling designs can be made to combat those effects. The work presented in this paper compares three different surface distortions on film cooling effectiveness including; surface deposition, film cooling hole blockage, and TBC spallation.

Relevant Past Studies

A number of studies in the literature have documented the effect of using alternate fuels on turbine surfaces. There are also studies showing the effect of surface roughness on film cooling. Only a few studies exist on the effect of blocked holes on film cooling effectiveness. In addition, there have been few studies simulating the effect of TBC spallation on film cooling effectiveness.

Studies concerning the effect of using coal and other solid fuels have focused on ash and other contaminant levels on deposition, corrosion, or erosion. A study by Wenglarz et al. [2] showed that high levels of ash, up to 40 t/year, can enter a turbine. DeCorso et al. [3] found that most coal derived fuels after conversion and purification had greater levels of impurity levels than those found in natural gas. They found that in natural gas sulfur levels are about 10 ppm, but a coal derived fuel after liquefaction and separation had about 1000 ppm of sulfur. Studies have also been carried out to see the effect of small amounts of ash flowing through a turbine. Moses and Bernstein [4] found that a fuel burning with 0.5% ash results in about 1.5 t/day of ash flowing through a turbine. A study by Wenglarz [5] yielded that the mass fraction of the ash particles adhering to surface and contributing to deposit buildup was 0.06 with an average particle diameter of 10 μm. Recent studies by Bons et al. [6] were carried out to study the effect of ash deposits present in coal fuels in an accelerated deposition test facility. They carried out their tests with ash particles at a slightly higher mean mass diameter of 13.3 μm than those found in coal fuels. For a test duration of 3 h, they found the net particle loading to be 165 ppmw/h (parts per million by weight per hour) resulting in an average deposit thickness of 1.3 mm.

Bonding of ash and other contaminants to turbine component surfaces is dependent on their surface properties [3]. Deposition of

---

Contributed by the International Gas Turbine Institute of ASME for publication in the Journal of Turbomachinery. Manuscript received July 17, 2006; final manuscript received July 25, 2006. Review conducted by David Wisler. Paper presented at the ASME Turbo Expo 2006: Land, Sea and Air (GT2006), Barcelona, Spain, May 8–11, 2006. Paper No. GT2006-90379.

contaminants and other particulate matter present in the mainstream gas takes place through impingement onto the surface. Typically in a gas turbine, the first rows of vanes are subjected to direct impingement resulting in particulate deposition [7]. The mechanism for this could be attributed to the fact that the particles are broken up and redistributed by impact [8]. Also, the leading edge film cooling regions on a vane endwall are more prone to deposition. Because this is the first cold surface the hot mainstream gas encounters before it enters a turbine and as mentioned before the molten contaminants would quench and adhere near the relatively colder regions. Bons et al. [9] showed through their turbine surface measurements that the leading edge region will have the greatest degradation. Also, actual turbine component measurements by Bons et al. [9], Taylor [10], and Tarada and Suzuki [11] revealed that all the regions of a turbine blade and vane are prone to deposition and roughness with varying levels.

A number of studies have been reported showing the effect of surface roughness on film cooling. Goldstein et al. [12] placed cylindrical roughness elements at the upstream and downstream location of film cooling holes on a flat plate. They observed that at low blowing rates, there is a decrease in adiabatic wall effectiveness by 10–20% over a smooth surface. However, at higher blowing rates they observed an enhancement of 40–50% in cooling performance. Schmidt et al. [13] did a similar study using conical roughness elements. They also found a higher degradation of film cooling effectiveness at lower momentum flux ratios than at higher momentum flux ratios. Barlow and Kim [14] studied the effect of a staggered row of roughness elements on adiabatic effectiveness. They found that roughness degraded cooling effectiveness compared to a smooth surface and the smaller elements caused a greater reduction than the larger elements.

There have been very few studies on the effect of roughness on endwall film cooling. In the study by Cardwell et al. [15], they showed that a uniformly rough endwall surface decreased cooling effectiveness at higher blowing ratios but at lower blowing ratios there was no significant change.

Not many studies are available in the literature showing the effect of blockage on film cooling effectiveness. The study done by Bunker [16] showed that for a partially blocked row of cylindrical holes there was significant degradation of local adiabatic effectiveness near the hole exit regions. The partial hole blockage was simulated by applying air plasma sprayed TBC over the holes without any protection. Bogard et al. [17] showed a cross section of a film cooling hole for an actual turbine part which depicted partial blockage of the hole downstream with the deposition extending outside of the hole.

Ekkad and Han [18,19] carried out heat transfer and film cooling measurements on a cylindrical model simulating TBC spallation. Ekkad and Han [18] found that spallation enhances heat transfer up to two times compared to a smooth surface. They also found that local heat transfer distributions were greatly affected by spallation depth and location. Ekkad and Han [19] found that higher freestream turbulence coupled with spallation greatly reduced film effectiveness. They found that spallation reduced film effectiveness inside the spallation cavity but increased it downstream of the spallation cavity.

In summary it is important to understand the effects of surface distortion due to contaminants present in fuel and combustion air. Though there have been many studies addressing the issue of surface deposition and surface distortion as a whole, there have been very few studies showing the effect of these distortions on a film cooled endwall.

Experimental Methodology

The experimental section was placed in a closed loop wind tunnel facility, as shown in Fig. 1. The flow encounters an elbow downstream of the fan and passes through a primary heat exchanger used to cool the bulk flow. The flow is then divided into three channels including the center passage and two cooled secondary passages located above and below the test section. Note that only the top secondary passage was used for this study. The primary core flow, located in the center passage, convects through a heater bank where the air temperature is increased to about 60°C. The secondary flow, in the outer passage, was cooled to about 20°C, thereby maintaining a temperature difference of 40°C between the primary and secondary flows. The secondary flow provided the coolant through the film cooling holes and through the leakage paths. Also, for all the tests carried out in this study a density ratio of 1.1 was maintained between the coolant and mainstream flows. Due to the fact that density ratios are not being matched to that of the engine, velocity ratios for the cooling holes will be significantly higher than those found in an engine for the same mass flux or momentum flux ratios. While there have been studies indicating that momentum flux scales jet liftoff for flat plate film cooling, it is unknown as to whether it best scales liftoff for endwall film cooling

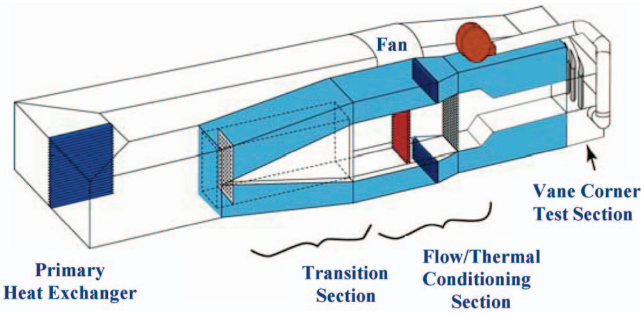

Fig. 1 Illustration of the wind tunnel facility

Downstream of the flow/thermal conditioning section is the test section that consists of two full passages with one center vane and two half vanes. Table 1 provides a description of turbine vane geometry and operating conditions. The vane geometry used in the current study is a commercial first-stage vane previously described by Colban et al. [20,21]. The passage under study consisted of an endwall surface with film cooling holes and leakage paths simulating the combustor-vane interface and vane-to-vane interface.

A detailed description of the endwall construction has been previously described by Knost and Thole [22] and Cardwell et al. [15], who used exactly the same film cooling and slot geometries as we used for this study. The endwall of the vane was constructed of foam because of its low thermal conductivity (0.033 W/m K). The endwall foam was 1.9 cm thick and was mounted on a 1.2 cm-thick Lexan plate. The cooling hole pattern on the endwall was cut with a five-axis water jet to ensure precision and integrity. The upstream slot was constructed with poplar wood as it had a low conductivity and was stiffer. The endwall surface was also covered with a 36 grit sandpaper to simulate a uniform surface roughness. Adiabatic endwall temperatures were measured for different flow rates through film cooling holes, through the

Table 1 Geometric and flow conditions

Scaling factor	9
Scaled up chord length (C)	59.4 cm
Pitch/chord (P/C)	0.77
Span/chord	0.93
Hole L/D	8.3
$\mathrm{Re}_{\mathrm{in}}$	2.1×10^5
Inlet and exit angles (deg)	0 and 72
Inlet, exit Mach number	0.017, 0.085
Inlet mainstream velocity	6.3 m/s
Upstream slot width	$0.024C$
Midpassage gap width	$0.01C$

combustor-to-turbine interface slot (referred to as upstream slot), and a constant flow rate through the vane-to-vane interface gap (referred to as midpassage gap).

The inlet turbulence intensity and length scales were measured to be 1.3% and 4 cm, respectively. For every test condition the dimensionless pressure coefficient distribution was verified to ensure periodic flow through the passages. Three separate plenums were used to control the flow rate through the film cooling holes, through the upstream slot, and through the midpassage gap. A global blowing ratio was calculated using an inviscid blowing ratio along with a global discharge coefficient, C_D, that was obtained from computational fluid dynamics (CFD) studies (as reported by Knost and Thole [23]).

The upstream slot flow was assumed to have a discharge coefficient of 0.6 which is the assumed value for a flow through a sharp-edged orifice and the flow rate was calculated accordingly. Flow through the midpassage gap was measured directly using a laminar flow element (LFE). In this study coolant flow rates are reported in terms of percent coolant mass flow rate per total passage mass flow rate for one vane pitch. Typical times to achieve steady-state conditions were 3 h.

Instrumentation and Temperature Measurements. A FLIR P20 infrared camera was used to spatially resolve adiabatic wall temperatures on the endwall. Measurements were taken at six different viewing locations to ensure that the entire endwall surface was mapped. The camera was placed perpendicular to the endwall surface at a distance 55 cm from the endwall. Each picture covered an area 24 cm by 18 cm with the area being divided into 320 by 240 pixel locations. The spatial integration of the camera was 0.715 mm (0.16 hole diameters). Thermocouples were also placed on the endwall surface at different locations to directly measure the temperature to post-calibrate the infrared images. For the post-calibration the emissivity was set at a constant value of 0.92 and the background temperature (~45°C) was adjusted until the temperatures from the infrared camera images were within 0.05°C of the corresponding thermocouple data. Six images were taken at each of the viewing locations to obtain an averaged picture using an in-house Matlab program. The same program was also used to assemble the averaged pictures at all locations to give a complete temperature distribution along the passage endwall.

Freestream temperatures were measured at multiple locations along the pitch and the average was determined by using a thermocouple rake consisting of three thermocouples along the span. It was found that the variations along the pitch were less than 0.2°C and that along the span were less than 1.5°C. Voltage outputs from the thermocouples were acquired by a 32 channel data acquisition module that was used with a 12-bit digitizing card. The temperature data were compiled after the system reached steady state.

A one-dimensional (1D) conduction correction as described by Ethridge et al. [24] was applied to all adiabatic effectiveness measurements. This correction involved measuring the endwall surface effectiveness with no blowing through the film cooling holes. This was done by blocking the film cooling holes on the endwall passage under study while maintaining similar flow rates through the adjacent passage to insure the correct boundary condition under the endwall. The resulting η correction was found to be 0.16 at the entrance for a η value of 0.9 and 0.02 at the exit region at a measured η value of 0.5.

Experimental Uncertainty. An uncertainty analysis was performed on the measurements of adiabatic effectiveness using the partial derivative method described at length by Moffat [25]. The precision uncertainty was determined by taking the standard deviation of six measurement sets of infrared (IR) camera images with each set consisting of six images. The precision uncertainty of the measurements was ±0.014°C. The bias uncertainty was ±1.0°C based on the uncertainty in the IR camera measurements specified by the manufacturer. The bias uncertainty of the thermocouples was ±0.5°C. The total uncertainty was then calculated as ±1.02°C for the images and ±0.51°C for the thermocouples. Uncertainty in effectiveness, η, was found based on the partial derivative of η with respect to each temperature in the definition and the total uncertainty in the measurements. Uncertainties in adiabatic effectiveness were calculated to be $\partial\eta = \pm 0.0303$ at a η value of 0.2 and $\partial\eta = \pm 0.0307$ at a η value of 0.9.

Simulations of Surface Distortions

Direct surface measurements on turbine engine hardware reported by Bons et al. [9], Taylor [10], and Tarada and Suzuki [11] all indicated an increase in surface roughness with an increase in turbine operational hours. Measurements by Taylor [10] were made on a blade with rms roughness heights varying from 30 μm to 50 μm. His measurements also revealed that the maximum peak-to-valley height of 79 μm at the leading edge was higher than at other regions of the blade. Tarada and Suzuki [11] did measurements on industrial and aero-engine blades. They also found that the specimens measured a higher distortion at the leading edge areas with a roughness center line average as high as 85 μm.

Most surface roughness measurements were done on engine blades with very little data available in the literature on measurements done on a vane and no data available for hardware used with synfuels. Bons et al. [9] performed measurements on vanes and blades of an actual land based gas turbine engine. Their findings also reported that on an average the roughness on the leading edge is greater than at the trailing edge. Their maximum roughness height (R_t) at different locations varied from 20 μm to as high at 440 μm.

For this simulation, the measurements completed by Bons et al. [9] were referenced and scaled up to match realistic vane endwall distortions. All the measurements done by Bons et al. [9] were represented in terms of center-line average roughness (R_a), rms roughness (R_q), and maximum peak to valley distance (R_t). Studies by Bogard et al. [17] showed that it is appropriate to represent uniform surface roughness in terms of equivalent sand grain roughness (k_s) instead of R_a. As this study primarily focuses on the effects of localized distortions on endwall film cooling effectiveness the authors thought that it be more appropriate to represent the deposit heights in terms of R_t. Bons et al. [9] measured an R_t value of 258 μm on the endwall surface and the simulated deposit heights on our endwall corresponded to 253 μm, 406 μm, and 609 μm at engine scale.

Even though deposits on an actual vane endwall do not have a characteristic shape and size, a methodical approach was taken to simulate cooling hole distortions by molding specific deposits with definable shapes and sizes. The endwall deposits (shown in Fig. 2(*a*)) were all semi-elliptical with varying minor radii (in the wall-normal direction) of 0.5*D*, 0.8*D* and 1.2*D*. As mentioned before, the heights at engine scale corresponded to 253 μm, 406 μm, and 609 μm, respectively. The streamwise length of all deposits was 2*D*.

The deposits were manufactured by injecting epoxy gel into a mold made of aluminum. The epoxy was allowed to dry in the mold for about 10 min before it was peeled out of the mold and left to dry until it was rigid enough to be placed onto the endwall. The dried epoxy was sprayed with adhesive to provide a sticky surface whereby sand was sprinkled on top of the deposit to make the surface rough. As mentioned previously the endwall surface was covered with a 36 grit sand paper [15] with an equivalent sand grain roughness (k_s) value of 0.42 mm at engine scale. Finally, the deposit was painted black and secured onto the sandpaper using a double sided tape.

The cooling hole blockages were manufactured similar to the deposits conforming to the required dimensions. Figure 2(*b*) shows the cross-sectional view of a blocked film cooling hole. The holes were blocked in such a manner as to reduce the exit hole

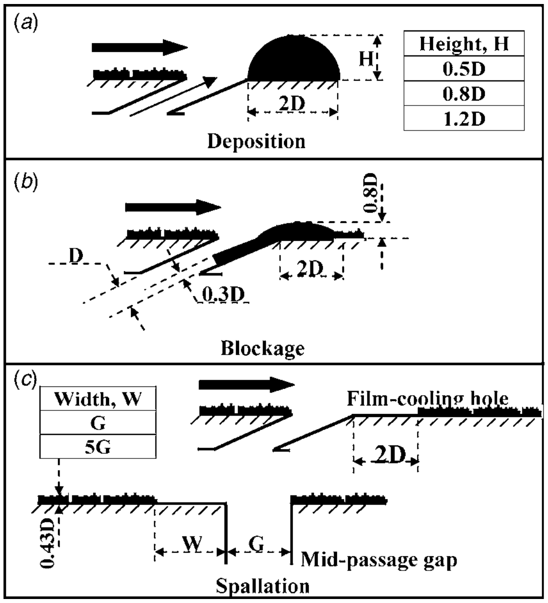

Fig. 2 Schematic of the surface distortions simulated on the endwall surface

area by 25%. The deposit extended one hole diameter into the hole and extended two hole diameters downstream of the cooling hole exit.

The sandpaper on the endwall simulating the uniform roughness corresponded to a thickness of 0.43*D* or 220 μm at engine scale. In most land-based gas turbine vanes and blades the TBC thickness is on the order of about 300 μm. As such, to simulate a spalled endwall the sand paper was removed from the surface to the specified width as shown in Fig. 2(*c*).

Because the mainstream gas flows from the pressure side to the suction side, heavy particles in the flow deposit along the pressure side surface and in the stagnation region. Considering these findings, the film cooling row at the leading edge region of the vane endwall was chosen to carry out deposition, blockage, and spallation studies, as shown in Fig. 3(*a*). In addition, deposition was also studied along the pressure side cooling holes and spallation was studied along the length of the midpassage gap.

Discussion of Results

Two baseline cases were measured whereby these included one with upstream slot coolant and one without upstream slot coolant. For the deposition and spallation studies, the upstream slot leakage flow was present. Blockage studies were done for the case without any upstream slot coolant flow. Figures 3(*a*)–3(*e*) show the surface distortions, the complete endwall contour, and the two baseline cases for this study. Figures 3(*c*)–3(*e*) compare lateral average effectiveness and contours of the two baseline cases only at the leading edge region. Adiabatic effectiveness levels were laterally averaged across the pitch (boxed region) from upstream of the cooling holes at a location $X/C=-0.05$, to a downstream location at $X/C=0.05$. It is important to note that for the baseline cases the endwall surface did not have localized surface distortions but did have a uniform surface roughness covering the entire endwall surface [15]. The coolant mass flow rate for the baseline cases was set at 0.5% of the core flow through the film cooling holes and 0.2% through the midpassage gap. For the baseline case with the upstream slot flow, 0.75% of the core flow passed through the upstream slot.

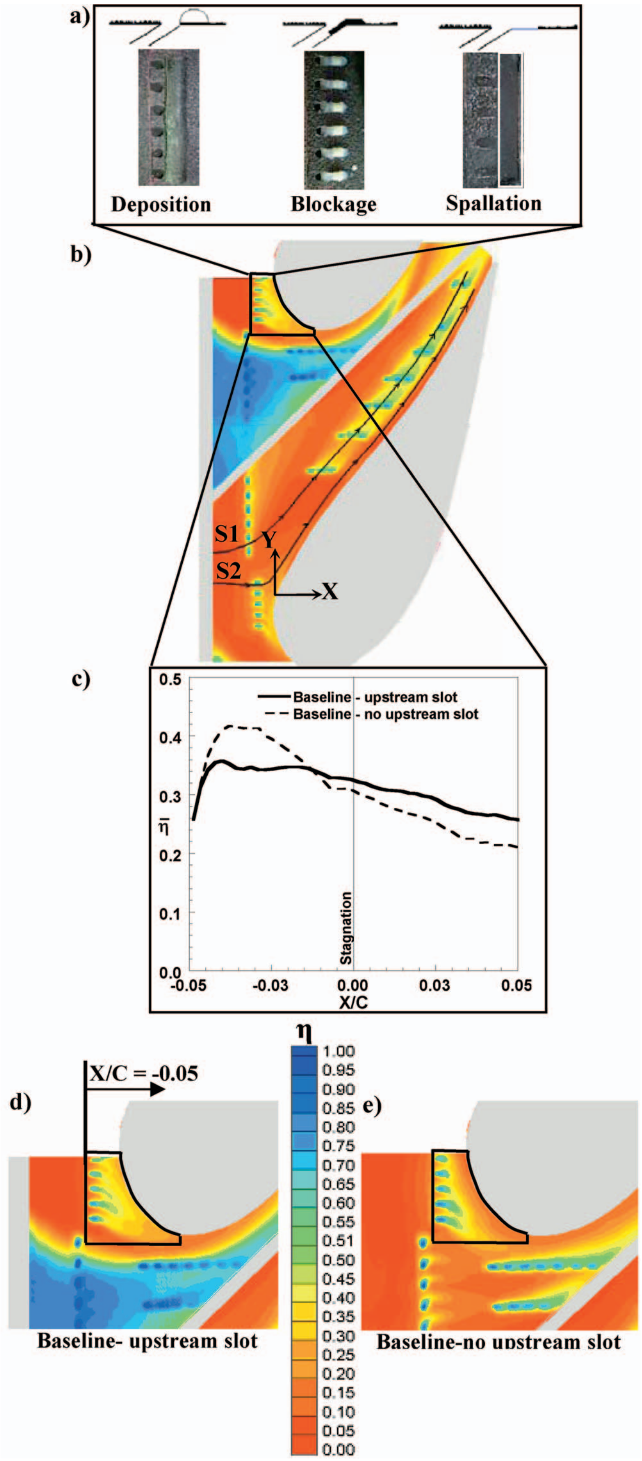

Fig. 3 Illustration of: (*a*) surface distortions simulated at leading edge; (*b*) baseline case with upstream slot flow; (*c*), (*d*), and (*e*) lateral average and effectiveness contours of the two baseline cases

There are some clear differences between the cases with and without upstream slot flow in terms of jet penetration towards the leading edge–endwall juncture as shown in Figs. 3(*d*) and 3(*e*). In the case where the slot flow is present, the cooling jets convect closer to the stagnation region. This may be due to the fact that just upstream of the holes the endwall boundary layer is most likely ingested into the upstream slot giving only a thin boundary layer thickness approaching the holes. The thinner boundary layer minimizes any horseshoe vortex formation which causes the coolant to be swept away from the endwall. It can be seen in Fig. 3(*e*)

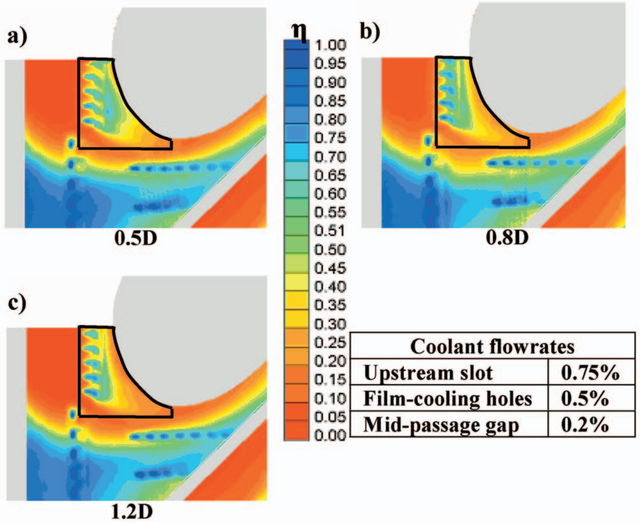

Fig. 4 Effectiveness contours comparing the effects of different deposit heights at the leading edge region

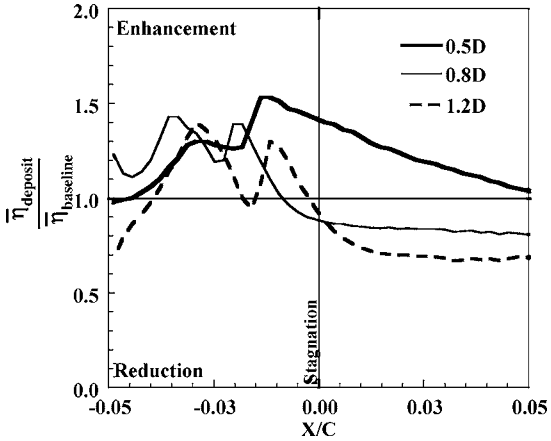

Fig. 5 Augmentation of laterally averaged effectiveness due to different deposit heights

that without the upstream slot flow, the horseshoe vortex effect is more dominant, resulting in the formation of a hot band around the stagnation region.

Deposition Studies. Figures 4(*a*)–4(*c*) show the local adiabatic effectiveness for different deposit heights at the leading edge region. For these cases, the coolant mass flow rates were 0.75% ($M_{\text{in}}=0.3$) through the upstream slot, 0.5% ($M_{\text{in}}=1.5$) through the film cooling holes, and 0.2% ($M_{\text{in}}=0.1$) through the midpassage gap.

Figure 3(*d*) shows that for the baseline case without any deposition downstream, the coolant from the leading edge holes was swept around the endwall junction from the stagnation region to the suction side. By placing a deposit that is 0.5*D* in height (refer to Fig. 4(*a*)) downstream of the cooling row, the coolant levels were much improved. The reason for this improved cooling is attributed to the fact that the coolant impacts the raised deposit as the jet is slightly separated from the wall for the baseline case. Moreover, it is speculated that a Coanda effect further contributes to the improvement, causing the coolant to move toward the endwall surface. With the increase in deposit height to 0.8*D* (refer to Fig. 4(*b*)), the coolant flow stagnates and is then deflected from the surface, thereby reducing the cooling effectiveness relative to that of the 0.5*D* case. In comparing Figs. 4(*b*) and 4(*c*) it can be seen that an increase in deposit height to 1.2*D* brought about the same effect for both deposit heights of 0.8*D* and 1.2*D*.

The above effects can be further quantified by looking at the lateral average plots. Figure 5 shows the change in laterally averaged adiabatic effectiveness between the deposit cases, relative to the baseline case. Note that the values greater than one are enhancements in effectiveness levels and less than one are reductions in effectiveness levels. Effectiveness was laterally averaged across the pitch downstream of the leading edge film cooling row as shown in Figs. 3(*b*) and 3(*c*). It can be seen that at a deposit height of 0.5*D* there is an overall enhancement of cooling effectiveness. The initial peak near the exit of the cooling holes is due to the obstruction and collection of the coolant flow caused by the deposit. Though there is decay in the enhancement of cooling effectiveness as the flow proceeds toward the vane–endwall junction it can be clearly seen that a deposit of height 0.5*D* enhances the overall cooling effectiveness. Figure 5 also shows that for deposits of height 0.8*D* and 1.2*D*, there is an improvement in effectiveness in the near hole region, but due to jet liftoff there is a sudden decrease with reduced cooling relative to the baseline case as the coolant flows toward the vane–endwall junction.

Deposition studies were also carried out along the pressure side cooling rows. For these tests a constant deposit height of 0.8*D* was used. Figures 6(*a*)–6(*c*) compare the adiabatic effectiveness along the pressure side cooling holes with deposits placed at the downstream, upstream, and on both sides of the cooling rows (indicated in the contours with lines). Note that the upstream deposits were similar to downstream deposits (Fig. 2(*a*)) except that the deposits were placed upstream of the cooling hole rows. Both sides refer to placing deposits on both downstream and upstream of the cooling hole rows. Downstream deposits shown in Fig. 6(*a*) deflected the cooling jets towards the vane–endwall junction,

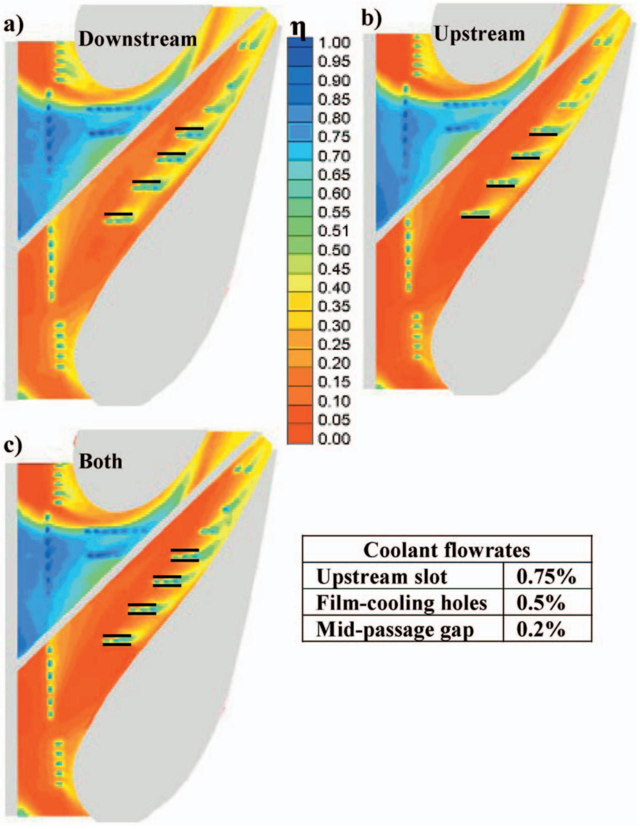

Fig. 6 Contours comparing the effects of pressure side deposition: (*a*) downstream; (*b*) upstream; and (*c*) downstream and upstream of holes

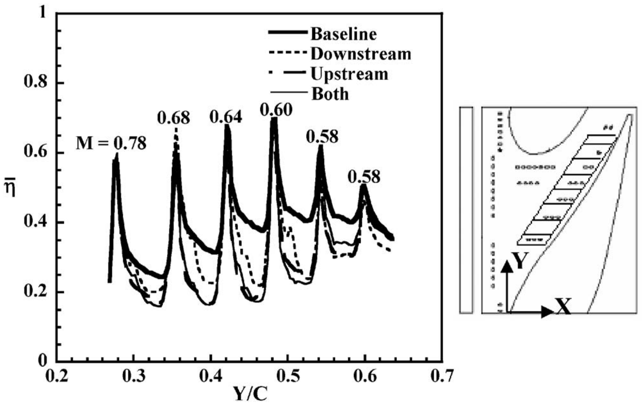

Fig. 7 Laterally averaged effectiveness along pressure side (boxed region on the right shows the averaged area)

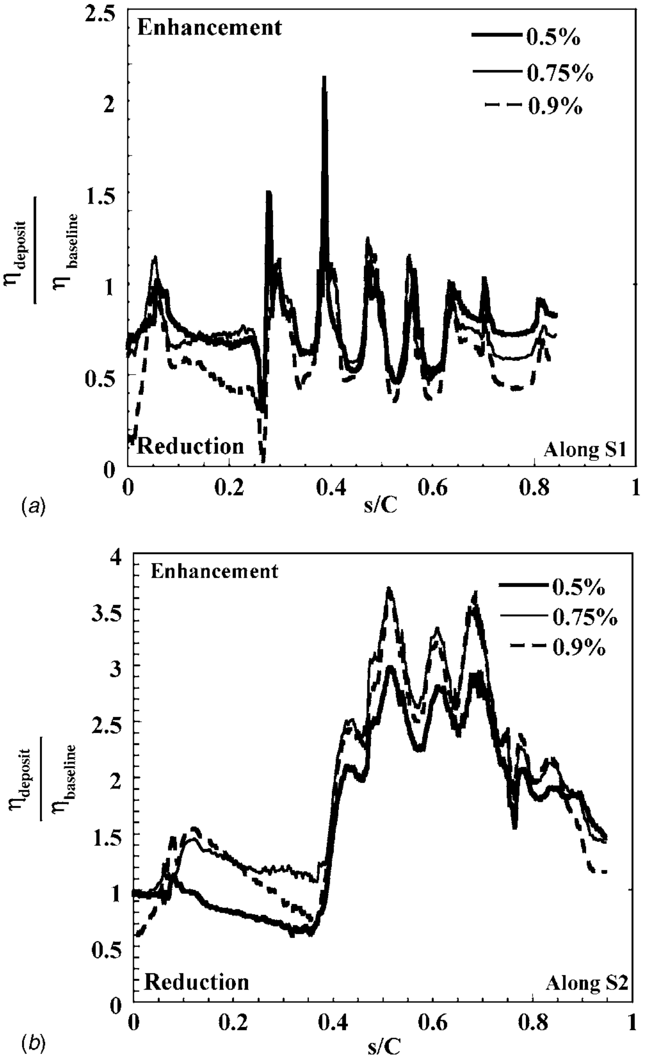

(*a*)

(*b*)

Fig. 8 Change in adiabatic effectiveness levels along streamlines S1 and S2 (refer to Fig. 3(*b*)) for deposits on both sides of the cooling rows

which is the direction that the jets are directed. As the coolant is directed more toward the juncture, there is an overall reduction in the cooling downstream of each row (compare with Fig. 3(*b*)). Upstream deposits (Fig. 6(*b*)) tended to cause the jets to have the same trajectory, but also cause a larger reduction in film cooling effectiveness relative to the downstream deposits. Similar to these results, placing deposits on both sides of the cooling rows (Fig. 6(*c*)) resulted in the bulk of the coolant getting even more streamlined toward the vane–endwall junction. From Fig. 3(*b*) it can be seen that for the baseline case, the coolant from the pressure side flowed toward the suction side increasing effectiveness levels downstream of the cooling rows. By placing deposits in this region the coolant was redirected toward the vane–endwall junction causing a reduction in the effectiveness levels downstream of the cooling rows. Though deposits at every location deflected the coolant, upstream deposition was found to cause the most severe reduction in adiabatic effectiveness.

The above effects can be quantified by comparing the laterally averaged adiabatic effectiveness. In this region effectiveness was laterally averaged streamwise as shown in Fig. 7. Shown in Fig. 7 are the laterally averaged local blowing ratios for each row of holes along the pressure side. Note that CFD results were used to quantify the local coolant flows from each cooling hole and the local static pressure was used to calculate the local freestream velocity that was used in the blowing ratio definition. It was seen that deposits upstream of the holes and on both sides of the cooling holes caused similar and higher degradation than deposits placed downstream of the cooling rows. Note that the deposits were placed on the first four cooling hole rows, but the effects are present on all the rows on the pressure side. It can be concluded that upstream deposition resulted in higher degradation than deposits at the downstream of the film cooling holes. This conclusion can be generated because the deposits on both upstream and downstream have nearly the same degradation as the upstream deposits alone.

As the coolant jets were directed toward the pressure–surface endwall junction, it was important to quantify the change in adiabatic effectiveness along flow streamlines passing through the cooling holes and also along the pressure–surface endwall junction. Figures 8(*a*) and 8(*b*) show the variation of adiabatic effectiveness along the flow streamlines at different film cooling flow rates with deposits placed on both sides of the cooling rows. Variation in adiabatic effectiveness was measured along two streamlines; S1 and S2 as shown in Fig. 3(*b*). The flow streamlines were computationally predicted at 2% span from the endwall surface using FLUENT 6.1.2. Figure 8(*a*) shows that by placing deposits on both upstream and downstream locations the adiabatic effectiveness levels decreased by about 50% along S1 for 0.5% film cooling mass flow rate. A similar effect was seen for 0.75% ($M_{\text{in}}=2.2$) and 0.9% ($M_{\text{in}}=2.7$) flow rate through the film cooling holes though there was a higher reduction at a mass flow rate of 0.9%.

As mentioned earlier, in the presence of deposits on both sides of the cooling rows the coolant was streamlined toward the vane–endwall junction. This was further quantified by measuring the adiabatic effectiveness along streamline S2 as shown in Fig. 8(*b*). It was seen that there was a twofold increase in adiabatic effectiveness levels in the presence of deposits along S2 for the nominal flow rate of 0.5% through the film cooling holes. A further increase in coolant mass flow rate to 0.75% and 0.9% increased the effectiveness levels nominally by 25%. Hence, it was seen that deposition on the pressure side decreased effectiveness downstream of the cooling rows, but increased the effectiveness levels along the vane–endwall junction.

Hole Blockage Studies. Partial blockages of film cooling holes were simulated at the leading edge film cooling row as mentioned previously. Tests were carried out by sequentially blocking each one of the five film cooling holes in the stagnation region though results are presented only for one hole, two hole, and five hole blockages. Similar to the other cases, the coolant mass flow rate for the baseline case for this study was set at 0.5% film cooling

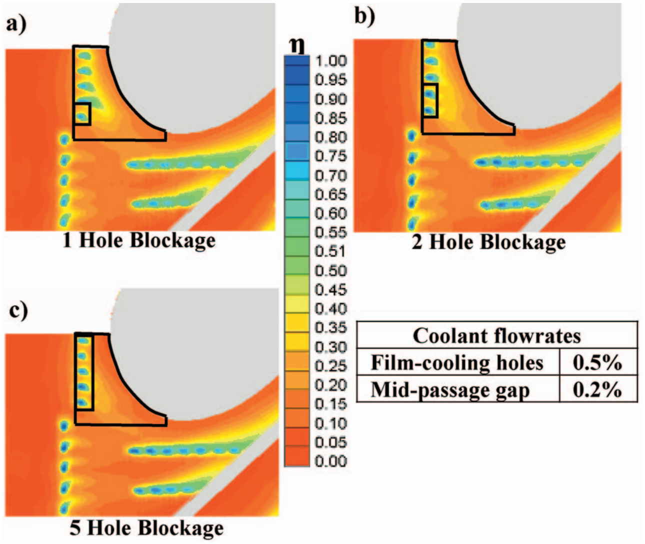

Coolant flowrates	
Film-cooling holes	0.5%
Mid-passage gap	0.2%

Fig. 9 Contours showing the effect of film cooling hole blockage on adiabatic effectiveness

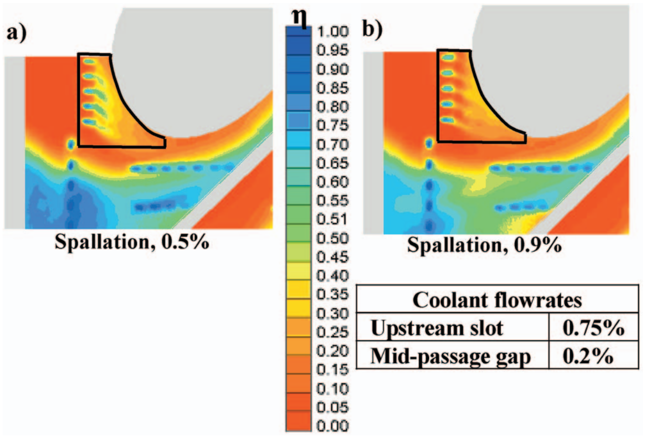

Coolant flowrates	
Upstream slot	0.75%
Mid-passage gap	0.2%

Fig. 11 Effectiveness contours showing the effect of leading edge spallation at 0.5% and 0.9% film cooling flow rate

holes, 0.2% midpassage gap, and no coolant injected through the upstream slot. There was no flow through the upstream slot as it was important to isolate any effect of the upstream flow at the leading edge cooling near the stagnation region.

Figures 9(*a*)–9(*c*) compare the adiabatic effectiveness contours with different number of holes partially blocked. The blockage extended one cooling hole diameter into the film cooling holes with a net flow area reduction of 25% at the cooling hole exit. Note that the same pressure ratio was used for the baseline and for the cases with blocked holes. Indicated with boxes in Figs. 9(*a*)–9(*c*) are the holes that are blocked. It can be seen that there is a dramatic decrease in effectiveness level with the increase in the number of holes being blocked as the coolant from the holes ceases to flow onto the endwall. The main reason for this is that when a hole is partially blocked, the momentum of the jet and the trajectory of the jet is increased, which causes the coolant to exit at a higher exit angle promoting separation. In this particular test the coolant from the partially blocked hole tended to flow directly into the mainstream resulting in lower adiabatic effectiveness on the endwall surfaces.

Figure 10 compares the degradation in laterally averaged effectiveness due to film cooling hole blockage. It can be seen that with the increase in the number of holes being partially blocked from 1 to 5 the laterally averaged effectiveness degrades from about 20% to about 50% of the baseline, respectively. It can be also seen that at upstream of the leading edge cooling holes (at $X/C=-0.05$) the effectiveness levels are higher due to the change in coolant jet trajectory caused by hole blockages. The study done by Bunker [16] showed a similar reduction of about 40% in the centerline adiabatic effectiveness for a row of blocked film cooling holes on a flat plate.

Spallation Studies. TBC spallation was simulated downstream of the leading edge film cooling row and also along the midpassage gap. The coolant mass flow rates for the baseline case for this study were set at 0.75% upstream slot, 0.5% film cooling holes, and 0.2% midpassage gap. Figures 11(*a*) and 11(*b*) compare the contours of adiabatic effectiveness of a spalled leading edge surface at film cooling mass flow rates of 0.5% and 0.9%.

The spalled endwall surface downstream of the cooling holes caused the coolant to flow over a forward facing step. This resulted in flow recirculation and prevented the coolant from sweeping across the vane–endwall junction. It was seen that at a mass flow rate of 0.5% although the near hole region is sufficiently cooled, effectiveness levels along the vane–endwall junction were relatively lower than the baseline case. By increasing the coolant mass flow rate to 0.9% the effectiveness levels were further reduced due to the combined effect of spallation and coolant jet liftoff of the surface.

Figure 12 compares the degradation in laterally averaged effectiveness due to spallation at the leading edge region. It can be seen

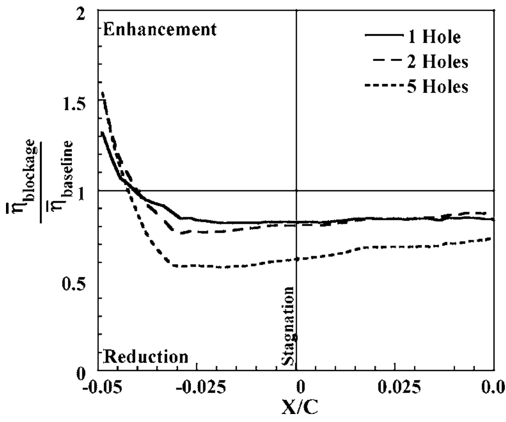

Fig. 10 Laterally averaged effectiveness showing the effect of hole blockages at the leading edge

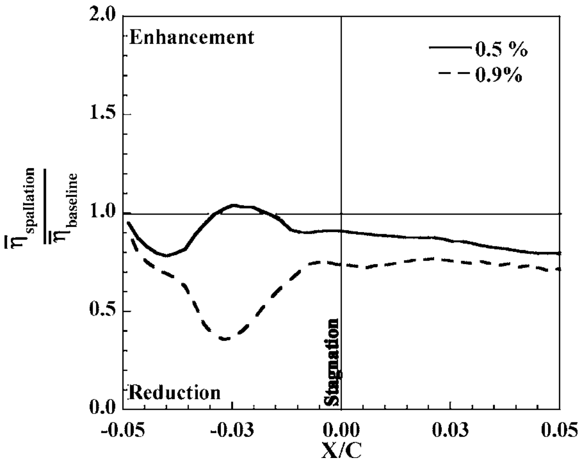

Fig. 12 Laterally averaged effectiveness showing the effect of leading edge spallation at different film cooling flow rates

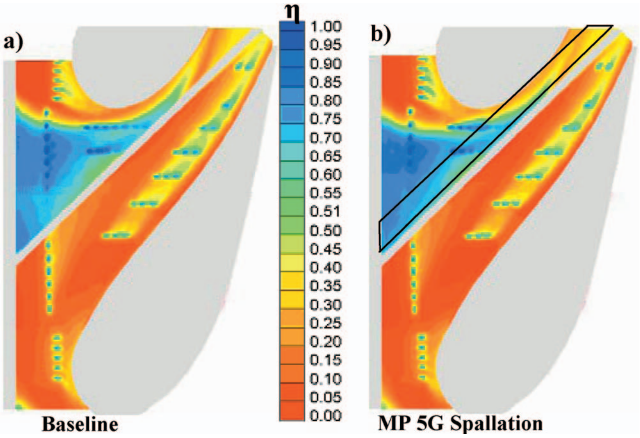

Fig. 13 Contours showing the effect of spallation along midpassage on endwall adiabatic effectiveness

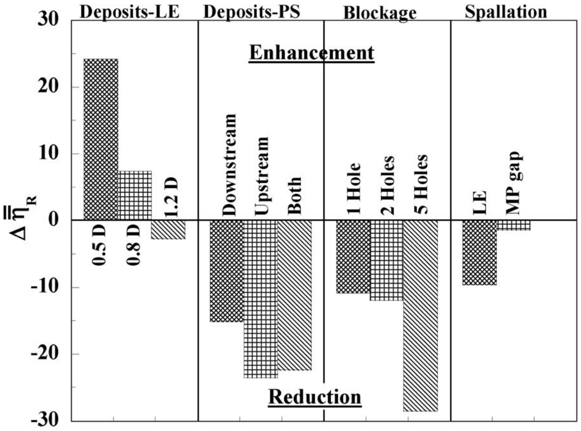

Fig. 14 Comparison of percent reduction on area-averaged adiabatic effectiveness due to surface distortions

that at a mass flow rate of 0.5%, the near hole regions have similar effectiveness levels as the baseline, but effectiveness levels decrease by about 20% near the vane–endwall region. At higher mass flow rate of 0.9%, due to jet liftoff, there is a reduction of about 50% downstream of cooling holes. Effectiveness levels increase near the junction due to jet reattachment, though these levels are still lower than the levels occurring in the baseline case. Note that the cooling holes lie between $-0.05 < X/C < -0.034$ and the spalled surface extends from $X/C = -0.034$ to $X/C = -0.02$.

Figures 13(*a*) and 13(*b*) compare the adiabatic effectiveness levels of the baseline and an endwall surface spalled five gap widths ($5G$) along the midpassage gap. The study by Cardwell et al. [15], showed that due to the presence of the midpassage gap, coolant from the upstream slot flows toward the suction side negating the need for endwall cooling in that region. Even though the surface was spalled along the midpassage gap there seemed to be no effect on the overall endwall effectiveness resulting from the large coolant flow over this region. It can be seen from Figs. 13(*a*) and 13(*b*) that the coolant from the upstream slot has the same coverage area and there is no significant reduction in adiabatic effectiveness levels. For the spallation studies along midpassage gap, tests were also carried out for smaller spalled regions. These tests also showed that spallation along midpassage gap had little effect on endwall effectiveness.

Summary of Cooling Reductions

The two factors that are important to quantify the effects of surface distortions are the film cooling effectiveness levels and heat transfer coefficients. This study focused primarily on film cooling effectiveness alterations due to surface distortion factors. It is important to understand which surface distortion brought about the maximum reduction in cooling effectiveness. This was done by calculating the percent reduction in area-averaged effectiveness. Figure 14 shows the combined effectiveness reduction for each endwall distortion study. This plot allows one to assess which is the most degrading effect.

Deposition studies had varied results. Deposits improved effectiveness at the leading edge, whereas along the pressure side deposits resulted in reducing the film cooling effectiveness. A very interesting result was observed that deposits directly downstream of the leading edge cooling row enhanced film cooling effectiveness at lower deposit heights ($0.5D$ and $0.8D$) and caused little reduction in effectiveness levels at a deposit of height $1.2D$. Along the pressure side it was seen that depositions typically degraded effectiveness levels downstream of the cooling rows by redirecting the coolant toward the vane–endwall junction. The reason for the degradation along the pressure side is because the jets are more attached to the surface and are easily deflected by deposits.

The maximum reduction in cooling effectiveness at the leading edge region was caused by film cooling hole blockages. At a mass flow rate of 0.5%, with the increase in the number of holes being blocked, the percent reduction in cooling effectiveness also increased. Blocking one and two holes brought similar effectiveness reductions, but with five holes blocked the effectiveness was significantly reduced by about 30%. This reduction in effectiveness due to blockages was expected given the lack of jet penetration.

Spallation along the midpassage gap had little to no effect on the overall endwall effectiveness, but spallation downstream of the leading edge film cooling row reduced the cooling effectiveness by about 10%.

Conclusions

Measurements of adiabatic effectiveness were presented for an endwall surface with simulated surface distortions namely, surface deposition, film cooling hole blockage, and TBC spallation. When the effects of these distortions were compared at the leading edge region, it was found that partial hole blockage and TBC spallation caused a higher reduction in adiabatic effectiveness levels than surface deposition.

Near hole depositions were studied with varying deposit heights and it revealed very interesting results. For a smaller deposit height of $0.5D$ the overall film cooling effectiveness downstream of the film cooling row was enhanced by about 25%. These deposits tended to deflect the coolant toward the endwall surface. With an increase in deposit height to $1.2D$ the coolant jet tends to lift off, lowering the film cooling effectiveness. Deposition along the pressure side lowered the effectiveness between successive cooling rows, but enhanced the effectiveness along the vane–endwall junction.

Hole blockage studies showed that partially blocked holes have the greatest detrimental effect on degrading film cooling effectiveness downstream of a film cooling row. At low blowing ratios, partially blocking five film cooling holes reduced film cooling effectiveness by about 30% and blocking a single hole resulted in a reduction in effectiveness of about 10%. Spallation studies conducted at the leading edge film cooling row showed a reduction in effectiveness of about 10%. Past studies have shown that spallation near film cooling holes is a significant form of surface distortion and hence it is very important to consider its effect while designing endwall cooling arrangements. Spallation was also studied along the midpassage gap which showed very little to no effect in endwall cooling effectiveness.

This study has shown the effects that cooling hole blockages can have on reducing endwall effectiveness levels. These effects should be considered in determining improved film cooling designs so that partial hole blockages can be avoided on turbine components.

Acknowledgment

This paper was prepared with the support of the US Department of Energy, Office of Fossil Fuel, and National Energy Technology Laboratory. However, any opinions, findings, conclusions, or recommendations expressed herein are solely those of the authors and do not necessarily reflect the views of the DOE. The authors would also like to specially thank Nick Cardwell for building and instrumenting the test section. The authors also thank Mike Blair (Pratt & Whitney), Ron Bunker (General Electric), and John Weaver (Rolls-Royce) for their input on the modeling of realistic turbine features.

Nomenclature

C = true chord of stator vane
D = diameter of film cooling hole
G = mid passage gap width
k_s = equivalent sand grain roughness
L = length of mid passage gap
LE = leading edge
M = local mass flux/blowing ratio, $M=\rho_j U_j/\rho_\infty U_\infty$
M_{in} = blowing ratio based on inlet mainstream velocity
MP = midpassage
P = vane pitch; hole pitch
PS = pressure side
Re_{in} = Reynolds number defined as $\text{Re}_{\text{in}}=CU_{\text{in}}/\nu$
R_a = center-line average roughness
R_q = rms roughness
R_t = maximum peak to valley distance
s = distance measured along a streamline
S = span of stator vane
T = temperature
X,Y,Z = local coordinates
U = velocity

Greek

η = adiabatic effectiveness, $\eta=(\text{T}_\infty-\text{T}_{\text{aw}})/(\text{T}_\infty-\text{T}_{\text{c}})$
$\bar{\eta}$ = laterally averaged effectiveness
$\bar{\bar{\eta}}$ = area-averaged effectiveness
$\Delta\bar{\bar{\eta}}_R$ = percent reduction in area-averaged effectiveness, $\Delta\bar{\bar{\eta}}_R=[(\bar{\bar{\eta}}_{\text{effect}}-\bar{\bar{\eta}}_{\text{baseline}})/\bar{\bar{\eta}}_{\text{baseline}}]\times 100$
ν = kinematic viscosity

Subscripts

aw = adiabatic wall
c = coolant conditions
in = inlet conditions
j = coolant flow through film cooling holes
∞ = local freestream conditions
R = reduction

References

[1] Wenglarz, R. A., 1985, "Deposition, Erosion, and Corrosion Protection for Coal-Fired Gas Turbines," ASME Paper No. 85-IGT-61.
[2] Wenglarz, R. A., Nirmalan, N. V., and Daehler, T. G., 1995, "Rugged ATS Turbines for Alternate Fuels," ASME No. 95-GT-73.
[3] Decorso, S. M., Newby, R. A., Anson, D., Wenglarz, R. A., and Wright, I. G., 1996, "Coal/Biomass Fuels and the Gas Turbine: Utilization of Solid Fuels and Their Derivatives," ASME No. 96-GT-76.
[4] Moses, C. A., and Bernstein, H. L., 1996, "Fuel-Specification Considerations for Biomass Pyrolysis Liquids to be Used in Stationary Gas Turbines," ASME No. 96-GT-406.
[5] Wenglarz, R. A., 1992, "An Approach for Evaluation of Gas Turbine Deposition," ASME J. Eng. Gas Turbines Power, **114**, pp. 230–234.
[6] Bons, J. P., Corsby, J., Wammack, J. E., Bentley, B. I., and Fletcher, T. H., 2005, "High Pressure Turbine Deposition in Land Based Gas Turbines From Various Synfuels," ASME No. GT2005-68479.
[7] Bornstein, N. S., 1996, "Reviewing Sulfidation Corrosion—Yesterday and Today," JOM, **48**(11), pp. 37–39.
[8] Wright, I. G., Leyens, C., and Pint, B. A., 2000, "An Analysis of the Potential for Deposition, Erosion, or Corrosion in Gas Turbines Fueled by the Products of Biomass Gasification or Combustion," ASME No. 2000-GT-0019.
[9] Bons, J. P., Taylor, R. P., McClain, S. T., and Rivir, R. B., 2001, "The Many Faces of Turbine Surface Roughness," J. Turbomach., **123**, pp. 739–748.
[10] Taylor, R. P., 1990, "Surface Roughness Measurements on Gas Turbine Blades," J. Turbomach., **112**, pp. 175–180.
[11] Tarada, F., and Suzuki, M., 1993, "External Heat Transfer Enhancement to Turbine Blading Due to Surface Roughness," ASME No. 93-GT-74.
[12] Goldstein, R. J., Eckert, E. R. G., and Chiang, H. D., 1985, "Effect of Surface Roughness on Film Cooling Performance," J. Eng. Gas Turbines Power, **107**, pp. 111–116.
[13] Schmidt, D. L., Sen, B., and Bogard, D. G., 1996, "Effects of Surface Roughness on Film Cooling," ASME No. 96-GT-299.
[14] Barlow, D. N., and Kim, Y. W., 1995, "Effect of Surface Roughness on Local Heat Transfer and Film Cooling Effectiveness," ASME No. 95-GT-14.
[15] Cardwell, N. D., Sundaram, N., and Thole, K. A., 2005, "Effects of Mid Passage Gap, Endwall Misalignment, and Roughness on Endwall Film Cooling," J. Turbomach., **128**, pp. 62–70.
[16] Bunker, R. S., 2000, "Effect of Partial Coating Blockage on Film Cooling Effectiveness," ASME No. 2000-GT-0244.
[17] Bogard, D. G., Schmidt, D. L., and Tabbita, M., 1998, "Characterization and Laboratory Simulation of Turbine Airfoil Surface Roughness and Associated Heat Transfer," J. Turbomach., **120**, pp. 337–342.
[18] Ekkad, S., and Han, J. C., 1997, "Detailed Heat Transfer Distributions on a Cylindrical Model With Simulated TBC Spallation," AIAA Paper No. 97-0595.
[19] Ekkad, S. V., and Han, J. C., 2000, "Film Cooling Measurements on Cylindrical Models With Simulated Thermal Barrier Coating Spallation," J. Thermophys. Heat Transfer, **14**(2), pp. 194–200.
[20] Colban, W. F., Thole, K. A., and Zess, G., 2002, "Combustor-Turbine Interface Studies: Part 1: Endwall Measurements," J. Turbomach., **125**, pp. 193–202.
[21] Colban, W. F., Thole, K. A., and Zess, G., 2002, "Combustor-Turbine Interface Studies: Part 2: Flow and Thermal Field Measurements," J. Turbomach., **125**, pp. 203–209.
[22] Knost, D. G., and Thole, K. A., 2004, "Adiabatic Effectiveness Measurements of Endwall Film Cooling for a First Stage Vane," J. Turbomach., **127**, pp. 297–305.
[23] Knost, D. G., and Thole, K. A., 2003, "Computational Predictions of Endwall Film Cooling for a First Stage Vane," ASME No. GT2003-38252.
[24] Ethridge, M. I., Cutbirth, J. M., and Bogard, D. G., 2000, "Scaling of Performance for Varying Density Ratio Coolants on an Airfoil With Strong Curvature and Pressure Gradient Effects," J. Turbomach., **123**, pp. 231–237.
[25] Moffat, R. J., 1988, "Describing the Uncertainties in Experimental Results," Exp. Therm. Fluid Sci., **1**, pp. 3–17.

Experimental Investigation of Turbine Leakage Flows on the Three-Dimensional Flow Field and Endwall Heat Transfer

Hans-Jürgen Rehder

Axel Dannhauer

Institute of Propulsion Technology,
Turbine Technology,
German Aerospace Center (DLR),
37073 Göttingen, Germany

Within a European research project, the tip endwall region of low pressure turbine guide vanes with leakage ejection was investigated at DLR in Göttingen. For this purpose a new cascade wind tunnel with three large profiles in the test section and a contoured endwall was designed and built, representing 50% height of a real low pressure turbine stator and simulating the casing flow field of shrouded vanes. The effect of tip leakage flow was simulated by blowing air through a small leakage gap in the endwall just upstream of the vane leading edges. Engine relevant turbulence intensities were adjusted by an active turbulence generator mounted in the test section inlet plane. The experiments were performed with tangential and perpendicular leakage ejection and varying leakage mass flow rates up to 2%. Aerodynamic and thermodynamic measurement techniques were employed. Pressure distribution measurements provided information about the endwall and vane surface pressure field and its variation with leakage flow. Additionally streamline patterns (local shear stress directions) on the walls were detected by oil flow visualization. Downstream traverses with five-hole pyramid type probes allow a survey of the secondary flow behavior in the cascade exit plane. The flow field in the near endwall area downstream of the leakage gap and around the vane leading edges was investigated using a 2D particle image velocimetry system. In order to determine endwall heat transfer distributions, the wall temperatures were measured by an infrared camera system, while heat fluxes at the surfaces were generated with electric operating heating foils. It turned out from the experiments that distinct changes in the secondary flow behavior and endwall heat transfer occur mainly when the leakage mass flow rate is increased from 1% to 2%. Leakage ejection perpendicular to the main flow direction amplifies the secondary flow, in particular the horseshoe vortex, whereas tangential leakage ejection causes a significant reduction of this vortex system. For high leakage mass flow rates the boundary layer flow at the endwall is strongly affected and seems to be highly turbulent, resulting in entirely different heat transfer distributions.

[DOI: 10.1115/1.2720484]

Keywords: shrouded turbine vane, tip leakage gap, leakage ejection, secondary flow field, endwall heat transfer

Introduction

Due to the necessity of a working clearance between the tips of rotating blades and the outer casing of a turbo machine, fluid leaks through this clearance and affects not only the efficiency of the stage but also the mass flow rate. Turbine blades may be shrouded or not, so the leakage processes are quite different for these two cases. In the case of unshrouded blades, the leakage flow is driven across the rotor tip by the pressure difference between the pressure and suction sides of the blade. For shrouded blades, the leakage is ejected from cavities in the outer casing through circumferential gaps between shrouds of neighboring blade rows. Typical tip geometries of a low pressure (LP) turbine with shrouded blades and vanes are shown in Fig. 1. The leakage air then interacts with the tip secondary flow field in the blade passages, forming a region of very complex flow. The accurate prediction of the distribution of leakage air as well as its influence on the surface heat transfer at the side wall, the blade, and the transient area in between is therefore important for the understanding of this flow region.

A comprehensive explanation of the secondary flow field in high and low pressure turbine cascades with plane endwalls, e.g., horseshoe vortex, passage vortex, corner vortices, etc., and their generation and interaction, is given in Langston [1], Sieverding [2], and Hodson et al. [3]. Recent investigations of secondary flow field features with endwall contouring and leakage ejection through different gap geometries were done by Piggush et al. [4]. They found that steps in the endwall and leakage ejection can lead to thicker boundary layers, stronger secondary flows, and possibly additional vortex structures in the passages. De la Rosa Blanco and Hodson [5] performed experiments with backward and forward facing steps of different heights in the hub endwall upstream of a low pressure turbine cascade. They also varied the thickness of the inlet endwall boundary layer.

A lot of literature exists concerning the effect of turbine passage secondary flow on the endwall heat transfer in linear and annular turbine cascades. Goldstein et al. [6] use the heat/mass transfer analogy to examine the local convection coefficients for two different endwall boundary layer thicknesses and two free-stream Reynolds numbers. The dominant roles of horseshoe vortex, pas-

---

Contributed by the International Gas Turbine Institute of ASME for publication in the Journal of Turbomachinery. Manuscript received July 14, 2006; final manuscript received July 20, 2006. Review conducted by David Wisler. Paper presented at the ASME Turbo Expo 2006: Land, Sea and Air (GT2006), Barcelona, Spain, May 08–11, 2006. Paper No. GT2006-90173.

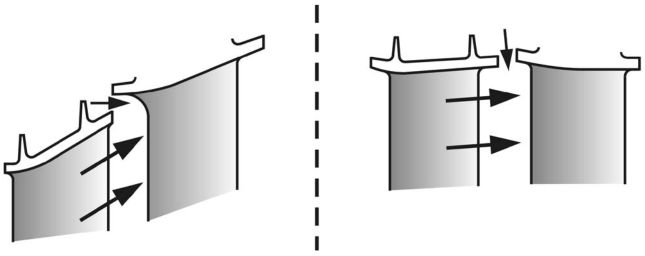

Fig. 1 Typical shroud geometries in a low pressure turbine

sage vortex, and blade wakes on the endwall heat transfer with and without film cooling are demonstrated by Graziani et al. [7] and Takeishi et al. [8]. Kost and Nicklas ([9,10]) carried out aerodynamic, heat transfer, and film cooling effectiveness measurements at the hub contour of a linear turbine stator cascade with a transonic flow field. Coolant was ejected through a slot and through holes in the endwall. They show that, in particular, the upstream location of a coolant slot can dramatically affect the strength of the horseshoe vortex system. The influence of high inlet free-stream turbulence intensities on the near-wall flow structure and endwall heat transfer in a linear cascade was investigated by Lee et al. [11]. Numerical simulations of the secondary flow field structure and heat transfer in a cascade with contoured endwall and air ejection through an upstream positioned slot and comparisons with experimental results can be found in Pasinato et al. [12].

The goal of the present work was to investigate the secondary flow field and endwall heat transfer with leakage ejection in the casing region of shrouded vanes. Therefore, aerodynamic flow field and heat transfer measurements were conducted in a linear cascade test section consisting of three large blades, a simplified contoured endwall, and a leakage gap in this wall just upstream of the cascade inlet plane. The investigations were part of the European research project AITEB (see Haselbach and Schiffer [13]).

Experimental Setup

Horizontal and vertical test section geometries and the cascade notation are presented in Figs. 2 and 3. The test section was designed and built for one cascade geometry with three large LP turbine vanes of 200 mm chord length. Upper and lower walls of the flow duct are shaped to streamlines through the cascade and were obtained from a computation fluid dynamics calculation. The contoured casing endwall of the cascade was designed with an opening angle of 15 deg, simulating the flow path opening in a real machine. A fillet contour with a radius of 10 mm is placed between vane and endwall junction. The opposite test section wall is equipped with a large observation window enabling access for optical measurement techniques. Varying experimental instrumentations can be employed because the center vane (including endwall) is easily exchangeable from the test section.

A small leakage gap is placed in the corner of a backward step 28 mm upstream of the vane leading edges. Leakage gap geometries for tangential (0 deg) and perpendicular (90 deg) ejection are shown in Fig. 4. The leakage gap is extended over the whole test section height.

The test section is part of a blow-down type wind tunnel with an atmospheric inlet. Atmospheric air from the laboratory hall passes an inlet duct, the cascade test section, an adjustable choking diffuser, and finally through a valve (o-ring flap) and a pipe system into a large vacuum vessel. The vessel with a capacity of 10,000 m^3 is evacuated by a set of vacuum pumps, enabling measuring times up to 20 min. The mass flow through the wind tunnel and hence the back pressure or the isentropic exit Mach number of the cascade is set by the adjustable diffuser. Due to constant (atmospheric) inlet conditions the Reynolds number cannot be varied independently, but is a function of the Mach number.

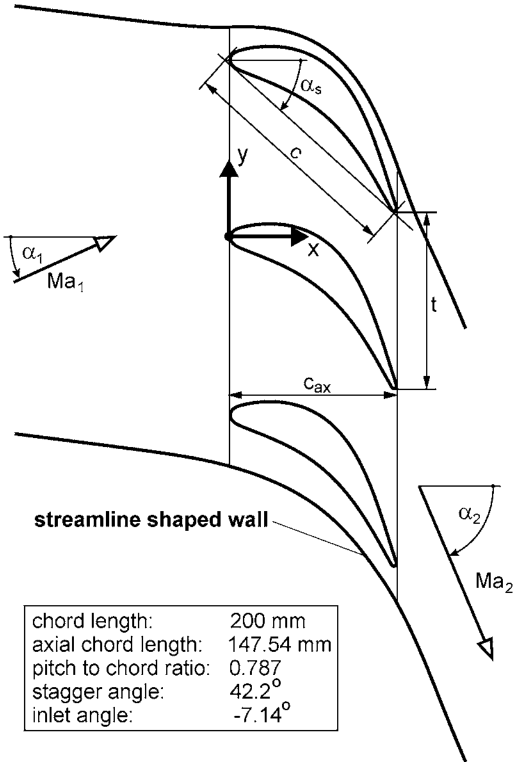

Fig. 2 Vertical test section (cascade) geometry

Engine relevant turbulence levels can be adjusted by an active turbulence generator mounted in the test section inlet. This is achieved by an independent up and downstream blowing of air

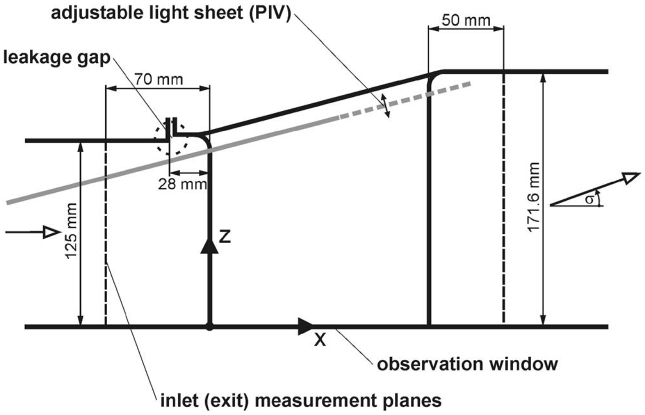

Fig. 3 Horizontal test section geometry

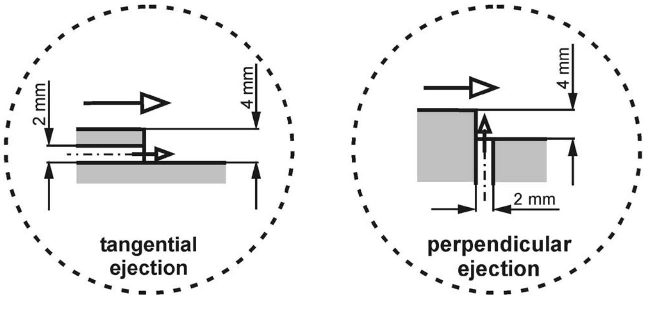

Fig. 4 Leakage gap geometries

through rows of small holes in the bars of the turbulence grid. Design and test of this turbulence generator are explained in more detail in Rehder et al. [14].

The leakage air is provided from the high pressure supply system of the DLR center. Passing a heat exchanger the leakage air is adjusted to a preset temperature level. However, for the experiments, a leakage temperature equal to the main flow temperature was chosen (iso-energetic condition). The leakage air supply is equipped with a remote controlled valve and a standard orifice plate for adjusting the desired mass flow rate. For more details about the wind tunnel, the test section design, and its equipment and instrumentation, see Rehder et al. [14].

Measurement Techniques

Flow Field Measurements. Standard aerodynamic measurement techniques were applied for the flow field survey, e.g., wall static pressure measurements, pneumatic probe traverses, particle image velocimetry (PIV), and surface oil flow visualization.

In order to measure static pressure distribution on surfaces the sidewall in the up- and downstream measuring planes of the cascade (see Fig. 3), the center vane, the fillet contour, and the contoured tip platform around the center vane are equipped with up to 227 pressure taps. The pressure taps are small holes with a diameter of 0.3 mm and are connected via tubes and plastic hoses to a PSI pressure transducer scanner.

Inlet total pressure and total temperature can be measured by a standard pitot probe and a thermocouple, located in the inlet duct of the test section. Without a turbulence generator these quantities are equivalent to the atmospheric conditions, but with a turbulence generator in place additional total pressure losses due to the bar wakes have to be taken into account. The losses were investigated by traversing a pitot probe in the upstream measuring plane of the cascade (see Fig. 3). A mean total pressure loss coefficient of the turbulence grid can then be calculated from an averaged value of this total pressure distribution. Thus, for all experiments with a turbulence generator, the cascade inlet total pressure is obtained from the atmospheric pressure corrected by the known loss coefficient.

Inlet sidewall boundary layers in the measuring plane were detected with the help of a flattened pitot probe of 0.3 mm thickness. The probe was inserted into the test section and traversed through holes in the opposite plane wall. An electrical circuit with an LED controls the contact of the probe head with the wall, allowing probe adjustments with an accuracy of about 0.02 mm. The static pressure within the boundary layer is measured directly from pressure taps in the sidewall.

The cascade exit flow field 50 mm downstream from the vane trailing edges was investigated applying a five-hole pyramid type probe. This probe with a head diameter of 3 mm allows the measurement of stagnation and static pressure (or Mach number) as well as the flow angles in the pitch- and spanwise planes. The probe is immersed into the flow field through a slot in the streamline shaped lower wall of the test section (see Fig. 2), and can be adjusted at any desired location between 50% and 100% flow channel height. Exit probe traverses cover at least one pitch around the center vane of the cascade.

Velocity vector measurements in the near-wall area downstream of the leakage gap and around the center vane leading edge were performed using a 2D PIV system. The principle of this nonintrusive measurement technique is rather simple. The flow is seeded with tiny tracer particles; e. g., oil or aerosol droplets in air and solid particles in fluids and frames. Using a light sheet, formed by a double pulsed laser beam through an optical head with cylindrical lenses, the particles are illuminated twice with a small time separation between. The light scattered by the particles is captured with a CCD camera positioned perpendicular to the light sheet plane and recorded as two single exposed images. The particle displacement between the two light pulses is then determined through evaluation of these images. Finally, the velocity vectors in the light sheet plane are calculated from the time delay between the illuminations and the particle displacements. A comprehensive description of the PIV technique is given in Raffel et al. [15].

Light sheet introduction into the test section is done via a periscope-like probe. The periscope with a diameter of 14 mm is inserted through a slant hole in the observation window sidewall upstream of the cascade, enabling alignment of the light sheet parallel to the tip platform contour (see Fig. 3). By slightly turning and traversing the probe in the longitudinal direction, the front parts of the passages around the center vane can be illuminated, and the distance of the light sheet from the platform is adjustable within a range of about 50 mm.

Oil flow visualization was performed by covering platform and center vane surface uniformly with a mixing of oil and titanium dioxide. Vane and platform are then mounted into the test section and exposed to the flow for a few seconds. The obtained wall streamline pattern indicates the local shear stress directions and reveals a lot of details about the flow behavior.

All pressure taps from surfaces and probes are measured by PSI pressure transducer scanners with an accuracy of about 0.1%. Due to a thorough calibration of the five-hole pyramid probe in a special facility (see Giess et al. [16]), the resulting experimental uncertainties (error bars) of probe measurements are lying within a range of 0.01 for the Mach number and about 0.5 deg for the flow angles. Errors in velocity measurements with PIV depend strongly on the estimation of the particle displacements and can be minimized by a proper setup of the experiment. Uncertainties basing on a 95% confidence level are on the order of 1% to 2%.

Heat Transfer Measurements. The principle of the measurement technique used is based on a well-known heat flux that is generated at the surface, the measured wall temperature distribution, as well as the temperature of the main flow. Thus, all causal parameters important for the heat transfer are available. Despite the fact that the heat flux has an inverse direction, the results of the accomplished investigations are nevertheless comparable with the phenomenology in a real gas turbine due to the usefulness concept of the heat transfer coefficient [17].

With constant property flows, the velocity distribution is independent of the temperature field and the heat transfer coefficient is nearly independent of the temperature boundary conditions, but is determined mainly by the flow field. In the absence of leakage blowing, T_{aw} would be equivalent to the free-stream temperature $T_{0\infty}$, or in the case of high speed flow the recovery temperature. Due to the fact that the influence of the leakage air on the heat transfer mechanism had to be investigated, it is helpful to use parts of the methods from film cooling examinations (see [18,19]). The so-called iso-energetic boundary condition is therefore used to eliminate the influence of the thermal diffusion of the leakage air. Due to this convention, the stagnation temperature of the ejected leakage air was adjusted to be equal to the stagnation temperature of the mainstream.

The setup for heat transfer measurements is depicted in Fig. 5. In order to generate the essential temperature difference between main stream and the surface of the test item, a precise heating system had to be established. Consequently, the test item was appended with electrically operated heating foils, which were generating a constant and homogeneous heat flux via the investigated area. To guarantee as accurate as possible stationary thermodynamic conditions inside of sidewall and blade, the platform as well as the blade was heated up to an expected average temperature under flow conditions before the wind tunnel was started. The remaining heat conduction losses into the sidewall were measured by the help of six heat flux sensors, which were distributed through the sidewall, and integrated 5 mm below the surface to avoid thermal disturbances at the surface.

An infrared camera was used to measure the surface temperatures T_{w} at distinct areas of the platform side. To receive the adiabatic wall temperature T_{aw}, reference pictures with deacti-

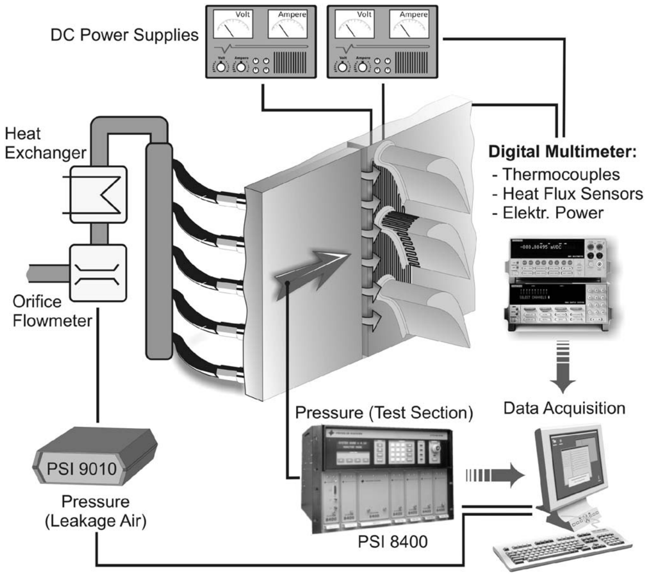

Fig. 5 Heat transfer measurement setup

vated heating foils were taken for each configuration. In a preprocessing step, these pictures were subtracted from the pictures containing the temperature distributions with activated heater. Besides its simplicity, this chosen method had the advantage of being able to take all camera-dependent errors into account. Because of the low isentropic exit Mach number of $Ma_{2is}=0.523$ that was used for the completed measurement campaign, the temperature distribution of the reference pictures is very homogeneous and corresponds well with the temperature $T_{0\infty}$ that was measured in the intake.

To accomplish the optical access to the test section at the infrared wavelengths, a zinc sulfide (ZnS) window as a part of the opposite endwall was substituted. Due to the immense size of the investigated area, it was not possible to receive the complete temperature distributions for the platform with only one infrared picture. As a result, the measurements had to be carried out under different observation positions through a smaller window, which could easily be altered between three different mount points. The received infrared pictures were transformed afterwards into the axial coordinate system of the wind tunnel and were finally merged. Additional thermocouples implemented at the surface of the observed area were used to validate the measured temperatures of the infrared camera in situ. All relevant data, such as the abovementioned as well as the data reflecting the condition of the flow field, were recorded simultaneously by the standard data acquisition of the wind tunnel.

Summing up the arisen uncertainties of the htc parameters, such as the heated area, the electric power, and of course the measured surface temperature, one receives a maximum error of 7.5% for the htc coefficient according to the error propagation law [20].

Test Conditions

Main flow parameters are summarized in Table 1. Inlet total pressure and total temperature depend from atmospheric conditions. The inlet total pressure is corrected taking into account the known loss coefficient of the turbulence generator. The inlet turbulence level was adjusted to 10% (Rehder et al. [14]). Inlet and isentropic exit Mach number of the cascade are defined by averaged values of the sidewall static pressure distributions in the measuring planes and the corrected inlet total pressure. During the experiments the isentropic exit Mach number was controlled by the adjustable diffuser. The resulting cascade flow field is overall subsonic. Reynolds numbers are based on the true chord length of 200 mm. The parameter c_m in Table 1 is the ratio of leakage mass flow to the mass flow through one passage of the cascade.

Table 1 Main flow parameters

Inlet total pressure	$P_{01}\approx 0.98$ bar
Inlet total temperature	$T_{01}\approx 293$ K
Inlet turbulence level	$Tu_1\approx 10\%$
Inlet Mach number	$Ma_1=0.250$
Isentropic exit Mach number	$Ma_{2,is}=0.523$
Inlet Reynolds number	$Re_1=1.10\times 10^6$
Exit Reynolds number	$Re_2=2.10\times 10^6$
Leakage mass flow rate	$c_m=0\%-2\%$

Velocity profiles of measured inlet sidewall boundary layers are plotted in Fig. 6. The diagram shows boundary layer profiles at three locations in the inlet measuring plane (see Fig. 3), covering approximate one pitch in front of the center vane. The velocity profiles were calculated from the measured total pressure distributions, by taking into account the sidewall static pressure measured at the boundary layer location and the total temperature measured in the inlet duct of the test section. Mean boundary layer parameters are summarized in Table 2. The boundary layer thickness is about 7% of the inlet duct height. Velocity profiles as well as the shape factor indicate a turbulent sidewall boundary layer, very similar to the one for a flat plate. This is not surprising because of the high inlet turbulence level during the experiments.

Results and Discussion

Distinct changes in the secondary flow behavior and endwall heat transfer mainly occurred for higher leakage mass flow rates between 1% and 2%. Therefore, only results with 2% leakage ejection will be presented and discussed in this paper and compared to a reference configuration without leakage ejection. The tangential leakage gap configuration with zero leakage flow but

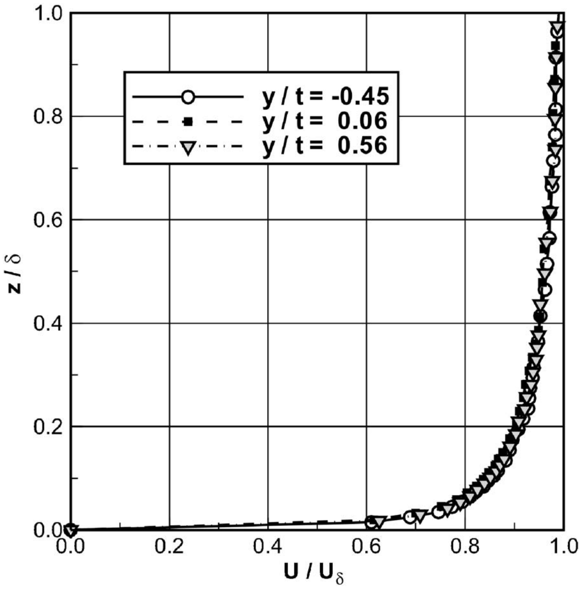

Fig. 6 Inlet sidewall boundary layer

Table 2 Mean inlet sidewall boundary layer parameters

Boundary layer thickness	$\delta=8.67$ mm
Displacement thickness	$\delta_1=0.64$ mm
Momentum thickness	$\delta_2=0.49$ mm
Shape factor	$H_{12}=1.29$

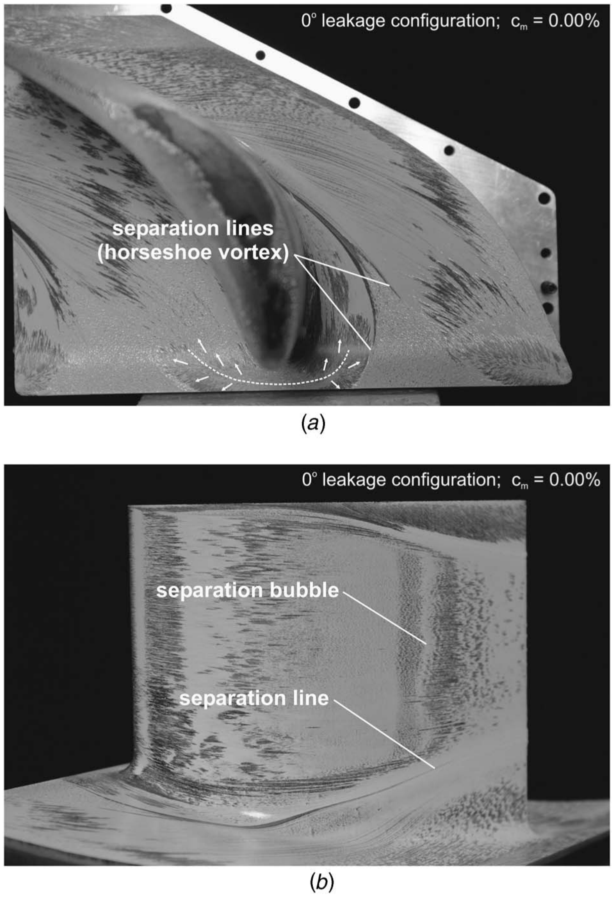

Fig. 7 Oil flow visualization on sidewall and vane suction side (zero leakage flow)

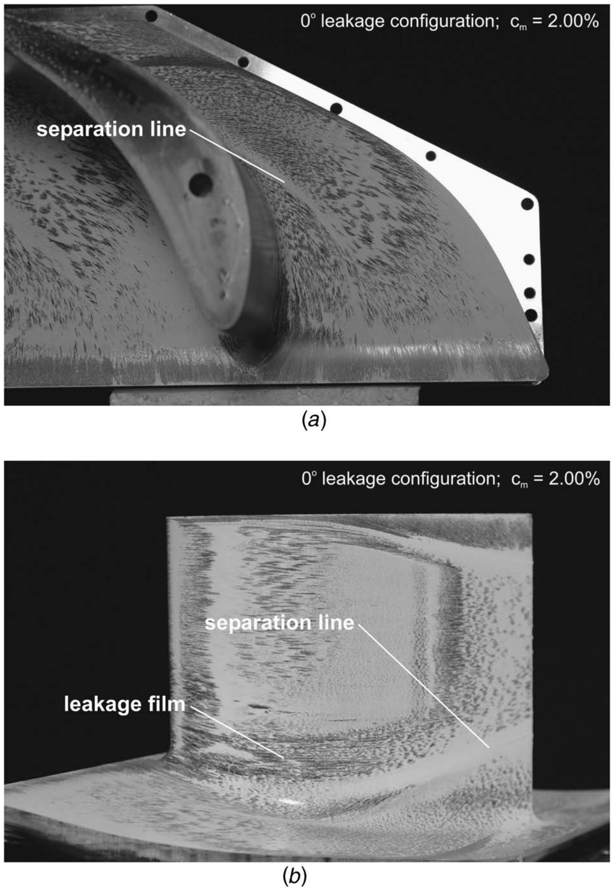

Fig. 8 Oil flow visualization on sidewall and vane suction side (tangential leakage ejection)

open gap was chosen for this reference case (Fig. 4). It was found that any secondary flow into and out of the small gap does not affect the overall flow field behavior of the cascade (for all leakage gap geometries).

Flow Field Measurements

Oil Flow Visualization. Oil flow visualization on the platform and vane suction surface for the zero leakage flow configuration is shown in Fig. 7. The backward facing step with the leakage gap is located 7 mm upstream of the platform leading edge. Two separation lines can be seen on the platform, indicating the presence of a horseshoe vortex system. The backward step forces the incoming boundary layer to separate at its edge and to roll up into this horseshoe vortex. A small dead water zone might occur just behind this step. The downstream reattachment of the horseshoe vortex flow on the platform around the vane leading edge is indicated by the dashed line. Additionally, some local flow (shear stress) directions are drawn into the picture. Further downstream in the passage, the pressure and suction side leg of the horseshoe vortex and the low momentum fluid within the platform boundary layer are strongly directed towards the vane suction side. The pressure drop across the vane passage is the main driving force for this behavior. The flow then separates from the suction surface forming the so-called passage vortex system. This is clearly revealed by the streamlines on the platform and vane suction side. A somewhat smaller secondary flow field at the opposite wall (with the observation window) can also be identified in Fig. 7. The stronger secondary flow on the platform side is induced mainly by the upstream backward facing step and the opening of the flow area. Outside the secondary flow regions, the oil flow pattern on the suction side at about 70% axial chord indicates the presence of a small separation bubble.

Oil flow visualization with tangential leakage ejection is shown in Fig. 8. A leakage flow parallel to the inlet flow direction mainly refills the incoming boundary layer and the separation region behind the backward facing step, resulting in a much thinner sidewall boundary layer reaching the vane leading edge and finally a weakening or reduction of the horseshoe vortex. It is seen from the oil flow visualization that for a high leakage mass flow rate of 2%, the horseshoe vortex system completely vanishes. The following strong turning of the passage flow towards the vane suction side and the passage vortex seem to be not affected. The leakage film can also be identified as a broad band of accelerated flow along the vane suction side. Further downstream, the secondary flow system (passage vortex) drives the fluid below the leakage film, forcing it to turn away from the platform contour into the main stream. The near-wall flow field behavior changes considerably when the leakage is ejected perpendicular to the main flow direction (see Fig. 9). The high leakage crossflow now amplifies the flow separation at the backward facing step and therefore the horseshoe vortex. Compared to the zero leakage configuration, a different shape of the leading edge part of this vortex and the following reattachment, indicated by the dashed line, can be observed in the picture. Due to the stronger horseshoe vortex, a lot of material was driven into the small regions between the suction and pressure side vortex legs from the neighboring vanes. In comparison with the zero leakage flow configuration, these areas are also significantly reduced. Two distinct separation lines from the pressure and suction side leg of the horseshoe vortex can now be recognized on the rear part of the passage and vane suction sur-

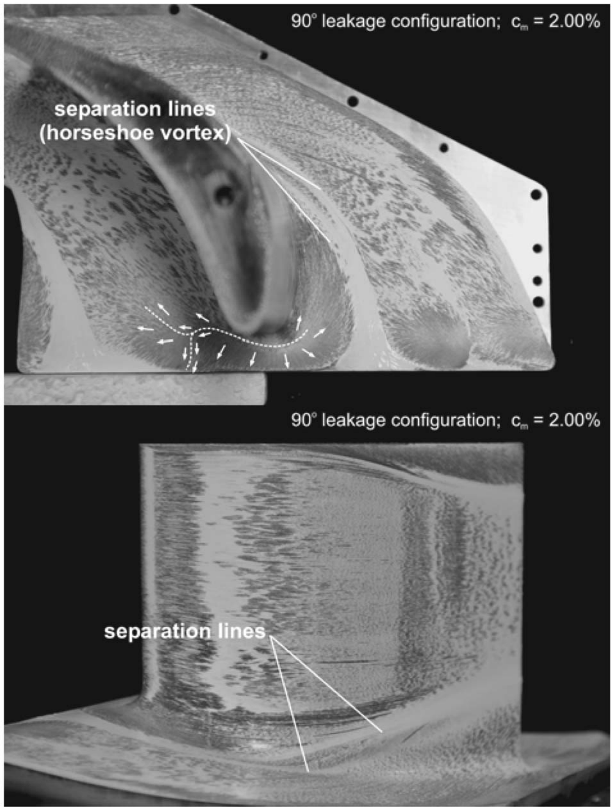

Fig. 9 Oil flow visualization on sidewall and vane suction side (perpendicular leakage ejection)

face. Again, the high turning of the near-wall flow towards the suction surface is clearly visible by the oil flow visualization in Fig. 9.

Static Surface Pressures. In Fig. 10, platform and fillet surface pressure measurements are presented as isentropic Mach number contours, calculated by taking into account the mean inlet total pressure of the cascade. Additionally, the leakage gap location is indicated in the diagrams. For zero leakage flow, the absolute Mach number distributions are plotted, while with leakage ejection, only the Mach number deviations from the flow field without leakage flow are shown.

The left diagram in Fig. 10 displays the absolute Mach number contours (no leakage flow). Maximum Mach numbers of about 0.7 were measured on the platform close to the vane suction surface.

The middle diagram in Fig. 10 shows the Mach number deviations due to tangential leakage ejection. Regions of accelerated flow are visible on the platform between gap and vane leading edges and near the first half of the vane suction surface, whereas along a small streak inside the passages the flow is slightly decelerated (indicated by the dark blue regions in the diagram). The dividing line between accelerated and decelerated flow areas is just the separation line of the horseshoe vortex system, as can be seen by the oil flow visualization in Fig. 7. Evidently, these results again indicate the reduction of the horseshoe vortex system by the tangential leakage flow.

Mach number deviations with perpendicular leakage ejection are given in the right diagram in Fig. 10. The flow on the platform is now heavily accelerated just downstream of the leakage gap, following by a strong deceleration in a small region around the vane leading edges. These abrupt changes are also a definite hint that crosswise leakage ejection in particular strengthens the leading edge part of the horseshoe vortex system. In contrast, any effect of perpendicular leakage ejection on the side wall Mach number distribution within the vane passages could not be detected.

Particle Image Velocimetry. PIV results are presented in Figs. 11 and 12. During the measurements, the light sheet plane was adjusted at five different heights above the platform contour between 5 mm and 35 mm distance from the wall (Fig. 3). Distances less than 5 mm could not be achieved due to higher light sheet deflections on the platform and fillet contour.

The diagrams in Fig. 11 show measured velocity vectors and Mach number contours in the light sheet plane at 5 mm distance from the sidewall. For the purpose of clarity, every second velocity vector was omitted. Three camera positions were used to investigate the flow field around the center vane leading edge. Mach numbers were calculated from the velocities by taking into account the total temperature measured in the inlet duct of the test section (assumption of adiabatic flow). Since the optical axis is adjusted perpendicular to the light sheet and is therefore not parallel in spanwise direction, a part of the flow field between gap and leading edge is covered by the vane and cannot be observed. The vane profile in the light sheet plane is indicated by the dashed line. The absolute velocity vectors in the diagrams are averaged values over 50 single images taken with the PIV system. Additionally, a standard deviation of about 10% was calculated, corresponding well with the adjusted inlet turbulence of the cascade.

Although a minimum distance of 5 mm from the platform contour was achieved only weak secondary flow effects can be observed from the results in Fig. 11. Solely the flow turning process to the vane suction side and a dividing line with convergent ve-

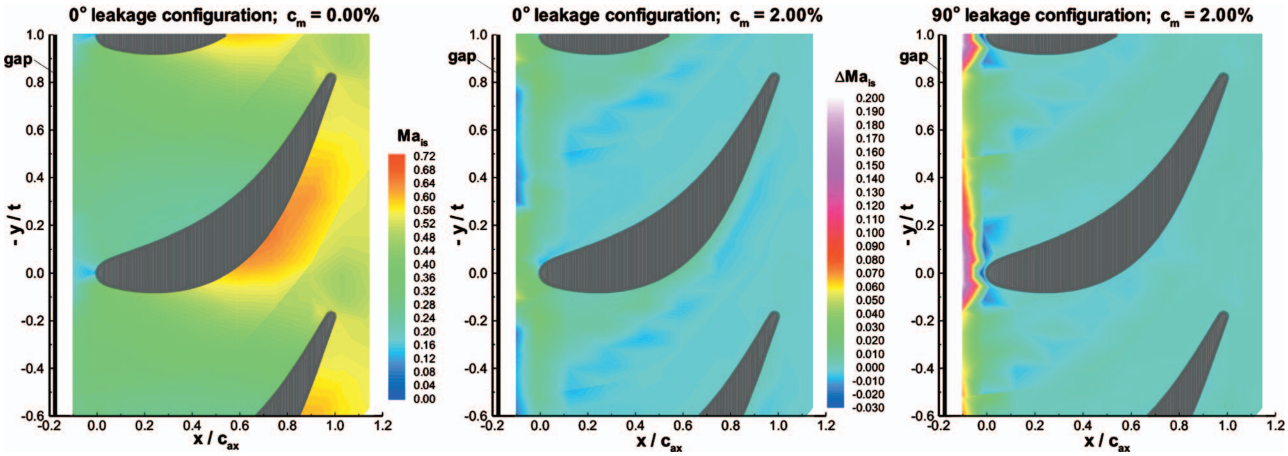

Fig. 10 Sidewall isentropic Mach number distributions

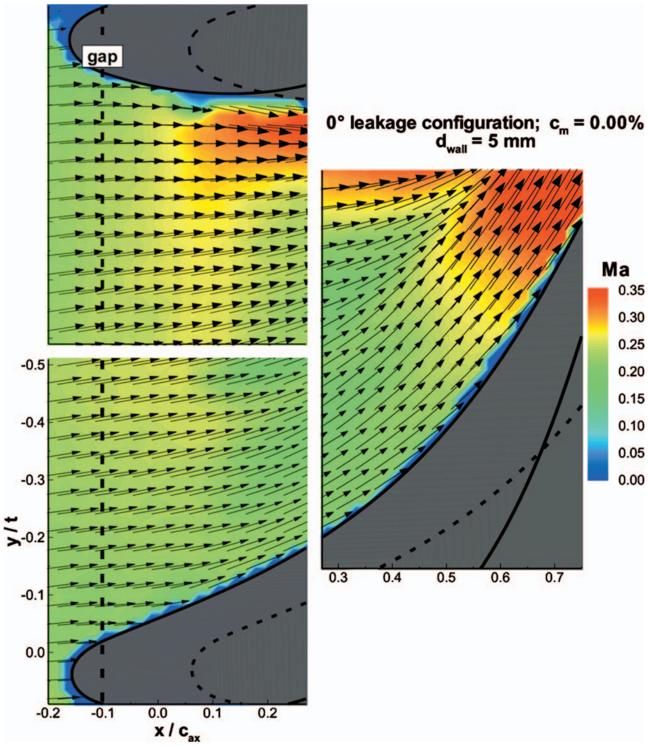

Fig. 11 Velocity vectors and Mach number contours at 5 mm distance from the sidewall (zero leakage flow)

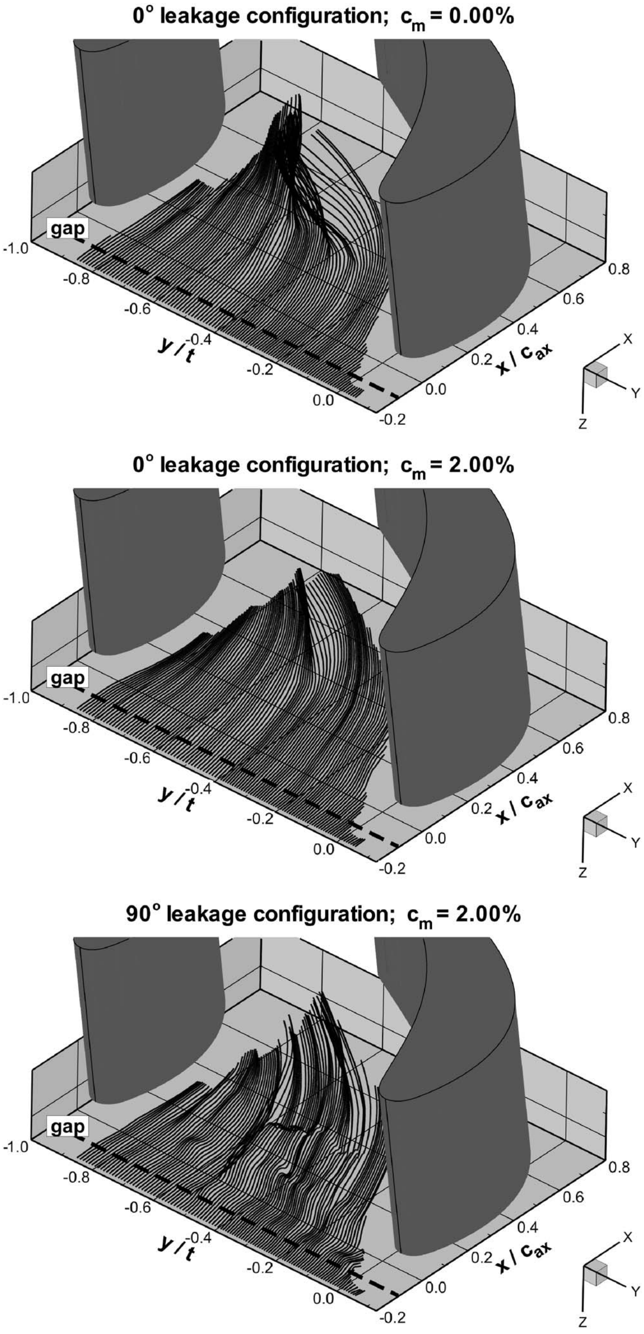

Fig. 12 Near wall 3D streamlines calculated from PIV measurements

locity vectors are visible in the right diagram. The location of this dividing line coincides with the location of the separation lines in Fig. 7, where the flow is driven away from the platform and enrolls into the passage vortex. Any horseshoe vortex effects downstream of the leakage gap and around the vane leading edge cannot be detected. In this region, the horseshoe vortex system is probably lying underneath the lowest measurement plane.

Since the PIV results indicate only small secondary flow effects, an attempt was made to determine 3D streamlines from the 2D velocity vectors in the measurement planes. The z-components of the velocity vectors were calculated taking into account the continuity equation for incompressible flow. Conservation of continuity then yields

$$\frac{\partial V_z}{\partial z} = -\left(\frac{\partial V_x}{\partial x} + \frac{\partial V_y}{\partial y}\right) \tag{1}$$

Equation (1) can be integrated in z-direction assuming $v_z = 0$ at the platform contour. From known vector components in all three directions within the measured volume, 3D streamlines were then calculated and plotted using Tecplot® software. Near-wall 3D streamlines are shown in Fig. 12.

Streamlines without leakage ejection are given in the upper diagram. The roll-up of the streamlines into the passage vortex is clearly visible. Tangential leakage ejection reduces this vortex, as can be seen in the middle diagram. In comparison, perpendicular leakage ejection leads to a more or less turbulent flow field behavior just downstream of the gap, indicated by the wavy form of the streamlines in the lower diagram. Apparently, the passage vortex in the downstream passage is increased and distributed over a bigger area of the flow field. It should be noted that the near-wall flow field with crosswise leakage ejection is highly three-dimensional and cannot be measured with sufficient accuracy by a two-dimensional PIV system.

Exit Flow Field Quantities. Exit flow field quantities from five-hole probe traverse measurements at 25% c_{ax} downstream of the vane trailing edges are presented in Figs. 13–16. Results from probe traverses closer to the sidewall (at $z/h_1 > 1.23$) are distorted due to interference effects between probe stem and wall and have been omitted. Secondary velocity vectors and total pressure contours are plotted in the upper diagrams, while the lower diagrams show axial vorticity contours. Pressure and suction side part of the wake, vortices, and the location of the platform sidewall are also indicated in the figures. The view is always in the axial direction. The secondary velocity vectors represent the deviation from the pitchwise averaged flow at midheight. The axial vorticity ω_{ax} was calculated by the following expression

$$\omega_{ax} = \frac{\partial V_y}{\partial z} - \frac{\partial V_z}{\partial y} \tag{2}$$

For this purpose the measured velocity vectors were interpolated

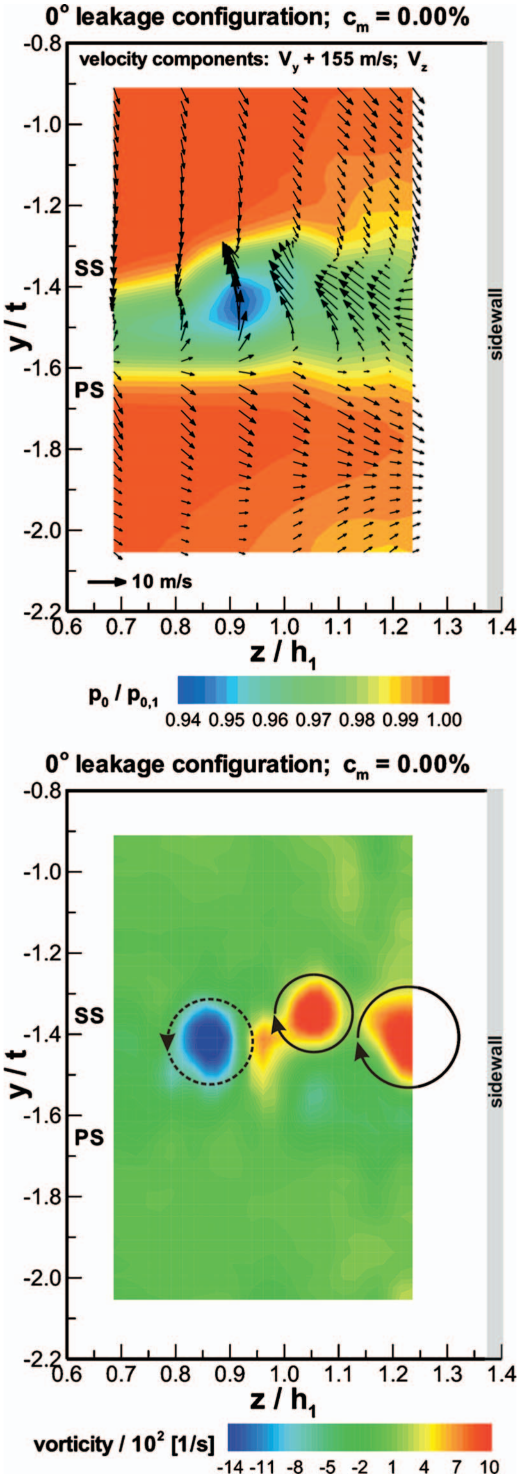

Fig. 13 Velocity vectors, total pressure, and vorticity contours in the exit flow field (zero leakage flow)

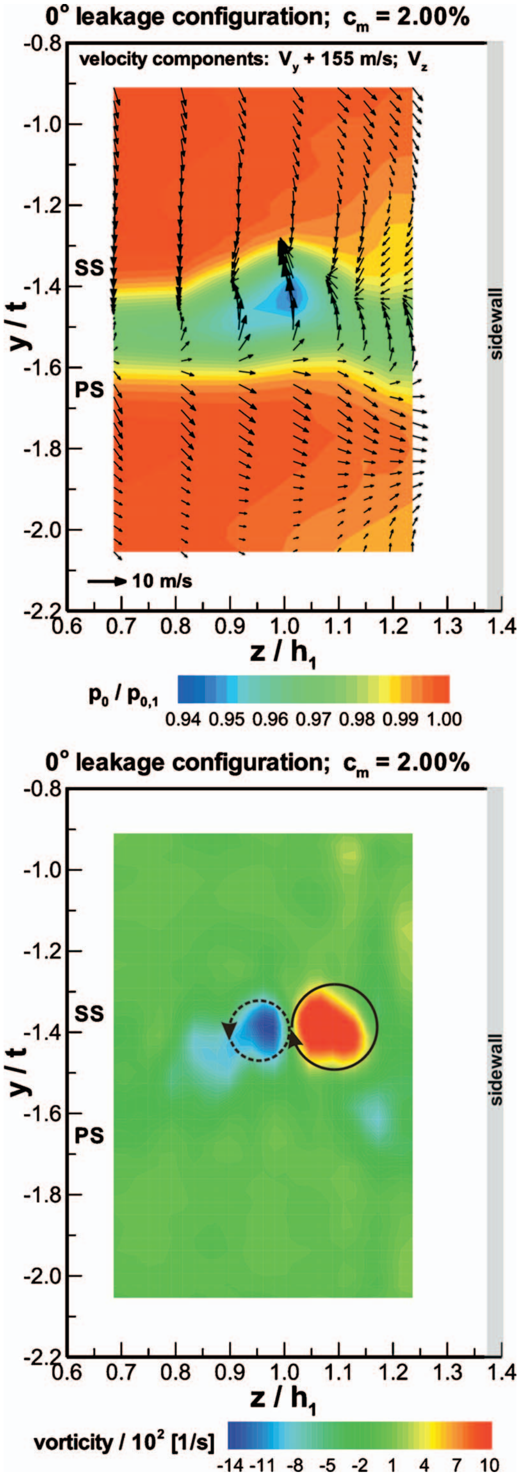

Fig. 14 Velocity vectors, total pressure, and vorticity contours in the exit flow field (tangential leakage ejection)

onto an equidistant grid.

In Fig. 13, exit flow field results with zero leakage flow are shown. Three regions with high axial vorticity appear in the flow field. The area of high positive vorticity close to the sidewall corresponds to the passage vortex, rotating in a clockwise direction. This can also be observed by the secondary velocity vectors in the upper diagram. The remaining vorticity regions are associated with the pressure side leg (rotating in a clockwise direction) and the suction side leg (rotating in anticlockwise direction) of the horseshoe vortex. Obviously, the pressure side leg of the horseshoe vortex is not merging with the passage vortex, although both are turning in the same direction.

Exit flow field results with tangential leakage ejection are plotted in Fig. 14. Compared to the no leakage case, the secondary flow area (wake width) near the platform is significantly reduced and the passage vortex is slightly shifted away from the sidewall. It was shown by the oil flow visualization in Fig. 8 that the horseshoe vortex completely vanishes due to the high tangential leak-

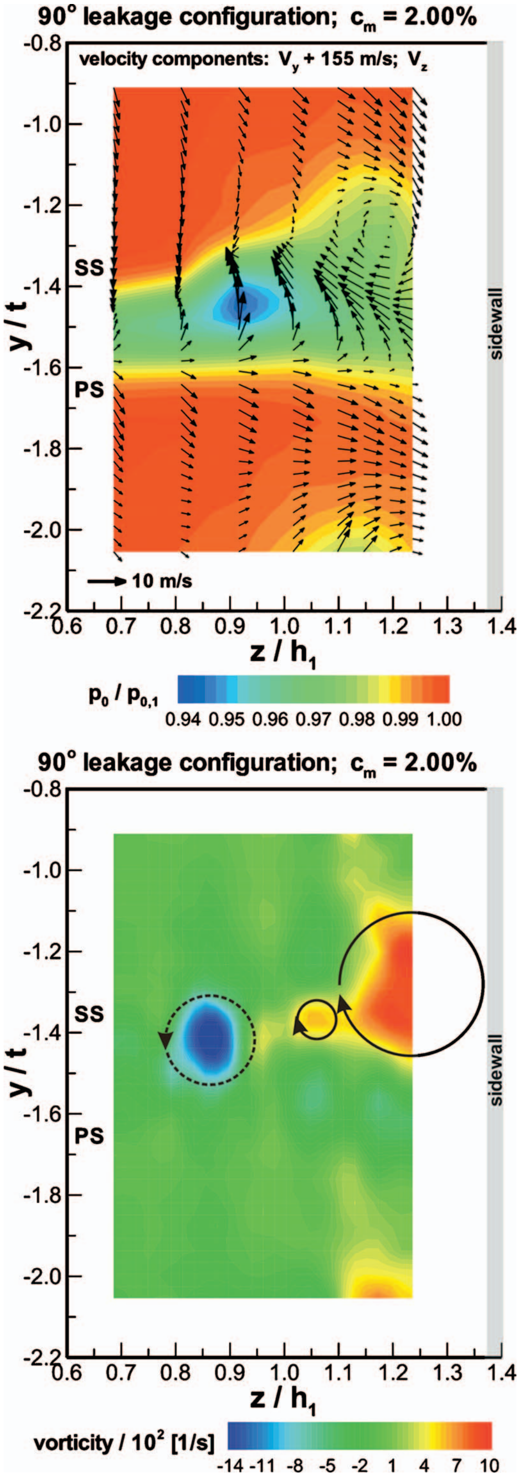

Fig. 15 Velocity vectors, total pressure, and vorticity contours in the exit flow field (perpendicular leakage ejection)

age flow. Apparently the leakage film, which can be seen as a streak along the vane suction side in Fig. 8, might contribute to the left region with high negative vorticity in Fig. 14, by turning into an anticlockwise rotating vortex.

Exit flow field quantities with high perpendicular leakage ejection are given in Fig. 15. Compared to the zero leakage flow configuration, a distinct growing of the wake width near the sidewall and the passage vortex now occurs. Location and strength of the pressure side leg of the horseshoe vortex remain unchanged, while the suction side leg is much smaller and tends to merge with the large passage vortex further downstream.

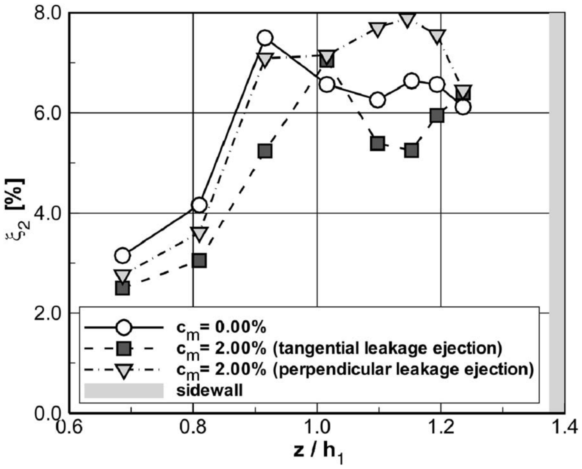

Fig. 16 Spanwise distributions of energy loss coefficient

Finally, a comparison of spanwise distributions of the energy loss coefficient is made. The distributions are plotted in Fig. 16. The coefficients were calculated from pitchwise homogeneous (mixed out) flow field quantities in the probe traverse planes, which can be determined taking into account the conservation laws of mass, momentum, end energy. The exact procedure is described by Amecke and Šafařík [21].

The spanwise distribution of the profile loss for zero leakage flow shows a maximum at $z/h_1=0.9$, which coincides with the spanwise location of the separation line on the vane suction side at the trailing edge, as can observed from the oil flow visualization in Fig. 7. The shear layer dividing the secondary flow region from the main flow region is a main source of loss in a cascade flow field. Closer to the sidewall, the losses then decrease to a minimum or plateau, but always at a much higher level than the one at midspan. With tangential leakage ejection, the overall loss level was lowered and the maximum in the spanwise distribution was shifted towards the sidewall. This behavior is clearly due to the disappearance of the horseshoe vortex system, which no longer contributes to the loss mechanism in the secondary flow field. In contrast to that perpendicular leakage ejection amplifies the passage vortex and therefore increases the loss level in the corresponding exit flow field region (for $z/h_1>1$ in Fig. 16).

Heat Transfer Measurements. Regarding the results of the htc measurements in Fig. 17, one realizes the typical heat transfer distributions for a plane turbine cascade (see Goldstein [6], Graziani et al. [7], and Takeishi et al. [8]). Shortly behind the leakage slit, the boundary layer seems to be separating, which is indicated by an accumulation of color in the oil flow pictures as well as some areas of higher heat transfer in the same regions. The through-flow boundary layer is therefore thick and turbulent.

The wedge shaped region of lower heat flux in the flow duct defines the area between the 3D separation lines of the pressure and suction side arm of the horseshoe vortex. Compared with the oil flow visualizations, the position of the separation lines corresponds very well. Downstream of these separation lines, a new and thinner boundary layer seems to be established associated with higher rates of heat transfer. The region between the separation lines and the leading edge is characterized by increased heat transfer, which is a result of the new boundary layer as well as mixing processes of the vortex that sweeps fluid of the outer boundary layer or the main stream in direction to the endwall. Despite these facts, the wall shear stresses are additionally increased because of the vortex motion. The strong flow accelera-

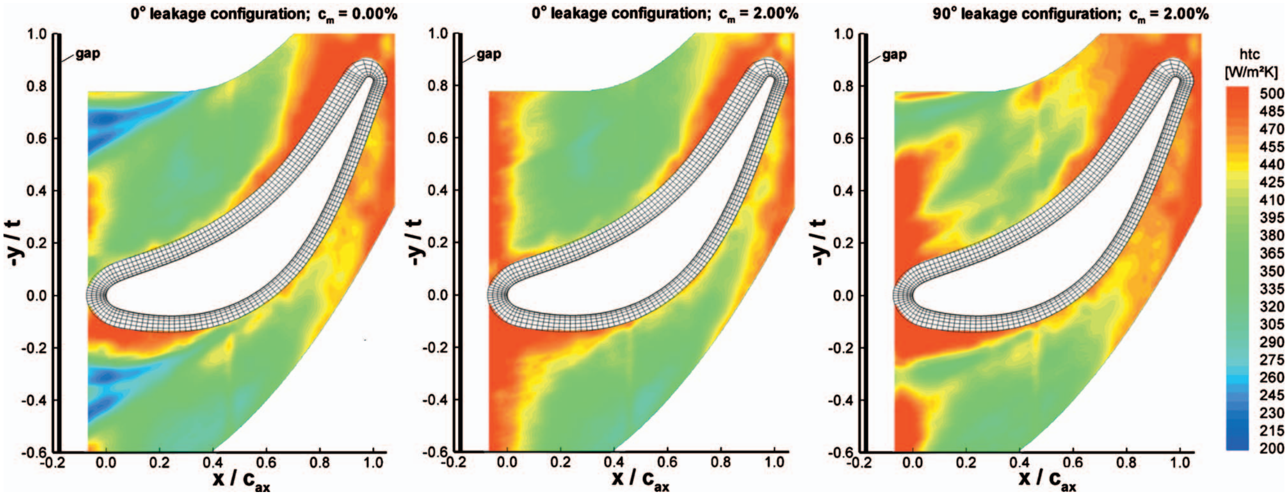

Fig. 17 Sidewall heat transfer distributions

tion around the nose region of the suction side is surely the main reason that the heat flux in this area appears much higher than on the pressure side. Just behind this high heat transfer region, the crossflow starts interfering with the suction surface; thus, this area should be the starting point of the passage vortex. In combination with the strong acceleration, which is indicated by the contour Mach number distribution, a slight increase of heat transfer until the trailing edge is visible. A thin endwall boundary layer and the reaction to the velocity field are also visible at the pressure side whereby the strongest increase appears across the throat.

The perpendicular leakage ejection leads, analogously to the tangential leakage ejection, to a reduction of the clearly noticeable separation lines as well as vortex stimulated high heat transfer regions. In contrast to the tangential configuration, it is not possible to re-energize the leading boundary layer. As a result of the perpendicular blowing, the separation areas behind the leakage slit are increasing; this is also indicated at the oil flow picture. The low htc area between the separation lines is still recognizable. Additionally, the increase of the heat transfer in the rear part of the duct is higher than in the tangential configuration, which correlates well with the Mach number distributions for this configuration.

With tangential leakage ejection a reduction of the wedge shaped regions can be seen. It seems that the leakage mass flow re-energizes the boundary layer in this area, whereby any indication of a vortex system is now vanished. As can be seen in Fig. 17 the heat transfer increases across the throat, as velocities are increasing.

Conclusions

This paper describes aerodynamic and thermodynamic experiments in a linear turbine cascade representing the casing endwall region of shrouded LP turbine guide vanes with the additional presence of leakage ejection. Leakage flow was simulated by blowing air through a small slot in the corner of a small backward facing step in the sidewall just upstream of the cascade. The experiments were performed with tangential and perpendicular leakage ejection and with zero and 2% leakage mass flow rates. In order to generate engine realistic boundary conditions a high inlet turbulence level of the cascade was adjusted by an active turbulence generator. A wide range of measurement techniques was employed, including surface pressure measurements, oil flow visualization, exit probe traverses, particle image velocimetry, and heat transfer measurements at the sidewall.

The aerodynamic results indicate that without leakage ejection, the incoming sidewall boundary layer always separates at the edge of the upstream backward facing step, rolling up into the so-called horseshoe vortex system. A strong interaction of leakage flow with the near wall secondary flow field in the cascade was then observed for high leakage mass flow rates. Tangential leakage ejection fills up the sidewall boundary layer and the dead water zone behind the backward facing step, leading to a significant reduction of the horseshoe vortex. At 2% leakage mass flow rate, the horseshoe vortex was completely removed. Additionally, the passage vortex was weakened. In contrast, perpendicular leakage ejection strengthens the horseshoe vortex system, in particular between gap and vane leading edge, and amplifies the passage vortex. Compared to the zero leakage case, the secondary losses decrease with tangential ejection, but increase in the sidewall region when the leakage is ejected perpendicular to the main inlet flow.

Heat transfer distributions at the sidewall are in good accord with the adopted flow visualization technique. Without leakage ejection, the secondary flows are strongly affecting the heat transfer. Thus, heat flux increases in the leading edge region of the suction side and decreases upstream of the three-dimensional separation of the suction and pressure side leg of the horseshoe vortex. Despite these effects, the heat transfer in the blade passage reacts strongly to the velocity field. Tangential leakage ejection re-energizes the boundary layer and reduces the influence of the secondary flows on the heat transfer.

Acknowledgment

The reported work was performed within the European research project "Aerothermal Investigation of Turbine Endwalls and Blades" (AITEB, 5FP, G4RD-CT-1999-00055). Permission for the publication is gratefully acknowledged by the authors.

Nomenclature

c = chord length (m)
c_{ax} = axial chord length (m)
c_m = leakage mass flow rate (%)
d_{wall} = distance from side wall (m)
htc = heat transfer coefficient (W/(m^2 K))
h_1 = inlet duct height (m)
H_{12} = boundary layer shape factor
Ma = Mach number
p = pressure (Pa)
PS = pressure surface
Re = Reynolds number
SS = suction surface
t = blade pitch (m)
T = temperature (K)
Tu = turbulence level (%)

U, V = velocity (m/s)
x, y, z = Cartesian coordinates (m)
α = circumferential flow angle (deg)
α_s = stagger angle (deg)
δ = boundary layer thickness (m)
δ_1 = displacement thickness (m)
δ_2 = momentum thickness (m)
ξ = kinetic energy loss coefficient (%)
σ = radial flow angle (deg)
ω = vorticity (1/s)

Subscripts

0 = total
1 = cascade inlet
2 = cascade outlet
aw = adiabatic wall
is = isentropic
w = wall
δ = boundary layer edge
∞ = free-stream condition

References

[1] Langston, S., 1980, “Crossflow in a Turbine Cascade Passage,” J. Eng. Power, **102**, pp. 866–874.
[2] Sieverding, C. H., 1985, “Recent Progress in the Understanding of Basic Aspects of Secondary Flows in Turbine Blade Passages,” ASME J. Eng. Gas Turbines Power, **107**, pp. 248–257.
[3] Hodson, H. P., and Dominy, R. G., 1986, “Three-Dimensional Flow in a Low-Pressure Turbine Cascade at Its Design Condition,” ASME Paper No. 86-GT-106.
[4] Piggush, J. D., and Simon, T. W., 2005, “Flow Measurements in a First Stage Nozzle Cascade Having Endwall Contouring, Leakage and Assembly Features,” ASME Paper No. GT2005-68340.
[5] De la Rosa Blanco, E., and Hodson, H. P., 2005, “Effect of Upstream Platform Geometry on the Endwall Flows of a Turbine Cascade,” ASME Paper No. GT2005-68938.
[6] Goldstein, R. J., and Spores, R. A., 1988, “Turbulent Transport on the Endwall in the Region between Adjacent Turbine Blades,” ASME J. Heat Transfer, **110**, pp. 863–869.
[7] Graziani, R. A., Blair, M. F., Taylor, J. R., and Mayle, R. E., 1980, “An Experimental Study of Endwall and Airfoil Surface Heat Transfer in a Large Scale Turbine Blade Cascade,” ASME J. Eng. Power, **102**, pp. 257–267.
[8] Takeishi, K., Matsuura, M., Aoki, S., and Sato, T., 1990, “An Experimental Study of Heat Transfer and Film Cooling on Low Aspect Ratio Turbine Nozzles,” ASME J. Turbomach., **112**, pp. 489–496.
[9] Kost, F., and Nicklas, M., 2001, “Film-Cooled Turbine Endwall in a Transonic Flow Field: Part I—Aerodynamic Measurements,” ASME Paper No. 2001-GT-0145.
[10] Nicklas, M., 2001, “Film-Cooled Turbine Endwall in a Transonic Flow Field: Part II—Heat Transfer and Film Cooling Effectiviness,” ASME Paper No. 2001-GT-0146.
[11] Lee, S. W., Park, B. K., and Lee, J. S., 2002, “Effects of High Free-Stream Turbulence on the Near-Wall Flow and Heat/Mass Transfer on the Endwall of a Linear Turbine Rotor Cascade,” ASME Paper No. GT2002-30187.
[12] Pasinato, H. D., Liu, Z., Roy, R. P., Howe, W. J., and Squires, K. D., 2002, “Prediction and Measurement of the Flow and Heat Transfer Along the Endwall and Within an Inlet Vane Passage,” ASME Paper No. GT2002-30189.
[13] Haselbach, F., and Schiffer, H. P., 2004, “Aerothermal Investigations on Turbine Endwalls and Blades (AITEB),” ASME Paper No. GT2004-53078.
[14] Rehder, H.-J., and Dannhauer, A., 2004, “DLR Rig Instrumentation—European Research Project AITEB,” DLR Internal Report IB 225-2004 A 08.
[15] Raffel, M., Willert, C., and Kompenhans, J., 1998, *Particle Image Velocimetry—A Practical Guide*, Springer-Verlag, Berlin.
[16] Giess, P.-A., Rehder, H.-J., and Kost, F., 2000, “A New Test Facility for Probe Calibration—Offering Independent Variation of Mach and Reynolds Number,” *15th Symposium on Measuring Techniques in Transonic and Supersonic Flow in Cascades and Turbomachines*, Firenze, Italy, September.
[17] Eckert, E. R. G., and Goldstein, R. J., *Measurements in Heat Transfer*, 2nd ed., McGraw-Hill, New York.
[18] Eckert, E. R. G., 1984, “Analysis of Film Cooling and Full-Coverage Film Cooling of Gas Turbine Blades,” ASME J. Eng. Gas Turbines Power, **106**, pp. 206–213.
[19] Teekaram, A. J. H., Forth, C. J. P., and Jones, T. V., 1984, “Cooling in the Presence of Mainstream Pressure Gradients,” ASME J. Turbomach., **113**, pp. 484–492.
[20] ISO, 1993, *Guide to the Expression of Uncertainty in Measurement*, Geneva, Switzerland, ISBN 92-67-10188-9.
[21] Amecke, J., and Šafařík, P., 1995, “Data Reduction of Wake Flow Measurements with Injection of an Other Gas,” Forschungsbericht DLR-FB 95-32, Cologne.

Scaling of Guide Vane Coolant Profiles and the Reduction of a Simulated Hot Streak

Sean C. Jenkins
e-mail: sjenkins@mail.utexas.edu

David G. Bogard
e-mail: dbogard@mail.utexas.edu

Mechanical Engineering Department,
The University of Texas at Austin,
Austin, TX 78712

The turbine section of a gas turbine engine is subjected to a nonuniform temperature distribution in the gas flow from the combustor. Regions of elevated temperatures, known as "hot streaks," subject the turbine airfoil to high heat loads. In this study, the reduction of hot streaks by coolant from a film cooled nozzle guide vane was experimentally evaluated. Experiments were conducted with an approach mainstream turbulence level of 20% to simulate actual turbine conditions. The coolant distributions downstream of the vane were measured for varying blowing ratios and varying coolant density, and scaling methods were found for variations in both parameters. For this study, the hot streak peak was positioned to impact the vane at the stagnation line. Measurements of the hot streak strength with coolant blowing showed as much as a 55% decrease in peak temperature compared with no coolant. [DOI: 10.1115/1.2447803]

Keywords: film cooling, hot streak, coolant distribution

Introduction

With the continued drive towards higher turbine inlet temperatures, accounting for temperature nonuniformities in the flow field becomes even more important. These temperature nonuniformities, commonly called "hot streaks," can cause premature failure of first stage turbine components. A clear understanding of how the film cooling flows from the first stage nozzle guide vanes can reduce the hot streak is also important, since this can change the expected flow field entering the rotor stage. For modern engines, an integer multiple of combustors to first stage nozzle guides vanes allows "clocking" or alignment of the hot streaks with the nozzle guide vanes. Since there are fewer combustors than guide vanes, only some would be impacted by the hot streak, in which case the effect of coolant flow on the hot streak becomes important. For the remaining vanes, the "cold streak" downstream of the vane caused by film cooling is also important to take into consideration. Documentation of the cold streaks downstream of a fully film cooled vane have not previously been performed. In addition, an analysis of the effects of film cooling blowing ratio and density ratio on hot streak reduction by film cooling has not previously been done.

Although several studies have looked at hot streaks through a turbine stage both experimentally and computationally, only two studies have looked at the effect of coolant on a hot streak. Previous work in our laboratory [1] investigated the effects of individual film cooling regions and full coverage film cooling on hot streak reduction. Relatively high levels of attenuation due to the mainstream turbulence level and film cooling were observed. However, the effects of blowing ratio and density ratio were not investigated.

The only other study of coolant flow effects on a hot streak was by Roback and Dring [2] who used trailing edge cooling only. In this study, performed at the United Technologies Low Speed Rotating Rig, CO_2 was used as a trace gas to follow the hot streak introduced through a pipe in the middle of the vane passage. Turbulence levels were not provided, however the description of the facility suggests that turbulence levels were low. In their study, a simulation of trailing edge coolant was performed by coolant ejection at several coolant-to-freestream velocity ratios. However, the focus of this study was on the surface heat transfer data for the first stage rotor for the combined hot streak and trailing edge coolant flow. Consequently no fluid temperatures approaching the rotor section were given.

In this study the effects of coolant injection from a highly cooled first vane on the reduction of a hot streak were investigated under engine realistic conditions of high mainstream turbulence. Nominal and high blowing ratios were used, and the coolant density ratio was varied. Particular attention was placed on determining how the coolant was dispersed at the trailing edge and farther downstream of the vane. Since blowing ratios and density ratios differ between engine applications and models, a clearer understanding of how these parameters affect hot streak reduction would be beneficial to engine designers.

Facilities and Experimental Conditions

The test facility used to make the experimental measurements was a closed-loop, low-speed wind tunnel, driven by a 50 hp variable pitch, variable speed fan. The test section, shown in Fig. 1, was a simulated three vane, two passage cascade with adjustable bleed and adjustable walls to maintain the proper flow around the test airfoil. A full description of the facility is given in Ref. [3].

The test airfoil was a scaled-up model of a first stage turbine guide vane with the Reynolds number matched to actual engine operating conditions. The vane had a true chord length of $C=594$ mm, a span of $S=550$ mm, and the pitch between airfoils was $P=460$ mm. The mainstream approach velocity was $U_0=5.8$ m/s for all experiments resulting in a Reynolds number of $\mathrm{Re}=1.2\times10^6$ based on chord length and exit velocity. The test vane was constructed of polyurethane foam selected for strength and low thermal conductivity, with a value of $k=0.048$ W/(m K). For all coolant regions, the coolant hole diameter was $d=4.11$ mm and the pitch in the vertical, or spanwise, direction between coolant hole centerlines was $5.55d$.

Three separate regions of coolant holes were available for performing experiments using film cooling. The showerhead region, shown in Fig. 2, had six rows of coolant holes with a row spacing of $3.33d$. These holes were oriented laterally, i.e., 90 deg to the streamwise direction, and had an injection angle of 25 deg relative

---

Contributed by the International Gas Turbine Institute of ASME for publication in the Journal of Turbomachinery. Manuscript received March 9, 2006; final manuscript received August 8, 2006. Review conducted by David Wisler. Paper presented at the ASME Turbo Expo 2005: Land, Sea and Air (GT2005), Reno, NV, USA, June 6–9, 2005. GT2005-69015.

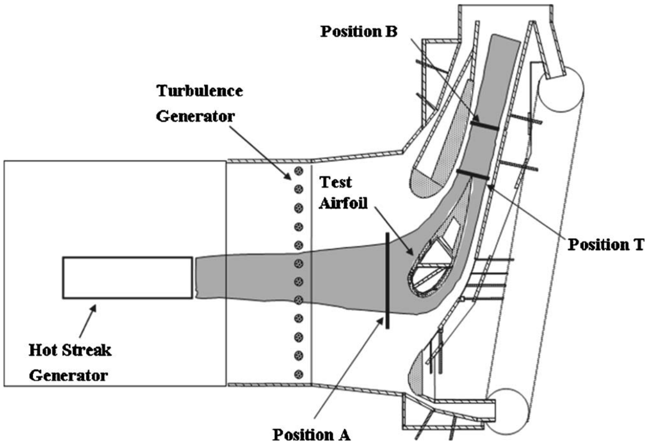

Fig. 1 Simulated vane cascade with hot streak generator

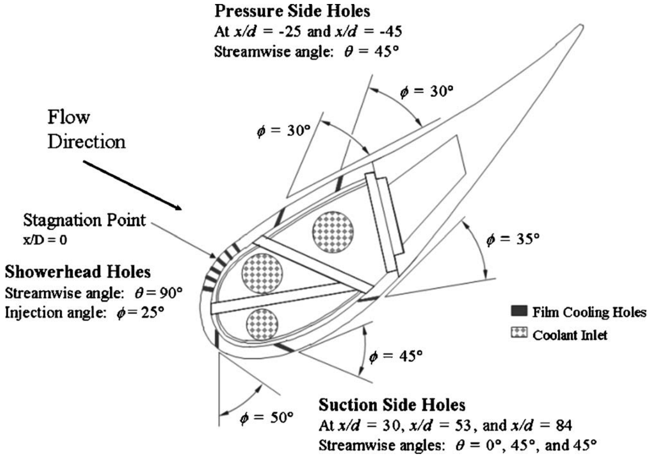

Fig. 3 Schematic of film cooling hole configuration

to the surface. This hole geometry had a "crossover" region, referring to the area where flow from holes angled downward interacts with flow from holes angled upward as indicated in the figure. The pressure side film cooling holes are also shown in Fig. 2, consisting of two rows of coolant holes. These rows were located at $s/d=-25$ and $s/d=-45$, where $s/d=0$ was located at the stagnation line at the leading edge of the airfoil, and s was the distance along the airfoil. The pressure side coolant holes had an injection angle of $\phi=30$ deg and a streamwise angle of $\theta=45$ deg. In addition to the showerhead and pressure side coolant holes, the film cooling schematic in Fig. 3 shows the three rows of suction side coolant holes. Their locations with respect to the stagnation line were $s/d=30$, $s/d=53$, and $s/d=84$. The injection angles were $\phi=50$ deg, 45 deg, and 35 deg, respectively, and the streamwise angles were $\theta=0$ deg, 45 deg, and 45 deg, respectively. The positions and injection angles for the suction and pressure side are tabulated in Table 1. The nominal mainstream temperature was 300 K, and for most experiments, coolant consisting of cryogenically cooled air supplied at 187.5 K resulted in a density ratio of 1.6. Each coolant region had a separate pressure plenum providing the coolant supply as shown in Fig. 3. Additional details of the film cooling supply and of the construction of the film cooling holes are given in Ref. [4].

The hot streak generator section was installed upstream of the test section as shown in Fig. 1. The exit of the hot streak generator was located 1.7C upstream of the vane leading edge and was designed to provide a nominal temperature ratio of $T_{0,\mathrm{HS}}/T_\infty=1.1$ under both low and high turbulence conditions at a location 0.21C upstream of the vane, noted as Position A in Fig. 1. It was designed to be continuously adjustable across the pitch of the vane cascade. The construction and adjustment of the hot streak generator section is fully described in Jenkins et al. [1]. Spanwise velocity profiles with the hot streak generator deactivated were uniform within ±4%. The velocity profile was also measured with the hot streak generator activated, and the velocities within the hot streak were found to increase following the relation $V_{\mathrm{hs}}=V_\infty*(T_{\mathrm{hs}}/T_\infty)^{1/2}$, consistent with a conserved total pressure. Additional details regarding the variations in the velocity field may also be found in Ref. [1].

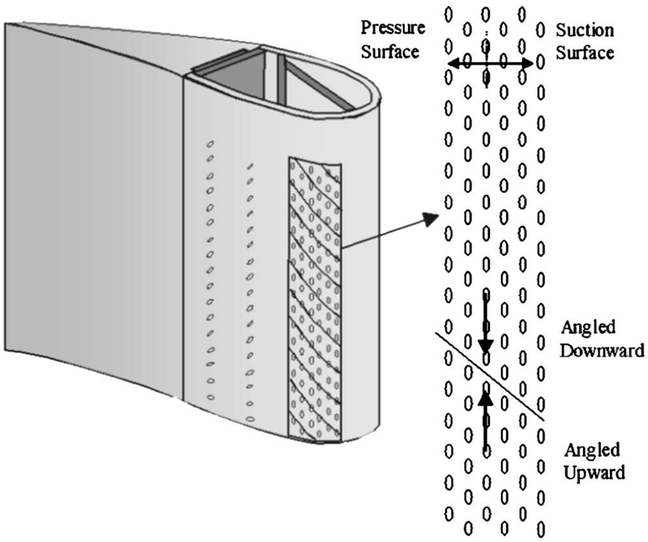

Fig. 2 Showerhead and pressure side cooling holes

Turbulence intensity and integral length scales were established using hot-wire anemometer measurements at Position A. High mainstream turbulence was generated using an array of 38-mm-diameter vertical rods, spaced 85 mm apart, and located 0.88C upstream of the stagnation point as shown in Fig. 1. The turbulence generator produced a turbulence intensity of Tu=20% with an integral length scale of $\Lambda_f=33$ mm at position A. This level of turbulence intensity has been shown to be representative of actual engine operating conditions [5]. The turbulence generation rods were constructed of a material with very low thermal conductivity to avoid interference with the hot streak. It should be noted that measurements were made in the facility by previous researchers showing that the turbulence field was isotropic at Position A. Additional details regarding the turbulence field and turbulence generator are available in Ref. [6].

Table 1 Coolant hole locations and angles

Region	s/d	Injection angle (ϕ) (deg)	Streamwise angle (θ) (deg)
Pressure side	−25	30	45
	−45	30	45
Showerhead	−7	25	90
	−3	25	90
	0	25	90
	3	25	90
	7	25	90
	10	25	90
Suction side	30	50	0
	53	45	45
	84	35	45

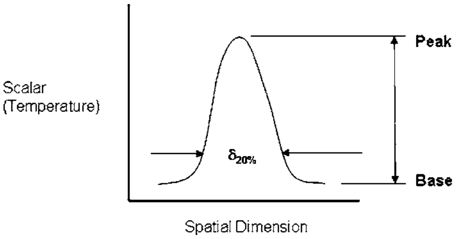

Fig. 4 Schematic of full width at 20%, $\delta_{20\%}$

Measured hot streak temperature profiles were acquired using a thermocouple rake consisting of 22 K-type thermocouples spaced 7.8 mm apart. Measurements were taken normal to the flow direction as shown in Fig. 1 as measurement planes at Positions A, T, and B. Temperature readings from the thermocouple rake and thermocouples placed in the mainstream were acquired using a National Instruments multiplexer and analog/digital (A/D) module, and LabVIEW software and time-averaged over a 6 s time span.

A normalized temperature ratio, Θ_R, was used to compare hot streak and coolant profiles. The normalized temperature ratio, Θ_R, was defined based on the peak hot streak temperature, $T_{0,\mathrm{HS}}$, measured at a standard reference position upstream of the vane leading edge (Position A). Since the local temperature is scaled by the peak value upstream, Θ_R may be thought of as the hot streak reduction, or as a percentage of the original hot streak. It is shown in Eq. (1) as follows

$$\Theta_R = \frac{T_{ij} - T_\infty}{T_{0,\mathrm{HS}} - T_\infty} \tag{1}$$

where Θ_R is computed at a point based on the temperature at that point T_{ij}; and the mainstream temperature at the measurement plane, T_∞.

For scaling coolant injection of different density ratios, the normalized coolant temperature, Θ_C, was more appropriate. The normalized coolant temperature relates the temperature at a point in the flow to the coolant temperature at the coolant hole exit, $T_{0,C}$, as shown in Eq. (2)

$$\Theta_C = \frac{T_{ij} - T_\infty}{T_\infty - T_{0,C}} \tag{2}$$

where the value of Θ_C, is calculated at a point based on the fluid temperature at that point, T_{ij}.

An important parameter in turbulent mixing of scalar quantities, such as temperature, is the full or half width of the scalar profile. In this study, the full width at 20% of the maximum was used to describe the relative sizes of hot streaks under different conditions or at different positions in the flow. The 20% width, $\delta_{20\%}$, is defined as the full profile width at 20% of the maximum of the difference between peak and base (or minimum for negative profiles such as coolant profiles) as shown in the schematic in Fig. 4.

To eliminate bias uncertainty of the measurements for the thermocouple rake, the equipment was tested against a known standard, i.e., an ice bath, and repeatable bias errors were computed. The bias errors between thermocouples were eliminated by adjusting the raw data according to the bias error previously determined. In this way, biases between thermocouples and thermocouple channels could be removed leaving only random or precision error. Based on statistical analysis of the temperature measurements, the precision uncertainty (95% confidence interval) of the time averaged temperature values ranged between ±0.1 K at the mainstream temperature and ±0.4 K at the peak hot streak temperature. This error was random error resulting from the data acquisition system. Based on the temperature uncertainties, the uncertainty in the normalized temperature ratio, Θ_R, was calculated to be ±0.02.

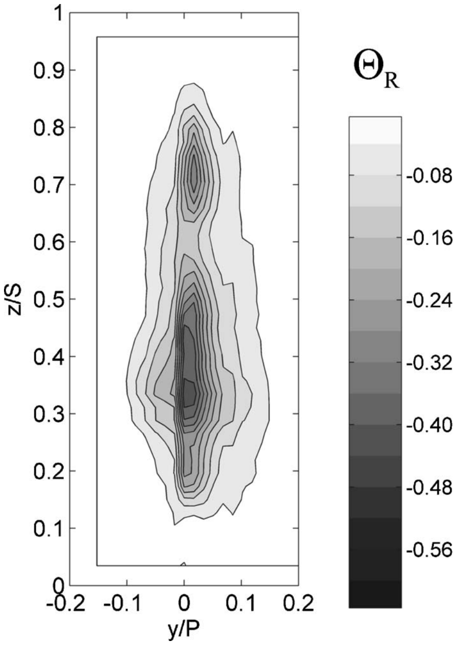

Fig. 5 Normalized temperature ratio (Θ_R) coolant contours at Position T for full coverage blowing at $M^*_{\mathrm{showerhead}}=1.6$, $M_{\mathrm{avg,suction}}=0.7$, and $M_{\mathrm{avg,pressure}}=0.6$, DR=1.6

Results

Coolant profiles were measured for a fully film cooled vane under conditions of high mainstream turbulence (Tu=20%). For these experiments blowing ratios were used corresponding to the optimum blowing ratios for adiabatic effectiveness. These blowing ratios were determined from previous studies made by researchers utilizing the same facility, the details of which may be found in Refs. [3,6,7]. A set of higher blowing ratios were also used to test the highest possible benefit of film cooling in hot streak reduction. These blowing ratios were also chosen based on previous studies and corresponded to the highest blowing ratios which still provided reasonable adiabatic effectiveness. Blowing ratios for optimum levels were $M^*=1.6$ for the showerhead, $M_{\mathrm{avg}}=0.7$ for the suction side, and $M_{\mathrm{avg}}=0.6$ for the pressure side. The higher blowing ratios were $M^*=2.0$ for the showerhead, $M_{\mathrm{avg}}=1.0$ for the suction side, and $M_{\mathrm{avg}}=1.0$ for the pressure side. Since the optimum blowing ratios for adiabatic effectiveness and for hot streak reduction may be different, these blowing ratio sets are later referred to as the "standard" blowing ratios and "high" blowing ratios to prevent confusion between what is optimum for adiabatic effectiveness and optimum for hot streak reduction.

Full Coverage Coolant Profiles. Contours for full coverage film cooling at standard blowing ratios ($M^*_{\mathrm{showerhead}}=1.6$, $M_{\mathrm{avg,suction}}=0.7$, and $M_{\mathrm{avg\ pressure}}=0.6$) and at a density ratio of DR=1.6 are shown in Fig. 5. Results are presented in terms of Θ_R even though no hot streak was used for these measurements so that the relative effect of the coolant on a hot streak would be evident. A large mass of coolant was centered pitchwise at the trailing edge and well below midspan at about $z/S=0.3$. The strong accumulation of coolant at this location was mainly due to the "crossover" region of the showerhead (Fig. 2). The showerhead coolant flow had a large downward (or upward) momentum due to the orientation of the coolant holes, causing the coolant to collect at one spanwise location. This region of low coolant temperatures (below the $\Theta_R=-0.16$ contour) stretched spanwise between $0.2<z/S<0.6$ with a pitchwise width that varied between about 6 and 13d (0.06–0.12P). The peak coolant temperature of $\Theta_R=-0.42$ coincided with the widest portion well below midspan

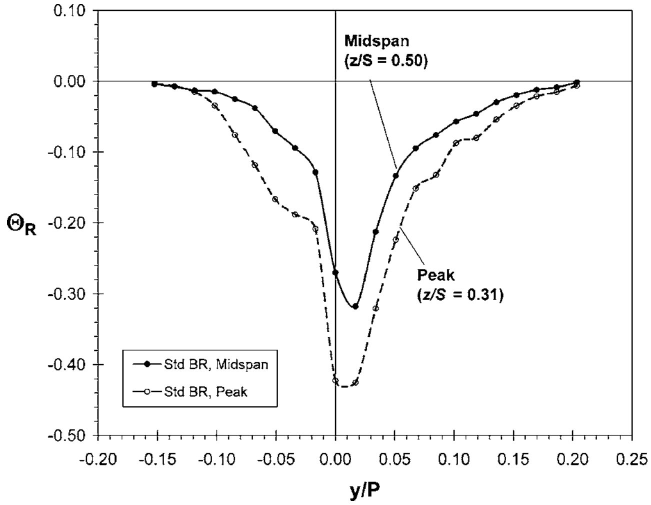

Fig. 6 Normalized temperature ratio (Θ_R) coolant profiles at Position T at midspan ($z/S=0.50$) and at the spanwise position of the peak coolant level ($z/S=0.31$) at standard blowing ratios ($M^*_{\text{showerhead}}=1.6$, $M_{\text{avg,suction}}=0.7$, and $M_{\text{avg,pressure}}=0.6$), DR=1.6

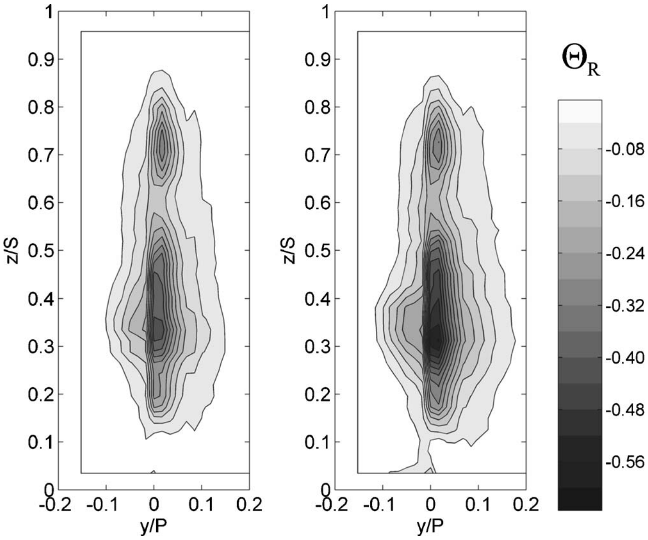

Fig. 7 Normalized temperature ratio (Θ_R) coolant contours at Position T, DR=1.6, for full coverage blowing at: (*a*) full coverage blowing at $M^*_{\text{showerhead}}=1.6$, $M_{\text{avg,suction}}=0.7$, and $M_{\text{avg,pressure}}=0.6$; and (*b*) full coverage blowing at $M^*_{\text{showerhead}}=2.0$, $M_{\text{avg,suction}}=1.0$, and $M_{\text{avg,pressure}}=1.0$

at about $0.35S$. Another large region of coolant was observed above midspan at about $z/S=0.7$. The deficiency in coolant at $z/S=0.6$ was due to blocked suction side holes at roughly this height due to the previous installation of a removable suction side coolant hatch used in other studies performed in the facility.

Normalized temperature profiles for the coolant flow are presented in Fig. 6 for positions at the midspan of the vane and the position where the maximum negative peak in Θ_R occurred. As shown in Fig. 2, the showerhead was split at the stagnation line, with $3\frac{1}{2}$ rows toward the suction side and $2\frac{1}{2}$ rows toward the pressure side. This, along with a greater total mass flow rate of coolant from the suction side coolant region compared with the pressure side coolant region, resulted in a greater amount of coolant present to the suction side of the vane at the trailing edge (Position T). At the midspan, where the hot streak was strongest, the coolant profile at midspan dipped to $\Theta_R=-0.32$ with a 20% width of nearly $17d$ $(0.15P)$. The spanwise position of peak coolant was well below midspan at $z=0.31S$. At this spanwise position, the coolant profile was nearly 50% wider than the midspan profile and peaked more than 35% lower at $\Theta_R=-0.43$. This suggests a very large potential for hot streak reduction if the center of the hot streak were positioned at approximately 1/3 span. For the current spanwise position of the hot streak, these results suggest that the hot streak should be positioned pitchwise just to the suction side of the stagnation line. The coincident peaks, negative for coolant, and positive for the hot streak, would likely result in a greater level of hot streak reduction.

As mentioned previously, two sets of full coverage blowing ratios were tested, corresponding to the optimum (standard) and above optimum (high) blowing ratios with respect to adiabatic effectiveness. The high blowing ratios had 35% more total mass flow rate than the standard blowing ratios. With respect to the approach flow to the vane, total coolant mass flow rates were 1.65% and 2.25% of the core flow for one vane pitch. Figure 7 compares coolant contours expressed in terms of Θ_R for standard blowing ratios ($M^*_{\text{showerhead}}=1.6$, $M_{\text{avg,suction}}=0.7$, and $M_{\text{avg,pressure}}=0.6$) and high blowing ratios ($M^*_{\text{showerhead}}=2.0$, $M_{\text{avg,suction}}=1.0$, and $M_{\text{avg,pressure}}=1.0$) at a density ratio of DR $=1.6$. While the shapes of the contours were similar with a large area of coolant centered below midspan and a small area of coolant above midspan, the main difference was the magnitude of the peak and size of the areas of coolant at a given contour level. For standard blowing ratios, the peak was $\Theta_R=-0.43$, while the peak for high blowing ratios was about 30% lower at $\Theta_R=-0.56$. In the small area of coolant above midspan, the magnitude of the coolant peak only increased slightly with increased blowing ratio. Since the showerhead holes directed coolant downward, this region of coolant changed little with increasing blowing ratio. With increased momentum at higher blowing ratios, the significant increases in coolant levels were only observed below $z=0.6S$. Therefore the primary source of increased coolant levels was the suction side,where small increases would be expected for the upper coolant area with an increase in blowing ratio from $M_{\text{avg,suction}}=0.7$ to 1.0.

Midspan and peak coolant profiles are shown in Fig. 8 where the effect of increased blowing is immediately evident. A marked increase in cooling potential occurred for high blowing ratios,

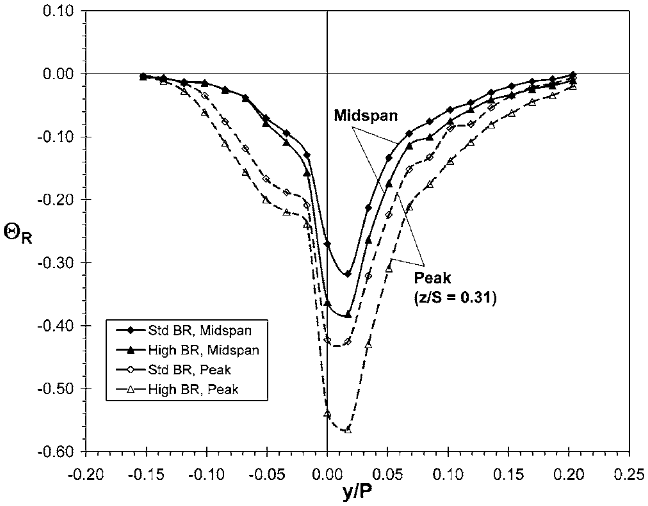

Fig. 8 Normalized temperature ratio (Θ_R) coolant profiles at Position T at midspan ($z/S=0.50$) and at the spanwise position of the peak coolant level ($z/S=0.31$) for standard blowing ratios ($M^*_{\text{showerhead}}=1.6$, $M_{\text{avg,suction}}=0.7$, and $M_{\text{avg,pressure}}=0.6$) and high blowing ratios ($M^*_{\text{showerhead}}=2.0$, $M_{\text{avg,suction}}=1.0$, and $M_{\text{avg,pressure}}=1.0$), DR=1.6

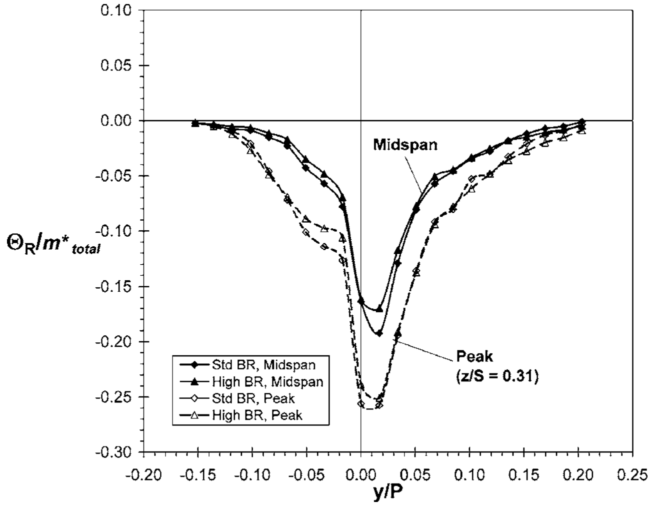

Fig. 9 Normalized temperature ratio scaled by the ratio of coolant to core flow ($\Theta_R/m^*_{\text{total}}$) for coolant profiles at Position T at midspan ($z/S=0.50$) and at the spanwise position of the peak coolant level ($z/S=0.31$) for standard blowing ratios and high blowing ratios, DR=1.6

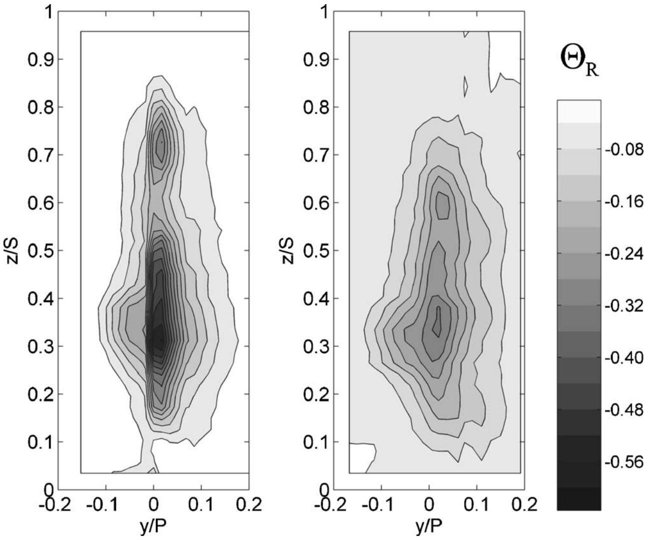

Fig. 10 Normalized temperature ratio (Θ_R) coolant contours for full coverage blowing at $M^*_{\text{showerhead}}=2.0$, $M_{\text{avg,suction}}=1.0$, and $M_{\text{avg,pressure}}=1.0$, DR=1.6 at: (a) Position T; and (b) Position B

where the negative peak increased nearly 25%, from $\Theta_R=-0.32$ to -0.38. However, the largest increase in coolant was observed well below midspan at about $0.3S$. This was mainly due to the behavior of the showerhead, where the higher blowing ratio resulted in higher fluid momentum, driving the coolant toward the crossover region well below midspan. This crossover region was the location shown in Fig. 2 where the directions of showerhead coolant holes were in opposition, creating an accumulation of coolant at this spanwise location. At this location, the negative peak increased more than 30%, representing a larger proportional increase in coolant at $z=0.31S$ than at midspan ($z=0.5S$).

To determine whether the coolant profiles scaled with the total mass flow rate of coolant, Θ_R values were divided by the total mass flow rate of coolant, and resulting profiles for the two mass flow rates of coolant were compared. Designating the ratio of the total mass flow rate of coolant to the mainstream flow rate as $m^*_{\text{total}}=\dot{m}_{\text{coolant}}/\dot{m}_{\text{mainstream}}$, the profiles of $\Theta_R/m^*_{\text{total}}$ were compared for the coolant flow rates of $m^*_{\text{total}}=1.65\%$ and 2.25%. Profiles of $\Theta_R/m^*_{\text{total}}$ for the two coolant mass flow rates tested were found to collapse quite well for the midspan and peak profiles as shown in Fig. 9. These results suggest that coolant profiles for varying mass flow rates of coolant are predictable using the profiles of $\Theta_R/m^*_{\text{total}}$ given in the figure.

The contrast between contour plots at the trailing edge and at Position B downstream of the vane for full coverage film cooling, shown in Fig. 10, indicated that the coolant was strongly diffused in the stator/rotor axial gap. Blowing ratios for these experiments were the high set of blowing ratios at $M^*_{\text{showerhead}}=2.0$, $M_{\text{avg,suction}}=1.0$, and $M_{\text{avg,pressure}}=1.0$ at a density ratio of DR $=1.6$. The location of $y/P=0.0$ at Position B was chosen as the peak position of a wake loss profile measured at the same position. Figure 10 shows that the top part of the coolant distribution at Position T moved downward by Position B. This was likely due to the high levels of dispersion between Position T and B, but also might be due to the passage vortex on the suction side of the vane causing a downward movement. Overall the coolant at Position B was significantly more dispersed than at Position T resulting in the peak magnitude decreasing 50% to $\Theta_R=-0.31$ at a spanwise location of $z/S=0.35$. This may be attributed to large scale, high turbulence levels.

Effect of Density Ratio on Coolant Profiles. For investigations of full coverage film cooling at low density ratios, the high set of blowing ratios were used, i.e., $M^*_{\text{showerhead}}=2.0$, $M_{\text{avg,suction}}=1.0$, and $M_{\text{avg,pressure}}=1.0$, since they were expected to have the largest effect on the hot streak. In Fig. 11, the coolant levels were roughly half as low for low density ratios (DR=1.2) as high density ratios (DR=1.6), but the shapes of the profiles were similar. In particular, the peak at low density ratio was $\Theta_R=-0.26$, with the magnitude of the peak at high-density ratio about 2.2 times higher. The similar shapes of profiles between the two density ratios at both midspan and at $z/S=0.31$ suggests that scaling would work well at both locations.

Since the normalized coolant temperature ratio, Θ_C, takes into account the difference in coolant temperature at the coolant hole exit, the data should collapse using this parameter. The results scaled by Θ_C are shown in Fig. 12. It is immediately obvious that the range and shape of the contour levels were very similar for the two density ratios using Θ_C scaling. This indicates that the spreading rate of the coolant and resulting distributions of initial coolant

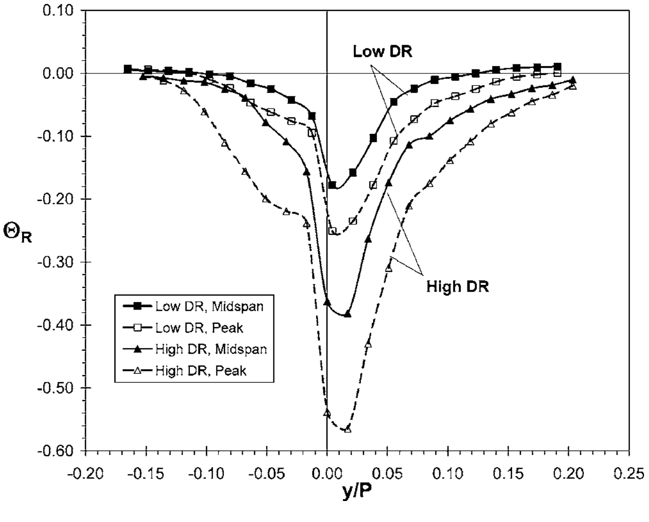

Fig. 11 Comparison of normalized coolant temperature (Θ_C) profiles at Position T at midspan ($z/S=0.50$) and the position of peak coolant ($z/S=0.31$) for full coverage blowing at $M^*_{\text{showerhead}}=2.0$, $M_{\text{avg,suction}}=1.0$, and $M_{\text{avg,pressure}}=1.0$, at low-density ratio (DR=1.2) and high-density ratio (DR=1.6)

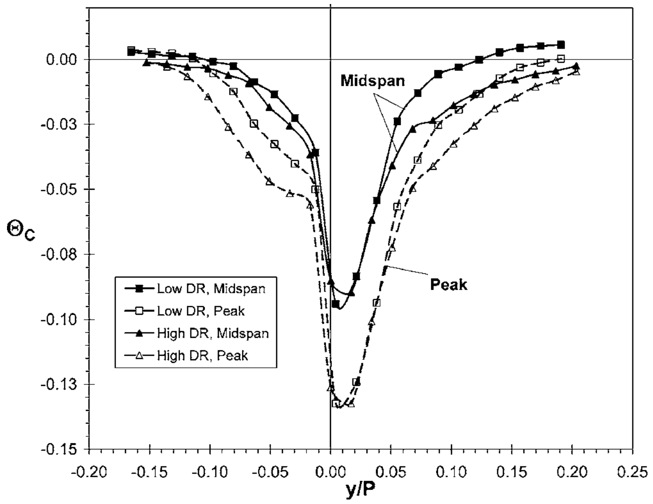

Fig. 12 Comparison of normalized coolant temperature (Θ_C) profiles at Position T at midspan ($z/S=0.50$) and the position of peak coolant ($z/S=0.31$) for full coverage blowing at $M^*_{\text{showerhead}}=2.0$, $M_{\text{avg,suction}}=1.0$, and $M_{\text{avg,pressure}}=1.0$, at low-density ratio (DR=1.2) and high-density ratio (DR=1.6)

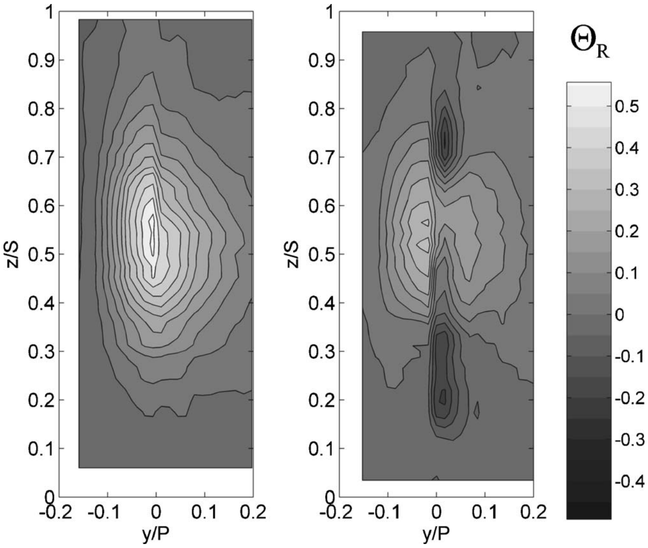

Fig. 13 Normalized temperature ratio (Θ_R) contours at Position T with the hot streak at the stagnation line: (*a*) no coolant; (*b*) full coverage blowing at $M^*_{\text{showerhead}}=1.6$, $M_{\text{avg,suction}}=0.7$, and $M_{\text{avg,pressure}}=0.6$, DR=1.6

were relatively independent of the density ratio within the range tested. Since the values of the coolant temperature at a given point were dependent on the coolant hole exit-to-mainstream temperature difference, this suggests that coolant profiles for other density ratios may be predicted from measured values using the definition of Θ_C near the vane. The agreement was very good at the peaks of the profiles with some deviations on the pressure side for the "peak" coolant profile and to the suction side well away from the peak for all profiles.

Effect of Full Coverage Film Cooling on Hot Streak Reduction. The effect of full coverage film cooling on the hot streak was considerable. For the following results, the hot streak was positioned pitchwise so that the center, or peak, of the hot streak would impinge the vane at the stagnation line at midspan (see Fig. 3 for stagnation line position). These experiments were also run under conditions of high mainstream turbulence. As shown in Fig. 13 for full coverage blowing at standard blowing ratios and a density ratio of DR=1.6, only a small portion of the hot streak remained at significant levels. With film cooling, the reduced hot streak peaked at $\Theta_R=0.33$ just to the pressure side of the vane at midspan, with a small region surrounding the peak at a contour level of $\Theta_R=0.30$. Overall, the reduction in the hot streak peak was 35% compared with no film cooling, while the reduction in the hot streak with respect to the reference position (Position A) upstream of the vane was 67%. Large amounts of excess coolant appeared above and below the hot streak to the suction side well below and above midspan, while the hot streak on the suction side of the trailing edge was reduced to $\Theta_R=0.19$.

Contour plots in Fig. 14 show the additional reduction in the hot streak due to increased blowing ratios for full coverage blowing. Blowing ratios for this comparison were standard blowing ratios ($M^*_{\text{showerhead}}=1.6$, $M_{\text{avg,suction}}=0.7$, and $M_{\text{avg,pressure}}=0.6$) and high blowing ratios ($M^*_{\text{showerhead}}=2.0$, $M_{\text{avg,suction}}=1.0$, and $M_{\text{avg,pressure}}=1.0$) at a density ratio of DR=1.6. There were increased coolant levels above and below the hot streak with increased blowing ratio. There was also a decrease in the size and magnitude of the remaining hot streak. At high blowing ratios the peaks on the pressure and suction sides were each reduced by at least one contour level ($\Delta\Theta_R=0.05$). However, significant decreases in the hot streak peak were not observed, primarily due to the nature of the individual coolant regions. The remaining hot streak was on the pressure side of the trailing edge. As discussed previously, increasing the blowing ratio had little effect at midspan because of the spanwise movement of the coolant. An increase in the blowing ratio led to higher coolant momentum from the showerhead resulting in higher coolant levels below midspan. This additional coolant contributed to the considerable drop in fluid temperature at $z=0.3S$, from $\Theta_R=-0.21$ to $\Theta_R=-0.38$. This helps to explain why the significant increase in mass flow did not have a correspondingly large effect on the hot streak peak value at midspan.

Comparing the same results at midspan, shown in Fig. 15, a considerable decrease was apparent in the center of the hot streak where the bulk of the coolant was located. Although the higher blowing ratios resulted in a 35% increase in coolant mass flow, the hot streak peaks at midspan were only reduced by an additional

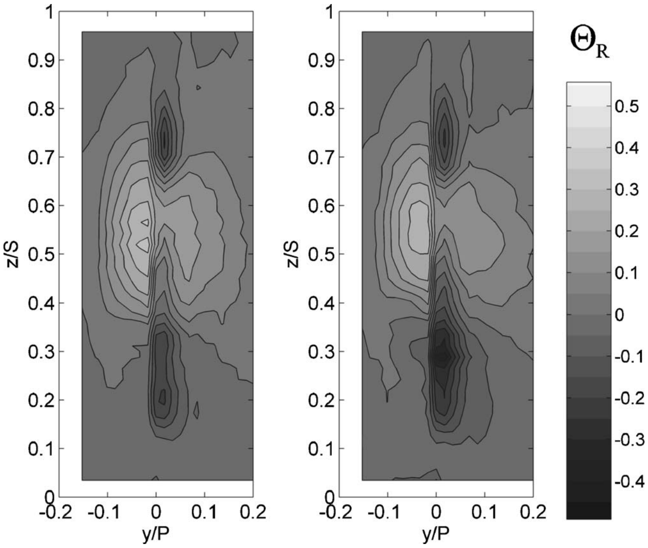

Fig. 14 Normalized temperature ratio (Θ_R) contours at Position T with the hot streak at the stagnation line: (*a*) full coverage blowing at $M^*_{\text{showerhead}}=1.6$, $M_{\text{avg,suction}}=0.7$, and $M_{\text{avg,pressure}}=0.6$, DR=1.6; and (*b*) full coverage blowing at $M^*_{\text{showerhead}}=2.0$, $M_{\text{avg,suction}}=1.0$, and $M_{\text{avg,pressure}}=1.0$, DR=1.6

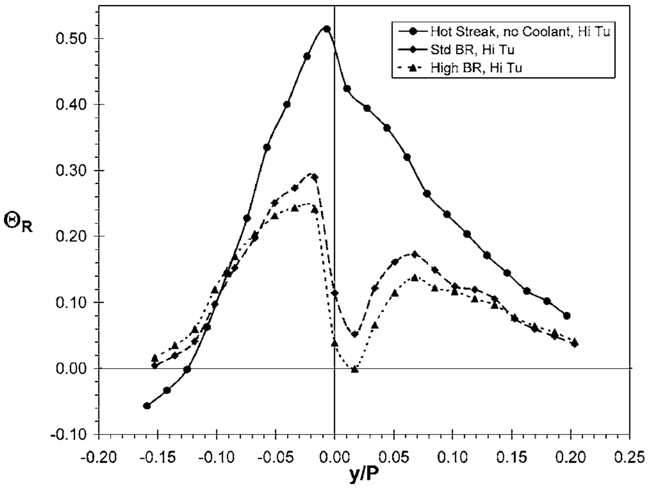

Fig. 15 Normalized temperature ratio (Θ_R) profiles at position *T* for the hot streak impacting the stagnation line without coolant and with full coverage blowing at adiabatic effectiveness optimum blowing ratios ($M^*_{\text{showerhead}}=1.6$, $M_{\text{avg,suction}}=0.7$, and $M_{\text{avg,pressure}}=0.6$) and above optimum blowing ratios ($M^*_{\text{showerhead}}=2.0$, $M_{\text{avg,suction}}=1.0$, and $M_{\text{avg,pressure}}=1.0$), DR=1.6

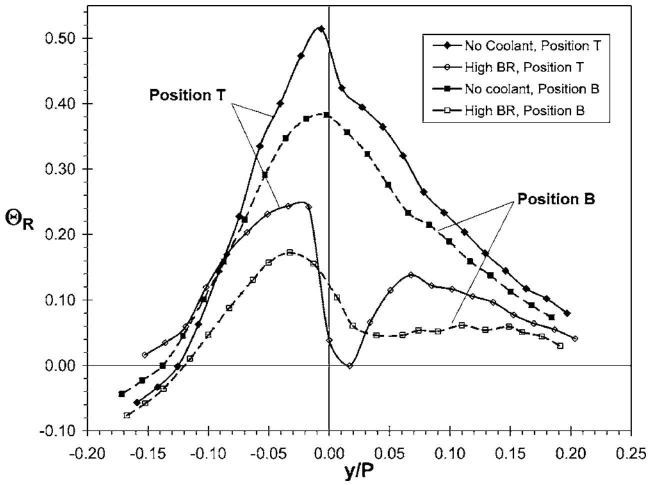

Fig. 17 Normalized temperature ratio (Θ_R) profiles at Position T and Position B for the hot streak impacting the stagnation line without coolant and with full coverage blowing at $M^*_{\text{showerhead}}=2.0$, $M_{\text{avg,suction}}=1.0$, and $M_{\text{avg,pressure}}=1.0$, DR=1.6

15–20% with the higher blowing ratios. Again this may be attributed to the spanwise movement of coolant from the showerhead at higher blowing ratios.

The rapid dispersion of coolant in the stator/rotor axial gap shown in Fig. 10 has important implications for hot streak reduction. As shown previously at the trailing edge of the vane, there were distinct regions of coolant and of hot streak fluid. These regions intermingled in the stator/rotor axial gap causing a significant drop in the sharp gradient at the trailing edge, as seen in the contours in Fig. 16. This comparison used the high set of blowing ratios ($M^*_{\text{showerhead}}=2.0$, $M_{\text{avg,suction}}=1.0$, and $M_{\text{avg,pressure}}=1.0$), the same set as for Fig. 10. At this downstream position the hot streak was reduced to a small region of low strength to the pressure side of the vane. The hot streak peak at $\Theta_R=0.17$ represented a reduction in hot streak strength of 83% compared with the upstream reference at Position A, and a 55% reduction in the hot streak compared with no film cooling at Position B.

The dispersion effect downstream of the vane is also evident from the midspan profiles in Fig. 17 showing the dip in the film cooled hot streak profile just to the suction side of the trailing edge being mixed out in the stator/rotor axial gap. Meanwhile, the peak on the pressure side was reduced an additional 40% to a value of $\Theta_R=0.17$.

Figure 18 shows the effect of density ratio in hot streak reduction for high blowing ratios ($M^*_{\text{showerhead}}=2.0$, $M_{\text{avg,suction}}=1.0$, and $M_{\text{avg,pressure}}=1.0$), the same as used for Fig. 11. Using low density ratio coolant, DR=1.2, with full coverage film cooling at high blowing ratios, Θ_R contours in Fig. 18(*a*) show the interaction with the hot streak was similar to the DR=1.6 case in Fig. 18(*b*), but the effect was smaller. This consistent pattern yet smaller level of reduction for smaller density ratio coolant compared to large

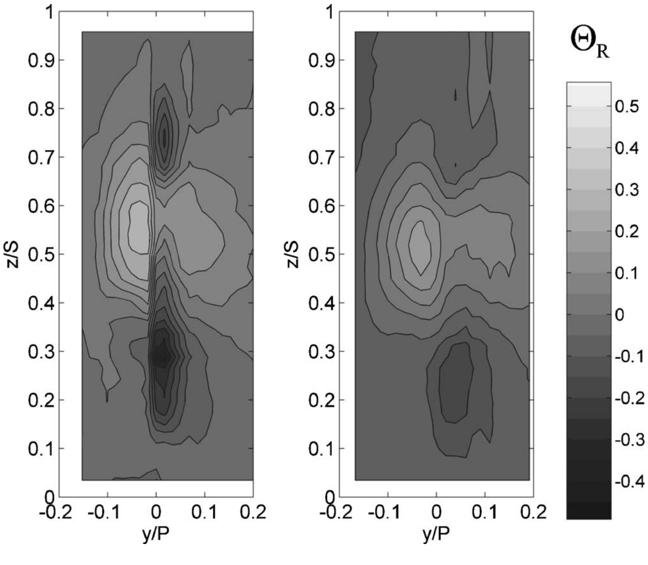

Fig. 16 Normalized temperature ratio (Θ_R) contours for full coverage blowing at $M^*_{\text{showerhead}}=2.0$, $M_{\text{avg,suction}}=1.0$, and $M_{\text{avg,pressure}}=1.0$, DR=1.6: (*a*) Position T (trailing edge); and (*b*) Position B

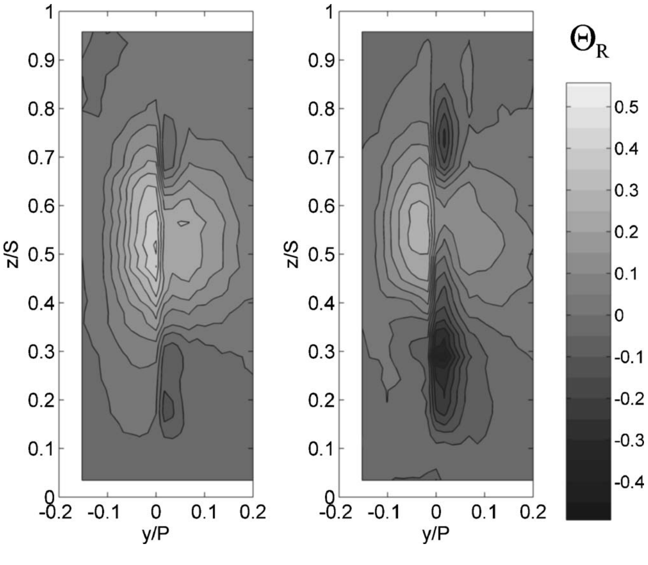

Fig. 18 Normalized temperature ratio (Θ_R) contours at Position T with the hot streak at the stagnation line with full coverage blowing at $M^*_{\text{showerhead}}=2.0$, $M_{\text{avg,suction}}=1.0$, and $M_{\text{avg,pressure}}=1.0$ at (*a*) DR=1.2; and (*b*) DR=1.6

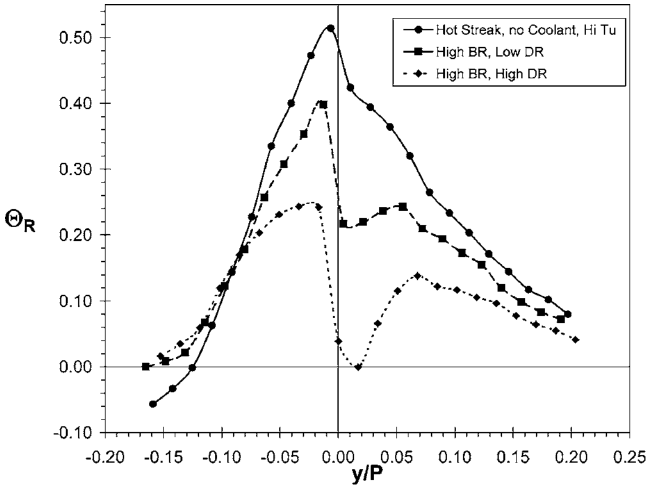

Fig. 19 Normalized temperature ratio (Θ_R) profiles at Position T for the hot streak impacting the stagnation line without coolant and with full coverage blowing at adiabatic effectiveness optimum blowing ratios ($M^*_{\text{showerhead}}=1.6$, $M_{\text{avg,suction}}=0.7$, and $M_{\text{avg,pressure}}=0.6$) and above optimum blowing ratios ($M^*_{\text{showerhead}}=2.0$, $M_{\text{avg,suction}}=1.0$, and $M_{\text{avg,pressure}}=1.0$), with density ratios of DR=1.2 and 1.6

density ratio coolant is evident in the midspan profiles given in Fig. 19. Overall the hot streak peak was reduced almost 20% to $\Theta_R=0.41$ compared with almost 40% with high density ratio coolant.

For the overall peak with low density ratio coolant, the drop in the peak hot streak temperature was $\Delta\Theta_R=0.10$, while the drop in the peak for high density ratio coolant was $\Delta\Theta_R=0.22$. The proportion of drops in the peak hot streak temperature is therefore $\Delta\Theta_{R,\text{LoDR}}:\Delta\Theta_{R,\text{HiDR}}=1:2.2$. This is about the same as the proportion of mainstream-to-coolant temperature differences for the two density ratios, i.e., $(T_\infty-T_c)_{\text{LoDR}}:(T_\infty-T_c)_{\text{HiDR}}=1:2.25$. This suggests that in addition to scaling the coolant profiles, the reduction in the hot streak could also be scaled according to the mainstream-to-coolant temperature difference.

Conclusions

The primary objective of this study was to determine the reduction of a hot streak impacting a highly film cooled nozzle guide vane. Initially, the coolant distribution downstream of the vane with no hot streak was quantified at the trailing edge and at 0.34C downstream of the vane. The downstream position corresponded to the typical position of the first rotor stage of a turbine. Experiments were conducted using an approach mainstream turbulence level of 20% in order to simulate actual engine conditions. Measurements showed a nonuniform distribution of coolant along the span of the vane. A significant accumulation of coolant was found to occur at a position where the coolant holes in the showerhead of the vane reversed direction. This suggests the possibility of greater reduction of hot streaks if the peak of the hot streak is positioned in the same location as the accumulated coolant.

As expected, with increasing blowing ratio the normalized temperature of the coolant distribution downstream of the vane showed a decreased temperature. However, the normalized temperature profile of the coolant was found to scale with the total mass flux of the coolant. Furthermore, experiments were conducted with coolant at density ratios of 1.2 and 1.6, and the downstream temperature profiles for these two cases were found to be very similar when scaled with the temperature difference between the coolant hole exit temperature and the mainstream temperature. These results indicate that the temperature distribution downstream of the vane for any blowing ratio and any density ratio is predictable when appropriately scaled.

The hot streak reduction due to the coolant injection was determined using measurements of the hot streak temperature profile downstream of the vane without and with film cooling injection. These experiments were conducted with coolant injection at blowing ratios that corresponded to the optimum for adiabatic effectiveness performance. These results were compared with experiments using higher blowing ratios with a total mass flow that was 36% higher. For all of the results, the hot streak peak was positioned to impact the vane at the stagnation line. Maximum reduction of the peak hot streak temperature occurred at the position 0.34C downstream of the vane trailing edge. At this position for the higher blowing ratios, there was a 55% reduction of the hot streak peak temperature compared with no film cooling, showing that very significant reduction of the hot streak can be achieved using the coolant from a highly film cooled nozzle guide vane.

Acknowledgment

We would like to thank Jay Rutledge and Dave Robertson for their assistance in running experiments and developing a new data acquisition system for the facility.

Nomenclature

BR = abbreviation for "blowing ratio"
C = vane chord length, 594 mm
d = film cooling hole diameter, 4.11 mm
DR = density ratio of coolant to mainstream, ρ_c/ρ_∞
k = thermal conductivity
m^*_{total} = ratio of the total mass flow rate of coolant to the mainstream flow rate
M = blowing ratio for the suction and pressure side, where U_∞ is the local freestream velocity at the hole location, $\rho_c U_c/\rho_\infty U_\infty$
M^* = blowing ratio for the showerhead region, where U_0 is the approach velocity to the vane, $\rho_c U_c/\rho_0 U_0$
p = film cooling hole pitch in the spanwise direction
P = pitch between vanes, 460 mm
s = surface length from leading edge stagnation line
S = span length of vane, 550 mm
T_{ij} = hot streak or coolant temperature at a point in the flow
$T_{0,C}$ = coolant temperature at the coolant hole exit
$T_{0,\text{HS}}$ = upstream peak hot streak temperature at the reference location, Position A
T_∞ = mainstream temperature
Tu = turbulence intensity, $u_{\text{rms}}/U\times 100\%$
U_0 = approach velocity to the vane
U_∞ = local freestream velocity
y = flow normal coordinate originating at the trailing edge or vane wall (positive from suction side of test vane, negative from pressure side of test vane)
z = spanwise coordinate

Greek Symbols

ϕ = injection angle with respect to the surface plane
θ = streamwise injection angle
ρ = density
Λ_f = turbulence integral length scale
Θ_C = normalized coolant temperature ratio, $(T_{ij}-T_\infty)/(T_\infty-T_{0,C})$

Θ_R = normalized hot streak temperature ratio, $(T_{ij}-T_{\infty})/(T_{0,\mathrm{HS}}-T_{\infty})$

Subscripts

C = coolant
HS = hot streak value
R = normalized
rms = root-mean-square
∞ = mainstream
0 = approach condition

References

[1] Jenkins, S. C., Varadarajan, K., and Bogard, D. G., 2003, "The Effects of High Mainstream Turbulence and Turbine Vane Film Cooling on the Dispersion of a Simulated Hot Streak," J. Turbomach., **126**(1), pp. 203–211.

[2] Roback, R. J., and Dring, R. P., 1993, "Hot Streaks and Phantom Cooling in a Turbine Rotor Passage: Part 1 – Separate Effects," J. Turbomach., **115**(4), pp. 657–666.

[3] Polanka, M. D., 1999, "Detailed Film Cooling Effectiveness and Three Component Velocity Field Measurements on a First Stage Turbine Vane Subject to High Freestream Turbulence," Ph.D. dissertation, The University of Texas at Austin, Austin, TX.

[4] Cutbirth, J. M., and Bogard, D. G., 2002, "Evaluation of Pressure Side Film Cooling With Flow and Thermal Field Measurements, Part I: Showerhead Effects," ASME Paper No. GT-2002-30174.

[5] Kuotmos, P., and McQuirk, J. J., 1989, "Isothermal Flow in a Gas Turbine Combustor—a Benchmark Experimental Study," Exp. Fluids, **7**, pp. 344–354.

[6] Cutbirth, J. M., 2000, "Turbulence and Three-Dimensional Effects on the Film Cooling of a Turbine Vane," Ph.D. dissertation, The University of Texas at Austin, Austin, TX.

[7] Robertson, D., 2004, "Roughness Impact on Turbine Vane Suction Side Film Cooling Effectiveness," Masters thesis, The University of Texas at Austin, Austin, TX.

Application of the Turbulent Potential Model to Heat Transfer Predictions on a Turbine Guide Vane

Rene Pecnik
e-mail: rene@ttm.tu-graz.ac.at

Wolfgang Sanz

Institute for Thermal Turbomachinery
and Machine Dynamics,
Graz University of Technology,
Graz 8010, Austria

The accurate numerical simulation of the flow through turbomachinery depends on the reliable prediction of laminar to turbulent boundary layer transition phenomena. The aim of this paper is to study the ability of the turbulent potential model to predict those nonequilibrium turbulent flows for several test cases. Within this model turbulent quantities are described by the turbulent scalar and turbulent vector potentials of the turbulent body force—the divergence of the Reynolds stress tensor. For model validation first flat plate test cases with different inlet turbulence intensities, zero pressure gradient, and nonuniform pressure gradient distributions along the plate were calculated and compared by means of skin friction values measured in the experiments. Finally the model was validated by heat transfer measurement data obtained from a highly loaded transonic turbine guide vane cascade for different operating conditions.

[DOI: 10.1115/1.2720494]

Introduction

In turbomachines and especially in aircraft engines the Reynolds numbers that determine the evolution of the boundary layers are relatively low. So a large part of the flow along the blade surfaces is often laminar or transitional. Bypass transition is the dominant form of transition in turbomachinery due to the high turbulence levels. The boundary layer development, losses, efficiency, and heat transfer are greatly affected by the laminar-to-turbulent transition. Therefore, the ability to accurately predict the transition process is crucial for the design of efficient and reliable machines.

Considerable effort has been spent on adapting standard two-equation turbulence models to predict transition for various kinds of flows. Schmidt and Patankar [1] showed the ability of two-equation low-Reynolds turbulence models to predict transition in boundary layer flows but they also investigated their limitations to specific applications. Further, more complex approaches are the addition of an intermittency transport equation based on highly empirical correlations to two-equation turbulence models [2,3]. These transport models have been tested on simple flat plate test cases and more complex transitional flows with reasonable results. More complex second moment turbulence closures show significant improvements in predicting nonequilibrium flow situations, but they tend to be less robust to be used in complex flow applications.

An innovative compromise between accuracy and numerical efforts promises the model of Chang and Perot [4], which solves turbulent potentials obtained by the divergence of the Reynolds stress tensor. This model contains the physical properties of a full Reynolds stress transport model, but solves a reduced number of transport equations. The source terms of the turbulent potential model (TPM) are directly related to that of full Reynolds stress transport models (RSTMs) and hence existing and proved RSTM can be used to derive the necessary terms for the TPM, e.g., pressure strain correlations. These pressure strain correlations describe the mechanism of the redistribution and relaxation of turbulence, and are usually separated into a slow and rapid part. How the rapid pressure strain term should behave in certain limits can be aided by the rapid distortion theory. Models that contain rapid distortion theory are able to predict transition with reasonable results [4].

Therefore in this work the ability of the TPM was investigated to accurately predict boundary layer transition. The TPM was first applied to predict the skin friction coefficient distribution on various flat plate test cases. But the main focus in this work was put on the ability of the model to predict the heat transfer distributions over a highly loaded transonic turbine guide vane.

Numerical Method

Flow Solver. The computations were performed using the in-house Navier–Stokes code LINARS, developed at the Institute for Thermal Turbomachinery and Machine Dynamics at Graz University of Technology, Austria.

The compressible Reynolds/Favre-averaged Navier–Stokes (RANS) equations are solved in conservative form by means of a fully implicit time-marching finite-volume method on structured curvilinear grids in multiblock alignment.

The inviscid (Euler) fluxes are discretized with the upwind flux-difference splitting method of Roe [5]. In order to achieve a high order of spatial accuracy a total variation diminishing (TVD) scheme with third-order interpolation was applied to get the state vector at each cell interface. The viscid flux vector at the cell interfaces is constructed with a second-order accurate central-differencing scheme, using Green's theorem.

To obtain a linear set of the governing equations the Newton–Raphson procedure is applied for the discretization in time. At the left-hand side of the equations system the inviscid fluxes are treated with first-order accuracy and the viscid fluxes with a thin-layer approximation to obtain a block tridiagonal matrix for each grid index line. This linear equation set is solved by the alternating direction implicit (ADI) scheme. In stationary simulations convergence is improved by using a local time step based on a local stability criterion and a three-level multigrid V-cycle. The main flow equations and the turbulence equations are solved sequentially.

Contributed by the International Gas Turbine Institute of ASME for publication in the Journal of Turbomachinery. Manuscript received July 17, 2006; final manuscript received July 27, 2006. Review conducted by David Wisler. Paper presented at the ASME Turbo Expo 2005: Land, Sea and Air (GT2005), Reno, NV, USA, June 6–9, 2005. Paper No. GT2006-90365.

Turbulence Closures. To close the RANS equations, additional equations have to be solved which model the turbulence in the flow field. The in-house code LINARS includes a number of low-Reynolds-number turbulence models as listed below:

- Spalart and Allmaras [6];
- standard k-ε model [7];
- k-ω model by Wilcox [8];
- shear stress transport (SST) k-ω model by Menter [9];
- v^2f turbulence model by Durbin [10]; and
- turbulent potential model by Perot and Moin [11].

The first four turbulence models are commonly used linear eddy-viscosity models as implemented in many computational fluid dynamics (CFD) codes. They use the Bousinesq approach to model the eddy viscosity, based on the assumption that a given shear level results in a given turbulence level. These models are not capable of predicting transitional boundary layer flows.

The advanced eddy viscosity model of Durbin includes turbulent anisotropy information by means of two additional equations: The first one is a transport equation for the turbulent normal strain component v'^2. The second one is an elliptic relaxation equation, which models the mechanism of the redistribution of turbulent kinetic energy and accounts for nonlocal pressure effects associated with velocity–pressure gradient correlations [10]. This model was used by the authors to simulate transitional boundary layers on flat plate test cases and to predict the secondary flow field through a transonic turbine guide vane [12].

In this work the last mentioned turbulent potential model was investigated. This model is akin with RSTM and is not an eddy viscosity model. The TPM was tested to its ability to predict transitional boundary layer flows on various turbomachinery relevant test cases.

Turbulent Potential Model

A detailed derivation of this model is given in Ref. [13] and will be summarized hereafter. The basic idea of the TPM is to keep the information of the Reynolds stresses tensor anisotropy and at the same time to reduce the number of transport equations compared to full RSTMs. The full second moment closures contain more information than required to close the RANS equations—only the divergence of the Reynolds stress tensor is therefore required [14].

The divergence of the Reynolds stress tensor can be decomposed into its scalar and vector potential using Helmholtz decomposition as given by

$$\nabla \cdot \mathbf{R} = \nabla\phi + \nabla \times \boldsymbol{\psi} \tag{1}$$

with the divergence free gauge restriction of $\nabla\cdot\boldsymbol{\psi}=0$. By means of this divergence free restriction of the vector potential the scalar and vector potential can be expressed explicitly as functions of the Reynolds stress tensor

$$\nabla^2\phi = \nabla \cdot (\nabla \cdot \mathbf{R}) \tag{2}$$

$$-\nabla^2\boldsymbol{\psi} = \nabla \times (\nabla \cdot \mathbf{R}) \tag{3}$$

The newly obtained variables ϕ and $\boldsymbol{\psi}$ are referred to in Ref. [11] as the average pressure drop in turbulent vortices (ϕ) and as a measure of the average vorticity magnitude of turbulent vortices ($\boldsymbol{\psi}$).

Transport equations were derived for these turbulent potentials. In these equations, similar to the derivation of a RSTM, unknown source terms appear. If only one inhomogeneous direction (only derivatives in the inhomogeneous direction remain) is assumed in order to guide the construction of the unknown source terms of the TPM, it can be shown that these source terms are directly related to the source terms of a RSTM. Hence existing RSTM can be used to derive the unknown source terms, which need to be modeled.

The transport equations given in the section below were proposed in Ref. [14]. This model is a further enhancement of the original one proposed in Ref. [13] in order to improve the model performance and stability.

TPM Transport Equations.

$$\frac{\partial k}{\partial t} + \frac{\partial \tilde{u}_j k}{\partial x_j} - \frac{\partial}{\partial x_j}\left[(\nu_l + \sigma_k \nu_t)\frac{\partial k}{\partial x_j}\right] = P - \varepsilon \tag{4}$$

$$\frac{\partial \varepsilon}{\partial t} + \frac{\partial \tilde{u}_j \varepsilon}{\partial x_j} - \frac{\partial}{\partial x_j}\left[(\nu_l + \sigma_\varepsilon \nu_t)\frac{\partial \varepsilon}{\partial x_j}\right] = \frac{\hat{\varepsilon}}{k}(C_{\varepsilon 1}P - C_{\varepsilon 2}\varepsilon) \tag{5}$$

$$\begin{aligned}\frac{\partial(\phi/k)^{1/2}}{\partial t} &+ \frac{\partial \tilde{u}_j(\phi/k)^{1/2}}{\partial x_j} - \frac{\partial}{\partial x_j}\left[(\nu_l + \sigma_\phi \nu_t)\frac{\partial(\phi/k)^{1/2}}{\partial x_j}\right] \\ &= \frac{1}{2}C_{p1}\beta\frac{\hat{\varepsilon}}{k}(2\alpha - 1)\left(\frac{\phi}{k}\right)^{1/2} - \frac{1}{2}(1 - C_{p2})\frac{P}{k}\left(\frac{\phi}{k}\right)^{1/2} \\ &\quad + \frac{1}{2}C_t\sqrt{\mathrm{Re}_t}\left(1 - 1.5\frac{\phi}{k}\right)\frac{P}{k} + \frac{1}{2}C_{p3}\left(\frac{(\psi_j/k)(\psi_j/k)}{f_{\mathrm{Re}\,t}\nu_t/k} - \frac{P}{k}\right)\left(\frac{\phi}{k}\right)^{1/2}\end{aligned} \tag{6}$$

$$\begin{aligned}\frac{\partial(\psi_i/k)}{\partial t} &+ \frac{\partial \tilde{u}_j(\psi_i/k)}{\partial x_j} - \frac{\partial}{\partial x_j}\left[(\nu_l + \nu_t)\frac{\partial(\psi_i/k)}{\partial x_j}\right] \\ &= C_\mu(2\alpha - 1)\frac{\phi}{k}\omega_i - 2\alpha\frac{\psi_i}{k}\frac{P}{k} - C_{p1}\beta\frac{\hat{\varepsilon}}{k}(1 - \alpha)\frac{\psi_i}{k} \\ &\quad - (1 - C_{p2})\left(\frac{\psi_i}{k}\frac{P}{k} - \frac{\phi}{k}\omega_i\right) + C_t\sqrt{\mathrm{Re}_t}\left(\frac{\phi}{k}\right)^{1/2}\omega_i\end{aligned} \tag{7}$$

with the model functions and constants

$$\begin{gathered}P = \psi_i\omega_i, \quad \nu_t = C_\mu\frac{\phi k}{\varepsilon}, \quad \alpha = \left(1 + \frac{3}{2}\frac{\phi}{k}\right)^{-1}, \quad f_{\mathrm{Re}\,T} = 1 + 25/\mathrm{Re}_t \\ \hat{\varepsilon} = \varepsilon k\left(k + 10\nu_l\left|\frac{\partial\sqrt{k}}{\partial x_i}\right|\right)^{-1}, \quad \beta = \frac{\nu_t}{\nu_l + 5\nu_t} \\ \mathrm{Re}_t = \frac{k^2}{\nu\varepsilon}, \quad \sigma_k = 1/3 + 2/3(P/\hat{\varepsilon}), \quad \sigma_\varepsilon = 1/3 + 1/2(P/\hat{\varepsilon}) \\ \sigma_\phi = 1/3, \quad C_{p1} = 1.7(0.5 + 0.5P/\varepsilon), \quad C_{p2} = 3/5 \\ C_{p3} = C_{p2} + 6/7, \quad C_\mu = 0.21, \quad C_{\varepsilon 1} = 1.45 \\ C_{\varepsilon 2} = 1.83 - 0.16e^{-0.1\,\mathrm{Re}_t}, \quad C_t = 0.0018\end{gathered} \tag{8}$$

The latter constant C_t controls the transition and is given to $C_t=0.001$ in the boundary layer code, which was kindly provided by Perot. In the boundary layer code the equations are based on the premise that streamwise second derivatives are small enough that they can be neglected. The code used in this work takes into account this streamwise derivative and therefore it is hypothesized that during the transition process (the assumption of small streamwise second derivatives in this region is not accurate) the derivatives add considerable diffusion. Hence, during the validation of the TPM this constant was modified to $C_t=0.0018$ to match the skin friction distribution along the flat plate test case T3A (zero pressure gradient) discussed below. In general the higher the value C_t the more upstream is the transition onset. This value was used for all investigated test cases presented in this work.

The transport equations for the turbulent kinetic energy and the turbulent dissipation are primarily supplementary equations to model the source terms in the turbulence potential equations. Further in this work the turbulent kinetic energy and the eddy viscosity were also coupled with the compressible Navier–Stokes equations (see section implementation Eqs. (13) and (14)).

In the current work only two-dimensional (2D) flow simulations were done with the implemented TPM. For these flows the vorticity vector $\boldsymbol{\omega}$ as well as the turbulent potential vector $\boldsymbol{\psi}$ have only one nonzero component. Hence the TPM model reduces to four transport equations to solve, namely k, ε, ϕ, and the component of the turbulent vector potential $\boldsymbol{\psi}$ that points out of the calculation plane ψ_3. In case of a fully 3D calculation one additional component of the potential vector must be solved (five transport equations), whereas the third component of the vector potential can be obtained from the gauge restriction $\nabla \cdot \boldsymbol{\psi}=0$.

Boundary Conditions. At the inlet the turbulent kinetic energy is specified with the turbulence intensity by $k_i=3/2\mathrm{Tu}_i^2 U_i^2$. With isotropic turbulence at the inlet the turbulent scalar ϕ_i is given by $\phi_i=2/3k_i$ and the turbulent vector potential $\psi_{3,i}=0$ in absence of walls. The turbulent dissipation rate ε_i at the inlet was evaluated with the turbulent Reynolds number $\varepsilon_i=k_i^2/\nu\,\mathrm{Re}_{t,i}$. The value $\mathrm{Re}_{t,i}$ is used as a free parameter, which was adjusted at the inlet by means of several calculations for the flat plate test cases to get the best agreement with the measured free-stream turbulence distribution along the flat plates. With this adjustment the same turbulence conditions were achieved compared to the experiments (see the section "Flat Plate Test Cases"). At the guide vane calculations the free parameter $\mathrm{Re}_{t,i}$ was assumed within reasonable magnitudes, as no turbulent dissipation or free-stream turbulent distribution was measured.

Dirichlet boundary conditions were imposed on the turbulent kinetic energy k, the turbulent potentials ϕ and ψ_3 at walls with $k=\phi=\psi_3=0$. The turbulent dissipation at walls was set with the relation

$$\varepsilon_W = 2\nu_l \frac{\partial\sqrt{k}}{\partial x_i}\frac{\partial\sqrt{k}}{\partial x_i} \tag{9}$$

Implementation. The compressible Reynolds/Favre averaged Navier–Stokes equations (higher order correlations not denoted) are given in this section to demonstrate the implementation of the TPM into the in-house code LINARS. If flows are subjected to high Mach numbers the density fluctuations cannot be neglected. Therefore it is necessary to perform (beside Reynolds averaging) density weighted time averaging, called Favre averaging. The Favre averaging does not—in contrast to the Reynolds averaging—alter the form of the conservation laws for compressible flows. The velocity vector u_i, the energy e, and the temperature T are Favre averaged by $\tilde{f}=\overline{\rho f}/\bar{\rho}$, with $f''=f-\tilde{f}$ and $\overline{f''}\neq 0$

$$\frac{\partial\bar{\rho}}{\partial t}+\frac{\partial\bar{\rho}\tilde{u}_j}{\partial x_j}=0$$

$$\frac{\partial(\bar{\rho}\tilde{u}_i)}{\partial t}+\frac{\partial(\bar{\rho}\tilde{u}_i\tilde{u}_j)}{\partial x_j}=-\frac{\partial\bar{p}}{\partial x_i}+\frac{\partial}{\partial x_j}(\bar{\tau}_{ij}-\overline{\rho u_i'' u_j''})$$

$$\frac{\partial(\bar{\rho}\tilde{e})}{\partial t}+\frac{\partial(\bar{\rho}\tilde{u}_j\tilde{e})}{\partial x_j}=-\frac{\partial\tilde{u}_j\bar{p}}{\partial x_j}+\frac{\partial[\tilde{u}_i(\bar{\tau}_{ij}-\overline{\rho u_i'' u_j''})]}{\partial x_j}-\frac{\partial(\dot{q}_{j,l}+\dot{q}_{j,t})}{\partial x_j} \tag{10}$$

The divergence of the Reynolds stress tensor is modeled with Eq. (1) given here in tensor notation

$$\frac{\partial(\overline{u_i'' u_j''})}{\partial x_j}=\frac{\partial\phi}{\partial x_i}+\varepsilon_{ijk}\frac{\partial\psi_k}{\partial x_j} \tag{11}$$

with the assumption of a constant density. ε_{ijk} represents the permutation tensor. In 2D this vector simplifies to

$$\frac{\partial(\overline{u_i'' u_j''})}{\partial x_j}=\begin{bmatrix}\dfrac{\partial\phi}{\partial x_1}\\[2ex]\dfrac{\partial\phi}{\partial x_2}\end{bmatrix}+\begin{bmatrix}\dfrac{\partial\psi_3}{\partial x_2}\\[2ex]-\dfrac{\partial\psi_3}{\partial x_1}\end{bmatrix} \tag{12}$$

Table 1 Boundary conditions for the flat plate test cases

	Re_L	$\mathrm{Tu}_{\mathrm{le}}$ (%)	$\mathrm{Re}_{t,\mathrm{le}}$
T3A	527,300	3.3	100
T3B	957,000	6.1	710
T3C1	772,200	6.6	190
T3C2	656,000	3.0	110

The following relations were used to determine the pressure and the energy

$$\bar{p}=R\tilde{T}\bar{\rho},\quad \tilde{e}=\frac{\bar{p}}{\kappa-1}+\frac{1}{2}\bar{\rho}\tilde{u}_i\tilde{u}_i+k \tag{13}$$

The turbulent heat transfer was modeled with the simple gradient diffusion hypothesis based on similarities to the molecular heat transfer for a first attempt in this work. The turbulent Prandtl number was set to a constant value of $\mathrm{Pr}_t=0.9$, the density was assumed to be constant again

$$\dot{q}_{j,t}=-c_p\overline{\rho \mathrm{Tu}_j''}=-\frac{c_p\mu_t}{\mathrm{Pr}_t}\frac{\partial\tilde{T}}{\partial x_j} \tag{14}$$

More accurate approaches are available but have not yet been tested.

The partial differential equations (PDEs) of the TPM have been solved uncoupled implicitly by means of the ADI scheme after each time step iteration of the main equations.

Results and Discussion

Flat Plate Test Cases. In this investigation numerical results were compared with experimental data obtained from transitional flows over adiabatic flat plates with sharp leading edges [15]. These experiments were chosen to test the ability of the turbulent potential model to predict transitional flow under the effects of free-stream turbulence, zero pressure gradient (ZPG), and varying pressure gradient conditions. In this work the test cases T3A and T3B with ZPG and T3C1 and T3C2 with nonuniform pressure gradients along the plate are presented. The boundary conditions are summarized in Table 1. The flow region is modeled with H-type grids; the first grid point has a y^+ value below 0.3. Calculations with a refined grid with double cell number showed the same results.

In Fig. 1 the symbols indicate the measured free-stream turbulence intensity (FSTI) distribution over Re_x for the test cases T3A and T3B. For the test case T3A two different distributions were plotted measured with single and crossed-wire probes (hot-wire anemometry), recorded at two different test runs. By analyzing the measurement data a lower FSTI distribution was observed at the test run with the crossed wire probe. Therefore the T3A test case calculations were done for both turbulence levels (indicated with low FSTI and high FSTI in the legend of Fig. 1), on the one hand to compare the measured skin friction distribution obtained by the single wire measurement and on the other to compare the measured Reynolds stresses obtained by the crossed wire measurement.

In order to match the measured FSTI distributions as shown in Fig. 1, several calculations with different turbulent dissipation rates at the inlet were done. Best results were obtained with the turbulent Reynolds number at the inlet $\mathrm{Re}_{t,\mathrm{le}}$, given in Table 1.

The skin friction and shape factor results for the test cases T3A and T3B are given in Fig. 2. The first two lines listed in the legend

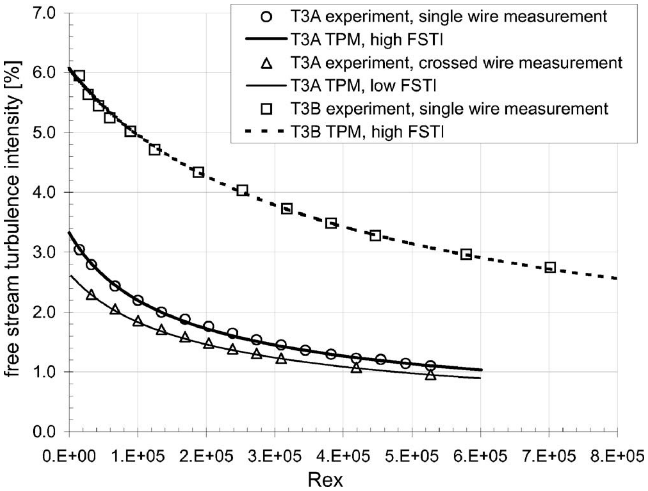

Fig. 1 FSTI distribution over Re_x for the flat plate test case T3A and T3B

represent the laminar Blasius and the fully turbulent skin friction distributions. The empirical fully turbulent friction distribution is obtained with the relation $c_f = 0.445/\ln^2 (0.06\,\mathrm{Re}_x)$.

The beginning and extent of the transition region is captured very well for the T3A test case with the high inlet FSTI calculation. Less agreement with the measurements was found for the test case T3B. The simulation overpredicts the pretransitional c_f values. The results for the ZPG test cases are almost identical to those presented in Ref. [4], which is also an evidence for the correct implementation of the TPM into the in-house code.

Furthermore, the result for the low FSTI calculation at inlet was also plotted in Fig. 2. For this case, detailed measurement data of the turbulence quantities are recorded and compared with the calculations in Fig. 3.

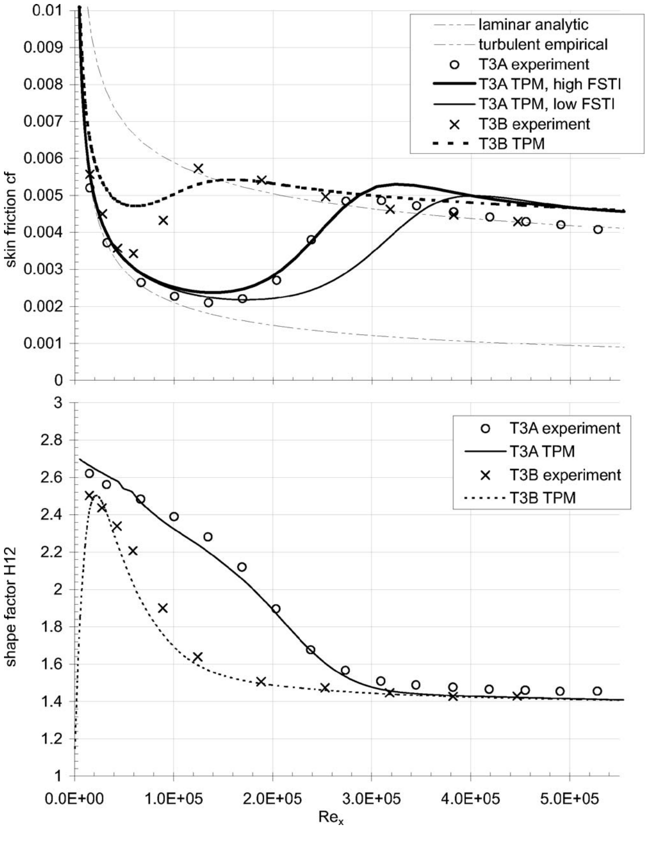

Fig. 2 Skin friction coefficient (top) and shape factor (bottom) for the test cases T3A and T3B

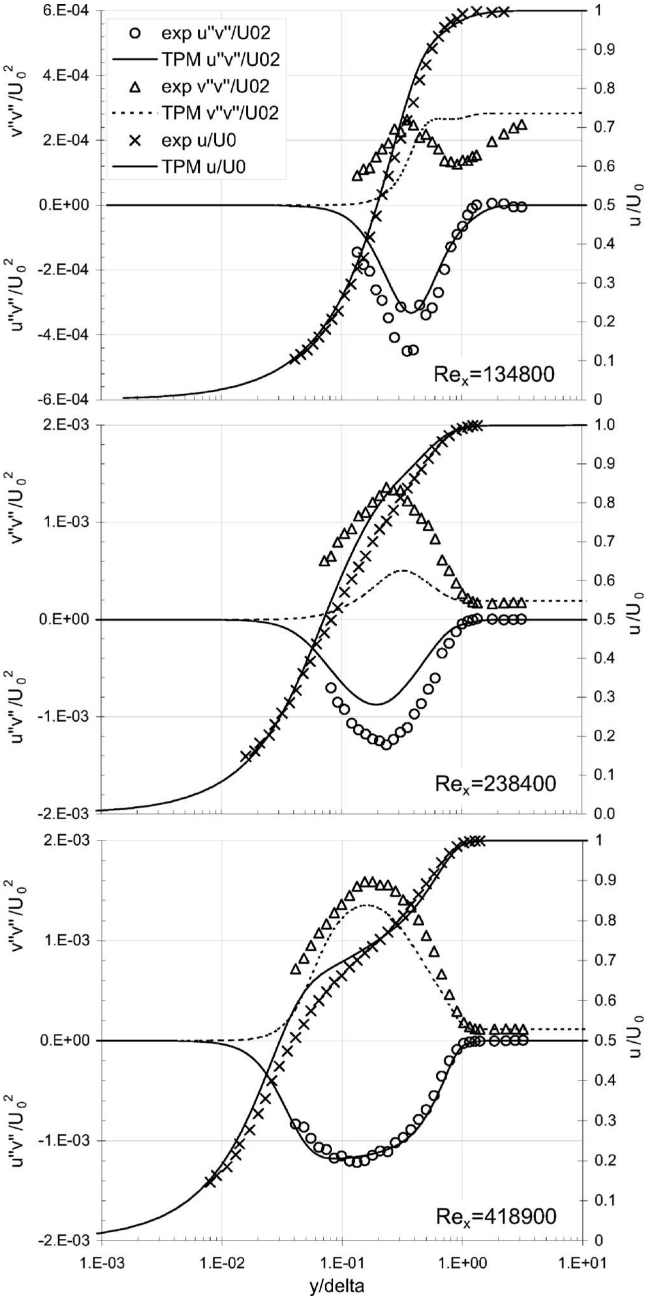

Fig. 3 Boundary layer velocity profiles and turbulence quantities at three different plate positions for the test case T3A

After the end of transition the numerical result shows an overpredicted friction coefficient for the fully developed turbulent boundary layer. The authors observed that the transition controlling terms in Eqs. (6) and (7) (with parameter C_t) increase the turbulent potentials, leading to this overprediction. A calculation with $C_t = 0$ (fully turbulent) shows a coincidence of the calculated and empirical curves for the friction coefficient at the fully developed turbulent boundary layer (not shown).

The shape factor H_{12}, shown in Fig. 2 (bottom), is defined as the ratio of displacement thickness to momentum thickness and indicates the influence of the free-stream turbulence prior to transition. The shape factor decreases from the laminar Blasius value

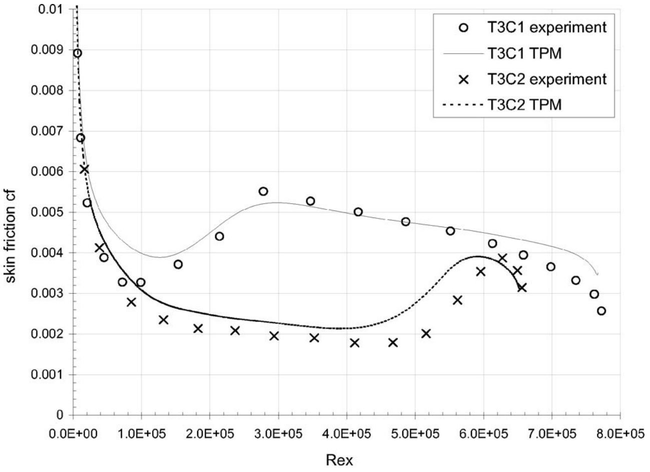

Fig. 4 Skin friction coefficient for the test cases T3C1 and T3C2

of $H_{12} \approx 2.6$ immediately after the flat plate leading edge and this is well captured for both calculated test cases as shown by a comparison with the experiments.

In flows with only one inhomogeneous direction, as it is the case for the investigated flat plate test case with ZPG, only the normal-to-wall derivations remain in Eqs. (2) and (3). Hence the turbulent scalar potential ϕ corresponds to the normal stress component of the Reynolds tensor $R_{22}=\overline{v''v''}=\phi$ and the turbulent vector potential ψ_3 to the shear stress component $R_{12}=\overline{u''v''}=\psi_3$.

Figure 3 shows a comparison between the measured distributions of R_{12} and R_{22} and the prediction with the TPM at three different stations on the flat plate. As mentioned before this investigation was done for the test runs with the lower FSTI condition at the inlet; and the calculated values for $\overline{v''v''}=2/3k$ coincide with the measured ones in the free-stream $(y/\delta > 1)$ at the three investigated locations. The three diagrams indicate laminar, transitional, and fully developed turbulent boundary layer profiles.

The turbulent scalar ϕ agrees well with the measurements in the fully turbulent region, whereas there is a strong deviation in the laminar and transitional region. The measurement shows an indentation of $\overline{v''v''}$ at $y/\delta=1$ and a following increase in the free-stream at $\mathrm{Re}_x=134{,}800$ (top), which is not predicted by the calculation.

For the flat plate test case the turbulent scalar ϕ has no direct impact on the Navier–Stokes equations as $\partial\phi/\partial x \approx 0$ in the x-momentum equation, but in conjunction with the mean shear magnitude it is responsible for the production of ψ_3. It is interesting that in spite of the underpredicted turbulent scalar ϕ the Reynolds shear stress $\overline{u''v''}$ is in relatively good agreement with the experiments. At the fully developed turbulent boundary layer at $\mathrm{Re}_x=418{,}900$ the distribution of the Reynolds shear stress $\psi_3=\overline{u''v''}$ even coincides with the experimental data.

Furthermore the nondimensional velocity profiles are compared with the measurements in Fig. 3 (right abscissa). The laminar profile is in very good agreement with the experiment (at this station the small turbulence values have no influence on the development of boundary layer profile), whereas the fully turbulent velocity profile shows a disagreement in the buffer layer (y/delta≈ 0.04) even though the Reynolds shear stress has been predicted correctly by the TPM.

The results for the nonuniform pressure gradient test cases are given in Fig. 4. These cases are characterized by a combined favorable and adverse pressure gradient over the plate typical for an aft loaded turbine blade. The overall results are well reproduced by the TPM. The turbulent Reynolds number at the leading edge was estimated to match the measured FSTI distribution along the plate and is given in Table 1. Similar to the test case T3B the skin friction coefficient is slightly overpredicted in the pretransitional boundary layer, due to the high inlet FSTI on both cases.

But the further development of the friction coefficient is well captured by the simulation. The transition with the lower FSTI is significantly delayed compared to the T3C1 case and does not start before the adverse pressure gradient region. This effect is also well captured by the TPM, although with a slightly earlier transition onset.

Table 2 Boundary conditions for the VKI turbine guide vane test cases

	$\mathrm{Re}_{c,2}$	$M_{2,\mathrm{is}}$	Tu_i (%)
MUR235	1.1e6	0.92	6.0
MUR241	2.1e6	1.09	6.0
MUR245	2.1e6	0.92	4.0
MUR247	2.1e6	0.92	1.0

Heat Transfer at the VKI Vane (MUR Test Cases). The ability of the turbulence potential model to predict transitional flow was also validated for the flow through a highly loaded transonic turbine guide vane, designed at the von Karman Institute [16].

The most important geometrical data of the blade are: chord =67.647 mm, pitch to chord ratio=0.85, throat to chord ratio =0.2207, and a stagger angle of 55 deg measured from the axial direction. The total inlet temperature is set at $T_{01}=420$ K and the wall temperature is considered to be close to a constant value of 300 K. The test runs were performed to investigate the influence of varying Reynolds numbers (based on the vane chord length and exit conditions) from 1.1e6 to 2.1e6, of varying flow conditions (the isentropic exit Mach number varies from 0.9 to 1.09) and of varying inlet turbulence level from 0.8% to 6%. In this work four different configurations, summarized in Table 2, were numerically investigated to validate the heat transfer rates on the vane surface using the TPM.

Figure 5 shows the blade contour of the MUR turbine guide vane designed by the VKI. The computational domain consists of

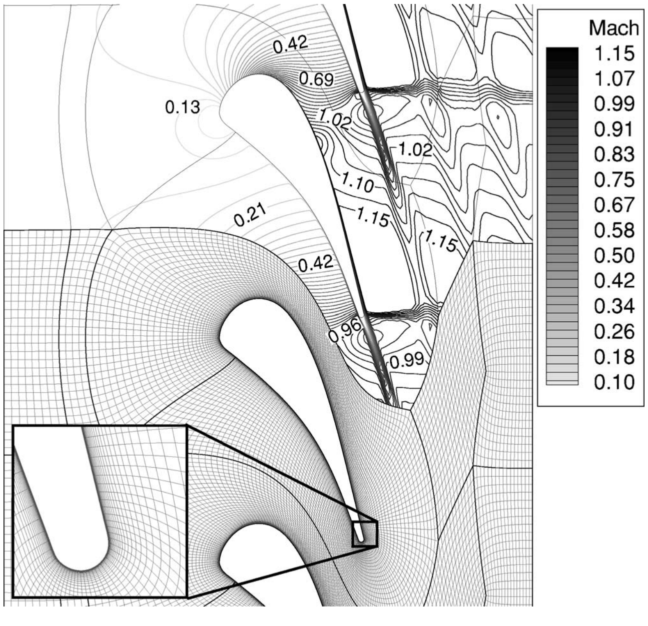

Fig. 5 Mach number distribution (MUR241) and grid topology of the investigated VKI test case

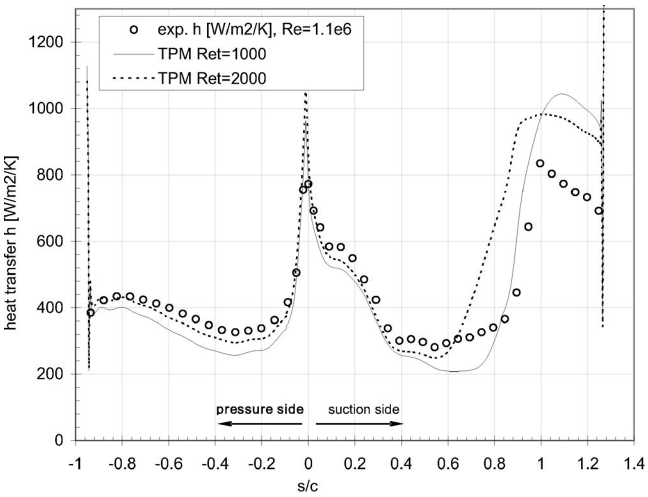

Fig. 6 Heat transfer for the VKI test case MUR235 (Tu_i =6.0%)

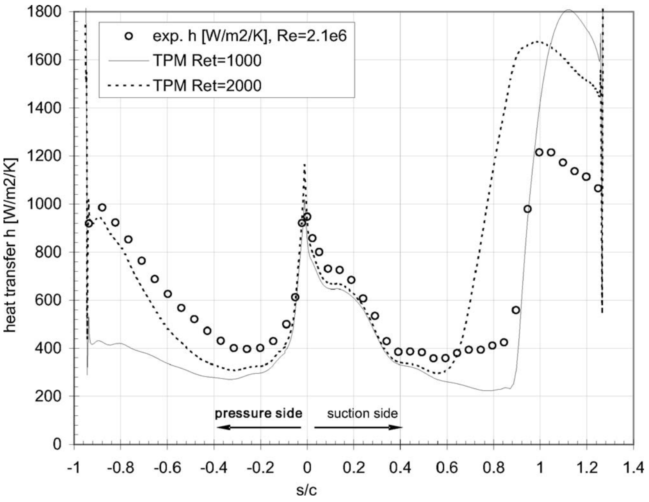

Fig. 8 Heat transfer for the VKI test case MUR245 (Tu_i =4.0%)

five blocks with a total of 16,000 cells; and the *O*-type block wrapped around the blade was meshed with 60 cells normal to the vane surface. The maximum value of $y+$ is about 0.3.

A comparison with a grid with twice as many points in streamwise and wall-normal direction showed grid independence for the grid used. The inlet plane of the computational grid was meshed at 55 mm upstream of the leading edge as at the turbulence intensity for the measurements was given at this location. Further, Mach number contours are shown in Fig. 5 for the test case MUR241 with an exit Mach number of 1.089. A strong suction side shock occurs close behind the trailing edge and extends in a nearly horizontal direction toward the outlet. A local maximum appears on the suction side close to mid chord. Nonreflecting boundary conditions were used as strong variation across the pitch occurs for all test run conditions for this test case at the outlet plane located 80 mm behind the trailing edge.

In Figs. 6–9 the results of the computed heat transfer distributions on the turbine guide vane are presented using the TPM. The heat transfer results on the pressure side are placed on the left-hand side, while the results on the suction side are placed on the right-hand side over the nondimensional vane surface length with the origin at the stagnation point. The heat transfer is evaluated by $h = \dot{q}_W/(T_\infty - T_W)$.

As no dissipation rate, respectively, turbulent Reynolds number was known for these test cases, two calculations with different inlet turbulent Reynolds numbers were done for the cases MUR235, MUR241, and MUR245. The inlet values for Re_t were assumed within a reasonable range of $\mathrm{Re}_{t,i} = 1000-2000$. For the last test case MUR247 with the lowest inlet turbulence intensity only the result for $\mathrm{Re}_{t,i} = 1000$ is given in Fig. 9. Further the study allows an insight of the model dependency on the turbulent Reynolds number at the inlet.

Standard two equation models often suffer in predicting the correct turbulent kinetic energy at regions with high rates of strain. This problem is known in literature as the stagnation point anomaly, as high rates of strain appear in that region. Physical and mathematical constraints have to be adopted for two-equation models as well as for RSTM to fix this problem [10]. The TPM does not suffer from these difficulties, hence no significant overprediction of the turbulent kinetic energy occurs and therefore the heat transfer is predicted in good agreement with the experiments at the leading edge region for all investigated test cases.

At the pressure side the inlet turbulent Reynolds number has little influence on the test cases MUR235 and MUR241 compared to the case MUR245 (see Figs. 6–8). The results with $\mathrm{Re}_t = 2000$

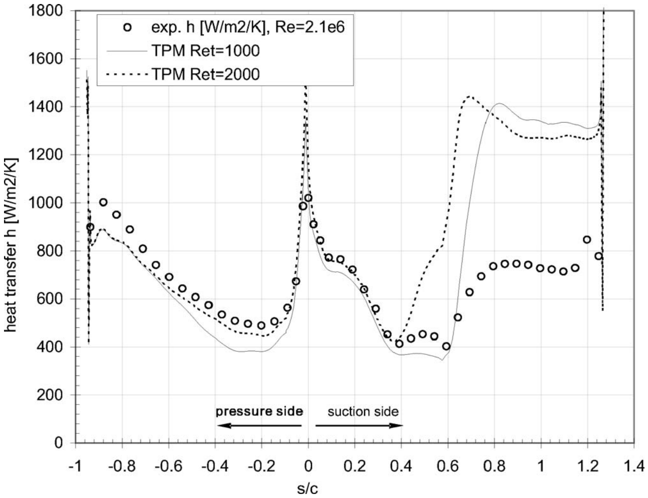

Fig. 7 Heat transfer for the VKI test case MUR241 (Tu_i =6.0%)

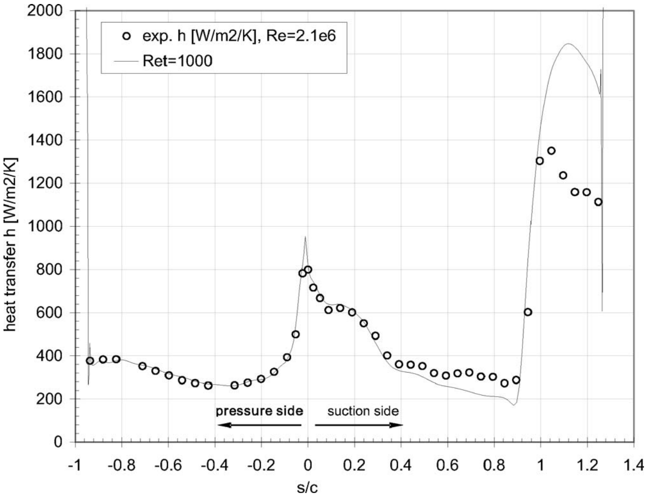

Fig. 9 Heat transfer for the VKI test case MUR247 (Tu_i =1.0%)

are slightly higher compared to the results with $\mathrm{Re}_t=1000$ and are in good agreement with the experiments of both test cases MUR235 and MUR241. The physical mechanism of the high turbulence level in the free stream, affecting the laminar boundary layer closely behind the leading edge on the pressure side, is well captured with the TPM. Investigations with intermittency transport equations have shown that they are not able to model the increase of the heat transfer on the pressure side prior to transition [2,17].

For the MUR245 case (Fig. 8) with a lower FSTI of 4% at the inlet the choice of the inlet turbulent Reynolds number has more impact on the development of the boundary layer on the pressure side. Setting $\mathrm{Re}_{t,i}=1000$ at the inlet, which leads to higher turbulent dissipation values, the turbulent kinetic energy reduces successively before it reaches the blade. As a result no transition occurs for this test case at the pressure side to the trailing edge.

For $\mathrm{Re}_t=2000$, numerical and experimental heat transfer agree reasonably well on the pressure side. Therefore the knowledge of the turbulent boundary conditions is of particular importance to validate and further to enhance statistical turbulence closures for RANS applications. On the other hand on the suction side the result for $\mathrm{Re}_{t,i}=1000$ is in better agreement with the measurement data. Nonetheless the authors believe that in the experiments a turbulent Reynolds number of approximately $\mathrm{Re}_{t,i}=2000$ is more reasonable, because the value h is predicted in closer agreement with the measured data on the pressure side, where the lower Mach number has less influence on the turbulent boundary layer development. On the suction side the higher Mach number flow affects the redistribution mechanism among the components of the Reynolds stress tensor. Recent experimental research on high-speed mixing layers shows that the anisotropy of the Reynolds stress tensor increases with Mach number, which finally reduces the growth rate. The nonconsideration of the Mach number influence on the TPM could explain the worse result for $\mathrm{Re}_t=2000$ on the suction side. A consideration of a pressure–dilatation model [18], turbulent mass flux model and a compressible turbulent dissipation model [19] could delay the transition on the suction side, which would also lead to a better agreement with measurements for the higher Re_t value at the inlet. These additional models for compressible turbulence could also prevent the too large overshot of h at the rear part of the blade's suction side for all investigated operating conditions.

Furthermore, for the lower inlet turbulent Reynolds number in the MUR245 case the same heat transfer distribution is obtained as for the test case MUR247 with a FSTI at the inlet of 1% (shown in Fig. 9). On the suction side of the blade all test case simulations predict the location of the rapid transition to a high heat transfer coefficient h very accurately, if the inlet turbulent Reynolds number is assumed to be $\mathrm{Re}_{t,i}=1000$.

For the test case MUR247 with the lowest investigated FSTI at the inlet, the value of Re_t has less influence on the heat transfer prediction, so that only the result for $\mathrm{Re}_{t,i}=1000$ is plotted in Fig. 9. The overall heat transfer distribution is captured very well, except for the large overshoot at the rear part of the suction side caused by the neglected compressibility effect as mentioned before.

Conclusion

A numerical study with a RANS code in conjunction with a nonequilibrium turbulence model was done. The turbulence model chosen for this investigation is an innovative "second moment closure" turbulence model and solves a reduced set of transport equations compared to that of full Reynolds stress transport models.

The aim of this work was to study the accuracy of this turbulent potential model for predictions in nonequilibrium turbulent flows. Laminar to turbulent transition in wall-bounded flows is a situation where nonequilibrium turbulence prevails. A prevalidation of the turbulent potential model was done by means of the skin friction distribution on an adiabatic flat plate test case with different inlet turbulence intensities for zero pressure gradient as well as for nonuniform pressure distributions along the flat plate. The results have shown a good agreement for these investigated test cases compared with the measured data.

Finally the model was tested for the prediction of heat transfer on a highly loaded transonic turbine guide vane cascade at different operating conditions. In general the heat transfer predictions with the turbulent potential model perform better compared to the results, which were achieved by the application of an intermittency transport model as investigated by the authors in a previous work [17]. On the pressure side of the vane for all investigated operating conditions the calculated heat transfer was well captured, if the inlet conditions are chosen adequately. The heat transfer after transition at the rear part of the guide vane's suction side was significantly overpredicted and this pleads for an extension of the turbulent potential model to account for compressible flow effects by means of additional correlations, which occur at the derivation of compressible Reynolds stress closures.

Acknowledgment

The support by the Austrian Science Foundation (FWF) within Grant No. P16761 "Steady and Unsteady Transition Modeling" is gratefully acknowledged.

Nomenclature

c = chord length
c_p = specific heat capacity at constant pressure
c_f = skin friction, $c_{\mathrm{f}}=\tau_w/(\rho_w U_w^2/2)$
H_{12} = shape factor, $H_{12}=\delta_1/\delta_2$
k = turbulent kinetic energy
Ma = Mach number
R = Reynolds stress tensor
Re = Reynolds number
Tu = turbulence intensity
q = heat transfer
U,u = velocity
y^+ = dimensionless wall distance

Greek Letters

δ = boundary layer thickness
ε = turbulence dissipation rate
ϕ = turbulence scalar potential
μ = dynamic viscosity
ν = kinematic viscosity
$\boldsymbol{\psi}$ = turbulent vector potential
τ = stress tensor
$\boldsymbol{\omega}$ = vorticity vector $\boldsymbol{\omega}=\boldsymbol{\nabla}\times\mathbf{u}$

Subscripts

2 = outlet value
i = inlet
is = isentropic
L = characteristic length
l = laminar
le = leading edge
t = turbulent

Other Symbols

$-$ = Reynolds averaged
$\sim$ = Reynolds/Favre averaged
$''$ = Favre fluctuating component

Abbreviations

FSTI = free-stream turbulence intensity
RSTM = Reynolds stress transport models
TPM = turbulent potential model
ZPG = zero pressure gradient

References

[1] Schmidt, R. C., and Patankar, S. V., 1991, “Simulating Boundary Layer Transition with Low-Reynolds k-ε Turbulence Models: Part 1—An Evaluation of Prediction Characteristics,” ASME J. Turbomach., **113**, pp. 10–17.
[2] Steelant, J. and Dick, E., 2001, “Modeling of Laminar-Turbulent Transition for High Freestream Turbulence,” J. Fluids Eng., **123**, pp. 22–30.
[3] Menter, F. R., Langtry, R. B., Likki, S. R., Suzen, Y. B., and Huang, P. G., 2004, “A Correlation-Based Transition Model Using Local Variables, Part 1—Model Formulation,” ASME Paper No. GT2004-53452.
[4] Chang, W., and Perot, B., 2002, “Prediction of Turbulent Transition in Boundary Layers Using the Turbulent Potential Model,” J. Turbul., **3**(22), pp. 1–15.
[5] Roe, P. L., 1981, “Approximate Riemann Solvers, Parameter Vectors and Differencing Scheme,” J. Comput. Phys., **43**, pp. 357–372.
[6] Spalart, P. R., and Allmaras S. R., 1994, “A One Equation Turbulence Model for Aerodynamic Flows,” Rech. Aerosp., **1**, pp. 5–21.
[7] Jones, W. P., and Launder, B. E., 1972, “The Prediction of Laminarization With a Two-Equation Model of Turbulence,” AIAA J., **15**, pp. 301–314.
[8] Wilcox, D. C., 1998, *Turbulence Modeling for CFD*, 2nd ed., DCW Industries, La Canada, CA.
[9] Menter, F. R., 1994, “Two-Equation Eddy-Viscosity Turbulence Models for Engineering Applications,” AIAA J., **32**(8), pp. 1598–1605.
[10] Medic, G., and Durbin, P. A., 2002, “Toward Improved Pre-diction of Heat Transfer on Turbine Blades,” ASME J. Turbomach., **124**, pp. 187–192.
[11] Perot, B., and Moin, P., 1996, “A New Approach to Turbulence Modelling,” *Proceedings of the Summer Program 1996*, Center for Turbulence Research, pp. 35–46.
[12] Pecnik, R., and Sanz, W., 2004, “Numerical Investigation of the Secondary Flow of a Transonic Turbine Stage Using Various Turbulence Closures,” ASME Paper No. GT2005–68754.
[13] Perot, B., 1999, “Turbulence Modeling Using Body Force Potentials,” Phys. Fluids, **11**(9), pp. 2645–2656.
[14] Sasanka, A., Xing, Z., and Perot, B., 2002, “Application of the Turbulent Potential Model to Unsteady Flows and Three-Dimensional Boundary Layers,” *Proceedings 9th International Symposium on Transport Phenomena and Dynamics of Rotating Machinery*, Honolulu, HI, February 10–14.
[15] Savill, A. M., 1992, *A Synthesis of T3 Test Case Predictions, Numerical Simulation of Unsteady Flows and Transition to Turbulence*, O. Pironneau et al., Cambridge University Press, Cambridge, U.K., pp. 404–442.
[16] Arts, T., Lambert de Rouvriot, M., and Rutherford, A. W., 1990, “Aero-Thermal Investigation of a Highly Loaded Transonic Linear Turbine Guide Vane Cascade,” Technical Note, 174, von Karman Institute for Fluid Dynamics, Belgium.
[17] Pecnik, R., Sanz, W., Gehrer, A., and Woisetschlaeger, J., 2003, “Modeling of Laminar-Turbulent Transition Using Two Different Intermittency Transport Equations,” Flow, Turbul. Combust., **70**, pp. 299–323.
[18] Sarkar, S., 1992, “The Pressure-Dilatation Correlation in Compressible Flows,” Phys. Fluids A, **4**, pp. 2674–2682.
[19] Adumitroaie, V., Ristorcelli, J. R., and Taulbee, D. B., 1998, “Progress in Favre-Reynolds Stress Closures for Compressible Flows,” NASA/CR-1998-2078423, ICASE Report No. 98–21, NASA, Washington, D.C.

Effects of Bleed Flow on Heat/Mass Transfer in a Rotating Rib-Roughened Channel

Yun Heung Jeon

Suk Hwan Park

Kyung Min Kim

Dong Hyun Lee

Hyung Hee Cho
e-mail: hhcho@yonsei.ac.kr

School of Mechanical Engineering,
Yonsei University,
Seoul 120-749, Korea

The present study investigates the effects of bleed flow on heat/mass transfer and pressure drop in a rotating channel with transverse rib turbulators. The hydraulic diameter (D_h) *of the square channel is* 40.0 mm. *20 bleed holes are midway between the rib turburators on the leading surface and the hole diameter* (d) *is* 4.5 mm. *The square rib turbulators are installed on both leading and trailing surfaces. The rib-to-rib pitch* (p) *is 10.0 times of the rib height* (e) *and the rib height-to-hydraulic diameter ratio* (e/D_h) *is 0.055. The tests were conducted at various rotation numbers (0, 0.2, 0.4), while the Reynolds number and the rate of bleed flow to main flow were fixed at 10,000 and 10%, respectively. A naphthalene sublimation method was employed to determine the detailed local heat transfer coefficients using the heat/mass transfer analogy. The results suggest that for a rotating ribbed passage with the bleed flow of* $\mathrm{BR}=0.1$, *the heat/mass transfer on the leading surface is dominantly affected by rib turbulators and the secondary flow induced by rotation rather than bleed flow. The heat/mass transfer on the trailing surface decreases due to the diminution of main flow. The results also show that the friction factor decreases with bleed flow.* [DOI: 10.1115/1.2720495]

Introduction

The design of an effective cooling system becomes more crucial in the development of high performance gas turbine engines. The turbine inlet temperature has been steadily increased to improve the thermal efficiency of turbine engines, but it resulted in high heat loads on turbine blades. To protect the blade materials from exceeding the maximum allowable temperature and being damaged, various cooling techniques are employed. Among them, internal passage cooling is to perform cooling inner turbulated surface using the cooling air coming from a compressor. Film cooling is to protect blade surfaces contacted with hot gases using the cooling air ejected through the holes on blade surface after cooling an internal passage. With the bleed flow, the flow structure of cooling air in the internal passage becomes different. Moreover, when the turbine blade rotates, more different flow structures are caused by the Coriolis force, accordingly it is necessary to understand how those parameters affect the cooling performance.

Rib conditions such as rib height, rib angle of attack, rib-to-rib pitch, rib shape, and rib arrangement have great effects on heat transfer and friction, and a number of studies have been made by many researchers [1–4]. The effect of channel geometry has also been of great interests to many researchers. Astarita et al. [5] measured heat transfer coefficients in rectangular channels of five different aspect ratios using an infrared scanner. Metzger and Vedula [6] investigated heat transfer characteristics in a triangular channel with various rib arrangements.

The rotation of cooling passage engenders complex internal flow and heat transfer characteristics so that many tests have been widely conducted to clarify the rotating effect. A study by Yang et al. [7] contains the results of heat transfer performance in a four-pass serpentine passage with various Reynolds numbers, Rossby numbers and rotational Rayleigh numbers. Iacovides et al. [8] reported the heat transfer and flow characteristics in a smooth two-pass duct, examining flow developments and local Nusselt number distributions. Dutta and Han [9] studied smooth rectangular passages with three channel orientations to understand the high rotation and rib arrangement effects on the heat transfer characteristics. Murata et al. [10] also investigated the influence of aspect ratio on heat transfer and fluid flow in a rotating smooth duct.

To perform a film cooling of gas turbine blades, bleed holes are formed on the surface of them and those holes have significant effects on heat transfer in the cooling passage. Therefore, the study of the effect of bleed flow is essential. Taslim et al. [11] measured local heat transfer coefficients in trapezoidal passages with bleed holes, and reported that bleed holes on the smooth surface (the side wall) consequently yield a more uniform distribution of spanwise heat transfer coefficient on the ribbed surface and the bleed flow caused lower friction factor than in the case of no effusion. Shen et al. [12] studied heat transfer enhancement by ribs and the combination of ribs and bleed holes. They found that the average heat transfer in the latter case was approximately 25% higher than that in the former case, but the heat transfer was decreased at high bleed ratios. Thurman and Poinsatte [13] investigated the interaction of 90 deg ribs and various bleed conditions on heat transfer. They reported that placing bleed holes after ribs widened the regions of high heat transfer due to removing the recirculation flow behind the ribs. Ekkad et al. [14] performed the experiments for various rib-roughened surfaces with bleed holes and reported that each rib arrangement generated similar heat transfer in the first pass.

Until now, most of the studies dealing with the heat transfer characteristics in the internal passages with bleed holes have been made under the stationary condition; therefore, to understand the cooling system of them it is necessary to study the heat transfer characteristics under the rotating condition.

Experimental Apparatus

Rotating Facility. A schematic view of the experimental apparatus is shown in Fig. 1. A blowing system, a rotating system, and a measuring system comprise the test rig. First, for a blowing system, one blower supplies room air into a test section and the other blower makes bleed flow through the test section. Those blowers are controlled using frequency inverters. Air temperature is regulated during the experiment using a heat exchanger. The

---

Contributed by the International Gas Turbine Institute of ASME for publication in the JOURNAL OF TURBOMACHINERY. Manuscript received July 18, 2006; final manuscript received July 25, 2006. Review conducted by David Wisler. Paper presented at the ASME Turbo Expo 2006: Land, Sea and Air (GT2006), May 8–11, 2006, Barcelona, Spain. Paper No. GT2006-91122.

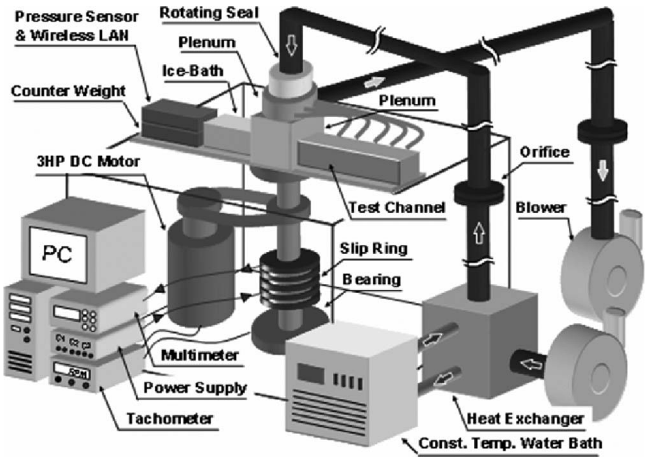

Fig. 1 Experimental apparatus

flows of blowing and bleeding are measured by orifice flow meters. The Reynolds number (Re) based on a hydraulic diameter and the ratio of the bleed flow to main flow (bleed ratio, BR) are monitored to be constant during the tests. The maximum difference of bleed flow through each bleed hole is verified within 3% for all cases by the test of differential pressure. A magnetic rotating seal and a rib seal are equipped in order to prevent any leakage through the rotating parts. A 3HP (2.24 kW) dc motor connected with a V-belt drives a rotating shaft, of which rotation speed is measured by an optical tachometer. Rotation numbers remain 0.0, 0.2, and 0.4 during the tests. The maximum rotation number ($\mathrm{Ro}=0.4$) corresponds to 400 rpm approximately. Lastly, for a measuring system an Agilent data logger and an PSI electronic pressure sensor interfaced to a computer via slip rings and a wireless LAN equipage respectively, record electrical output signals from the test section. To measure naphthalene surface temperature accurately, *J*-type thermocouples are embedded in the test plate because the vapor pressure of naphthalene is sensitive to temperature, and varies about 10% per temperature change of $1^\circ\mathrm{C}$. The temperature of bulk air is also obtained by the thermocouples installed in the channel inlet and outlet.

Test Section. Figure 2 presents the geometry of the test channel and Fig. 3 shows the coordinate system of the test section. The test channel has a hydraulic diameter (D_h) of 40.0 mm and a cross-sectional area of 40 mm$(W) \times 40$ mm(H). Its streamwise coordinate ranges from $x/D_h=2.0$ to $x/D_h=13.8$. The square rib turbulators are installed on both leading and trailing surfaces of the test channel and the array of them is inlined. The rib height-to-hydraulic diameter ratio (e/D_h) is 0.055 and the rib-to-rib pitch is 10.0 times of the rib height. The test channel has 20 bleed holes midway between the rib turbulators on the midleading surface and the diameter of them (d) is 4.5 mm. The 10 bleed holes are located at the test section and the last holes at the flow developing region. The ratio of hole-spacing to the diameter (p/d) is 4.9. The ratio of maximum rotating radius to the hydraulic diameter (R/D_h) is 14.5. The coordinate system of the test section is depicted in Figs. 2(a) and 2(b). The streamwise, lateral and vertical direction corresponds to the axis of x, y, and z, respectively. The test section is covered with naphthalene from $x/D_h=8.45$ to $x/D_h=13.8$ and has 10 bleed holes. The lateral domain of it ranges from $y/D_h=-0.5$ to $y/D_h=0.5$.

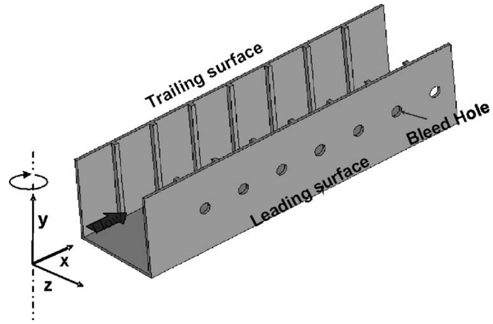

Fig. 2 Geometry of the test channel

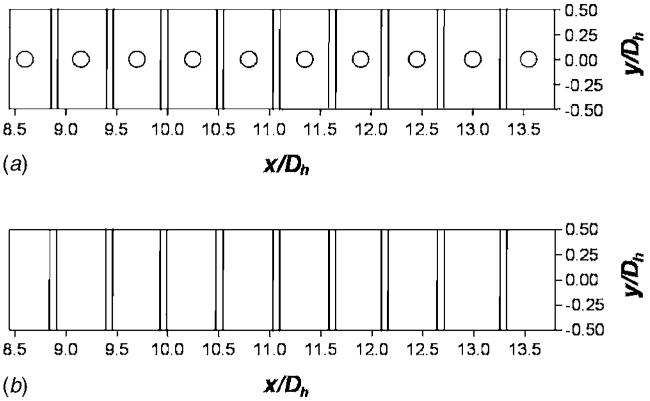

Fig. 3 Coordinate system of the test section: (*a*) leading surface; (*b*) trailing surface

To measure the pressure drop through the channel, pressure tests were conducted using the electronic pressure sensor. Pressure taps numbering 8 are drilled at $z/D_h=0.0$ on the one of the sidewalls, of which spacing and diameter are 66 mm and 1 mm, respectively.

Experimental Procedure and Data Reduction

A naphthalene sublimation method is employed to obtain detailed heat/mass transfer coefficients using the analogy between heat and mass transfer. The leading and trailing surface of the test section are cast with naphthalene to simulate a cooling channel's two-sided heating condition of a gas turbine blade. Naphthalene surfaces where mass transfer occurs correspond to a uniform wall temperature boundary condition of heat transfer experiments. The local naphthalene sublimation depth is measured to attain mass transfer coefficients on each position using a liner variable differential transformer, LBB-375TA-020 and an automated positioning table. It is expressed as

$$h_m = \frac{\dot{m}}{\rho_{v,w} - \rho_{v,b}} = \frac{\rho_s(\Delta z/\Delta t)}{\rho_{v,w} - \rho_{v,b}} \tag{1}$$

where $\dot{m}$ is the local mass transfer rate of naphthalene per unit area which is determined from the density of solid naphthalene, ρ_s, and the sublimation rate, $\Delta z/\Delta t$. The $\rho_{v,w}$ and $\rho_{v,b}$ are the vapor density of naphthalene on the surface and the bulk air, respectively. The former is calculated from the ideal gas law using the vapor pressure and the surface temperature as

$$\rho_{v,w} = \frac{P_{\mathrm{naph}}}{R_{\mathrm{naph}} T_w} \tag{2}$$

The naphthalene vapor pressure, P_{naph}, is determined from the equations suggested by Ambrose et al. [15]. The latter, or the bulk vapor density of naphthalene, is obtained from the average naphthalene sublimation depth, $\overline{z_{\mathrm{sub}}}|_x$, measured at each position in the mainstream direction as

$$\rho_{v,b} = \frac{\rho_s W x}{\dot{Q}_{\mathrm{air}} \Delta t} \, \overline{z_{\mathrm{sub}}}|_x \tag{3}$$

From the local mass transfer coefficient, the Sherwood number is calculated as

$$\mathrm{Sh} = h_m D_h / D_{\mathrm{naph}} \tag{4}$$

where D_{naph} is the diffusion coefficient of naphthalene in air. The properties of naphthalene suggested by Ambrose et al. [15] and Goldstein and Cho [16] are used in the present study. The uncertainty in the Sherwood number is estimated to be within ±8.0% at a 95% confidence level using the uncertainty estimation method of Kline and McClintock [17]. The Nusselt numbers can be obtained from the Sherwood numbers by the correlation $\mathrm{Nu}/\mathrm{Sh} = (\mathrm{Pr}/\mathrm{Sc})^{0.4}$, which is for turbulent flows.

The mass transfer results are presented as the Sherwood number ratios, $\mathrm{Sh}/\mathrm{Sh}_0$, to estimate the heat/mass transfer augmentation effectively, where Sh_0 is the Sherwood number for a fully developed turbulent flow in a stationary smooth circular tube correlated by McAdams [18] and converted to mass transfer parameters as

$$\mathrm{Sh}_0 = 0.023\,\mathrm{Re}^{0.8}\,\mathrm{Sc}^{0.4} \tag{5}$$

The line and the regional averaged Sherwood number, $\overline{\mathrm{Sh}}_L$ and $\overline{\mathrm{Sh}}_R$, are calculated by the integration of the local Sherwood numbers weighted by constant area.

The average pressure drop is obtained from the slope calculated by a linear curve-fitting of the local pressure difference data in the middle region of the channel $(\Delta P/\Delta L)$ where the static pressure decreases linearly. The friction factor is calculated with the average pressure drop as

$$f = \Delta P / [4(\Delta L/D_h)(1/2)\rho u_b^2] \tag{6}$$

The uncertainty of the friction factor is within 4.4%. The friction loss results are presented as the friction factor ratios, f/f_0, where f_0 represents the friction factor for a fully developed turbulent flow in a stationary smooth circular tube. The empirical equation that closely fits the Kármán-Nikuradse equation proposed by Petukhov [19] is employed as $f_0 = 2(2.236 \ln \mathrm{Re} - 4.639)^{-2}$.

The thermal performance, η, obtained by considering both the heat/mass transfer augmentation and the friction loss increment is presented based on the constant pumping power condition and it is expressed as the following equation:

$$\eta = (\overline{\mathrm{Sh}}_R/\mathrm{Sh}_0)/(f/f_0)^{1/3} \tag{7}$$

Results and Discussion

To investigate the flow patterns and local heat/mass transfer characteristics for the rotating rib-roughened passage with bleed flow, our preceding experimental data for the smooth channel are compared as baseline data.

Heat/Mass Transfer Characteristics

Cases Without Bleed Flow. For a smooth channel, when the passage rotates (Ro=0.2), the discrepancy of the heat/mass transfer between the leading and trailing surfaces is observed. For the leading surface, on the middle region (the remnant region except the corner of the passage), the heat/mass transfer is weakened, while it is augmented on the corner region. For the trailing surface, on the overall region, the heat/mass transfer is augmented. The reason is that the Coriolis force acts toward the trailing surface for the radially outward flow. At the higher rotation number of Ro=0.4, the high heat/mass transfer region on the leading surface becomes smaller and the overall heat/mass transfer decreases. For the trailing surface, the heat/mass transfer is more augmented by the effect of the strengthened Coriolis force.

Figure 4 presents the local Sherwood number ratio distributions and Fig. 5 shows the line averaged Sherwood number ratio distributions in the ribbed channel without bleed flow. The data are presented in the range of $11.5 \leq x/D_h \leq 13.0$ due to the periodical patterns in the fully developed region.

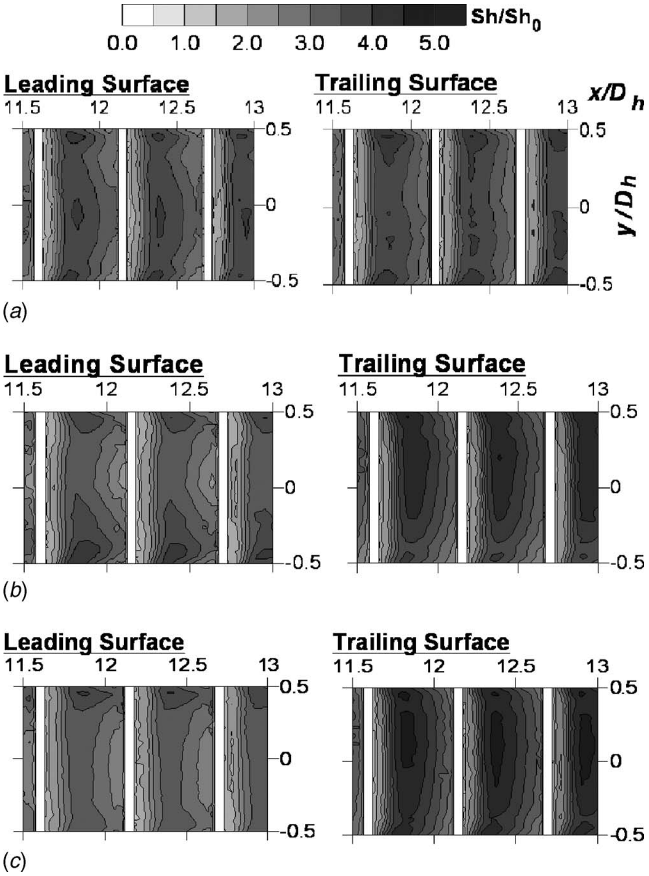

Fig. 4 Sh ratio distributions in the ribbed channel at BR=0.0: (*a*) Ro=0.0; (*b*) Ro=0.2; (*c*) Ro=0.4

At the rotation number of Ro=0.0 (stationary case), there are two peaks of the heat/mass transfer coefficients in an inter-rib region: the first peak appears at the upstream of the middle of the inter-rib region by the flow reattachment and the second sharp peak just before the rib due to the corner vortex. On the outer region around the corner of the passage, the heat/mass transfer is lowered due to the weakened reattachment with the redeveloping flows caused by the wall friction. This is a typical pattern of the heat heat/mass transfer distributions on the ribbed surfaces with flow separation and reattachment and this pattern agrees well with

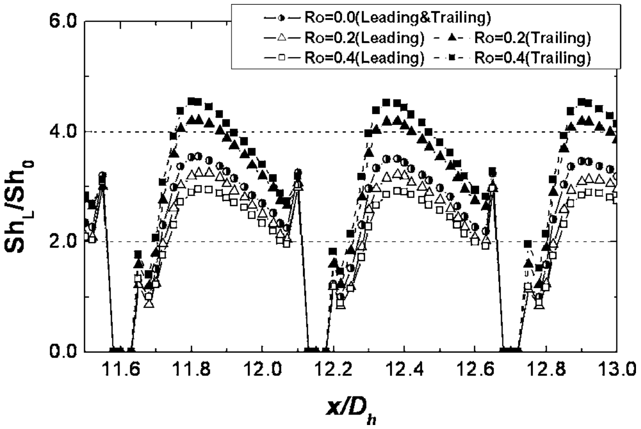

Fig. 5 Line averaged Sh ratio distributions in the ribbed channel at BR=0.0

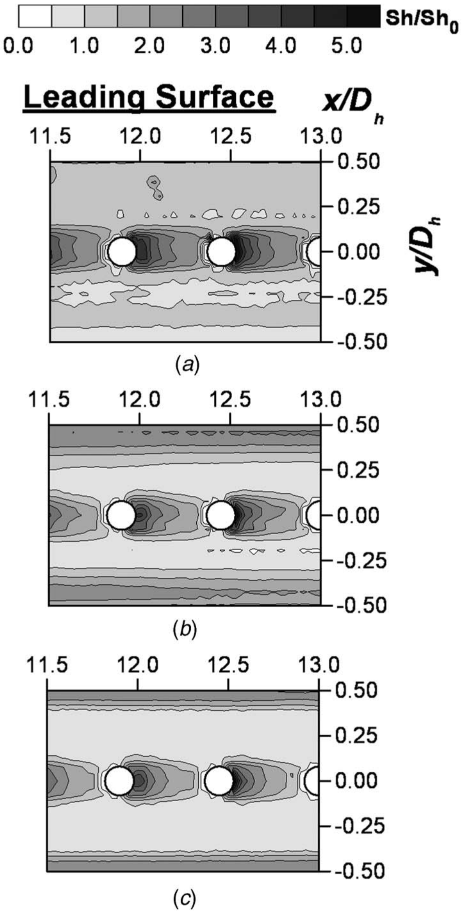

Fig. 6 Sh ratio distributions on the leading surface in the smooth channel at BR=0.1: (*a*) Ro=0.0; (*b*) Ro=0.2; (*c*) Ro=0.4

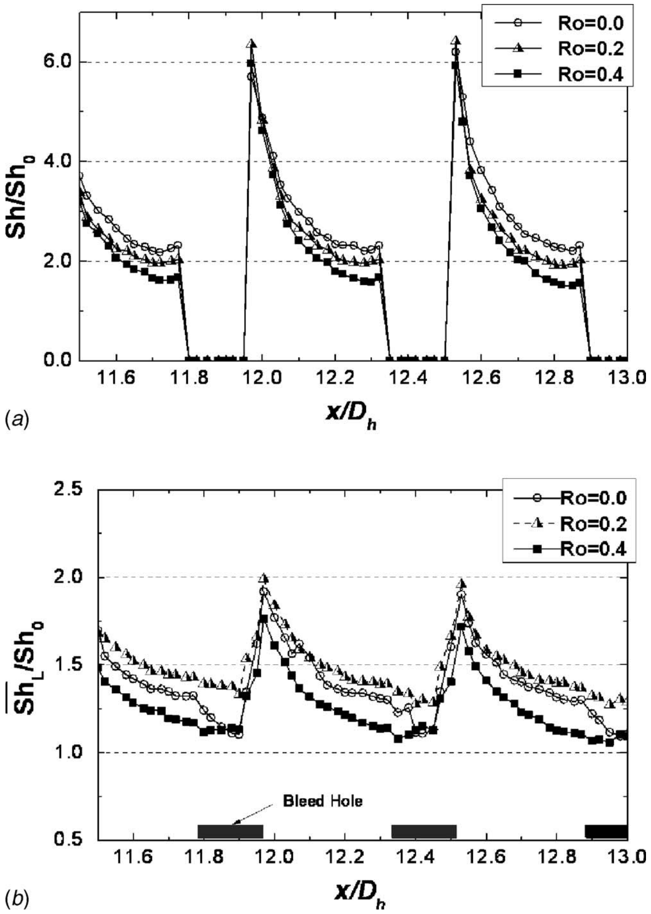

Fig. 7 Sh ratio distributions on the leading surface in the smooth channel at BR=0.1: (*a*) Sh ratio distributions on the center line; (*b*) Line averaged Sh ratio distributions

the results of the previous studies such as Kukreja et al. [2], Aliaga et al. [3], and Acharya et al. [4]. When the passage rotates (Ro=0.2), the heat/mass transfer decreases on the leading surface and increases on the trailing surface. For the leading surface, on the middle region except the corner of the passage, the reattachment becomes weak due to the Coriolis force acting toward the trailing surface. On the corner region, the high heat/mass transfer appears due to the impingement of the secondary flow returning from the trailing surface by the Coriolis force. On the overall region of the trailing surface, the heat/mass transfer becomes high because the separated flow by the rib turbulators is strongly reattached by the Coriolis force. As the rotation number increases, the heat/mass transfer on the leading surface decreases and that on the trailing surface becomes higher because of the strengthened secondary flow by rotation.

Cases With Bleed Flow. Figure 6 presents the local Sherwood number ratio distributions on the leading surface in the smooth channel with bleed flow. The contour patterns near bleed holes appear similar for all cases. At the rotation number of Ro=0.0, the heat/mass transfer on the leading surface is enhanced by the effect of the tripping flow which impinges around the bleed holes due to the drawing flow by suction and augments the heat/mass transfer on the vicinity of them, while that on the trailing surface decreases due to the diminution of main flow. Figure 7(*a*) presents the local Sherwood number ratios on the center line of the leading surface in the smooth channel with bleed flow, showing the effect of the tripping flow. The peak of heat/mass transfer is formed immediately behind the bleed holes and decreases sharply along the center line after impinging on the surface. Figure 7(*b*) shows the line averaged Sherwood number ratio distributions on the leading surface. At the rotation number of Ro=0.2, the heat/mass transfer on the leading surface is the highest value for all cases unlike the smooth passage without bleed flow. It is due to the effect of the tripping flow and the high heat/mass transfer on both corner regions by the Coriolis force. The heat/mass transfer on the trailing surface increases. At the higher rotation number of Ro=0.4, the heat/mass transfer on the leading surface decreases because of the strengthened Coriolis force acting toward the trailing surface. For the trailing surface, the heat/mass transfer becomes higher but reduced as compared with the case without bleed flow because of the diminution of the main flow.

Figure 8 presents the local Sherwood number ratio distributions and Fig. 9 shows the line averaged Sherwood number ratios in the channel with ribs and bleed flow. The contour patterns for all cases are similar to them without bleed flow. At the rotation number of Ro=0.0, the heat/mass transfer on the leading surface is higher than that without bleed flow because the reattachment becomes strong on both sides of bleed holes by the effect of the tripping flow. On the other hand, the heat/mass transfer on the trailing surface is lower than that without bleed flow because of the diminution of the main flow.

When the passage rotates (Ro=0.2), the heat/mass transfer on the leading surface decreases. This is because the reattachment becomes weakened on the middle region except the corner of the passage due to the Coriolis force acting toward the trailing surface. On the corner region of the leading surface, however, the reattachment becomes strong by the impingement of the second-

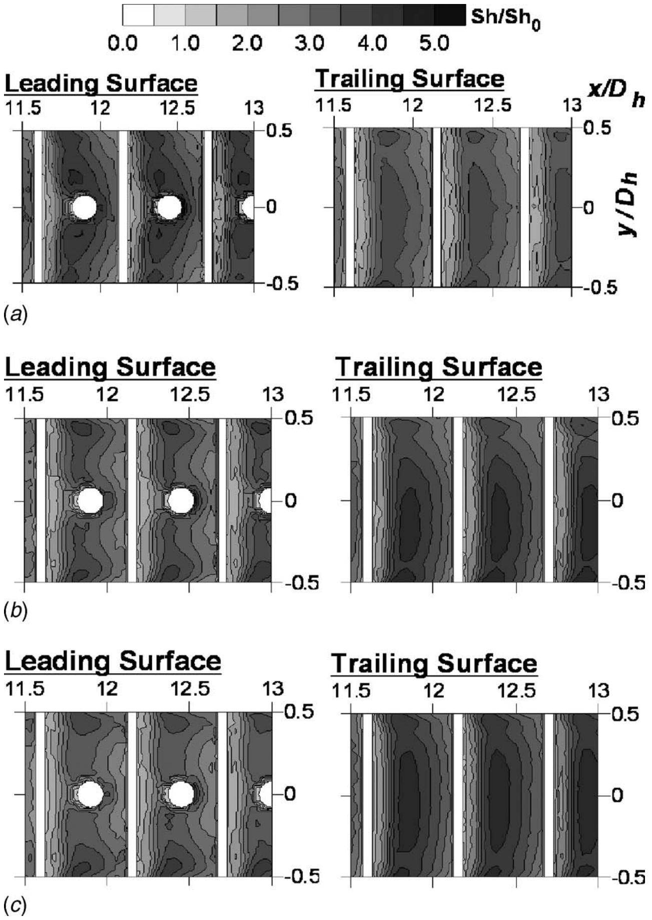

Fig. 8 Sh ratio distributions in the ribbed channel at BR=0.1: (*a*) Ro=0.0; (*b*) Ro=0.2; (*c*) Ro=0.4

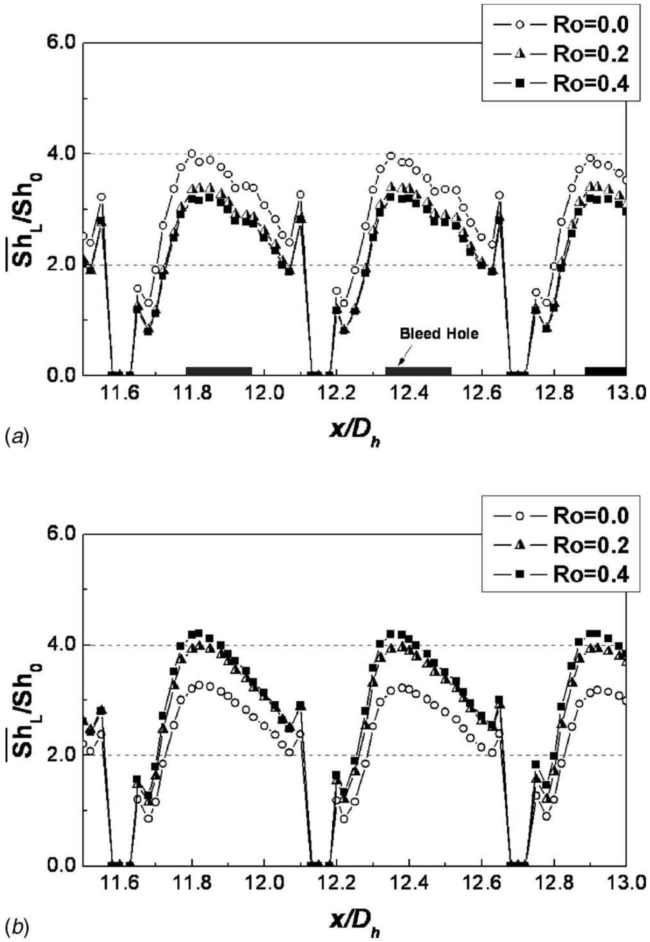

Fig. 9 Line averaged Sh ratio distributions in the Ribbed channel at BR=0.1: (*a*) leading surface; (*b*) trailing surface

ary flow returning from the trailing surface by rotation. For the trailing surface, on the overall region, the heat/mass transfer is augmented by the Coriolis force. At the higher rotation number of Ro=0.4, the heat/mass transfer on the leading surface is more reduced and that on the trailing surface becomes more augmented by the effect of the strengthened Coriolis force.

Comparison. Figure 10 presents the regional averaged Sherwood number ratios ($10.5 \leq x/D_h \leq 13.25$) for all tests. For the smooth and ribbed passages, as the rotation number increases, the heat/mass transfer on the leading surface gradually decreases except the case of the smooth passage with bleed flow but that on the trailing surface increases by degrees. With bleed blow, at all rotation numbers, the heat/mass transfer on the trailing surface decreases due to the diminution of the main flow.

For the stationary ribbed passage with bleed flow, the heat/mass transfer on the leading surface increases approximately 11% over that without bleed flow by the effect of the tripping flow. When the passage rotates, at the same rotation number, the heat/mass transfer on the leading surface is almost the same as that without bleed flow. This result suggests that at the bleed flow of BR =0.1, the tripping flow has hardly effect on the heat/mass transfer on the leading surface. That is, at that bleed flow, the primarily factors affecting the heat/mass transfer on the leading surface in the rotating ribbed passage are the Coriolis force and the effect of rib turbulators.

Figure 11 presents the Sherwood number ratios at some lateral positions ($y/D_h=0.00, 0.26$) on the leading surface in the ribbed channel. At the stationary case with bleed flow, the heat/mass transfer is augmented both at $y/D_h=0.00$ and 0.26 by the effect of the tripping flow as shown in Fig. 11(*a*). For the rotating cases with bleed flow, the effect of the tripping flow appears only behind the bleed holes as shown in Figs. 11(*b*) and 11(*c*). Therefore, we can see that at the bleed flow of BR=0.1 the heat/mass transfer on the leading surface of the rotating ribbed passage is almost the same as that without bleed flow.

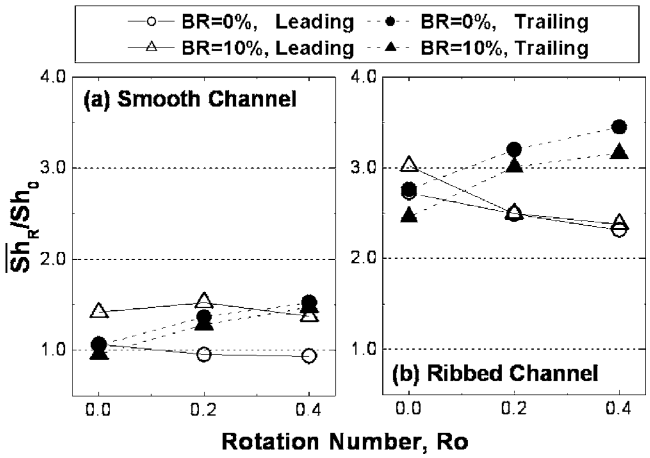

Fig. 10 Regional averaged Sherwood number ratios ($10.5 \leq x/D_h \leq 13.25$)

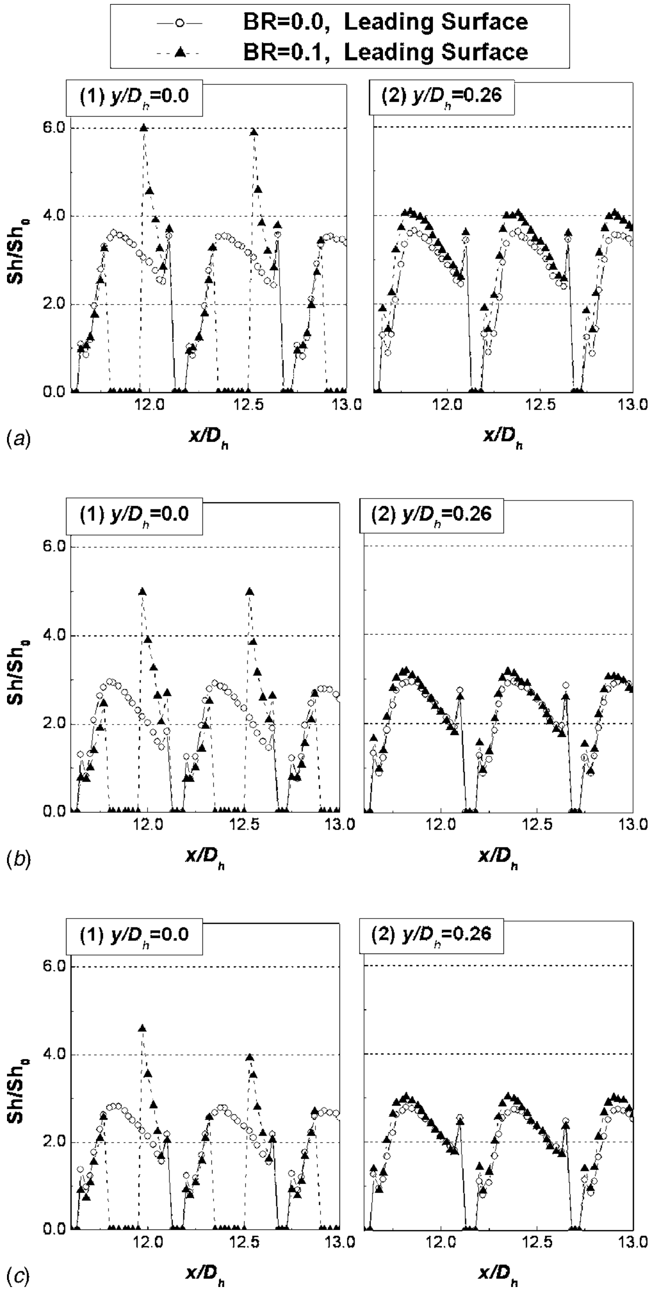

Fig. 11 Sh ratio distributions on the leading surface in the ribbed channel: (*a*) Ro=0.0; (*b*) Ro=0.2; (*c*) Ro=0.4

Friction Loss and Performance. Figure 12 presents the friction loss results in the form of the friction factor ratios. First, for all cases, friction factors remain nearly constant at all rotation numbers. This result agrees with that of Prabhu et al. [20]. Second, with bleed flow, the friction factors decrease in both the smooth and ribbed channels. The declination results from the diminution of main flow due to the bleed flow and the reduction of the area where the flow contact.

Figure 13(*a*) presents the mean Sherwood number ratios on both the leading and trailing surfaces of the smooth and ribbed channels at the tested rotation numbers. The mean values of the ribbed channel are about 2 times higher than those of the smooth channel because of the effect of rib turbulators. For the smooth channel, the mean values with bleed flow are higher than those without bleed flow due to the effect of the tripping flow on the leading surface. For the ribbed channel, at the stationary state, the mean value with bleed flow is similar to that without bleed flow. The reason is that with bleed flow, the increase in heat/mass transfer on the leading surface by the tripping flow is nearly the same as the decrease in that on the trailing surface by the diminution of main flow. When the channel rotates, the mean values with bleed flow are a little lower than those without bleed flow because the diminution of the main flow reduces the heat/mass transfer on the trailing surface.

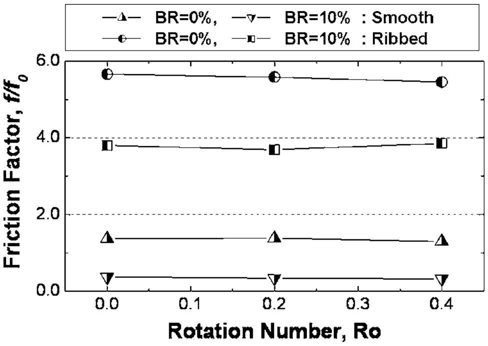

Fig. 12 Friction factor ratios at various rotation numbers

Figure 13(*b*) shows the thermal performance in the smooth and ribbed channels. The thermal performance for all tests has the same pattern as that of the mean Sherwood number ratios, and that of the smooth channel with bleed flow is the highest value under rotation.

Conclusions

In the present study, the heat/mass transfer characteristics in a rotating rib-roughened channel with bleed flow are investigated experimentally, and compared with the smooth passage. The results are summarized as follows.

Cases Without Bleed Flow

- For the rotating smooth passage, the heat/mass transfer decreases on the leading surface, but increases on the trailing surface due to the effect of the Coriolis force.
- For the rotating ribbed passage, the heat/mass transfer decreases on the leading surface, but increases on the trailing surface like the smooth channel. For the leading surface, the flow reattachment becomes weak on the middle region except the corner of the duct.

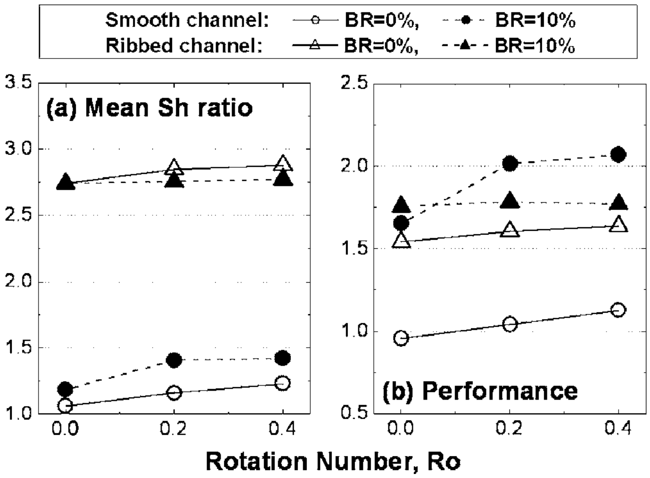

Fig. 13 Mean Sherwood number ratios and thermal performance ($10.5 \leqslant x/D_h \leqslant 13.25$)

Cases With Bleed Flow

- For the smooth passage, the heat/mass transfer on the leading surface is augmented by the effect of the tripping flow. The local peak of heat/mass transfer is formed immediately behind the bleed holes and decreases sharply along the center line after tripping flow attachment on the surface. However, the heat/mass transfer on the trailing surface decreases due to the diminution of main flow.
- For the stationary ribbed passage, the heat/mass transfer on the leading surface increases approximately 11% over that without bleed flow by the tripping flow. On the other hand, the heat/mass transfer on the trailing surface decreases due to the diminution of main flow. When the passage rotates, the heat/mass transfer is reduced on the leading surface. However, that on the trailing surface is augmented due to the Coriolis force. At the same rotation number, the heat/mass transfer on the leading surface is similar to that without bleed flow; therefore, the dominant factors affecting heat/mass transfer on the leading surface are the Coriolis force and the secondary flow (separation and reattachment) induced by rib turbulators.

Friction Loss and Performance

- For all cases, the friction factors remain nearly constant at all rotation numbers. With bleed flow, the friction factors decrease in both the smooth and ribbed channels. The thermal performance of the smooth channel with bleed flow is the highest value under rotation.

Acknowledgment

This work was supported partially by the Electric Power Industry Technology Evaluation and Planning.

Nomenclature

BR = ratio of bleed flow rate to main flow rate
D = bleed hole diameter
D_h = hydraulic diameter
D_{naph} = mass diffusion coefficient of naphthalene vapor in air ($\text{m}^2\,\text{s}^{-1}$)
e = rib height
f = friction factor, Eq. (6)
f_0 = friction factor of a fully developed turbulent flow in a stationary smooth pipe
h = heat transfer coefficient ($\text{W m}^{-2}\,\text{K}^{-1}$)
h_m = mass transfer coefficient (m s^{-1})
H = passage height
k = turbulent kinetic energy ($\text{m}^2\,\text{S}^{-2}$)
k_c = thermal conductivity of coolant ($\text{W m}^{-1}\,\text{K}^{-1}$)
$\dot{m}$ = local naphthalene mass transfer rate per unit area ($\text{kg m}^{-2}\,\text{s}^{-1}$)
Nu = Nusselt number, hD_h/k_c
p = hole to hole pitch
P_{naph} = naphthalene vapor pressure (N m^{-2})
Pr = Prandtl number, $\mu C_p/k_c$
$\dot{Q}_{\text{air}}$ = volume flow rate of air ($\text{m}^3\,\text{s}^{-1}$)
R = maximum radius of rotating arm
R_{naph} = gas constant of naphthalene ($\text{J mol}^{-1}\,\text{K}^{-1}$)
Re = Reynolds number, $D_h u_b/v$
Ro = Rotation number, $D_h\Omega/u_b$
Sc = Schmidt number, v/D_{naph}
Sh = Sherwood number, $h_m D_h/D_{\text{naph}}$
Sh_0 = Sherwood number of a fully developed turbulent flow in a stationary smooth pipe, Eq. (5)
$\overline{\text{Sh}}_L$ = line averaged Sherwood number, $\int_{-W/2}^{W/2}\text{Sh}\,dy/\int_{-W/2}^{W/2}dy$
$\overline{\text{Sh}}_R$ = regional averaged Sherwood number, $\int_{x_1}^{x_2}\int_{-W/2}^{W/2}\text{Sh}\,dydx/\int_{x_1}^{x_2}\int_{-W/2}^{W/2}dydx$
T_w = wall temperature (K)
u_b = passage averaged bulk velocity (m s^{-1})
W = passage width
x = coordinate and distance in the streamwise direction
y = coordinate and distance in the lateral direction
Z = coordinate and distance in the vertical direction
$\overline{z_{\text{sub}}}$ = average naphthalene sublimation depth
Δt = runtime
Δz = sublimation depth of the naphthalene surface
μ = dynamic viscosity ($\text{kg m}^{-1}\,\text{s}^{-1}$)
ν = kinematic viscosity ($\text{m}^2\,\text{s}^{-1}$)
η = thermal performance, Eq. (7)
ρ_s = density of solid naphthalene (kg m^{-3})
$\rho_{v,b}$ = bulk vapor density of naphthalene (kg m^{-3})
$\rho_{v,w}$ = vapor density of naphthalene on the surface (kg m^{-3})
Ω = angular velocity (rad s^{-1})

References

[1] Han, J. C., Glicksman, L. R., and Rohsenow, W. M., 1978, “An Investigation of Heat Transfer and Friction for Rib-Roughened Surfaces,” Int. J. Heat Mass Transfer, **21**, pp. 1143–1156.
[2] Kukreja, R. T., Lau, S. C., and McMillin, R. D., 1993, “Local Heat/Mass Transfer Distribution in a Square Channel With Full and V-Shaped Ribs,” Int. J. Heat Mass Transfer, **36**, pp. 2013–2020.
[3] Agliga, D. A., 1994, “Convective Heat Transfer Distributions Over Plates with Square Ribs From Infrared Thermography Measurements,” Int. J. Heat Mass Transfer, **36**(3), pp. 363–374.
[4] Acharya, S., Myrum, T., Qiu, X., and Sinha, S., 1997, “Developing and Periodically Developed Flow, Temperature and Heat Transfer in a Ribbed Duct,” Int. J. Heat Mass Transfer, **40**, pp. 461–479.
[5] Astarita, T., Cardon, G., and Carlomagno, G. M., 1998, “Average Heat Transfer Measurements Near a Sharp 180 Degree Turn Channel for Different Aspect Ratios,” *IMechE Conference Transaction: In Optical Methods and Data Processing in Heat and Fluid Flow*, London, pp. 137–146.
[6] Metzger, D. E., and Vedula, R. P., 1987, “Heat Transfer in Triangular Channels With Angled Roughness Ribs on Two Walls,” Exp. Heat Transfer, **1**(1), pp. 31–44.
[7] Yang, W.-J., Zhang, N., and Chiou, J., 1992, “Local Heat Transfer in a Rotating Serpentine Flow Passage,” ASME J. Heat Transfer, **114**, pp. 354–361.
[8] Iacovides, H., Jackson, D. C., Kelemenis, G., Launder, B. E., and Yuan, Y. M., 1999, “Experiments on Local Heat Transfer in a Rotating Square-Ended U-Bend,” Int. J. Heat Fluid Flow, **20**, pp. 302–310.
[9] Dutta, S., and Han, J. C., 1996, “Local Heat Transfer in Rotating Smooth and Ribbed Two-Pass Square Channels With Three Channel Orientations,” ASME J. Heat Transfer, **118**, pp. 578–576.
[10] Murata, A., and Mochizuki, S., 1999, “Effect of Cross-Sectional Aspect Ratio on Turbulent Heat Transfer in an Orthogonally Rotating Rectangular Smooth Duct,” Int. J. Heat Mass Transfer, **42**, pp. 3803–3814.
[11] Taslim, M. E., Li, T., and Spring, S. D., 1995, “Experimental Study of the Effects of Bleed Holes on Heat Transfer and Pressure Drop in Trapezoidal Passages With Tapered Turbulators,” ASME J. Turbomach., **117**, pp. 281–289.
[12] Shen, J. R., Wang, Z., Ireland, P. T., Jones, T. V., and Byerley, A. R., 1996, “Heat Transfer Enhancement Within a Turbine Blade Cooling Passage Using Ribs and Combinations of Ribs With Film Cooling Holes,” ASME J. Turbomach., **118**, pp. 428–434.
[13] Thurman, D., and Poinastte, P., 2001, “Experimental Heat Transfer and Bulk Air Temperature Measurements for a Multipass Internal Cooling Model With Ribs and Bleed,” ASME J. Turbomach., **123**, pp. 90–96.
[14] Ekkad, S. V., Huang, Y., and Han, J. C., 1998, “Detailed Heat Transfer Distributions in Two-Pass Square Channels With Rib Turbulators and Bleed Holes,” Int. J. Heat Mass Transfer, **41**, pp. 3781–3791.
[15] Ambrose, D., Lawrenson, I. J., and Sparke, C. H. S., 1975, “The Vapor Pressure of Naphthalene,” J. Chem. Thermodyn., **7**, pp. 1173–1176.
[16] Goldstein, R. J., and Cho, H. H., 1995, “A Review of Mass Transfer Measurements Using Naphthalene Sublimation,” Exp. Therm. Fluid Sci., **10**, pp. 416–434.
[17] Kline, S. J., and McClintock, F. A., 1953, “Describing Uncertainty in Single-Sample Experiments,” Mech. Eng. (Am. Soc. Mech. Eng.), **75**, pp. 3–8.
[18] McAdams, W. H., 1942, *Heat Transmission*, 2nd ed., McGraw-Hill, New York.
[19] Petukhov, B. S., 1970, “Heat Transfer and Friction in Turbulent Pipe Flow With Various Physical Properties,”Adv. Heat Transfer, **6**, pp. 503–504.
[20] Prabhu, S. V., Arora, N., and Vedula, R. P., 2005, “Effect of Channel Orientation and Rib Pitch-to-Height Ratio on Pressure Drop in a Rotating Square Channel With Ribs on Two Opposite Surfaces,” Int. J. Rotating Mach., **1**, pp. 67–76.